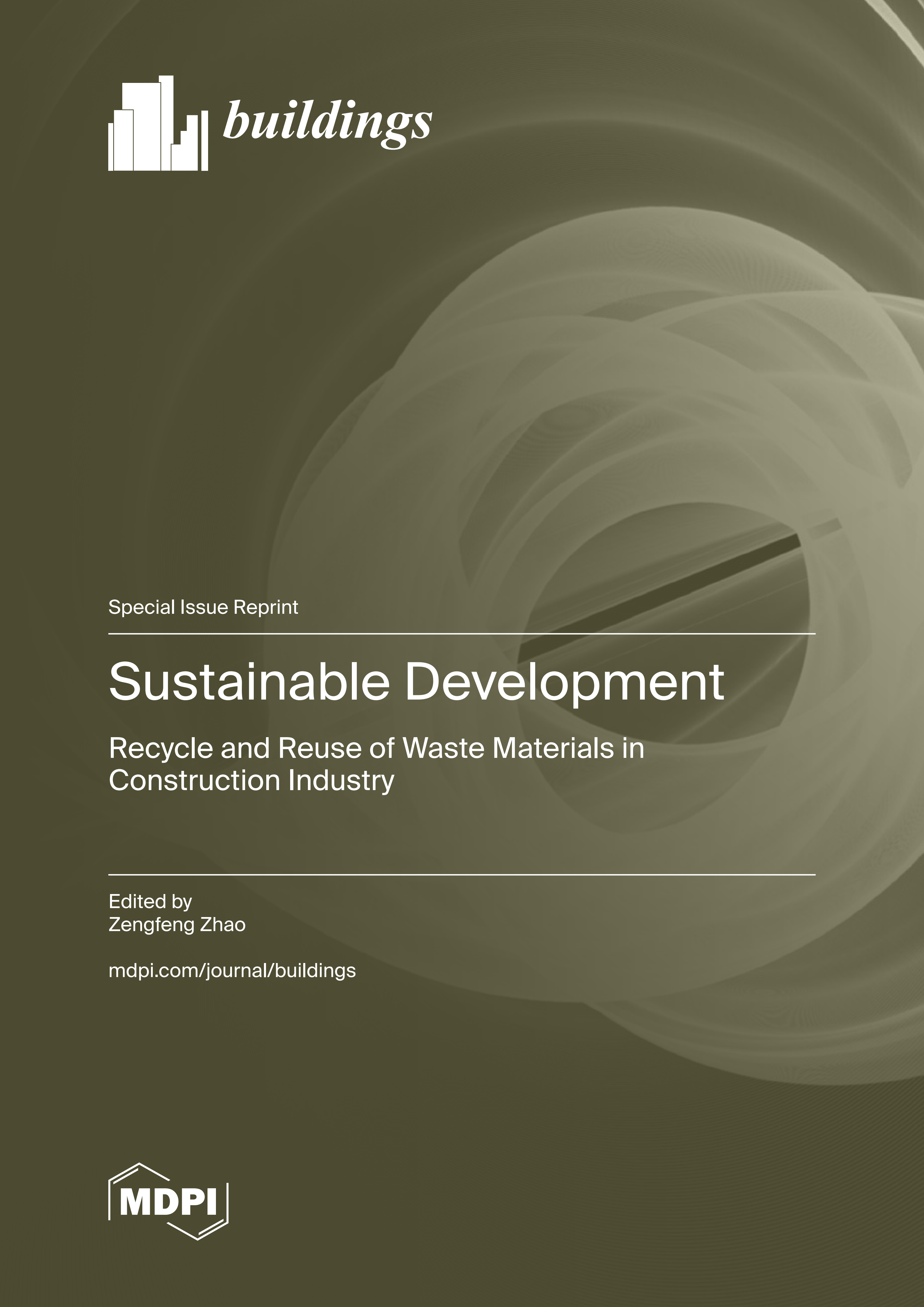

buildings

Special Issue Reprint

Sustainable Development

Recycle and Reuse of Waste Materials in Construction Industry

Edited by
Zengfeng Zhao

mdpi.com/journal/buildings

MDPI

Sustainable Development: Recycle and Reuse of Waste Materials in Construction Industry

Sustainable Development: Recycle and Reuse of Waste Materials in Construction Industry

Guest Editor

Zengfeng Zhao

MDPI

Basel • Beijing • Wuhan • Barcelona • Belgrade • Novi Sad • Cluj • Manchester

Guest Editor
Zengfeng Zhao
Department of Structural
Engineering
College of Civil Engineering
Tongji University
Shanghai
China

Editorial Office
MDPI AG
Grosspeteranlage 5
4052 Basel, Switzerland

This is a reprint of the Special Issue, published open access by the journal *Buildings* (ISSN 2075-5309), freely accessible at: https://www.mdpi.com/journal/buildings/special_issues/Recycle_Reuse.

For citation purposes, cite each article independently as indicated on the article page online and as indicated below:

Lastname, A.A.; Lastname, B.B. Article Title. *Journal Name* **Year**, *Volume Number*, Page Range.

ISBN 978-3-7258-4429-6 (Hbk)
ISBN 978-3-7258-4430-2 (PDF)
https://doi.org/10.3390/books978-3-7258-4430-2

Contents

About the Editor

Zengfeng Zhao

Zengfeng Zhao is currently a research professor at the College of Civil Engineering at Tongji University. He received his Ph.D. in civil engineering from the University of Lille l in France in 2014. He has been selected for the Marie Curie fellowship, Chief Scientist of the National Key R&D Program International Cooperation Project, the Shanghai Leader Oversea Program, and the Shanghai Pujiang Talents Program. His research interests encompass the use of recycled aggregates and by-products in concrete to reduce their environmental impact and CO2 emissions. He has participated in four European research projects dealing with the use of recycled materials in the concrete industry. He has worked as a PI on more than ten research projects in China. He has been involved with members of ACI, FIB, and RILEM, e.g., eight technical committees of RILEM, including 273-RAC, 281-CCC, 282-CCL, 303-PFC, 304-ADC, 309-MCP, 313-MMS, and CUC. He also serves as the managing editor of Low-Carbon Materials and Green Construction and guest editor of Buildings. To date, Zengfeng Zhao has published over 120 fully reviewed scientific publications, 60 of which are in international refereed journals.

Preface

With the development of the urbanization and globalization, the construction industry is facing unprecedented challenges and opportunities. This Reprint, titled ”Buildings’ Sustainable Development: Recycle and Reuse of Waste Materials in Construction Industry” is designed to explore and share the latest research findings and practical experiences in the recycling and reuse of waste materials within the construction industry.

The theme of this Special Issue focuses on the recycling and reuse of construction and demolition waste (C&DW), a global issue with a significant impact on environmental and resource sustainability. The scope of the issue is broad, including 14 papers that cover a range of topics, including recycled aggregates, recycled powder, macro and micro properties characterization of concrete based on recycled materials, and low-carbon construction methods. Research on the application of various waste materials, including glass, bricks, slag, and waste concrete, in the production of new building materials/elements is also featured.

Our aim is to provide an academic exchange platform to showcase the latest scientific research and industrial case studies in reducing the environmental impact of the construction industry. By publishing interdisciplinary articles, we hope to stimulate further research and discussion, promoting the construction industry in a more sustainable direction.

The reasons for writing these scientific works are manifold: firstly, the global construction industry has a significant impact on the environment, necessitating innovative solutions to reduce carbon emissions and resource waste; secondly, the supply of high-quality building materials is increasingly scarce, and recycling and reusing waste materials can alleviate this pressure; and lastly, by sharing and exchanging knowledge, we can accelerate the dissemination of information and promote technological advancement.

This Special Issue is aimed at professionals, researchers, engineers, policymakers, and scholars interested in sustainable construction practices. We have invited authors who have in-depth research and practical experience in this field, and their contributions have enriched the content and depth of this Special Issue.

Last but certainly not least, we would like to express our gratitude to all the authors, reviewers, and the MDPI editorial team who have participated in this Special Issue. Their efforts and contributions have made the successful publication of this Special Issue possible. We look forward to your reading and feedback, and together, we can contribute to the sustainable development of the construction industry.

Zengfeng Zhao
Guest Editor

buildings

Article

Effect of Crushing Method on the Properties of Produced Recycled Concrete Aggregates

Julien Hubert [1], Zengfeng Zhao [2,*], Frédéric Michel [1] and Luc Courard [1]

[1] Urban and Environmental Engineering, University of Liège, Allée de la Découverte 9, 4000 Liège, Belgium; julien.hubert@uliege.be (J.H.); frederic.michel@uliege.be (F.M.); luc.courard@uliege.be (L.C.)
[2] Department of Structural Engineering, College of Civil Engineering, Tongji University, Shanghai 200092, China
* Correspondence: zengfengzhao@tongji.edu.cn

Abstract: Construction and Demolition Waste (C&DW) is generated around the world and its quantity will increase in the future. Recycling has become the favored method of dealing with concrete waste but, to avoid its downcycling, it is important to develop a recycling process which is able to produce high-grade recycled concrete aggregates (RCA). To that end, studying the influence of the production process on the properties of RCA can prove to be a crucial step toward a more circular construction industry. In this study, the influence of the crushing method is investigated. Samples of five laboratory-made concretes have been crushed using the most common mechanical crushing methods (impact crusher and jaw crusher), and the particle size distribution, morphology, hardened cement paste content and water absorption of the produced RCA have been measured and analyzed. The findings indicate that the use of impact crushers results in the production of RCA possessing more spherical geometric characteristics, albeit with a broader particle size distribution and a relatively higher content of fine particles as compared to those obtained from jaw crushers. Additionally, it is observed that the employed crushing technique seemingly exerts no discernible impact on the hardened cement paste content and the water absorption in the context of the studied concretes.

Keywords: construction and demolition waste; recycling; crushing; recycled concrete aggregates; morphology; water absorption

1. Introduction

The ongoing expansion and replacement of existing real estate leads to the production of important amount of Construction and Demolition Wastes (C&DW). The construction industry is responsible for one of the heaviest and most voluminous waste streams in the EU [1]. It accounts for at least one third of the waste generated in the EU and represents an amount of about 850 Mt (Mt: Megaton). The most widely used building material is concrete with a global production increasing by as much as 25 Gt (Gt: Gigaton) per year [2,3] which means that most of the C&DW are composed of concrete. Due to environmental and economic pressure, recycling has become an increasingly popular method of disposing of C&DW that can provide a sustainable source of aggregates for future concrete production [4–6].

Recycling C&DW starts with the selective demotion of a building to separate the different waste materials [7,8] after which it is transferred to the recycling plant. C&DW recycling plants bear a resemblance to natural aggregate production facilities, as they employ a range of equipment such as crushers, screens, transfer devices and filtering systems to produce granular materials of a predetermined grain size distribution. The degree of processing of the C&DW depends on their intended future application [9]. The recycling plants can be divided into mobile or stationary styles. Considering fixed recycling plants [10,11], the recycling process starts with the reception and storage of the materials to be treated. It is followed by a scalping step where the materials are screened to separate fine particles and soil before crushing. Next, the material is crushed (primary and occasionally secondary crushing), then it goes on a conveyor band equipped with an electromagnet to remove any metallic elements (such as rebars), and through a manual or automatic extraction of impurities. Finally, it is screened for the different desired particle sizes.

The preparation phase is particularly important, specifically for large reinforced concrete elements, as it may impact crushing and purification systems. It is also used to reduce waste dimensions before crushing. The produced aggregates are mainly used in less demanding applications such as bulk fill, fill in drainage, primary foundations, embankments and levelling work [9,12–14] which leads to concrete "down cycling".

A very low percentage of recycled concrete aggregates (RCA) are used for the production of new concrete products because typical state-of-the-art recycling plants usually yield "lower-grade" RCA, presenting a lower density, higher water absorption [15–19], lower resistance to abrasion and higher sulfate content compared to the natural aggregates (NA) [20–27]. These properties of RCA, including its fine content and shape [28–31], have been shown to have a negative impact on the workability, strength and durability of recycled concrete prepared using RCA [32–37]. The lower quality of RCA is attributed to their composition which comprises a mixture of NA and adherent hardened cement paste [38–44]. Some scholars have experimentally studied the mechanical properties of recycled concrete slabs and pointed out the feasible use of recycled concrete in practical engineering applications [20,23–25], whereas the properties of RCA were good enough (this could be improved by updating the crushing procedure).

Given that the recycling of C&DW has become one of the most important topics in concrete research, and because of the correlation between mortar content and RCA properties, many research works have been conducted to identify the factors responsible for the adherent hardened cement paste content. It is mostly influenced by the properties of the parent concrete, the crushing procedure and the final particle size of the RCA produced [45–49].

Weaker parent concrete has usually been linked to RCA with better densities and thus less adherent hardened paste [50–52], which is due to the mortar in the weaker parent concrete being more easily removed during the crushing process. De Juan and Gutteriez [38] did not directly observe a relation between parent concrete strength and mortar content (they used RCA of unknown origin), but they reported a proportional relationship between mortar content and Los Angeles abrasion resistance, and between Los Angeles resistance and parent concrete compressive strength. It could then be expected that a similar relationship exists between mortar content and parent concrete strength. Grubl and Ruhl [53] have reported, however, that the compressive strength of the original concrete had little to no influence on the cement paste content and that it was only controlled by the crushing procedure. The maximum size of the NA in the parent concrete also affects the properties of RCA. Padmini et al. [51] reported that the water absorption of RCA (closely related to the adherent hardened cement paste content) decreases with increasing NA maximum size.

The effect of the RCA particle size is abundantly present in the literature. Ghorbani et al. [54] have shown that the compressive strength and tensile strength, as well as the workability of concrete made with RCA, all decreased as coarser aggregates were used. In terms of cement paste content, most have reported an increase in adherent hardened cement paste content with decreasing granular fraction. Exteberria et al. [46] have reported that the quantity of adherent mortar increases with a decreasing granular fraction. They observed a variation from 20% to 40% (in mass) in the amount of attached mortar for the granular fractions 10/25 mm and 4/10 mm, respectively. Hansen [55] reported values of attached mortar of up to 60% (in mass) for 4/8 mm coarse RCA and up to 65% for the 0/0.3 mm filler fraction. More recently, Zhao et al. [56] showed variation in hardened cement paste content from 10% to 17% for the granular fractions 14/20 mm and 0/2 mm, respectively. But some authors have also reported contradictory results with mortar content increasing as the grain sizes increased [57].

It was found that most studies on RCA either do not refer to the crushing process at all or only consider the number of crushing steps. Indeed, several authors have indicated that increasing the crushing times results in a reduction in the content of adherent hardened cement paste [38,45,58–62]. However, few results are available related to the influence of the crushing method itself in the literature. This study endeavors to fill this gap. It will clarify the impact of the crushing method on the properties of the produced RCA scientifically, which could play the role of guiding production for the recycling plant. The goal of this research is thus to evaluate the effect of the crushing method on the properties of RCA. Samples of five laboratory-made concretes have been crushed using the most common mechanical crushing methods (impact crusher and jaw crusher). The particle size distribution, morphology, hardened cement paste content and water absorption of the produced RCA have been measured and analyzed.

2. Experimental Program

2.1. Materials Used for the Production of Concrete

In this study, five different compositions of laboratory-made concrete have been crushed using a jaw crusher and an impact crusher at the semi-industrial level. Many studies have demonstrated the correlation between the compressive strength of the original concrete and the quantity of the adherent cement paste [38,50,51]. A different aspect of the parent concrete has thus been chosen for study: its composition. All five compositions are in the same compressive strength range; this study chooses to modify the cement quantity, the type of cement, the nature of the aggregates and the water-to-cement (W/C) ratio selected to investigate the influence of these key parameters on the crushability of concrete and on the properties of the RCA produced. A total of 120 L of each concrete mix was cast and prepared for the production of RCA. In accordance with EN 206 [63], cubes (150 × 150 × 150 mm) were produced and stored in a room with a temperature of 20 ± 2 °C and relative humidity of 90 ± 5% for 90 days before being crushed. The reference concrete was designed using limestone aggregates (2/7, 7/14, and 14/20 mm) and calcareous sand (0/4 mm). The CEM III 52.5 cement based on slag was used for the production of concrete "C2-CEM III" (since slag-blended cement is very often used in the production of cement on the market and the same grade of 52.5 has to be used in this study; thus, CEM III 52.5 was chosen for investigation in this study). CEM I 52.5 produced in the CBR company wasused for the other four types of concrete. The relative proportion between each mix was established according to the standard EN 480-1 [64]. This approach led to the following design for the reference concrete: 35%, 20%, 20% and 25% by mass for the sand 0/4 mm, NA 2/7 mm, 7/14 mm and 14/20 mm, respectively. The quantities of each constituent (expressed in kg/m^3) are given in Table 1. The other concretes only differ from the reference concrete by one parameter. Note that since the sandstone aggregates used present a very close grain size distribution to the limestone aggregates used, the same relative proportions of each constituent have been used. Mixtures with a low cement quantity and low W/C ratio required a superplasticizer to reach the desired slump class (S3/S4). The experimental grain size distribution curve is fitted as much as possible on a theoretical curve linking the mean values defined in the standard EN 480-1 [64]. Concerning the mixing procedure used in the production of concrete, the air-dried coarse aggregates and natural sand were firstly introduced in the mix, and then half of the total water was added and mixed for 1 min. The water compensation was adjusted according to the water content and water absorption of natural sand and coarse aggregates during concrete batching. The other half of the total water was added after the introduction of the cement. In the case of using the superplasticizer, additional mixing of 1 min was carried out to reach the desired slump.

Table 1. Compositions of concrete made in the laboratory.

Name of Concrete	C1-Reference	C2-CEM III	C3-Sandstone	C4-Low Cement	C5-Low W/C
Type of aggregate	Limestone	Limestone	Sandstone	Limestone	Limestone
NA 2/7 mm (kg/m^3)	368.8	368.8	368.8	405.1	367.1
NA 7/14 mm (kg/m^3)	345	345	345	379	343.4
NA 14/20 mm (kg/m^3)	433.5	433.5	433.5	476.2	431.5
Sand 0/4 mm (kg/m^3)	604.9	604.9	604.9	664.4	602.1
Type of cement	CEM I 52.5	CEM III 52.5	CEM I 52.5	CEM I 52.5	CEM I 52.5
Cement quantity (kg/m^3)	400	400	400	320	452
Cement paste volume (dm^3/m^3)	351	358	351	282	351
Efficient water (kg)	224.2	224.2	224.2	180.6	207.1
W/C ratio	0.56	0.56	0.56	0.56	0.46
Superplasticizer (g/kg cement)	0	0	0	6.8	3.3

2.2. Concrete Characteristics

Concretes have been characterized in fresh and hardened states: fresh concrete slump (NBN EN 12350–2 [65]), density (NBN EN 12350-6 [66]) and compressive strengths (NBN EN 12390-3 [67]) were measured. Table 2 shows the properties of the produced concrete.

Table 2. Properties of the produced concrete.

Properties	C1-Reference	C2-CEM III	C3-Sandstone	C4-Low Cement	C5-Low W/C
Slump (mm)	155	176	182	135	146
Slump class	S4	S4	S4	S3	S3
Density (g/cm^3)	2.35	2.31	2.31	2.36	2.31
Compressive strength (MPa) (mean and standard deviation)	56.0 (±2.4)	61.6 (±0.7)	52.7 (±2.5)	56.0 (±6.4)	66.9 (±0.7)

2.3. RCA Production

The crushing mechanism directly impacts the properties of RCA such as grain size distribution, fine content and shape, as well as the adherent hardened cement paste content. Mechanical crushing can be performed with different types of crushers according to a survey conducted in the SeRaMCo project [11]; the most used equipment for C&DW recycling are the impact, jaw and cone crushers. This choice is mainly influenced by acquisition and maintenance costs and does not consider the properties of the end product [68].

Crushing was performed using semi-industrial crushers owned by the CTP (Centre Terre et Pierre asbl) in Tournai (Belgium). Approximately 240 kg of each mix was crushed using the two primary crushers: the impact crusher and the jaw crusher.

A jaw crusher consists of two plates fixed at an angle. One plate remains stationary while the other oscillates back and forth, crushing the material in between. The particle size reduction depends on the maximum and minimum size of the gap between the plates. In an impact crusher, materials fall onto the rotor and are caught by blow bars, which throw them against the impact plates (smashing them into smaller particles).

The crusher's parameters were defined to produce aggregates with a diameter between 0 and 25 mm. For this reason, the jaw spacing was fixed at 22 mm for the jaw crusher. The produced aggregates were sieved at 4/6.3/8/12.5/20/25 mm.

2.4. Characterization of RCA

The particle size distribution was obtained following the European standard method EN 933-1 [69].

The flakiness index was measured on the RCA produced according to the European standard method EN 933-3 [70]. The shape index was also measured on the RCA according to the standard EN 933-4 [71].

There is no standard method to measure the attached mortar content in RCA. In the literature, the following methods are presented:

- The first method consists of a thermal treatment [38]. It is based on several cycles where the aggregates are soaked in water then heated to 300 °C progressively to detach adherent mortar from the surface of NA. This is due to the micro-cracking presented at the interface between aggregates and mortar because of their different thermal dilation coefficients. This method is only suitable for coarse RCA, since mortal removal needs "brushing" of the RCA which is difficult with fine RCA.
- The second method [61,72] involves the dissolution of cement paste in a hydrochloric acid solution. Regrettably, it cannot be utilized when working with limestone aggregates and fillers, as they are susceptible to be dissolved when exposed to hydrochloric acid.
- The third method uses image analysis [61,73] to quantify the amount of residual mortar on a flat polished section, which is efficient with coarse RCA, but the distinction between fine aggregates and cement paste is difficult. Moreover, a statistical approach is needed and it is time-consuming to obtain the reliable results.
- The last method had been developed by Zhao [44] and is based on the dissolution of cement paste in a solution of salicylic acid. This method has been shown not to dissolve calcareous aggregates.

This latter method has been chosen to measure the adherent hardened cement paste content (HCPC) because it is easy to perform and can be applied to RCA obtained by crushing concrete containing natural limestone aggregates. The sample is dried at 105 °C and then ground until it is smaller than 0.2 mm. A small quantity of this dried sample is then immersed into a solution of salicylic acid and methanol and stirred for an hour. The solid fraction is filtered using a glass filter and washed (at least four times) using methanol. The solid residue is then dried at 70 °C for 30 min and weighed. The hardened cement paste content is obtained through:

$$HCPC = \frac{(M_a - M_b)}{M_a} \times 100 \quad (1)$$

where M_a and M_b are the mass of the dried material before dissolution and the mass of the dried filtrate, respectively.

The water absorption of each granular class of RCA has been determined according to the European standard method EN 1097-6 [74], while the details have been also presented in Zhao et al. [44].

3. Results and Discussion

3.1. Particle Size Distribution

Figure 1 shows the variation in the particle size distribution of the RCA produced with the jaw crusher and the impact crusher. It can be seen that the impact crusher curves stop before reaching 100%. The goal of the crushing process was to produce aggregates with a grain size distribution between 4 mm and 25 mm, and this highlights the fact that the impact crusher produces around 30% of aggregates outside the desired range. It also produces more fine particles than the jaw crusher because it crushes mortar and aggregate particles alike; in contrast, a jaw crusher only breaks a small proportion of the original aggregate, thus generating almost half the amount of fine particles for the same maximum size of particle [10,75,76]. These points are in clear favor of the jaw crusher, which is more efficient in terms of material use and produces fewer fine particles which have a high water absorption. Based on these results, we can conclude that the composition (for the formulations considered) has little to no impact on the particle size distribution of RCA.

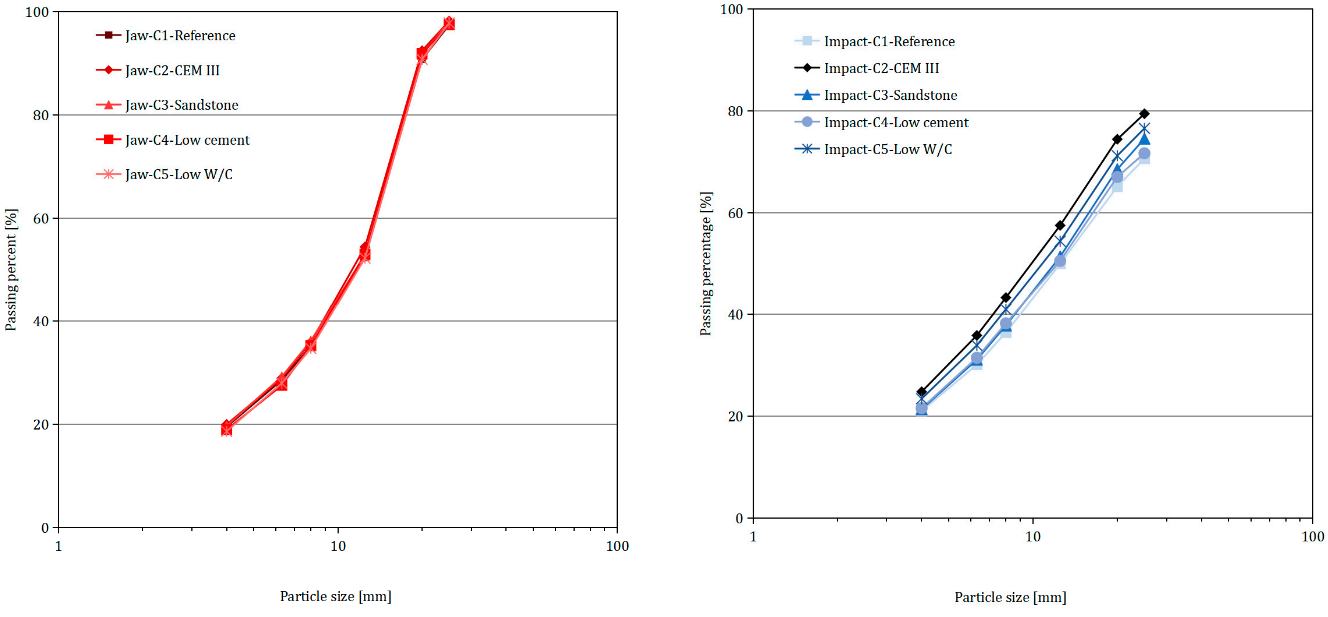

(**a**) (**b**)

Figure 1. Particle size distribution for all the considered concrete mix processed with a jaw crusher (**a**) and an impact crusher (**b**).

3.2. Morphology

Figure 2 shows the flakiness index increasing with decreasing granular fraction for both crusher types. A smaller value of the flakiness index denotes less elongated (“more cubic”) aggregates. The jaw crusher also produces flakier aggregates than the impact crusher. This can be explained by the breakage mechanism involved [11,22]. Composition does not seem to have any significant impact on the flakiness index, since the curves for the different compositions cross each other. It is worth noting that the jaw crusher curves all present a minimum value of the flakiness index for the 16/20 mm granular fraction, which can be explained by the fact that the maximum grain size of the NA used to produce the parent concrete is 20 mm. This means that recycled aggregates of nearly 20 mm in diameter are mostly composed of unbroken NA surrounded by a little cement paste. A similar observation was made by Florea [59], who found a maximum value of RCA densities around 8 mm which corresponds to the D_{max} of the gravel used for the initial concrete. This led them to the same interpretation that RCA with a granular fraction above the D_{max} of the parent concrete most likely contains a larger amount of cement paste than those around the D_{max}. This trend cannot be observed for the impact crusher because of the breakage mechanism. Indeed, impact crushers, contrary to jaw crushers, crush mortar and aggregates alike [76].

The global flakiness index varies from 11% to 14% for the jaw crusher and from 6% to 8% for the impact crusher (Table 3), which is calculated by the percentage of granular fraction and each flakiness index. These values are lower than the maximum value defined in the national standards related to aggregates used for concrete production in a series of North West European countries (maximum overall flakiness index: Belgium, 20%; France and Luxembourg, 35%; Germany, 50%, i.e., varying from 20% to 50% depending on the country).

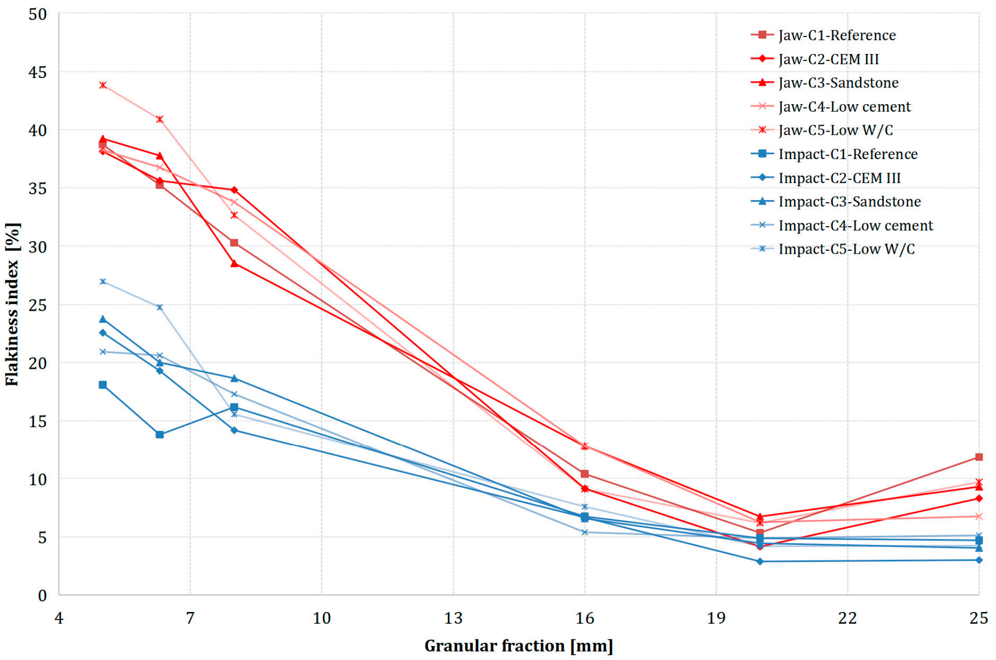

Figure 2. Flakiness index of RCA crushed by jaw and impact crushers.

Table 3. Global flakiness index for the concrete mix crushed by impact and jaw crushers (as a percentage).

	C1-Reference	C2-CEM III	C3-Sandstone	C4-Low Cement	C5-Low W/C
Jaw crusher	14	11	13	11	12
Impact crusher	8	6	6	7	7

The same trend was observed as for the shape index (Figure 3). The shape index increases with decreasing granular fraction (as for the flakiness index, a smaller value of the shape index denotes a more "spherical" aggregate). Once again, the jaw crusher produces more elongated aggregates and the concrete mix does not seem to have any influence for the range investigated. The measured global shape index varies from 34% to 46% for the jaw crusher and from 11% to 18% for the impact crusher.

3.3. Hardened Cement Paste Content

Figure 4 presents the hardened cement paste content (HCPC) for the different granular fractions for the RCA obtained from the reference composition. This shows that a larger granular fraction of RCA presents a lower hardened cement paste content; the HCPC values of RCA obtained in this study are similar to the results given in previous research works [44,56]. This is well correlated with the results obtained on flakiness and shape indexes' variation. Similar trends have also been described by many authors [22,46,55,56].

Based on Figure 4, the HCPC values of RCA obtained by the jaw crusher and impact crusher are similar for each granular fraction (except for the granular fraction 16/20 mm). It can be concluded that the crushing method (whether the jaw crusher or impact crusher) has no clear influence on the hardened cement paste content.

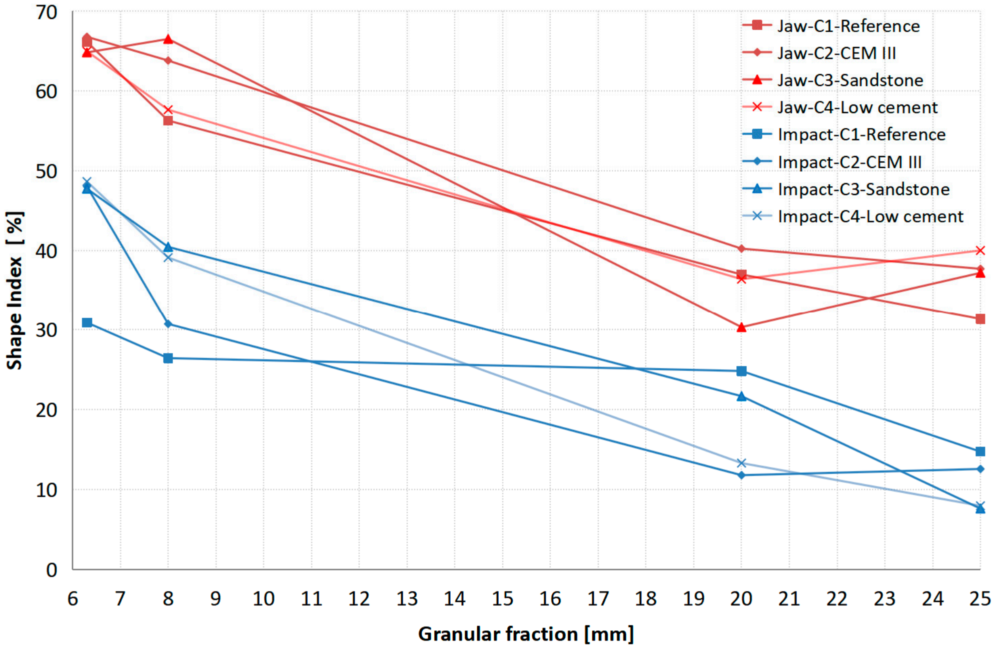

Figure 3. Shape index of RCA crushed by jaw and impact crushers.

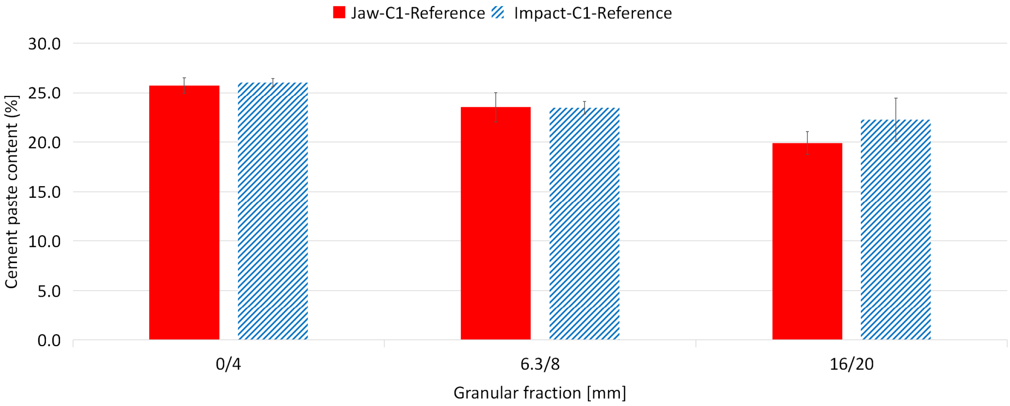

Figure 4. Hardened cement paste content for the RCA obtained from the reference concrete mix.

3.4. Water Absorption

Figure 5 shows the variation in water absorption of the RCA produced by the jaw crusher for all of the considered compositions. These results are concordant with the trend observed for the cement paste content. The larger the granular fraction, the lower the water absorption, which is logical given the lower cement paste content. The water absorption of the fraction 0/4 mm presents the highest values (ranging between 8.6% and 12.5% for all five studied compositions), which is consistent with the water absorption of RCA presented in other studies [17,30,38,44]. In addition, the difference in the water absorption values obtained in the fractions 6.3/8, 12.5/20 and 20/25 mm is less than that of the fraction 0/4 mm, which is also confirmed in the previous work [56]. Another trend visible in Figure 5 is the slight increase in water absorption for the granular fraction 20/25 mm when compared to the granular fraction 12.5/20 mm, which validates our previous hypothesis that RCA of a granular size close to the D_{max} of the parent concrete is mostly composed of NA.

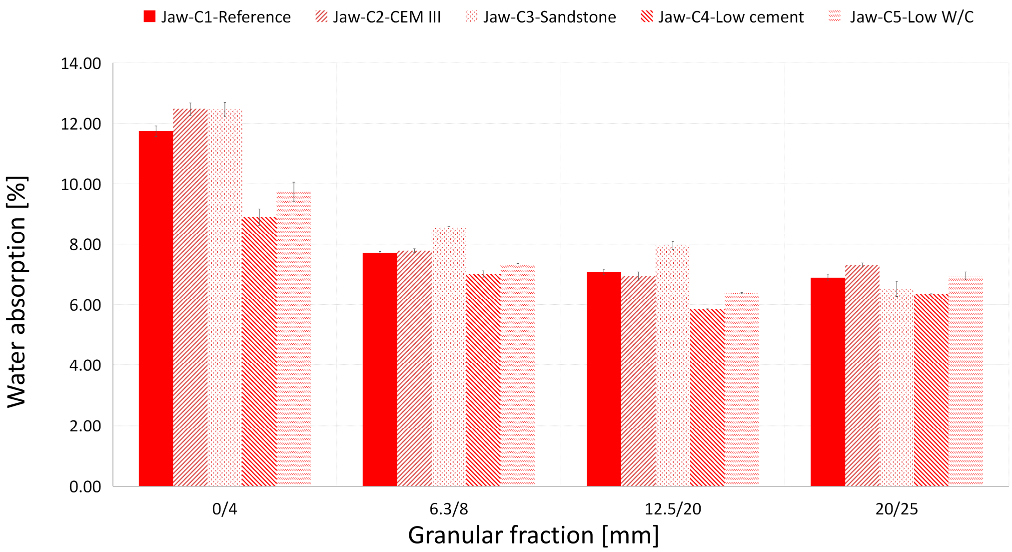

Figure 5. Water absorption for the RCA produced with the jaw crusher.

It is worth noting that, the results obtained for the series of the reference, CEM III and sandstone are very similar. Conversely, the water absorption obtained with all of the granular fractions of RCA produced from the concrete "C4-Low cement" are significantly lower than other RCAs, which can be linked to a low cement content used in the parent concrete, which results in a lower porosity of the hardened cement paste. The lower values obtained for the RCA produced from concrete "C5-Low W/C" can be attributed to the lower W/C ratio of the cement paste in the parent concrete. Both compositions (low cement composition and low W/C composition) produce a lower porosity of the cement paste presented in the parent concrete, leading to the lower absorption of the RCA [27,38,44]. The same trends are observed in Figure 6 for the results obtained by the impact crusher.

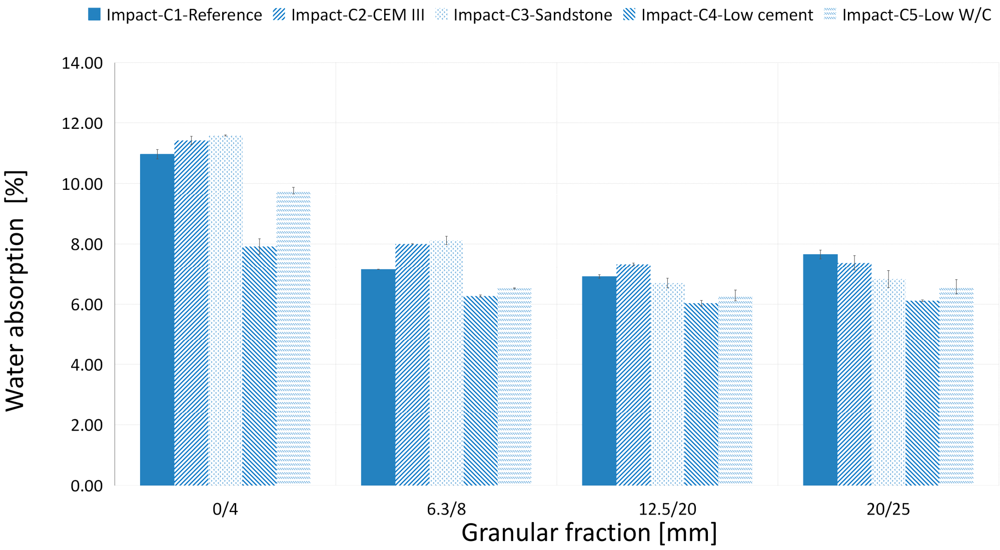

Figure 6. Water absorption for RCA produced with the impact crusher.

Figure 7 shows the water absorption of the RCA obtained from the reference composition. As can be seen in this figure, there is no clear influence of the crushing methods on the water absorption, as was the case with the hardened cement paste content. Based on these results, we can conclude that the composition (for the formulations considered) has little to no impact on the water absorption or cement paste content of RCA.

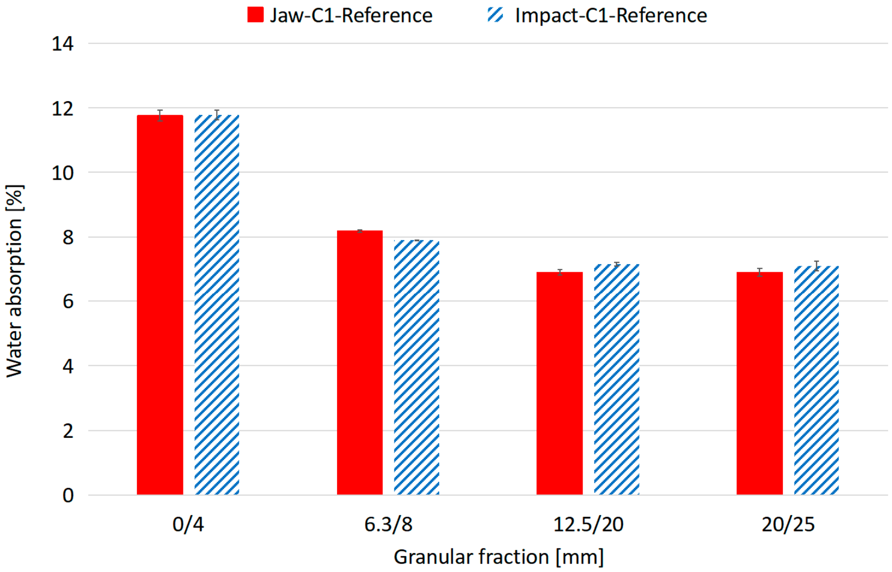

Figure 7. Water absorption for the RCA obtained from the reference concrete by different crushers.

Based on the above discussion, the findings indicate that the use of impact crushers results in the production of RCA possessing more spherical geometric characteristics, albeit with a broader particle size distribution and a relatively higher content of fine particles as compared to those obtained from jaw crushers. Additionally, it is observed that the employed crushing technique seemingly exerts no discernible impact on the hardened cement paste content or the water absorption in the context of the studied concretes.

4. Conclusions

In this study, the impact of the crushing method was investigated. The RCAs obtained by the mechanical crushing of five laboratory-made concretes were characterized. The effect of the parent concrete mix on the properties of the RCA was also investigated. The main conclusions can be drawn as follows:

(a) The impact crusher results in the production of aggregates possessing more spherical geometric characteristics, a broader spectrum of grain sizes and a relatively higher content of fine particles as compared to those obtained from the jaw crusher. In addition, the crushing method exerts no discernible impact on the hardened cement paste content and the water absorption in the context of the studied concretes. The W/C ratio in the range from 0.46 to 0.56, as well as the type of NA in the parent concrete, do not seem to have any influence on the properties of the produced RCA.

(b) The flakiness and shape indexes decrease with the increase in the granular fraction. The larger granular fractions have a lower residual hardened cement paste content and water absorption than the smaller fractions, which indicates that larger fractions of RCA are mostly composed of NA with a bit of adherent mortar.

(c) In the case of using a jaw crusher to produce RCA, the water absorption and morphology indicators of RCA show their minimum values when the granular fraction is close to the maximum diameter of the NA in the parent concrete. This correlation indicates that the breakage mechanism of the jaw crusher does not affect the RCA in a similar manner to the impact crusher.

This study presents the impact of the crushing method on the properties of produced RCA scientifically, which could play the role of guiding production for the recycling plant. Further investigations using more sophisticated morphology measurement techniques (such as laser optical measurements) could potentially discriminate the crushing operating system more appropriately. A wider range of variation in the concrete mix could also affect the the produced RCA, which needs to be investigated in the future. In addition, the properties of concrete based on the RCA produced by different crushers are worth future study.

Author Contributions: J.H.: conceptualization, methodology, writing—original draft preparation, data curation; Z.Z.: writing—review and editing, formal analysis, funding acquisition, validation; F.M.: investigation, visualization, formal analysis; L.C.: writing—review and editing, validation, funding acquisition. All authors have read and agreed to the published version of the manuscript.

Funding: This research was supported by the INTERREG North West Europe program through the project SeRaMCo (Secondary Raw Materials for Concrete Precast Products); and the Fundamental Research Funds for the Central Universities, funding number: 22120230250 (Tongji University). This work was also sponsored by the Shanghai Pujiang Program (funding number: 22PJ1422700).

Data Availability Statement: Not applicable.

Acknowledgments: The authors would like to thank the INTERREG North West Europe program for financial support through the project SeRaMCo. The authors would also like to thank the Centre Terre et Pierre for performing crushing operations. The authors would also like to thank Ziying Pu from Tongji University for her help in the format changing.

Conflicts of Interest: The authors declare no conflict of interest.

References

1. Delvoie, S.; Zhao, Z.; Michel, F.; Courard, L. Market analysis of recycled sands and aggregates in North West Europe: Drivers and barriers. In Proceedings of the IOP Conference Series: Earth and Environmental Science, Banda Aceh, Indonesia, 19–20 June 2019; p. 012055.
2. Gursel, A.P.; Masanet, E.; Horvath, A.; Stadel, A. Life-cycle inventory analysis of concrete production: A critical review. *Cem. Concr. Compos.* **2014**, *51*, 38–48. [CrossRef]
3. Georgiades, M.; Shah, I.H.; Steubing, B.; Cheeseman, C.; Myers, R. Prospective life cycle assessment of European cement production. *Resour. Conserv. Recycl.* **2023**, *194*, 106998. [CrossRef]
4. Ravindrarajah, R.S.; Loo, Y.H.; Tam, C.T. Recycled concrete as fine and coarse aggregates in concrete. *Mag. Concr. Res.* **1987**, *39*, 214–220. [CrossRef]
5. Ong, K.; Ravindrarajah, S.R. Mechanical Properties and Fracture Energy of Recycled-Aggregate Concretes. 1987. Available online: http://scholarbank.nus.edu.sg/handle/10635/74242 (accessed on 30 August 2023).
6. Zhang, T.; Chen, M.; Wang, Y.T.; Zhang, M.Z. Roles of carbonated recycled fines and aggregates in hydration, microstructure and mechanical properties of concrete: A critical review. *Cem. Concr. Compos.* **2023**, *138*, 104994. [CrossRef]
7. Coelho, A.; de Brito, J. Economic analysis of conventional versus selective demolition—A case study. *Resour. Conserv. Recycl.* **2011**, *55*, 382–392. [CrossRef]
8. Pereira, P.M.; Vieira, C.S. A literature review on the use of recycled construction and demolition materials in unbound pavement applications. *Sustainability* **2022**, *14*, 13918. [CrossRef]
9. Hansen, E. *Recycling of Demolished Concrete and Masonry*; CRC Press: Boca Raton, FL, USA, 1992.
10. Silva, R.V.; de Brito, J.; Dhir, R.K. Availability and processing of recycled aggregates within the construction and demolition supply chain: A review. *J. Clean. Prod.* **2017**, *143*, 598–614. [CrossRef]
11. Delvoie, S.; Zhao, Z.; Michel, F.; Courard, L. *WPT1-Technical REPORT of the Best-Practice in Producing Recycled Aggregates and Sands*; Université de Liège: Liège, France, 2018.
12. Everaert, M.; Stein, R.; Michaux, S.; Goovaerts, V.; Groffils, C.; Delvoie, S.; Zhao, Z.F.; Snellings, R.; Nielsen, P.; Broos, K. Microwave radiation as a pre-treatment for standard and innovative fragmentation techniques in concrete recycling. *Materials* **2019**, *12*, 488. [CrossRef] [PubMed]
13. Huang, W.L.; Lin, D.H.; Chang, N.B.; Lin, K.S. Recycling of construction and demolition waste via a mechanical sorting process. *Resour. Conserv. Recycl.* **2002**, *37*, 23–37. [CrossRef]
14. Omer, M.M.; Rahman, R.A.; Almutairi, S. Strategies for enhancing construction waste recycling: A usability analysis. *Sustainability* **2022**, *14*, 5907. [CrossRef]
15. Marinkovic, S.; Radonjanin, V.; Malesev, M.; Ignjatovic, I. Comparative environmental assessment of natural and recycled aggregate concrete. *Waste Manag.* **2010**, *30*, 2255–2264. [CrossRef] [PubMed]
16. Nedeljkovic, M.; Visser, J.; Savija, B.; Valcke, S.; Schlangen, E. Use of fine recycled concrete aggregates in concrete: A critical review. *J. Build. Eng.* **2021**, *38*, 102196. [CrossRef]
17. Tam, V.W.Y.; Soomro, M.; Evangelista, A.C.J. Quality improvement of recycled concrete aggregate by removal of residual mortar: A comprehensive review of approaches adopted. *Constr. Build. Mater.* **2021**, *288*, 123066. [CrossRef]
18. Ruiz, L.A.L.; Ramon, X.R.; Mercedes, C.M.L.; Domingo, S.G. Multicriteria analysis of the environmental and economic performance of circularity strategies for concrete waste recycling in Spain. *Waste Manag.* **2022**, *144*, 387–400. [CrossRef]

19. Shi, C.; Li, Y.; Zhang, J.; Li, W.; Chong, L.; Xie, Z. Performance enhancement of recycled concrete aggregate—A review. *J. Clean. Prod.* **2016**, *112*, 466–472. [CrossRef]
20. Setkit, M.; Leelatanon, S.; Imjai, T.; Garcia, R.; Limkatanyu, S. Prediction of Shear Strength of Reinforced Recycled Aggregate Concrete Beams without Stirrups. *Buildings* **2021**, *11*, 402. [CrossRef]
21. Leelatanon, S.; Imjai, T.; Setkit, M.; Garcia, R.; Kim, B. Punching Shear Capacity of Recycled Aggregate Concrete Slabs. *Buildings* **2022**, *12*, 1584. [CrossRef]
22. Krampitz, T.; Lieberwirth, H.; Hartl, S.; Nüsse, A. Zerkleinerung von Porenbeton in konventionellen Zerkleinerungsmaschinen der Bauschuttaufbereitung. *Chem. Ing. Tech.* **2022**, *95*, 1–12. [CrossRef]
23. Revilla-Cuesta, V.; Fiol, F.; Perumal, P.; Ortega-López, V.; Manso, J.M. Using recycled aggregate concrete at a precast-concrete plant: A multi-criteria company-oriented feasibility study. *J. Clean. Prod.* **2022**, *373*, 133873. [CrossRef]
24. Imjai, T.; Kefyalew, F.; Aosai, P.; Garcia, R.; Kim, B.; Abdalla, H.M.; Raman, S.N. A new equation to predict the shear strength of recycled aggregate concrete Z push-off specimens. *Cem. Concr. Res.* **2023**, *169*, 107181. [CrossRef]
25. Imjai, T.; Garcia, R.; Kim, B.; Hansapinyo, C.; Sukontasukkul, P. Serviceability behaviour of FRP-reinforced slatted slabs made of high-content recycled aggregate concrete. *Structures* **2023**, *51*, 1071–1082. [CrossRef]
26. Xiao, J.Z.; Pham, T.L.; Wang, P.J.; Gao, G. Behaviors of semi-precast beam made of recycled aggregate concrete. *Struct. Des. Tall Spec. Build.* **2014**, *23*, 692–712. [CrossRef]
27. Yang, X.; Liu, Y.; Liang, J.; Meng, Y.; Rong, H.; Li, D.; Chen, Y.; Lv, J.; Jiang, Y.; Liu, Y. Straightening methods for RCA and RAC—A review. *Cem. Concr. Compos.* **2023**, *141*, 105145. [CrossRef]
28. Hansen, T.C.; Boegh, E. Elasticity and drying shrinkage concrete of recycled aggregate. *J. Am. Concr. Inst.* **1985**, *82*, 648–652.
29. He, H.; Stroeven, P.; Stroeven, M.; Sluys, L.J. Influence of particle packing on elastic properties of concrete. *Mag. Concr. Res.* **2012**, *64*, 163–175. [CrossRef]
30. Khatib, J.M. Properties of concrete incorporating fine recycled aggregate. *Cem. Concr. Res.* **2005**, *35*, 763–769. [CrossRef]
31. Assaad, J.J.; Mardani, A. Limestone replacements by fine crushed concrete and ceramic wastes during the production of Portland cement. *J. Sustain. Cem. Based Mater.* **2023**. [CrossRef]
32. Lippiatt, N.R.; Bourgeois, F.S. Recycling-oriented investigation of local porosity changes in microwave heated-concrete. *Kona Powder Part. J.* **2014**, *31*, 247–264. [CrossRef]
33. Guo, Y.C.; Zhang, J.H.; Chen, G.M.; Xie, Z.H. Compressive behaviour of concrete structures incorporating recycled concrete aggregates, rubber crumb and reinforced with steel fibre, subjected to elevated temperatures. *J. Clean. Prod.* **2014**, *72*, 193–203. [CrossRef]
34. Zhang, H.H.; Xiao, J.Z.; Tang, Y.X.; Duan, Z.H.; Poon, C.S. Long-term shrinkage and mechanical properties of fully recycled aggregate concrete: Testing and modelling. *Cem. Concr. Compos.* **2022**, *130*, 104527. [CrossRef]
35. Rashwan, M.S.; Abou Rizk, S. The properties of recycled concrete. *Concr. Int.* **1997**, *19*, 56–60.
36. Silva, R.V.; de Brito, J.; Dhir, R.K. Establishing a relationship between modulus of elasticity and compressive strength of recycled aggregate concrete. *J. Clean. Prod.* **2016**, *112*, 2171–2186. [CrossRef]
37. Zhao, Z.F.; Courard, L.; Groslambert, S.; Jehin, T.; Leonard, A.; Xiao, J.Z. Use of recycled concrete aggregates from precast block for the production of new building blocks: An industrial scale study. *Resour. Conserv. Recycl.* **2020**, *157*, 104786. [CrossRef]
38. de Juan, M.S.; Gutierrez, P.A. Study on the influence of attached mortar content on the properties of recycled concrete aggregate. *Constr. Build. Mater.* **2009**, *23*, 872–877. [CrossRef]
39. Dhir, R.; Paine, K.; Dyer, T. Recycling construction and demolition wastes in concrete. *Concrete* **2004**, *38*, 25–28.
40. Mazhoud, B.; Sedran, T.; Cazacliu, B.; Cothenet, A.; Torrenti, J.M. Influence of residual mortar volume on the properties of recycled concrete aggregates. *J. Build. Eng.* **2022**, *57*, 104945. [CrossRef]
41. dos Santos, J.R.; Branco, F.; De Brito, J. Mechanical properties of concrete with coarse recycled aggregates. *Struct. Eng. Int.* **2004**, *14*, 213–215. [CrossRef]
42. Tam, V.W.; Tam, C.M. *Re-Use of Construction and Demolition Waste in Housing Developments*; Nova Science Publishers: New York, NY, USA, 2008.
43. Bai, G.L.; Zhu, C.; Liu, C.; Liu, B. An evaluation of the recycled aggregate characteristics and the recycled aggregate concrete mechanical properties. *Constr. Build. Mater.* **2020**, *240*, 117978. [CrossRef]
44. Zhao, Z.; Remond, S.; Damidot, D.; Xu, W. Influence of hardened cement paste content on the water absorption of fine recycled concrete aggregates. *J. Sustain. Cem.-Based Mater.* **2013**, *2*, 186–203. [CrossRef]
45. Akbarnezhad, A.; Ong, K.C.G.; Tam, C.T.; Zhang, M.H. Effects of the parent concrete properties and crushing procedure on the properties of coarse recycled concrete aggregates. *J. Mater. Civ. Eng.* **2013**, *25*, 1795–1802. [CrossRef]
46. Etxeberria, M.; Vazquez, E.; Mari, A.; Barra, M. Influence of amount of recycled coarse aggregates and production process on properties of recycled aggregate concrete. *Cem. Concr. Res.* **2007**, *37*, 735–742. [CrossRef]
47. Sun, D.S.; Shen, S.S.; Huang, W.; Liu, K.W.; Wang, A.G.; Chen, J. A review of quality of recycled aggregate and its effect on durability of recycled aggregate concrete. *Mater. Express* **2022**, *12*, 1415–1426. [CrossRef]
48. Touzé, S.; Bru, K.; Ménard, Y.; Weh, A.; Von der Weid, F. Electrical fragmentation applied to the recycling of concrete waste—Effect on aggregate liberation. *Int. J. Miner. Process.* **2017**, *158*, 68–75. [CrossRef]
49. Ulsen, C.; Tseng, E.; Angulo, S.C.; Landmann, M.; Contessotto, R.; Balbo, J.T.; Kahn, H. Concrete aggregates properties crushed by jaw and impact secondary crushing. *J. Mater. Res. Technol. JMRT* **2019**, *8*, 494–502. [CrossRef]

50. Haase, R.; Dahms, J. Material cycles on the example of concrete in the northern parts of Germany. *Beton* **1998**, *48*, 350–355.
51. Padmini, A.K.; Ramamurthy, K.; Mathews, M.S. Influence of parent concrete on the properties of recycled aggregate concrete. *Constr. Build. Mater.* **2009**, *23*, 829–836. [CrossRef]
52. Pani, L.; Francesconi, L.; Rombi, J.; Stochino, F.; Mistretta, F. The role of parent concrete in recycled aggregate concrete. In Proceedings of the 20th International Conference on Computational Science and Its Applications (ICCSA), Cagliari, Italy, 1–4 July 2020; pp. 368–378.
53. Grubl, P.; Ruhl, M. German committee for reinforced concrete (DafStb)–Code: Concrete with recycled aggregates. In Proceedings of the International Symposium Organised by the Concrete Technology Unit, University of Dundee, London, UK, 11–12 November 1998.
54. Ghorbani, S.; Sharifi, S.; Ghorbani, S.; Tam, V.W.Y.; de Brito, J.; Kurda, R. Effect of crushed concrete waste's maximum size as partial replacement of natural coarse aggregate on the mechanical and durability properties of concrete. *Resour. Conserv. Recycl.* **2019**, *149*, 664–673. [CrossRef]
55. Hansen, T.C. Recycled aggregates and recycled aggregate concrete second state-of-the-art report developments 1945–1985. *Mater. Struct.* **1986**, *19*, 201–246. [CrossRef]
56. Zhao, Z.; Courard, L.; Michel, F.; Remond, S.; Damidot, D. Influence of granular fraction and origin of recycled concrete aggregates on their properties. *Eur. J. Environ. Civ. Eng.* **2018**, *22*, 1457–1467. [CrossRef]
57. Yagishita, F. Behavior of reinforced concrete beams containing recycled coarse aggregate. *Demolition Reuse Concr. Masn.* **1994**, *43*, 331–342.
58. Fleischer, W.; Ruby, M. *Recycled Aggregates from Old Concrete Highway Pavements*; Thomas Telford Publishing: London, UK, 1999.
59. Florea, M.V.A.; Brouwers, H.J.H. Properties of various size fractions of crushed concrete related to process conditions and re-use. *Cem. Concr. Res.* **2013**, *53*, 278. [CrossRef]
60. Nagataki, S. Recycling of demolished concrete. *Spec. Publ.* **2001**, *200*, 1–20.
61. Nagataki, S.; Gokce, A.; Saeki, T.; Hisada, M. Assessment of recycling process induced damage sensitivity of recycled concrete aggregates. *Cem. Concr. Res.* **2004**, *34*, 965–971. [CrossRef]
62. Ibrahim, M.; Alimi, W.; Assaggaf, R.; Salami, B.A.; Oladapo, E.A. An overview of factors influencing the properties of concrete incorporating construction and demolition wastes. *Constr. Build. Mater.* **2023**, *367*. [CrossRef]
63. NBN EN 206. Concrete—Specification, Performance, Production and Conformity. CEN: Brussels, Belgium, 2014.
64. NBN EN 480-1. Admixtures for Concrete, Mortar and Grout—Test Methods—Part 1: Reference Concrete and Reference Mortar for Testing. CEN: Brussels, Belgium, 2014.
65. NBN EN 12350-2. Testing Fresh Concrete—Part 2: Slump Test. CEN: Brussels, Belgium, 2019.
66. NBN EN 12350-6. Testing Fresh Concrete—Part 6: Density. CEN: Brussels, Belgium, 2019.
67. NBN EN 12390-3. Testing Hardened Concrete—Part 3: Compressive Strength of Test Specimens. CEN: Brussels, Belgium, 2019.
68. Wilson, J. Recycling of construction and demolition waste: The Dutch experience. *Quarry Manag.* **1996**, *23*, 03059421.
69. NBN EN 933-1. Tests for Geometrical Properties of Aggregates—Part 1: Determination of Particle Size Distribution—Sieving Method. CEN: Brussels, Belgium, 2012.
70. NBN EN 933-3. Tests for Geometrical Properties of Aggregates—Part 3: Determination of Particle Shape—Flakiness Index. CEN: Brussels, Belgium, 2012.
71. NBN EN 933-4. Tests for Geometrical Properties of Aggregates—Part 4: Determination of Particle Shape—Shape Index. CEN: Brussels, Belgium, 2008.
72. Tam, V.W.Y.; Tam, C.M.; Le, K.N. Removal of cement mortar remains from recycled aggregate using pre-soaking approaches. *Resour. Conserv. Recycl.* **2007**, *50*, 82–101. [CrossRef]
73. Abbas, A.; Fathifazl, G.; Fournier, B.; Isgor, O.B.; Zavadil, R.; Razaqpur, A.G.; Foo, S. Quantification of the residual mortar content in recycled concrete aggregates by image analysis. *Mater. Charact.* **2009**, *60*, 716–728. [CrossRef]
74. NBN EN 1097-6. Tests for mechanical and physical properties of aggregates-Part 6: Determination of particle density and water absorption. CEN: Brussels, Belgium, 2000.
75. Cazacliu, B.; Le Guen, L.; Hamard, E.; Roux, S.; Braymand, S. Chapter 2: Elaboration des granulats de béton recyclé. *Ouvrages Sci.* **2018**, 31–55.
76. O'Mahony, M. Recycling of Materials in Civil Engineering. Ph.D. Thesis, Oxford University, Oxford, UK, 1990.

buildings

Article

Fresh and Hardened Properties of Cementitious Composites Incorporating Firebrick Powder from Construction and Demolition Waste

Ozer Sevim [1,*], **Erdinc H. Alakara** [2] and **Selahattin Guzelkucuk** [3]

[1] Department of Civil Engineering, Kırıkkale University, Kırıkkale 71451, Türkiye
[2] Department of Civil Engineering, Tokat Gaziosmanpasa University, Tokat 60150, Türkiye
[3] Department of Civil Engineering, Kırsehir Ahi Evran University, Kırsehir 40360, Türkiye
* Correspondence: ozersevim@kku.edu.tr; Tel.: +90-318-357-4242

Abstract: Firebricks are generally used in furnace basins where glass, ceramics, and cement are produced. Firebricks have an important place in construction and demolition waste (CDW). However, there is a limited understanding of the effects on fresh and hardened state properties of cementitious composites. This study investigates the mechanical, physical, and microstructural properties of cementitious composites incorporating firebrick powder (FBP) from CDW. In this regard, the FBP was used at 5, 10, 15, 20, and 25% replacement ratio by weight of cement to produce cementitious composites. The consistency, setting characteristics, and 3, 7, and 28 days compressive and flexural strength tests of produced cementitious composites were performed. In addition, ultrasonic pulse velocity, water absorption, porosity, unit weight, and microstructure analysis of cementitious composites were conducted. As a result, the 28-day compressive strength of the cementitious composite mortars containing up to 10% firebrick powder remained above 42.5 MPa. The flow diameters increased significantly with the increase of the FBP. Therefore, it has been determined that the FBP can be used up to 10% in cementitious composites that require load-bearing properties. However, FBP might be used up to 25% in some cases. Using waste FBP instead of cement would reduce the amount of cement used and lower the cost of producing cementitious composites.

Keywords: firebrick powder; construction and demolition waste; cementitious composites; setting characteristics; compressive strength

1. Introduction

Today, the construction sector is one area that benefits greatly from the developments in industry and technology. Concrete is the most preferred building material in construction [1]. Concrete, produced in more than 10 billion tons in the world every year, has many advantages in terms of workability, strength, and durability compared to other building materials [2]. One of the most important components determining the properties of concrete is cement. Cement is also the material with the highest cost in concrete production [3]. Cement production is a process that has huge environmental impacts in terms of raw material consumption, energy consumption, and high CO_2 emissions. Approximately one ton of CO_2 is released into the atmosphere during each ton of ordinary Portland cement (OPC) production [2]. Global cement production, responsible for around 8% of worldwide CO_2 emissions, has increased more than 30 times since 1950 [4]. The high CO_2 emissions of cement production have motivated researchers to conduct various research for a sustainable environment [5–8]. At the beginning of these studies is using construction and demolition wastes (CDW) together with cement. The most important aim of CDW is to reduce cement costs and CO_2 emissions.

Technological developments in the construction industry have facilitated the demolition of structures. Large amounts of CDW occur during the demolition and rehabilitation phases in the construction industry [9]. CDW accounts for 30–40% of total municipal solid waste, corresponding to 10 billion tons of CDW each year worldwide [10]. Concrete and ceramic wastes constitute more than 50% of the total CDW worldwide [11]. These wastes cause adverse effects such as energy consumption, greenhouse gas emissions, water pollution, raw material consumption, and land occupation [12]. Brick wastes occupy an important place in CDWs. There are many studies on the use of different types of brick waste [13–16]. One of these wastes is firebrick (FB).

FBs, which have completed their service life and are demolished yearly to be replaced with new ones, have an important place in CDWs. FB is generally used in furnace basins where glass, ceramics, and cement are produced [17]. Therefore, recycling these wastes is of great importance for a sustainable environment. One of the best ways to deal with FB wastes is to use these wastes as aggregate or cement-based complementary material in concrete production. Nematzadeh et al. [18] investigated the compressive behavior of concrete containing fine recycled FB aggregate together with calcium aluminate cement (CAC) and polyvinyl alcohol (PVA) fibers under an acidic environment. In general, the results showed that the samples containing CAC together with PVA fibers showed suitable mechanical properties in terms of corrosion control against acid attack, while the samples containing fine FB aggregate performed quite poorly in this regard. Khattab et al. [19] investigated the high-temperature addition of FB aggregates, substituting 20% as coarse aggregate into concrete mixes. It has been determined that FB aggregate substituted concretes improve compressive strength at high temperatures. Kavas et al. [20] investigated using FB aggregate as a fine aggregate in mortar mixes. The high-temperature performance of the mortars prepared with FB aggregate containing magnesium chromite showed better performance when compared to the HCl absorption percentages control mortars. El-Didamony et al. [21] studied the pozzolanic activity of FBs containing calcium oxide. It has been determined that FB powder (FBP) used by substituting up to 20% by mass of ordinary Portland cement (OPC) has pozzolanic activity. Substitution of 5–10% FBP to OPC provided higher compressive strength than control mixes up to 90 days of cure time.

Firebricks have an important place in construction and demolition waste (CDW). However, there is a limited understanding of the effects on fresh and hardened state properties of cementitious composites. The literature studies on FB showed limited studies on using the powder form of firebrick obtained by grinding this waste as a supplementary cementitious material (SCM) [21–23]. In the studies, FB was generally used as an aggregate. In addition, in the studies conducted, no studies were found on the effect of FBP on the physical and mechanical properties such as setting time, workability, porosity, water absorption, unit weight, ultrasonic pulse velocity, flexural and compressive strength, and microstructure analyzes on cementitious composites.

2. Experimental Program

2.1. Materials

CEM I 42.5 R (OPC), ground waste FBP, standard sand, and tap water were used in cementitious composite production. The physical and chemical properties of the cement and FBP are given in Table 1. Table 1 shows that the ratios of SiO_2 and Al_2O_3, which are important for pozzolanic reactions, are 51.43% and 37.46%, respectively.

Firebrick powder used in cementitious composite mortar mixtures was obtained by grinding waste firebricks from CDW. For this, the material, which was first turned into small pieces in the jaw crusher, was further reduced with the help of the mill. Finally, it was pulverized using a ball mill. Figure 1 shows the production of firebrick powder.

Table 1. Physical and chemical properties of cement and FBP.

Chemical Composition (%)	Cement	FBP
SiO_2	21.34	51.43
Al_2O_3	4.58	37.46
Fe_2O_3	3.85	2.14
CaO	62.26	0.71
MgO	1.73	0.60
Na_2O	0.38	0.32
K_2O	0.40	0.35
SO_3	3.69	0.29
TiO_2	-	4.81
Other elements	1.77	1.89
Physical Properties	**Cement**	**FBP**
Specific gravity	3.14	2.38
Specific surface area (cm^2/g)	3410	2610
Loss on ignition (%)	1.83	6.87

Figure 1. Production stages of firebrick powder.

2.2. Methods

2.2.1. Sample Preparation

Cementitious composite mortars were produced per EN 196-1 [24] by substituting FBP at 0% (Control), 5, 10, 15, 20, and 25% by weight of cement. The water : binder ratio of the cementitious composite mortars remains constant at 0.50 in all mixture groups. A summary of the mixing proportions for different mixtures is given in Table 2.

Table 2. Mixing plan of cementitious composite mortars incorporating FBP.

Mix Coding	FBP (%)	FBP (g)	Cement (g)	Water (g)	Sand (g)
Control	0	0.0	450.0	225	1350
FBP5	5	22.5	427.5	225	1350
FBP10	10	45.0	405.0	225	1350
FBP15	15	67.5	382.5	225	1350
FBP20	20	90.0	360.0	225	1350
FBP25	25	112.5	337.5	225	1350

2.2.2. Setting Time Test

Setting characteristics for cementitious composites incorporating FBP are determined according to EN 196-3 [25] standard. The initial and final setting times of six different cement composites were determined.

2.2.3. Consistency

This test aims to determine the workability of cementitious composite mortars incorporating FBP. The mortar mixtures, prepared according to the EN 196-1 [24] standard, were filled into the truncated cone mold on the flow table in two layers and were tamped twenty-five times in each layer. After the filling, the truncated conical mold was slowly lifted. Then flow table was stroked 25 times in 15 s per EN 12350-5 [26] by turning the shaking device. Finally, the flow diameters in both directions of the mortar were measured, and the average of these two results was accepted as the final flow diameter.

2.2.4. Unit Weight, Water Absorption, and Porosity Tests

Unit weight, water absorption, and porosity of all mixture groups were determined according to EN 480-5 [27]. The samples were kept in water curing for 28 days and removed from the curing pool. After the surfaces of the samples were dried with a cloth, the saturated surface dry weights were measured (W_1). Then, to determine the weight of the samples in the air, they were dried in an oven at 110 °C for 24 h. After the samples taken out of the oven were cooled to room temperature, their weight in the air was measured (W_0). W_2 represents the weight of the sample in water. Then, unit weight, water absorption, and porosity results were calculated with the help of the formulas given in Equations (1)–(3). All measurements were carried out using three samples for each mixture group, and the obtained results were averaged to get the final result.

$$\text{Unit weight} = \frac{W_0}{V},\ (\text{g/cm}^3) \tag{1}$$

$$\text{Water absorption} = \frac{W_1 - W_0}{W_0} \times 100,\ (\%) \tag{2}$$

$$\text{Porosity} = \frac{W_1 - W_0}{W_1 - W_2} \times 100,\ (\%) \tag{3}$$

2.2.5. Determination of Flexural and Compressive Strengths and Ultrasonic Pulse Velocity

The flexural and compressive strengths of the cementitious composite mortars incorporating FBP were determined per EN 196-1 [24]. The flexural strength results of 40 × 40 × 160 mm prismatic cementitious composite mortars were measured after water curing for 3, 7, and 28 days. Compressive strength results were measured using 40 × 40 mm samples obtained after the flexural strength test. Flexural and compressive strength tests were carried out at loading rates per EN 196-1 [24]. Ultrasonic pulse velocity of the cementitious composite mortars incorporating FBP was determined per EN 12504-4 [28]. An ultrasonic pulse velocity test of the cementitious composites was performed using the Proceq Pundit Lab+.

2.2.6. Microstructure Analysis

The microstructural analyses of 7- and 28-day Control, FBP5, and FBP10 samples were performed with scanning electron microscopy (SEM). Microstructure analyses of the cementitious composites were conducted using a Zeiss EVO 40XP SEM device. SEM analyses were performed on small samples obtained after compressive strength. Small samples were coated with gold to obtain clear images in SEM analyses.

3. Results and Discussion

3.1. Setting Characteristics of Cementitious Composites

The test results of the initial and final setting times of cement composites incorporating FBP performed in complying with EN 196-3 [25] are shown in Figure 2.

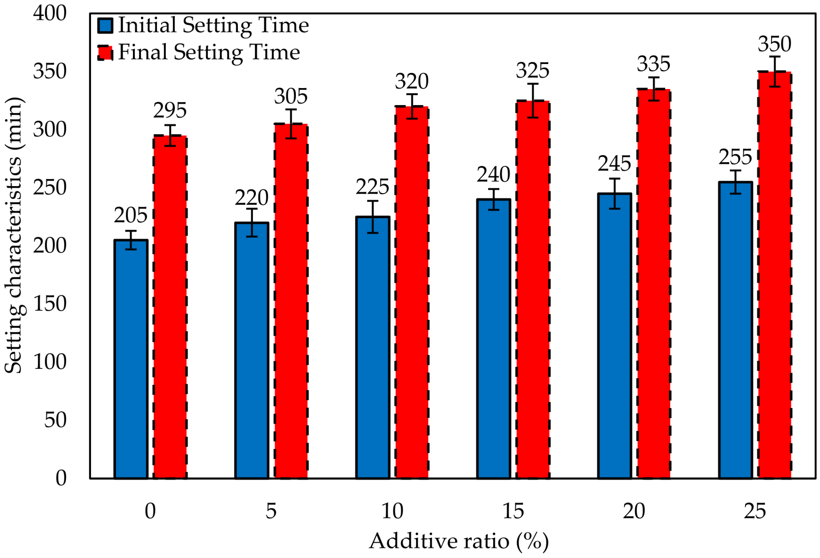

Figure 2. Setting characteristics of cement composites.

As shown in Figure 2, it was observed that the initial and final setting times were prolonged with the increase in the FBP ratio. The main reason for this situation is the delayed beginning of hydration and the prolongation of setting times of pozzolans. Initial setting times of 5%, 10%, 15%, 20%, and 25% FBP substituted cement composites increased by 7.32, 9.76, 17.07, 19.51, and 24.39%, respectively, while the final setting times of 5, 10, 15, 20, and 25% FBP substituted cement composites increased by 3.39, 8.47, 10.17, 13.56, and 18.64%, respectively, compared to cement composites without FBP. Since the specific surface area of FBP is lower than that of cement and the particle size is larger, the initial and final times were prolonged as the FBP replacement ratio increased. This situation was similar to the studies conducted in [29,30] on the effect of SCM on the setting time of cement pastes.

3.2. Consistency of Results

The flow diameters of cementitious composite mortars incorporating FBP are shown in Figure 3. The results of the FBP-substituted cementitious composites show that the flow diameters increase with the replacement ratio. This situation is thought to be due to the specific surface area of FBP, as stated in [21]. The fact that the specific surface area of FBP is lower than cement reduces the water requirement for mortar mixtures. Since the amount of water was kept constant in all mixture groups, the flow diameters increased with the FBP replacement ratio. Flow diameters of FBP5, FBP10, FBP15, FBP20, and FBP25 samples increased by 7.69, 15.38, 19.23, 26.92, and 30.77%, respectively, compared to control mortars. FBP is a pozzolanic material and provides secondary hydration. As the pozzolanic reactions take place over long periods and are delayed, an excess of water is present during mixing and placement. This situation increases workability, as stated in [31,32].

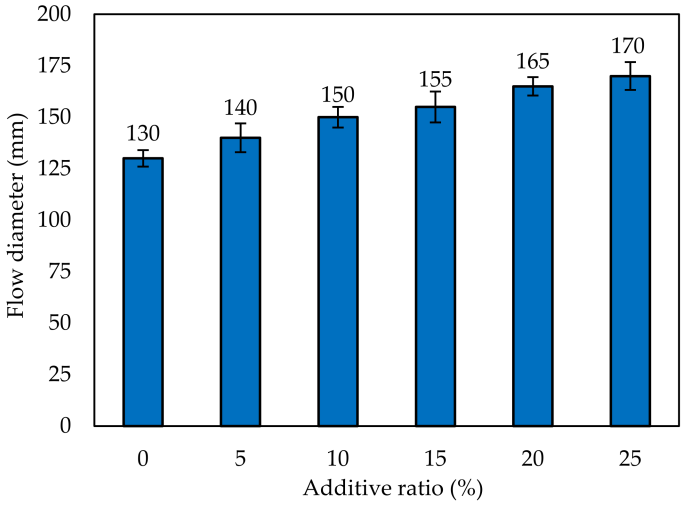

Figure 3. Flow diameters of cementitious composites.

3.3. Unit Weight, Water Absorption, and Porosity Test Results

The porosity test results of the cementitious composite mortars incorporating FBP are shown in Figure 4. It was observed that the porosity results of the FBP-substituted cementitious composites increased with the increase in the FBP replacement ratio. The porosity test results of FBP5, FBP10, FBP15, FBP20, and FBP25 samples increased by 1.76, 4.57, 6.45, 8.63, and 11.15%, respectively, compared to control mortars.

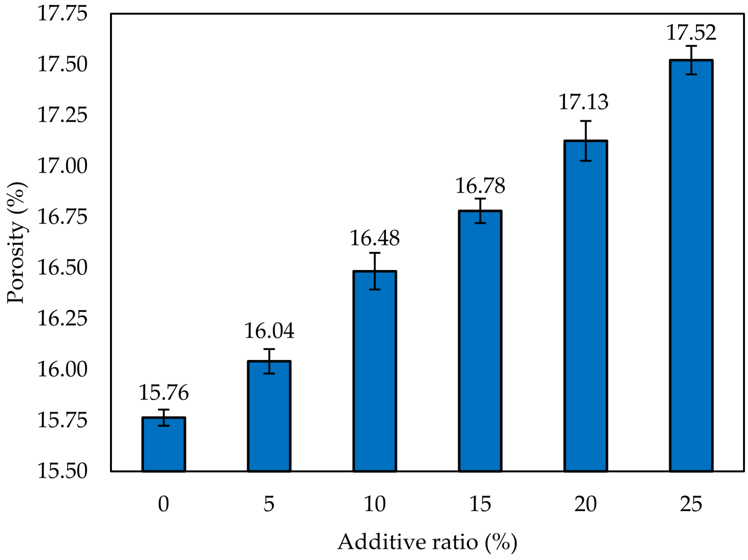

Figure 4. Porosity test results of the cementitious composites.

The water absorption test results of the cementitious composite mortars incorporating FBP are given in Figure 5. It was observed that an increase was observed in the porosity results. It was observed that 25% FBP substituted cementitious composite mortars had the maximum water absorption results. It was also observed that there was an increase of 3.83, 6.47, 7.64, 11.31, and 14.51%, respectively, for 5, 10, 15, 20, and 25% FBP additive ratios, compared to the control sample.

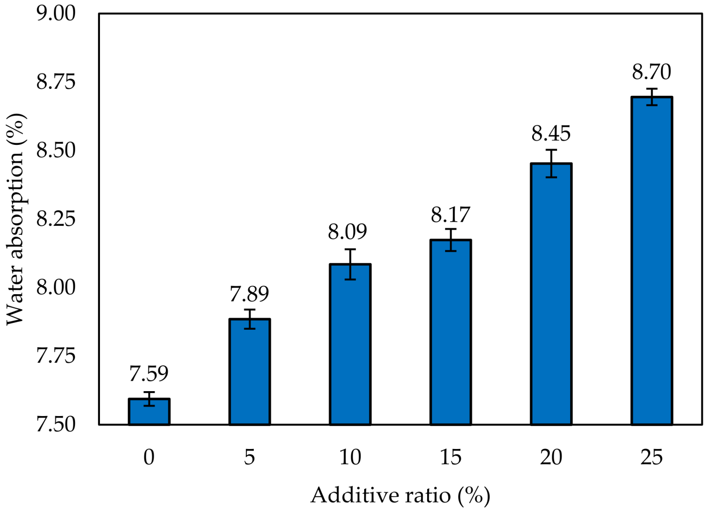

Figure 5. The water absorption test results of cementitious composites.

Figure 6 shows the relationship between porosity and water absorption. The result showed a strong relationship between these two physical properties of the cementitious composite samples incorporating FBP.

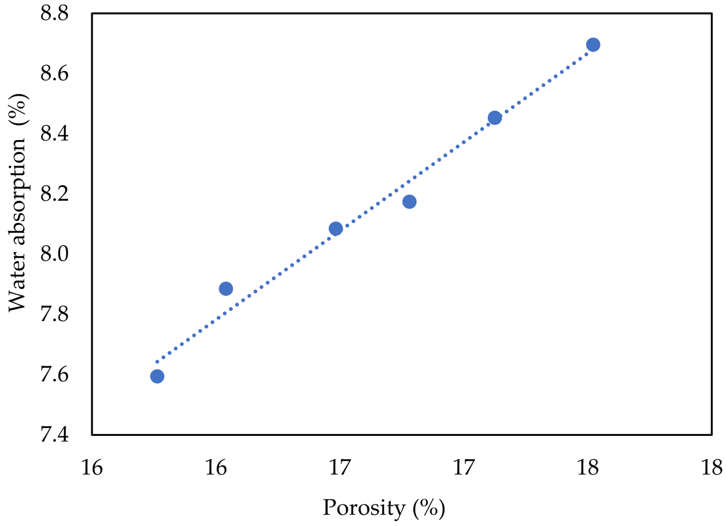

Figure 6. Relationship between porosity and water absorption.

The unit weight test results of the cementitious composite mortars incorporating FBP are shown in Figure 7. Since the unit weight is inversely proportional to the porosity and water absorption data, it is seen that the unit weight test results of the FBP substituted cementitious composite mortars, having high porosity and water absorption, are low. The highest unit weight result was obtained from the control sample without FBP. The unit weight test results of FBP5, FBP10, FBP15, FBP20, and FBP25 samples decreased by 0.86, 1.29, 1.86, 2.95, and 4.09%, respectively, compared to control mortars. With the increase in the FBP replacement ratio, the unit weights of cementitious composites decrease. This situation can be attributed to the fact that FBP has lower specific gravity than cement. Reducing the unit weight reduces dead loads in the structures, which is a beneficial effect, as mentioned in [33].

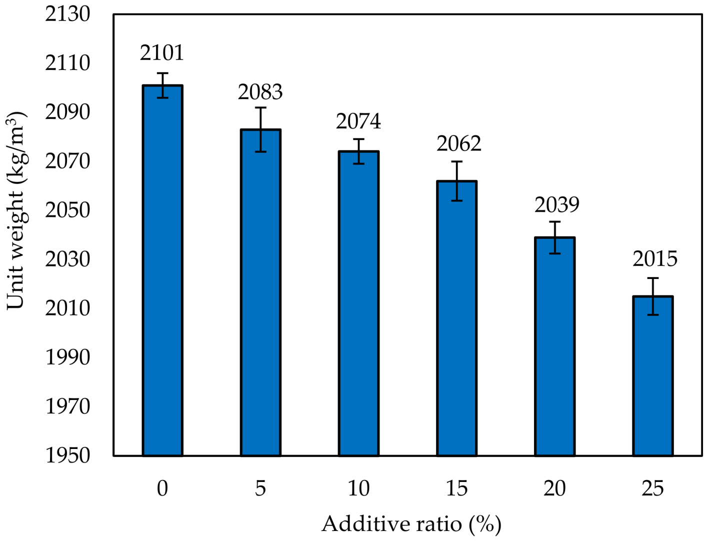

Figure 7. The unit weight test results of the cementitious composites.

The results of porosity, water absorption, and unit weight are evaluated. The increase in porosity and water absorption values and decrease in unit weights with the rise of the FBP replacement ratio was attributed to the dilution of the OPC by FBP, which is present in higher amounts in the cementitious composite [21]. With increasing FBP content, C-S-H and C-A-S-H amounts decrease, hydration development slows down, and the porosity of cementitious composites increases.

3.4. Ultrasonic Pulse Velocity Results

The ultrasonic pulse velocity test results performed on cementitious composite mortar samples incorporating FBP that have completed their 28-day curing period are shown in Figure 8. With the increase of FBP replacement ratios, decreases in ultrasonic pulse velocity test results were observed.

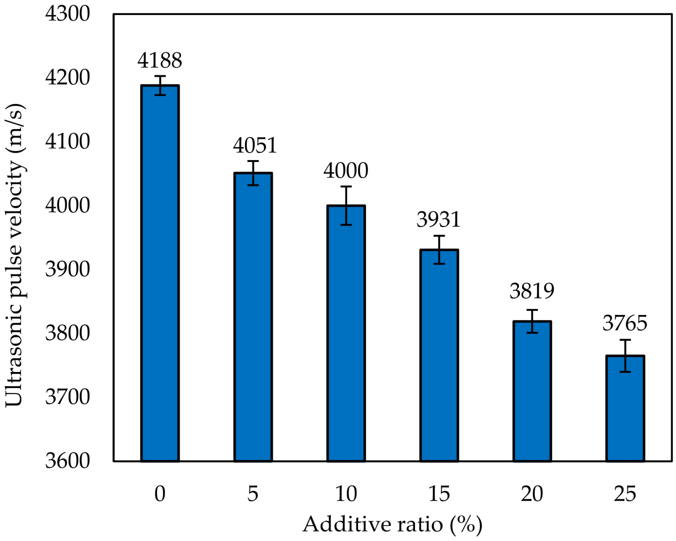

Figure 8. The ultrasonic pulse velocity test results of cementitious composites.

The relationship between the ultrasonic pulse velocity and the porosity, water absorption, and unit weight results are shown in Figure 9. Results showed a strong relationship between the physical properties of the cementitious composites incorporating FBP and the ultrasonic pulse velocity test results.

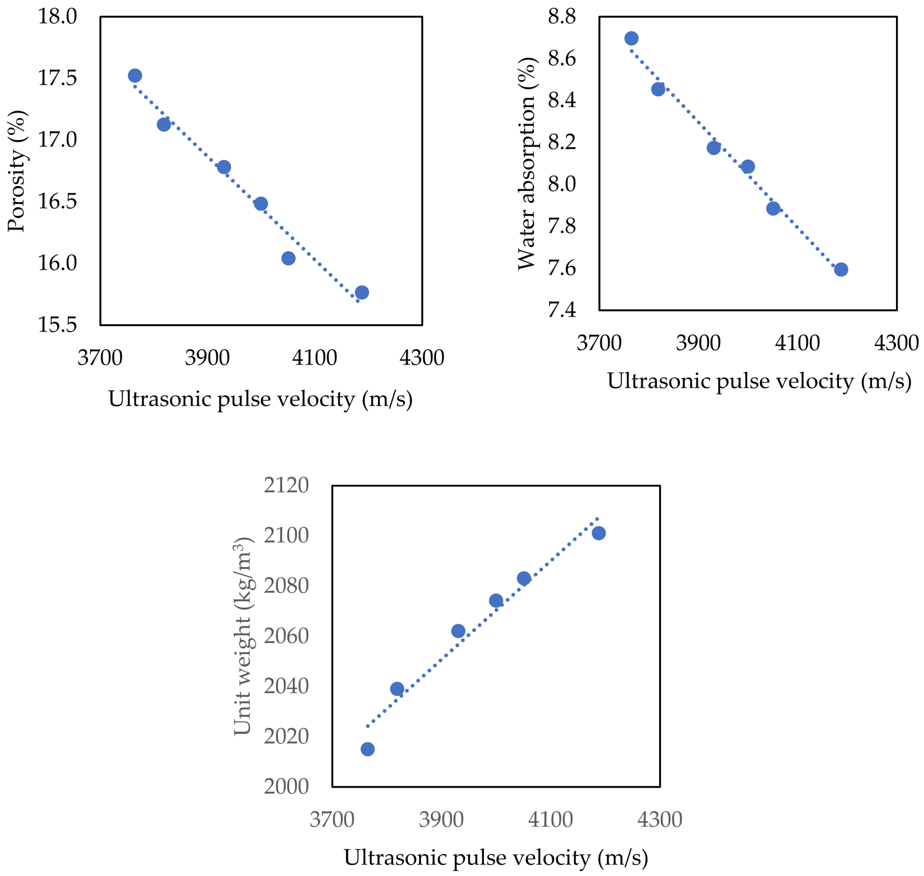

Figure 9. The relationship between the ultrasonic pulse velocity, porosity, water absorption, and unit weight results.

The ultrasonic pulse velocity (UPV) is transmitted through the solid phases. The UPV of cementitious materials has an inverse relationship to porosity, proportional to the volume fraction of the solid phase [34,35]. Therefore, as in Figure 9, UPV increased with increasing unit weight and decreasing porosity and water absorption. However, UPV has a nonlinear relationship with the FBP replacement ratio, as shown in Figure 8. In addition, the UPV of cementitious composites significantly depends on the microstructure and the densities of the samples as a result of the chemical reaction between cement, FBP, and water, as explained in [36].

3.5. Flexural Strengths Results

Figure 10 shows the flexural strength test results of cementitious composite mortars incorporating FBP after 3, 7, and 28 days of water curing, with the error bar indicating the standard deviation.

Results showed that the flexural strengths decreased as the FBP replacement ratio increased. While the 3-day flexural strength test results of FBP5, FBP10, FBP15, FBP20, and FBP25 samples decreased by 4.38, 11.35, 15.46, 19.56, and 25.99%, respectively, the 7-day flexural strength test results were reduced by 3.35, 6.47, 11.50, 15.69, and 19.88%, respectively, compared to control mortar. The 28-day flexural strength test results decreased by 2.17, 4.35, 8.70, 13.04, and 15.22% for FBP5, FBP10, FBP15, FBP20, and FBP25, respectively. When the reduction rates of flexural strength test results of cementitious composite mortars incorporating FBP compared to control mortar are examined, it is seen that the reduction rates decrease with increasing curing time. This situation proves that the strength of pozzolans increases over the 3-day strength. When the results of Figure 10 are evaluated, the flexural strength test results decreased with the increase of the FBP replacement ratio, but the strength gain rate showed continuous growth. This situation shows that the flexural strength test results of cementitious composites incorporating FBP can catch up to that of the control mortars at later ages [23]. In addition, the results proved once again that pozzolans complete their hydration late. The flexural strengths were similar to the study by Zeghad et al. [22]. Since there are limited studies on replacing FBP in cement, this section was evaluated by considering other studies on brick powder in the literature. Naceri and Hameri [37] reported that as the brick powder replacement ratio increased, the 7- and 28-day flexural strengths decreased compared to the reference mortars. They also determined that mortars containing 5 and 10% brick powder had higher flexural strength than reference mortars at 90-day flexural strengths. The linear decrease in the 28-day flexural strengths with the increase in the brick powder replacement rate was also seen in similar studies by Liu [38] and Xue et al. [39].

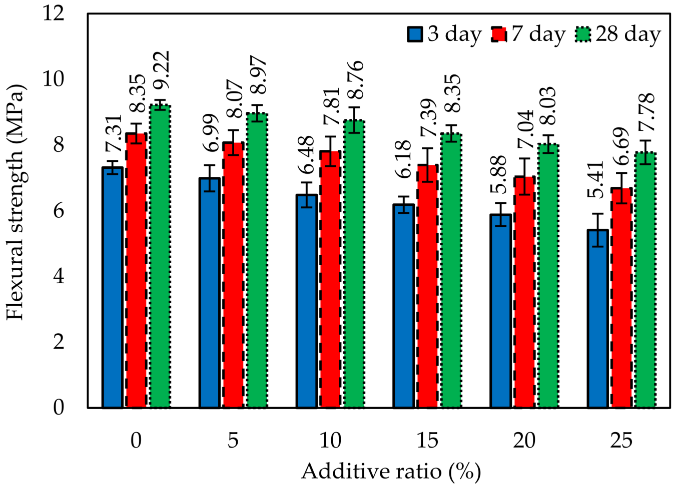

Figure 10. The flexural strength test results of cementitious composite mortars.

3.6. Compressive Strength Results

Figure 11 shows the compressive strength test results of cementitious composite mortars incorporating FBP after 3, 7, and 28 days of water curing, with the error bar indicating the standard deviation.

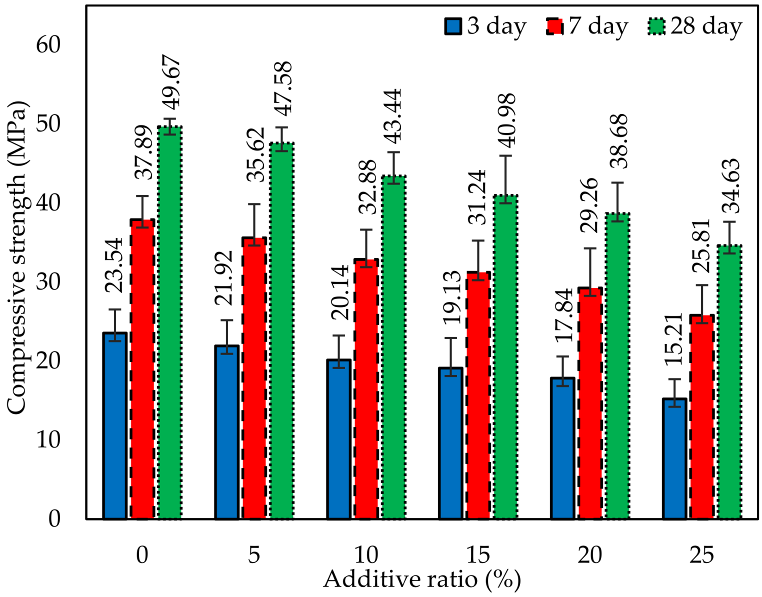

Figure 11. The compressive strength test results of cementitious composite mortars.

When the results were examined, the compressive strength decreased as the FBP replacement ratios increased. While the 3-day compressive strength test results of FBP5, FBP10, FBP15, FBP20, and FBP25 samples decreased by 6.88, 14.44, 18.73, 24.21, and 35.39%, respectively, the 7-day compressive strength test results decreased 5.99, 13.22, 17.55, 22.78, and 31.88%, compared to the control mortar. The 28-day compressive strength test results decreased by 4.21, 12.54, 17.50, 22.13, and 30.28%, respectively. This situation proves that the strength of pozzolans increases over the 3-day strength. Figure 12 shows the increment rate in compressive strength test results for each mixture group.

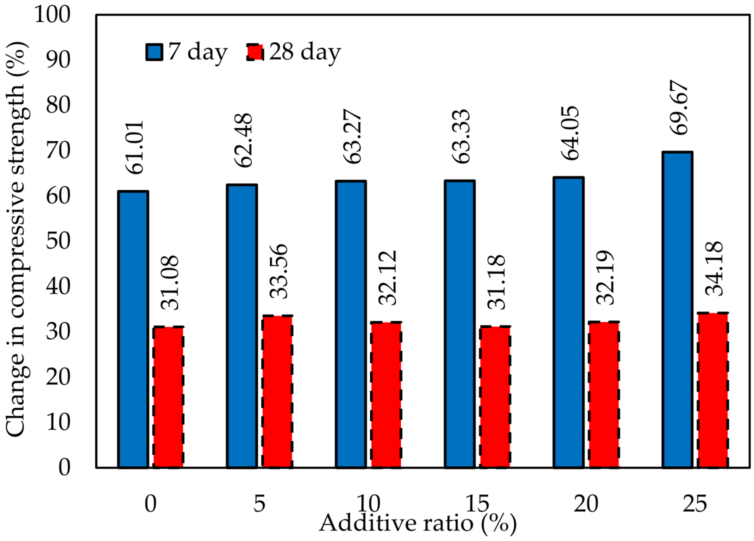

Figure 12. Change in compressive strength of FBP-based cementitious composites.

As shown in Figure 12, the 7-day increase rate percentages represent the increase according to 3-day compressive strength, while the 28-day increase rate percentages represent the increase according to 7-day compressive strength. Looking at the increase rates, both the 7-day and 28-day increase rates are higher than that of the control sample with the increase in FBP. Especially in the first days (7 days), the increase rate is higher compared to later ages. When the results of Figures 11 and 12 are evaluated, although the compressive strengths decreased with the increase of the FBP replacement ratio, the strength gain rate showed a continuous increase as in the flexural strength. This situation again showed that the compressive strength test results of cementitious composite mortars incorporating FBP at prolonged days could catch up with the compressive strength of control mortars, as in flexural strength [23]. The compressive strength results were similar to the study by Zeghad et al. [22]. When the studies on the use of brick powder in cement-based composites are examined, the 28-day compressive strengths generally decrease with the increase in the brick powder replacement ratio [38,40]. With the rise of the FBP replacement ratio, the OPC in the cement-based composite is diluted, which reduces the amount of C-S-H, C-A-S-H, and CH. For this reason, the compressive strength of cementitious composites with additives decreases [21].

Figure 13 shows the relationship between ultrasonic pulse velocity and 28-day compressive strength results. According to this result, it is possible to say that there is a strong relationship between compressive strength and ultrasonic pulse velocity.

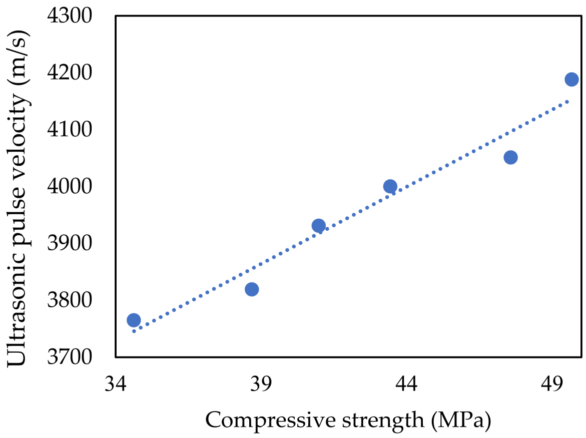

Figure 13. The relationship between ultrasonic pulse velocity and compressive strength.

3.7. Microstructure Analysis

Figure 14 shows images of the SEM analyses of control, FBP5, and FBP10 samples after 7 days of water curing. When the SEM images are examined, it is seen that the amount of Calcium silicate hydrate (C-S-H) in the control samples is more intense than in cementitious composite mortars incorporating FBP. The low C-S-H concentration in cementitious composite mortars containing FBP can be attributed to the slow hydration development of pozzolans in the first days. Again, the reason for this situation is the late hydration reactions.

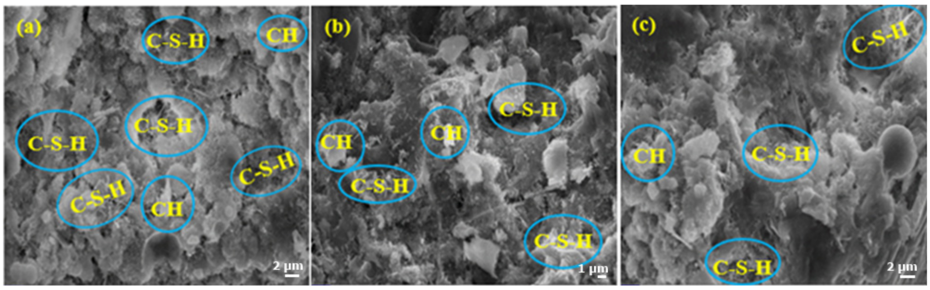

Figure 14. 7-days SEM images of (**a**) Control, (**b**) FBP5, and (**c**) FBP10 samples.

Figure 15 shows images of the SEM analyses of control, FBP5, and FBP10 samples after 28 days of water curing. When SEM images are examined, it is seen that a result similar to the 7-day SEM analysis is obtained. It is seen that the C-S-H density in the control sample is higher than in FBP5 and FBP10 samples. The C-S-H density of FBP5 samples is higher than that of FBP10. When compared to the 7-day SEM images, it is seen that the C-S-H density increases, and the hydration development of the pozzolans are better in the following days. When the results of SEM analyses are evaluated, they are determined to support the compressive and flexural strength results.

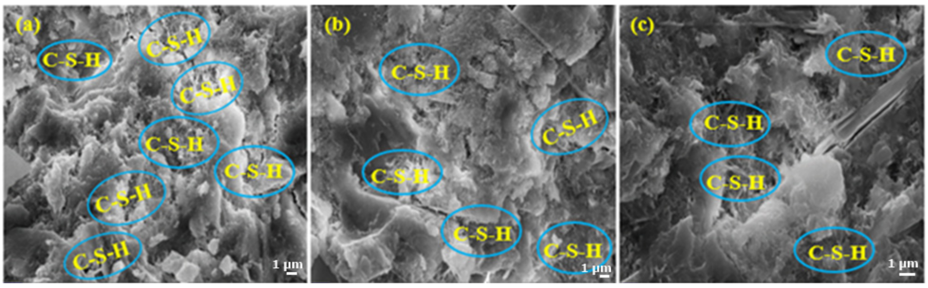

Figure 15. 28-days SEM images of (**a**) Control, (**b**) FBP5, and (**c**) FBP10 samples.

4. Conclusions

This study investigated the mechanical, physical, and microstructural properties of cementitious composites incorporating firebrick powder (FBP). In this regard, the firebrick powder was used at 5, 10, 15, 20, and 25% replacement ratio by weight of cement to produce cementitious composites. The consistency, setting characteristics, and 3, 7, and 28 days compressive and flexural strength tests of produced cementitious composites were performed. In addition, ultrasonic pulse velocity, water absorption, porosity, unit weight, and microstructure analysis of cementitious composites were conducted. The key outcomes of the study are as follows:

- As the FBP ratio increased, the initial and final setting times got longer. This situation shows that the FBP retards the setting characteristics. The main reason for this situation is the delayed beginning of hydration and the prolongation of setting times of pozzolans. The flow diameters increased significantly with the increase of the replacement ratio of the FBP. This shows that the water requirement for workability can be reduced in cementitious composite mortar mixtures thanks to FBP. This situation can be attributed that the specific surface area of FBP being lower than cement.
- The mechanical strength results decreased as the replacement ratio of FBP increased. However, as the replacement ratio of FBP increased, a general increase in the strength gain rate was observed.
- It has been observed that the FBP obtained by grinding the waste firebrick can be used up to a 10% replacement ratio in cementitious composites that would require load-bearing properties to comply with the specification. However, FBP might be used up to 25% in some cases. Since cement production causes ~8% of the world's CO_2 emissions and energy, using waste FBP instead of cement would reduce the amount of cement used and lower the cost of producing cementitious composites.

In future studies, FBP can be ground more so that the specific surface area is close to cement and can be substituted for cement in different proportions. This way, the strength decreases can be at a lower level. In addition, no study has been found on using FBP in geopolymer or alkali-activated slag (AAS) mortars. The use of FBP in geopolymer or AAS mortars can also be investigated in future studies.

Author Contributions: Conceptualization, O.S. and E.H.A.; methodology, O.S. and E.H.A.; validation, O.S. and E.H.A.; investigation, O.S. and E.H.A.; resources, O.S., E.H.A. and S.G.; writing—original draft preparation, O.S. and E.H.A.; writing—review and editing, O.S., E.H.A. and S.G.; supervision, O.S. All authors have read and agreed to the published version of the manuscript.

Funding: This research received no external funding.

Institutional Review Board Statement: Not applicable.

Informed Consent Statement: Not applicable.

Data Availability Statement: Not applicable.

Conflicts of Interest: The authors declare no conflict of interest.

References

1. Mehta, P.K.; Monteiro, P.J.M. *Concrete Microstructure, Properties, and Materials*, 3rd ed.; McGraw-Hill: New York, NY, USA, 2006.
2. Meyer, C. The greening of the concrete industry. *Cem. Concr. Compos.* **2009**, *31*, 601–605. [CrossRef]
3. Dunuweera, S.P.; Rajapakse, R.M.G. Cement types, composition, uses and advantages of nanocement, environmental impact on cement production, and possible solutions. *Adv. Mater. Sci. Eng.* **2018**, *2018*, 4158682. [CrossRef]
4. Andrew, R.M. Global CO_2 emissions from cement production. *Earth Syst. Sci. Data* **2018**, *10*, 195–217. [CrossRef]
5. Tantri, A.; Nayak, G.; Kamath, M.; Shenoy, A.; Shetty, K.K. Utilization of cashew nut-shell ash as a cementitious material for the development of reclaimed asphalt pavement incorporated self-compacting concrete. *Constr. Build. Mater.* **2021**, *301*, 124197. [CrossRef]
6. Shaaban, M. Properties of concrete with binary binder system of calcined dolomite powder and rice husk ash. *Heliyon* **2021**, *7*, e06311. [CrossRef]

7. Sarıdemir, M.; Çelikten, S.; Yıldırım, A. Mechanical and microstructural properties of calcined diatomite powder modified high strength mortars at ambient and high temperatures. *Adv. Powder Technol.* **2020**, *31*, 3004–3017. [CrossRef]
8. Demir, İ.; Sivrikaya, B.; Sevim, O.; Baran, M. A study on ASR mitigation by optimized particle size distribution. *Constr. Build. Mater.* **2020**, *261*, 120492. [CrossRef]
9. Wu, H.; Zuo, J.; Zillante, G.; Wang, J.; Yuan, H. Construction and demolition waste research: A bibliometric analysis. *Archit. Sci. Rev.* **2019**, *62*, 354–365. [CrossRef]
10. Wu, H.; Zuo, J.; Yuan, H.; Zillante, G.; Wang, J. A review of performance assessment methods for construction and demolition waste management. *Resour. Conserv. Recycl.* **2019**, *150*, 104407. [CrossRef]
11. Hwang, C.L.; Yehualaw, M.D.; Vo, D.H.; Huynh, T.P.; Largo, A. Performance evaluation of alkali activated mortar containing high volume of waste brick powder blended with ground granulated blast furnace slag cured at ambient temperature. *Constr. Build. Mater.* **2019**, *223*, 657–667. [CrossRef]
12. Ding, Z.; Wang, Y.; Zou, P.X. An agent based environmental impact assessment of building demolition waste management: Conventional versus green management. *J. Clean. Prod.* **2016**, *133*, 1136–1153. [CrossRef]
13. Li, L.G.G.; Lin, Z.H.; Chen, G.M.; Kwan, A.K.H. Reutilizing clay brick dust as paste substitution to produce environment-friendly durable mortar. *J. Clean. Prod.* **2020**, *274*, 122787. [CrossRef]
14. Zhao, Z.; Grellier, A.; Bouarroudj, M.E.K.; Michel, F.; Bulteel, D.; Courard, L. Substitution of limestone filler by waste brick powder in self-compacting mortars: Properties and durability. *J. Build. Eng.* **2021**, *43*, 102898. [CrossRef]
15. Ortega, J.M.; Letelier, V.; Solas, C.; Moriconi, G.; Climent, M.Á.; Sánchez, I. Long-term effects of waste brick powder addition in the microstructure and service properties of mortars. *Constr. Build. Mater.* **2018**, *182*, 691–702. [CrossRef]
16. Zhao, Z.; Xiao, J.; Duan, Z.; Hubert, J.; Grigoletto, S.; Courard, L. Performance and durability of self-compacting mortar with recycled sand from crushed brick. *J. Build. Eng.* **2022**, *57*, 104867. [CrossRef]
17. Horckmans, L.; Nielsen, P.; Dierckx, P.; Ducastel, A. Recycling of refractory bricks used in basic steelmaking: A review. *Resour. Conserv. Recycl.* **2019**, *140*, 297–304. [CrossRef]
18. Nematzadeh, M.; Dashti, J.; Ganjavi, B. Optimizing compressive behavior of concrete containing fine recycled refractory brick aggregate together with calcium aluminate cement and polyvinyl alcohol fibers exposed to acidic environment. *Constr. Build. Mater.* **2018**, *164*, 837–849. [CrossRef]
19. Khattab, M.; Hachemi, S.; Al Ajlouni, M.F. Evaluating the physical and mechanical properties of concrete prepared with recycled refractory brick aggregates after elevated temperatures' exposure. *Constr. Build. Mater.* **2021**, *311*, 125351. [CrossRef]
20. Kavas, T.; Karasu, B.; Arslan, O. Utilization of refractory brick wastes in concrete production as aggregates. *Sohn. Int. Symp. Adv. Process. Met. Mater.* **2006**, *5*, 479–483.
21. El-Didamony, H.; Amer, A.A.; El-Hoseny, S. Recycling of low-grade aluminosilicate refractory brick waste product in blended cement. *J. Therm. Anal. Calorim.* **2016**, *125*, 23–33. [CrossRef]
22. Zeghad, M.; Mitterpach, J.; Safi, B.; Amrane, B.; Saidi, M. Reuse of refractory brick wastes (RBW) as a supplementary cementitious material in a concrete. *Period. Polytech. Civ. Eng.* **2017**, *61*, 75–80. [CrossRef]
23. Alakara, E.H.; Sevim, O.; Demir, I.; Şimşek, O. Experimental study on firebrick powder-based cementitious composites under the effect of elevated temperature. *J. Build. Eng.* **2022**, *61*, 105277. [CrossRef]
24. *TS EN 196-1*; Methods of Testing Cement–Part 1: Determination of Strength. Turkish Standards Institution: Ankara, Turkey, 2016.
25. *TS EN 196-3*; Methods of Testing Cement-Part 3: Determination of Setting Time and Soundness. Turkish Standards Institution: Ankara, Turkey, 2017.
26. *TS EN 12350-5*; Testing Fresh Concrete-Part 5: Flow Table Test. Turkish Standards Institution: Ankara, Turkey, 2019.
27. *TS EN 480-5*; Admixtures for Concrete, Mortar and Grout—Test Methods—Part 5: Determination of Capillary Absorption. Turkish Standards Institution: Ankara, Turkey, 2008.
28. *TS EN 12504-4*; Testing Concrete in Structures—Part 4: Determination of Ultrasonic Pulse Velocity. Turkish Standards Institution: Ankara, Turkey, 2021.
29. Brooks, J.J.; Johari, M.M.M.; Mazloom, M. Effect of admixtures on the setting times of high-strength concrete. *Cem. Concr. Compos.* **2000**, *22*, 293–301. [CrossRef]
30. Kula, I.; Olgun, A.; Erdogan, Y.; Sevinc, V. Effects of colemanite waste, cool bottom ash, and fly ash on the properties of cement. *Cem. Concr. Res.* **2001**, *31*, 491–494. [CrossRef]
31. Rogers, S.B. Evaluation and Testing of Brick Dust as A Pozzolanic Additive to Lime Mortars for Architectural Conservation. Master's Thesis, University of Pennsylvania, Philadelphia, PA, USA, 2011.
32. Arif, R.; Khitab, A.; Kırgız, M.S.; Khan, R.B.N.; Tayyab, S.; Khan, R.A.; Anwar, W.; Arshad, M.T. Experimental analysis on partial replacement of cement with brick powder in concrete. *Case Stud. Constr. Mater.* **2021**, *15*, e00749. [CrossRef]
33. Sutter, L.L.; Hooton, R.D.; Schlorholtz, S. *Methods for Evaluating Fly Ash for Use in Highway Concrete*; Transportation Research Board: Washington, DC, USA, 2013.
34. Ye, G.; Lura, P.; Van Breugel, K.; Fraaij, A.L.A. Study on the development of the microstructure in cement–based materials by means of numerical simulation and ultrasonic pulse velocity measurement. *Cem. Concr. Compos.* **2004**, *26*, 491–497. [CrossRef]
35. Hong, G.; Oh, S.; Choi, S.; Chin, W.J.; Kim, Y.J.; Song, C. Correlation between the compressive strength and ultrasonic pulse velocity of cement mortars blended with silica fume: An analysis of microstructure and hydration kinetics. *Materials* **2021**, *14*, 2476. [CrossRef]

36. Bogas, J.A.; Gomes, M.G.; Gomes, A. Compressive strength evaluation of structural lightweight concrete by non–destructive ultrasonic pulse velocity method. *Ultrasonics* **2013**, *53*, 962–972. [CrossRef]
37. Naceri, A.; Hamina, M.C. Use of waste brick as a partial replacement of cement in mortar. *Waste Manag.* **2009**, *29*, 2378–2384. [CrossRef]
38. Liu, S.; Dai, R.; Cao, K.; Gao, Z. The role of sintered clay brick powder during the hydration process of cement pastes. *Iran. J. Sci. Technol. Trans. Civ. Eng.* **2017**, *41*, 159–165. [CrossRef]
39. Xue, C.Z.; Shen, A.Q.; Chang, Y.T.; Liang, D. The study of the construction waste brick powder's activity. *Adv. Mater. Res.* **2015**, *1079*, 309–311. [CrossRef]
40. Lin, K.L.; Chen, B.Y.; Chiou, C.S.; Cheng, A. Waste brick's potential for use as a pozzolan in blended Portland cement. *Waste Manag. Res.* **2010**, *28*, 647–652. [CrossRef]

buildings

Article

Investigation on Dynamic Mechanical Properties of Recycled Concrete Aggregate under Split-Hopkinson Pressure Bar Impact Test

Wenping Du [1,2], Caiqian Yang [1,3,*], Hans De Backer [2], Chen Li [3], Kai Ming [1], Honglei Zhang [4] and Yong Pan [5]

[1] Key Laboratory of Concrete and Prestressed Concrete Structures of the Ministry of Education, School of Civil Engineering, Southeast University, Nanjing 210096, China; diploma0802@163.com (W.D.); 220201184@seu.edu.cn (K.M.)
[2] Department of Civil Engineering, Ghent University, 9052 Zwijnaarde, Belgium; hans.debacker@ugent.be
[3] College of Civil Engineering and Mechanics, Xiangtan University, Xiangtan 411105, China; 230179447@seu.edu.cn
[4] Jiangsu Huatong Engineering Testing Co., Ltd., Nanjing 210000, China; dwpyls0802@gmail.com
[5] Jiangsu Eastern Expressway Management Co., Ltd., Lianyungang 222000, China; 201921002244@smail.xtu.edu.cn
* Correspondence: ycqixx@seu.edu.cn

Abstract: The dynamic mechanical properties of recycled concrete (RC) and natural concrete (NC) were studied by impact tests and numerical simulation. The quasi-static tests were conducted by a servo-hydraulic machine, while the impact test used a 50 mm diameter split-Hopkinson pressure bar (SHPB). The ANSYS/LS-DYNA software simulation was selected to validate the experimental results. The recycled coarse aggregates (RCAs) came from the housing demolition and were conducted with the microwave-assisted beneficiation method. The stress–strain curves, compressive strength, dynamic increase factor (DIF), initial elastic modulus and failure modes were analyzed and discussed. The results showed that the quasi-static compressive strengths of the RC were lower than that of the NC by 5.0%. The maximum dynamic compressive strengths of the NC increased by 105.9% when the strain rates varied from 46–108, while the RC increased by 102.2% when the strain rates varied from 42 to 103. The stress–strain curves of the RC and NC demonstrated a similar pattern. The DIF showed an increasing tendency with the increasing of strain rates, while the initial elastic modulus showed a decreasing tendency. The failure modes first initiated from the edge of specimens and then propagated to the center of specimens. An empirical equation was proposed for the estimation of the DIF of the RC which was obtained from the microwave-assisted beneficiation. The simulation results for the prediction of stress–strain curves of the RC showed good agreement with the experimental results. In addition, these results suggested that the RCAs were obtained by the microwave-assisted beneficiation can be recycled and may be used in some actual engineering.

Keywords: SHPB; RC; compressive strength; DIF; initial elastic modulus; failure modes

1. Introduction

In the entire world, construction generates 2.2 billion tons of waste every year [1], and this increasing trend will reach approximately 6.2 billion tons by 2025 [2]. The concrete waste from the demolition of old city buildings constituted 58% of the 18 million tons of waste generated in China over the past year. However, the recycling coefficient of utilization is low. The recycling of waste concrete not only purifies the environment, but also reduces the over consumption of natural resources [3]. To solve the above problem, many novel, efficient technologies are being continuously developed. Examples include conventional heating [4], particle-shape-collecting technology [5], thermal–mechanical technology [6], a chemical immersion method [7,8], hybrid techniques [9] and microwave-assisted beneficiation [10,11]. Scholars mainly focus on mechanical and chemical properties to obtain high-quality coarse aggregate. The quasi-static mechanical properties method of obtaining recycled concrete (RC) is mature. However, the dynamic behavior of concrete under different strain rates is more complex than that of the quasi-static mechanical properties. Therefore, related investigation of impact behaviors is scarce. The dynamic tests mainly concentrated on split-Hopkinson pressure bar (SHPB) and drop-hammer impact tests [12]. However, the dynamic mechanics of RC according to different beneficiation methods were investigated. The investigation of the dynamic mechanism of natural concrete (NC) was started by Abrams. It was then expanded by a large number of scholars. The relationship between strain rate and other mechanical properties was the primary focus of scholars [13–15]. The dynamic mechanism of RC was investigated mainly according to the same method as NC. Then, the mechanisms and models of dynamic failure modes, strength [16], stress–strain curves [6,17] and fragmentation [18] were summarized. The dynamic behavior of recycled aggregate concrete was simulated by the SHPB with different diameters and drop weight impact loads [19]. Although the fundamental behaviors had been investigated, the environmental, economic and durability aspects of the RC also required investigation because they were important to concrete structures' serviceability [20–23]. To study the influence of nanoparticle chemical composite on the dynamic mechanical performance of the RC, the impact load was simulated by a 100 mm diameter SHPB. The results showed that some nanoparticles can improve the RC's dynamic compressive strength [24]. In the field of concrete, concrete-filled steel tubes are widely applied in engineering. Therefore, it was necessary to study the dynamic mechanics performance of recycled-aggregate-concrete-filled steel tubes under different conditions. Combined with the experiment and simulation, the mechanical behavior of the recycled-aggregate-concrete-filled steel tube was investigated. The results showed that reinforcement ratio and strength can improve impact behaviors [25,26]. Construction and demolition wastes were obtained from different districts. Therefore, the recycled coarse aggregate (RCA) may contain different materials. However, the rubber [11,27,28] and asphalt may have had a significant influence on the performance of the RC. There were some other investigations into the integrated assessment of RCA [29], the splice strength of steel reinforcement embedded in the RCA [30] and recycled aggregate concrete under daily temperature variations [31].

Although there have been many achievements in investigating the dynamic behaviors of RC (coarse aggregate from the tradition methods), The investigations of RCAs obtained from microwave-assisted beneficiation are scarce. In this paper, according to the most recent investigations, the dynamic behaviors of RC and NC were thoroughly investigated using the SHPB impact test. Then, the finite element method was selected to verify the dynamic behaviors. The stress–strain curves, compressive strength, dynamic increase factor (DIF), initial elastic modulus and failure modes were the main parameters that were investigated. Finally, a model was developed for the prediction of the stress–strain curve of the RC under dynamic loading, which showed good agreement with the impact experiment results.

2. Materials and Methods

2.1. Materials and Specimens

In quasi-static and dynamic tests, the NC included Portland cement (42.5R), fine aggregate, coarse aggregate and water. The difference between the NC and RC was the coarse aggregate, as shown in Figure 1. The design strength grade of concrete specimens was C40. The fine aggregate was river sand. The coarse aggregate of the NC was crushed stone (see Figure 1a) the maximum diameter of which was less than 6 mm, while the coarse aggregate of the RC was gravel (see Figure 1b) which was obtained from demolition waste and treated by microwave-assisted beneficiation. Then, the RCAs were crushed (see Figure 1c) and used as recycling materials for cost-effectiveness and environmental purification. The coarse aggregate replacement rate was 100% in the RC, i.e., the coarse aggregate of the RC was totally replaced by RCA. Differently from the most prior investigations, the beneficiation method was microwave-assisted beneficiation. Figures 2 and 3 present the scanning electron microscope (SEM) images and X ray diffraction (XRD) patterns of natural coarse aggregate and RCA. It was found that the microwave-assisted beneficiation had a slight influence on the coarse aggregate. The related tests indicated that the natural coarse aggregate and RCA showed similar mechanical properties [10]. Therefore, the RCA may be recovered and reused.

(**a**) (**b**) (**c**)

Figure 1. Coarse aggregate, (**a**) Natural, (**b**) RCA, (**c**) Crushed RCA.

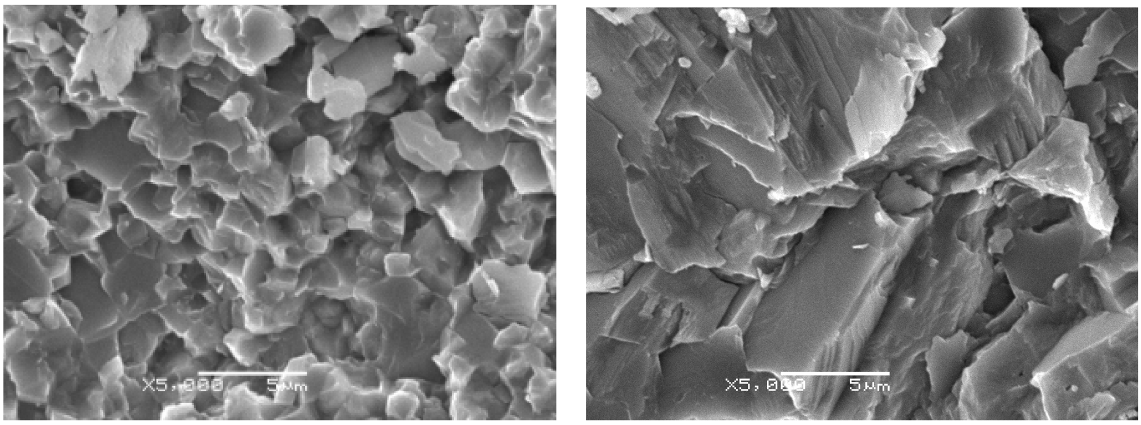

(**a**) (**b**)

Figure 2. SEM images of natural coarse aggregate and RCA. (**a**) Natural coarse aggregate; (**b**) RCA.

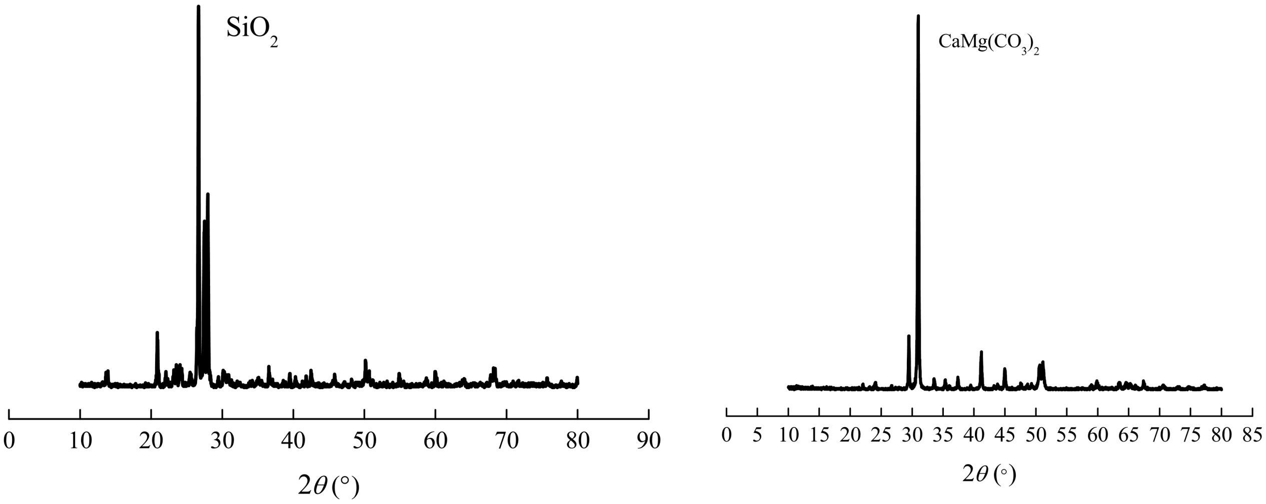

(**a**) (**b**)

Figure 3. XRD pattern of natural coarse aggregate and RCA: (**a**) Natural coarse aggregate; (**b**) RCA.

The impact test was selected to investigate the dynamic behavior of the NC and RC specimens. For the RC specimens, the water absorption was higher than that of the NC. Therefore, it was necessary to use additional water to assure the same water–binder ratio. According to the mix design specification of the concrete (JGJ55-2011), The water–binder ratio was 0.38. The additional water in the RC specimens was 4.6%. Five cubic specimens with dimensions of 150 mm were fabricated and cured for 28 days at room temperature. Their compressive strengths were measured according to the standard compression tests. The SHPB specimens had diameters of 50 mm and heights of 25 mm [29]. The specimens were divided into two groups and tested after 28 days of standard curing. Each specimen is named using a X40-Y format, where X denotes NC or RC, and Y represents the number of specimens, as shown in Figure 4.

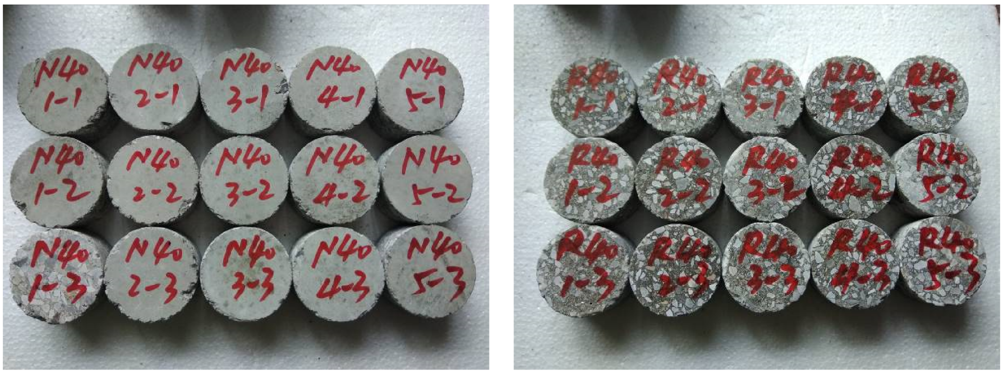

(**a**) (**b**)

Figure 4. Concrete specimens. (**a**) NC; (**b**) RC.

2.2. SHPB Test

The SHPB device used in the dynamic impact testing is shown in Figure 5a,b. The SHPB apparatus consisted of the following parts: gas tank, cylindrical striker (50 mm in diameter, 400 mm in length), incident bar (50 mm in diameter, 3000 mm in length), transmitter bar (50 mm in diameter, 3000 mm in length), absorption bar, damper, dynamic strain indicator, oscilloscope, data processing system and testing specimen. The specimens are sandwiched between the incident and transmitter bars, as shown in Figure 5c. During the test, the pressurized gas promoted the striker bar, and a stress pulse was produced in the incident bar. The stress pulse impinged the specimen. The achieved strain rates in the SHPB test were not constant throughout the test. The dynamic impact process of the SHPB is shown in Figure 6. Five rating air pressures (0.1 MPa, 0.2 MPa, 0.3 MPa, 0.4 MPa and 0.5 MPa) were investigated. Figure 7 shows the typical pulse signals during SHPB impact test. According to the impulses, the stress, strain and strain rates can be obtained [22].

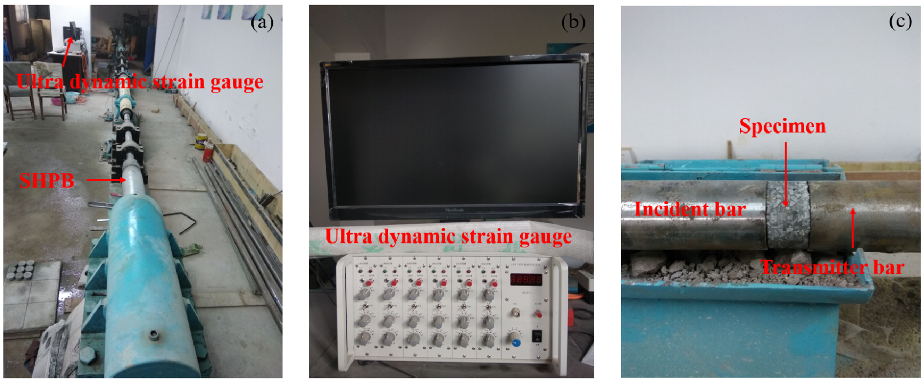

Figure 5. 50 mm diameter cross-sectional SHPB for impact test. (**a**) SHPB device; (**b**) ultra-dynamic strain gauge; (**c**) specimen.

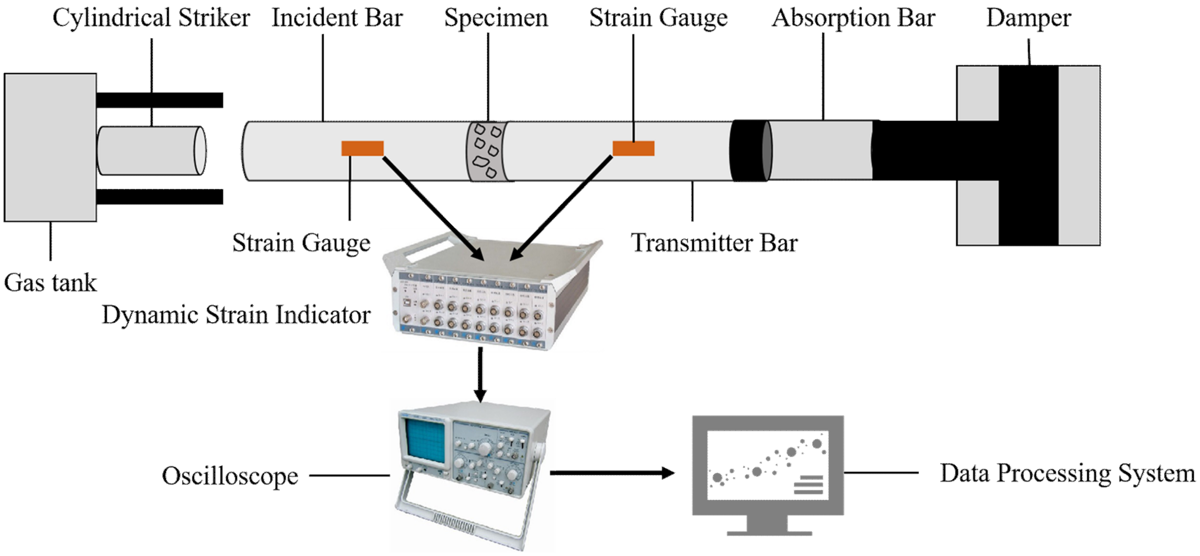

Figure 6. Split-Hopkinson pressure bar (SHPB).

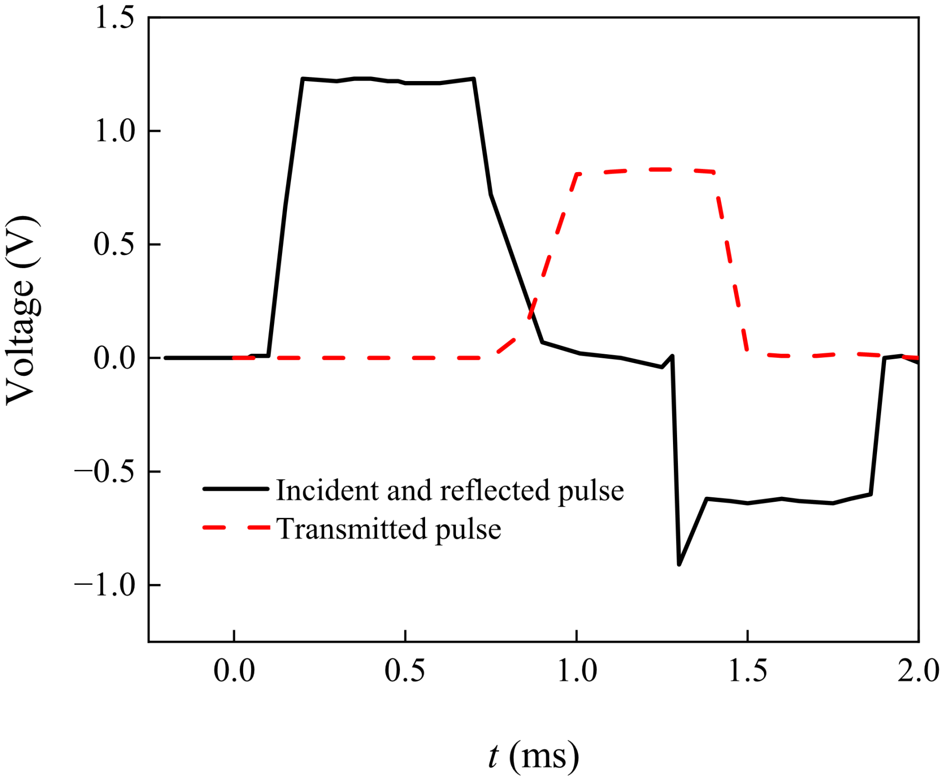

Figure 7. Typical pulse signals during SHPB impact test.

3. Experimental Results

The experimental results of the quasi-static compressive strength testing are given in Table 1. The average compressive strengths of the NC and RC were 41.52 MPa and 39.44 MPa, respectively. It can be concluded that the compressive strength of the NC was higher than that of the RC by 5.0%. This phenomenon indicated that the waste concrete blocks conducted with microwave-assisted beneficiation had a certain recycling value [10]. The micro-cracks propagated in the longitudinal direction; there were several cracks running through the specimens. Simultaneously, concrete spalling occurred on the edge of specimens.

Table 1. Results of quasi-static compressive strength.

Specimens	Load (kN)	Compressive Strength (MPa)	Average (MPa)
N40-1	929	41.3	41.52
N40-2	918	40.8	
N40-3	936	41.6	
N40-4	947	42.1	
N40-5	941	41.8	
R40-1	880	39.1	39.44
R40-2	884	39.3	
R40-3	891	39.6	
R40-4	887	39.4	
R40-5	896	39.8	

Table 2 gives the results of dynamic compressive strength testing. Compared to Table 1, the dynamic strengths were higher than the quasi-static strengths. The dynamic compressive strength of the RC increased by 12.9%, 39.6%, 63.2%, 83.3% and 102.2% under five strain rates when compared to the quasi-static compressive strength, respectively, while the NC increased by 17.8%, 44.3%, 67.6%, 87.4% and 105.9%, respectively. The relationship between dynamic compressive strength and strain rate was linear. This also indicated the dynamic strengthening characteristics of concrete.

Table 2. Results of dynamic compressive strength testing.

Specimens	Impact Velocity (m/s)	Strain Rate (s^{-1})	Compressive Strength (MPa)	Specimens	Impact Velocity (m/s)	Strain Rate (s^{-1})	Compressive Strength (MPa)
NC-100-1	4.8	50	48.6	RC-100-1	4.5	37	44.7
NC-100-2	4.7	47	47.4	RC-100-2	4.7	43	46.2
NC-100-3	4.6	41	46.8	RC-100-3	4.6	46	45.3
NC-200-1	7.3	66	58.8	RC-200-1	7.2	63	56.6
NC-200-2	7.1	57	57.6	RC-200-2	7.1	54	55.5
NC-200-3	7.2	63	58.5	RC-200-3	7.3	60	56.2
NC-300-1	9.7	80	67.7	RC-300-1	9.5	74	64.3
NC-300-2	9.8	86	68.1	RC-300-2	9.9	78	66.7
NC-300-3	9.6	77	67.3	RC-300-3	9.7	79	65.8
NC-400-1	10.7	90	75.3	RC-400-1	10.9	87	74.6
NC-400-2	11.1	98	76.2	RC-400-2	10.7	92	72.6
NC-400-3	10.9	94	75.6	RC-400-3	10.8	94	73.9
NC-500-1	12.3	107	83.1	RC-500-1	12.3	105	82.1
NC-500-2	12.2	112	82.8	RC-500-2	12.1	100	80.6
NC-500-3	12.4	105	83.7	RC-500-3	12.2	104	81.2

Note: 100, 200, 300, 400 and 500 represent impact pressures of 0.1 MPa, 0.2 MPa, 0.3 MPa, 0.4 MPa and 0.5 MPa, respectively; 1, 2 and 3 represent the number of concrete specimens.

3.1. Stress–Strain Curves

Figure 8 demonstrates the stress–strain curves of concrete specimens under different impact pressures. It can be concluded that the relationship between stress and strain was linear at the elastic stage. The deformation of concrete was mainly influenced by the coarse aggregate and cement mortar. Then, the specimen entered an elastic–plastic state; the increasing rate of strain was faster than that of the stress. The strain further accelerated, while the stress increased slightly. The plastic deformation played a major role at this stage. The micro-cracks originated inside the concrete. However, the concrete was in a stable state before the stress reached its compressive strength. When the stress reached the peak values, the curves presented a decreasing tendency. The bearing capacity of concrete specimens decreased with the increasing of strain. This phenomenon was defined as strain softening.

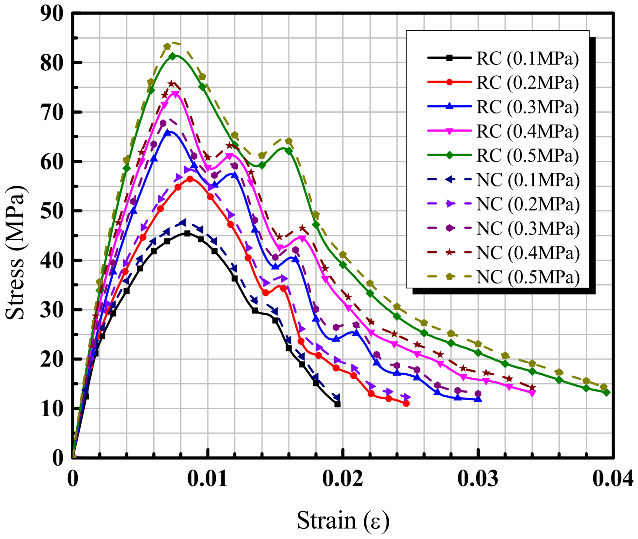

Figure 8. Stress–strain curves of concrete specimens under different impact pressures.

Compared to the NC and RC impact tests results, it can be found that the impact time was longest when the impact pressure was 0.1 MPa. When the stress increased up to the maximum value, the stress was found to descend gradually and slowly with the increase in strain. This stage was an elastic strengthening stage, and the pores and cracks were compacted. Therefore, the concrete presented a strain hardening phenomenon under the impact loading. The overall impact resistance improved and had an excellent energy dissipation effect. During this initial stage, the relationship between stress and strain was linear when the impact pressure varied from 0.2 MPa to 0.5 MPa. The stress increased up to the peak values in a short time; the specimen was rapidly destroyed. The curves began to decrease rapidly, and the stress value decreased immediately with the increase in strain. When the strain rate increased gradually, the curvatures of the stress–strain curves on the ascending stage became smaller. It was indicated that the concrete damage evolution occurred completely. i.e., it was the strain rate strengthening effect of concrete.

Compared to the stress–strain curves at descending phase, an oscillating reaction was found when the impact pressure varied from 0.2 MPa to 0.5 MPa. This oscillation reaction was illustrated the softening property of the concrete. The slope of the stress–strain curves increased with the increasing of impact pressure. The linear line segment become longer and showed the obvious brittle failure advantages. It can also be seen that the higher impact pressure made the concrete harden easily. The higher the strength, the higher the corresponding brittleness. When the impact pressure increased, the stress corresponding to the high impact pressure was greater than that of the low impact pressure. That is, when the impact pressure increased gradually, the strain rate was higher. The relationship between the stress and strain of concrete also developed from strain hardening to strain softening.

3.2. Parameters Study

3.2.1. Dynamic Compressive Strength

As shown in Figure 9, it can be concluded that the relationship between impact velocity and dynamic compressive strength is linear. The dynamic compressive strength increased linearly when the impact velocity of the NC and RC varied from 4.7 m/s to 12.3 m/s (0.1 MPa–0.5 MPa). At the same the impact velocity, the dynamic compressive strength of the NC was greater than that of the RC. The absolute error between the NC and RC is shown in Figure 9 (in green). With the increase in impact velocity, the growth rate of dynamic compressive strength became smaller. This indicated that the influence of impact on concrete—first more obviously and then more slowly—approached smoothness.

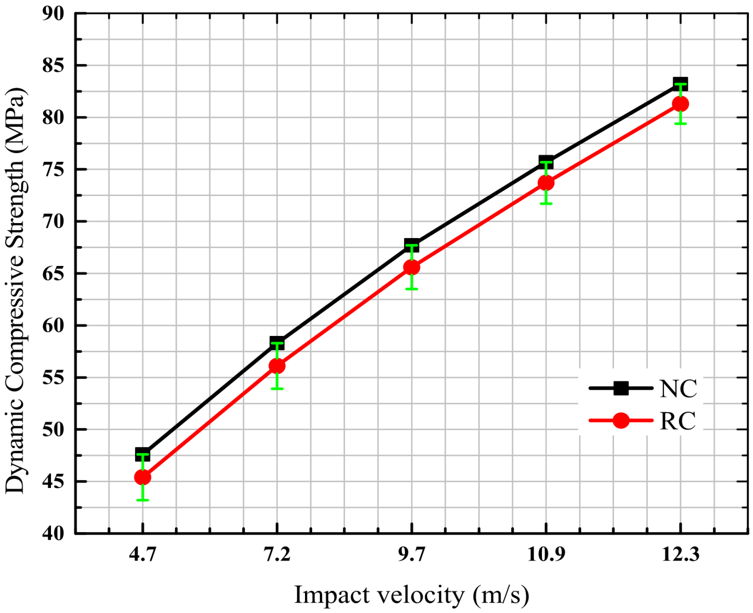

Figure 9. Relationship between impact velocity and dynamic compressive strength.

3.2.2. Dynamic Increase Factor

The influence of strain rates on the dynamic compressive strength is shown in Figure 10. The relationship between the strain rate and DIF was a logistic function form, and the coefficients between the NC and RC were different. The *R* square values of the NC and RC are 0.994 and 0.996, respectively. According to the experimental results and fitting curves, the expression of the DIF is shown in Equation (1) and Figure 11. The *R* square values of the NC and RC are 0.994 and 0.997, respectively, which was different from the expression [32]; the same function was logarithmic. Equation (1) has reasonable accuracy for evaluating the DIF of the RC.

$$\text{DIF} = a + b/\left[1 + (\dot{\varepsilon}_d/c)^d\right] \tag{1}$$

where a, b and c are constants, $\dot{\varepsilon}_d$ is the strain rate and d is the index.

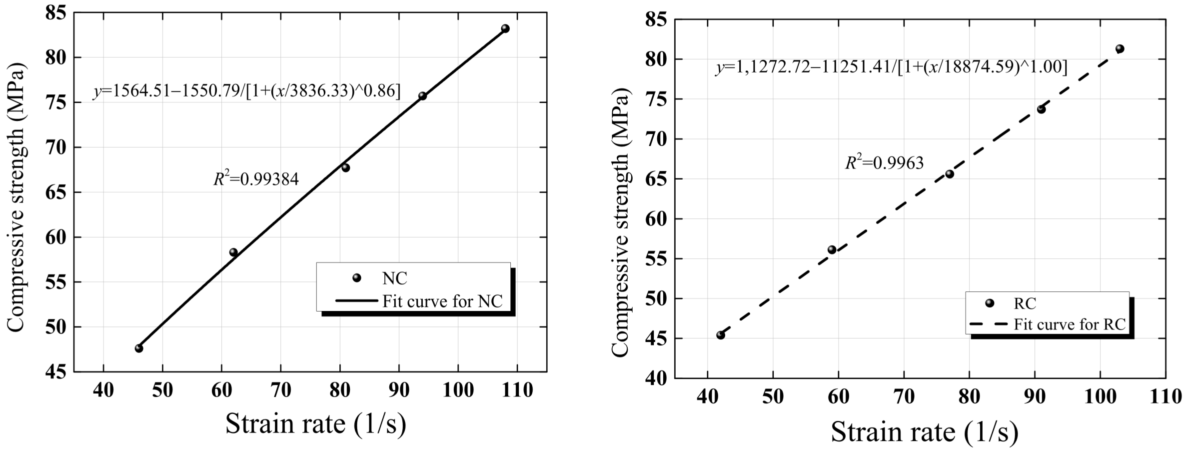

(**a**) (**b**)

Figure 10. Effect of strain rates on dynamic compressive strength. (**a**) Natural concrete; (**b**) recycled concrete.

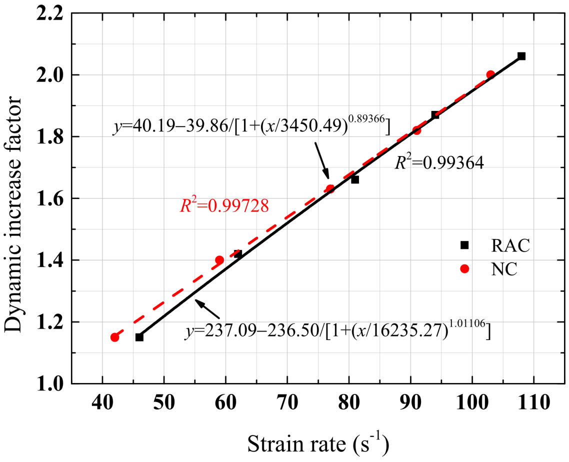

Figure 11. Dynamic increase factor of concrete.

3.2.3. Initial Elastic Modulus

To further study the initial elastic modulus of concrete, the stress–strain curves of concrete were fitted when the impact pressure was 0.3 MPa. The fitting curves (as shown in Figure 12) and initial elastic modulus (as shown in Figure 13) were obtained.

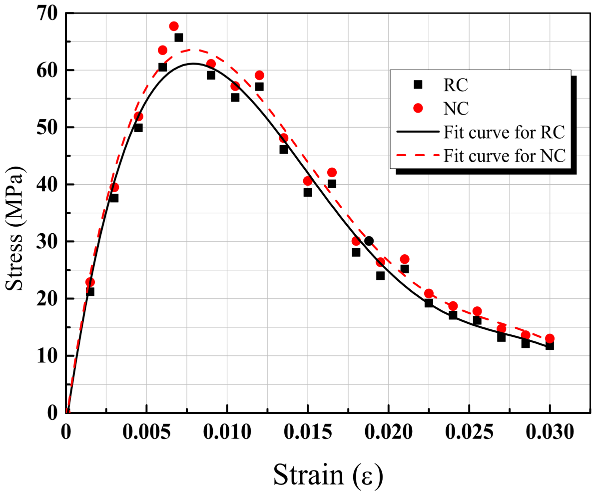

Figure 12. Dynamic compressive strength.

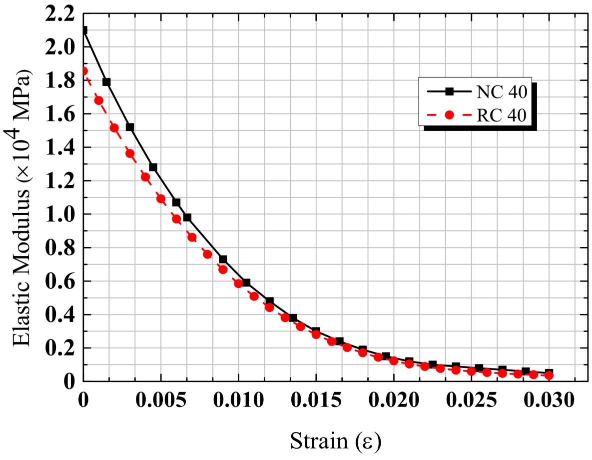

Figure 13. Initial elastic modulus.

According to the experimental results of the NC and RC, the fitting curve of stress is proportional to the biquadrate of the strain, as shown in Figure 12. A derivative of the stress is obtained the initial elastic modulus, as shown in Figure 13. It can be concluded that there was much difference between the initial elastic modulus of the NC and RC when the strain was less than 0.010, while they were in good agreement with each other when the strain was more than 0.010. Therefore, it can be concluded that RC can replace NC in some specific conditions.

3.2.4. Failure Modes

According to Figures 14 and 15, the failure modes of the NC and RC specimens under different impact loads can be obtained. Two cracks were observed on cross section of the NC when the impact pressure was 0.2 MPa. Figures 14a and 15a show that the RC is completely destroyed when compared to the NC. Concrete spalling occurred on the edge of specimens, which was accompanied by many micro-cracks, and the cracks presented as "H"-type. The NC specimen showed good integrity, while the RC specimen showed a more severe degree of damage. Some micro-cracks originated near the main crack of the NC specimen. When the impact pressure was 0.3 MPa, the concrete is crushed as shown in Figures 14b and 15b. However, the size of the NC was larger than that of the RC. There were about six fragments on the NC. When the impact pressure was 0.4 MPa, the concrete specimens were completely broken. Figures 14c and 15c show that the RC was seriously damaged. At the same impact pressure, the failure modes of the RC specimen were more damaged than those of the NC specimen. For the quasi-static test, the concrete cracking occurred from the edge of specimens to the center, while in the dynamic test, the concrete cracking occurred from the center to the edge.


(**a**) (**b**) (**c**)

Figure 14. Failure modes of NC specimen. (**a**) 0.2 MPa; (**b**) 0.3 MPa; (**c**) 0.4 MPa.


(**a**) (**b**) (**c**)

Figure 15. Failure modes of the RC specimen. (**a**) 0.2 MPa; (**b**) 0.3 MPa; (**c**) 0.4 MPa.

4. Numerical Model Validation

4.1. Numerical FEM Model

To estimate the accuracy of impact test results, ANSYS/LS-DYNA finite element software, developed by Ansys, Inc., Canonsburg, Pennsylvania, USA, was used to establish a three-dimensional finite element calculation model of SHPB impact tests. During the ANSYS/LS-DYNA simulation, the constitutive model of concrete is Holmquist-Johnson-Cook (HJC) model, as given in Table 3. The HJC model of the RC is given in Table 4. Figure 16 shows stress–strain curves of concrete. It included elastic stage (OA segment), plastic stage (AB segment) and close-grained stage components after crushing. At the elastic stage, the relationship between the stress and strain was linear. At the point of A, the stress reached the tensile strength of concrete. The corresponding stress was cracking stress. Then, the specimen entered the plastic stage after concrete cracking. Many cracks initiated with the increase in strain rate. Finally, the specimen entered the close-grained stage after crushing.

Table 3. HJC model of concrete.

Density ($kg{\cdot}m^{-3}$)	Shear Modulus (GPa)	Strength	Hardening Coefficient	Strain Rate Coefficient	Hardening Exponent	Compressive Strength (MPa)	Tensile Strength (MPa)	Strain Rate	Minimum Plastic Strain
2400	14.86	0.79	1.6	0.007	0.61	48	4	1×10^{-6}	0.01
Normalize strength (MPa)	Compressive strain	Volume strain	Stress (GPa)	Strain rate (compacted)	Damage constant 1	Damage constant 2	Material constant 1 (MPa)	Material constant 2 (MPa)	Material constant 3 (MPa)
7	16	1×10^{-3}	0.80	0.1	0.04	1.0	85	−171	208

Table 4. HJC model of the RC.

Density ($kg{\cdot}m^{-3}$)	Shear Modulus (GPa)	Strength	Hardening Coefficient	Strain rate Coefficient	Hardening Exponent	Compressive Strength (MPa)	Tensile Strength (MPa)	Strain Rate	Minimum Plastic Strain
2450	18.47	0.79	1.8	0.007	0.99	45	4	1×10^{-6}	0.01
Normalize strength (MPa)	Compressive strain	Volume strain	Stress (GPa)	Strain rate (compacted)	Damage constant 1	Damage constant 2	Material constant 1 (MPa)	Material constant 2 (MPa)	Material constant 3 (MPa)
7	15	8.0×10^{-4}	1.3	0.07	0.04	1.0	85	−171	208

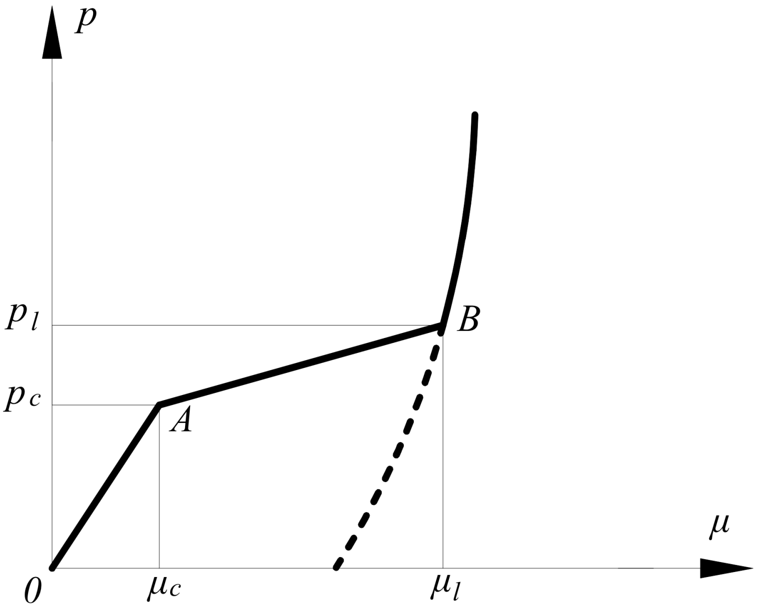

Figure 16. Stress–strain curve of concrete.

The contact automatic types were selected to simulate the interface between the specimen and the SHPB (surface to surface). The reliability and validity of model were verified when compared to the experimental values. The dynamic mechanics of the RC were further improved and proved whether RC can be used in actual engineering. For the SHPB, the parameters of the striker and pressure bar are given in Table 5. A quarter-scale model was established to simulate the whole SHPB impact process.

Table 5. Parameters of Striker and pressure bars.

Density (g/mm^3)	Elastic Modulus (MPa)	Poisson's Ratio	Yield Strength (MPa)	Tangent Modulus (MPa)	Failure Strain
7.8×10^{-3}	2.1×10^{5}	0.3	500	6×10^{2}	0.28

Impact velocities of 4.7 m/s (0.1 MPa), 9.6 m/s (0.3 MPa) and 12.2 m/s (0.5 MPa) were selected to simulate the impact process of the SHPB. The wave forms can be obtained through using the post-processing software LS-PREPOST, developed by Ansys, Inc., Canonsburg, Pennsylvania, USA. The direction of impact loads is shown in Figure 17a along the left to right. Figure 17b shows the model after meshing. The relationship between stress–strain and time was recorded by two different cements along the velocity direction of incident and transmitter bar. The final stress–strain curves were obtained after recalculation. This paper mainly investigated the dynamic mechanical properties of recycled concrete aggregate at the impact velocity of 9.6 m/s (0.3 MPa).

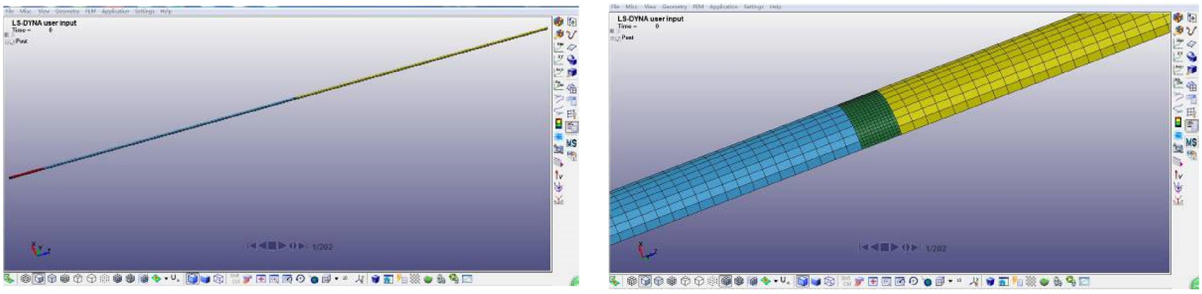

(**a**) (**b**)

Figure 17. Finite Element Model. (**a**) SHPB model; (**b**) mesh.

4.2. Impact Stress–Strain Curves

A monitoring unit was set on the surface of incident and transmitter bar. The wave form tendencies of the different concretes were basically similar to each other. The stress wave propagated in the bar, and the reflection phenomenon occurred on the contact interface between the input bar and the specimen. Because the strength of concrete was relatively low, the transmission wave was negligible. It was found that the NC's stress maximum of incident and transmission waves was higher than that of the RC. Nevertheless, the difference between the NC and RC specimens was small. These simulation results were coincident with the impact test results, while the peak value of the simulation results was higher than that of the test value.

According to Figure 18, it is obvious that the NC's dynamic compressive strength was larger than that of the RC. At the same impact pressure, the increasing tendency of stress was similar to the impact test results. However, the oscillating reaction did not occur at the descending stage. The reason was that the stress wave was assumed to be a constant and unchanged by the increase in simulation duration, while the stress wave varied with the increase in impact test duration.

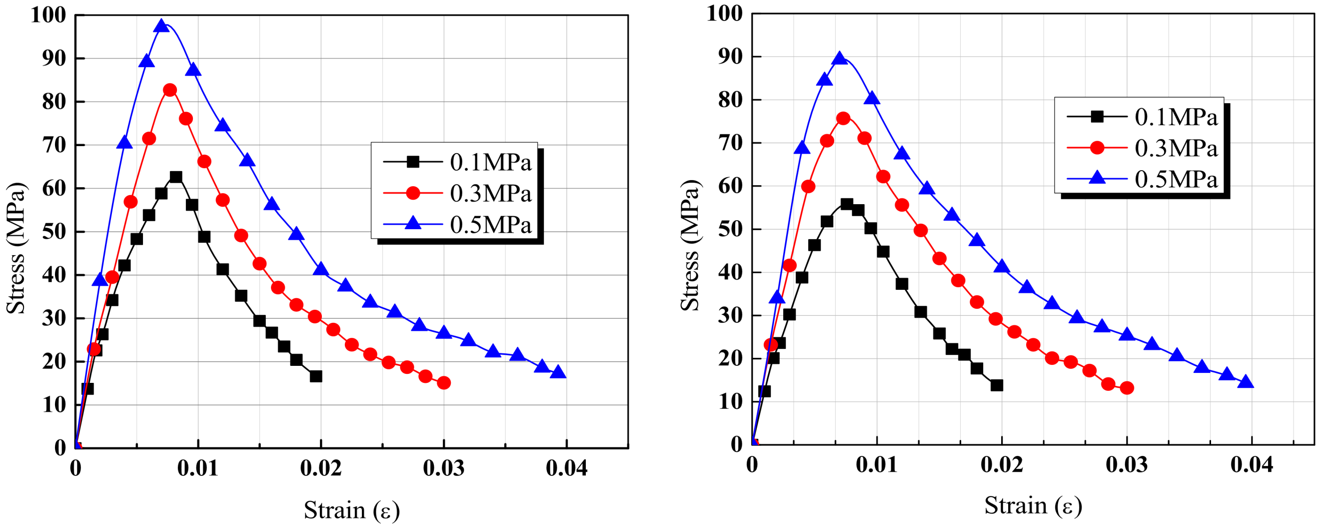

(**a**) (**b**)

Figure 18. Stress–strain curves of concrete. (**a**) Natural concrete; (**b**) recycled concrete.

The compressive stress–strain curves of concrete specimens under the same impact velocities are presented in Figure 19. In the figure, N/RC*i* (*i* = *S* and *T*) represents the simulation and test values of the NC and RC. The stress–strain curves presented similar tendencies under three different impact velocities. The test and simulation values of concrete specimens are in good agreement with each other, expect that the strain varied from 0.005 to 0.010. At the ascending stage, the stress–strain curves were consistent with each other when the strain was less than 0.001. With the increasing of impact velocities, the relative error of peak stress became smaller. At the descending stage, the stresses were approximately close to each other. This phenomenon became more obvious with increasing impact velocity. The simulation results showed good accuracy with the experimental results. It can be verified that the NC and RC had the same mechanical behavior under the impact loads, and the accuracy of the finite element model was validated. Therefore, RC can replace NC in some actual engineering.

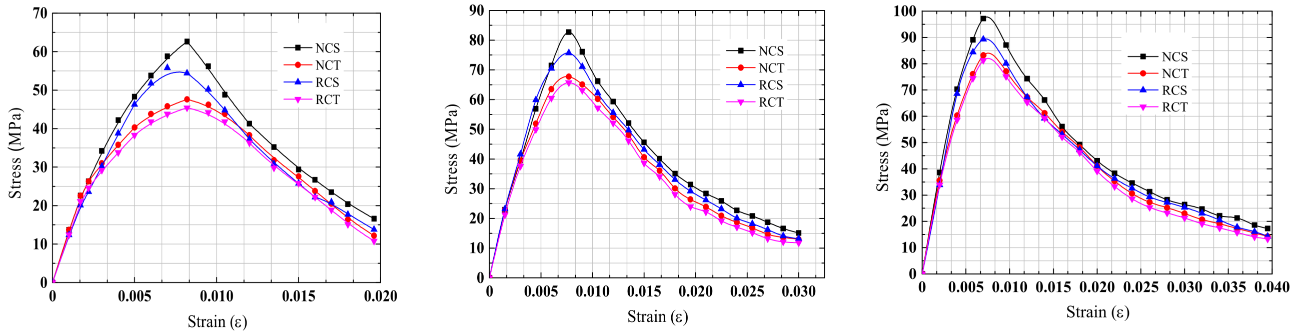

(**a**) (**b**) (**c**)

Figure 19. Compressive stress–strain curves of concrete. (**a**) 4.7 m/s; (**b**) 9.6 m/s; (**c**) 12.2 m/s.

4.3. Failure Modes

The failure modes of the RC (as shown in Figure 20) and NC (as shown in Figure 21) specimens showed similar behavior at three impact velocities. In this paper, only the failure modes at an impact velocity of 9.6 m/s were given. Figures 20 and 21 display the failure modes of concrete at different times. It was found that the failure tendencies of the NC and RC were very similar. At the initial impact velocities, the center elements were not destroyed and maintained good integrity, as shown in Figures 20a and 21a. With the increase in impact time, the concrete on the edge begins to fall and show damage, as shown in

Figures 20b and 21b. This means that a failure mode was developed. Then, the cracks gradually propagated to the center of the specimen, as shown in Figures 20c and 21c. Due to the size of the concrete specimens, the terminal of the specimens will easily produce the stress concentration phenomenon during loading. The failure modes of the specimens gradually extend from the edge to the center, as shown in Figures 20d and 21d. Figures 20e and 21e show that many through-cracks originate at the center of the specimens. The main parts of the specimens were completely separated and destroyed, as shown in Figures 20f and 21f. The overall failure process can be described as the stress wave having had a significant influence on the dynamic behavior. Compared to Figures 20 and 21, it can be concluded that multiple cracks initiate on the RC specimens at the same time. The damage degree of the RC was relatively heavier than that of the NC. The RC specimens were completely crushed. This also indicates that the impact resistance of the RC was slightly worse than that of the NC. This conclusion is basically consistent with the impact test results. Therefore, it was feasible to use the simulation software to make qualitative analysis of the SHPB impact test of the RC.

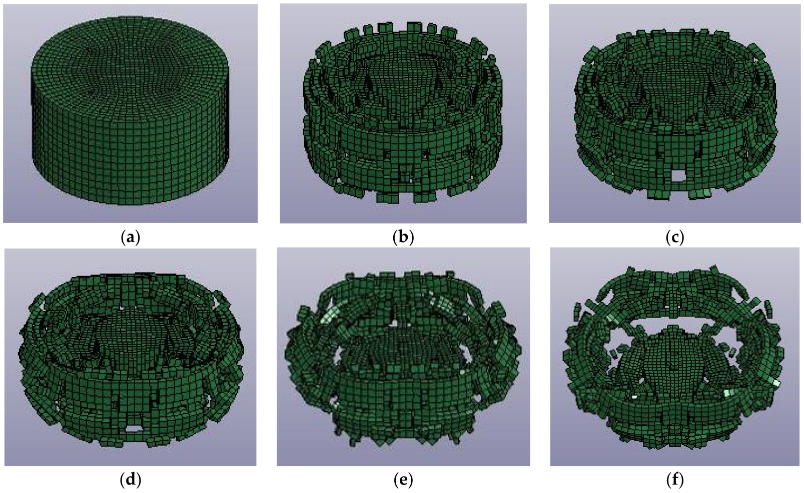

Figure 20. Failure modes of recycled concrete. (**a**) t = 0.0 ms; (**b**) t = 0.5 ms; (**c**) t = 0.7 ms; (**d**) t = 1.0 ms; (**e**) t = 1.5 ms; (**f**) t = 2.0 ms.

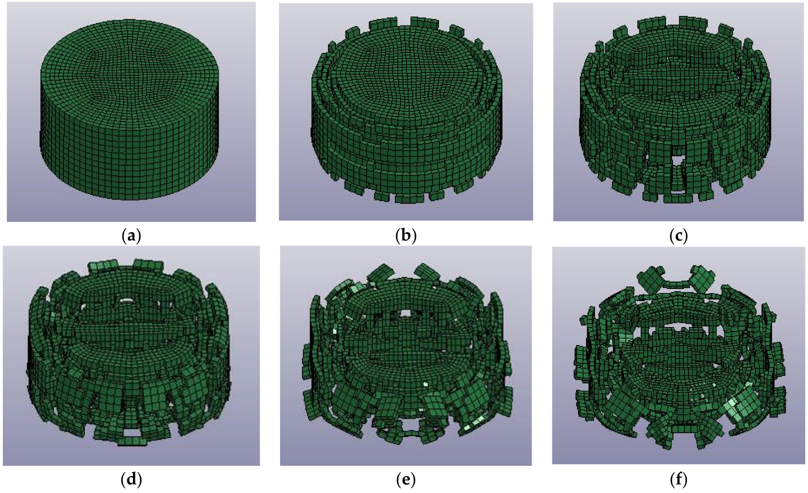

Figure 21. Failure modes of natural concrete. (**a**) t = 0.0 ms; (**b**) t = 0.5 ms; (**c**) t = 0.7 ms; (**d**) t = 1.0 ms; (**e**) t = 1.5 ms; (**f**) t = 2.0 ms.

5. Conclusions

In this paper, quasi-static and dynamic tests of the NC and RC specimens were investigated. The relationship between stress and strain, compressive strength, dynamic increase factor, initial elastic modulus and failure modes were studied in detail. Combined with the ANSYS/LS-DYNA finite element software, the whole impact process of the concrete was simulated. Finally, the main results were obtained as follows:

(1) Quasi-static test results showed that the compressive strength of the NC was about 1.05 times higher than that of the RC. The dynamic results obtained suggest that the compressive strength of the NC was higher than that of the RC. With the increase in impact velocity, the compressive strength and the dynamic increase factor increased gradually. According to the impact tests, the logistic function expression of dynamic increase factor was obtained.

(2) From the relationship between stress and the varying strain rates, it can be concluded that the stress–strain curves showed a linear behavior at the initial stage of loading. When the stress reached the maximum value, the curves presented a decreasing tendency. The concrete specimens presented the strain softening phenomenon.

(3) With the increase in impact velocity, the growth rate of dynamic compressive strength became smaller. The expression of DIF gives an adequate estimate of the dynamic compression strength of the RC and NC within the strain rate range of 40–100 s^{-1}. The proposed empirical model gives an adequate estimate of stress–strain curves of the RC and NC at the impact velocity of 9.6 m/s.

(4) The initial elastic modulus showed a decreasing tendency with the increase in strain. The strain had a significant influence on the initial elastic modulus when the strain was less than 0.010, while they were in good agreement with each other when the strain was more than 0.010.

(5) Failure modes can conclude that the damage degree of concrete developed from the edge of specimens. Then, the failure gradually extends to the center of the specimens. With the increase in impact time, many through-cracks originated at the center of specimens. Then, the main part of the specimens were completely separated and destroyed. The simulation results showed good agreement with the SHPB impact test. Therefore, this model was feasible for performing qualitative analysis of the SHPB impact test of the RC.

Author Contributions: W.D.: investigation, data curation, writing—original draft preparation. C.Y.: conceptualization, supervision, project administration, writing—review and editing. H.D.B.: writing—review and editing, supervision. C.L.: methodology, investigation. K.M.: methodology, investigation. H.Z.: resources, project administration. Y.P.: resources, project administration. All authors have read and agreed to the published version of the manuscript.

Funding: This research was funded by the National Science Foundation of China (Grant No. 52078122), Innovative Venture Technology Investment Project of Hunan Province (2018GK5028), Key R&D Program of Hunan Province (2018WK2111) and China Scholarship Council (202006090229).

Institutional Review Board Statement: Not applicable.

Informed Consent Statement: Not applicable.

Data Availability Statement: All data, models, and code generated or used during the study appear in the submitted article.

Acknowledgments: The authors would like to acknowledge the financial support from the National Science Foundation of China, Innovative Venture Technology Investment Project of Hunan Province, Key R&D Program of Hunan Province and China Scholarship Council.

Conflicts of Interest: The authors declare no conflict of interest.

References

1. Islam, M.J.; Islam, K.; Shahjalal, M.; Khatun, E.; Islam, S.; Razzaque, A.B. Influence of different types of fibers on the mechanical properties of recycled waste aggregate concrete. *Constr. Build. Mater.* **2022**, *337*, 127577. [CrossRef]
2. Huang, Y.J.; Wang, T.C.; Sun, H.L.; Li, C.X.; Yin, L.; Wang, Q. Mechanical properties of fibre reinforced seawater sea-sand recycled aggregate concrete under axial compression. *Constr. Build. Mater.* **2022**, *331*, 127338. [CrossRef]
3. McGinnis, M.J.; Davis, M.; Rosa, A.D.L.; Weldon, B.D.; Kurama, Y.C. Strength and stiffness of concrete with recycled concrete aggregates. *Constr. Build. Mater.* **2017**, *154*, 258–269. [CrossRef]
4. Akbarnezhad, A.; Ong, K.C.G.; Zhang, M.H.; Tam, C.T.; Foo, T.W.J. Microwave-assisted beneficiation of recycled concrete aggregates. *Constr. Build. Mater.* **2011**, *25*, 3469–3479. [CrossRef]
5. Braga, A.M.; Silvestre, J.D.; Brito, J.D. Compared environmental and economic impact from cradle to gate of concrete with natural and recycled coarse aggregates. *J. Clean. Prod.* **2017**, *162*, 529–543. [CrossRef]
6. Wang, C.Q.; Xiao, J.Z. Evaluation of the stress-strain behavior of confined recycled aggregate concrete under monotonic dynamic loadings. *Cement. Concrete. Comp.* **2018**, *87*, 149–163. [CrossRef]
7. Xuan, D.X.; Zhan, B.J.; Poon, C.S. Durability of recycled aggregate concrete prepared with carbonated recycled concrete aggregates. *Cement. Concrete. Comp.* **2017**, *84*, 214–221. [CrossRef]
8. Saravanakumar, P.; Abhiram, K.; Manoj, B. Properties of treated recycled aggregates and its influence on concrete strength characteristics. *Constr. Build. Mater.* **2016**, *111*, 611–617. [CrossRef]
9. Song, I.H.; Ryou, J.S. Hybrid techniques for quality improvement of recycled fine aggregate. *Constr. Build. Mater.* **2014**, *72*, 56–64. [CrossRef]
10. Du, W.P. *Research on Beneficiation Technique of High Quality Recycled Concrete Aggregate*; Xi'an University of Science and Technology: Xi'an, China, 2017. (In Chinese)
11. Aslani, F.; Ma, G.W.; Wan, D.L.Y.; Muselin, G. Development of high-performance self-compacting concrete using waste recycled concrete aggregates and rubber granules. *J. Clean. Prod.* **2018**, *182*, 553–566. [CrossRef]
12. Feng, W.H.; Tang, Y.C.; He, W.M.; Wei, W.B.; Yang, Y.M. Mode I dynamic fracture toughness of rubberised concrete using a drop hammer device and split Hopkinson pressure bar. *J. Build. Eng.* **2022**, *48*, 103995. [CrossRef]
13. Bai, W.F.; Shen, J.X.; Guan, J.F.; Wang, J.Y.; Yuan, C.Y. Study on compressive mechanical properties of reycled aggregate concrete with silica fume at different strain rates. *Mater. Today. Commun.* **2022**, *31*, 103444. [CrossRef]
14. Tang, Y.X.; Xiao, J.Z.; Zhang, H.H.; Duan, Z.H.; Xia, B. Mechanical properties and uniaxial compressive stress-strain behavior of fully recycled aggregate concrete. *Constr. Build. Mater.* **2022**, *323*, 126546. [CrossRef]
15. Chen, A.J.; Han, X.Y.; Chen, M.; Wang, X.Y.; Wang, Z.H.; Guo, T.T. Mechanical and stress-strain behavior of basalt fiber reinforced rubberized recycled coarse aggregate concrete. *Constr. Build. Mater.* **2020**, *260*, 119888. [CrossRef]
16. Xiao, J.Z.; Li, L.; Shen, L.M.; Poon, C.S. Compressive behaviour of recycled aggregate concrete under impact loading. *Cement. Concrete. Res.* **2015**, *71*, 46–55. [CrossRef]
17. Xiao, J.Z.; Zhang, K.J.; Akbarnezhad, A. Variability of stress-strain relationship for recycled aggregate concrete under uniaxial compression loading. *J. Clean. Prod.* **2018**, *181*, 753–771. [CrossRef]
18. Ramesh, K.T.; Hogan, J.D.; Kimberley, J.; Stickle, A. A review of mechanisms and models for dynamic failure, strength, and fragmentation. *Planet. Space. Sci.* **2015**, *107*, 10–23. [CrossRef]
19. Rao, M.C.; Bhattacharyya, S.K.; Barai, S.V. Behaviour of recycled aggregate concrete under drop weight impact load. *Constr. Build. Mater.* **2011**, *25*, 69–80.
20. Kong, X.Z.; Fang, Q.; Chen, L.; Wu, H. A new material model for concrete subjected to intense dynamic loadings. *Int. J. Impact. Eng.* **2018**, *120*, 60–78. [CrossRef]
21. Guo, H.; Shi, C.J.; Guan, X.M.; Zhu, J.P.; Ding, Y.H.; Ling, T.C.; Zhang, H.B.; Wang, Y.L. Durability of recycled aggregate concrete—A review. *Cement. Concrete. Comp.* **2018**, *89*, 251–259. [CrossRef]
22. Luccioni, B.; Isla, F.; Forni, D.; Cadoni, E. Modelling UHPFRC tension behavior under high strain rates. *Cement. Concrete. Comp.* **2018**, *91*, 209–220. [CrossRef]
23. Jin, L.; Yu, W.X.; Du, X.L.; Zhang, S.; Li, D. Meso-scale modelling of the size effect on dynamic compressive failure of concrete under different strain rates. *Int. J. Impact. Eng.* **2019**, *125*, 1–12. [CrossRef]
24. Li, W.G.; Luo, Z.Y.; Long, C.; Wu, C.Q.; Duan, W.H.; Shah, S.P. Effects of nanoparticle on the dynamic behaviors of recycled aggregate concrete under impact loading. *Mater. Design.* **2016**, *112*, 58–66. [CrossRef]
25. Li, W.G.; Luo, Z.Y.; Wu, C.Q.; Tam, V.W.Y.; Duan, W.H.; Shah, S.P. Experimental and numerical studies on impact behaviors of recycled aggregate concrete-filled steel tube after exposure to elevated temperature. *Mater. Design.* **2017**, *136*, 103–118. [CrossRef]
26. Li, W.G.; Luo, Z.Y.; Wu, C.Q.; Duan, W.H. Impact performances of steel tube-confined recycled aggregate concrete (STCRAC) after exposure to elevated temperatures. *Cement. Concrete. Comp.* **2018**, *86*, 87–97. [CrossRef]
27. Li, L.J.; Tu, G.R.; Lan, C.; Liu, F. Mechanical characterization of waste-rubber-modified recycled-aggregate concrete. *J. Clean. Prod.* **2016**, *124*, 325–338. [CrossRef]
28. Liu, F.; Chen, G.X.; Li, L.J.; Guo, Y.C. Study of impact performance of rubber reinforced concrete. *Constr. Build. Mater.* **2012**, *36*, 604–616. [CrossRef]
29. Wijayasundara, M.; Mendis, P.; Crawford, R.H. Integrated assessment of the use of recycled concrete aggregate replacing natural aggregate in structural concrete. *J. Clean. Prod.* **2018**, *174*, 591–604. [CrossRef]

30. Prince, M.J.R.; Gaurav, G.; Singh, B. Splice strength of steel reinforcement embedded in recycled aggregate concrete. *Constr. Build. Mater.* **2018**, *160*, 156–168. [CrossRef]
31. Liu, F.; Feng, W.H.; Xiong, Z.; Tu, G.R.; Li, L.J. Static and impact behaviour of recycled aggregate concrete under daily temperature variations. *J. Clean. Prod.* **2018**, *191*, 283–296. [CrossRef]
32. Bui, N.K.; Satomi, T.; Takahashi, H. Improvement of mechanical properties of recycled aggregate concrete basing on a new combination method between recycled aggregate and natural aggregate. *Constr. Build. Mater.* **2017**, *148*, 376–385. [CrossRef]

buildings

MDPI

Article

Effect of Moisture Condition and the Composition of Aggregate from Demolition Waste on Strength and Workability Properties of Recycled Concrete

Saied Kashkash [1,2], Oliver Czoboly [2,3] and Zoltan Orban [2,*]

[1] Department of Civil Engineering, Marcel Breuer Doctoral School of Architecture, University of Pécs, H-7624 Pécs, Hungary; saied.kashkash@mik.pte.hu
[2] Structural Diagnostics and Analysis Research Group, Faculty of Engineering and Information Technology, University of Pécs, H-7624 Pécs, Hungary; czobolyo@btclabor.hu
[3] Beton Technológia Centrum Ltd., H-1107 Budapest, Hungary
* Correspondence: orban.zoltan@mik.pte.hu

Abstract: Large quantities of construction and demolition waste are generated annually, and in many parts of the world, it is disposed of in landfills. Utilizing this waste to produce coarse aggregates for concrete production offers a potentially sustainable approach that mitigates environmental impacts. Despite the widespread encouragement of using recycled aggregates as a substitute for natural coarse aggregates, practical applications remain limited, and the concrete production industry continues to primarily rely on exploiting natural resources. The recycling of concrete waste derived from the demolition of obsolete or damaged buildings as structural concrete has been seldom realized thus far, primarily due to regulatory constraints and concerns regarding technological difficulties. This paper presents a case study to demonstrate that, with meticulous preparation, concrete waste from a demolished building can be rendered suitable for use as structural concrete. The experimental investigation examined how the proportion of recycled aggregates obtained from a demolished building and the moisture content influenced the properties of fresh and hardened concrete. The results revealed an increase in the compressive strength of the hardened recycled concrete as a higher proportion of recycled coarse aggregate was incorporated into the mixture. Moreover, pre-soaked recycled coarse aggregates were found to improve the workability of the recycled concrete mixture significantly. The results highlight the significant potential of utilizing concrete waste as a valuable resource in the production of ready-mix concrete for structural applications, provided that appropriate measures are taken to optimize its properties.

Keywords: recycled aggregates moisture condition; recycled concrete workability; recycled concrete compressive strength; construction waste recycling; sustainable concrete

1. Introduction

Concrete, as the most widely used construction material, plays a vital role in meeting the growing demand for new buildings, infrastructure, and roads, especially as global population increases [1,2]. However, the conventional production of concrete, which relies on cement, fine aggregates, coarse aggregates, and water, is associated with significant environmental challenges [3,4]. Cement production, a key component of concrete, consumes vast amounts of energy and is a major contributor to global carbon dioxide (CO_2) emissions, accounting for approximately 5–7% of anthropogenic CO_2 emissions worldwide [5,6]. The urgent need to address climate change and achieve sustainability in the construction industry has prompted global efforts to reduce CO_2 emissions and enhance environmental protection and resource management.

Over the past few decades, governments worldwide have been actively promoting sustainable policies aimed at reducing environmental impacts and achieving economic gains [7]. These policies employ economic instruments such as taxation to discourage waste disposal in landfills while incentivizing the recovery and reintegration of construction and demolition waste (C&DW) into the production cycle. Although concrete offers numerous advantageous physical and mechanical properties, its structural lifespan is typically limited to 50–100 years, after which structures are often dismantled. In Europe, a significant number of structures constructed after World War II are approaching the end of their design life, resulting in a projected increase in C&DW volumes in the near future [8]. In fact, C&DW accounted for approximately 36% of Europe's total waste in 2016 [9].

The concept of finding beneficial applications for demolition waste is not new and applications following World War II have been documented by Gluzhge [10]. Presently, C&DW is either disposed of in landfills, as predominantly observed in developing countries, or processed in recycling plants in more developed nations. Recycled aggregates derived from C&DW are primarily employed in low-grade applications, such as raw material for the cement industry, soil stabilization, pavement bricks, road construction subbase material, and embankment fill [11]. Notably, during the reconstruction project of Puskas Stadium in Hungary, approximately 60% of the demolished waste was successfully re-used on-site or for other construction projects, while the remaining 40% was sent to landfills [12].

The properties of recycled aggregates can vary significantly, influenced by factors such as the acquisition method, particle size, attached mortar, and original concrete quality [13]. Demolished rubble from construction sites often contains various materials, including concrete, tiles, soil, bricks, and wood [14]. These additional contaminants diminish the quality of recycled aggregate, particularly when the rubble results from disasters such as wars, earthquakes, or floods. Several studies have explored various methods and treatments aimed at improving the quality of recycled aggregates. Ouyang et al. [15] concluded that the production of high-quality recycled aggregate could be achieved by either removing or strengthening the attached mortar. A comparative study by Katz [16], used silica fume impregnation to enhance the surface porosity of recycled aggregate and ultrasonic cleaning in removing loose particles from the surface of recycled aggregates. The results indicated that silica fume impregnation resulted in a greater enhancement in the compressive strength of the recycled concrete when compared to ultrasonic cleaning. In a study conducted by Junak et al. [17], geopolymer slurry was applied to coat the recycled concrete aggregates (RCA) with the aim of improving its surface characteristics. The findings revealed that this treatment led to an increase in the density of the RCA and a decrease in its water absorption capacity. According to Pandurangan et al. [18], various treatments such as mechanical, thermal, or chemical methods for removing attached mortar from recycled aggregates have shown positive effects on bond strength and increased compressive strength when compared to untreated recycled aggregate. In their study, it was observed that polymer impregnation had the most significant impact on enhancing the physical and mechanical properties of the recycled concrete aggregates (RCA), followed by the attached mortar (AM) removal method and the accelerated carbonation curing process. Although it is possible to produce high-quality recycled aggregate with properties comparable to natural aggregates, achieving such quality necessitates costly, time-consuming, and energy-intensive treatments involving the removal of contaminants, classification, washing, screening, and multiple crushing stages [19]. Recycled aggregates (R.A) generally exhibit lower density and higher water absorption than natural aggregates due to the presence of attached mortar [20]. The fine fraction of recycled aggregate tends to have a higher mortar content, making it unsuitable for use in structural concrete production [21]. Ensuring the quality of the original concrete also presents challenges in standardization. RILEM (International Union of Laboratories and Experts in Construction Materials, Systems, and Structures) guidelines recommend avoiding the use of recycled coarse aggregates with water absorption exceeding 7% in concrete production [22]. However, European standards allow for the substitution of up to 50% of natural coarse aggregates with recycled coarse aggregates under certain conditions [23]. Studies by Corinaldesi [24] and Limbachiya et al. [25] have found no significant influence on the compressive strength of recycled concrete when replacing up to 30% of natural aggregates with recycled aggregates. Moisture conditions of recycled aggregates significantly affect the workability of recycled concrete due to the higher water absorption of recycled aggregates. Several studies have investigated the effects of different moisture conditions on the properties of RA and the resulting concrete mixtures. The findings from these studies have been inconsistent and influenced by multiple variables. In 2004, Poon et al. [26] observed that high percentages of recycled aggregate, particularly in the saturated surface dried (SSD) state, resulted in less cohesive concrete mixtures and potential bleeding during casting, leading to reduced compressive strength. Also, it was noted that the optimal moisture condition was found to be the air-dried condition. Brand et al. [27] reported the highest compressive strengths were achieved using 80% SSD state, and the strength properties for recycled concrete aggregates (RCA) concrete were greatest when the RCA was at least in the partially-saturated moisture state. Other studies [28–31], reported that the presaturation of recycled aggregate negatively impacts concrete strength and durability. The duration of presoaking has been identified as a determining factor in the flowability of fresh recycled concrete. Zhang et al. [32] concluded that partially saturated RA is beneficial for the performance of recycled concrete. Given the existing technological uncertainties, further investigations are necessary to promote the use of sustainable concrete incorporating recycled aggregate.

This paper presents the outcomes of a case study conducted in Pécs, Hungary, where recycled aggregates were obtained from a demolished reinforced concrete building constructed in the 1970s. The mechanical and physical properties of the recycled aggregates were examined, and subsequent concrete production incorporated these aggregates in two moisture conditions: dried and partially saturated. The results highlight the significant potential of utilizing concrete waste as a valuable resource in the production of ready-mix concrete for structural applications, provided that appropriate measures are taken to optimize its properties.

2. Materials and Methods

2.1. Materials

2.1.1. Cement

All concrete mixes were produced using CEM II/B-S 42.5N Portland Slag Cement as the binder material. The cement was supplied by a local supplier and complied with EN 197-1:2011 [33] without any cementitious replacement.

2.1.2. Natural Aggregates

Two types of coarse natural aggregates were used, each with different characteristics. The first type was natural round aggregate (N) extracted from riverbeds or lakes, that had a round shape and smooth surface. The second type was natural crushed stone (NC), which had an angular shape and rough surface as shown in Figure 1a.

(**a**) (**b**)

Figure 1. (**a**) Illustrates the distinction between natural (N) and recycled (R) fine and coarse aggregates, (**b**) Coarse aggregates: Natural (N), Crushed Stone (NC), and Recycled (R).

2.1.3. Recycled Aggregate

For this study, recycled aggregate (R)—see Figure 1b—was obtained from the demolition of a 25-story building in Pécs, Hungary in 2016. It is estimated that approximately 22,549 t of debris were generated from the demolition (see Figure 2a). During the demolition, the reinforced concrete elements were dismantled using a tower crane (see Figure 2b) and then broken into transportable pieces by a demolition machine equipped with a crushing head, while separating the recyclable reinforcing steel. The collected debris was transported to a landfill site where it was crushed into smaller. After primary and secondary crushing, the debris size ranged between 0/40 mm. The rubble was stored in a landfill near Pécs for several years. Although the demolished concrete rubble was considered a good-quality raw material being relatively homogeneous, its recycling as a raw material for concrete has not yet been fully realized. A significant portion of the debris remains in the landfill awaiting further use (see Figure 2c). Samples were collected from two storage locations and then graded to the required sizes for concrete mixing. Only the coarse recycled aggregate RCA with a diameter of 4/16 mm was used in the preparation of concrete mixes. On the other hand, the fine recycled portion, measuring 0/4 mm, which constitutes approximately 35% of the total weight of the collected rubble, was not included in the concrete mixture due to its composition primarily consisting of crushed mortar. (see Figure 1b). The preparation method and mixing approach were specifically designed to facilitate the implementation of recycled aggregate in ready-mix concrete production. By simplifying the processing steps and ensuring compatibility with existing concrete plant production lines, encouraging the industrial sector to adopt sustainable practices without significant modifications to their existing processes.

Figure 2. (**a**) High rise building that was the source of recycled aggregate ; (**b**) Demolition technique; (**c**) Stored debris ; **(d)** Steps for partially saturating the recycled aggregates.

2.1.4. Chemical Admixtures

Different dosages of a water-reducing admixture were used to achieve the desired workability. The superplasticizer used was Sika ViscoCrete-7710, with a recommended dosage ranging from 0.2% to 2% of the cement content (mc%).

2.2. Experimental Work

Eight concrete mixes were prepared, each varying in the content of recycled coarse aggregate and moisture conditions. Mix N served as the control mix and utilized natural round aggregates (N). Mix NC was a conventional concrete mix in which 50% of the coarse round aggregates were replaced with crushed stone (NC). The remaining six mixes incorporated different proportions of recycled coarse aggregate (15%, 30%, and 50%) and were prepared in both dried and partially saturated conditions. The recycled aggregates were submerged in water for 1 h, drained, and then left at room temperature for an additional 1 h before mixing (see Figure 2d). Table 1 provides an overview of the coarse aggregate content and moisture condition for each mix.

Table 1. Coarse aggregates content in each mix.

Mix Code	N	NC	R	RW *
Mix N	100%	-	-	-
Mix NC	50%	50%	-	-
Mix R15	85%	-	15%	-
Mix R30	70%	-	30%	-
Mix R50	50%	-	50%	-
Mix RW15	85%	-	-	15%
Mix RW30	70%	-	-	30%
Mix RW50	50%	-	-	50%

* Recycled aggregates partially saturated.

2.2.1. Mix Design

The targeted concrete class for all mixes was C30/37, with a desired workability class of F3 according to MSZ EN 12350-5 standards [34]. The water/cement ratio was fixed at 0.52, and the maximum aggregate diameter (Dmax) was set to 16 mm. The type and content of cement remained constant across all mixes. The concrete composition was determined using the absolute volume method. The specific mixture proportions for each mix are presented in Table 2.

Table 2. Concrete mix proportions.

Concrete Mix	Cement (kg)	Water (kg)	W/C	Sand (kg)	Coarse Aggregate (kg)				Plasticizer (mc% *)	Density kg/m^3
					Natural		Recycled			
					N	NC	R	RW		
N	350	182	0.52	732	1098	-	-	-	0.18	2363
NC	350	182	0.52	732	549	549	-	-	0.13	2372
R15	350	182	0.52	732	933	-	165	-	0.31	2356
R30	350	182	0.52	732	769	-	329	-	0.51	2361
R50	350	182	0.52	732	549	-	549	-	0.50	2315
RW15	350	182	0.52	732	933	-	-	165	0.23	2326
RW30	350	182	0.52	732	769	-	-	329	0.31	2322
RW50	350	182	0.52	732	549	-	-	549	0.10	2312

* The percentage of superplasticizer to the weight of cement.

The same mixing method and sequence were followed for all mixes. The natural coarse aggregates (N&NC) and fine aggregates were in an oven-dried condition by drying them at 105 °C for 24 h and then were cooled at room temperature before mixing. While the recycled aggregate (R) was used in two states: oven-dried (as in mixes R15, R30, and R50) and partially saturated (RW) (as in mixes RW15, RW30, and RW50). Tests were conducted on the aggregates to determine their characteristics. The grading curves for recycled and natural aggregates exhibited similar trends, as depicted in Figure 3. These curves were generated in accordance with the EN 933-1 standard [35].

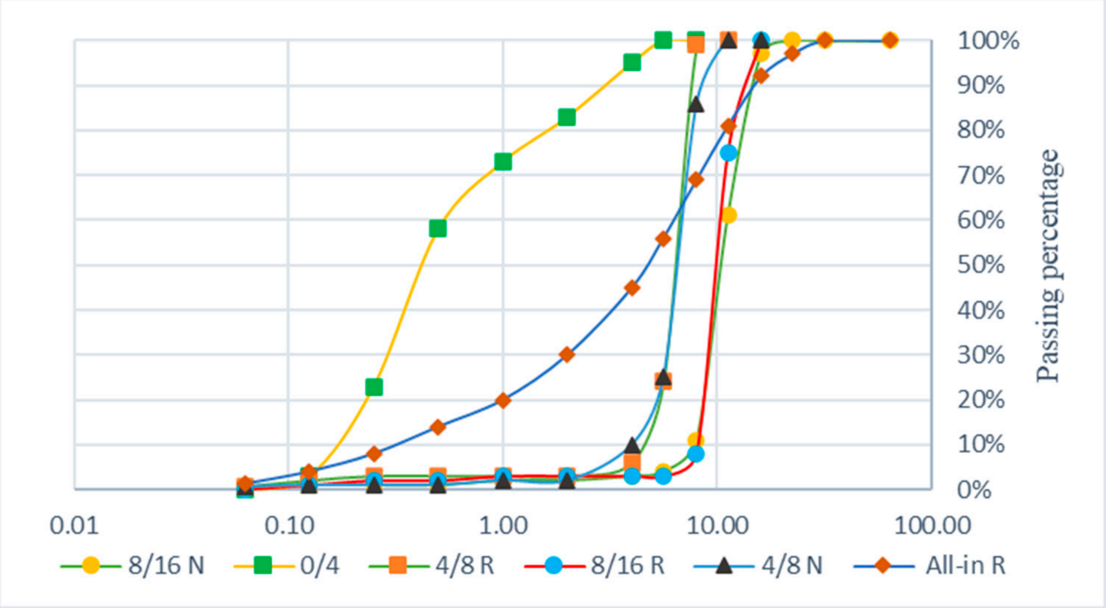

Figure 3. Grading curves of the fine and coarse aggregates.

The physical properties of the aggregates, such as particle density and water absorption, were tested in compliance with the requirements of EN standards [36]. The quality of the recycled aggregate was further assessed by evaluating its mechanical properties, including resistance to fragmentation, as determined by the Los Angeles and Micro-Deval aggregate impact tests. These tests were carried out in accordance with standard EN-1097-2 [37,38] procedures. In addition, shape index and bulk density tests were carried out to gain an overall understanding of the aggregate properties [39,40]. Contaminants, including wood, paper, tiles, bricks, and metal debris, were present in the recycled aggregates (R) and were removed during the separation process to obtain the required fractions. The total mass of these contaminants was less than 10% (Rc 90 and Rcu 95), classifying the recycled aggregate as type A according to EN 206 standards [23]. The coarse aggregate with sizes ranging from 4–16 mm was divided into two standard fractions: 4/8 mm and 8/16 mm using vibrating mechanical sieves, constituting 44% and 56% respectively of the coarse aggregate volume. The volume of the different aggregate fractions was the same in each mixture: 0/4 fraction accounted for 40%, 4/8 fraction accounted for 26%, and 8/16 fraction accounted for 34%.

2.2.2. Concrete Batching Procedure

The concrete batching procedure involved using a pan-type mixer with a 50-L capacity for preparing all the concrete mixtures. To simplify the process and make it more practical, the conventional mixing sequence was followed. The coarse aggregate was added first, followed by cement, and then the sand was added to cover the cement and prevent it from dusting. Dry mixing was performed for approximately 60 s. Water was then gradually added during mixing to ensure a uniform mixture. The wet mixture was then mixed for an additional 1–3 min, during which the superplasticizer was gradually added to achieve the desired workability. If needed, this final step was repeated. Following the mixing process, the fresh properties of the concrete were tested to assess the quality of the mixture.

After that, the concrete mixtures were cast in standard size moulds with dimensions of (150 × 150 × 150) mm and compacted using a mechanical vibrating table. After casting the specimens were stored at room temperature of (20 ± 2) °C and 95% relative humidity (RH) for 24 h, and then cured in water until the designated testing time after 28 days (according to the Hungarian standard, MSZ 4798:2016) [41].

2.2.3. Concrete Testing Methods

Tests were conducted to evaluate various properties of the concrete mixes. Regarding the fresh concrete properties, the consistency class was determined by performing the flow table test in accordance with the EN 12350-5:2009 standard [34]. The fresh density of the concrete was measured and calculated following the guidelines provided in the EN 12350-6:2009 standard [42]. Additionally, the air content was determined using the pressure gauge method specified in the EN 12350-7:2009 standard [43].

Moving on to the hardened concrete properties, the compressive strength of the concrete mixes was assessed at 28 days using three standard-sized (150 mm) cubical specimens per mix following the EN 12390-3:2009 standard [44]. The hardened density of each concrete mix was calculated in accordance with the EN 12390-7:2009 standard [45].

Furthermore, the splitting tensile strength of the concrete mixes was evaluated at 28 days using three standard-sized (150 mm) cubical specimens per mix following the EN 12390-6:2009 standard [46].

3. Results and Discussion

3.1. Recycled Aggregates

Table 3 presents the mechanical and physical properties of the recycled aggregate.

Table 3. Recycled aggregates properties.

Type of Test	Recycled Aggregate Size (mm)		Standard
	4/8	8/16	
Water absorption (24 h)	7.9%	6.1%	EN 1097-6 [36]
Density	2.32 g/cm^3	2.37 g/cm^3	EN 1097-6 [36]
Los Angeles (L.A%)	34.8%		EN 1097-2 [37]
Micro-Deval MDE	25%		EN 1097-1 [38]
Bulk density	1.11 g/cm^3	1.13 g/cm^3	EN 1097-3 [39]
Shape index SI	18.3	22.1	EN 933-4 [40]

3.2. Aggregate Moisture Content and Fresh Concrete Properties

3.2.1. Workability

To assess the influence of the moisture condition and recycled aggregate content on the workability of the concrete mixes, the flow table test was conducted directly after mixing according to MSZ EN 12350-5:2009 Testing fresh concrete—Part 5 [34]. The results are shown in Figure 4.

As the substitution ratio of dried recycled aggregate increased, it was anticipated that the workability would decrease due to its higher water absorption. To ensure the desired flowability comparable to the control mix, a higher dosage of superplasticizer was required.

When recycled aggregates or crushed stone were used in the mixes (Mix R15, R30, R50, and Mix NC), the angular shape and rough surface texture of the aggregate affected the flowability of the fresh concrete. Angular shapes have a larger surface area compared to rounded shapes, and the rough surface texture requires more cement paste, leading to higher water absorption and lower concrete consistency which is in line with the findings from other studies [29,47,48].

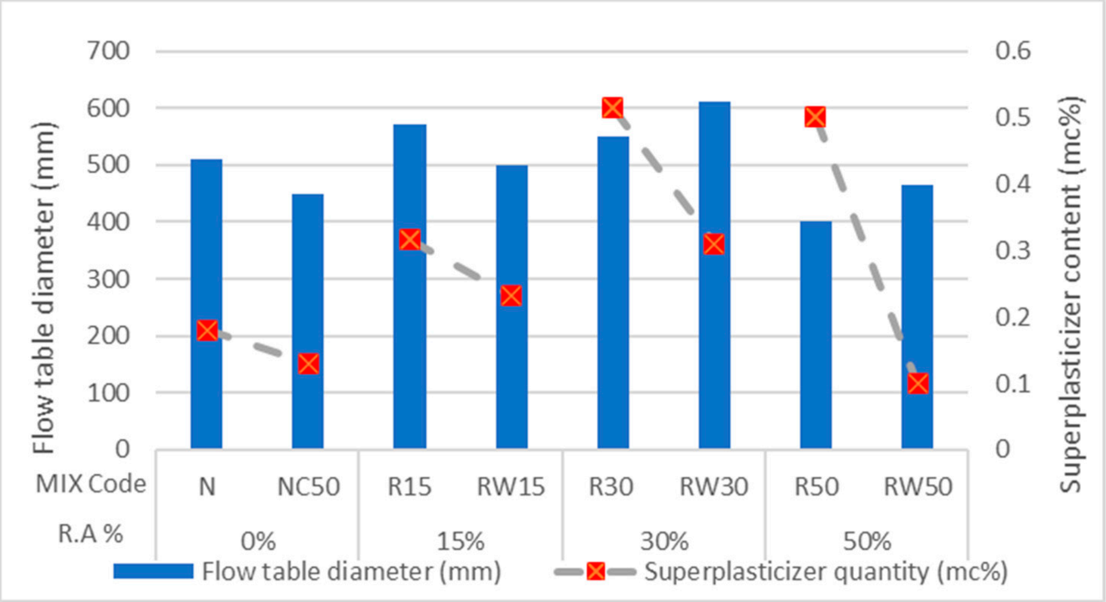

Figure 4. Flow table results and superplasticizer content for both the dried and partially saturated conditions of recycled aggregates.

In contrast to fully saturated wet aggregate or saturated surface dried (SSD) conditions, where excessive free water leads to aggregate segregation and decreased compressive strength as concluded in previous studies [26,48], partially saturating the recycled aggregate improved the workability of recycled concrete and reduced the need for superplasticizer, without any significant effects on the hardened concrete properties.

Through a process of pre-soaking the recycled aggregate for 1 h and subsequently exposing it to air at room temperature for 1 h, the moisture condition of the aggregate was partially saturated, as shown in Figure 5.

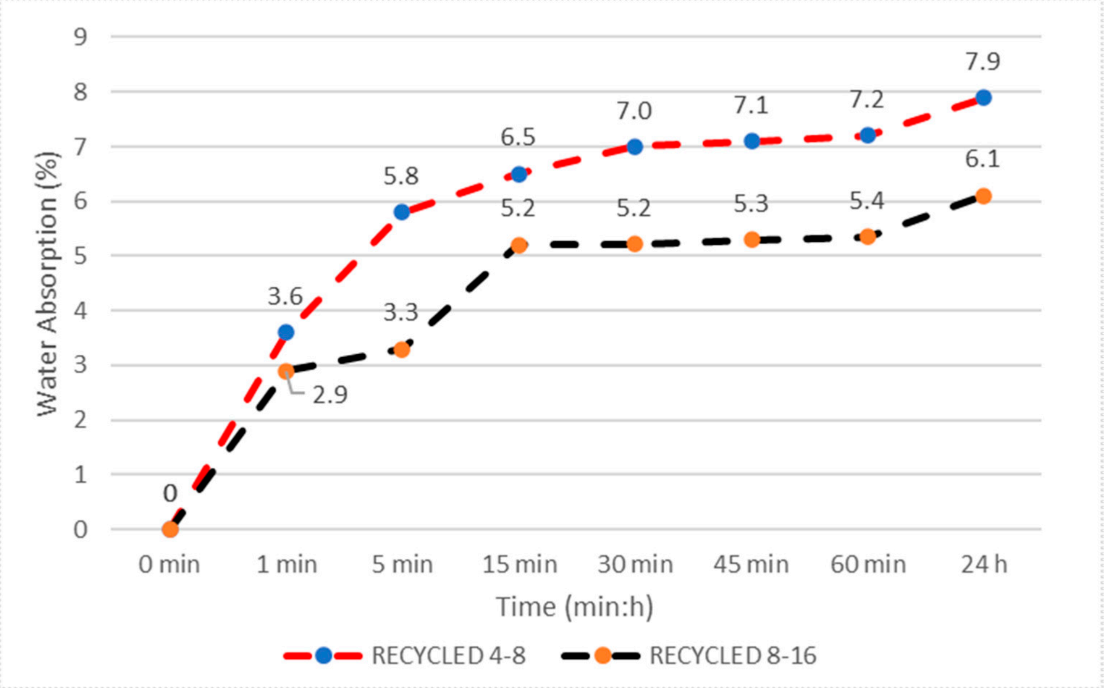

Figure 5. Water absorption of recycled aggregate over 24 h period.

This approach provided improved control over the water content in the mixture and enhanced the overall workability of the concrete mixture. Additionally, reducing the dosage of superplasticizer is more cost effective.

3.2.2. Density and Air Content

The density of recycled aggregate is approximately 5–8% lower than that of natural aggregates due to the presence of attached mortar, which is more porous compared to natural round aggregates. However, the density of recycled concrete did not exhibit significant differences compared to conventional concrete. This can be attributed to the cubical shape of the recycled aggregate, which facilitates better packing. There was an observed increase in the air content of the recycled concrete, likely caused by factors such as the higher porosity of the recycled aggregate, resulting in an elevated entrained air content see Figure 6.

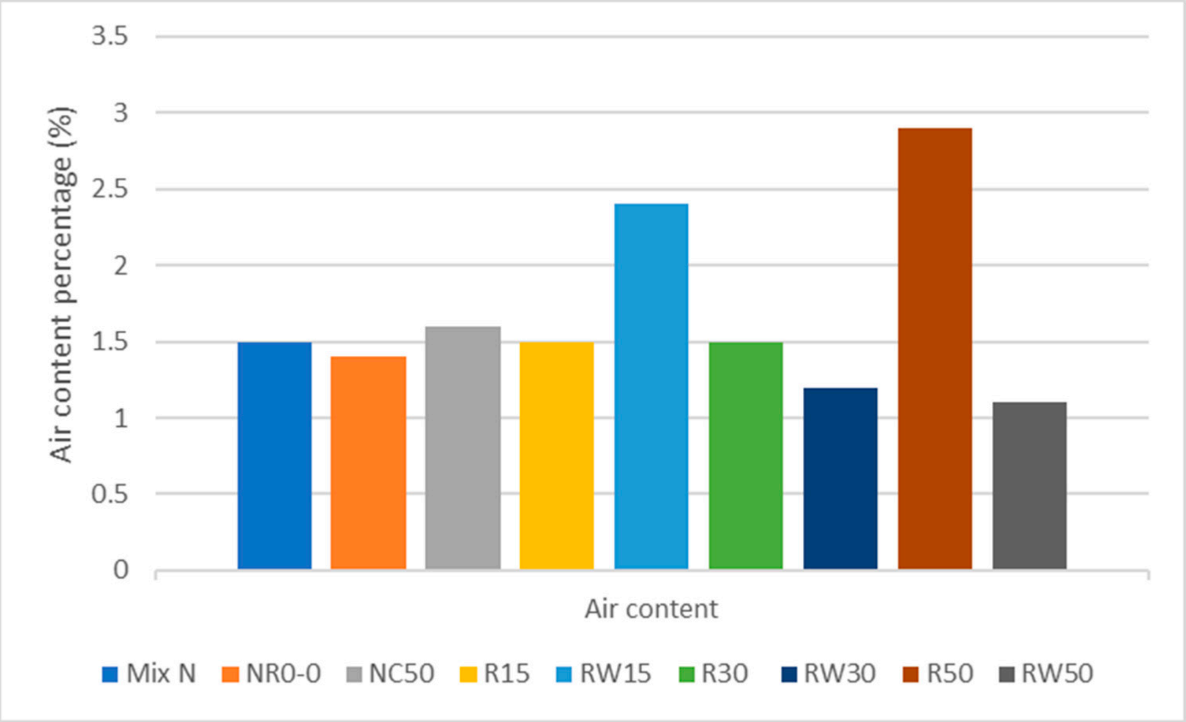

Figure 6. Air content results of fresh concrete.

3.3. Hardened Concrete Properties

3.3.1. Compressive Strength and Hardened Density

The incorporation of dried recycled aggregate demonstrated a slight increase in the compressive strength with a higher percentage of replacement, as depicted in Figure 6. This indicates that the dried recycled aggregate can contribute to the overall strength of the concrete, even at higher replacement percentages.

In contrast, when presoaked recycled aggregate was utilized, the compressive strength remained comparable to that of the control mix. This suggests that the partial saturation of the recycled aggregate aided in preserving its strength properties and preventing any substantial decrease in compressive strength, see Figure 7.

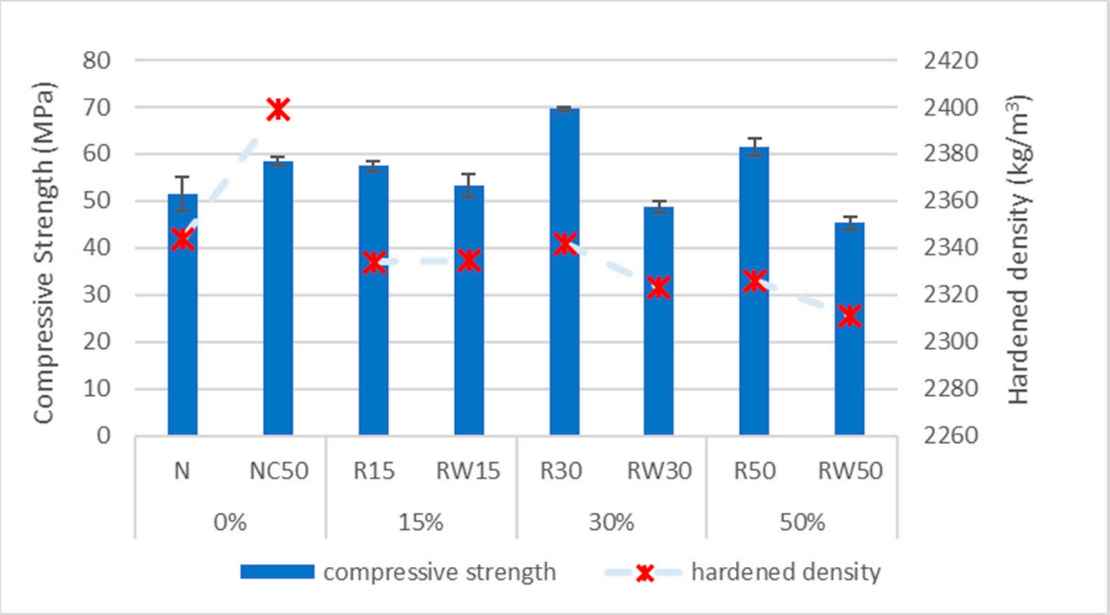

Figure 7. The compressive strength and the hardened density results (average values and ranges).

3.3.2. Splitting Tensile Strength

With 15% and 30% substitution with recycled coarse aggregate, the splitting tensile increased by 10% and 20% respectively while partially saturating the recycled aggregates had a slight impact. However, using 50% recycled aggregates dried or partially saturated aggregates led to lower splitting tensile strength as shown in Figure 8.

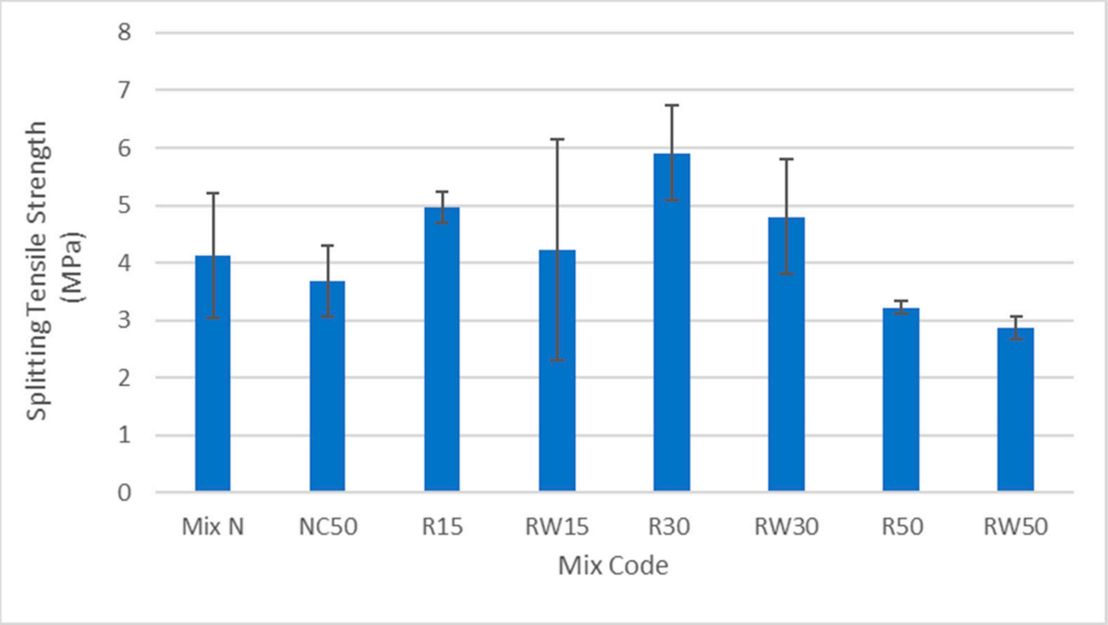

Figure 8. Splitting tensile strength results (average values and ranges).

4. Conclusions

The results of the research demonstrate that recycled coarse aggregate (RCA) can serve as a viable alternative to natural coarse aggregates in various concrete applications. It has been demonstrated through a case study that the appropriate use of RCA in the concrete production process not only reduces the reliance on natural resources in the construction industry, but also provides the opportunity to achieve concrete properties required for structural applications.

The use of recycled aggregate, whether in dried or partially saturated condition, can yield recycled concrete with comparable properties to conventional concrete mixes, even for structural applications. However, the optimal saturation level of the recycled aggregate to mitigate workability loss without compromising compressive strength can vary depending on factors such as the source, quality, composition of the recycled material, and other environmental conditions.

Conducting comprehensive testing and evaluation of the specific recycled aggregate being employed is essential to determine the ideal saturation level for achieving the desired workability while maintaining the compressive strength of the concrete. Partial saturation, where the recycled aggregate is soaked in water for a limited duration without reaching full saturation, has shown promise in enhancing the properties of recycled concrete compared to using fully saturated recycled aggregate or adding excess water directly to the mix. This approach improves workability without introducing excessive water content, which can lead to aggregate segregation and reduced compressive strength. By finding the right balance between moisture content and aggregate proportions, it is feasible to optimize the fresh and hardened properties of recycled concrete while minimizing potential adverse effects. Although the attained compressive strength of recycled concrete proves its suitability for structural applications, additional research is needed to evaluate its durability and performance under various exposure conditions.

This highlights the importance of understanding the specific characteristics of the recycled aggregate and tailoring the concrete mixture accordingly to achieve the desired concrete performance while considering environmental conditions and sustainability goals.

5. Recommendations and Future Research Directions

In addition to the findings of this study, there are several areas that warrant further research and could provide valuable opportunities for future work. Firstly, investigating the long-term durability of concrete utilizing recycled aggregates in various exposure conditions, such as freeze-thaw cycles or when exposed to chemicals, would provide insights into the performance and resilience of recycled concrete over time. Additionally, exploring the potential of incorporating additives or admixtures to enhance the properties and performance of recycled concrete could allow the optimization of its characteristics for different applications. Conducting life cycle assessment studies to assess the environmental impact and sustainability aspects of using recycled aggregates would provide a comprehensive understanding of its benefits and contribute to informed decision-making in construction projects. Moreover, assessing the feasibility of utilizing recycled aggregates in specialized concrete applications, including high-strength concrete or self-compacting concrete, would further expand the potential applications of recycled materials.

In terms of recommendations for practice, it is crucial to promote the adoption of guidelines and standards for the production, quality control, and use of recycled aggregates in concrete. Establishing clear criteria and regulations ensures consistent and reliable performance and fosters confidence in utilizing recycled materials. Increasing awareness and educating industry professionals about the potential benefits of recycled aggregates is also vital to encourage their widespread use. Collaboration with regulatory bodies and stakeholders to develop policies and incentives that support the use of recycled aggregates will further drive the adoption of sustainable practices in the construction industry. Lastly, establishing partnerships between researchers, manufacturers, and contractors can facilitate the transfer of knowledge and best practices, promoting the effective implementation of recycled aggregates in construction projects. By addressing these future research directions and implementing the recommended practices, the utilization of recycled aggregates can be maximized, contributing to a more sustainable and environmentally friendly construction industry.

Author Contributions: Conceptualization, methodology, validation; formal analysis; investigation; resources, data curation, S.K., O.C. and Z.O.; writing—original draft preparation, S.K.; writing—review and editing, S.K. and Z.O.; visualization, S.K.; supervision, Z.O.; project administration, Z.O.; funding acquisition, Z.O. All authors have read and agreed to the published version of the manuscript.

Funding: This research received no external funding.

Data Availability Statement: Not applicable.

Acknowledgments: The authors would like to thank the Faculty of Engineering and Information Technology of the University of Pécs for their financial support.

Conflicts of Interest: The authors declare no conflict of interest.

References

1. Naik, T.R. Sustainability of Concrete Construction. *Pract. Period. Struct. Des. Constr.* **2008**, *13*, 98–103. [CrossRef]
2. Zhong, X.; Hu, M.; Deetman, S.; Steubing, B.; Lin, H.X.; Hernandez, G.A.; Harpprecht, C.; Zhang, C.; Tukker, A.; Behrens, P. Global Greenhouse Gas Emissions from Residential and Commercial Building Materials and Mitigation Strategies to 2060. *Nat. Commun.* **2021**, *12*, 6126. [CrossRef]
3. Serres, N.; Braymand, S.; Feugeas, F. Environmental Evaluation of Concrete Made from Recycled Concrete Aggregate Implementing Life Cycle Assessment. *J. Build. Eng.* **2016**, *5*, 24–33. [CrossRef]
4. Bravo, M.; De Brito, J.; Pontes, J.; Evangelista, L. Mechanical Performance of Concrete Made with Aggregates from Construction and Demolition Waste Recycling Plants. *J. Clean. Prod.* **2015**, *99*, 59–74. [CrossRef]
5. Worrell, E.; Price, L.; Martin, N.; Hendriks, C.; Meida, L.O. Carbon Dioxide Emissions from the Global Cement Industry. *Annu. Rev. Energy Environ.* **2001**, *26*, 303–329. [CrossRef]
6. Prakash, R.; Raman, S.N.; Subramanian, C.; Divyah, N. Eco-Friendly Fiber-Reinforced Concretes. In *Handbook of Sustainable Concrete and Industrial Waste Management: Recycled and Artificial Aggregate, Innovative Eco-Friendly Binders, and Life Cycle Assessment*; Woodhead Publishing: Thorston, UK, 2022; pp. 109–145. [CrossRef]
7. Piccinali, A.; Diotti, A.; Plizzari, G.; Sorlini, S. Impact of Recycled Aggregate on the Mechanical and Environmental Properties of Concrete: A Review. *Materials* **2022**, *15*, 1818. [CrossRef]
8. Lotfi, S.; Eggimann, M.; Wagner, E.; Mróz, R.; Deja, J. Performance of Recycled Aggregate Concrete Based on a New Concrete Recycling Technology. *Constr. Build. Mater.* **2015**, *95*, 243–256. [CrossRef]
9. European Statistics-Eurostat. *Energy, Transport and Environment Statistics*, 2020 Ed. ed; European Commission: Luxembourg, 2020; ISBN 9789276207375.
10. World Business Council for Sustainable Development. *The Cement Sustainability Initiative: Executive Brief*; World Business Council for Sustainable Development: Geneva, Switzerland, 2012; p. 42.
11. Kox, S.; Vanroelen, G.; Van Herck, J.; de Krem, H.; Vandoren, B. Experimental Evaluation of the High-Grade Properties of Recycled Concrete Aggregates and Their Application in Concrete Road Pavement Construction. *Case Stud. Constr. Mater.* **2019**, *11*, e00282. [CrossRef]
12. The Demolition of the Puskás Ferenc Stadium Will Last for 8 Months-Daily News Hungary. Available online: https://dailynewshungary.com/the-demolition-of-the-puskas-ferenc-stadium-will-last-for-8-months/ (accessed on 23 July 2022).
13. Sim, G.; Quattrone, M.; Monteiro, W.; Cazacliu, B.G. Current Applications of Recycled Aggregates from Construction and Demolition: A Review. *Materials* **2021**, *14*, 1700.
14. Tam, V.W.Y.; Soomro, M.; Evangelista, A.C.J. A Review of Recycled Aggregate in Concrete Applications (2000–2017). *Constr. Build. Mater.* **2018**, *172*, 272–292. [CrossRef]
15. Ouyang, K.; Shi, C.; Chu, H.; Guo, H.; Song, B.; Ding, Y.; Guan, X.; Zhu, J.; Zhang, H.; Wang, Y.; et al. An Overview on the Efficiency of Different Pretreatment Techniques for Recycled Concrete Aggregate. *J. Clean. Prod.* **2020**, *263*, 121264. [CrossRef]
16. Katz, A. Treatments for the Improvement of Recycled Aggregate. *J. Mater. Civ. Eng.* **2004**, *16*, 597–603. [CrossRef]
17. Junak, J.; Sicakova, A. Effect of Surface Modifications of Recycled Concrete Aggregate on Concrete Properties. *Buildings* **2017**, *8*, 2. [CrossRef]
18. Pandurangan, K.; Dayanithy, A.; Om Prakash, S. Influence of Treatment Methods on the Bond Strength of Recycled Aggregate Concrete. *Constr. Build. Mater.* **2016**, *120*, 212–221. [CrossRef]
19. Quattrone, M.; Angulo, S.C.; John, V.M. Energy and CO_2 from High Performance Recycled Aggregate Production. *Resour. Conserv. Recycl.* **2014**, *90*, 21–33. [CrossRef]
20. Wang, B.; Yan, L.; Fu, Q.; Kasal, B. A Comprehensive Review on Recycled Aggregate and Recycled Aggregate Concrete. *Resour. Conserv. Recycl.* **2021**, *171*, 105565. [CrossRef]
21. Chen, X.; Li, Y.; Kang, X.; Fan, Y. Study on Recycled Concrete Powders as Mineral Admixture in Recycled Concrete Study on Recycled Concrete Powders as Mineral Admixture in Recycled Concrete. *IOP Conf. Ser. Earth Environ. Sci.* **2019**, *330*, 022113. [CrossRef]
22. Silva, R.V.; De Brito, J.; Dhir, R.K. Properties and Composition of Recycled Aggregates from Construction and Demolition Waste Suitable for Concrete Production. *Constr. Build. Mater.* **2014**, *65*, 201–217. [CrossRef]

23. *MSZ EN 206:2013*; Concrete-Specification, Performance, Production and Conformity. Hungarian Standards Institution: Budapest, Hungary, 2017.
24. Corinaldesi, V. Structural Concrete Prepared with Coarse Recycled Concrete Aggregate: From Investigation to Design. *Adv. Civ. Eng.* **2011**, *2011*, 283984. [CrossRef]
25. Limbachiya, M.C.; Leelawat, T.; Dhir, R.K. Use of Recycled Concrete Aggregate in High-Strength Concrete. *Mater. Struct. Mater. Constr.* **2000**, *33*, 574–580. [CrossRef]
26. Poon, C.S.; Shui, Z.H.; Lam, L.; Fok, H.; Kou, S.C. Influence of Moisture States of Natural and Recycled Aggregates on the Slump and Compressive Strength of Concrete. *Cem. Concr. Res.* **2004**, *34*, 31–36. [CrossRef]
27. Brand, A.S.; Roesler, J.R.; Salas, A. Initial Moisture and Mixing Effects on Higher Quality Recycled Coarse Aggregate Concrete. *Constr. Build. Mater.* **2015**, *79*, 83–89. [CrossRef]
28. Ferreira, L.; De Brito, J.; Barra, M. Influence of the Pre-Saturation of Recycled Coarse Concrete Aggregates on Concrete Properties. *Mag. Concr. Res.* **2011**, *63*, 617–627. [CrossRef]
29. Kebaili, O.; Layachi, B.; Nourredine, A. Influence of Moisture Conditioning of Recycled Aggregates on the Properties of Fresh and Hardened Concrete. *J. Clean. Prod.* **2013**, *54*, 282–288. [CrossRef]
30. Guerzou, T.; Mebrouki, A.; Castro-Gomes, J. Influence of Pre-Saturation of Recycled Aggregates on Concrete Workability and Strength. *Int. J. Eng. Res. Afr.* **2019**, *42*, 76–85. [CrossRef]
31. García-González, J.; Rodríguez-Robles, D.; Juan-Valdés, A.; del Pozo, J.M.M.; Guerra-Romero, M.I. Pre-Saturation Technique of the Recycled Aggregates: Solution to the Water Absorption Drawback in the Recycled Concrete Manufacture. *Materials* **2014**, *7*, 6224–6236. [CrossRef]
32. Zhang, H.; Xu, X.; Liu, W.; Zhao, B.; Wang, Q. Influence of the Moisture States of Aggregate Recycled from Waste Concrete on the Performance of the Prepared Recycled Aggregate Concrete (RAC)—A Review. *Constr. Build. Mater.* **2022**, *326*, 126891. [CrossRef]
33. *MSZ EN 197-1:2011*; Cement—Part 1: Composition, Specifications, and Conformity Criteria for Common Cements. Hungarian Standards Institution: Budapest, Hungary, 2011.
34. *MSZ EN 12350-5:2009*; Testing Fresh Concrete—Part 5: Flow Table Test. Hungarian Standards Institution: Budapest, Hungary, 2009.
35. *MSZ EN 933-1:1998*; Tests for Geometrical Properties of Aggregates—Part 1: Determination of Particle Size Distribution—Sieving Method. Hungarian Standards Institution: Budapest, Hungary, 1998.
36. *MSZ EN 1097-6:2006*; Tests for Mechanical and Physical Properties of Aggregates—Part 6: Determination of Particle Density and Water Absorption. Hungarian Standards Institution: Budapest, Hungary, 2006.
37. *MSZ EN 1097-2:2006*; Tests for Mechanical and Physical Properties of Aggregates—Part 2: Methods for Determination of Resistance to Fragmentation (Los Angeles Test). Hungarian Standards Institution: Budapest, Hungary, 2006.
38. *MSZ EN 933-5:1998*; Tests for Geometrical Properties of Aggregates—Part 5 Determination of Percentage of Crushed and Broken Surfaces in Coarse Aggregate Particles Essais. Hungarian Standards Institution: Budapest, Hungary, 2005.
39. *MSZ EN 1097-3:2006*; Tests for Mechanical and Physical Properties of Aggregates—Part 3: Determination of Loose Bulk Density and Voids. Hungarian Standards Institution: Budapest, Hungary, 2006.
40. *MSZ EN 933-4:2008*; Tests for Geometrical Properties of Aggregates—Part 4: Determination of Particle Shape—Shape Index. Hungarian Standards Institution: Budapest, Hungary, 2008.
41. *MSZ 4798:2016*; Aggregates for Concrete. Hungarian Standards Institution: Budapest, Hungary, 2016.
42. *EN 12350-6:2009*; Testing Fresh Concrete—Part 6: Density. European Committee for Standardization: Luxembourg, 2009.
43. *EN 12350-7:2009*; Testing Fresh Concrete—Part 7: Air Content—Pressure Methods. European Committee for Standardization: Luxembourg, 2009.
44. *EN 12390-3:2009*; Testing Hardened Concrete—Part 3: Compressive Strength of Test Specimens. European Committee for Standardization: Luxembourg, 2009.
45. *EN 12390-7:2009*; Testing Hardened Concrete—Part 7: Density of Hardened Concrete. European Committee for Standardization: Luxembourg, 2009.
46. *EN 12390-6:2009*; Testing Hardened Concrete—Part 6: Tensile Splitting Strength of Test Specimens. European Committee for Standardization: Luxembourg, 2009.
47. Sagoe-Crentsil, K.K.; Brown, T.; Taylor, A.H. Performance of Concrete Made with Commercially Produced Coarse Recycled Concrete Aggregate. *Cem. Concr. Res.* **2001**, *31*, 707–712. [CrossRef]
48. de Andrade Salgado, F.; de Andrade Silva, F. Recycled Aggregates from Construction and Demolition Waste towards an Application on Structural Concrete: A Review. *J. Build. Eng.* **2022**, *52*, 104452. [CrossRef]

buildings

Article

Microscopic Mechanism and Reagent Activation of Waste Glass Powder for Solidifying Soil

Yuze Hong [1,2], Xinyi Xu [3,4], Chaojie Zhang [2,4,*], Zehai Cheng [1,*] and Guanshe Yang [5]

[1] Institute of Civil and Architectural Engineering, Zhejiang University of Science and Technology, Hangzhou 310023, China; hongyuze2021@163.com
[2] Zhejiang Provincial Key Laboratory of Water Conservancy Disaster Prevention and Mitigation, Hangzhou 310020, China
[3] Houston International Institute, Dalian Maritime University, Dalian 116026, China; xinyi_xu2003@163.com
[4] Zhejiang Institute of Hydraulics & Estuary, Hangzhou 310020, China
[5] Ningbo Raw Water Co., Ltd., Ningbo 315000, China; bgs.bx@163.com
* Correspondence: zcjie2004@126.com (C.Z.); chengzh2008@163.com (Z.C.)

Abstract: Glass waste products represent a significant environmental concern, with an estimated 1.4 billion tons being landfilled globally and 200 million tons annually. This results in a significant use of land resources. Therefore, it would be highly advantageous to develop a new method for disposing of waste glass. Waste glass can be recycled and ground into waste glass powder (WGP) for use in solidified soil applications as a sustainable resource. This study is based on solidified soil research, wherein NaOH, $Ca(OH)_2$, and Na_2SO_4 were incorporated as activators to enhance the reactivity of WGP. The optimal solidified soil group was determined based on unconfined compressive strength tests, which involved varying the activator concentrations and WGP content in combination with cement. X-ray diffraction (XRD) was used to study the composition of solidified soil samples. Microscopic pore characteristics were investigated using scanning electron microscopy (SEM), and the Image J software was employed to quantify the number and size of pores. Fourier-transform infrared spectroscopy (FTIR) was employed to examine the activation effect of waste glass powder. This study investigated the solidification mechanism and porosity changes. The results demonstrate that the addition of activated WGP to solidified soil enhances its strength, with a notable 12% increase in strength achieved using a 6% $Ca(OH)_2$ solution. The use of 2% concentration of Na_2SO_4 and NaOH also shows an increase in strength of 7.6% and 8.6%, respectively, compared to the sample without WGP. The XRD and SEM analyses indicate that activated WGP enhances the content of hydrates, reduces porosity, and fosters the formation of a more densely packed solidified soil structure.

Keywords: activation; solidified soil; strength; pore pattern; material content; Fourier-transform infrared spectroscopy

1. Introduction

Waste glass can be effectively reused by converting it into waste glass powder (WGP) and incorporating it into solidified soil. Previous studies have explored the feasibility of reusing WGP [1,2]. However, the utilization of WGP poses several challenges despite its potential benefits. Firstly, glass and other utensils are typically found in a stable SiO_4 state, which complicates the transformation process from broken glassware to activated WGP. Furthermore, while WGP obtained through various processes contains essential hydroxide elements such as silicon and aluminum, it lacks calcium, which impedes its ability to achieve cohesive properties independently. Experiments have shown that substituting cement with inactivated WGP can reduce sample strength [3–5]. The successful resolution of the aforementioned challenges makes the potential of manufactured WGP immensely significant. Many scholars have focused on glass powder as an auxiliary cement component. Gao X. [6] illustrated through in-depth thermal analysis that while the reactivity of WGP in a silicate cement system may be lower compared to fly ash, it shows remarkable similarity in an alkali-activated system, thereby substantiating the feasibility of using WGP as a substitute for fly ash. Additionally, it has been observed that WGP ground from glass of varying colors shows distinctive levels of reactivity [7–9]. In the area of particle dimensions, finely ground WGP possesses unique pozzolanic activity, Research has found [10–15] that glass contains a large amount of amorphous SiO_2, and there is also a high content of oxides such as Fe_2O_3 and Al_2O_3 in glass. As the particle size of glass powder decreases, it promotes the release of more amorphous SiO_2 and oxides, thus unveiling its promising potential as an adjunct cementitious component [16,17]. The particle size of WGP can be significantly diminished through the use of physical grinding techniques [18,19]. Studies have highlighted that WGP particles measuring below 100 µm are more adept at manifesting pozzolanic activity [20], particularly demonstrating the heightened reactivity of WGP particles beneath 38 µm [20–23]. Moreover, several academics posit [24] that the refinement of WGP plays a pivotal role in fortifying the strength of composite glass powder structures. This enhancement could be attributed to the meticulous dispersion of tiny WGP particles within the cement paste, ultimately contributing to a superior particle-size distribution of the cementitious material. Furthermore, the work of Yue Long [25] underscores the efficacy of alkaline activation in leaching WGP to generate active SiO_2. However, it is important to note that excessive alkali may incite alkali-aggregate reactions, which could reduce the strength and durability of the sample. Kong Qingqiu [26] conducted experiments which showed that WGP activated by a reagent has a significant early excitation effect and a later weakening effect. Conversely, Shi [27] believes that excitation of WGP by reagents can not only improve the early strength of the sample but also improve its later strength. In the area of microstructural examination, Li Zhuocai's electron microscopic investigations [28] unveiled a profusion of hydration byproducts that emerged during the latter phases of WGP specimens, crafting a compact, plate-like configuration. Meanwhile, the scholarly discourse exemplified by Zhang Chi et al. [29] postulates that the incorporation of WGP can diminish the macropores within a specimen. Conversely, Yu Xuanliang [30] suggests that WGP exhibits minimal impact on the quantity of macropores and capillary pores in a sample, but offers a moderate reduction in transition pore prevalence.

There are numerous applications of solidified soil, including roadbed backfilling, slope protection, and land reclamation. The incorporation of glass powder into this material could significantly enhance the global utilization rate of waste glass. Additionally, the selection of agents for solidifying soil is relatively extensive. This allows for the identification of the most suitable agent for a given engineering project based on factors such as strength and hazard classification. Therefore, in acid–base activation systems, reagent-activated WGP has great research potential in replacing silica fume, fly ash, and other materials. At present, there are many studies on the application of WGP in cement mortar or concrete, but there are few articles on the application of chemically activated WGP in cement-based solidified soil. This study focuses on the effect of activated WGP on the strength improvement of solidified soil, the changes in the microstructure of activated glass powder, the changes in sample composition, and the corrosive effect of reagents on waste glass powder.

This study activates glass powder through different concentrations of reagents and prepares solidified soil by mixing the activated WGP with cement according to different dosages. The mechanical properties of the soil are analyzed for its unconfined compressive strength. Additionally, the microstructure is characterized to evaluate changes in pore-size distribution through scanning electron microscopic (SEM) tests and the utilization of the Image J software for machine learning image processing. The composition of WGP-solidified soil and the alterations under different WGP activators are examined via X-ray diffraction (XRD) and Fourier-transform infrared spectroscopy (FTIR).

2. Experimental Section

2.1. Production of Glass Powder

This study explores the use of WGP as a coagulant additive, with cement as the main curing agent, by preparing solvent solutions with varying concentrations of 2%, 4%, and 6% using NaOH, $Ca(OH)_2$, and Na_2SO_4 as ingredients. The nuances of alkaline activation of OH^- ions versus sulfate ion activation, the solubility of Na ions, and the essential Ca^{2+} ion supplementation to counteract the natural calcium deficiency in WGP were explored, and a thorough evaluation of the activation effects and mechanisms was undertaken. In this experimental procedure, WGP was pre-activated, taking into consideration the weak acidic nature of the soil. Directly blending alkaline activators with WGP and introducing them to the soil may risk neutralizing the alkalinity. To prevent such disruptions and to enhance the interaction between the alkaline activator and WGP, as well as to promote the ease of pre-activating the WGP, the activation process unfolded as follows: (1) Opt for transparent and colorless glass vessels to ensure comparability during experimentation. (2) Employ ball milling for durations of 0 h, 6 h, and 12 h to produce distinct particle sizes of WGP. The particle-size distribution resulting from varying the ball milling durations is detailed in Table 1. (3) Immerse the utilized WGP from the 12 h ball milling process in 2%, 4%, and 6% concentrations of the reagent. (4) After a 3-day aging period in the solution, desiccate the WGP in a curing chamber at 40 °C until its moisture content is below 2%. (5) Following activation, reinstall the WGP in the ball mill for a final milling session, and sieve it through a 0.075 mm filter to yield the ultimate product for detecting the composition of glass, as shown in Table 2.

Table 1. Composition of WGP particle size at different milling times.

0 h	Particle-size composition			
Particle size (mm) Content (%)	0.5–1 0.9	0.25–0.5 5.8	0.075–0.25 57.97	0–0.075 35.33
6 h			Particle-size composition	
Particle size (mm) Content (%)			0.075–0.25 20.6	0–0.075 79.4
12 h		Particle-size composition		
Particle size (μm) Content (%)	0–5.23 29.16	5.23–14.78 28.37	14.78–41.8 42.47	

Table 2. Chemical composition of transparent bottle and jar glass.

SiO_2 (%)	Al_2O_3 (%)	CaO (%)	MgO (%)	Na_2O (%)	Fe_2O_3 (%)
72	2.5	8.25	2	14.6	0.1

2.2. Selection of Activators

The activator selection was evaluated based on two factors: the impact of the reagent itself on the hydration performance of cement and and the influence of the reagent on the WGP activity. The erosion effect of alkaline agents on WGP is closely related to the type of cation present, particularly Ca^{2+}. The solubility of the calcium salt formed on the glass surface is relatively low. However, in the presence of Na^+ as the cation, the resulting sodium salt can rapidly dissolve on the glass surface, hastening the erosion of the glass at greater depths [31]. Concurrently, the corrosive potential of OH^- ions is also notably strong. This highlights the noteworthy advantage of NaOH as an activator, with its corresponding reaction formula depicted as follows when SiO_2 is dissolving in an alkaline solution [32]:

$$\equiv\text{Si-O-Si}\equiv+\text{OH}- \rightarrow \equiv\text{Si-O}- + \text{HO-Si}\equiv \tag{1}$$

The reactions that can occur on the surface of WGP due to the presence of an alkaline solution are as follows:

$$Si(OH)_4 + NaOH \rightarrow [Si(OH)_3O]{-}Na^+ + H_2O \quad (2)$$

The properties of Na_2SO_4 render it an effective sulfate with activating qualities on WGP. When the partially reacted Na_2SO_4 is combined with the energized WGP in a cemented solidified soil system, $Ca(OH)_2$ produced post cement hydration interacts with Na_2SO_4, resulting in the formation of NaOH. This has further stimulating effect on cement and glass:

$$Na_2SO_4 + Ca(OH)_2 + 2H_2O \rightarrow CaSO_4 \cdot 2H_2O + 2NaOH \quad (3)$$

Simultaneously, the partially used Na_2SO_4 engages in a reaction with $Ca(OH)_2$ produced during cement hydration, releasing Ca^{2+} ions and initiating the formation of AFt. This process can be explained by the following chemical equation: Na_2SO_4 swiftly consumes the $Ca(OH)_2$ released during cement hydration, expediting the early stages of hydration:

$$AlO_{2-} + Ca^{2+} + OH^- + SO_4{}^{2-} \rightarrow 3CaO \cdot Al_2O_3 \cdot CaSO_4 \cdot 32H_2O \quad (4)$$

Glass powder, akin to fly ash, lacks inherent strength when used alone or combined with NaOH stimulation [33]. Furthermore, $Ca(OH)_2$, acting as an activator, exerts a corrosive influence on the WGP itself. To give cementitious properties to mixtures containing WGP and fly ash, substances with lime-like properties must be added to the composite system to supplement the element of "calcium" in order to activate the reactivity of WGP and generate cementitious products similar to the hydration reaction of Portland cement. The presence of quicklime (CaO) or hydrated lime ($Ca(OH)_2$) is required.

2.3. Preparation

Different concentrations [8,26,34] (2%, 4%, and 6%) of solutions of different reagents (NaOH, $Ca(OH)_2$, and Na_2SO_4) were prepared to explore the optimal dosage of WGP after activation. Different concentrations and pH values result in different activation effects, and increasing the concentration of OH^- is beneficial for Si-O and Al-O. The unconfined compressive strength of WGP was analyzed to evaluate the effectiveness of different reagents in activating its reactivity. Microscopic analysis was conducted using X-ray diffraction (XRD), scanning electron microscopy (SEM), and Fourier-transform infrared spectroscopy (FTIR). Machine learning with the Image J software was used to process the electron microscopic images to study the mechanical properties and microscopic features of WGP within the cemented solidified soil system, and to investigate its curing mechanism and changes in porosity.

The concentration of the solidifying agent (cement) for the solidified soil was 20% (by mass percentage), with a certain moisture content. WGP was added to the solidified soil post activation in the form of an external additive. The designed dosage of WGP as an external additive was 1%, 3%, 5%, and 7% (calculated per individual specimen). Each group of WGP was activated with 2%, 4%, and 6% solvent concentrations, with 36 groups in total. To demonstrate the effect of activated WGP, non-activated WGP at 1%, 3%, 5%, and 7% was used as the control group. Three horizontal samples were taken from each group after curing for 14 days, and the average of the results was calculated (same as below); the unconfined compressive strength test results are shown in Figure 1.

According to Figure 1, with an increase in the dosage of non-activated WGP, the unconfined compressive strength shows a decreasing trend. A moderate amount of non-activated WGP has little impact on the strength of the specimens. Strength is controlled by cement, but when the dosage is excessive, a decreasing trend in strength is observed. Excessive WGP actually inhibits the hydration of cement, as also noted by Niyomukiza

JB [35] in their study, where a decrease in strength was observed for specimens after a WGP dosage of 7%.

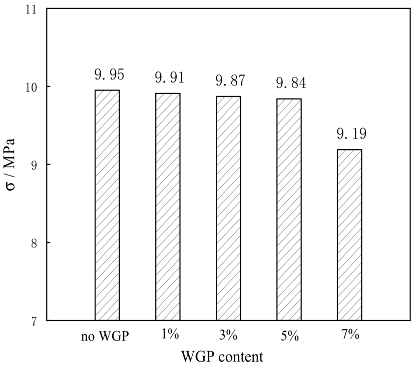

Figure 1. WGP content vs. unconfined compressive strength.

3. Results and Discussion

3.1. Unconfined Compressive Strength

Utilizing NaOH, $Ca(OH)_2$, and Na_2SO_4 as the reagents, the activators were prepared at concentrations of 2%, 4%, and 6% for glass activation. Post activation, WGP was blended at levels of 1%, 3%, 5%, and 7% into the samples, and the resultant powders were designated as NaOH waste glass powder (NWGP), $Ca(OH)_2$ waste glass powder (CWGP), and Na_2SO_4 waste glass powder (SWGP). Subsequent strength evaluation entailed the use of unconfined compressive strength testing. The strain rate of the experiment was 1 mm/min, and the maximum pressure of the sensor was 2000 kg. The unconfined pressure gauge and sensor are shown in Figure 2. Unconfined compressive strength is the most basic indicator for testing material properties in geotechnical tests. As it is not constrained by lateral forces, the results obtained can reflect the strength of the material. The WGP samples after testing are shown in Figure 3, and the results are shown in Figure 4.

Figure 2. Unconfined pressure instrument.

Figure 3. Damaged samples.

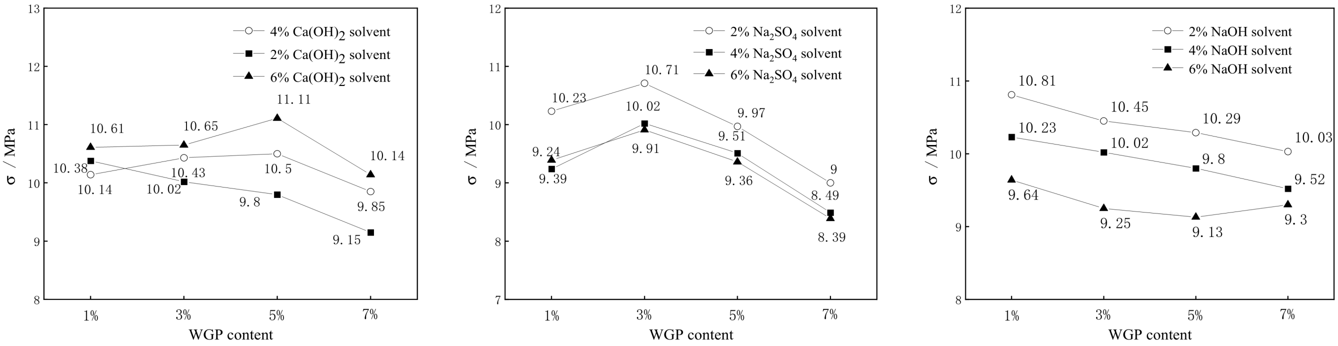

(**a**) (**b**) (**c**)

Figure 4. Curve of WGP content vs. strength. Ca(OH)$_2$ solvent (**a**), Na$_2$SO$_4$ solvent (**b**), NaOH solvent (**c**).

Based on the insights from Figure 4, it is evident that the WGP activated by a 6% concentration of Ca(OH)$_2$ solvent shows superior strength in comparison to powders activated by 2% and 4% concentrations. Furthermore, the WGP samples activated by 4% and 6% concentrations of Ca(OH)$_2$ exhibit an increase in strength with increasing dosage, with the 5% CWGP demonstrating the highest strength, suggesting that a 5% dosage is the most suitable. This finding aligns closely with the research by Wenwen Zhang [36]. Conversely, the strength of the WGP activated by 2% concentration Ca(OH)$_2$ tends to decrease as the dosage increases.

As shown in Figure 4b, the glass powder activated by 2% concentration of Na$_2$SO$_4$ solvent exhibits the most effective results. The SWGP samples produced by the three groups of solvents with different concentrations reflect a similar trend, showing an increase in strength as the SWGP dosage increases, with the highest unconfined compressive strength observed at a 3% SWGP. In Figure 4c, the activation effect of NWGP gradually diminishes with an increasing concentration of NaOH, resulting in a decrease in sample strength as the NWGP dosage increases.

These figures demonstrate that an inappropriate reagent dosage can weaken the WGP solidified soil after activation. Figure 4 shows that the unconfined compressive strength of each test group generally exceeds the corresponding control group's strength in Figure 1, indicating that utilizing the WGP activated by a 6% Ca(OH)$_2$ solvent has a noticeable effect on sample strength. Activation with Ca(OH)$_2$ serves to enhance the alkalinity of the samples and provides an ample supply of Ca^{2+} ions. This alkalinity is conducive to the pozzolanic activity of WGP, promoting the release of Al$_2$O$_3$, SiO$_2$, and other oxides. These oxides can interact with Ca^{2+} ions to generate hydration products like C-S-H and C-A-H, which are crucial for cement hardening. Therefore, the inclusion of WGP necessitates increased generation of Ca(OH)$_2$. Li Fang [24] conducted an experiment which showed a decrease in calcium and an increase in silicon and sodium content in the samples. This suggests that in the later stages of the experiment, the calcium element was consumed to produce hydration products like C-S-H, while Ca(OH)$_2$ separated the sodium and silicon elements from the WGP, further depleting the calcium content. Therefore, regardless of whether it is required to replenish the Ca^{2+} ion content or activate WGP, Ca(OH)$_2$ is a more suitable option. In terms of dosage, CWGP has an upper limit as excessive dosages increase the OH$^-$ concentration in the solution, impacting the cement hydration process.

By analyzing the visual data depicted in Figure 4b, it is evident that at a 3% SWGP, each solvent concentration shows a peak unconfined compressive strength within its corresponding group. However, as the solvent concentration increases, the strength of the SWGP samples decreases. The addition of Na$_2$SO$_4$ accelerates the breakdown of the glass structure within the powder, thereby releasing more active SiO$_2$ and Al$_2$O$_3$, It also reacts chemically with Ca(OH)$_2$ decomposed from cement to generate C-S-H and C-A-H compounds (see Equations (5) and (6)). The generation of C-S-H and C-A-H compounds results in a higher strength and increases the volume of hydration products, thus filling the pores of the sample and improving its strength. Yet, a high dosage of Na_2SO_4 (6%) triggers the formation of expansive ettringite, compromising the internal stability of the samples. Furthermore, the surplus ettringite stemming from an elevated Na_2SO_4 content depletes the levels of other hydration products. This conclusion is consistent with that of Xu Y.D. [37].

As shown in Figure 4c, it can be inferred that the critical threshold is reached at a 4% concentration of NaOH solvent. When the solvent concentration reaches 6%, the increased presence of OH^- ions in the solution interferes with the cement hydration process, resulting in a lower strength compared to the control group. During hydration, the concentration of Ca^{2+} is significantly affected by OH^-, whereby a higher liquid-phase OH^- content corresponds to a lower Ca^{2+} content. The decrease in Ca^{2+} concentration slows down the reaction rate and inhibits the formation of C-S-H and C-A-H compounds [38]. As noted in M. Ben Haha's study [39], it is observed that the potent activation of sodium hydroxide promptly engenders a C-S-H gel to envelope the WGP, impeding a substantial fraction of the powder from dispersing with free water to fill the larger pores, thereby contributing to the lowered strength. Similar reports have been conveyed by Ahmad S. Omran [40].

$$Ca(OH)_2 + A1_2O_3 + nH_2O \rightarrow CaO \cdot A1_2O_3\ (n + 1)\ H_2O \tag{5}$$

$$Ca(OH)_2 + SiO_2 + nH_2O \rightarrow CaO \cdot SiO_2 \cdot (n + 1)\ H_2O \tag{6}$$

3.2. Scanning Electron Microscopic (SEM) Analysis

Following a 14-day period of curing in a standard curing box, several representative groups of samples were selected from a large number of samples for this experiment. Each complete sample was dried in the shade and then cut into circular pieces with a diameter of 1 cm and a thickness of 0.5 mm, as shown in Figure 5. Attention was paid to break the observation surface of the sample to obtain a fresh cross-sectional opening. Finally, the sample was placed in a glass beaker, weighed, and dried in a vacuum drying oven. The vacuum pump was turned and the sample was dried in a vacuum environment at approximately 40 °C and 0.08 MPa for at least 24 h for later use. Before electron microscopic observation, it was necessary to fix the slices and apply a spray-gold treatment. The slices were adhered to the sample stage with conductive adhesive and a conductive film was sprayed on the surface of the slices, as shown in Figure 6. Once the spray coating process was finished, the sample was observed under an electron microscope. An electron microscopic image with a magnification of 10,000 X was selected to facilitate observation of the microstructure between the pores of the specimen.

Figure 5. Ring-cut specimen.

Figure 6. Samples on the loading platform.

Figure 7 shows a pure cement-based solidified soil sample, while Figures 8–10 show WGP solidified soil samples activated by NaOH, $Ca(OH)_2$, and Na_2SO_4, respectively. After pressure forming, the micrograph of the pristine cement-based solidified soil, depicted in Figure 7, in the cement control group displays an unconventional arrangement of particles. The surfaces of the soil particles are predominantly characterized by flake-like structures that spread out in a scattered manner, contributing to a loosely structured composition. The primary contact mode between particles was observed to be face-to-face. The sample, overall, shows a continuous, flattened clay mineral matrix, with visible localized accumulations of flat soil particles. After the original sample was magnified by 10,000 times, the flocculent hydration products of the thin film were observed to be stacked together in a face-to-face contact form. Locally, the oriented arrangement of the aggregates is visible, and a significant amount of C-S-H and AFt hydrates is distributed on the concave surface and pores. In contrast, following the introduction of WGP, the porosity of the sample surface notably decreases. The flake-like hydrated products exhibit an increase in surface area and thickness, become more uniform, and have greater integrity.

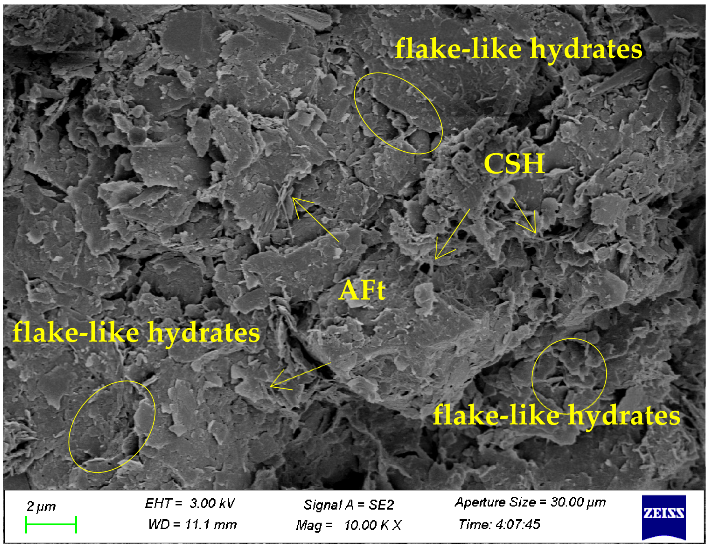

Figure 7. Cement-based solidified soil.

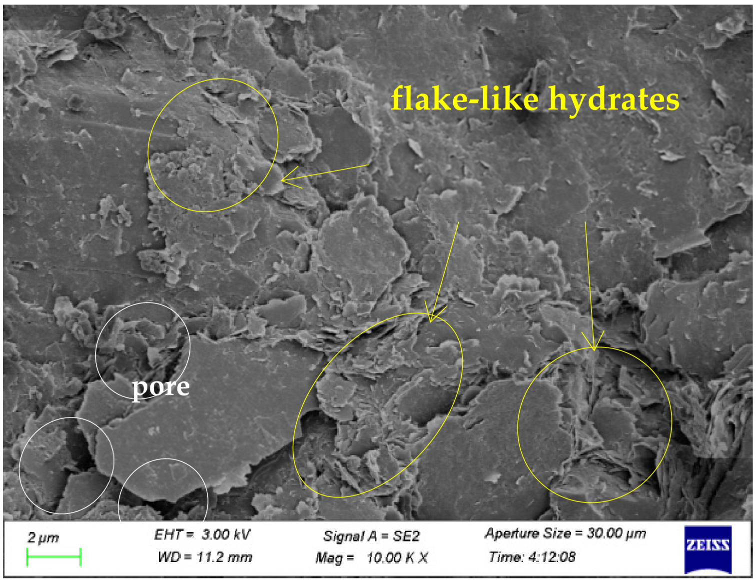

Figure 8. Solidified soil with CWGP.

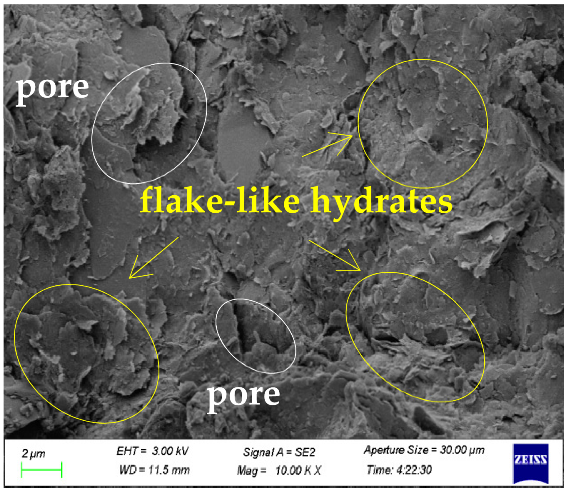

Figure 9. Solidified soil with SWGP.

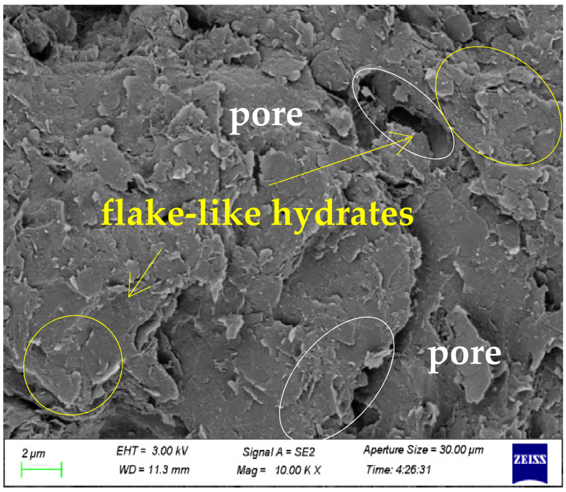

Figure 10. Solidified soil with NWGP.

From Figure 8, it can be observed that the sample surface is more compact, characterized by the distribution of thin flake-like hydrated products on top of plate-like solidified soil particles or within the interparticle voids. A comprehensive observation of the various hydrated flake-like products in the solidified soil reveals that the plate-like hydrated products in the group activated by $Ca(OH)_2$ and WGP exhibit larger areas and tighter integration. By observing Figures 9 and 10, it can be seen that despite having large plate-like hydration products, there are still pores between them. The key distinction between Figures 8–10 lies in the use of different activators for the WGP. The incorporation of $Ca(OH)_2$ leads to an increase in the area of hydrated products, enhancing uniformity and compactness. Based on the mechanical performance results in the previous section, the unconfined compressive strength of the WGP group activated by $Ca(OH)_2$ is the highest, corresponding to the denser hydration described in this section.

Figure 9 shows the NWGP group, which exhibits a small amount of flake-like hydrates. A large amount of the flat solidified soil mineral matrix is exposed to the outside. The flake-like hydrates do not attach as much to the surface of the solidified soil, as shown in Figures 7, 8 and 10. Some of them grow and are embedded between solidified soil particles, with a small amount attached to the surface. The hydration products attached to the solidified soil are relatively dense, with small pores, which also provides a certain strength for the sample. The distribution of flake-like hydration products in Figures 7 and 10 is similar, with the difference being that the flake-like hydration products in Figure 10 have a larger area. Compared with Figure 7, the larger flake-like hydration products cover or effectively fill the pores, providing a better overlap effect between soil particles. The surface of the sample is denser, which improves its mechanical properties.

3.3. ImageJ Microstructure Analysis

The image processing in this study employed a consistent electron microscopic magnification of 10,000 times. The software's advanced Intelligent processing capabilities were used for automated learning, a series of images underwent processing, pores were segmented, and different pore sizes were distinguished, culminating in the creation of Figures 11 and 12.

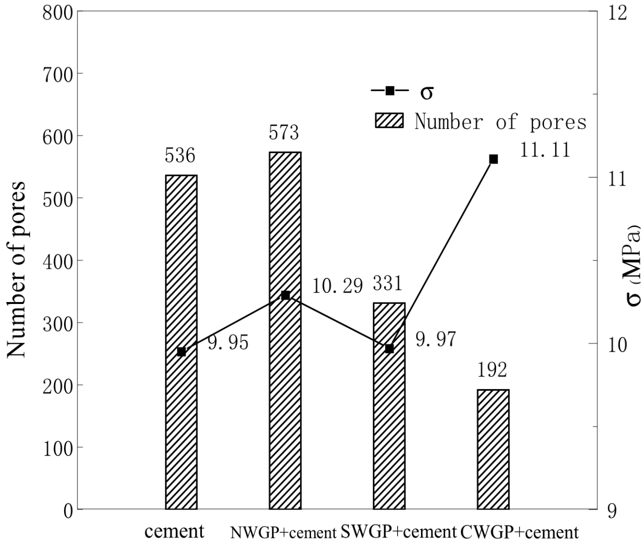

Figure 11. Diagram of the relationship between stress and pore quantity.

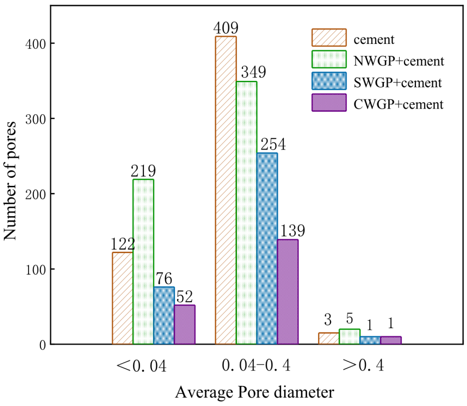

Figure 12. Pore sizes of glass powders with different activators.

The changes in pore quantities have a marginal impact on the samples' unconfined compressive strength, as demonstrated by the results shown in Figure 11, where a marked reduction in pores is evident in the CWGP samples, resulting in a significant increase in unconfined compressive strength compared to the other three groups. From Figure 12, it can be seen that the introduction of SGWP and CWGP led to a reduction in the range of pore sizes (pores less than 0.04 µm, pores between 0.04 µm and 0.4µm, and pores exceeding 0.4 µm) to varying degrees, The introduction of NWGP noticeably decreased the size of pores with a diameter of 0.04 µm to 0.4 µm to smaller dimensions (below 0.4 µm). In summary, the activated WGP can significantly improve the porosity of the samples compared to the pure cement experimental group, and the WGP activated by $Ca(OH)_2$ has the best porosity improvement effect.

Firstly, when analyzing for the main causes, compared with the experimental group without WGP, the medium porosity is significantly reduced and the waste glass powder particles are mostly angular in shape, which have the effect of filling the pores with micro-aggregates and are beneficial for improving the pore structure of the system and increasing density [41]. Secondly, the samples mixed with glass powder are prone to $Ca(OH)_2$ reaction, and a circle of hydrates forms around the glass powder, making the pores filled by the glass powder more dense [33]. In addition, excess $Ca(OH)_2$ is prone to $CaCO_3$ reaction when in contact with CO_2, as shown in reaction Formula (7). $CaCO_3$ is a sheet-like crystal attached to the surface of the sample, which is similar to the morphology shown in Figure 4, playing a role in reducing pores and increasing density. Moreover, it can be seen from reference [42] that the product of the reaction between SO_2 dissolved in WGP and $Ca(OH)_2$ is denser than the product of cement hydration.

$$Ca(OH)_2 + CO_2 \rightarrow CaCO_3 + H_2O \tag{7}$$

3.4. X-ray Diffractometer (XRD) Analysis

To further explore the influence of different activators on the composition of cement-based solidified soil samples, we used a multi-group trial and selected three representative groups from a large number of samples. In the early stage of the experiment, it was necessary to dry the samples using traditional shade drying and other drying methods. After shade drying, the samples were placed in a vacuum drying oven to ensure complete evaporation of moisture. After the samples were dried, they were ground into powder with a hammer and screened through a 0.074 mm sieve. About 10 g of each sample was prepared for testing.

Figure 13a–c show the X-ray diffraction patterns of the samples resulting from the introduction of WGP within the cemented solidified soil system. The patterns indicate that the chemical reactions began within 14 days. A detailed analysis uncovers that the mineral micro-components predominantly consist of kaolinite ($Al_2Si_2O_5(OH)_4$), silica (SiO_2), illite ($KAl_2[(SiAl)_4O_{10}]\cdot(OH)_2\cdot nH_2O$), albite ($Na(AlSi_3O_8)$), and the cementitious material, hydrated calcium silicate (C-S-H). Each detected component displays distinct characteristic peaks on the diffraction profile. These components' relative proportions are visually represented in Figure 13a–c, which portray the primary constituents formed within the samples. From the detected components, it can be observed that the main components of WGP activated by different solvents did not change after being added to the solidified soil, but the proportion of its components changed slightly.

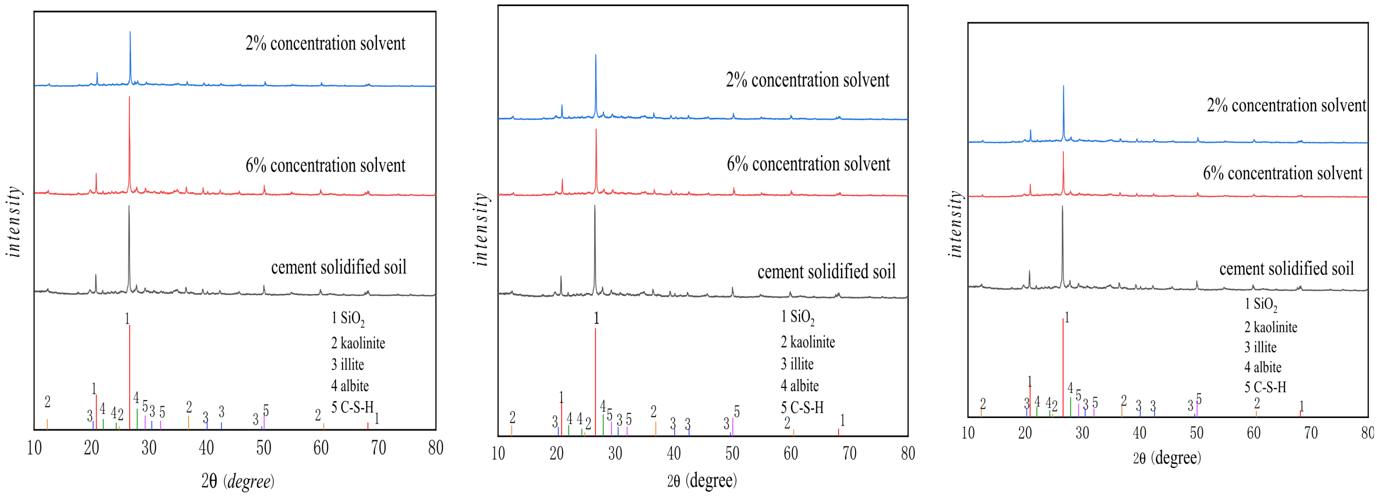

(**a**) (**b**) (**c**)

Figure 13. Different solvent concentrations of $Ca(OH)_2$ (**a**), Na_2SO_4 (**b**), and NaOH (**c**).

With the addition of glass powder, it can be seen that the SiO_2 content in Figure 14b and Figure 14c increases by 2% and 2.2%, respectively, compared to 30.9% in Figure 14a. The proportion of SiO_2 in Figure 14b is lower than that in Figure 14c, and the corresponding proportion of C-S-H gel in Figure 14b is higher. It can be seen that a certain amount of active SiO_2 has reacted to form C-S-H gel. This phenomenon is consistent with the above conclusion that the strength of WGP with 6% solvent is higher than that with 2% solvent. At the same time, the mineral composition of the original clay, such as kaolinite and illite sodium feldspar, shows slight changes in content due to the heterogeneity of the soil.

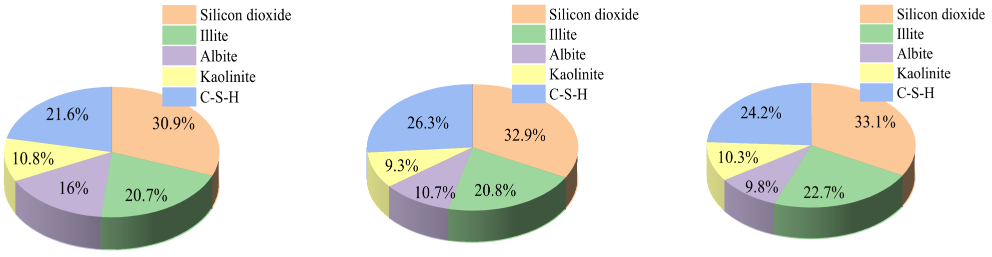

(**a**) (**b**) (**c**)

Figure 14. Mineral content ratio of $Ca(OH)_2$ WGP solidified soil. Solidified soil with (**a**) no glass powder; (**b**) 6% concentration solvent; and (**c**) 2% concentration solvent.

It is evident that the SiO_2 and C-S-H gel contents in Figure 15c surpass those in Figure 15b. The heightened presence of Na_2SO_4 causes a fracturing of the SiO_4 tetrahedra structure, rendering the reactive SiO_2 more vulnerable to hydration reactions. Consequently, there is a decline in SiO_2 content, as depicted in the compositional charts. In Figure 15b, the C-S-H gel content is lower than in Figure 15c, potentially attributed to the excessive consumption of $Ca(OH)_2$ by the increased Na_2SO_4 content during cement hydration. This leads to an overabundance of AFt, which depletes Ca^{2+} ions and impedes the formation of additional C-S-H gel, thereby contributing to the decrease in sample strength.

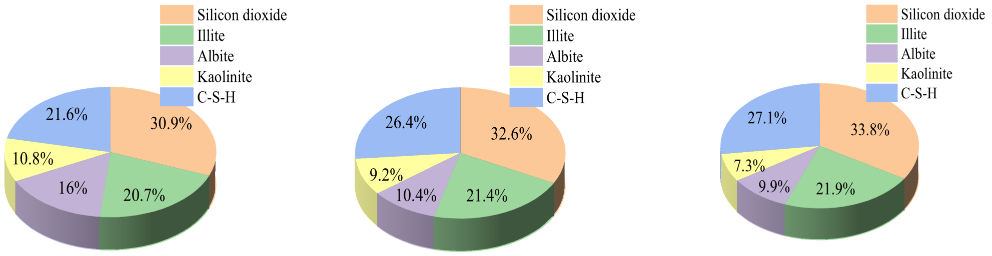

(**a**) (**b**) (**c**)

Figure 15. Mineral content ratio of Na_2SO_4 WGP solidified soil. Solidified soil with (**a**) no glass powder; (**b**) 6% concentration solvent; and (**c**) 2% concentration solvent.

Although sodium salts dissolve readily in water, an excess of NaOH increases the internal alkalinity of the sample, accelerating the reaction. Activated Al_2O_3 and SiO_2 in cement accelerate dissolution. The accelerated reactions promote the rapid formation of C-S-H gel surrounding the WGP, limiting the activation of most of the WGP; this explains the noticeable decrease in SiO_2 content in Figure 16c compared to Figure 16b. The increased active SiO_2 then participates in reactions that result in a greater abundance of C-S-H gel.

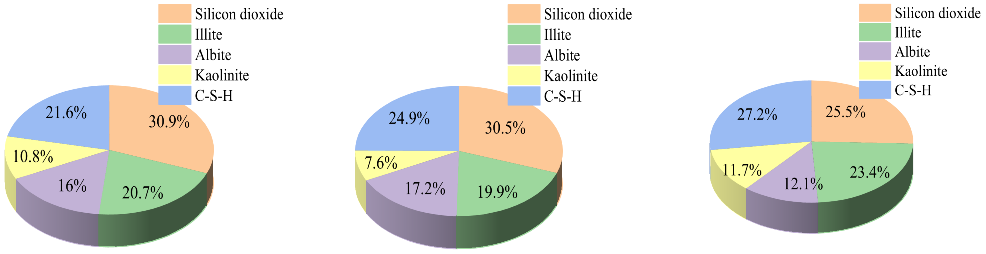

(**a**) (**b**) (**c**)

Figure 16. Mineral content ratio of NaOH WGP solidified soil. Solidified soil with (**a**) no glass powder; (**b**) 6% concentration solvent; and (**c**) 2% concentration solvent.

3.5. Fourier-Transform Infrared Spectroscopic (FTIR) Analysis

Based on the composition analysis of XRD described in the previous section, this study investigated the effect of activators on SiO_2 in WGP and further investigated the activation effect of NaOH, $Ca(OH)_2$, and Na_2SO_4 on WGP. Fourier-transform infrared (FTIR) spectroscopy was employed in the investigation. Inactive WGP and activators at 2% and 6% concentrations were chosen to enhance comparability. The experimental results are illustrated in Figures 17–19.

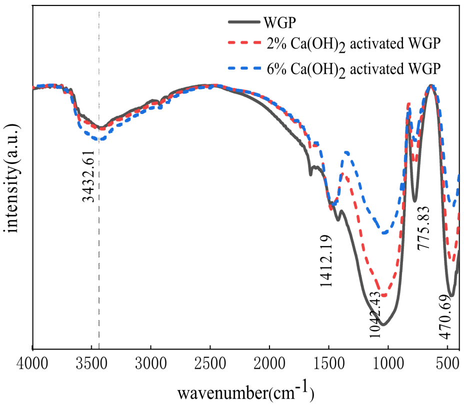

Figure 17. WGP activated by $Ca(OH)_2$ solvent.

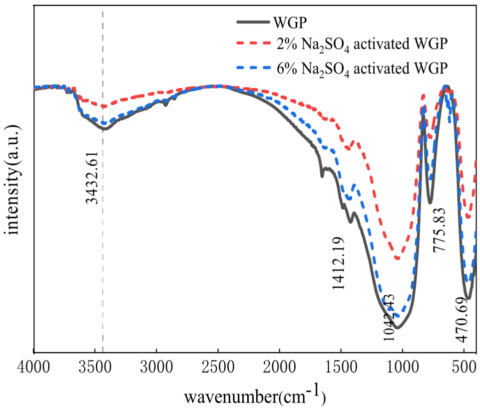

Figure 18. WGP activated by Na_2SO_4 solvent.

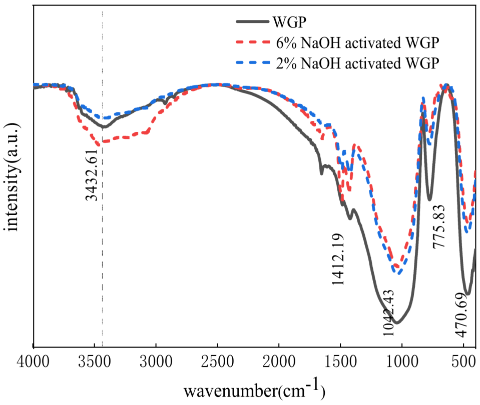

Figure 19. WGP activated by NaOH solvent.

In these figures, it is clear that the vibration peak position of the activated WGP closely matches that of the inactive WGP. However, there is a noticeable shift in the (Si-O-Si) bending vibration peak around 470.69 cm^{-1}, indicating the interaction of the activator with SiO_2 in the WGP. When comparing these three sets of graphs, it is evident that as the activator concentrations increase, the vibrational peak intensity decreases to varying degrees. This indicates the corrosive effect of activator concentration on SiO_2, causing chemical bonds to break.

The Si-O bond exhibits a symmetric stretching vibration peak at 775.83 cm^{-1}, while the Si-O-Si bond displays an antisymmetric stretching vibration peak at 1042.43 cm^{-1}. Both peaks vary proportionally with changes in the reagent concentration.

The distinctive peak residing near 1412.19 cm^{-1} arises from the presence of C-O bonds. This is likely due to carbonization effects during the meticulous sample preparation process, which might have led to the formation of carbonates within the sample [43–47]. Notably, the interaction of $Ca(OH)_2$ with CO_2 results in the production of $CaCO_3$, accentuating the peak broadening near 1412.19 cm^{-1} shown in Figure 17.

The intensification of the OH vibration peak at 3432.61cm^{-1}, displayed in both Figures 13 and 15, could be due to the nuanced alterations in vibration peaks induced by the introduction of NaOH and $Ca(OH)_2$. Conversely, in Figure 17, the peak's attenuation may be attributed to further consumption throughout the reaction process due to the absence of OH doping.

Moreover, an analysis of Figures 17 and 19 reveals that the vibration peaks of the $Ca(OH)_2$ solvents at 2% and 6% concentrations are significantly weaker compared to the 6% NaOH solvent, indicating the former has a greater ability to promote OH^- reactions, which may be due to a better activation effect. The vibration peak of NaOH solvent with a concentration of 2% is shallower than that of the original WGP, indicating the solvent consumes both the original OH^- and itself. This further demonstrates that an appropriate concentration has a better activation effect, which is consistent with the previous results.

4. Conclusions

This study excited glass activity through different types of reagents and solvents at different concentrations. It used WGP of different dosages after activation to mix with cement-based solidified soil. The optimal dosage, optimal activator, and optimal concentration of the activator were obtained through unconfined compressive strength analysis. Scanning electron microscopic (SEM) experiments were performed and the Image J software for machine learning was used to process the electron microscopic images, characterizing their microstructure and analyzing the changes in pore size. Through X-ray diffraction (XRD) experiments, the composition of the glass powder solidified soil and the changes in composition content under different glass powder activators were analyzed, and the activation effect of waste glass powder was demonstrated through Fourier-transform infrared (FTIR) spectroscopy. The conclusions are as follows:

(1) The activation effect of different reagents on glass powder is influenced by their concentration. Unconfined compressive strength tests were conducted on samples of solidified soil mixed with glass powder to characterize their strength. The optimal concentration for the $Ca(OH)_2$ solvent is 6%, while the optimal concentration for the Na_2SO_4 and NaOH solvents is 2%.

(2) The comparative experiments revealed that the strength of the WGP solidified soil samples exhibited a gradual decline with the addition of glass powder. However, when glass powder was activated by the 6% $Ca(OH)_2$ solvent and was added at a dosage of 5%, the optimal dosage was obtained. The highest strength of the solidified soil produced was 11.11 MPa, which represented a 13% increase in strength compared to the inactive 5% dosage.

(3) Through SEM testing, it was found that the experimental group with added activated glass powder had a more uniform and denser microstructure compared to the pure cement experimental group. At the same time, compared with NWGP and SWGP groups, the pore size of the CWGP solidified soil group significantly reduced, and the large pore size tended to transform into a small pore size. The main reason is that CWGP can fill the pores and induce crystallization of $Ca(OH)_2$.

(4) The X-ray diffraction (XRD) analysis revealed that the predominant components of the solidified soil mixture with glass powder are kaolinite, silica, illite, albite, and cementitious material C-S-H. The addition of WGP is reflected in the pie chart by an increase in the content of SiO_2. With an appropriate solvent concentration, the C-S-H gel exhibits varying degrees of increase in the pie chart, thereby enhancing the strength of the solidified soil to a certain extent. This phenomenon reflects the activating effect of the activator and the feasibility of adding activated WGP to solidified soil.

(5) According to the Fourier-transform infrared (FTIR) spectroscopic analysis, as the reagent concentration increases, SiO_2 in the WGP continues to corrode the bond cleavage and the content of OH^- decreases accordingly.

Author Contributions: Conceptualization, Y.H., C.Z. and Z.C.; Methodology, Y.H., C.Z. and Z.C.; Software, Y.H. and X.X.; Validation, Y.H.; Formal analysis, Z.C.; Investigation, Y.H. and X.X.; Data curation, Y.H. and X.X.; Writing—original draft, Y.H.; Writing—review & editing, Y.H. and X.X.; Supervision, G.Y.; Project administration, Y.H. and G.Y.; Funding acquisition, G.Y. All authors have read and agreed to the published version of the manuscript.

Funding: This study was conducted by the Science and Technology Project of Zhejiang Provincial Depart- 312 ment of Water Resources, grant number RA1910; Science and Technology Project of Zhejiang Pro- 313 vincial Department of Water Resources, grant number RB2021.

Data Availability Statement: The original contributions presented in the study are included in the article, further inquiries can be directed to the corresponding authors.

Conflicts of Interest: Author Yang Guanshe was employed by the company Ningbo Raw Water Co., Ltd. The remaining authors declare that the research was conducted in the absence of any commercial or financial relationships that could be construed as a potential conflict of interest.

References

1. Jain, J.A.; Neithalath, N. Chloride transport in fly ash and glass powder modified concretes—Influence of test methods on microstructure. *Cem. Concr. Compos.* **2010**, *32*, 148–156. [CrossRef]
2. Nassar, R.U.D.; Soroushian, P. Green and durable mortar produced with milled waste glass. *Mag. Concr. Res.* **2012**, *64*, 605–615. [CrossRef]
3. Li, A.; Qiao, H.; Li, Q.; Hakuzweyezu, T.; Chen, B. Study on the performance of pervious concretemixed with waste glass powder. *Constr. Build. Mater.* **2021**, *300*, 123997. [CrossRef]
4. Khmiri, A.; Chaabouni, M.; Samet, B. Chemical behaviour of ground waste glass when usedas partial cement replacement in mortars. *Constr. Build. Mater.* **2013**, *44*, 74–80. [CrossRef]
5. Shayan, A.; Xu, A. Value-added utilisation of waste glass in concrete. *Cem. Concr. Res.* **2004**, *34*, 81–89. [CrossRef]
6. Gao, X.; Yu, Q.; Li, X.; Yuan, Y. Assessing the modification efficiency of waste glass powder in hydraulic construction materials. *Constr. Build. Mater.* **2020**, *263*, 120111. [CrossRef]
7. Song, B. Experimental Study on Activation of Waste Glass Powder. Master's Thesis, Nanhua University, Chiayi, China, 2013.
8. Du, H.J.; Tan, K.H. Use of waste glass as sand in mortar: Part II-alkali-silicareaction and mitigation methods. *Cem. Concr. Compos.* **2013**, *35*, 118–126. [CrossRef]
9. Zhao, H.; Ke, G.; Song, B.; Zou, P. Effect of waste glass pow der on hydration products of cement paste and structure of plastic sand. *Concrete* **2018**, *10*, 106–109+122.
10. Ali, E.E.; Al-Tersawy, S.H. Recycled glass as a partial replacement for fine aggregate in self compacting concrete. *Constr. Build. Mater.* **2012**, *35*, 785–791. [CrossRef]
11. Lam, C.S.; Poon, C.S.; Chan, D. Enhancing the performance of pre-cast concrete blocks incorporating waste glass e ASR consideration. *Cem. Concr. Compos.* **2007**, *29*, 616–625. [CrossRef]
12. De Moura, A.A.; Effting, L.; Moisés, M.P.; Carbajal, G.G.A.; Tarley, C.R.T.; Câmara, E.; Gracioli, A.; Bail, A. The influence of calcium-rich environments in siliceous industrial residues on the hydration reaction of cementitious mixtures. *J. Clean. Prod.* **2019**, *225*, 152–162. [CrossRef]
13. Geng, C.; Wu, X.; Yao, X.; Wang, C.; Mei, Z.; Jiang, T. Reusing waste glass powder to improve the strength stability of cement at HTHP. *J. Pet. Sci. Eng.* **2022**, *213*, 110394. [CrossRef]
14. Varma, D.N.; Singh, S.P. A Review on Waste Glass-based Geopolymer Composites as a Sustainable Binder. *Silicon* **2023**, *15*, 7685–7703. [CrossRef]
15. Cai, Y.; Xuan, D.; Poon, C.S. Effects of nano-SiO_2 and glass powder on mitigating alkali-silica reaction of cement glass mortars. *Constr. Build. Mater.* **2019**, *201*, 295–302. [CrossRef]
16. Schwarz, N.; Cam, H.; Neithalath, N. Influence of a fine glass powder on the durability characteristics of concrete and its comparison to fly ash. *Cem. Concr. Compos.* **2008**, *30*, 486–496. [CrossRef]
17. Yang, J. Study on the Auxiliary Cementitious Effect of Waste Glass Micro Powder in Recycled Concrete. Master's Thesis, Kunming University of Science and Technology, Kunming, China, 2010.
18. Shi, C.J.; Day, R.L. Comparison of different methods for enhancing reactivity of pozzolans. *Cem. Concr. Res.* **2001**, *31*, 813–818. [CrossRef]
19. Idir, R.; Cyr, M. Pozzolanic properties of fine coarse color-mixed glass cullet. *Cem. Concr. Compos.* **2011**, *33*, 19–29. [CrossRef]
20. Shi, C.; Zheng, K. A review on the use of waste glasses in the production of cement and concrete. *Resour. Conserv. Recycl.* **2007**, *52*, 234–247. [CrossRef]
21. Dyer, T.D.; Dhir, R.K. Chemical Reaction of Glass Cullet used as Cement Component. *Mater. Civ. Eng.* **2001**, *13*, 412–417. [CrossRef]
22. Shi, C.; Wu, Y.; Riefler, C.; Wang, H. Characteristics and pozzolanic reactivity of glass powders. *Cem. Concr. Res.* **2005**, *35*, 987–993. [CrossRef]
23. Archibald, J.F.; DeGagne, D.O.; Lausch, P.; De Souza, E.M. Ground waste glass as a pozzolanic consolidation agent for mine backfill. *CIM Bull.* **1995**, *88*, 80–87.
24. Fan, L.; Liu, G.; Su, H.; Jin, D.; Lu, R.; Li, L. The influence of glass powder particle size distribution on the properties of cementitious materials. *Sci. Technol. Eng.* **2016**, *16*, 271–274.
25. Yue, L.; Ji, T.; Zhou, Y.; Wang, S.; Jiang, M.; Fu, T.; Zhang, S. Active Excitation of Waste Glass Powder and Its Effect on the Properties of Mortar. *Concr. Cem. Prod.* **2022**, *7*, 97–100.
26. Kong, Q. Research on the Activity of Waste Glass Powder by Chemical Excitation and Hydrothermal Excitation. Master's Thesis, South China University, Chiayi, China, 2014.
27. Shi, C.; Day, R.L. Pozzolanic reaction in the presence of chemical activators Part I. Reaction kinetics. *Cem. Concr. Res.* **2000**, *30*, 51–58. [CrossRef]
28. Li, Z. Study on Characterizing the Volcanic ash Activity of Waste Glass Powder Using pH Value and Conductivity. Master's Thesis, South China University, Chiayi, China, 2014.

29. Zhang, C.; Wang, J.; Song, W.; Fu, J. *Effect of Waste Glass Powder on Pore Structure, Mechanical Properties and Microstructure of Cemented Tailings Backfill*; Elsevier Ltd.: Amsterdam, The Netherlands, 2023.
30. Yu, X. Study on The Influence of Glass Powder on The Microcosmic and Mechanical Properties of Concrete. Master's Thesis, Guilin University of Technology, Guilin, China, 2020.
31. Zhao, Y.; Yin, H. *Glass Technology*; Chemical Industry Press: Beijing, China, 2006; Volume 412.
32. Wang, Z.; Zheng, H.; Qian, J. Comparison of sulfate activation on fly ash activity. *Compr. Util. Fly Ash* **1999**, *12*, 15–18.
33. Li, F.; Yang, J.; Li, L. Effect and Mechanism of Waste Glass Powder as Supplementary Cementitious Material on Mortar Properties. *Silic. Bull.* **2022**, *41*, 3208–3218.
34. Lei, F. The Research on Hydration Activity and Mechanism of Cement Paste with Glass Powder. Master's Thesis, Guilin University of Technology, Guilin, China, 2017.
35. Niyomukiza, J.B. Use of waste glass powder in improving the properties of expansive clay soils. *Glob. NEST Int. J. Glob. NEST J.* **2023**, *25*, 139–145.
36. Zhang, W.; Li, S.; Song, L.; Sheng, Y.; Xiao, J.; Zhang, T. Studying the Effects of Varied Dosages and Grinding Times on the Mechanical Properties of Mortar. *Sustainability* **2023**, *15*, 5936. [CrossRef]
37. Xu, Y.; He, T. Effect of Mitigating Strength Retrogradation of Alkali Accelerator by the Synergism of Sodium Sulfate and Waste Glass Powder. *J. Renew. Mater.* **2021**, *9*, 1991–1999. [CrossRef]
38. Dan, J.; Wang, P. Research on the variation law of ion concentration in early cement hydration liquid phase. *J. Shihezi Univ. (Nat. Sci. Ed.)* **2007**, *25*, 494–499.
39. Haha, M.B.; Le Saout, G.; Winnefeld, F.; Lothenbach, B. Influence of activator type on hydration kinetics, hydrate assemblage and microstructural development of alkali activated blast-furnace slags. *Cem. Concr. Res.* **2011**, *41*, 301–310. [CrossRef]
40. Omran, A.F.; Etienne, D.; Harbec, D.; Tagnit-Hamou, A. Long-term performance of glass-powder concrete in large-scale field applications. *Constr. Build. Mater.* **2017**, *135*, 43–58. [CrossRef]
41. Ke, G.; Zou, P.; Gan, Y.; Song, B.; Zeng, D. Strength Activity Characteristic and Mechanism of Waste Glass Powders. *Chin. Powder Technol.* **2015**, *21*, 87–92.
42. Zheng, K.R.; Chen, L.; Zhou, J. Pozzolanic Reaction of Soda-lime Glass and Its influences on Composition of Calcium Silicate Hydrate. *J. Ceram.* **2016**, *44*, 202–210.
43. Tang, Q. Engineering Properties and Mechanism of Soft Soil Solidified by Phosphogypsum—Mineral Powder—Carbide Slag Composite Solid Waste Gelling Agent l. Master's Thesis, Donghua University, Shanghai, China, 2023.
44. Wang, W. Study on the Effect of Stone Powder on the Properties of Alkali-Activated Slag System. Master's Thesis, Guangzhou University, Guangzhou, China, 2023.
45. Li, J. Research on Carbonization of Waste Concrete Powder and Its Application in Brickmaking. Master's Thesis, Guangzhou University, Guangzhou, China, 2023.
46. Liu, G.; Florea, M.V.A.; Brouwers, H.J.H. Waste glass as binder in alkali activated slag–fly ash mortars. *Mater. Struct.* **2019**, *52*, 101. [CrossRef]
47. Bernal, S.A.; Provis, J.; Rose, V.; De Gutierrez, R.M. Evolution of binder structure in sodium silicate-activated slag-metakaolin blends. *Cem. Concr. Compos.* **2011**, *33*, 46–54. [CrossRef]

buildings

Article

Experimental Study on the Mechanical Properties of Recycled Spiral Steel Fiber-Reinforced Rubber Concrete

Jinqiu Yan [1], Yongtao Gao [2,*], Minggao Tang [2], Nansheng Ding [2], Qiang Xu [2], Man Peng [2] and Hua Zhao [2]

[1] School of Architecture and Civil Engineering, Xihua University, Jinzhou Road 999#, Chengdu 610039, China; shang1597533@163.com
[2] State Key Laboratory of Geohazard Prevention and Geoenvironment Protection, No. 1, East Third Road, Erxianqiao, Chengdu 610059, China; tomyr2008@163.com (M.T.); dingnansheng@cdut.edu.cn (N.D.); xuqiang_68@126.com (Q.X.)
* Correspondence: gaoyongtao06@cdut.edu.cn

Abstract: Recycled rubber (RR) and recycled spiral steel fiber (RSSF) were added to plain concrete (PC) to prepare recycled spiral steel fiber rubber concrete (SSFRC) with matrix strengths of C30, C40, and C50. Strength tests on the PC, rubber concrete (RC), and SSFRC were carried out, including the cube compressive strength, splitting tensile strength, and flexural strength. The effects of RSSF and RR on the mechanical properties of concrete were analyzed. Simultaneously, the stress–strain curve of the SSFRC was obtained through axial compressive testing, and the toughness of SSFRC was evaluated by three indexes: the tensile compression ratio, bending compression ratio, and toughness index. The results show that adding RR to PC results in a decrease in the mechanical properties of concrete with different matrix strengths, and the addition of RSSF can make up for the strength loss of the rubber. The mechanical strength of SSFRC with different matrix strengths increased first and then decreased with the increase in RSSF content. The cubic compressive strength reached its peak value when the content of RSSF was 1%, and the splitting tensile strength and flexural strength reach their peak values when the content of RSSF was 1.5%. RSSF works best with rubber particles at the right dosage to further increase the toughness of the concrete. When the rubber content is 10%, and the RSSF content is 1.5%, the mechanical strength enhancement effect of SSFRC is at its best, and the toughness is also at its best.

Keywords: recycled spiral steel fiber rubber concrete; strength test; reinforcement; toughness

1. Introduction

With the rapid development of the global transportation industry, hundreds of millions of discarded tires are produced by the elimination of vehicles every year [1,2]. According to statistics, about 50 million tires are directly discarded every year, with only a small portion able to be recycled, and 500 million tires will be discarded by 2030 [3,4]. A landfill of waste tires can cause serious fire hazards and environmental pollution, and the accumulated tires can also harbor bacteria that can cause diseases in humans [5–7]. The existing pyrolysis treatment measures for waste tires not only have a long investment return cycle but also produce a large amount of carbon dioxide, which promotes the greenhouse effect of the atmosphere to a certain extent [8]. In order to maximize the recycling of waste tires and reduce their harm to the environment and society, waste tires can be made into rubber particles instead of natural sand so as to partially replace the fine aggregate in concrete and achieve the purpose of saving resources [9].

B.S. Thomas et al. [10] added waste tire rubber particles to concrete and studied the fatigue performance of rubber concrete under constant amplitude cyclic loading, finding that the fatigue performance of rubber concrete is better than that of ordinary concrete. Han Q. et al. [11] found that when the rubber particle size and content reached the optimum, the performance of concrete under cyclic load could be effectively improved, making it suitable for the construction of rigid pavement. P.N. Pham et al. [12] added waste rubber particles to high-strength concrete, and the results showed that the impact resistance of concrete increased by 83%. Hassanli R. et al. [13] added modified waste rubber particles to recycled aggregate concrete, and its impact resistance increased significantly compared with recycled aggregate concrete. O. Youssf et al. [14] found that rubber particles at a specific particle size and dosage could enhance the freeze-thaw resistance of concrete. T.M. Pham et al. [15] found that modified recycled rubber particles can improve the vibration reduction and sound insulation ability of light aggregate concrete.

Due to its low strength and low elastic modulus, rubber will reduce the mechanical properties of concrete [16–18]. In order to improve this strength loss, the current main methods are to modify the rubber surface, add other fiber materials, etc. [19]. G.A. Issa et al. [20] optimized the mix ratio of rubber concrete, and the loss of its force-flow and mechanical properties was limited. K. Shahzad et al. [21] et al. studied the surface changes of NAOH- and urea-modified rubber. Both materials reduced the hydrophobicity of the rubber surface to varying degrees. NAOH treatment can remove part of the hydrophobic substances on the surface of rubber particles, increase the surface roughness and surface area of rubber particles, and slightly reduce the water contact angle of rubber, where the reduced rubber water contact angle is 36.9°. The treatment method is simple to operate and low in cost. Z. Keshavarz et al. [22] treated rubber particles with NAOH, silane coupling agent (SCA), and a sulfuric acid solution, and the mechanical properties of the rubber concrete were significantly enhanced. In addition to fiber materials, at present, the best effect is mainly from adding steel fiber to rubber concrete. M.K. Ismail et al. [23] added steel fiber to waste rubber concrete and found that the synergistic effect of the steel fiber and rubber could improve the compressive strength of the concrete. I. Guerra et al. [24] found that steel fiber could significantly enhance the dynamic and static tensile strength of concrete, and its ductility was also significantly improved. H. Gharibi, D.G. Aggelis, and J. Xu et al. [25–27] showed that the combination of steel fiber and rubber particles yielded a significant improvement in the tensile properties. The addition of steel fiber can also reduce the loss of flexural strength, and the crack width of steel fiber rubber concrete is much smaller than that of steel fiber concrete. Q. Han and J. Xu et al. [28–30] found that the combination of waste rubber and steel fiber can further improve the toughness of concrete, and the synergistic effect of the two can greatly increase the fracture mode of concrete. A.A. Abouhussien et al. [31] believed that steel fiber orientation could improve the flexural strength and crack resistance of concrete. Z. Keshavarz, D. and M.S.S. Ahamad et al. [32,33] added steel fiber to rubber concrete, and the peak deflection, toughness, and ductility of the rubber concrete under bending and shearing all increased with the increase in steel fiber content. J. Xu and L.A. Jimoda et al. [34,35] found that the bending strength and tensile strength were related to the steel fiber content, and the strain, hardening. and softening behaviors of steel fiber rubber concrete were mainly affected by the steel fiber content.

In current research methods, primary steel fibers or steel fibers extracted from waste tires are mainly used to reinforce rubber concrete, but these steel fibers have a planar shape. Spiral-shaped recycled steel fibers have a three-dimensional spatial shape, which can form a three-dimensional bonding structure with rubber and concrete and have obvious spatial mechanical characteristics. They can form bonds with concrete in multiple dimensions, thereby preventing concrete from bonding in multiple directions. In order to explore the influence of spiral recycled steel fiber on rubber concrete, this experiment adopts the basic mechanical properties of recycled spiral steel fiber-reinforced rubber concrete with different volume contents. We study the cube compressive strength, splitting tensile strength, flexural strength, and prismatic axial compressive strength of various SSFRCs at 28 d. At the same time, the tensile compression ratio, folding compression ratio, and toughness index were used to evaluate the toughness of RSSFRC, and the measured values of the axial compressive strength and cubic compressive strength of SSFRC were fitted, while a more suitable formula for calculating the axial compressive strength of RSSFRC was established. Through the experimental research of RSSFRC, the three-dimensional model mechanism of the improvement of the mechanical properties of rubber concrete by recycled spiral steel fibers was revealed, and the ductility working mechanism of recycled spiral steel fiber rubber concrete was explored. This provides a new approach for the utilization of renewable resources and the green application of civil engineering materials.

2. Materials and Test Methods

2.1. Materials

Common Portland cement P.O 42.5 was used as the test cement. The packing density was 3.05×10^3 kg/m^3, and its related performance indexes are shown in Table 1. The coarse aggregate was gravel with a particle size d < 40 mm, and the packing density was 2.5×10^3 kg/m^3. The fine aggregate was medium coarse sand with an apparent density of 2.65 kg/cm^3, and ordinary tap water was used for mixing, with the particle size range of the sand being between 0.5 and 2.0 mm. The RSSF came from the residual material of machining, and its density was 7.8×10^3 kg/m^3. It had a three-dimensional helical structure with an average length of 20~40 mm, a width from 2 to 4 mm, a thickness of less than 0.5 mm, an average tensile strength of no less than 350 MPa, and an elastic modulus of 2.1×10^5 N/mm^2. The rubber came from the broken particles of waste tires, where the packing density was 0.9×10^3 kg/m^3, the particle size was from 1 to 3 mm, and it was washed with 5% NaOH solution to pH = 7. The raw materials are shown in Figure 1.

Table 1. Cement performance index.

Standard Consistency (%)	**Setting Time (min)**		**Compressive Strength of Cube (MPa)**		**Flexural Strength (MPa)**	
24.2	Initial condensation	Termination condensation	3 d	28 d	3 d	28 d
	180	260	25.5	52.5	5.2	8.8

(**a**) (**b**) (**c**) (**d**)

Figure 1. Raw materials for testing: (**a**) coarse aggregate; (**b**) RSSF inspection; (**c**) treated RSSF; and (**d**) alkali washed rubber.

2.2. Specimen Making and Maintenance

According to the existing research results and the actual situation of this test, the rubber content was determined to be 10%, replacing fine aggregate sand with rubber at a volume content of 10% sand. The volume content of the RSSF was 0%, 0.5%, 1.0%, 1.5%, and 2%. The matrix strength of the SSFRC specimens was C30, C40, and C50. The concrete mix ratios of the specimens with different strength grades are shown in Table 2. Since the design strength of all concrete specimens was between C30 and C60, non-standard specimen sizes were used in all kinds of tests. For details on the size of the test blocks, see Table 3.

Table 2. Mix ratio of each specimen.

Strength Grade of Concrete Matrix	RSSF Volume Content (%)	Amount of Each Material per Unit Volume (kg/m^3)					
		Cement	Gravel	Sand	Water	Rubber	RSSF
C30	0	380	1251	644	180	0	0
	0	380	1251	580	180	32	0
	0.5	380	1251	580	180	32	39
	1	380	1251	580	180	32	79
	1.5	380	1251	580	180	32	118
	2	380	1251	580	180	32	157
C40	0	420	1241	577	180	0	0
	0	420	1241	519	180	28	0
	0.5	420	1241	519	180	28	39
	1	420	1241	519	180	28	79
	1.5	420	1241	519	180	28	118
	2	420	1241	519	180	28	157
C50	0	470	1200	617	165	0	0
	0	470	1200	555	165	30	0
	0.5	470	1200	555	165	30	39
	1	470	1200	555	165	30	79
	1.5	470	1200	555	165	30	118
	2	470	1200	555	165	30	157

Table 3. Test specimen.

Intensity Type	Specimen Size (mm)	Number of Specimens	Number per Group	Total	Total
Compressive strength of cube	100 × 100 × 100	18	3	54	216
Splitting tensile strength	100 × 100 × 100	18	3	54	
Flexural strength	100 × 100 × 400	18	3	54	
Axial compressive strength	100 × 100 × 300	18	3	54	

When the specimen was made, it was carried out in strict accordance with the specification of "steel fiber reinforced concrete (JG/T472-2015)", and the raw materials required for weighing were reserved. First, we poured the coarse aggregate gravel, fine aggregate river sand, and cement into the raw materials on an impervious steel plate that was soaked in advance and dry mixed for 2 min. After the dry mixing, we evenly sprinkled the rubber particles and continued to stir it. After fully mixing, we added water and then the RSSF. The whole process of adding RSSF had to include stirring, and the RSSF had to be input three times. When each RSSF was input, we waited for the previous batch of RSSF to be fully and evenly mixed with the mixture. With the increase in RSSF content, the input times of the RSSF could be appropriately increased, and the wet mixing time was not less than 3 min. The resulting SSFRC mixture was subjected to slump testing to evaluate its workability. Then, the SSFRC mixture was poured into a clean mold coated with waste oil, and the shaking table was used to vibrate and compact the mixture until the surface of the mix was slurry, and a small amount of waste oil was spilled. When the vibration was over, we smoothed and removed air bubbles with a scraper. The mold was removed 24 h after casting and placed in water at 20 ± 2 °C for maintenance for 28 d.

2.3. Test Method

2.3.1. Slump

The slump test could be carried out after the SSFRC mixture was evenly mixed, Relevant test operations were carried out in accordance with the "steel fiber reinforced concrete (JG/T472-2015)"of China.

2.3.2. Mechanical Strength

The compressive strength of the cube was tested with a WHY-1000 microcomputer controlled pressure testing machine with a maximum measuring range of 1000 kN. The splitting tensile strength was tested with a CSS-555000 microcomputer controlled electro-hydraulic servo testing machine, which was combined with a steel splitting tensile fixture. The flexural strength was measured with a YA-500 microcomputer hydraulic pressure testing machine. The axial compression strength was tested with a CSS-MAM600DL electro-hydraulic servo universal testing machine. The relevant test operation and strength calculations were carried out in accordance with the "Fiber Concrete Test Method Standard", and the test equipment and installation are shown in Figure 2.

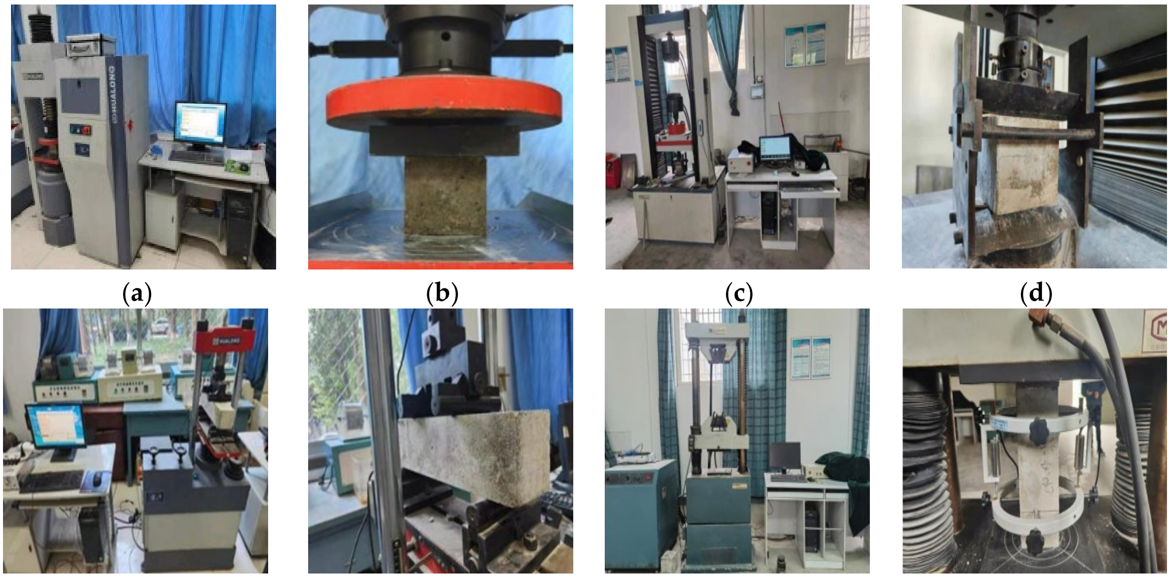

(**a**) (**b**) (**c**) (**d**)

(**e**) (**f**) (**g**) (**h**)

Figure 2. Installation diagram of test equipment and specimens: (**a**) WHY-1000 testing machine; (**b**) installation diagram of compressive strength testing machine; (**c**) CSS-555000 testing machine; (**d**) installation diagram of tensile strength testing machine; (**e**) YA-500 testing machine; (**f**) installation drawing of flexural strength testing machine; (**g**) CSS-MAM600DL testing machine; and (**h**) installation drawing of axial compression testing machine.

3. Test Results and Discussion

3.1. Slump

Figure 3 shows the variation trend of the slump values of concrete with different strengths. Table 4 shows the slump values of the PC, RC, and SSFRC mixes with different volumes. As can be seen in Figure 3, the addition of rubber particles and steel fibers reduced the slump of the concrete to a certain extent, making its working performance worse. The higher the RSSF content was, the more the slump would be reduced. The higher the strength of the concrete matrix, the lower the slump.

The reason for the above phenomenon is that the surface of the rubber particles after alkali washing was uneven, and the shape was irregular, which enhanced the water absorption capacity of the rubber surface and increased the friction force of the internal flow of the mix, thereby reducing the fluidity of the mix. The RSSF used in the test had a three-dimensional helical structure and good spatial characteristics, and the particles were connected to each other in the concrete, which enhanced the internal connection of the concrete, increased the friction force of the internal flow of the concrete mix, and restricted the movement of each. The slump of the mixture was decreased by the synergistic effect of the RSSF and rubber. This is because the addition of a large amount of RSSF makes the RSSF occasionally cross, and it cannot significantly bridge the effect, forming a network structure.

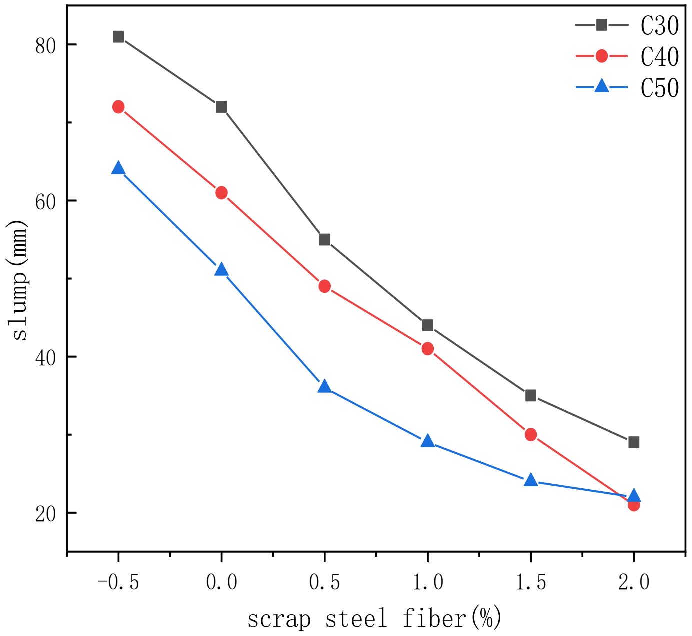

Figure 3. Slump test results.

Table 4. Slump values of concrete with different strengths.

Specimen Number	Slump (mm)
C30—PC	81
C30—RC	72
C30—SSFRC—0.5%	55
C30—SSFRC—1.0%	44
C30—SSFRC—1.5%	35
C30—SSFRC—2.0%	29
C40—PC	72
C40—RC	61
C40—SSFRC—0.5%	49
C40—SSFRC—1.0%	41
C40—SSFRC—1.5%	30
C40—SSFRC—2.0%	21
C50—PC	64
C50—RC	51
C50—SSFRC—0.5%	36
C50—SSFRC—1.0%	29
C50—SSFRC—1.5%	24
C50—SSFRC—2.0%	22

3.2. Mechanical Strength

Figure 4 shows the variation trend of the mechanical strength of the PC, RC, and SSFRC with different strengths at 28 d, including the cube compressive strength, splitting tensile strength, flexural strength, and axial compressive strength.

As can be seen in Figure 4, after adding 10% rubber particles to the PC, the mechanical strength of the RC decreased to varying degrees. The cubic compressive strength, splitting tensile strength, and flexural strength of the C30 concrete decreased by about 10%. Those of the C40 concrete decreased by about 14%, while those of the C50 concrete decreased by about 21%. This shows that the addition of rubber has the same influence on the mechanical strength of concrete with the same matrix strength, and the influence on the mechanical properties of high-strength concrete is greater when the matrix strength is different.

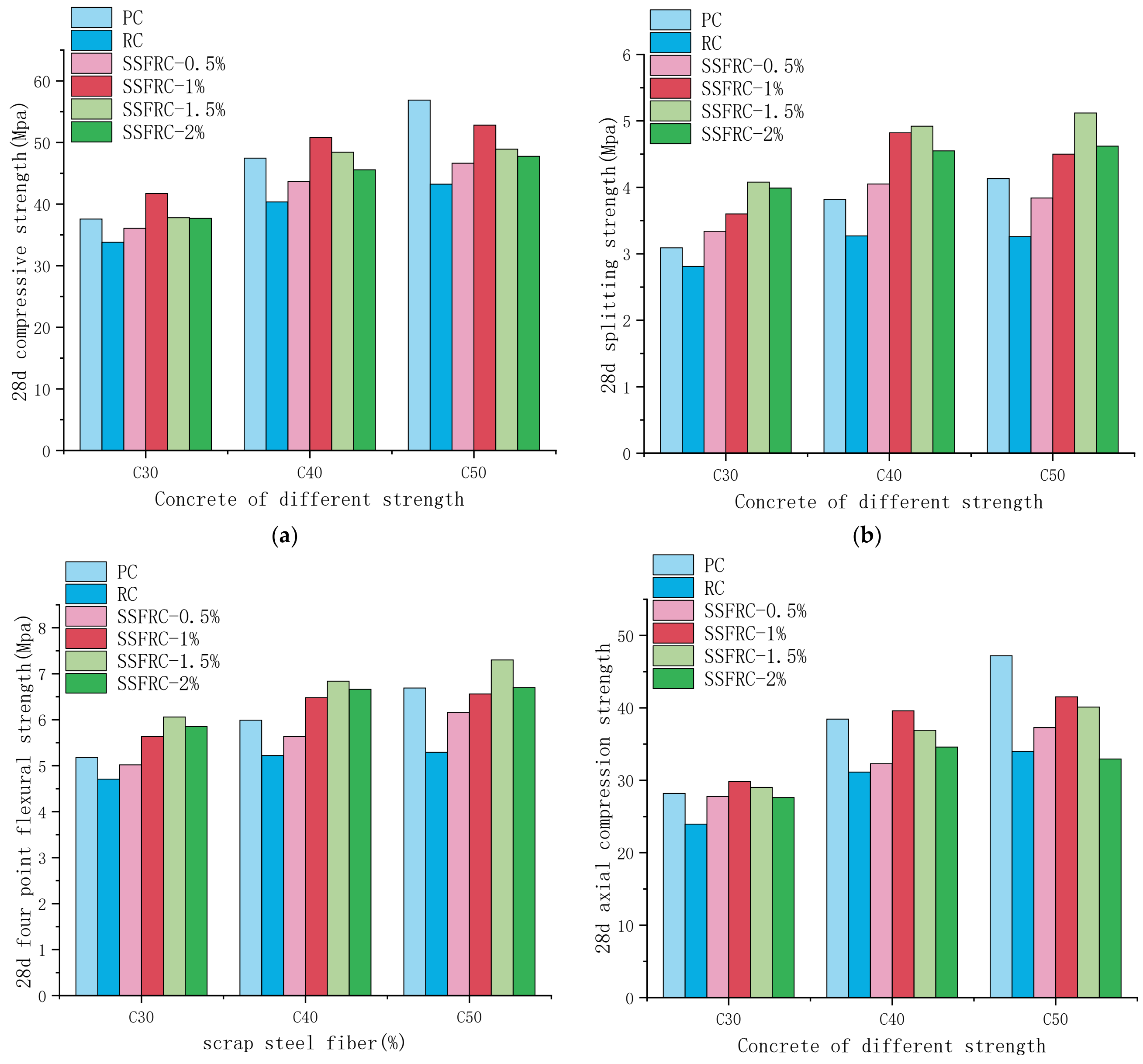

(**a**) (**b**) (**c**) (**d**)

Figure 4. Strength variation trends of different types of concrete: (**a**) cube compressive strength; (**b**) splitting tensile strength; (**c**) flexural strength; and (**d**) axial compressive strength.

The reason for this result is that the structural weakness of the rubber itself, as well as the hydrophobicity of the rubber particles after alkali washing, made the interface transition zone between the rubber particles and the cement stone clear. Studies have shown that the strength of the interface area between rubber and mortar is only 35% of the strength of mortar [36–38], and the surface of rubber particles cannot become completely hydrophilic with this alkaline washing treatment [39,40]. The hydrophobicity of rubber particles will prevent water molecules from contacting the rubber surface, thus inhibiting the hydration of cement on the rubber surface, resulting in a reduction in calcium silicate hydrate (C-S-H) gel, the hydration product of the main strength source in RC, and a reduction in compressive strength [41–43].

It can also be seen in Figure 4 that after adding RSSF, the mechanical strength of concrete with different matrix strengths presented a trend of first increasing and then decreasing with the increase in RSSF content. The compressive strength of SSFRC with different matrix strengths reached its peak value when the content of RSSF was 1%. The peak compressive strength of the C30 and C40 concrete increased by 23% and 26% compared with the RC, respectively, with both exceeding that of plain PC. The peak compressive strength of the C50 concrete increased by 22% compared with the RC but only reached 93% of the RC's strength. The splitting tensile strength and flexural strength both reached their peak values when the content of RSSF was 1.5%. Compared with the RC, the peak tensile strengths of the C30, C40, and C50 concrete increased by 45%, 50%, and 56%, respectively, all exceeding that of the PC. The corresponding peak bending strength increased by 28%, 31%, and 37% compared with the RC, respectively, which also exceeded that of the PC.

Figure 5 shows three mechanical strength ratios of different types of concrete, including the cube compressive strength ratio, splitting tensile strength ratio, and flexural strength ratio. Table 5 shows the 28 d mechanical strengths of the PC, RC, and SSFRC.

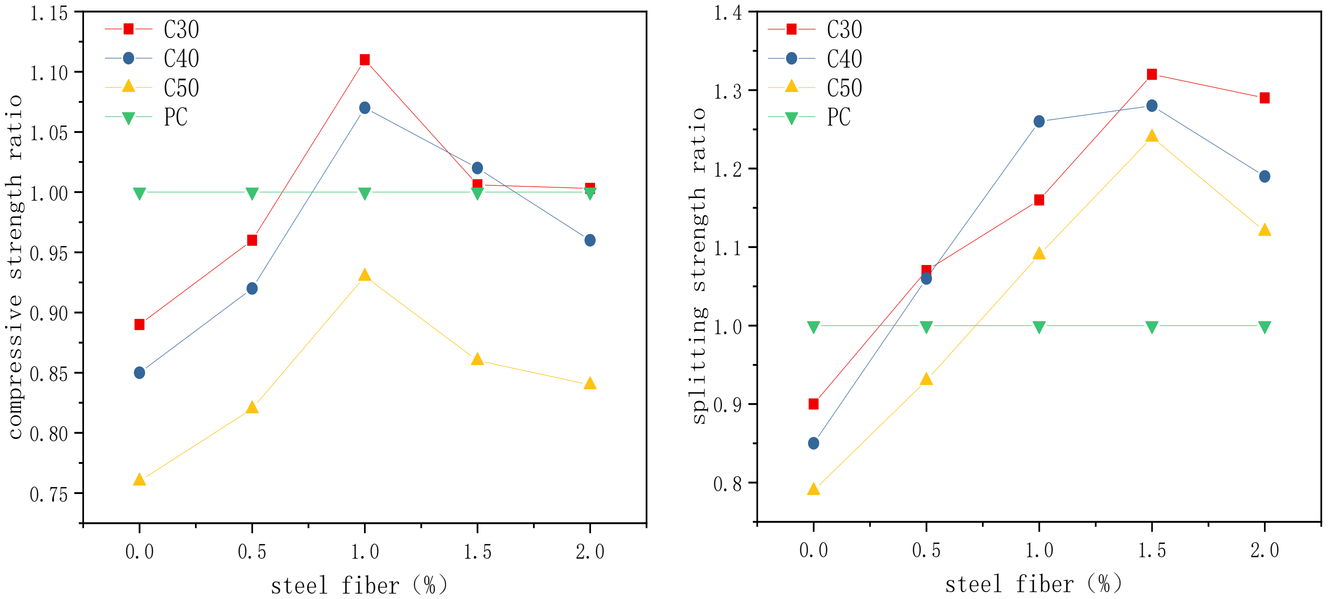

(**a**) Cube compressive strength ratio (**b**) Splitting tensile strength ratio

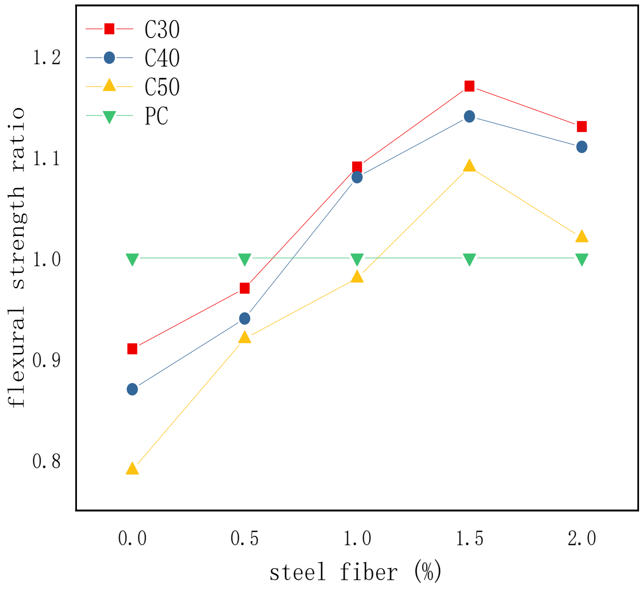

(**c**) Flexural strength ratio

Figure 5. Mechanical strength ratios of different types of concrete: (**a**) cube compressive strength ratio; (**b**) splitting tensile strength ratio; and (**c**) flexural strength ratio.

Table 5. Different types of concrete mechanical strength values at 28 d.

Specimen Number	Compressive Strength of Cube (MPa)	Splitting Tensile Strength (MPa)	Flexural Strength (MPa)	Axial Compressive Strength (MPa)
C30-PC	37.58	3.09	5.18	28.18
C30-RC	33.8	2.81	4.71	23.95
C30-SSFEC-0.5%	36.07	3.34	5.02	27.77
C30-SSFEC-1%	41.71	3.6	5.64	29.87
C30-SSFEC-1.5%	37.8	4.08	6.06	29.03
C30-SSFEC-2%	37.69	3.99	5.85	27.62
C40-PC	47.47	3.82	5.99	38.45
C40-RC	40.35	3.27	5.22	31.14
C40-SSFEC-0.5%	43.67	4.05	5.64	32.29
C40-SSFEC-1%	50.79	4.82	6.48	39.6
C40-SSFEC-1.5%	48.42	4.92	6.84	36.91
C40-SSFEC-2%	45.57	4.55	6.66	34.60
C50-PC	56.87	4.13	6.69	47.2
C50-RC	43.23	3.26	5.29	33.98
C50-SSFEC-0.5%	46.63	3.84	6.16	37.28
C50-SSFEC-1%	52.82	4.50	6.56	41.53
C50-SSFEC-1.5%	48.92	5.12	7.30	40.12
C50-SSFEC-2%	47.76	4.62	6.70	32.95

It can be seen in Figure 5 that the mechanical strength of the C30, C40, and C50 SSFRC increased compared with the PC. In addition to the C50 cube compressive strength being lower than that of the PC, the rest exceeded that of the PC. According to the data in Figure 5, it can be seen that the addition of RSSF could greatly improve the tensile and flexural strength of RC, but the improvement in compressive strength was not obvious. Moreover, 1% RSSF had the best effect on the cube compressive strength, and the 1.5% RSSF had the best effect on the splitting tensile strength and flexural strength.

The ratio of the axial compressive strengths and cube compressive strengths of different kinds of concrete was different, and the ratio of the two was between 0.69 and about 0.83 in this test. Based on the measured values of the axial compressive strength and cube compressive strength, a new calculation relationship suitable for SSFRC was fitted [44–46], as shown in Equation (1), and the relationship between the two is shown in Figure 6:

$$\mathrm{f_c} = 0.92\mathrm{f_{cu}} - 6.72 \tag{1}$$

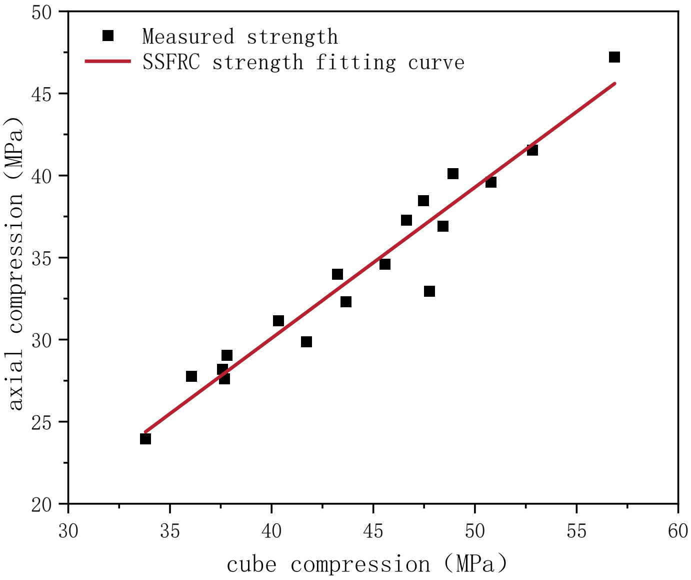

Figure 6. Relationship between SSFRC cube compression and axial compression.

In Equation (1), f_c is the axial compressive strength test value of the SSFRC, and f_{cu} is the cube compressive strength test value of the SSFRC.

3.3. Toughness Evaluation

Figure 7 shows the stress–strain curves of the PC, RC, and SSFRC with different strengths under axial pressure, while Figures 8 and 9 show the variation trends of the tensile and compressive ratios of the SSFRC, respectively. Table 6 shows the tensile compression ratio, folding compression ratio, and toughness index of various concrete types.

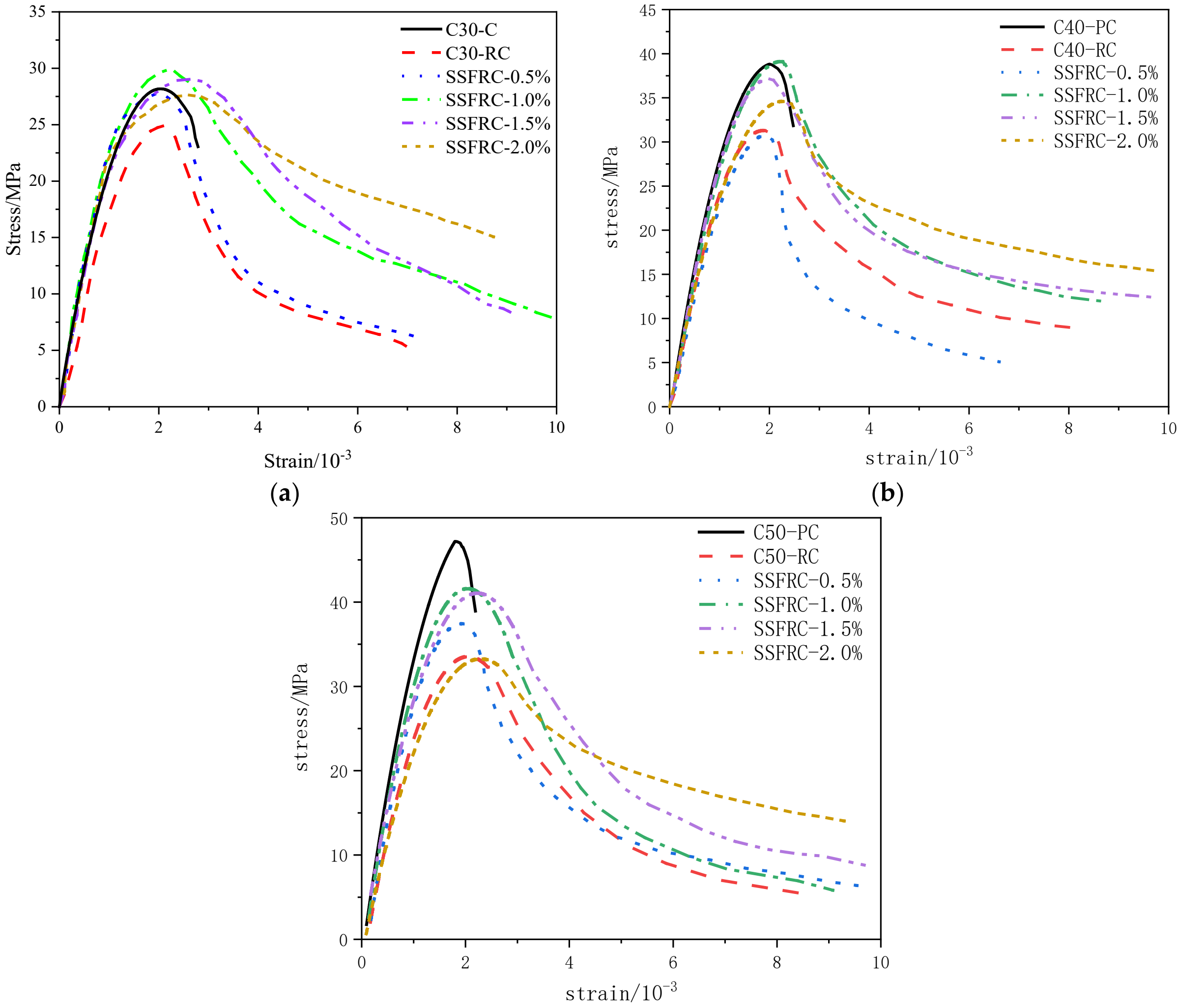

(**a**) (**b**)

(**c**)

Figure 7. Stress—strain curves of different types of concrete: (**a**) C30; (**b**) C40; and (**c**) C50.

As can be seen in Figure 7, the curve was divided into an ascending section (a linear ascending stage before the initial crack point and a nonlinear ascending stage from the initial crack point to the peak stress) and a descending section (a failure stage of the specimen after the peak stress). The full stress–strain curve could be obtained for the RC and SSFRC except for the latter half of the stress–strain curve, which could not be obtained for the PC due to brittle failure. It can be seen from Figure 7a–c that the addition of rubber reduced the peak stress of the PC. This is because rubber reduces the strength of PC, which is the same reason why the compressive strength of the cubes in Section 3.2 decreased.

After adding the RSSF, the peak stress of the specimen first increased and then decreased. This is because after the content of RSSF reaches a certain value, the continuous increase in content will make the RSSF overlap with each other and increase the weak point in the matrix, thus weakening the strengthening effect. The addition of rubber increased the peak strain of the PC, indicating that rubber can improve the deformation capacity of PC and increase its ductility. After the addition of RSSF, the peak strain of the SSFRC with different matrix strengths increased compared with that of the RC, and the stress–strain area increased with different amplitudes compared with that of the RC. The results show that RSSF has positive effect on RC's crack resistance at different strengths, and the C30 matrix strength was the most significant. With the increase in RSSF content, the decline trend of the post-peak curve was slower than that of the RC, and the compressive toughness of the SSFRC was further improved.

Table 6. Tensile compression ratios, folding pressures, and toughness indexes of different types of concrete.

Specimen Number	Tension and Compression Ratio	Flexural Strength and Compressive Strength Ratio	Toughness Index
C30-PC	0.0823	0.13783	-
C30-RC	0.0831	0.13934	1.51
C30-SSFRC-0.5%	0.0926	0.13917	1.48
C30-SSFRC-1.0%	0.0863	0.13521	1.88
C30-SSFRC-1.5%	0.1079	0.16031	1.77
C30-SSFRC-2.0%	0.1058	0.15521	2.05
C40-PC	0.0804	0.12618	-
C40-RC	0.0810	0.12936	1.32
C40-SSFRC-0.5%	0.0927	0.1291	1.75
C40-SSFRC-1.0%	0.0949	0.12758	1.60
C40-SSFRC-1.5%	0.1016	0.14126	1.67
C40-SSFRC-2.0%	0.0997	0.14614	1.97
C50-PC	0.0726	0.11763	-
C50-RC	0.0754	0.12236	1.64
C50-SSFRC-0.5%	0.0824	0.13210	1.72
C50-SSFRC-1.0%	0.0852	0.12419	1.49
C50-SSFRC-1.5%	0.1047	0.14922	1.73
C50-SSFRC-2.0%	0.0967	0.14028	1.98

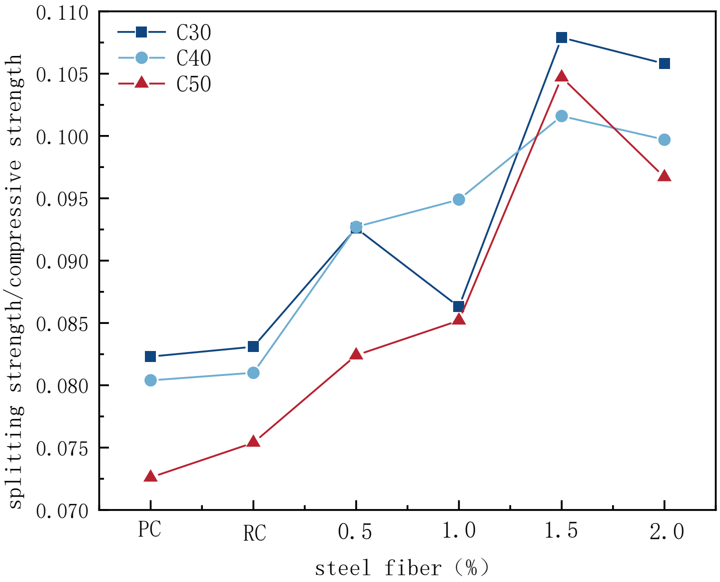

Figure 8. Tensile compression ratio curves of different types of concrete.

In Table 5, the compressive strength of the cube is the compressive strength value obtained by testing a cube with a size of 100 × 100 × 100 mm. This value is mainly used to determine the strength grade of the concrete. The axial compressive strength is the value obtained by conducting tests on 100 × 100 × 300 mm test blocks, which is mainly used to determine the design value of the concrete's compressive strength.

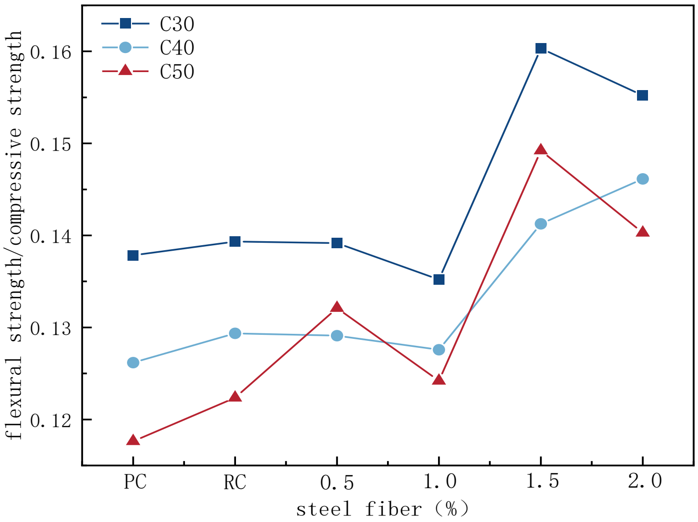

Figure 9. Ratio curves of flexural and compressive strengths of different types of concrete.

4. Conclusions

By adding different volumes of RSSF into RC, the mechanical properties and toughness characteristics of RSSF rubber concrete were studied by means of test methods. The main conclusions are as follows:

(1) Rubber particles and different volumes of RSSF will reduce the slump of concrete to a certain extent. The higher the RSSF content, the more the slump decreases. The higher the concrete strength, the lower the slump. But the slump of concrete with a high RSSF content does not decrease continuously.

(2) The addition of rubber particles has similar effects on different mechanical properties of concrete with the same matrix strength. When the matrix strength is different, the mechanical properties of high-strength concrete are affected more. When the RSSF content is 1%, the compressive strength of concrete with different matrix strengths is the best. When the RSSF content is 1.5%, the tensile strength and flexural strength are the best, but the strength improvement effect on high-strength concrete is limited.

(3) Rubber can improve the toughness of PC. The toughness of RC with different matrix strengths is further improved by different dosages of RSSF. When the content of RSSF is 1.5%, the folding ratio and tension ratio of each SSFRC reach the peak value, and the toughness index increases with the increase in the content of RSSF. The synergistic effect of RSSF with rubber particles at a certain amount further increases the toughness of RC. When the content of rubber is 10%, and the content of RSSF is 1.5%, the mechanical properties and compressive toughness of concrete can be improved the most, and the defects of PC brittleness can be effectively improved.

Author Contributions: Conceptualization, Q.X.; methodology, M.T.; software, M.P.; validation, H.Z.; formal analysis, J.Y.; investigation, J.Y.; resources, M.T.; data curation, Y.G.; writing—original draft preparation, N.D.; writing—review and editing, J.Y. All authors have read and agreed to the published version of the manuscript.

Funding: This research was funded by the National Science and Technology Support Program of China, the National Natural Science Foundation of China, and the State Key Laboratory of Geological Disaster Prevention and Geological Environmental Protection of Chengdu University of Technology under grant numbers 2015BAK09B01, 41877273, and SKLGP2019K019.

Data Availability Statement: Data will be made available upon request.

Acknowledgments: The authors of the paper would like to thank the editors and reviewers for their guidance and feedback on the paper.

Conflicts of Interest: The authors declare that they have no known competing financial interests or personal relationships that could have appeared to influence the work reported in this paper.

References

1. Straka, P.; Auersvald, M.; Vrtiska, D.; Kittel, H.; Simacek, P.; Vozka, P. Production of transportation fuels via hydrotreating of scrap tires pyrolysis oil. *Chem. Eng. J.* **2023**, *460*, 141764. [CrossRef]
2. AbdelAleem, B.H.; Ismail, M.K.; Hassan, A.A. The combined effect of crumb rubber and synthetic fibers on impact resistance of self-consolidating concrete. *Constr. Build. Mater.* **2018**, *162*, 816–829. [CrossRef]
3. Abdelmonem, A.; El-Feky, M.S.; Nasr, E.S.A.; Kohail, M. Performance of high strength concrete containing recycled rubber. *Constr. Build. Mater.* **2019**, *227*, 116660. [CrossRef]
4. Aly, A.M.; El-Feky, M.S.; Kohail, M.; Nasr, E.S.A. Performance of geopolymer concrete containing recycled rubber. *Constr. Build. Mater.* **2019**, *207*, 136–144. [CrossRef]
5. Sofi, A. Effect of waste tyre rubber on mechanical and durability properties of concrete—A review. *Ain Shams Eng. J.* **2018**, *9*, 2691–2700. [CrossRef]
6. Yi, O.; Zhuge, Y.; Ma, X.; Gravina, R.J.; Mills, J.E.; Youssf, O. Push-off and pull-out bond behaviour of crc composite slabs—An experimental investigation. *Eng. Struct.* **2021**, *228*, 111480. [CrossRef]
7. Siddika, A.; Al Mamun, M.A.; Alyousef, R.; Amran, Y.H.M.; Aslani, F.; Alabduljabbar, H. Properties and utilizations of waste tire rubber in concrete: A review. *Constr. Build. Mater.* **2019**, *224*, 711–731. [CrossRef]
8. Roychand, R.; Gravina, R.J.; Zhuge, Y.; Ma, X.; Youssf, O.; Mills, J.E. A comprehensive review on the mechanical properties of waste tire rubber concrete. *Constr. Build. Mater.* **2020**, *237*, 117651. [CrossRef]
9. Richardson, A.; Coventry, K.; Edmondson, V.; Dias, E. Crumb rubber used in concrete to provide freeze–thaw protection (optimal particle size). *J. Clean. Prod.* **2016**, *112*, 599–606. [CrossRef]
10. Thomas, B.S.; Chandra Gupta, R. Properties of high strength concrete containing scrap tire rubber. *J. Clean. Prod.* **2016**, *113*, 86–92. [CrossRef]
11. Han, Q.; Yang, G.; Xu, J. Performance of crumb rubber concrete made with high contents of heat pre-treated rubber and magnetized water. *J. Mater. Res. Technol. JMR&T* **2018**, *25*, e2240.
12. Youssf, O.; Swilam, A.; Tahwia, A.M. Application of rubberized cement-based composites in pavements: Suitability and considerations. *Constr. Build. Mater.* **2023**, *23*, 2160–2176.
13. Hassanli, R.; Youssf, O.; Vincent, T.; Mills, J.E.; Manalo, A.; Gravina, R. Experimental Study on Compressive Behavior of FRP-Confined Expansive Rubberized Concrete. *J. Compos. Constr.* **2020**, *24*, 04020034. [CrossRef]
14. Youssf, O.; Mills, J.E.; Hassanli, R. Assessment of the mechanical performance of crumb rubber concrete. *Constr. Build. Mater.* **2016**, *125*, 175–183. [CrossRef]
15. Pham, T.M.; Renaud, N.; Pang, V.; Shi, F.; Hao, H.; Chen, W.S. Effect of rubber aggregate size on static and dynamic compressive properties of rubberized concrete. *Struct. Concr.* **2022**, *23*, 2510–2522. [CrossRef]
16. Abd-Elaal, E.; Araby, S.; Mills, J.E.; Youssf, O.; Roychand, R.; Ma, X.; Zhuge, Y.; Gravina, R.J. Novel approach to improve crumb rubber concrete strength using thermal treatment. *Constr. Build. Mater.* **2019**, *229*, 116901. [CrossRef]
17. Ismail, M.K.; Hassan, A.A.A. Influence of mixture composition and type of cementitious materials on enhancing the fresh properties and stability of self-consolidating rubberized concrete. *J. Mater. Civ. Eng.* **2016**, *28*, 04015075. [CrossRef]
18. Ismail, M.K.; Hassan, A.A.A. Use of metakaolin on enhancing the mechanical properties of self-consolidating concrete containing high percentages of crumb rubber. *J. Clean. Prod.* **2016**, *125*, 282–295. [CrossRef]
19. Abu Bakar, B.H.; Noaman, A.T.; Akil, H.M. Cumulative effect of crumb rubber and steel fiber on the flexural toughness of concrete. *Eng. Technol. Appl. Sci. Res.* **2017**, *7*, 1345–1352. [CrossRef]
20. Issa, G.A.; Salem, G. Utilization of recycled crumb rubber as fifine aggregates in concrete mix design. *Constr. Build. Mater.* **2013**, *42*, 48–52. [CrossRef]
21. Shahzad, K.; Zhao, Z. Experimental study of NaOH pretreated crumb rubber as substitute of fine aggregate in concrete. *Constr. Build. Mater.* **2022**, *358*, 129448. [CrossRef]
22. Keshavarz, Z.; Mostofinejad, D. Porcelain and red ceramic wastes used as replacements for coarse aggregate in concrete. *Constr. Build. Mater.* **2019**, *195*, 218–230. [CrossRef]
23. Ismail, M.K.; Hassan, A.A.A. Impact resistance and mechanical properties of self-consolidating rubberized concrete reinforced with steel fibers. *J. Mater. Civ. Eng.* **2017**, *29*, 04016193. [CrossRef]
24. Guerra, I.; Vivar, I.; Llamas, B.; Juan, A.; Moran, J. Eco-efficient concretes: The effects of using recycled ceramic material from sanitary installations on the mechanical properties of concrete. *Waste Manag.* **2009**, *29*, 643–646. [CrossRef] [PubMed]
25. Gharibi, H.; Mostofinejad, D. Thermal and mechanical properties of concrete containing porcelain ceramic tile waste as fine and coarse aggregates. *Mag. Concr. Res.* **2023**, *75*, 123–134. [CrossRef]
26. Aggelis, D.G.; Mpalaskas, A.C.; Matikas, T.E. Investigation of different fracture modes in cement-based materials by acoustic emission. *Cem. Concr. Res.* **2013**, *48*, 1–8. [CrossRef]

27. Xu, J.; Fu, Z.; Han, Q.; Li, H. Fracture monitoring and damage pattern recognition for carbon nanotube-crumb rubber mortar using acoustic emission techniques. *Struct. Control Health Monit.* **2019**, *26*, e2422. [CrossRef]
28. Han, Q.; Xu, J.; Carpinteri, A.; Lacidogna, G. Localization of acoustic emission sources in structural health monitoring of masonry bridge. *Struct. Control Health Monit.* **2015**, *22*, 314–329. [CrossRef]
29. Xu, J.; Niu, X.L.; Yao, Z.Y. Mechanical properties and acoustic emission data analyses of crumb rubber concrete under biaxial compression stress states. *Constr. Build. Mater.* **2021**, *298*, 123778. [CrossRef]
30. Xu, J.; Shu, S.R.; Han, Q.H.; Liu, C. Experimental research on bond behavior of reinforced recycled aggregate concrete based on the acoustic emission technique. *Constr. Build. Mater.* **2018**, *191*, 1230–1241. [CrossRef]
31. Abouhussien, A.A.; Hassan, A.A.A. Classification of damage in self-consolidating rubberized concrete using acoustic emission intensity analysis. *Ultrasonics* **2020**, *100*, 105999. [CrossRef] [PubMed]
32. Ahamad, M.S.S.; Maizul, E.N.M. Digital analysis of geo-referenced concrete scanning electron microscope (SEM) images. *Civ. Environ. Eng. Rep.* **2020**, *30*, 65–79. [CrossRef]
33. Keshavarz, Z.; Mostofinejad, D. Steel chip and porcelain ceramic wastes used as replacements for coarse aggregates in concrete. *J. Clean. Prod.* **2019**, *230*, 339–351. [CrossRef]
34. Xu, J.; Niu, X.L.; Ma, Q.; Han, Q.H. Mechanical properties and damage analysis of rubber cement mortar mixed with ceramic waste aggregate based on acoustic emission monitoring technology. *Constr. Build. Mater.* **2021**, *309*, 125084. [CrossRef]
35. Jimoda, L.A.; Sulaymon, I.D.; Alade, A.O.; Adebayo, G.A. Assessment of environmental impact of open burning of scrap tyres on ambient air quality. *Int. J. Environ. Sci. Technol.* **2018**, *15*, 1323–1330. [CrossRef]
36. Abd Allah Abd-Elaty, M.; Farouk Ghazy, M.; Hussein Khalifa, O. Mechanical and thermal properties of fibrous rubberized geopolymer mortar. *Constr. Build. Mater.* **2022**, *354*, 129192. [CrossRef]
37. Wu, Y.F.; Kazmi, S.M.S.; Munir, M.J.; Zhou, Y.; Xing, F. Effect of compression casting method on the compressive strength, elastic modulus and microstructure of rubber concrete. *J. Clean. Prod.* **2020**, *264*, 121746. [CrossRef]
38. Xie, J.H.; Guo, Y.C.; Liu, L.S.; Xie, Z.H. Compressive and flexural behaviours of a new steel-fibre-reinforced recycled aggregate concrete with crumb rubber. *Constr. Build. Mater.* **2015**, *79*, 263–272. [CrossRef]
39. Alsaif, A.; Albidah, A.; Abadel, A.; Abbas, H.; Almusallam, T.; Al-Salloum, Y. Behavior of ternary blended cementitious rubberized mixes reinforced with recycled tires steel fibers under different types of impact loads. *Structures* **2022**, *45*, 2292–2305. [CrossRef]
40. Hilal, N.N. Hardened properties of self-compacting concrete with different crumb rubber size and content. *Int. J. Built Environ. Sustain.* **2017**, *6*, 191–206. [CrossRef]
41. Stallings, K.A.; Durham, S.A.; Chorzepa, M.G. Effect of cement content and recycled rubber particle size on the performance of rubber-modified concrete. *Int. J. Sustain. Eng.* **2019**, *12*, 189–200. [CrossRef]
42. Li, Y.; Zhang, S.; Wang, R.; Dang, F. Potential use of waste tire rubber as aggregate in cement concrete—A comprehensive review. *Constr. Build. Mater.* **2019**, *225*, 1183–1201. [CrossRef]
43. Albidah, A.; Alsaif, A.; Abadel, A.; Abbas, H.; Al-Salloum, Y. Role of recycled vehicle tires quantity and size on the properties of metakaolin-based geopolymer rubberized concrete. *J. Mater. Res. Technol. JMR&T* **2022**, *18*, 2593–2607.
44. Pham, T.M.; Davis, J.; Ha, N.S.; Pournasiri, E.; Shi, F.; Hao, H. Experimental investigation on dynamic properties of ultra-high-performance rubberized concrete (UHPRuC). *Constr. Build. Mater.* **2021**, *307*, 125104. [CrossRef]
45. Shi, Y.; Long, G.; Ma, C.; Xie, Y.; He, J. Design and preparation of ultra-high performance concrete with low environmental impact. *J. Clean. Prod.* **2019**, *214*, 633–643. [CrossRef]
46. Tayeh, B.A.; Zeyad, A.M.; Agwa, I.S.; Amin, M. Effect of elevated temperatures on mechanical properties of lightweight geopolymer concrete. *Case Stud. Constr. Mater.* **2021**, *15*, e00673. [CrossRef]

buildings

Article

Sustainable Pavement Construction in Sensitive Environments: Low-Energy Asphalt with Local Waste Materials and Geomaterials

Miguel A. Franesqui [1,*], Jorge Yepes [2] and Samuel Valencia-Díaz [3]

[1] Grupo de Fabricación Integrada y Avanzada—Departamento de Ingeniería Civil, Universidad de Las Palmas de Gran Canaria (ULPGC), Campus de Tafira, 35017 Las Palmas de Gran Canaria, Spain
[2] Departamento de Ingeniería Civil—IOCAG, Universidad de Las Palmas de Gran Canaria (ULPGC), Campus de Tafira, 35017 Las Palmas de Gran Canaria, Spain; jorge.yepes@ulpgc.es
[3] Departamento de Ingeniería Civil, Universidad de Las Palmas de Gran Canaria (ULPGC), Campus de Tafira, 35017 Las Palmas de Gran Canaria, Spain; samuel.valencia@ulpgc.es
* Correspondence: miguel.franesqui@ulpgc.es

Abstract: Low-energy asphalt techniques, such as warm mix asphalt (WMA), combined with the rational consumption of geomaterials and waste recycling would promote more sustainable and energy-efficient asphalt pavements. In volcanic environments, a significant proportion of aggregate production is discarded due to its extreme porosity, and used tires generate a main environmental issue as well. While recycled rubber powder from tire waste can enhance the mechanical behavior of asphalt, it also raises its viscosity. Therefore, joining rubberized asphalt containing local waste geomaterials with WMA technologies is crucial to reduce the manufacturing temperatures and emissions and to produce more eco-efficient pavements. For this purpose, the most relevant technological characteristics of rubberized warm mix asphalt with residual aggregates from highly vesiculated volcanic rocks are tested in the laboratory and contrasted with conventional mixtures. The outcomes demonstrate not only the feasibility of the production of such mixtures in line with the current specifications, but also show a significant improvement in the resistance to moisture and to plastic deformations, and an improvement in the stiffness modulus. The eco-efficiency indicators conclude that the energy consumption and emissions are reduced by 9%, enabling the reuse of waste materials by more than 95%.

Keywords: sustainable asphalt pavement; low-energy asphalt; construction waste; used tire; reclaimed rubber; residual geomaterial; porous volcanic aggregate; eco-efficiency analysis

1. Introduction

Today's society is challenged by the depletion of natural resources, increase in environmental pollution, and the reduction in biodiversity, and is increasingly aware of the need to protect the environment to achieve social development and economic growth. Sustainability in industrial processes must be based on the fact that innovations in new technologies incorporate sustainability principles, with an adequate analysis of their different dimensions and the creation of methodologies to maximize sustainable development [1].

The production of hot mix asphalt (HMA) for paving is among the most energy- and emission-intensive construction activities [2], with an annual global production of nearly 1.2 billion metric tons. The mixing temperatures are typically between 160 and 170 °C. This implies a yearly fuel consumption of over 9 billion liters (2.4 billion gallons) and CO_2 emissions of approximately 26 million metric tons per year worldwide (based on an average of 7.5 L of fuel consumption and 21.5 kg of CO_2 per metric ton of HMA [3]).

Low-energy asphalt technologies would enable the sustainable long-term use of these fundamental materials for transport infrastructures. In this regard, warm mix asphalt

(WMA) is a technique for manufacturing and compacting asphalt mixes at lower temperatures than conventional hot mixes (HMA), while maintaining their workability and mechanical characteristics. The reduction in temperature during the production of the mixture translates into lower energy requirements (i.e., fuel and electricity consumption) and lower emissions into the atmosphere. It also brings other notable benefits: (a) an improvement in workers' health and safety conditions, by reducing the risk of burns, smoke, and aerosol emissions [4,5]; (b) a reduction in binder aging due to oxidation [6]; and (c) longer transport distances regardless of climatic conditions [7].

WMA techniques can be grouped into diverse types, although all of them try to reduce the binder viscosity to produce the mixture at lower temperature, favoring its workability and compactability. These techniques are the following [7]: (a) binder foaming processes, by injection of sprayed water on the previously heated bitumen, which causes the violent expansion of steam, foaming the bitumen and reducing its viscosity; (b) organic additives of low melting point (i.e., paraffinic resins, waxes with long aliphatic chains) that reduce the viscosity of the mixture; (c) microfoaming inorganic additives (zeolites); and (d) surfactant additives, which promote the coating and adhesion of the binder with the mineral aggregates, decreasing the surface tension of the hot bitumen and the friction between both components, thus enhancing the workability of the mixture during its production and compaction. A comparative life cycle assessment of WMA technologies can be found in some previous research [8]; and the effect of certain chemical additives on the mechanical properties of recycled mixtures has also been assessed [9].

In asphalt mixtures, aggregates account for up to 95% of the total mass, which in general represents an economic and ecological problem for the mining industry [10,11], particularly in volcanic islands, where the impact of quarrying can be rather significant due to the limited territory and the impact of the extractive activities.

Most of the recent previous studies concerning bituminous mixtures containing recycled geomaterials are focused on Reclaimed Asphalt Pavement (RAP) [12,13] or Recycled Concrete Aggregates (RCA) [14,15], but those using residual volcanic aggregates are very limited [16,17]. However, on average, more than 75% of volcanic rocks are scoriaceous and vesicular types which are likely to produce aggregates whose mechanical properties do not satisfy the standard technical requirements due to their extreme heterogeneity, porosity, alveolar structure, and absorption, as well as the non-cubic particle shape [18]. The latter shape property also depends on the crushing method [19].

Consequently, most of the extraction of volcanic geomaterials is discarded because they are considered marginal aggregates and they are not recommended for structural applications. Furthermore, in these volcanic regions, the high degree of environmental protection of the territory prevents the opening of new quarries and landfills. For example, in the Canary Islands (28° N; 15.5° W), the protected natural areas cover the 60% of the territory; there are biosphere reserves (UNESCO) on every island, and five of the seven main islands are biosphere reserve on their own (i.e., the whole territory) [20,21]. Such territories have environmental attributes that need to be protected because of their special natural value, fragility, or vital ecosystem functions and are therefore considered sensitive environments. There are other characteristics commonly associated with these regions: (a) geographical limitations of the territory; (b) isolation and remoteness from the main economic areas; (c) the need to obtain the construction materials from their own local resources; (d) the difficulty of opening new extractive areas due to environmental protection constraints; (e) the fact that waste and residues must be processed and recovered in the same territory, contributing to the development of the local industry and economy.

As a result, the use of residual and marginal aggregates is a key issue to provide eco-friendly solutions to the building industry in these sensitive environments. Some other engineering applications of pyroclastic geomaterials such as volcanic ashes have been previously suggested [22,23] in other volcanic territories.

Another type of waste that generates a major environmental issue in sensitive environments is used tires, since they cannot be incinerated as fuels for clinker production, as is often carried out elsewhere. However, reclaimed granulated rubber from End-of-Life Tires (ELT) can boost the mechanical behavior of bituminous mixtures if it is incorporated by replacing part of the mineral aggregate (also called rubberized mixtures by the "dry" process [24]) or previously blended with the bitumen to produce a Crumb Rubber-Modified Binder (CRMB), also called rubberized bitumen by the "wet" process [25–27]. In the last decade, a "semi-dry" method using a Reacted and Activated Rubber (RAR) that can be added directly to the asphalt plant has been used in the construction of pavements in certain countries [28], and more recently, some authors have proposed a "semi-dry/semi-wet" process technology [29]. In all cases, the blend of the recycled rubber particles with the bitumen at high temperature promotes the rubber swelling and chemical reactions that modify the elastomeric chains, the devulcanization (breaking of sulfur bonds), the absorption of aromatic fractions of the asphalt bitumen, and thus the modification of the rheological properties [30].

All these techniques aim to ensure that bituminous mixtures incorporating crumb rubber produce paving materials than can offer enhanced performance and durability [31]. They could also contribute to reduce the traffic noise [32–34] as well as the grain size degradation of the extremely porous aggregates during compaction works. However, the elastomeric properties of the rubber particles raise the asphalt viscosity, which also forces an increase in the manufacturing temperature of the asphalt admixture and, consequently, the energy consumption and emissions [35]. Therefore, combining rubberized asphalt with WMA technologies is crucial for the long-term sustainability of this asphalt rubber technique.

The amalgamation of these three technologies (WMA + CRMB + residual geomaterials) could lead to not only eco-friendly bituminous mixtures for paving applications, which would make it possible to achieve the emission reduction targets set by government policies, but also to increase their mechanical properties and durability, by reducing the pavement maintenance. For this purpose, a liquid chemical surfactant additive—composed of renewable components—is used in this study for the mixture manufacture and compaction at lower temperatures. This additive is more economical than granular microcrystalline waxes because it is used in smaller proportions, avoids cracking problems due to crystallization at low temperatures [36], and facilitates the additive dosage. In this study, the main technological characteristics of these rubberized warm asphalt mixtures with residual aggregate from highly vesiculated volcanic rocks are analyzed in the laboratory and confronted with conventional HMA with the same aggregate. Furthermore, their eco-efficiency is assessed.

2. Materials and Methods

2.1. Residual Volcanic Aggregate

All the mixtures were made with an olivine-pyroxene grey basalt of scoriaceous and vesicular structure, obtained from the same quarry (Figure 1). This type of high porosity aggregate is the most common in volcanic regions (approx. 75% of the exploitable resources), but it is considered a marginal or residual aggregate for the production of structural materials, and it is therefore relegated to being used only for embankments and fillings.

Table 1 shows the most relevant properties of the different aggregate fractions. These were determined by laboratory tests that were also carried out within the framework of this research. Ten samples of each of the aggregate fraction were obtained by quartering procedures using riffle sample splitters and the laboratory analysis according to the test methods of the European Standards (EN).


(**a**) (**b**) (**c**)

Figure 1. Vesicular volcanic aggregates: (**a**) rock structure of a lava flow; (**b**) typical heterogeneity, variability, and discontinuous special distribution of volcanic rocks in a quarry; (**c**) detail of the fraction 10–20 mm.

Table 1. Main characteristics of the asphalt mixture components.

	Aggregate (Scoriaceous and Vesicular Grey Basalt)			**Mineral Filler (CEM II/B-P 32.5 R)**	**Penetration Grade Binders**		
	# 10–20 mm	**# 4–10 mm**	**# 0–4 mm**	**(# <0.063 mm)**	**35/50**	**CRMB 35/50**	**CRMB 35/50 + 0.5% (3) of Cecabase RT®**
Proportion (%)	20.93 (1)	36.27 (1)	38.88 (1)	3.92 (1)	6 (2)	6 (2)	6 (2)
ρ_a (g/cm^3)	2.45	2.88	2.89	-	-	-	-
ρ_{SSD} (g/cm^3)	2.36	2.56	2.63	-	-	-	-
ρ_{rd} (g/cm^3)	2.23	2.37	2.35	-	-	-	-
WA_{24} (%)	15.5	8.3	5.8	-	-	-	-
FI	-	6	6	-	-	-	-
Cc	56	60	-	-	-	-	-
SE_4	-	-	73	-	-	-	-
LA	29	28	-	-	-	-	-
PSV	60	60	-	-	-	-	-
Dens. (g/cm^3)	-	-	-	-	1.042	1.028	1.027
Pen. ($\times 10^{-1}$ mm)	-	-	-	-	44	38	30
SP [R&B] (°C)	-	-	-	-	51.6	64.2	67.4
Visc. [at 60 °C] (cP)	-	-	-	-	51,000	215,000	211,000
Visc. [at 150 °C] (cP)	-	-	-	-	250	900	850

(ρ_a) Particle density [apparent]; (ρ_{SSD}) Particle density [saturated surface dry]; (ρ_{rd}) Particle density [dry], according to EN 1097-6; (WA_{24}) Water absorption of particles after 24 h, according to EN 1097-6; (FI) Flakiness index, according to EN 933-3; (Cc) Particles with more than 50% of their surface crushed or broken, according to EN 933-5; (SE_4) Sand equivalent of fraction 0–4 mm, according to EN 933-8; (LA) Los Angeles coefficient (resistance to fragmentation), according to EN 1097-2; (PSV) Polished stone value (resistance to polishing), according to EN 1097-8; (Dens.) Binder density, according to EN 15326; (Pen.) Penetration at 25 °C, 100 g, 5 s, according to EN 1426; (SP) Softening point [Ring and Ball test], according to EN 1427; (Visc.) Dynamic viscosity by Brookfield rotational viscometer, according to EN 13302. (1) Percentage by weight of total aggregate; (2) Percentage by weight of mixture; (3) Percentage by weight of bitumen.

As aggregate fraction # <0.063 mm (mineral filler), a Portland cement with pozzolanic addition was employed (designated CEN II/B-P 32.5 R, according to the EN 197-1). This type of cement is the most common in volcanic territories due to the presence of pozzolans in certain volcanic rocks.

2.2. Waste Crumb Rubber from Used Tires

The waste crumb rubber modifier (CRM) was produced by mechanical grinding at ambient temperature and its composition is from car tires (50%) and from trucks (50%). It was supplied by a local company in charge of the treatment of this waste. This company carries out the recovery and separation of the raw material components of discarded tires in the region. Fifty percent of the rubber comes from passenger car tires and the rest from truck tires.

The thermogravimetric analysis revealed the following: 57.41% polymeric rubber, 32.22% carbon black, 6.02% ash, and 4.67% plasticizer and additives. Up to 94% (by weight of CRM) was below 0.5 mm in size. As for its size distribution, the particle size was smaller than 1.0 mm (i.e., 94.1% passed through sieve 0.5 mm, 23.7% through 0.25 mm, 3.7% through 0.125 mm, and 0.4% through 0.063 mm).

2.3. Binders

The bitumen used for the control mixture without rubber—conventional mixture of the type hot mix asphalt (HMA)—was a commercial penetration grade bitumen 35/50. The bitumen for the rubberized hot mixture (RHMA) was a crumb rubber-modified binder of the same penetration grade (CRMB 35/50). This rubberized binder was previously manufactured at the laboratory by blending the CRM with a penetration grade bitumen 50/70. Because the elastomer raises both viscosity and consistency, the resulting binder (CRMB) had a penetration grade 35/50. To achieve this, each sample (600 g) of bitumen 50/70 was heated to 180 ± 1 °C in an oil bath and then 10% (by weight) of CRM was added in the blending unit. It was mixed for 60 min at 4000 rpm with a propeller agitator maintaining the same temperature.

The rubberized warm mixture (RWMA) was produced with a CRMB 35/50 binder previously blended with 0.5% (by wt. of rubberized bitumen) of a surfactant liquid additive (Cecabase RT$^{®}$) at 180 ± 1 °C for 10 min at 4000 rpm in the same mixer, ensuring that the additive is properly homogenized into the bitumen.

Ten samples of each binder type were obtained to characterize them following the European Standards (EN). The main properties of the binders are also summarized in Table 1.

2.4. Bituminous Mixtures

The type of mixture selected for this study was a Semi-dense Asphalt Concrete (AC16 surf S), following the European Standard EN 13108-1, which is an asphalt mixture typically employed for wearing courses of different roads, traffic types, and climatic conditions because of its adequate macrotexture and its lower susceptibility to plastic deformations, and because its production involves lower costs compared to a dense asphalt concrete. The aggregate gradation is shown in Figure 2a.

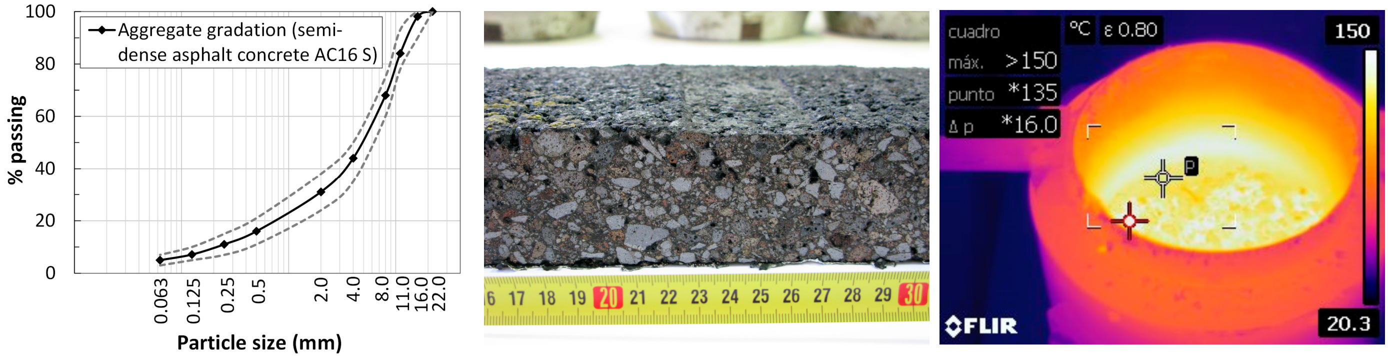

(**a**) (**b**) (**c**)

Figure 2. Rubberized warm mix asphalt (RWMA) mixed at 155 °C and compacted at 145 °C: (**a**) particle size distribution curve; (**b**) slab specimen after Wheel Tracking Test; (**c**) infrared photography during the mixing process.

A total of 201 cylindrical specimens, 46 slab specimens (Figure 2b), and 27 non-compacted samples (for theoretical maximum density tests) were prepared in the laboratory following the Spanish technical specifications for roads (PG-3), which are in accordance with the European Standards.

The effect of the CRM binders and the warm mix asphalt (WMA) additive on the physical and mechanical properties of this Semi-dense Asphalt Concrete (AC-S) with scoriaceous and vesicular basalt was compared by preparing three types of mixtures with a binder content of 6% in reference to the total weight of the mixture. Previous tests showed this was the optimum binder content for this porous mineral aggregate. This percentage is higher compared to conventional aggregates and similar to recycled aggregates (RCA), as highlighted by previous research [14], due to the increased binder absorption. The three types of asphalt mixes used in this research were as follows: (a) the control hot mixture with conventional bitumen (HMA), mixed at 170 ± 1 °C; (b) the rubberized hot mixture with CRM bitumen (RHMA), mixed at 180 ± 1 °C; and (c) the low-energy warm mix asphalt with CRM bitumen (RWMA), mixed at 155 ± 1 °C (Figure 2c). In all cases, the compaction temperatures were 10 °C below the mixing temperatures.

The mixing and compaction temperatures of the RWMA had to be at least 10 °C higher than the control HMA in order to meet the values required by the specifications for road pavements. At lower compaction temperatures, certain properties of the RHMA with this poor-quality aggregate were particularly critical, especially the air void content, the rutting resistance, and the dynamic stiffness modulus, as described in Section 3.

The production temperature of the RWMA was selected based on the results of different mixture properties obtained from previous tests on specimens manufactured between 140 and 180 °C. At mixing temperatures below 140 °C the air void content of the RWMA was above 12% (due to the difficulty of compaction as a result of the higher viscosity of the CRM bitumen and the aggregate roughness), the proportional rut depth at 10,000 cycles by wheel tracking test in air was over 6%, and the indirect tensile strength ratio drop below 70%, therefore failing to comply with most of the specifications for paving mixtures. In contrast, above 150–155 °C (depending on the property being evaluated), the RWMA met these specifications.

2.5. Laboratory Tests

The cylindrical specimens (D = 101.6 mm; h = 63.5 mm) were compacted by the Marshall method (EN 12697-30) with either 50 or 75 blows per side, based on the lab test. The slab specimens of 300 × 300 × 60 mm were compacted by the rolling method (EN 12697-33). Three series of characterization tests for each type of mixture were carried out on the compacted specimens and non-compacted samples, with a total number of 552 tests for the entire investigation:

(a) Volumetric properties: theoretical maximum density (EN 12697-5, Procedure A: volumetric) of non-compacted samples, bulk density (EN 12697-6, Procedure B: saturated surface dry, SSD), and void characteristics (EN 12697-8) of cylindrical specimens compacted by impact with 75 blows per side;
(b) Moisture resistance (EN 12697-12, by Indirect Tensile Test, ITT [EN 12697-23]) of cylindrical specimens compacted by impact with 50 blows per side;
(c) Resistance to permanent deformation: Wheel Tracking Test, WTT (EN 12697-22, Procedure B: in air, small device, at 60 °C and 10,000 cycles), on slab specimens compacted by metallic roller, and Marshall Test (EN 12697-34) of cylindrical specimens compacted by impact with 75 blows/side;
(d) Dynamic stiffness modulus (EN 12697-26) by Indirect Tensile Test on cylindrical specimens [IT-CY] compacted by impact with 75 blows per side, k = 0.6, T = 20 °C, f = 2.2 Hz;
(e) Resistance to fatigue (EN 12697-24) by Four-Point Bending Test on prismatic specimens [4PB-PR] with 1 million load cycles, at 20 °C, 10 Hz).

3. Results and Discussion

3.1. Physical Properties

Figure 3 shows the average values of the main volumetric properties of the rubberized mixtures, allowing comparison of results with respect to the control hot mixture with conventional bitumen (HMA), all of them manufactured following the same procedure and the same type of residual volcanic aggregate. The bulk density of the rubberized mixtures

(RHMA and RWMA) was superior to the HMA; for the RWMA, it was 3.4% higher and the results were more homogenous (lower statistical deviation). Both the air void content and voids in mineral aggregate of the RWMA comply with the standard specifications for this type of asphalt concrete for wearing courses, and proved to be inferior to the RHMA, whose air void contents are superior to the HMA because of the higher theoretical maximum density of the rubberized mixtures.

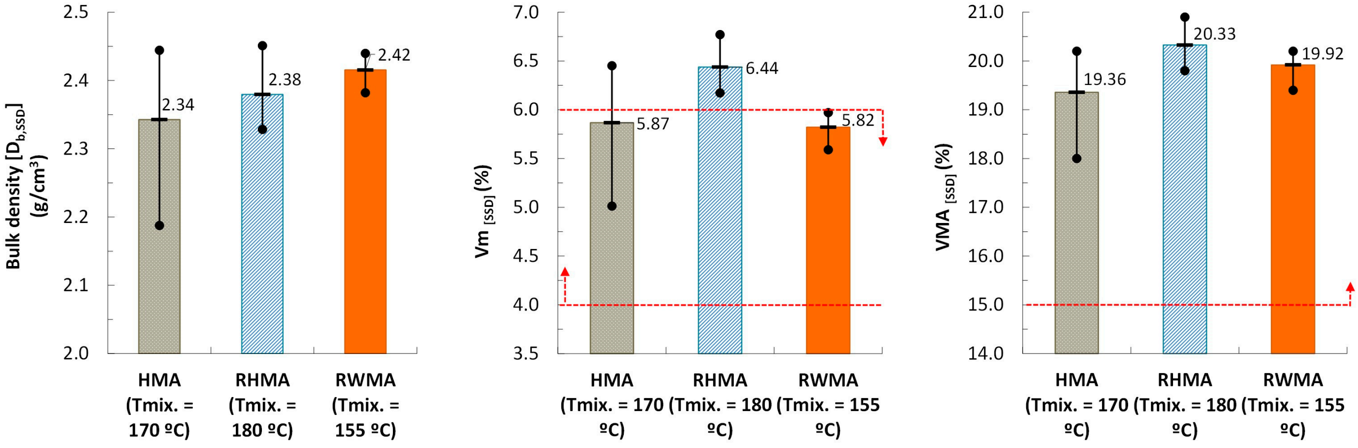

(**a**) (**b**) (**c**)

Figure 3. Volumetric characteristics of the asphalt mixtures: (**a**) bulk density by procedure B: saturated surface dry, SSD; (**b**) air voids in the mixture; (**c**) voids in mineral aggregate.

3.2. Strength Properties

Figure 4a clearly shows the improvement of the resistance to moisture action of the rubberized mixtures with respect to the hot mixture with conventional bitumen (HMA) in terms of the indirect tensile strength ratio (ITSR). The ITSR of the RWMA increased by 36.6%, thus complying with pavement technical specifications. Although the indirect tensile resistance of dry specimens (ITS_d) decreased with respect to the HMA (Figure 4c), with the saturated specimens (ITS_W) it was similar (Figure 4b), showing the favorable effect on the adhesion under wet conditions of the combined action of the surfactant additive and the rubber on these mixtures with highly porous aggregates.

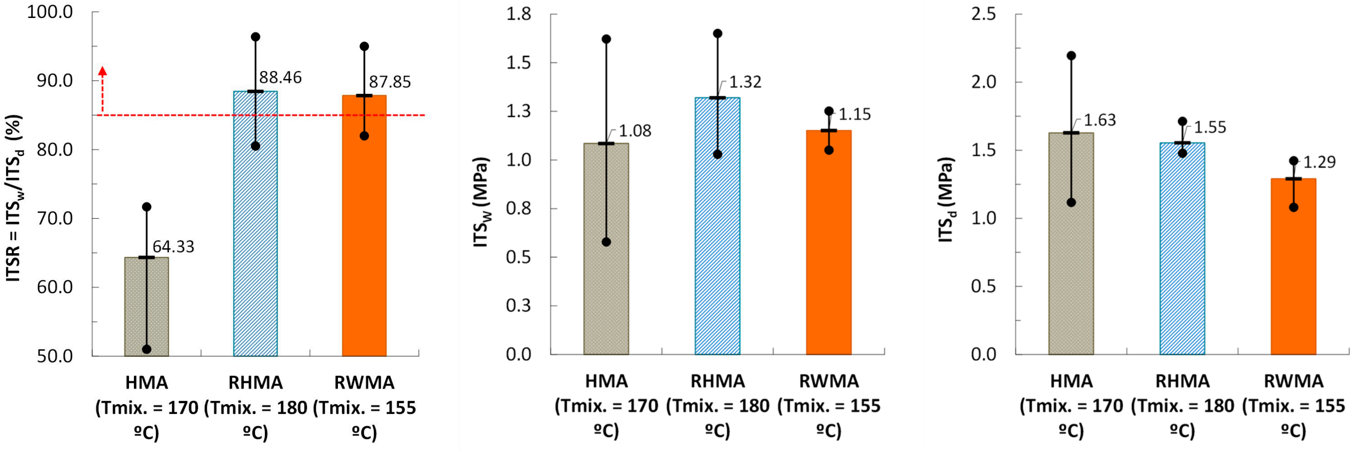

(**a**) (**b**) (**c**)

Figure 4. Resistance to water action of the asphalt mixtures: (**a**) indirect tensile strength ratio; (**b**) indirect tensile strength of saturated specimens (72 h at 40 °C); (**c**) indirect tensile strength of dry specimens.

Figure 5a–c highlight the enhanced rut resistance of the rubberized mixtures (lower wheel tracking slope by 47.12%, rut depth by 51.3%, and proportional rut depth by 54.1%) with respect to the control mixture. Similar results are shown by the Marshall tests, in which the stability (Figure 6a), deformation (Figure 6b), and Marshall Quotient (Figure 6c) of the RWMA were significantly higher than the average values of the HMA (by 99.3%, 12.8% and 45.7%, respectively). This improvement suggests a noteworthy finding for the practical reuse of waste vesicular aggregates from volcanic islands in pavement construction.

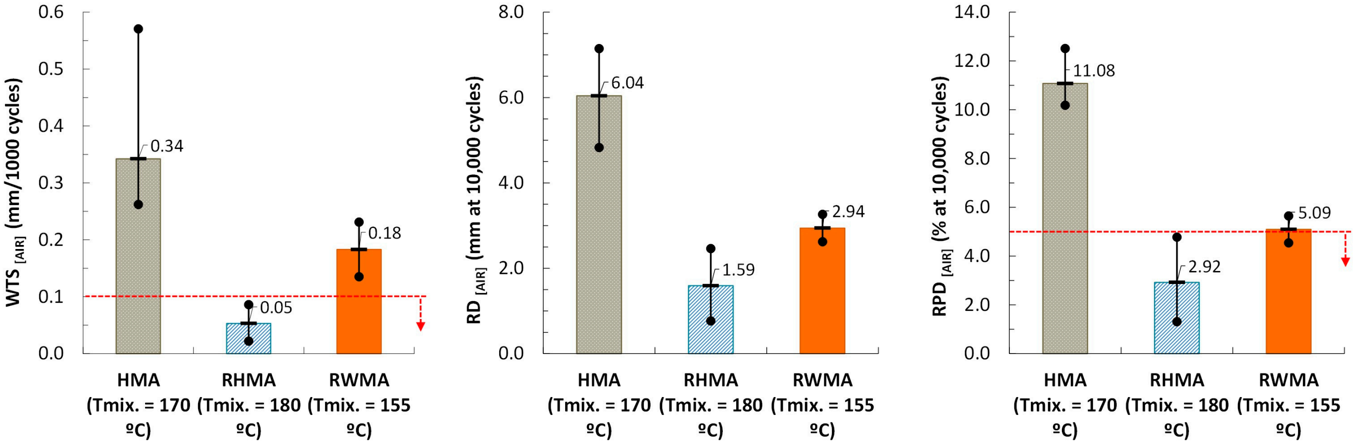

(**a**) (**b**) (**c**)

Figure 5. Resistance to plastic deformations by Wheel Tracking Test (WTT) in air at 60 °C and 10,000 cycles: (**a**) wheel tracking slope between 5000 and 10,000 rolling cycles; (**b**) rut depth at 10,000 cycles; (**c**) proportional rut depth at 10,000 cycles.

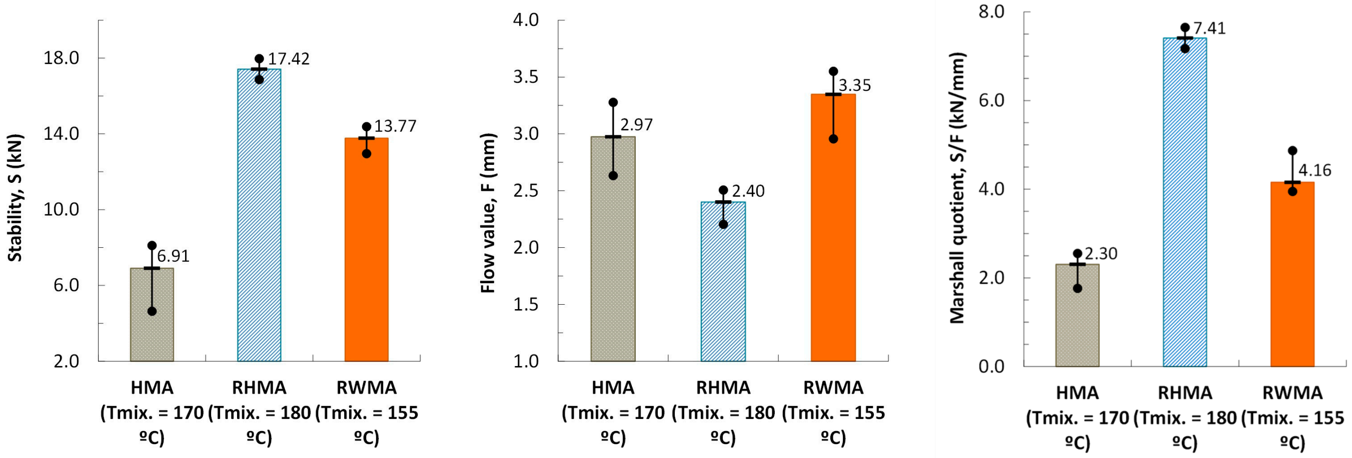

(**a**) (**b**) (**c**)

Figure 6. Resistance to plastic deformations by Marshall Test: (**a**) stability; (**b**) flow value; (**c**) Marshall Quotient.

These results are consistent with those reported by other previous studies using recycled aggregates (RCA), which showed better performance in terms of moisture sensitivity and rutting resistance [14].

3.3. Mechanical Properties under Dynamic Loading

The dynamic stiffness modulus by Indirect Tensile Test on cylindrical specimens of the RWMA was 34.5% higher than the hot mixture with conventional binder (HMA) and up to 51.9% superior to the RHMA (Figure 7a). These results prove that the stiffness increment is not due to the rubberized binder as expected, but the favorable effect on the adhesion and coating between aggregates and bitumen promoted by the surfactant additive.

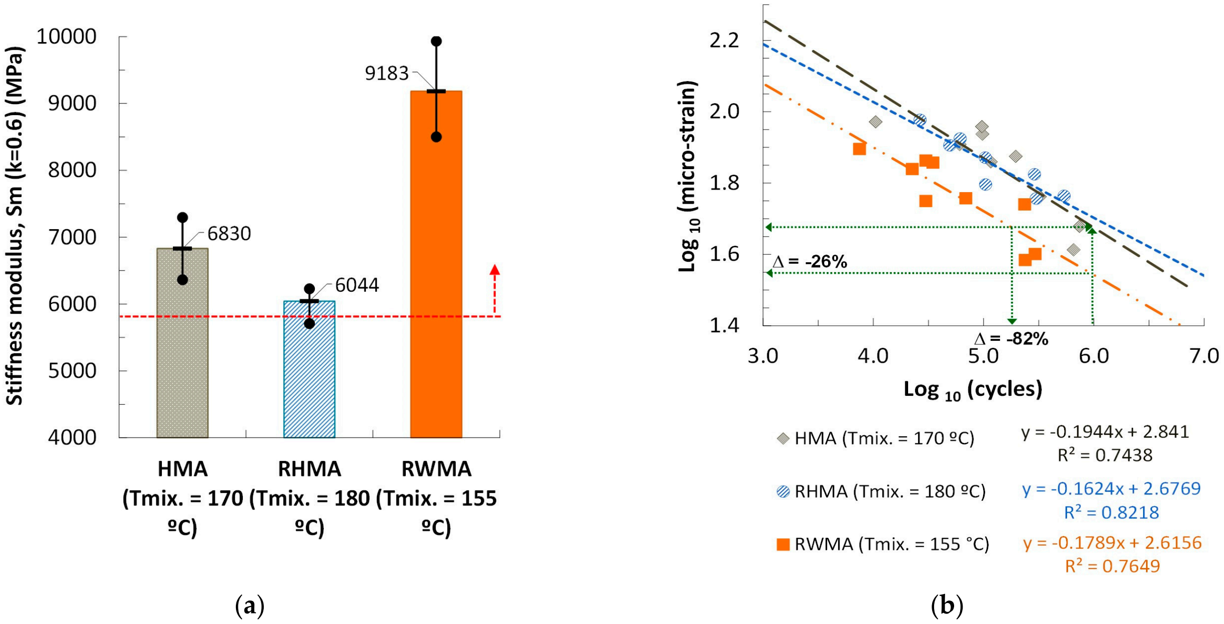

(**a**) (**b**)

Figure 7. Dynamic performance characteristics: (**a**) stiffness modulus by Indirect Tensile Test (ITT) at 20 °C; (**b**) fatigue laws by four-point bending test at 20 °C, 1 million cycles, 10 Hz.

Fatigue resistance of RWMA mixtures is reduced compared to the HMA, even though the fatigue law of the RHMA slightly improved with respect to the mixture with conventional bitumen (HMA). The initial micro-strain for an expected service life of 1 million load cycles until fatigue failure decreased by 26%, which supposes a reduction in the expected number of fatigue cycles by 82% (Figure 7b). This result is in accordance with previous research, which stated the reduced cracking resistance of WMA by bending tests on semi-circular specimens, albeit produced with a foam-based additive [37]. However, this apparent reduction in the durability of these asphalt mixes can be counterbalanced at the design stage by using thicker asphalt layers for the pavement structure or by the disposition of the constituent materials in the pavement layers, and it is justified by the sustainability improvement with the use of natural materials and waste products that this technology offers for highly sensitive environments such as volcanic islands.

3.4. Statistical Analysis of the Experimental Results

The data collected from the laboratory tests were analyzed following the next steps:

(1) An Exploratory Data Analysis (EDA) was performed to evaluate the quality of the data by using descriptive statistics tools (i.e., relevant statistics about the deviation and error of the laboratory results, basic plots, normality tests). The main statistics related with deviation are summarized in Table 2.

(2) Based on the results of the normality test and the dependency of the samples, a non-parametric statistical approach was used to assess the effect of the mixture type on the different properties evaluated. In this case, the Kruskal–Wallis test was chosen (non-parametric analogue of the one-way ANOVA).

(3) A Dunn's post hoc test was also performed along with Kruskal–Wallis to answer two main questions, namely, whether at least one type of mixture is different from the other two, and between which types exactly this difference is. The *p*-values are shown in Table 3.

Table 2. Statistics of dispersion of the laboratory results for each property and type of mixture, and Shapiro–Wilk normality test.

		N	**Mean**	**SD**	**CoV (%)**	**Std. Error**	**MAD**	**Shapiro–Wilk**	**Shapiro–Wilk *p*-Value**
$D_{b,SSD}$ (g/cm^3)	HMA	18	2.34	0.09	3.73	0.021	0.061	0.891	0.0414
	RHMA	18	2.38	0.04	1.64	0.009	0.028	0.924	0.155
	RWMA	18	2.42	0.02	0.90	0.005	0.018	0.842	0.006
$D_{m,V}$ (g/cm^3)	HMA	16	2.49	0.18	7.21	0.045	0.045	0.696	<0.001
	RHMA	16	2.54	0.02	0.64	0.004	0.001	0.566	<0.001
	RWMA	15	2.54	0.01	0.52	0.003	0.008	0.750	<0.001
ITS_W (MPa)	HMA	16	1.08	0.41	37.56	0.102	0.366	0.846	0.012
	RHMA	16	1.32	0.25	19.31	0.064	0.213	0.827	0.006
	RWMA	16	1.15	0.10	9.03	0.026	0.101	0.644	<0.001
ITS_d (MPa)	HMA	14	1.63	0.41	25.28	0.110	0.371	0.855	0.026
	RHMA	12	1.55	0.10	6.31	0.028	0.030	0.715	0.001
	RWMA	12	1.29	0.16	12.15	0.045	0.054	0.701	<0.001
ITSR (%)	HMA	14	64.33	9.78	15.20	2.524	1.383	0.644	<0.001
	RHMA	12	88.46	8.29	9.37	2.392	7.934	0.650	<0.001
	RWMA	12	87.85	5.85	6.65	1.688	5.597	0.650	<0.001
$WTS_{[air]}$ (mm/1000 cycles)	HMA	12	0.34	0.14	40.22	0.040	0.007	0.579	<0.001
	RHMA	12	0.05	0.03	51.20	0.008	0.024	0.819	0.016
	RWMA	12	0.18	0.05	27.40	0.014	0.048	0.650	<0.001
$RD_{[air]}$ (mm at 10^4 cycles)	HMA	12	6.04	0.86	14.27	0.249	0.578	0.856	0.043
	RHMA	12	1.59	0.63	39.34	0.181	0.415	0.840	0.027
	RWMA	12	2.94	0.33	11.38	0.097	0.321	0.650	<0.001
$PRD_{[air]}$ (%at 10^4 cycles)	HMA	12	11.08	1.07	9.64	0.308	0.357	0.699	<0.001
	RHMA	12	2.92	1.49	51.04	0.430	1.373	0.799	0.009
	RWMA	12	5.09	0.58	11.29	0.166	0.551	0.650	<0.001
S (kN)	HMA	16	6.91	1.41	20.41	0.352	0.529	0.739	<0.001
	RHMA	16	17.42	0.57	3.29	0.143	0.555	0.644	<0.001
	RWMA	15	13.77	0.62	4.49	0.159	0.410	0.759	0.001
F (mm)	HMA	16	2.97	0.29	9.69	0.072	0.255	0.758	<0.001
	RHMA	15	2.40	0.14	5.989	0.037	0.016	0.635	<0.001
	RWMA	15	3.35	0.29	8.52	0.074	0.010	0.614	<0.001
Marshall Quotient [S/F] (kN/mm)	HMA	16	2.30	0.31	13.30	0.082	0.081	0.678	<0.001
	RHMA	15	7.41	0.25	3.33	0.062	0.239	0.644	<0.001
	RWMA	15	4.16	0.54	12.93	0.139	0.300	0.741	<0.001
$S_{m[IT\text{-}CY]}$ (k = 0.6) (MPa)	HMA	20	6829.97	510.51	7.47	114.153	523.000	0.864	0.009
	RHMA	30	6043.72	312.51	5.17	57.057	313.600	0.909	0.014
	RWMA	30	9182.84	633.28	6.90	115.620	509.005	0.896	0.007

(N) Number of valid results; (Mean) Averaged result; (SD) Standard Deviation; (CoV) Coefficient of Variation; (Std. Error) Standard Error of the Mean; (MAD) Median Absolute Deviation; ($D_{m,V}$) Theoretical maximum density: Volumetric procedure, according to EN 12697-5.

The statistical tests have proven that the differences in the properties of the mixtures manufactured with CRM binders with respect to the control mix without rubber (HMA) are statistically significant, except for a limited number of them (i.e., density properties and ITS_W). However, it is known that the dispersion of these laboratory tests is usually higher due to the heterogeneous nature of these materials. These differences are evident when comparing RWMA mixtures not only with the HMA control mixture but also with respect to the RHMA mixture, according to the *p*-values.

Table 3. Statistical test results about the effect of the mixture type on the different properties.

Property of the Mixture	Kruskal–Wallis Test	Dunn's Post Hoc Test	
	p-Value	Mixtures to Compare	Holm's *p*-Value
$D_{b,SSD}$ (g/cm^3)	0.020	HMA-RHMA	0.596
		HMA-RWMA	0.024 (1)
		RHMA-WMA	0.068
$D_{m,V}$ (g/cm^3)	0.061	HMA-RHMA	0.088
		HMA-RWMA	0.123
		RHMA-WMA	0.785
ITS_W (MPa)	0.272	HMA-RHMA	0.445
		HMA-RWMA	0.760
		RHMA-WMA	0.382
ITS_d (MPa)	0.003	HMA-RHMA	0.718
		HMA-RWMA	0.009 (2)
		RHMA-WMA	0.006 (2)
ITSR (%)	<0.001	HMA-RHMA	<0.001 (3)
		HMA-RWMA	<0.001 (3)
		RHMA-WMA	1.000
$WTS_{[air]}$ (mm/1000 cycles)	<0.001	HMA-RHMA	<0.001 (3)
		HMA-RWMA	0.010 (2)
		RHMA-WMA	0.010 (2)
$RD_{[air]}$ (mm at 10^4 cycles)	<0.001	HMA-RHMA	<0.001 (3)
		HMA-RWMA	0.010 (2)
		RHMA-WMA	0.010 (2)
$PRD_{[air]}$ (%at 10^4 cycles)	<0.001	HMA-RHMA	<0.001 (3)
		HMA-RWMA	0.002 (2)
		RHMA-WMA	0.061
S (kN)	<0.001	HMA-RHMA	<0.001 (3)
		HMA-RWMA	0.003 (2)
		RHMA-WMA	0.003 (2)
F (mm)	<0.001	HMA-RHMA	<0.001 (3)
		HMA-RWMA	0.031 (1)
		RHMA-WMA	<0.001 (3)
Marshall Quotient [S/F] (kN/mm)	<0.001	HMA-RHMA	<0.001 (3)
		HMA-RWMA	0.003 (2)
		RHMA-WMA	0.003 (2)
$S_{m[IT-CY]}$ (k = 0.6) (MPa)	<0.001	HMA-RHMA	0.004 (2)
		HMA-RWMA	<0.001 (3)
		RHMA-WMA	<0.001 (3)

A *p*-value less than 0.05 indicates that there is a significant statistical difference: (1) $p < 0.05$; (2) $p < 0.01$ (strong difference); (3) $p < 0.001$ (very strong difference).

3.5. Eco-Efficiency Analysis

A preliminary eco-efficiency assessment was carried out using the main indicators in the manufacture of asphalt mixes: energy consumption, atmospheric emissions, and waste generation. Only the mixing, laying, and compaction processes of the three types of mixtures were compared, considering the following: (1) heating of the aggregates, including the mineral filler; (2) heating of the binder; (3) mixing temperature; and (4) compaction temperature.

Energy consumption and emissions are directly related to the temperature required to manufacture the asphalt mix, and the latter depends on the content of rubber powder incorporated, the quality, adhesion and porosity of the aggregate used, as well as the type and bitumen content. With the "wet" method used in this research incorporating the waste rubber powder to obtain a rubber-modified bitumen (10% of rubber by bitumen weight), and with the extremely porous aggregates (water absorption up to 16%, see Table 1), the required manufacturing temperature for the RHMA (with a binder content of 6%) increased 10 ºC with respect the control mixture. It is precisely this drawback that justifies this research, and aims to reduce the manufacturing temperature using a chemical surfactant.

3.5.1. Energy Consumption

Vesicular volcanic aggregates, due to their high porosity, require longer heating time to completely dry out their moisture, which means an additional 0.7 L of fuel per metric ton for each increase by 1% in moisture, consuming 5.1 L of additional fuel per metric ton compared to mixtures with conventional low-porosity aggregates. A conventional asphalt concrete mixture with neat bitumen 35/50 and limestone aggregate involves approximately 271.1 MJ/metric ton of fuel (natural gas) [38]. Assuming the linear relationship between energy consumption and manufacturing temperature above the water vaporization temperature (Figure 8a), the RHMA mixture accounts for an increase in fuel consumption of 7.1% over the HMA. However, the RWMA allows a reduction in fuel consumption of 8.4% (14.5% compared to the RHMA) (Figure 8b). These results have been calculated from statistical analysis of data provided by local asphalt mix manufacturers using dense volcanic aggregates (mainly dense basalt and phonolite). For conversion to mixtures with highly porous aggregates, a proportional calculation has been applied (proportionally to their porosity, according to Table 1), since more energy is needed to evaporate the moisture from their pores and the required binder content is also increased proportionally.

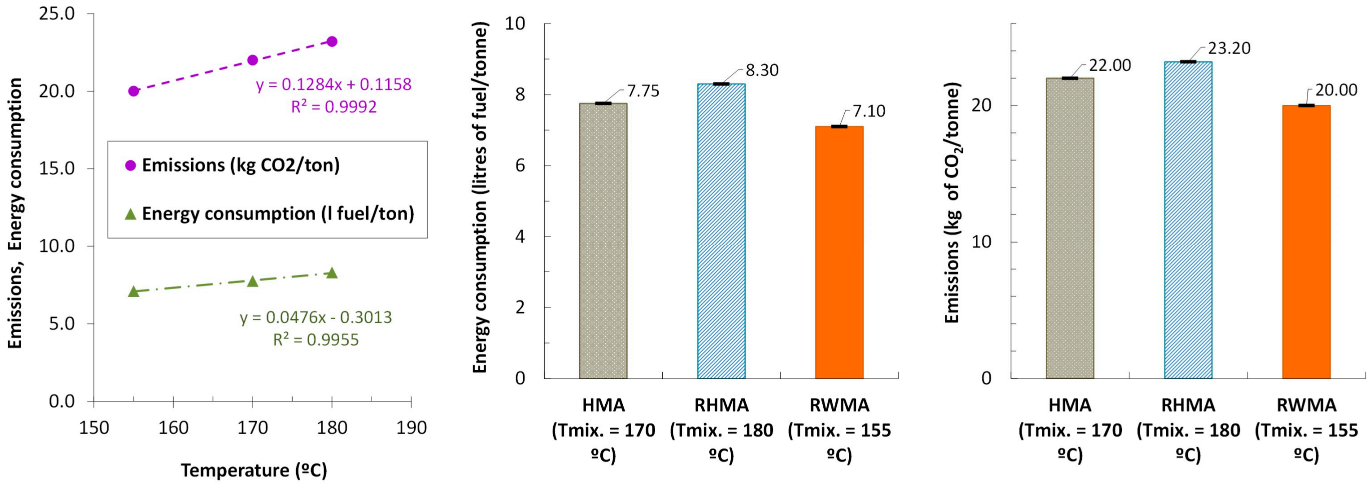

(**a**) (**b**) (**c**)

Figure 8. Eco-efficiency indicators: (**a**) influence of the manufacturing temperature; (**b**) fuel consumption; (**c**) CO_2 emissions.

To evaluate the consumptions involved in the manufacture of each component material of asphalt rubber mixtures, the following results of Refs. [39,40] can be used: (a) production of crushed aggregate: 57.6–78.6 MJ/metric ton; (b) obtaining the raw materials for the binder: 40,200 MJ/metric ton; (c) binder manufacture: 2890–5320 MJ/metric ton.

3.5.2. Emissions

CO_2 emissions for the RHMA mixture are increased by 5.5% compared to the HMA, considering that they also depend linearly on fuel consumption and, thus, on temperature (Figure 8a). However, the RWMA leads to a reduction of 9.1% (13.8% compared to the RHMA) (Figure 8c). Emissions were obtained from in situ measurements in local asphalt plants using dense volcanic aggregates. As indicated above, the appropriate conversion was made to take into account the higher porosity of the aggregates used in this study based on the proportional relationship of the emissions with the higher energy consumption.

According to Ref. [41], for an asphalt concrete of type WMA with conventional aggregates, the following reductions in gases to the atmosphere are achieved: NO_X: 73.5%; CO: 12.2%; SO_2: 74.6%.

3.5.3. Waste Recycling

The use of rubber from used tires in these bituminous mixtures allows a proportion of 10% of the bitumen weight, which means 6 kg of rubber per metric ton of mixture. Although this may seem a small percentage of this waste, this would mean recovering 25 metric tons of rubber for each kilometer of conventional road (i.e., 10 m wide roadway) that would be taken to landfill sites otherwise. This figure would increase to more than 50 metric tons per kilometer in the case of dual carriageways.

4. Conclusions

The results presented in this experimental study lead to the following conclusions:

- The bulk density of the rubberized warm mixture (RWMA) was 3.4% higher than the hot mixture with conventional binder (HMA). The volumetric properties of the RWMA meet the standard specifications for this type of asphalt concrete, even the most stringent requirements for wearing courses.
- The resistance to water action of the RWMA is increased by 37%, complying with pavement technical specifications. This shows the favorable effect on the adhesion under wet conditions of the combined action of the surfactant additive and the rubber on these mixtures with highly porous aggregates.
- It is important to highlight the enhanced rut resistance of the rubberized mixtures by approximately 50%. Similar results show the increased stability (by 99%), and reduced permanent (plastic) deformation (by 13%). This improvement supposes a noteworthy finding for the practical reuse of waste vesicular aggregates from volcanic rocks in pavement construction, especially for infrastructures under heavy traffic and at high weather temperatures.
- The dynamic stiffness modulus of the RWMA was 35% superior to the HMA, due to the favorable effect on the adhesion and coating between aggregates and bitumen promoted by the surfactant additive. This increase in the modulus of the asphalt mixture would allow a reduction in the thickness of the asphalt layers estimated at 13% (for an equivalent heavy-vehicle traffic of 300 trucks/day).
- The enhancements in the properties above mentioned lead to asphalt mixtures for paving that require less maintenance due to rutting damages and degradation promoted by the moisture action.
- The fatigue resistance of the RWMA mixtures is reduced compared to the HMA. However, this apparent worsening in the durability of these asphalt mixes can be addressed at the design stage of the pavement structure, and it is justified by the sustainability improvement with the use of raw materials and the waste recycling that this technology offers for extremely sensitive environments such as volcanic islands.
- The eco-efficiency analysis revealed that the RWMA mixture reduce fuel consumption and thus, CO_2 emissions to the atmosphere by about 9% if compared to the HMA, and 15% if compared to RHMA. The use of rubber from used tires in these bituminous mixtures facilitates the recovery of between 25 and 50 metric tons of waste per roadway kilometer (in single roadways and dual carriageways, respectively). Additionally, this mixture enables the reuse of more than 95% of residual materials (ELT) and geomaterials (marginal aggregates).
- Experimentally, it has been shown that it is technically possible to produce asphalt mixtures with a lower energy consumption, certain improved properties, and a reduced environmental impact by recycling two large volume residues, while meeting specifications for paving.

- The amalgamation of these three technologies (WMA + CRMB + residual geomaterials) promotes cleaner and more sustainable pavements, contributing to a zero waste society, and enhances their performance by reducing the maintenance.

Although this research has been carried out with residual materials and geomaterials from volcanic islands, the proposed technique, method, and conclusions are applicable elsewhere, since residual poor-quality aggregates are common, and the accumulation of used tires together with the need to limit emissions are global challenges. On the other hand, high porosity volcanic rocks can also be found in large extensions of continental areas in East and Southeast Asia, America and Africa.

For future research, it would be of interest to compare the performance properties and the eco-efficiency of these warm mixtures with high porosity marginal volcanic aggregates manufactured by the "wet" process and the "dry" or "semi-dry" process in order to optimize the production method. A life cycle assessment (LCA) would also make it possible to determine the sustainability over several life cycles after recycling.

Author Contributions: M.A.F.: Conceptualization, Methodology, Formal analysis, Investigation, Resources, Data curation, Writing—original draft, Writing—review and editing, Supervision, Project administration, Funding acquisition. J.Y.: Conceptualization, Methodology, Formal analysis, Investigation, Project administration. S.V.-D.: Methodology, Investigation, Resources. All authors have read and agreed to the published version of the manuscript.

Funding: This work was funded by the Regional Government of the Canary Islands (Spain), through the research project: "Technical regulations for the design and construction of road pavements in the road network of the Canary Islands" (Agreement C2020/143, "Convenio de cooperación con la Consejería de Obras Públicas, Transportes y Vivienda para la elaboración de la Guía de recomendaciones técnicas para el diseño y ejecución de firmes en la red de carreteras de Canarias"). The APC was supported by the same funder.

Data Availability Statement: Data will be made available on request.

Conflicts of Interest: The authors declare no conflicts of interest. The funder had no role in the design of the study; in the collection, analyses, or interpretation of data; in the writing of the manuscript; or in the decision to publish the results.

References

1. Huang, Y. Technology innovation and sustainability: Challenges and research needs. *Clean. Technol. Environ. Policy* **2021**, *23*, 1663–1664. [CrossRef]
2. Aryan, Y.; Dikshit, A.K.; Shinde, A.M. A critical review of the life cycle assessment studies on road pavements and road infrastructures. *J. Environ. Manag.* **2023**, *336*, 117697. [CrossRef] [PubMed]
3. Milad, A.; Babalghaith, A.M.; Al-Sabaeei, A.M.; Dulaimi, A.; Ali, A.; Reddy, S.S.; Bilema, M.; Yusoff, N.I.M. A Comparative Review of Hot and Warm Mix Asphalt Technologies from Environmental and Economic Perspectives: Towards a Sustainable Asphalt Pavement. *Int. J. Environ. Res. Public Health* **2022**, *19*, 14863. [CrossRef] [PubMed]
4. Kumar, R.; Saboo, N.; Kumar, P.; Chandra, S. Effect of warm mix additives on creep and recovery response of conventional and polymer modified asphalt binders. *Constr. Build. Mater.* **2017**, *138*, 352–362. [CrossRef]
5. Martin, H.; Kerstin, Z.; Joachim, M. Reduced emissions of warm mix asphalt during construction. *Road Mater. Pav. Des.* **2019**, *20*, S568–S577. [CrossRef]
6. Lakshmi Roja, K.; Roy, N.; Murali Krishnan, J. Influence of Aging on the Rheological Behavior of Warm Mix Asphalt Binders. In Proceedings of the 8th RILEM International Symposium on Testing and Characterization of Sustainable and Innovative Bituminous Materials, Ancona, Italy, 7–9 October 2015; Canestrari, F., Partl, M., Eds.; RILEM Bookseries. Springer: Dordrecht, The Netherlands, 2016; Volume 11. [CrossRef]
7. Sukhija, M.; Saboo, N. A comprehensive review of warm mix asphalt mixtures-laboratoryto field. *Constr. Build. Mater.* **2021**, *274*, 121781. [CrossRef]
8. Cao, R.; Zhen Leng, Z.; Yu, H.; Shu-Chien Hsu, S.C. Comparative life cycle assessment of warm mix technologies in asphalt rubber pavements with uncertainty analysis. *Resour. Conserv. Recycl.* **2019**, *147*, 137–144. [CrossRef]
9. Barraj, F.; Khatib, J.; Castro, A.; Elkordi, A. Effect of Chemical Warm Mix Additive on the Properties and Mechanical Performance of Recycled Asphalt Mixtures. *Buildings* **2022**, *12*, 874. [CrossRef]
10. de Bortoli, A. Understanding the environmental impacts of virgin aggregates: Critical literature review and primary comprehensive life cycle assessments. *J. Clean. Prod.* **2023**, *415*, 137629. [CrossRef]

11. Upadhyay, A.; Laing, T.; Kumar, V.; Dora, M. Exploring barriers and drivers to the implementation of circular economy practices in the mining industry. *Resour. Policy* **2021**, *72*, 102037. [CrossRef]
12. Wang, P.; Chen, J.; Wang, J.; Li, J.; Ning, H.; Liang, C.; Ge, X.; Wang, X. Evaluation of the Refined Decomposition Effect of Reclaimed Asphalt Pavement Materials. *Buildings* **2023**, *13*, 2240. [CrossRef]
13. Wei, W.; Ji, C.; Song, H.; Li, Z.; Liu, Z.; Sun, L.; Zhou, Z. Effect of Fractionation Process and Addition of Composite Crumb Rubber-Modified Asphalt on Road Performance Variability of Recycled Asphalt Mixtures with High Reclaimed Asphalt Pavement (RAP) Content. *Buildings* **2023**, *13*, 2729. [CrossRef]
14. Gedik, A. A review on the evaluation of the potential utilization of construction and demolition waste in hot mix asphalt pavements. *Resour. Conserv. Recycl.* **2020**, *161*, 104956. [CrossRef]
15. Al-Bayati, H.K.A.; Tighe, S.L.; Achebe, J. Influence of recycled concrete aggregate on volumetric properties of hot mix asphalt. *Resour. Conserv. Recycl.* **2018**, *130*, 200–214. [CrossRef]
16. Han, S.; Baek, C. Evaluation of Properties of Asphalt Concrete Mixture Using Basalt Aggregate from Jeju Island. *Buildings* **2023**, *13*, 3119. [CrossRef]
17. Zhang, X.; Ma, Y.; Zhu, Z.; Xu, J.; Zhang, Y.; Tang, B. Water Damage Resistance of Tuff Asphalt Mixtures with Admixtures Based on Surface Energy Theory. *Buildings* **2023**, *13*, 3105. [CrossRef]
18. Heap, M.J.; Violay, M.E.S. The mechanical behaviour and failure modes of volcanic rocks: A review. *Bull. Volcanol.* **2021**, *83*, 33. [CrossRef]
19. Hubert, J.; Zhao, Z.; Michel, F.; Courard, L. Effect of Crushing Method on the Properties of Produced Recycled Concrete Aggregates. *Buildings* **2023**, *13*, 2217. [CrossRef]
20. UNESCO. Biosphere Reserves in Europe & North America. Gran Canaria Biosphere Reserve, Spain. Available online: https://en.unesco.org/biosphere/eu-na/gran-canaria (accessed on 21 January 2024).
21. Regional Government of the Canary Islands. Canary Network of Protected Natural Areas. Available online: http://www.gobcan.es/cmayot/espaciosnaturales/informacion/quees.html (accessed on 21 January 2024).
22. Lemougna, P.N.; Wang, K.; Tang, Q.; Nzeukou, A.N.; Billong, N.; Chinje Melo, U.; Xue-min, C. Review on the use of volcanic ashes for engineering applications. *Resour. Conserv. Recycl.* **2018**, *137*, 177–190. [CrossRef]
23. Hossain, K.M.A.; Lachemi, M.; Easa, S. Stabilized soils for construction applications incorporating natural resources of Papua New Guinea. *Resour. Conserv. Recycl.* **2007**, *51*, 711–731. [CrossRef]
24. Cao, W. Study on properties of recycled tire rubber modified asphalt mixtures using dry process. *Constr. Build. Mater.* **2007**, *21*, 1011–1015. [CrossRef]
25. Hosahally Nanjegowda, V.; Prapoorna Biligiri, K. Recyclability of rubber in asphalt roadway systems: A review of applied research and advancement in technology. *Resour. Conserv. Recycl.* **2020**, *155*, 104655. [CrossRef]
26. Hosahally Nanjegowda, V.; Prapoorna Biligiri, K. Utilization of high contents of recycled tire crumb rubber in developing a modified-asphalt-rubber binder for road applications. *Resour. Conserv. Recycl.* **2023**, *192*, 106909. [CrossRef]
27. Mohamed, A.S.; Han, Y.; Cao, Z.; Xu, X.; Xiao, F. Investigating bonding mechanism of rubberized RAP asphalt mastic from rheological and physiochemical perspectives. *J. Clean. Prod.* **2023**, *404*, 136978. [CrossRef]
28. Zhang, P.; Li, D.; Li, B.; Wang, Y.; Wei, Y.; Wang, B.; Zhang, B. The Properties of Sodium-Hypochlorite-Activated Crumb Rubber and the Influence of Aging on the Rheological Properties of Activated Asphalt Rubber. *Buildings* **2023**, *13*, 712. [CrossRef]
29. Hosahally Nanjegowda, V.; Prapoorna Biligiri, K. Modified asphalt-rubber green pavement (MARGPave) mixtures: Product development and performance assessment. *Resour. Conserv. Recycl.* **2023**, *198*, 107125. [CrossRef]
30. He, Y.; Wang, Q.; Zhang, J.; Li, Y.; He, H.; Huang, G. Foamed crumb rubber asphalt binder: Preparation, rheological properties and adhesion characteristics. *J. Clean. Prod.* **2023**, *396*, 136516. [CrossRef]
31. Irfan, M.; Ali, Y.; Ahmed, S.; Hafeez, I. Performance Evaluation of Crumb Rubber-Modified Asphalt Mixtures Based on Laboratory and Field Investigations. *Arab. J. Sci. Eng.* **2018**, *43*, 1795–1806. [CrossRef]
32. Bollard, K. *Report on the Status of Rubberized Asphalt Traffic Noise Reduction in Sacramento County*; County of Sacramento Public Works Agency—Transportation Division, Sacramento: Sacramento, CA, USA, 1999.
33. Freitas, E. *Contribution of Asphalt Rubber Mixtures to Noise Abatement—Time Effect*; IN: Inter Noise 2010 (13–16 June); University of Minho: Braga, Portugal, 2010.
34. Pacholak, R.; Plewa, A.; Gardziejczyk, W. Analysis of the Behavior of Low-Noise Asphalt Mixtures with Modified Binders under Sinusoidal Loading. *Materials* **2022**, *15*, 5476. [CrossRef]
35. Tushar, Q.; Santos, J.; Zhang, G.; Bhuiyan, M.A.; Giustozzi, F. Recycling waste vehicle tyres into crumb rubber and the transition to renewable energy sources: A comprehensive life cycle assessment. *J. Environ. Manag.* **2022**, *323*, 116289. [CrossRef]
36. Edwards, Y.; Redelius, P. Rheological Effects of Waxes in Bitumen. *Energy Fuels* **2003**, *17*, 511–520. [CrossRef]
37. Li, D.; Leng, Z.; Zhang, S.; Jiang, J.; Yu, H.; Wellner, F.; Leischner, S. Blending efficiency of reclaimed asphalt rubber pavement mixture and its correlation with cracking resistance. *Resour. Conserv. Recycl.* **2022**, *185*, 106506. [CrossRef]
38. Moins, B.; Bech, C.; Hernando, D.; Van den bergh, W.; Audenaert, A. An investigation on the use of lean asphalt as an alternative base material in asphalt pavements by means of laboratory testing, life cycle assessment, and life cycle cost analysis. *Resour. Conserv. Recycl.* **2023**, *194*, 106992. [CrossRef]
39. Athena Institute. *A Life Cycle Perspective on Concrete and Asphalt Roadways: Embodied Primary Energy and Global Warming Potential*; Cement Association of Ottawa: Ottawa, ON, Canada, 2006.

40. Stripple, H. *Life Cycle Assessment of Road, a Pilot Study for Inventory Analysis*; IVL Swedish Environmental Research Institute: Gothenburg, Sweden, 2001; 182p.
41. Peilong, L.; Zhan, D. Analysis of environmental and ecological effects on new techniques for asphalt pavement materials. In Proceedings of the International Symposium on Water Resource and Environmental Protection, Xian, China, 20–22 May 2011; pp. 3090–3092.

buildings

Article

An Experimental Study on Innovative Concrete Block Solutions for Reconstruction

Mahmut Cem Yılmaz [1], Ahmad Aswad [1] and Ömer Mercimek [2,*]

[1] Civil Engineering Department, Ankara Yıldırım Beyazıt University, 06010 Ankara, Turkey; mahmutcemyilmaz@aybu.edu.tr (M.C.Y.); 185110119@ybu.edu.tr (A.A.)
[2] Civil Engineering Department, Ankara University, 06830 Ankara, Turkey
* Correspondence: omercimek@ankara.edu.tr

Abstract: In this study, an experiment was conducted to innovate a new design of interlocking concrete blocks (ICBs) containing recycled aggregates (RAs) by reducing the consumed time and cost in construction using an environmental approach. Accordingly, the designed ICBs were produced manually using RAs, and wallettes were easily built with a mortarless mechanism by stacking the blocks without any mortar layers. In the experiments, besides the individual compression tests of the two types of ICB with natural and recycled aggregates, the wallette samples that were produced using ICBs, containing either 100% natural aggregates or 100% Ras, were tested under axial compressive loading. The experimental results were assessed considering the compressive strength, displacement, and failure mode. In the obtained results, we noticed that the average compressive strengths of the wallettes that were produced with natural or recycled aggregate ICBs were large enough to meet the standards of Syrian regulations, which are considered an example reference. The resulting displacement values were acceptable and could be negligible in some wallette specimens. It was concluded that the innovative ICBs with both normal or recycled aggregates could be a good alternative to traditional blocks, especially in post-disaster or post-war areas.

Keywords: reconstruction; recycled concrete aggregate; concrete blocks; interlocking block

1. Introduction

Within the cement sector, Türkiye, which is among the world's leading cement-producing countries, is ranked fifth in the world, and it is ranked seventh among the main cement consumer countries. In 2012, Türkiye was ranked second after Iran in the world's cement sector exports. In Europe, Türkiye's cement industry was ranked first in both production and export. While sector exports were focused in the north and west of Africa in 2012, Iraq, Libya, and Russia remained the major markets for sector exports in 2013. China leads globally within the building business. The building industry has grown to be one of the most important sectors of the national economy of China, but rising construction activity in recent years has resulted in a considerable volume of construction trash. According to data, China is the world's largest consumer of cement, and the cement consumed there accounts for 55% of global consumption [1]. Global cement consumption in 2021 grew steadily across many parts of the world and was projected to increase by 6%, excluding China. In 2022, IA cement expected a 2–4% growth in Turkish cement consumption, supported by a strong infrastructure pipeline with high-speed railways and renewable energy projects at the forefront [2]. However, compared to the previous year, cement production decreased by 6.6 percent to 73,708,000 tons. In the January–May period of 2023, there was an increase of 7.9% in cement production compared to 2022 [3].

The economic growth of many developing countries in the world is adversely affected by resource scarcity, global warming, epidemic diseases, and environmental conditions [1,4–10]. The conservation of the world's resources and the sustainability of natural habitats have emerged as the most pressing and critical issues for the survival and well-being of humans. Due to rapid industrialization and population growth in the last two hundred years, material and natural energy resources have been consumed in large quantities, which has led to global environmental changes that human beings have never experienced before.

Besides Türkiye, EU economies are heavily dependent on the construction sector. The building industry consumes a lot of natural resources and produces a lot of waste. According to a previous European Commission declaration [11], the building industry utilizes more than half of all minerals mined from the ground and creates more than 500,000 tonnes of trash every year in the EU. In addition, the management and disposal of old buildings have become a problematic issue [12]. However, in industrialized nations, the secondary utilization of building debris is extremely common. For many years, the recycling of building debris has been carried out, particularly for recycled concrete in the United States, Japan, and certain European nations. Construction and demolition trash is recycled at a rate of around 75% in certain wealthy European nations [12]. The use of leftover concrete as aggregates in the production of recycled concrete is an important developmental trend in environmentally friendly construction materials. Concrete recycling not only allows for the effective reuse of construction materials, but it also addresses the issue of natural aggregate shortages [12].

In recent years, many studies have been conducted on recycled aggregate concrete (RAC). The authors of [13] concentrated on the material characterization and modification of recycled concrete aggregates (RCAs), as well as RAC mix designs. In general, it is considered that the larger the percentage of RCAs, the greater the decline in RAC strength. Strength fluctuation is another key obstacle limiting the broad use of RAC [14–16]. Research on RAC components, included columns, beams, and joints, demonstrated that their mechanical characteristics are essentially similar to conventional concrete [1]. Also, RAC frame construction has recently been examined for earthquake performance [17].

The study by Ferriz-Papi and Thomas (2020) [18] aimed to investigate in depth the use of recovered aggregates from building and demolition wastes in concrete mixtures in order to enhance upcycling. A review of the research and regulations on concrete block manufacturing in the United Kingdom has been created as a part of this study. The initial studies were conducted as part of a case study with a sample of a building and demolition waste recycled aggregate from a Swansea demolition and construction waste factory. Visual inspection and screening procedures were used to create a composition of the two samples, which was then compared to the original aggregates. Up to 70% of the material was earthen debris from the excavation, with the remainder being a combination of plaster, glass, and organic materials, with tiny residues of mortar, concrete, and ceramic waste. Two concrete mixes were created using 80% recycled aggregates and various water/cement ratios. Testing included compressive strength, absorption, slump, and density. When the findings were compared with the reference specimen, we discovered that the quality of both combinations declined dramatically. However, in order to successfully employ these recycled aggregates in concrete block manufacturing, they needed to be analysed, and encouraging findings were discovered.

Guo et al. (2018) [19] sought to investigate the potential application of RCAs in the production of concrete construction blocks. Concrete construction blocks containing 75% RCA were produced via laboratory research and plant trials. The durability and mechanical qualities of RAC blocks were investigated via a variety of experiments. The shear and compressive performances of wall prisms fabricated using RAC blocks were proven to be comparable to those of standard concrete walls. The authors proposed that RCAs can be used to manufacture environmentally friendly concrete construction blocks. They concluded that the usage of RAC blocks plays a significant role in the building life cycle and will benefit the long-term development of masonry structures.

There has been increasing interest in the design and manufacture of novel interlocking masonry blocks for sustainable and cost-effective structures in recent years [20–24]. One such option is to make interlocking blocks with tongue and groove portions as well as projections that exactly fit together; this has been accomplished by partially replacing fly ash for cement in the block's manufacture. This concept seeks to develop mortar-free, earthquake-resistant structures while reducing construction time and cost by up to 65%, using less labour and fewer resources [25].

Another study focuses on the production of interlocking masonry blocks using local materials such as Portland cement and water, without the use of mortar. Various shapes and dimensions (toe shape, bottom and top) of wall blocks were used. The compaction effort and compressive strength of these interlocking concrete blocks were found to be 3.687 (K.J./m^3) and 4.80 (MPa), respectively [26]. These values are well below the values of some specially mixed concrete specimens [27].

One study focuses on developing a new wall prospect using an interlocking concrete block model. The blocks were then exposed to compressive and axial loads. The author concluded that the new models made from the interlocking blocks may work for concrete wall construction and could be employed in typical load-bearing walls. It was shown that the new model, which is made up of interlocking blocks, may work as a concrete wall construction and be employed in typical load-bearing walls [28].

Finally, one research study explored the novel design of a hollow interlocking concrete block with a good finish that may be utilized to build steel-fibre-reinforced load-bearing walls. The blocks were examined to explore this possibility and compare their failure patterns and load capacity to those of nearby solid and hollow blocks. According to the study's findings, the load-bearing capacity of the wall was 12% and 22% greater than that of the local solid and hollow block walls, respectively. Furthermore, as compared to local blocks, the usage of steel fibre reduced the dead load by 28% and 11%, respectively [29].

Interlocking reinforced concrete blocks (IRCBs) emerged as sustainable solutions in various construction applications due to their cost and time effectiveness. This study specifically explores the potential advantages of IRCBs, particularly in disaster and war-torn countries like Syria.

The advantages of adopting IRCBs are numerous. Firstly, they are simple to install and need no specific masonry labour skills, making them appropriate for wall building. Second, IRCBs may be utilized for both structural and non-structural applications including columns, walls, and beams. They may also be used to create single or multi-story buildings, making them extremely useful in rural locations. IRCBs may be employed in both horizontal and vertical orientations, providing an architecturally pleasing perspective of the structure. Moreover, IRCBs can be dry-stacked without mortar, which significantly reduces cement usage. They also come with embedded holes for electrical and plumbing installations, making them suitable for different building requirements. IRCBs can also be sound- and heat-insulated, increasing their utility in various settings. Lastly, IRCBs are resistant to earthquakes, making them an appropriate solution for disaster-prone countries.

In summary, IRCBs offer numerous advantages, making them an innovative material in construction. Their versatility and sustainability make them suitable for various applications, especially in disaster-prone countries like Syria. With the growing need for cost-effective and sustainable construction solutions, IRCBs have the potential to be a game-changer in the construction industry.

The construction of basic structures with interlocking blocks fashioned from aggregate obtained from the transformation of concrete waste generated in war zones was seen as an efficient and cost-effective solution to the issue of shelter provision for individuals. Interlocking dry-stack bricks may require very little mortar alignment. The blocks are set with a cement slurry using an interlocking system to resist applied stresses; ICB walls may be erected at least three times faster than conventional block walls [19]. Masonry dry-stack technology based on blocks interlocking with grooves and tongues allows for proper building alignment. This wall structure is capable of withstanding a variety of external forces, due to steel rods inserted via holes. A dry-stacking wall technique would minimize shrinkage cracks on a concrete wall [30].

As can be understood from the literature, studies on interlocking blocks created using RAs are relatively limited. Moreover, examining RAs and natural aggregates simultaneously has become a very important issue. In this study, experiments are conducted to innovate a new design of interlocking concrete blocks containing recycled aggregates by reducing the consumed time and cost in construction, together with an environmental approach. According to this, the designed interlocking concrete blocks were produced manually by using recycled aggregates, and wallettes were easily built with a mortarless mechanism by stacking the blocks without any mortar layers. In the experiments, besides the individual compression tests of the two types of interlocking concrete blocks with natural and recycled aggregates, wallette specimens produced by interlocking blocks containing either 100% natural aggregates or 100% recycled aggregates were tested under axial compressive loading.

2. Experimental Study

2.1. Materials

Portland cement and tap water from the laboratory were used for the production of test elements. Coarse and fine aggregates were sourced from a factory and from construction debris from different regions.

Preparing Recycled Concrete Aggregate

Working Steps In Situ

There are several steps to produce RCAs, as shown in Figure 1:

- Collecting and selecting construction and demolition concrete waste;
- The classification of concrete aggregates;
- Crushing large and medium aggregates manually with a hammer;
- Cleaning and sieving small aggregates.


(**a**) (**b**)

Figure 1. Some steps of preparing RCAs.

The recycling process in a laboratory using a single-toggle jaw crusher:

- Putting concrete waste aggregates in the hopper and crushing between fixed and swing jaws to small aggregates, and slipping down through the opening gap at the bottom, as shown in Figure 2. The size of the broken course concrete aggregate is between 4 and 12 mm;
- Screening crushed aggregates in 3.35–12.5 mm sieves to obtain the appropriate coarse aggregate;
- Separating invalid aggregates to obtain fine aggregates (sand).

2.2. Preparing Concrete Mixture

Trial Mix Design

At this stage, different mix ratios of sand, coarse aggregates, cement, and water were tried to find the appropriate mixture that would be used to produce a concrete block.

The experimental mixtures were prepared in a laboratory, and the materials were manually mixed. Therefore, water was splashed slowly with a water sprayer, as shown in Figure 3. The mixture ratio was specified as follows: for the NCA mixture, 4:1:1:1 (4 units of sand, 1 unit of coarse aggregate, 1 unit of cement, 1 unit of water = 2000 mL); for the RCA mixture, 4:1:1:1.5 (4 units of sand, 1 unit of coarse aggregate, 1 unit of cement, 1.5 units of water = 3000 mL).

Mould Design

Figure 2. Recycling concrete process (**1**) collecting waste concrete, (**2**) and (**3**) reducing the size of concrete pieces in the crusher, (**4**) obtaining RA.

RCA Mixture **NCA Mixture**

Figure 3. Mixture prepared in the laboratory.

When designing the ICB, a concrete block that is used in construction, the size and shape of the block were carefully considered to ensure its structural integrity and ease of use. The wooden mould used to create the block was inspired by Portuguese design [31], specifically the traditional use of wooden moulds in their construction industry.

It has two hinges at the backside and two hasps at the front to remove it easily and flexibly after turning the mould over without collapsing the block wall. To produce a standard block that would be portable for construction workers and bear more pressure with a long top protrusion (24 cm), the following was designed:

- The back piece, to obtain the block's groove; bottom and half-bottom blocks can be made by turning the front part over;
- The front piece, to obtain the block's protrusion; top and half-top blocks can be made by turning the back piece over;
- The bottom base, to fix the mould and prevent the block from sliding while compacting the mixture, which helps us to hold the mould when we want to turn the mould over;
- A wooden hand, to compact the levels manually 3 or 4 times in the mixture, especially the last one.

This block wall system includes a standard block (24 × 12 × 18 cm), a bottom block, a top block, a half-bottom block, and a half-top block, as shown in Figures 4–6.

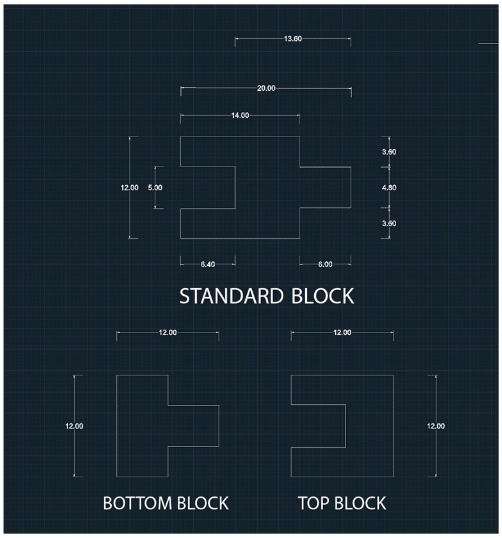

Figure 4. Interlocking block system design (**standard**, **bottom**, and **top**).

Figure 5. Main plywood mould, back piece, front piece, and wooden hand.

The height of the protrusion measured 6 cm, while its width measured 4.8 cm. On the other hand, the height of the groove was augmented to 6.4 cm, and the width to 5 cm. Such an increase in both the height and width of the backside piece facilitates the placement of mortar between the blocks when interlocking them to form a wall. Additionally, it enables the removal of the wooden back piece easily, without causing any collapse in the protrusion.

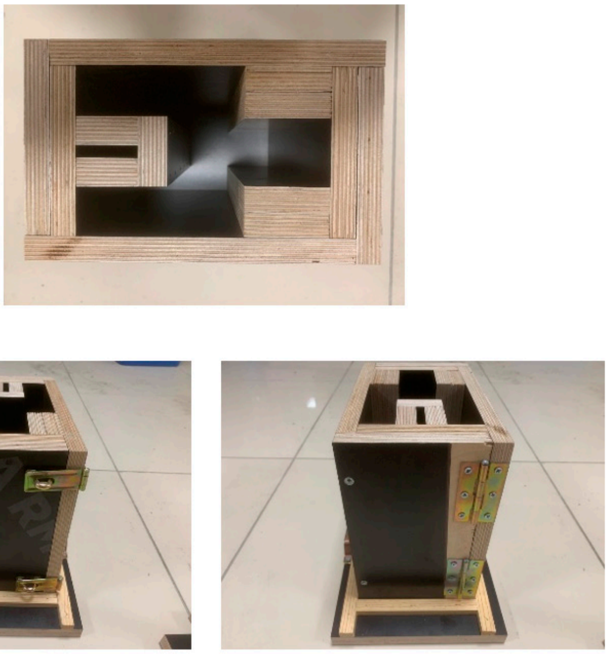

Figure 6. Plywood mould in three views.

2.3. *Casting Process of Interlocking Concrete Block Specimens*

After preparing the mixture using a 4:1:1:1 ratio and obtaining the necessary tools, such as a metal rod, hammer, and wooden hand, the production process for interlocking concrete blocks (ICBs) is shown in Figure 7. The process includes the following steps:

- Painting all mould faces with oil;
- Placing the mould base on the ground;
- Placing the wooden mould on the base and closing the hasps with a thin wooden rod;
- Filling the mould with the concrete mixture;
- Consolidating and compacting the mixture three times for three levels by hammering the wooden hand;
- Shaking the mixture three times manually by using a metal rod for each level;
- Turning the mould over and knocking the base with a plastic hammer;
- Extracting the concrete block by opening the hasps and carefully removing one side of the front wooden piece.

Figure 7. Production process of interlocking concrete blocks (**1**) preparing the mixture, (**2**) placing it in the mold, (**3**) and (**4**) compressing the mixture, (**5**), (**6**), (**7**) and (**8**) dismantling the mold.

2.4. Curing Blocks

After removing the mould, we sprayed water on each block periodically, morning and evening, for seven days.

2.5. Fabrication of ICB Wallette

The wallette panels were constructed using the interlocking block system, which consists of five blocks: the standard block, top block, bottom block, half-bottom block, and half-top block. The standard blocks serve as the primary unit in wallette construction, while the bottom blocks provide structural support for the wall. The top blocks are used to seamlessly terminate the wallette without interlocking keys, whereas the half-bottom and half-top blocks are used to achieve accurate completion of the wall course.

Each wall specimen is composed of one bottom block, two half-bottom blocks, two standard blocks, one top block, and two half-top blocks. These blocks interlock easily with each other using their protrusion key. The wallette's construction entails stacking each dry block one by one, without mortar between them, resulting in a mortarless or dry-stack wall system. The wallette panel specimen's dimensions are L = 480 mm × H = 30 mm.

In this study, the authors constructed five wallette panel specimens using interlocking block systems containing 100% normal aggregates, and five other specimens containing 100% recycled aggregates.

2.6. Specimens and Instrumentation Setup

Axial Compression Tests on Blocks

The compressive strength test is a crucial property used to determine the load-bearing capacity of blocks. This is provided by utilizing the Automatic Compression Testing Machine (ASTM), as shown in Figure 8, to measure blocks' ability to withstand loads before failure. The compressive strength test is particularly significant when using the blocks to construct load-bearing walls. The test involves placing a block between two steel plates, ensuring that it is centred on the loading axis. The load is then gradually increased (0.2 kN/s) until the block fails, and the compressive strength of the block is measured. To prepare for the compression test, multiple tests were conducted using standard blocks with varying mix ratios and ages. Subsequently, five standard natural blocks (NBs) made entirely of natural aggregates and five recycled blocks (RBs) made entirely of recycled aggregates were casted. After curing for seven days, both sets of blocks were subjected to a compression test after 28 days of age, as listed in Table 1.

Axial Compression Tests on ICB Wallettes

Figure 8. Standard interlocking concrete block in the compression test machine.

Table 1. Standard blocks with 100% NCAs and 100% RCAs.

%	Block ID	Age (Day)	Water Treatment Time (Day)	Mix Ratio (Sand:C.Agg:C:W)
100% NA	NB1	28	7	4:1:1:1
	NB2			
	NB3			
	NB4			
	NB5			
100% RA	RB1	28	7	4:1:1:1$\frac{1}{2}$
	RB2			
	RB3			
	RB4			
	RB5			

During the compression test, the panel specimen was positioned between a metal beam at the bottom and a hydraulic vertical load jack. Additionally, two rectangular metal plates were placed over the top end of the panel to ensure that the load was evenly distributed. The load was then gradually increased (0.2 kN/s) until the wallette failed. To measure the vertical displacement accurately, linear variable differential transformer (LVDT) instruments are attached to each wall specimen on the wallette's side in the vertical direction, as illustrated in Figure 9.

Figure 9. ICB wallette specimen test setup.

3. Experimental Results

3.1. Chemical Properties of Recycled Concrete Aggregates

The recycled fine and coarse aggregates were analysed using a scanning electron microscope (SEM). The elemental mapping of our sample surface layer was obtained through X-ray diffraction (XRD) and energy dispersive spectroscopy (EDX). Additionally, SEM can capture high-resolution and three-dimensional images, which provide information on the topography, morphology, and composition.

The SEM-EDS measurements indicated the presence of such constituent elements as O, Ca, C, Au, Si, Al, Fe, S, Mg, K, and Na. The shape and size of the recycled aggregates were irregular because of crushed concrete debris. The RCA particles had irregular shapes, and the surface was acute. Small particles were adhered to the RCA particles, as shown in Figures 10 and 11. The presence of oxygen, carbon, and calcium was determined with high percentages, and they were classified as prominent elements. In Figure 10b, the micro-analysis data of the coarse aggregate show the concentrations of several chemical elements in weight percentages It was indicated that the coarse aggregate particles contained mostly 46.8% oxygen, 24.5% calcium, and 13% carbon. However, the micro-analysis data of the fine aggregates in Figure 11b show that their particles had mostly 43.5% oxygen, 30% calcium, and 12% carbon. Figure 11c shows the scanning electron microscopy (SEM) images of the recycled fine aggregate used.

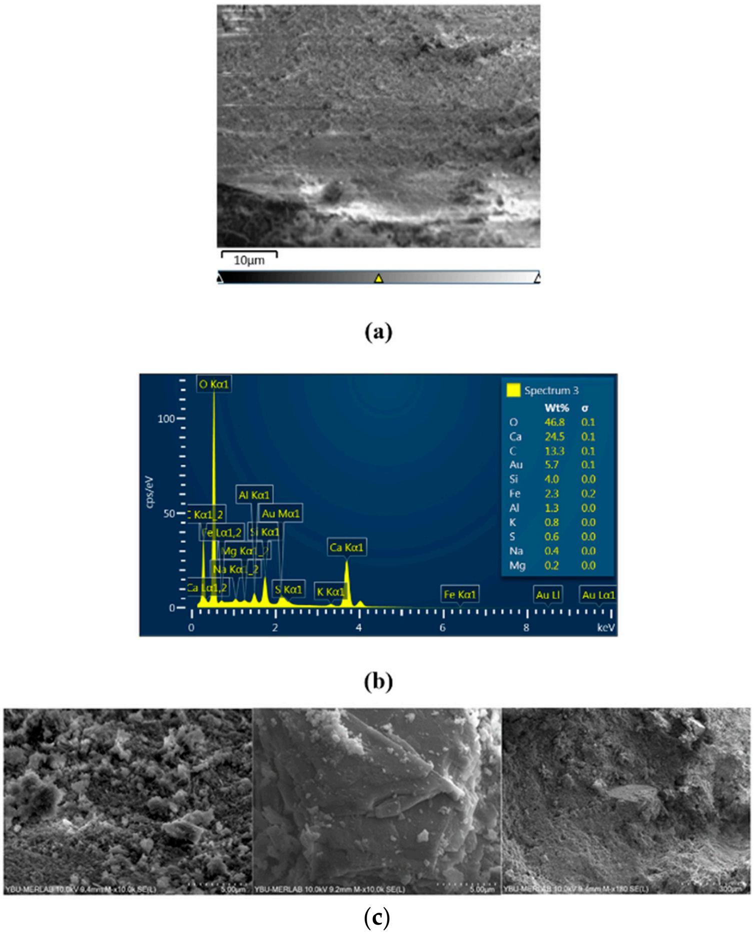

Figure 10. SEM-EDS results of recycled coarse aggregate sample: (**a**) general SEM pattern, (**b**) overall EDS analysis, and (**c**) local SEM images.

3.2. Compressive Strength Results of Block Specimens

The compressive strength results of the experimental standard block specimens are reported in Table 2. Figures 12 and 13 show the comparison between the NB and RB block groups.

Table 2. Compressive strength results of standard block specimens.

%	Block ID	Surface Area (cm^2)	Maximum Load (KN)	Maximum Stress (MPa)	Average Stress (MPa)
100% NA	NB-1	4.8 × 24	101.1	8.7	9.22 (with a standard deviation of 0.43)
	NB-2		112.3	9.7	
	NB-3		106.2	9.2	
	NB-4		111.9	9.7	
	NB-5		101.7	8.8	
100% RA	RB-1	4.8 × 24	56.8	4.9	4.9 (with a standard deviation of 0.99)
	RB-2		49.1	4.2	
	RB-3		73.3	6.3	
	RB-4		64.8	5.6	
	RB-5		40.9	3.5	

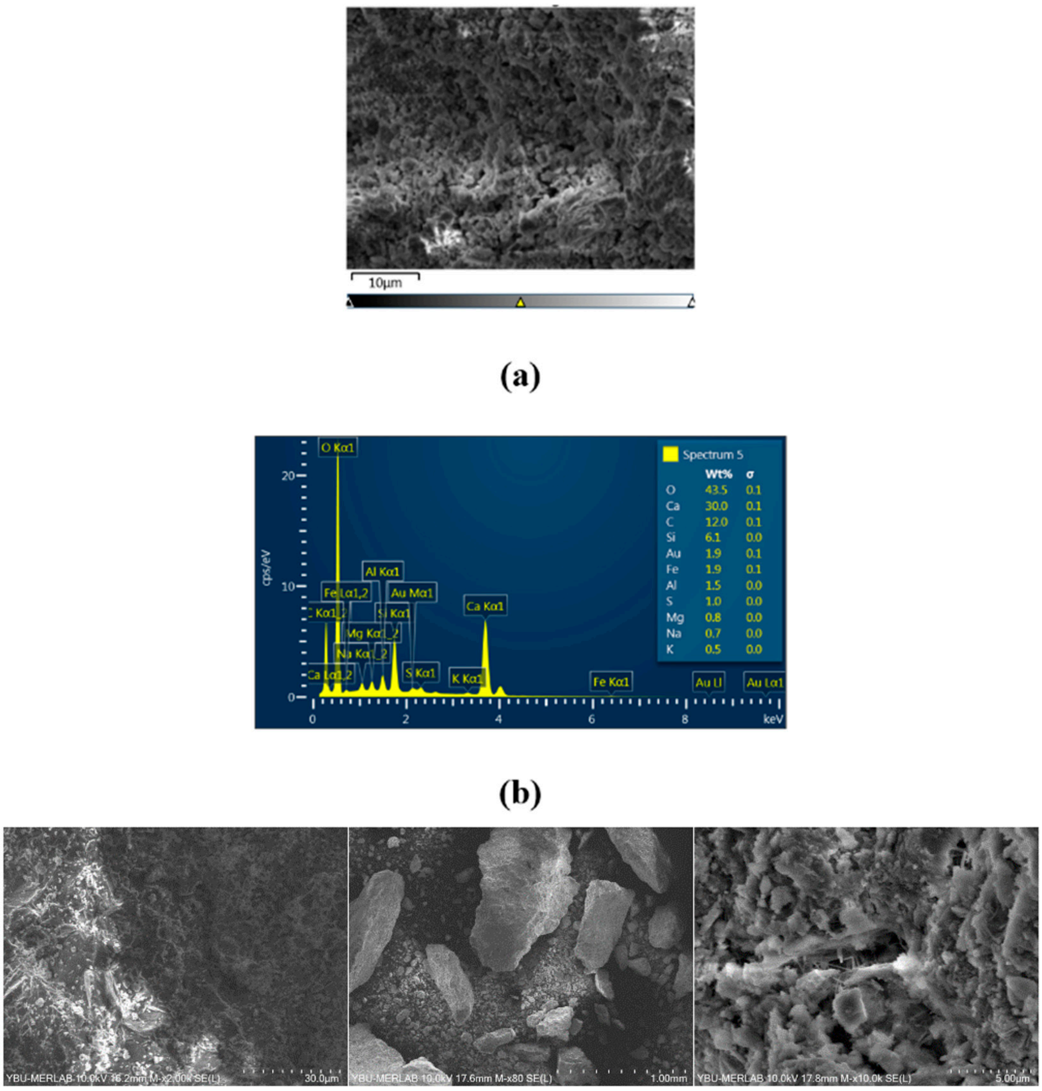

(a)

(b)

(c)

Figure 11. SEM-EDS results of recycled fine aggregate sample: (**a**) general SEM view, (**b**) overall EDS analysis, and (**c**) local SEM images.

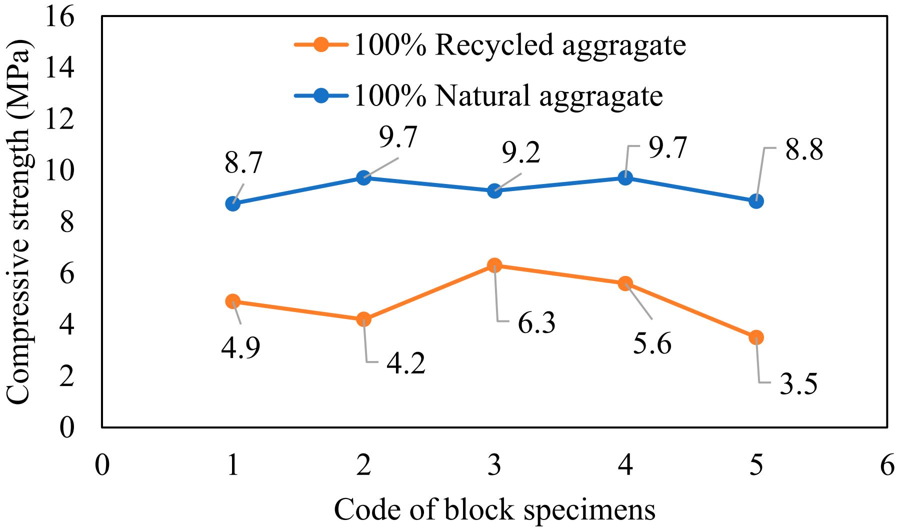

Figure 12. Compressive strength results of standard block specimens.

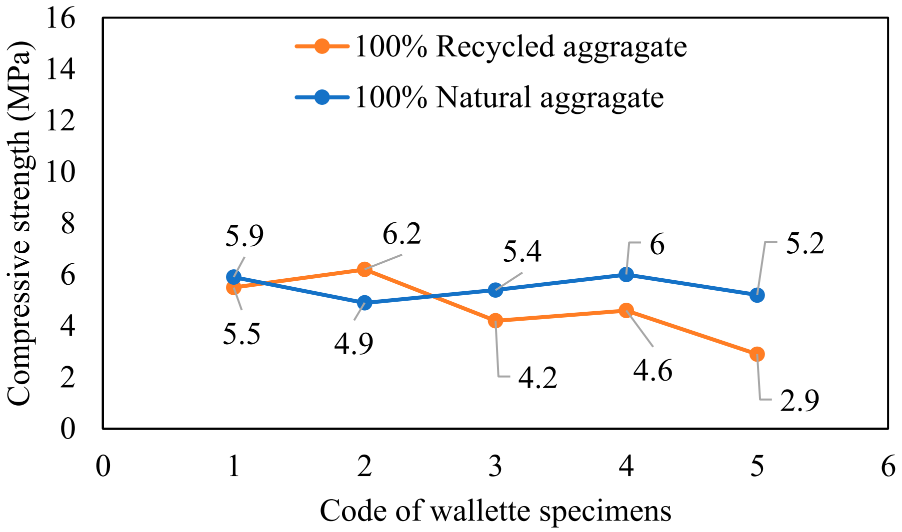

Figure 13. Compressive strength results of wallette specimens.

3.3. Compressive Strength Results of Wallette Panel Specimens

Table 3 summarizes the compressive strength results of the wallettes. The average compressive strength of the NW wallette specimens is 5.48 MPa, while the average compressive strength of the RW wallette specimens is 4.68 MPa.

Table 3. Compressive strength results of wallette specimens.

%	Code of Wall	Surface Area (cm^2)	Max. Load (KN)	Max. Stress (MPa)	Average Stress (MPa)	Δ (mm)	Average Δ (mm)
100% NA	NW1	48 × 7	199.7	5.9	5.48 (with a standard deviation of 0.43)	3.16	2.12 (with a standard deviation of 1.05)
	NW2		165.6	4.9		1.61	
	NW3		181.3	5.4		3.57	
	NW4		200.7	6		0.86	
	NW5		173.3	5.2		1.44	
100% RA	RW1	48 × 7	183.9	5.5	4.68 (with a standard deviation of 1.13)	1.97	1.67 (with a standard deviation of 1.05)
	RW2		208.8	6.2		0.9	
	RW3		140.8	4.2		2.12	
	RW4		155.1	4.6		1.85	
	RW5		95.8	2.9		1.53	

The curves in Figures 14 and 15 show that the displacement values of both the NWs and RWs range between 0.86 and 3.57 mm for the NWs, and range between 0.9 and 2.12 mm for the RWs.

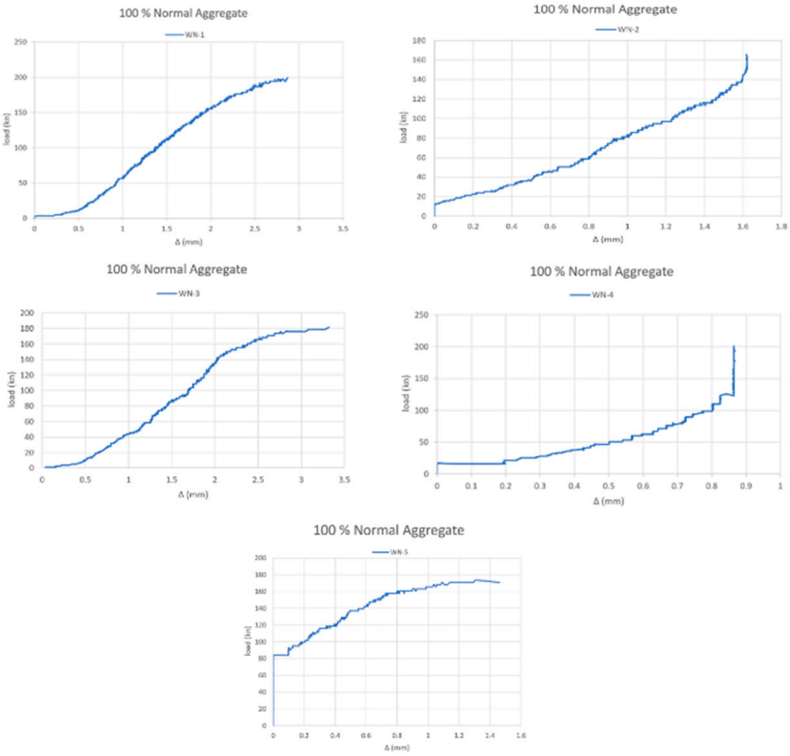

Figure 14. Load–displacement curves of the NW wallette panels.

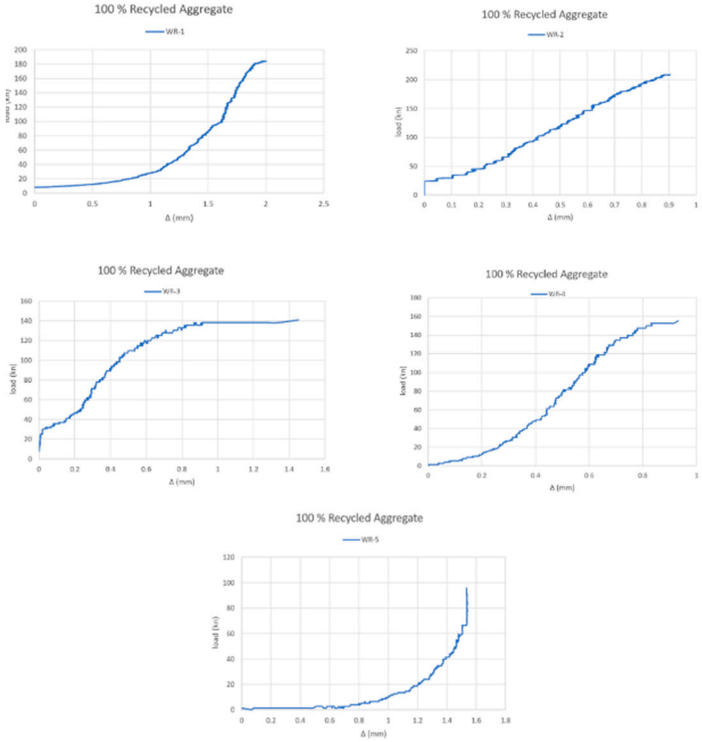

Figure 15. Load–displacement curves of the RW wallette panels.

4. Discussion

This study involved testing specimens using a compression test machine to measure the compressive strength of individual standard blocks (NB, RB) and wallette panels (NW, RW). Prior to the experiment, the optimal mixture for the interlocking concrete blocks was determined through several attempts. Various standard blocks with different mixture ratios were constructed and tested to determine their strengths. The Syrian Arab Code for unreinforced load-bearing walls on buildings [6] was used to define the permissible value of compressive strength. The current study aimed to investigate the use of 100% recycled concrete aggregates (RCAs) in mortarless interlocking concrete blocks, which could provide economic and environmental benefits. Two groups, each containing five blocks, were produced: the first group contained 100% RCAs, and the second group contained 100% natural concrete aggregates (NCAs). The experimental results indicated that the average compressive strength of the standard ICB containing 100% NCAs was 9.22 MPa, while that of the standard ICB containing 100% RCAs was 4.9 MPa. Figure 12 shows a comparison between the NB and RB block groups, indicating that the average compressive strength of the NCA blocks was almost twice that of the RCA ones. The low strength of the RCA blocks could be attributed to the inadequate homogenization of the RCA particles in both the fine and coarse aggregates, as well as the highly porous adhered mortar structure in the RCA mixture, which led to a weak concrete. Manual compaction and vibration mechanisms during preparation may also reduce concrete strength. After loading the axial force, a failure occurred along the protrusion, as indicated with the long line crack that extended to the bottom of the blocks, as shown in Figure 16.

Figure 16. Vertical lines of cracks after loading axial force.

Two sets of tests were carried out on the wallette panels to investigate their compressive strength. Ten wallette samples were constructed using an interlocking block system: five with 100% natural coarse aggregates (NCAs) and five with 100% recycled coarse aggregates (RCAs). A load was applied along the surface face of the wallette (480 mm × 120 mm) to ensure uniform distribution. The results of the compressive strength tests are summarized in Table 3. The average compressive strength of the NCA wallette specimens was 5.48 MPa, with a maximum of 5.9 MPa and a minimum of 4.9 MPa. The average compressive strength of the RCA wallette specimens was 4.68 MPa, with a maximum of 6.2 MPa and a minimum of 2.9 MPa. The compressive strength results of both types of wallette specimens, were similar and met the Syrian load-bearing wall code, with the average compressive strength of the RCAs being nearly six times higher than 0.8 MPa and that of the NCAs being nearly seven times higher than 0.8 MPa.

Based on these results, interlocking recycled concrete block walls (IRCBWs) can be considered as load-bearing walls for single- and multi-story buildings, using a mortarless interlocking block wall system. This system increases construction productivity and reduces labour and construction duration in war/disaster-affected areas. However, as seen in Figure 17, the grooves are not sufficiently connected to the tongue key, which may adversely affect the wall strength. This is because the dry bed joints between interlocking block layers play a significant role in the performance of the mortarless masonry wall system. Moreover, some design imperfections were evident during the casting stage when producing half of the top and bottom blocks. The length of the mould was 24 cm, but the half-block was only 12 cm, resulting in the inadequate compaction of the last layer of the block. As a result, some half-blocks did not complete the wall entirely, leaving part of the tongue or groove outside the wallette.

Figure 17. Interlocking three types of blocks.

Vertical cracks were observed as starting from the top of the wallette and extending through the three compaction layers of the block. This occurrence can be attributed to inadequate contact between the groove's lower surface and the protrusion's upper surface for each type of block. As a result, the crack propagates from one block to another until the entire wallette fails. The failure mode is presented in Figures 18 and 19.

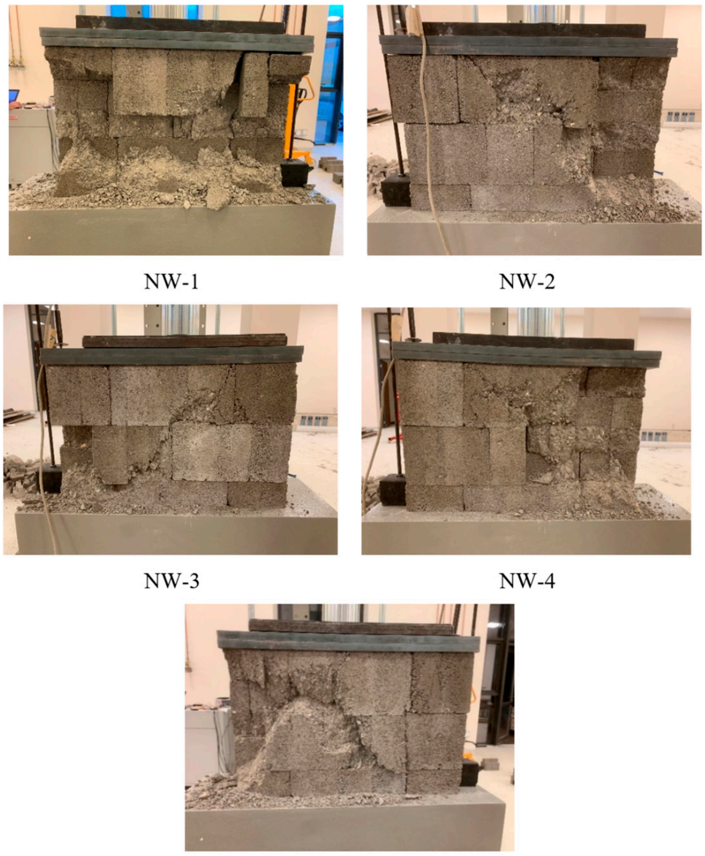

NW-1

NW-2

NW-3

NW-4

NW-5

Figure 18. Failure pattern of the NW wallette panels.

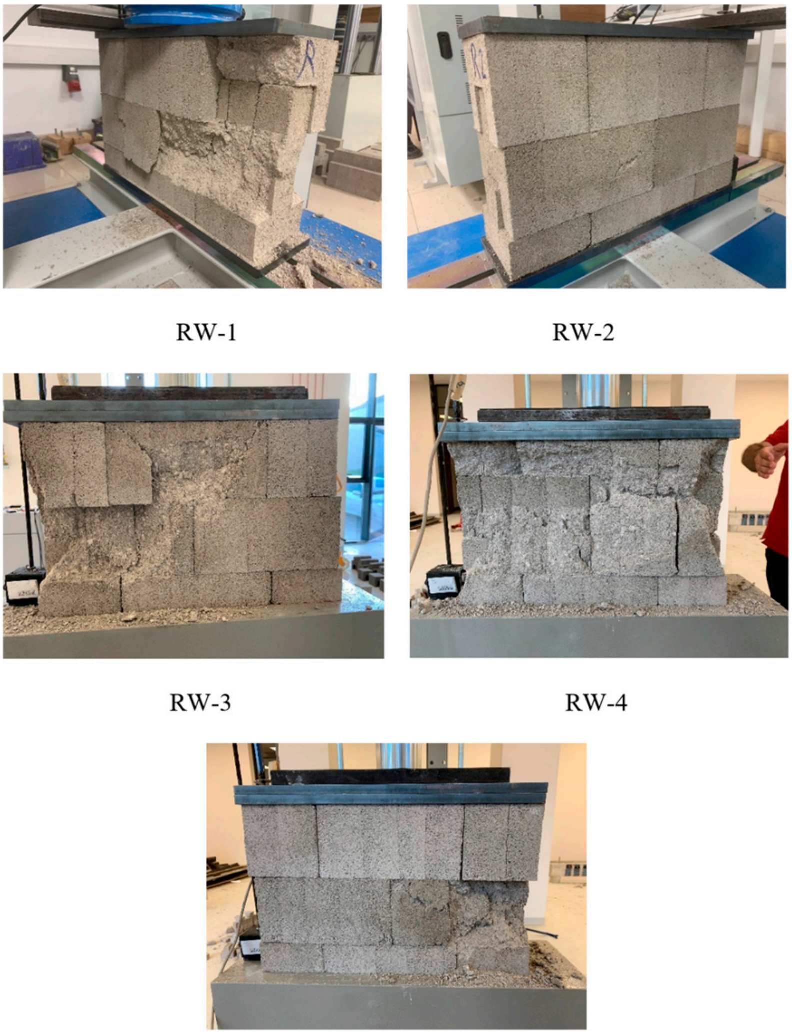

RW-1 RW-2

RW-3 RW-4

RW-5

Figure 19. Failure pattern of the RW wallette panels.

Figures 14 and 15 illustrate the displacement values of both the NWs and RWs. The NW displacement ranges between 0.86 and 3.57 mm, while the RW displacement ranges between 0.9 and 2.12 mm. Notably, the average displacement value of the NWs (2.12 mm) is higher than that of the RWs (1.67 mm). Overall, the wallette structure does not exhibit significant displacement.

As a general evaluation with the mechanical results obtained, it was understood that the natural and recycled aggregates that were used in the production of interlocking blocks gave close results in the concrete compressive strength of the walls. In other words, the use of recycled aggregates, which is a very environmentally friendly approach, has proven to be quite suitable for the production of interlocking blocks. However, it is obvious that more successful results will be obtained when the production defects shown in Figure 17 are eliminated. The simple and fast construction of walls with the three types of blocks proposed in this study was demonstrated during the production of the test elements. That is, when these blocks are available for sale on the market, people will build their houses and other basic structures in a simple way, since no skilled labour is required. Finally, the fact that the material used is recycled and that the production of the blocks is simple will reduce the cost considerably and provide cheap access to the market.

5. Conclusions

In the present study, the potential and feasibility of using recycled concrete aggregates (RCAs) obtained from construction and demolition (C&D) waste were evaluated. This study explored the possibility of constructing a load-bearing wall using interlocking concrete blocks (ICBs) through a dry-stack mechanism. The system comprised five types of inter-locking concrete blocks, namely standard, bottom, top, half-top and half-bottom, designed to be placed and stacked easily without mortar. This study further examined the compressive strength, displacement, and failure mode of wallette panel specimens using ICBs containing 100% NCAs and 100% RCAs. As a result, the following conclusions were made:

- The average compressive strength of the NCA wallette specimens was 5.48 MPa, with a maximum of 5.9 MPa and a minimum of 4.9 MPa;
- The average compressive strength of the RCA wallette specimens was 4.68 MPa, with a maximum of 6.2 MPa and a minimum of 2.9 MPa;
- The compressive strength results of both types of wallette specimens were similar and met the Syrian load-bearing wall code, with the average compressive strength of the RCAs being nearly six times higher than 0.8 MPa, and that of the NCAs being nearly seven times higher than 0.8 MPa.

Author Contributions: Conceptualization, M.C.Y. and A.A.; methodology, M.C.Y. and A.A.; validation, M.C.Y., A.A. and Ö.M.; formal analysis, M.C.Y. and A.A.; investigation, M.C.Y., A.A. and Ö.M.; resources, M.C.Y. and Ö.M.; data curation, M.C.Y. and Ö.M.; writing—original draft preparation, M.C.Y. and Ö.M.; writing—review and editing, M.C.Y. and Ö.M.; visualization, M.C.Y. and Ö.M.; supervision, M.C.Y. and Ö.M.; project administration, M.C.Y.; funding acquisition, M.C.Y. All authors have read and agreed to the published version of the manuscript.

Funding: This research received no external funding

Data Availability Statement: No new data were created.

Conflicts of Interest: The authors declare no conflict of interest.

References

1. Xiao, J.; Li, W.; Fan, Y.; Huang, X. An overview of study on recycled aggregate concrete in China (1996–2011). *Constr. Build. Mater.* **2012**, *31*, 364–383. [CrossRef]
2. Cement 2022 Research Report. 2022. IA Cement. Available online: https://www.iacement.com/reports/ (accessed on 10 October 2023).
3. Türk Çimento. Available online: https://www.turkcimento.org.tr/tr/haber_detay/cimento-ve-klinker-istatistikleri (accessed on 10 October 2023).
4. Xiao, J.Z. *Recycled Concrete*; China Building Industry Press: Beijing, China, 2008; p. 26.
5. Sun, Y.; Zhou, D. The present study state and problems to be solved on recycled concrete in China. *Concrete.* **2006**, *4*, 25–28.
6. Sengar, B.S.; Garg, V.; Kumar, A.; Awasthi, V.; Kumar, S.; Atuchin, V.V.; Mukherjee, S. Band alignment of Cd-free (Zn, Mg) O layer with Cu2ZnSn (S, Se) 4 and its effect on the photovoltaic properties. *Opt. Mater.* **2018**, *84*, 748–756. [CrossRef]
7. Prosekov, A.Y.; Ivanova, S.A. Food security: The challenge of the present. *Geoforum* **2018**, *91*, 73–77. [CrossRef]
8. Dragunov, V.P.; Dorzhiev, V.Y.; Ostertak, D.I.; Atuchin, V.V. A new autostabilization mechanism in the Bennet doubler circuit-based electrostatic vibrational energy harvester. *Sens. Actuators A Phys.* **2018**, *272*, 259–266. [CrossRef]
9. Vesnina, A.; Prosekov, A.; Atuchin, V.; Minina, V.; Ponasenko, A. Tackling atherosclerosis via selected nutrition. *Int. J. Mol. Sci.* **2022**, *23*, 8233. [CrossRef] [PubMed]
10. Atuchin, V.V.; Asyakina, L.K.; Serazetdinova, Y.R.; Frolova, A.S.; Velichkovich, N.S.; Prosekov, A.Y. Microorganisms for Bioremediation of Soils Contaminated with Heavy Metals. *Microorganisms* **2023**, *11*, 864. [CrossRef]
11. European Commission—Science for Environment. Available online: http://ec.europa.eu/environment/integration/research/newsalert/pdf/39si10.pdf (accessed on 3 October 2023).
12. Kanellopoulos, A.; Nicolaides, D.; Petrou, M.F. Mechanical and durability properties of concretes containing recycled lime powder and recycled aggregates. *Constr. Build. Mater.* **2014**, *53*, 253–259. [CrossRef]
13. Tsujino, M.; Noguchi, T.; Tamura, M.; Kanematsu, M.; Maruyama, I. Application of conventionally recycled coarse aggregate to concrete structure by surface modification treatment. *J. Adv. Concr. Technol.* **2007**, *5*, 13–25. [CrossRef]
14. Tavakoli, M.; Soroushian, P. Strengths of recycled aggregate concrete made using field-demolished concrete as aggregate. *Mater. J.* **1996**, *93*, 178–181.
15. Kou, S.C.; Poon, C.S.; Wan, H.W. Properties of concrete prepared with low-grade recycled aggregates. *Constr. Build. Mater.* **2012**, *36*, 881–889. [CrossRef]

16. Younis, K.H.; Pilakoutas, K. Strength prediction model and methods for improving recycled aggregate concrete. *Constr. Build. Mater.* **2013**, *49*, 688–701. [CrossRef]
17. Xiao, J.; Wang, C.; Li, J.; Tawana, M.M. Shake-table model tests on recycled aggregate concrete frame structure. *ACI Struct. J.* **2012**, *109*, 777–786.
18. Ferriz-Papi, J.A.; Thomas, S. Recycled aggregates from construction and demolition waste in the production of concrete blocks. *J. Constr. Mater.* **2020**, *2*, 1–6. [CrossRef]
19. Guo, Z.; Tu, A.; Chen, C.; Lehman, D.E. Mechanical properties, durability, and life-cycle assessment of concrete building blocks incorporating recycled concrete aggregates. *J. Clean. Prod.* **2018**, *199*, 136–149. [CrossRef]
20. Abdullah, E.S.R.; Mirasa, A.K.; Asrah, H.; Lim, C.H. Review on Interlocking Compressed Earth Brick. *IOP Conf. Ser. Earth Environ. Sci.* **2020**, *476*, 012029. [CrossRef]
21. Omoregie, A.D.; Alabi, A.O.; Imuetinyan, A.E. Providing sustainability in educational buildings through the use of compressed stabilized interlocking earth blocks. *J. Constr. Eng. Technol. Manag.* **2016**, *6*, 130–140.
22. Sathiparan, N.; Jaasim, J.H.M.; Banujan, B. Sustainable production of cement masonry blocks with the combined use of fly ash and quarry waste. *Materialia* **2022**, *26*, 101621. [CrossRef]
23. Arunachalam, K.P.; Henderson, J.H. Experimental study on mechanical strength of vibro-compacted interlocking concrete blocks using image processing and microstructural analysis. *Iran. J. Sci. Technol. Trans. Civ. Eng.* **2023**, 1–19. [CrossRef]
24. Silva, W.; Picado-Santos, L.; Barroso, S.; Cabral, A.E.; Stefanutti, R. Assessment of Interlocking Concrete Block Pavement with By-Products and Comparison with an Asphalt Pavement: A Review. *Appl. Sci.* **2023**, *13*, 5846. [CrossRef]
25. Kumar, T.P.; Vigneshvar, R. Development of an Innovative Interlock Blocks. *J. Civ. Eng. Environ. Technol. Print* **2014**, *1*, 114–118.
26. Onyeakpa, C.; Onundi, L. Improvement on the Design and Construction of Interlocking Blocks and Its Moulding Machine. *IOSR J. Mech. Civ. Eng.* **2014**, *11*, 49–66. [CrossRef]
27. Garg, A.; Aggarwal, P.; Aggarwal, Y.; Belarbi, M.O.; Chalak, H.D.; Tounsi, A.; Gulia, R. Machine learning models for predicting the compressive strength of concrete containing nano silica. *Comput. Concr.* **2022**, *30*, 33.
28. Ganesh, S.J.; Lokeshwaran, N. Experimental investigation on behavior of shear wall assembled with interlocking concrete block. *Int. J. Civ. Eng. Technol.* **2017**, *8*, 111–117.
29. Sarath, P.; Pradeep, P.; Shemy, S.B. Performance of Steel Fibre Reinforced Interlocking Hollow Block as Load Bearing Wall. *IOSR J. Mech. Civ. Eng.* **2015**, *12*, 38–46.
30. Tatheer, Z. Strategies for Improving the Response of Drystack Masonry to Compression. Ph.D. Thesis, Queenland University of Technology, Queenland, Australia, 2017.
31. de Blocos, E. How To Make an Adjustable Cinder Block Mold. 2021. Available online: https://www.youtube.com/watch?v=Lyq_H0yQKyQ (accessed on 10 October 2023).

buildings

Article

Stabilization of Shield Muck Treated with Calcium Carbide Slag–Fly Ash

Jinzhe Wang [1], Ying Fan [1,*], Xixi Xiong [1,2] and Fucai Zhao [1,3]

[1] School of Civil Engineering Architecture and the Environment, Hubei University of Technology, Wuhan 430068, China; wangjingzhe51@icloud.com (J.W.)
[2] Wuhan Hanyang Municipal Construction Group Co., Ltd., Wuhan 430000, China
[3] Wuhan Institute of Rock and Soil Mechanics, Chinese Academy of Sciences, Wuhan 430064, China
* Correspondence: 102111017@hbut.edu.cn

Abstract: Solidifying shield muck with calcium carbide slag and fly ash as curing agents was proposed as a highly efficient method for reusing waste shield muck. The compaction test, unconfined compression test, and dry–wet cycle test were used to evaluate the compressive strength, water immersion stability, and durability of the cured soil. The stress–strain curve and microscopic test were employed to analyze the compression damage law, mineral composition, and microscopic morphology of the cured soil, and to analyze the mechanism of calcium carbide slag–fly ash-cured shield muck. It was found that calcium carbide slag–fly ash can significantly improve the compressive strength of shield muck, and the strength of cured soil increases and then decreases with an increase in calcium carbide slag and fly ash and increases with curing age. The strength was highest when the content of calcium carbide slag and fly ash was 10% and 15%, respectively. Dry–wet cycle tests showed that the specimens had good water immersion stability and durability, and the stress–strain curve of the specimen changed from strain hardening to strain softening after dry–wet cycles. The internal particles of the cured soil were mainly cemented and filled with C-(A)-S-H colloid and calcium alumina (AFt), which both support the pores between the soil and form a skeleton structure to enhance the strength of the soil and lend it good mechanical properties.

Keywords: shield muck; industrial waste; unconfined compressive strength; dry–wet cycle; stress–strain curve; microstructure

1. Introduction

With the increasing demand for underground space utilization in urban construction, the shield method, as a safe and efficient fully mechanized concealed excavation construction method with a low impact on the environment around the construction site, has been widely used in the construction of rail transit, tunnels, municipal highways, urban integrated pipeline corridors, and other projects. Shield residue is the waste engineering residue produced by the city in the process of shield construction. It is generated in large amounts, has poor engineering properties, and has high processing costs. This residue is often not disposed of directly, making the processing cost of engineering residue high in terms of the process of transporting it out of the residue disposal site. Also, the spilling of residue on the road results in pollution of the environment [1–3]. Curing/stabilization technology is a commonly used technology for soil reuse today. Most residue curing materials are inorganic chemical materials, such as cement, gypsum, lime, etc. [4–6]. This type of curing method, which consumes a significant amount of energy, produces cement, and leads to the lime process, will produce a large amount of CO_2, accompanied by SO_2 and other harmful gases. Calcined slag will cause secondary pollution, leading to new pressure on the environment [7,8]. Therefore, developing more environmentally friendly and effective curing technology is necessary from the perspective of sustainable development and the economy. Calcium carbide slag (CS) is a secondary product of calcium carbide hydrolysis, a method for obtaining acetylene gas. Fly ash (FA) is an industrial waste produced in thermal power generation that has a high content of active SiO_2. They all belong to the category of industrial waste, with a large annual output but a low utilization rate, and accumulating waste will encroach on land and damage the soil and water environment. It has been found that the combination of calcium carbide slag and fly ash has a good effect on curing soil, based on the ecological civilization concept of "treating waste with waste", combined with the current situation of the low utilization rate of waste engineering slag generated from subway and tunnel projects. Using calcium carbide slag and fly ash as curing agents to improve the mechanical properties of shield muck and using the improved slag for road construction has thus been proposed.

Recently, scholars at home and abroad have studied how to use shield residues and technology utilizing calcium carbide slag and fly ash curing soil [9]. Zhang et al. [10] used shield slag and lime as the main raw materials and calcium carbide slag and iron powder as stabilizing materials. The formation mechanism of low-heat Portland cement under different doping conditions was investigated via X-ray diffraction (XRD), a scanning electron microscope (SEM), and differential thermal analysis. It was found that the shield residue could be prepared as a high-belite cementitious material for secondary use. Baskar et al. [11] cured clayey soils with calcium carbide slag and fly ash as raw materials and found a 52% increase in the compressive strength of soil specimens, with minimal strength loss after the 12th cycle of the cyclic unconfined compressive strength test, significantly improving strength and durability. Xu et al. [12] investigated the mechanical properties of cured soil using an unconfined compressive strength test (UCS), XRD, SEM, and a corrosion resistance test using shield residues as a raw material, blast furnace slag as a curing agent, and water glass and sodium hydroxide as alkali exciters. The results show that alkali-excited blast furnace slag (GGBFS) has a good curing ability for shield residues, and an appropriate amount of GGBFS (GGBFS/shield residues = 0.3) can be used to achieve a high early strength (20 MPa) and late strength (30 MPa) of the cured shield residues. Liu et al. [13] investigated the swelling and shrinking characteristics and strength properties of expanded soils stabilized with calcium carbide slag and rice husk ash. It was found that calcium carbide slag and rice husk ash could significantly increase the unconfined compressive strength, cohesion, and internal friction angle of the swelling soil while decreasing the swelling properties of the cured soil. Guo et al. [14] investigated the mechanical properties of lime–alkali slag, lime–desulfurized, gypsum-stabilized shield residue soil and its water immersion stability and durability using the indoor compaction test, CBR test, UCS, dry–wet cycle test, XRD test, and SEM test. The results show that the mechanical properties of the shield residue soil were greatly improved after mixing it with the improved material, and the water stability and durability were also greatly improved. The improved soil also had good road performance and can be used as roadbed filling material.

In summary, previous researchers have treated shield residues mostly with slag, lime, gypsum, and other materials. Calcium carbide slag, as a curing agent, is mainly used in swelling soil, silt soil, etc. Calcium carbide slag and fly ash are forms of industrial waste. If the mechanical properties of slag can be improved by combining them in a certain proportion, they can be applied to roadbed fillers so that they can be "taken from the soil and used in the soil." These wastes can be used effectively to protect the environment and, at the same time, enrich the choice of materials for road construction.

Therefore, this paper proposes treating shield slag soil with calcium carbide slag–fly ash. The unconfined compression test can be used to study the change in the compressive strength of cured soil and the optimal amount of curing agent. Dry–wet cycle tests were used to study the stability and durability of the cured soil via water immersion. Microscopic tests such as XRD and SEM were used to analyze the mineral composition and microstructure of the cured soil. The stress–strain curves of the cured soil were considered alongside the calcium carbide slag–fly ash curing mechanism of shield slag soil. This study aims to provide theoretical support for the reuse of shield residues as engineering fill material.

2. Materials and Methods

2.1. Materials

The test muck was taken from the fifth-section interval of the second phase of the Wuhan City Rail Transit Line 11 East project, near the proposed stopping point shown in Figure 1. The muck is composed of clay and is grayish–yellow in color, and its basic physical index is shown in Table 1. The gradation curve of shield residues is shown in Figure 2, with a uniformity coefficient Cu > 5 and curvature coefficient 1 < Cc < 3. The gradation is good.

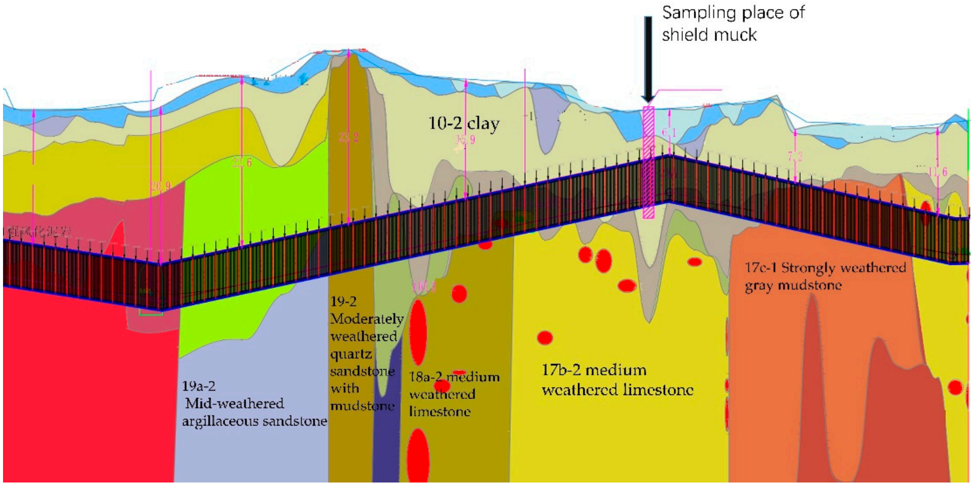

Figure 1. Longitudinal section view of shield muck taking material.

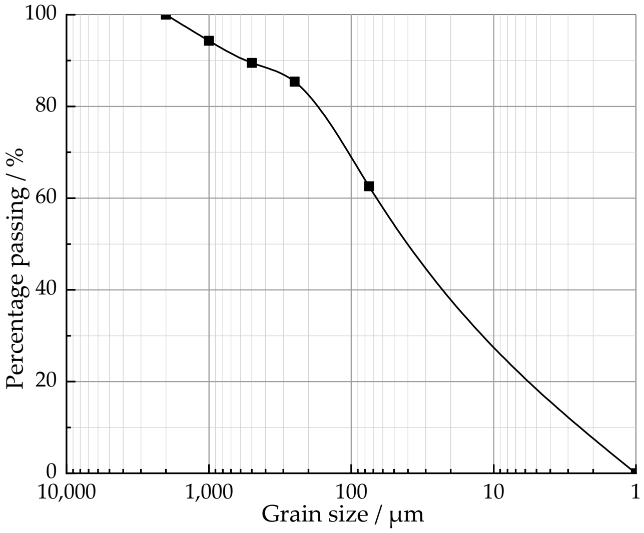

Figure 2. Shield muck grading curve.

Calcium carbide slag was produced by a limited company in Henan that produces water purification materials. The slag had the appearance of an off-white powder with a certain irritating odor and a specific gravity of 2.03. The fly ash was produced by a power plant in Henan Province, and it had the appearance of gray powder. The content of SiO_2 and Al_2O_3 in the fly ash reaches 79.42%, and the content of CaO and MgO is 6.23%, meaning that it constitutes silica–alumina type fly ash. The cement was produced by Huaxin Cement Co. The shield muck, calcium carbide slag, fly ash, and Portland cement are shown in Figure 3, and their chemical compositions are shown in Table 2.

Table 1. Basic physical properties of shield muck.

Properties of Shield Muck	Shield Muck Sample
Initial Water Content (ω/%)	42.3
Liquid Limit (ω_L/%)	43.7
Plastic Limit (ω_P/%)	23.5
Plasticity Index (I_P)	20.2
Liquidity Index (I_L)	0.931
Specific Density (P)	2.54
Maximum Dry Density (g/cm^3)	1.802
Optimum Moisture Content (%)	17.27
Coefficient of Curvature, Cc	2.48
Coefficient of Uniformity, Cu	59


(**a**) (**b**) (**c**) (**d**)

Figure 3. Test material: (**a**) Fly ash; (**b**) Calcium carbide slag; (**c**) Portland cement; (**d**) Shield muck.

Table 2. Chemical composition of calcium carbide slag, fly ash, and cement (%).

Sample Name	CaO	SiO_2	Al_2O_3	MgO	Fe_2O_3	TiO_2	SO_3	Na_2O
Calcium Carbide Slag	86.25	2.21	1.93	0.42	1.07	0.10	2.75	0.05
Fly Ash	5.38	54.84	24.58	0.85	5.85	—	—	—
Portland Cement	62.34	21.17	5.48	2.76	3.85	—	—	—

2.2. Test Protocol

The shield muck has a high water content, a high viscosity, and a flow plastic state. To facilitate the subsequent test, it was necessary to pretreat the undisturbed shield muck.

The shield muck was dried naturally and then crushed by a soil crusher. The crushed shield muck was then passed through a 2 mm standard sieve by a vibrating sorter according to geotechnical test specifications [15]. After sieving, the soil samples were put into an oven at 105 °C, dried to a constant weight, and removed for use. The compaction test was carried out using the heavy compaction method to determine the specimens' maximum dry density and optimum water content under the dosing of plain soil and each curing agent. The unconfined compressive strength test was based on the maximum dry density and optimum moisture content obtained from the compaction test, and the specimen dosage was calculated by controlling 96% compaction. The sample was pressed into a cylindrical shape of Φ50 mm × 100 mm using the static pressure method. The molded specimens were wrapped in cling film and placed in a standard maintenance box for 7, 14, and 28 days [16]. Three parallel specimens were set for each curing agent dose, and the results were averaged. Based on previous research [17–23], the dosing amounts of calcium carbide slag and fly ash were designed as shown in Table 3, and the unconfined compression test was carried out according to the dosing amounts presented in Table 3. The specimens were loaded until they were destroyed, and the dosing amounts of calcium carbide slag and fly ash that were optimal for stabilizing the shield slag soil in the selected dosing interval were obtained according to the results of the unconfined compression test. After the strength test, the specimens were taken for XRD and SEM tests to determine their internal composition and microstructure under different doping ratios.

Table 3. Tests on unconfined compressive strength.

Sample	Dosage	Curing Age (Day)
Control Group 1	0%CS + 0%FA + 0% cement	
Control Group 2	0%CS + 0%FA + 5% cement	
Sample 1	6%CS + 15%FA	
Sample 2	8%CS + 15%FA	
Sample 3	10%CS + 15%FA	7 days
Sample 4	12%CS + 15%FA	14 days
Sample 5	14%CS + 15%FA	28 days
Sample 6	10%CS + 12%FA	
Sample 7	10%CS + 18%FA	
Sample 8	10%CS + 21%FA	
Sample 9	10%CS + 24%FA	

Note: CS is calcium carbide slag and FA is fly ash in the doping amount; control group 1 is plain soil, and control group 2 is mixed with 5% cement. Curing agent admixture is the ratio of curing agent to dry soil mass.

Dry–wet cycle tests were conducted to further investigate the stability and durability of the cured residual soil. The dry–wet cycle test was carried out following the method described in previous research [24]. Three kinds of samples with the lowest, medium, and highest strength were selected to carry out the dry–wet cycle test.

2.3. Methods

According to the test specification [15], the sieved and dried plain soil, as well as the cured soil mixed with different proportions of the curing agent, was subjected to light compaction tests to obtain the optimum moisture content and maximum dry density, and the samples were mixed with different proportions of calcium carbide slag and fly ash.

Carbide slag and fly ash were added to the shield muck according to the predetermined proportions and mixed evenly; water was added until the mixture reached the optimum moisture content; the mixture was thoroughly mixed again; and then it was put into a sealed bag and left for 24 h. When making the specimens, the resting mixture was put into a light compaction steel mold with an inner diameter of 50 mm and a height of 100 mm in 3 layers. After compression molding, the sponges were wrapped with cling film and placed in a standard curing box with a temperature of (20 ± 2) °C and a humidity of 95%. After reaching the maintenance curing age, the specimens were removed. A WDW-10E-microcomputer-controlled electronic universal testing machine was used to carry out the unconfined compression test on the test block. The vertical strain rate was set to 1 mm/min. The value was recorded when the strength of the specimen reached its peak. At this point, the specimen was destroyed internally. The test continued until the specimen surface showed obvious cracks, at which point it was stopped. The average value of three parallel specimens measured in each group of tests was taken as the experimental result for analysis. After the compression test, the specimens were finely crushed internally and processed to a constant weight in the freeze-dryer. The dried, crushed pieces were internally ground into a powder and passed through a 0.075 mm sieve for the XRD test. The XRD scanning speed was 5 (°)/min, and the range was 5~80°. The internal section of the dried specimen block was selected for the SEM test. In the dry–wet cycle test, the specimen was standardized for 28 d and then dried at room temperature (20 ± 3) °C for 24 h. The specimen was numbered, and its mass, diameter, and height measured; then, the specimen was placed in a water bath, which was slowly filled with water until the top surface of the specimen was submerged. The specimens were immersed in a water bath at (20 ± 0.5) °C for 24 h, and their morphology was observed. Then, the specimen was taken out and put on the absorbent paper for 1 h; the moisture on the specimen's surface was wiped off; the specimen's mass, diameter, and height were measured; and the specimen's appearance was recorded. This constitutes a dry–wet cycle. It was repeated five times to complete a five-stage dry–wet cycle. The compressive strength without a lateral limit of the

3 groups of ratios was measured after completing 1, 3, and 5 dry–wet cycles, and 2 parallel specimens were taken from each group.

3. Analysis of Test Results

3.1. Compaction Characteristic Analysis

Keeping the proportion of fly ash constant, the trends of optimum moisture content and maximum dry density were investigated for different calcium carbide slag ratios against plain soil (Control Group 1) and mixed with 5% cement (Control Group 2), and the test results are shown in Figure 4.

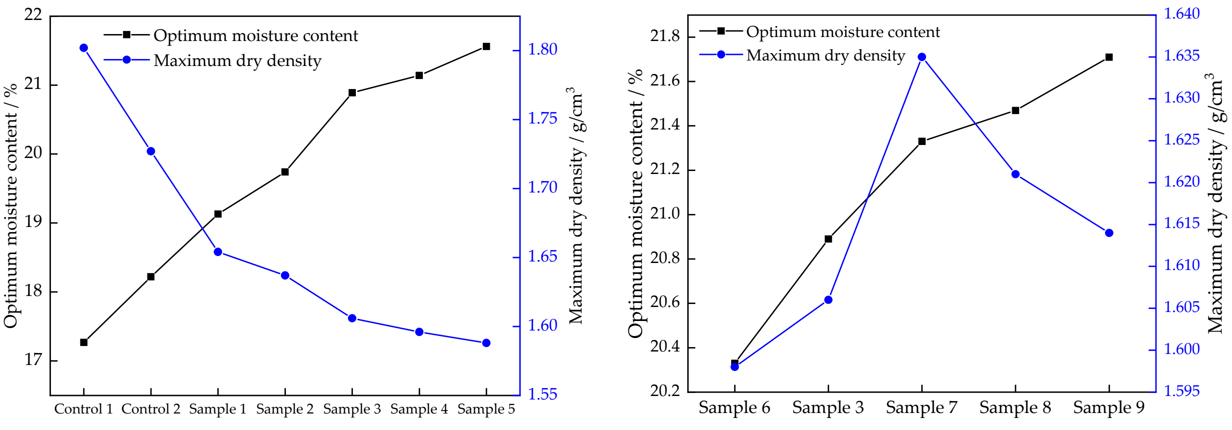

(**a**) (**b**)

Figure 4. The trend of compaction test of specimens with different proportions: (**a**) Trend of compaction tests with different calcium carbide slag ratios; (**b**) Trend of compaction tests with different fly ash ratios.

Figure 4a shows that the optimum moisture content of the treated soil tends to increase, and the maximum dry density tends to decrease with the increase in cement incorporation and calcium carbide slag incorporation. This is because the main component of calcium carbide slag is CaO, which more easily ionizes with the OH− ions in a water hydrolysis reaction to form Ca^{2+}, compared to plain soil without the addition of a curing agent. The reaction consumes a large amount of water, while the products generated by the reaction increase the cementation between soil particles, and a stable agglomerate structure is formed inside the soil, preventing water from continuing to enter the interior. Therefore, the optimum moisture content of the bonding material increases with the increase in the calcium carbide slag admixture. The maximum dry density decreases with increasing curing agent dosing; this is mainly because the specific gravity of cement, calcium carbide slag, and fly ash is smaller than that of shield muck, resulting in the relative density of the mixture being lower than that of the shield residues. The maximum dry density of the specimens showed an overall decreasing trend under the compaction action.

Figure 4b shows that the optimum moisture content of the binding material increases continuously with the increase in the fly ash admixture. The maximum dry density increased first and reached its peak when 18% fly ash was mixed in, and the maximum dry density decreased gradually after the fly ash continued to be mixed in. This phenomenon was mainly due to the small specific surface area of fly ash and the large voids between the particles of calcium carbide slag. For amounts of fly ash lower than 18%, calcium carbide slag and fly ash in the compaction effect mean that the internal particles between the voids fill each other and become more compact, resulting in increasing dry density. When the fly ash admixture exceeds 18%, the amount of calcium carbide slag admixture remains unchanged. Currently, as the compaction effect has been unable to further fill its internal voids, the skeleton between fly ash particles has difficulty achieving further compaction under the compaction effect, resulting in a gradual decrease in its maximum dry density.

3.2. Analysis of UCS

The effect of calcium carbide slag-fly ash on the strength of cured shield muck is shown in Figure 5. The addition of calcium carbide slag and fly ash can significantly improve the lateral limitless compressive strength of shield muck.

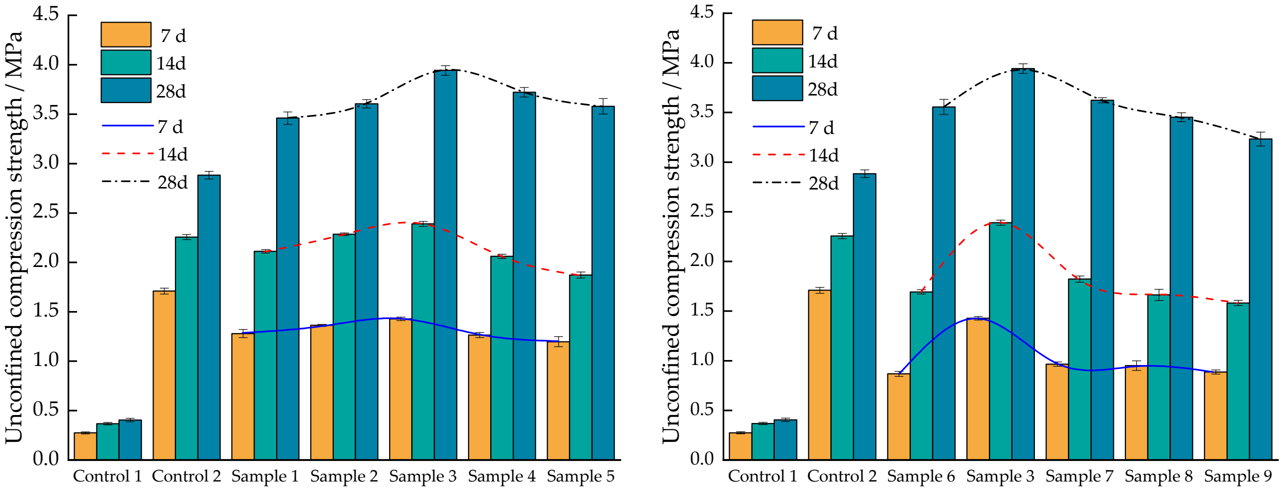

(**a**) (**b**)

Figure 5. Unlimited compressive strength under different dosages: (**a**) Different calcium carbide slag content; (**b**) Different fly ash content.

Figure 5a shows that the compressive strength of the specimens increased with the amount of calcium carbide slag and then decreased, and the strength reached its maximum at 10% calcium carbide slag and 15% fly ash (Sample 3). With the best curing effect, the unconfined compressive strength of the shield residue soil (Control Group 1) was 0.275 MPa at 7 days of maintenance. When 6% calcium carbide slag and 15% fly ash (Sample 1) were added, the unconfined compressive strength of the cured soil reached 1.280 MPa, an increase of 365% compared to Control Group 1, representing a significant increase in strength. The compressive strength increased from 1.280 MPa to 1.428 MPa when the dosing of the calcium carbide slag increased from 6% to 10%, reaching its maximum. When the dosing of calcium carbide slag continued to increase from 10% to 14%, the compressive strength of the cured soil gradually decreased to 1.197 MPa when 14% calcium carbide slag was incorporated, which was still an increase of 335% compared to Control Group 1. The unconfined compressive strength of Control Group 2 mixed with 5% ordinary Portland cement for 7 days was 1.710 MPa, and the curing effect was better than that of Sample 3. However, after 28 days of maintenance, the unconfined compressive strength of Sample 3 was 3.942 MPa, which was 1.37 times that of Control Group 2. This indicates that under certain conditions, the calcium carbide slag-fly ash curing of shield slag soil can achieve a better effect than that of cement.

Figure 5b shows that the compressive strength of the specimen increases with the increase in the fly ash admixture and then decreases, and it also reaches its maximum in Sample 3. The compressive strength of the cured soil increases significantly with the increase in curing age. The longer the age of maintenance, the greater the increase in the unconfined compressive strength of the specimens.

Short-term and long-term reactions of carbide slag-fly ash can occur in slag soil. The short-term reactions include dehydration, flocculation, and carbonization, while the long-term reactions are related to the formation of various gel compounds in the soil matrix [24]. The test results show that the greater the dosing of calcium carbide slag, the more significant the dewatering effect. This is due to the ability of the CaO in calcium carbide slag to undergo hydration to produce $Ca(OH)_2$, which provides strength to the mix after carbonization and precipitation. At the same time, $Ca(OH)_2$ can react with the active

SiO_2 and Al_2O_3 in fly ash in a volcanic ash reaction to produce gelling substances such as hydrated calcium silicate (C-S-H) and hydrated calcium silicate aluminate (C-A-S-H). These gelling substances enhance the skeleton's strength and fill the pore; the pores are reduced, resulting in lower porosity, which improves the mix gradation to some extent, resulting in greater inter-particle cohesion and increased mix strength. In addition, the increase in the inter-particle adhesion force causes the volume of flocculent gel agglomerates to become larger, further increasing the strength of the cured soil. The reaction process of volcanic ash is longer, less gelatinous material is generated in the early stage of the reaction, and the flocculent gel agglomeration process is slow. However, with increasing age, the volcanic ash reaction continues, prompting more and more gelatinous material to be generated and the flocculent gel agglomerates to become larger and larger, so the increase in strength after 14 to 28 days of maintenance is more significant than that after 7 to 14 days of maintenance. The early reaction rate of cement is faster than that of carbide slag-fly ash, and the compressive strength of Control Group 2 was the highest at 7 days of maintenance. However, as the reaction of the volcanic ash proceeded, the compressive strength of the test group increased more rapidly; the compressive strength of Sample 3 exceeded that of Control Group 2 at 14 days, and the compressive strength of all test groups exceeded that of Control Group 2 at 28 days.

With increasing amounts of calcium carbide slag, excessive calcium carbide slag particles absorb some of the water, making the hydration reaction process exhibit slow coagulation and inhibiting the volcanic ash reaction. Meanwhile, the excess calcium carbide slag affects the shield muck particle gradation, reducing the friction between the shield muck particles so that the unconfined compressive strength decreases. Figure 5b shows that by increasing the content of fly ash, more active SiO_2 and Al_2O_3 are added to the mixture, and they react in the mixture to form a silicon aluminum geopolymer gel, which improves the compressive strength of the solidified soil. However, the strength is reduced after too much fly ash is added, partly because there are few calcium-rich components in fly ash. The greater the amount of fly ash admixture, the lower the percentage of calcium content in the mixture, and the less C-S-H and C-A-S-H are formed by hydration, which directly affects the strength of the mixture. On the other hand, with the increase in fly ash content, more of the structurally stable sodium aluminosilicate (N-A-S-H) polymer is formed. Although it has good strength, it cannot function the same as bonding and polymerizing soil particles such as C-S-H and C-A-S-H, so too much fly ash is not conducive to improving the mixture's strength [25]. At the same time, the formation of the monomer in the geopolymer matrix depends entirely on the Si/Al ratio in the raw material. The Si/Al ratio is one of the most important factors affecting geotechnical synthesis. Ratios that are too high or too low significantly limit the formation of the polymer. The incorporation of excessive fly ash affects the Si/Al ratio of the mixture [26].

3.3. Characteristics of the Stress–Strain Curve Relationship

Figure 6a–c show the stress–strain curves of the specimens after 7, 14, and 28 days of maintenance with different doping levels of calcium carbide slag. The figures show that the stress–strain process exists in the pore fracture compacting stage, the elastic deformation to microplastic fracture stable development stage, the progressive rupture stage, and the post-rupture stage [27].

Comparing Figure 6a–c, it can be seen that the growth rate of each stress–strain stage of the specimens with different calcium carbide slag content is about the same at 7 and 14 days of curing, and the growth rate of each stage of the stress–strain of the specimens with different calcium carbide slag content appears significantly different at 28 days of curing. When the cured soil has a low maintenance age, the stress–strain curve reaches peak stress with relatively small, sudden drop changes. However, as the age increases, the peak stress of the cured soil increases, the stress–strain curve rises, and the sudden drop changes obviously; plasticity decreases and brittleness increases. It exhibits typical strain-softening characteristics. Soil structural damage accumulates, and it eventually breaks down.

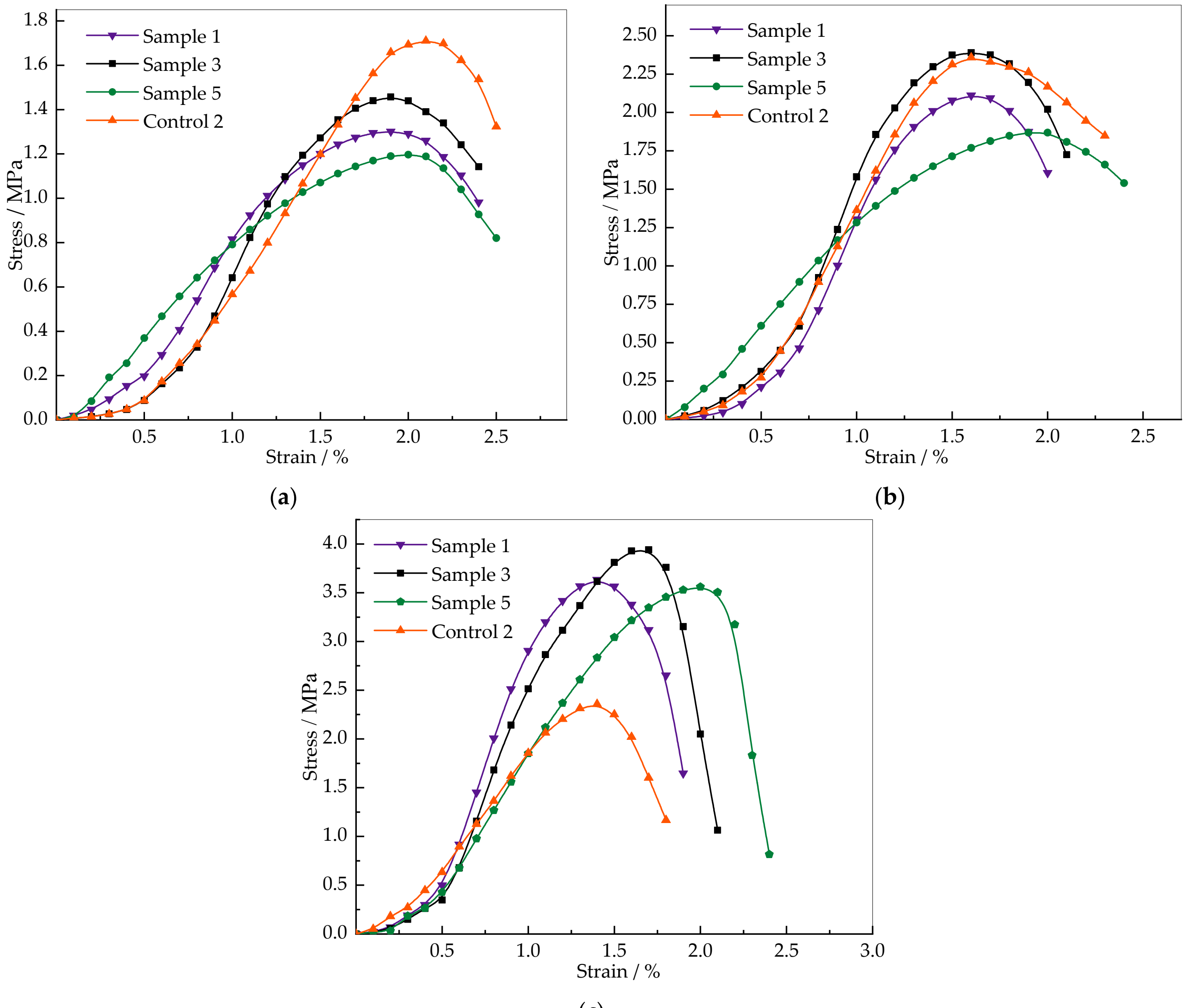

(**a**)

(**b**)

(**c**)

Figure 6. Stress-strain curves under different calcium carbide slag dosages: (**a**) 7 d; (**b**) 14 d; (**c**) 28 d.

The ultimate strain is the strain value corresponding to the peak stress on the stress–strain relationship curve, and its magnitude is an important indicator of a material's toughness and compression deformation [28]. Generally, the ultimate strains of the specimens at 7 days of curing were greater than those at 14 and 28 days of curing. The ultimate strains of soil cured with calcium carbide slag–fly ash were mainly distributed between 1% and 2.2%, which is similar to Tang's conclusion that the ultimate strains of cement-cured soil were mainly distributed between 1% and 2.5% [29–31].

The deformation modulus is the ratio of the compressive stress to the corresponding compressive strain under unconfined conditions, which reflects the ability of the material to resist elastic–plastic deformation. Therefore, E_{50} (the secant modulus corresponding to 50% of the peak stress, also known as the deformation coefficient) was chosen to characterize the deformation properties of the material.

The variation pattern of the E_{50} of soil cured under different amounts of the calcium carbide slag admixture and at different maintenance ages is shown in Figure 7. It can be seen that the deformation modulus E_{50} of the cured soil does not vary significantly with the amount of calcium carbide slag in the range of calcium carbide slag admixture selected for the test. However, the deformation modulus E_{50} increased significantly as the maintenance age increased. According to Chen [32] and Horpibulsuk [18], this is because the specimen reacted with the highly reactive SiO_2 in the fly ash and with Ca^{2+} in the calcium carbide slag, resulting in a filling effect and the generation of colloidal hydration products such as C-S-H. This reduces the soil pores and makes the soil structure denser and more stable. Thus, the deformation resistance of soil solidified with carbide slag-fly ash solidified soil is improved.

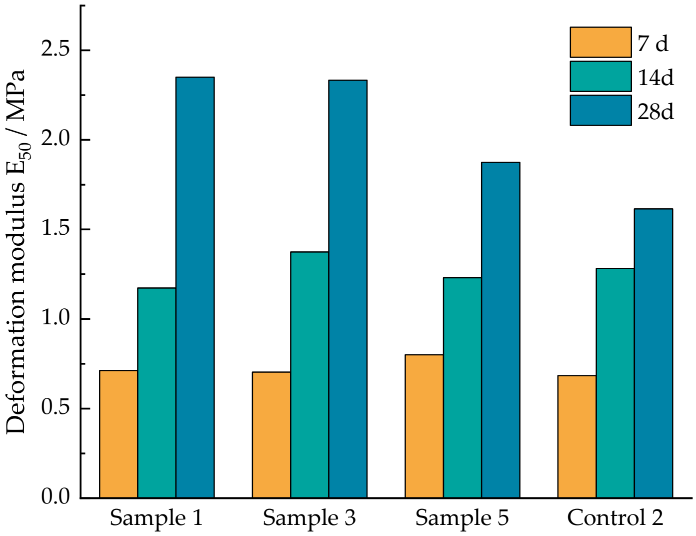

Figure 7. The change of deformation modulus E_{50} of specimen.

3.4. Effect of the Dry–Wet Cycle on Solidified Shield Muck

The lowest strength (Sample 9), the medium strength (Sample 1), and the highest strength (Sample 3) were selected for the dry–wet cycle test. It was found that the overall structure of the three specimens remained intact after five levels of dry–wet cycles, but there were different degrees of mass loss and damage to the specimens' surfaces after each level of dry–wet cycles. As shown in Figure 8, the surface of Sample 3 did not show obvious changes at the end of the dry–wet cycle. With the dry–wet cycle, the surface of Sample 1 gradually turned from relatively smooth to rough, producing small holes, and the holes in the specimen at the end of the three cycles were more obvious. The surface of Sample 9 produced a large number of pores and fine cracks at the end of three dry–wet cycles. After each dry–wet cycle, it was obvious that the powder shed from the specimen was suspended and precipitated in distilled water.

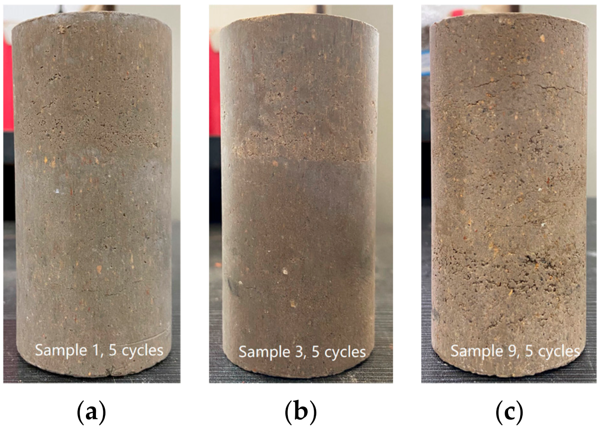

Figure 8. After the dry–wet cycle, the sample surface: (**a**) Sample 1, 5 cycles; (**b**) Sample 3, 5 cycles; (**c**) Sample 9, 5 cycles.

The effects of the number of dry–wet cycles on the specimen mass and unconfined compressive strength are shown in Figure 9. Figure 9a shows that the mass and strength of all three specimens decreased with the increase in the number of dry–wet cycles. Specifically, the specimen's mass decreased the most after the first dry–wet cycle, and, with continued dry–wet cycles, the specimen's mass loss gradually stabilized. The mass loss rates of Sample 1, Sample 3, and Sample 9 were 2.91%, 1.79%, and 3.52% after the end of 5 dry–wet cycles, respectively. In general, the rate and degree of mass reduction of Sample 3 were much smaller than those of the other specimens, and the rate and degree of mass reduction of Sample 9 were the largest. Figure 9b shows that the unconfined compressive strength of specimens decreased significantly after the first dry–wet cycle, and the continued dry–wet cycles had little effect on the strength of the specimens; the strengths of Sample 1, Sample 3, and Sample 9 after the first dry–wet cycle were 0.62, 0.67, and 0.69 of the strength of the specimens without dry–wet cycles, respectively. After 5 dry–wet cycles, the unconfined compressive strength of Sample 1 decreased from 3.632 MPa to 2.342 MPa; Sample 3's unconfined compressive strength decreased from 3.942 MPa to 2.826 MPa; and Sample 9's unconfined compressive strength decreased from 3.232 MPa to 1.793 MPa.

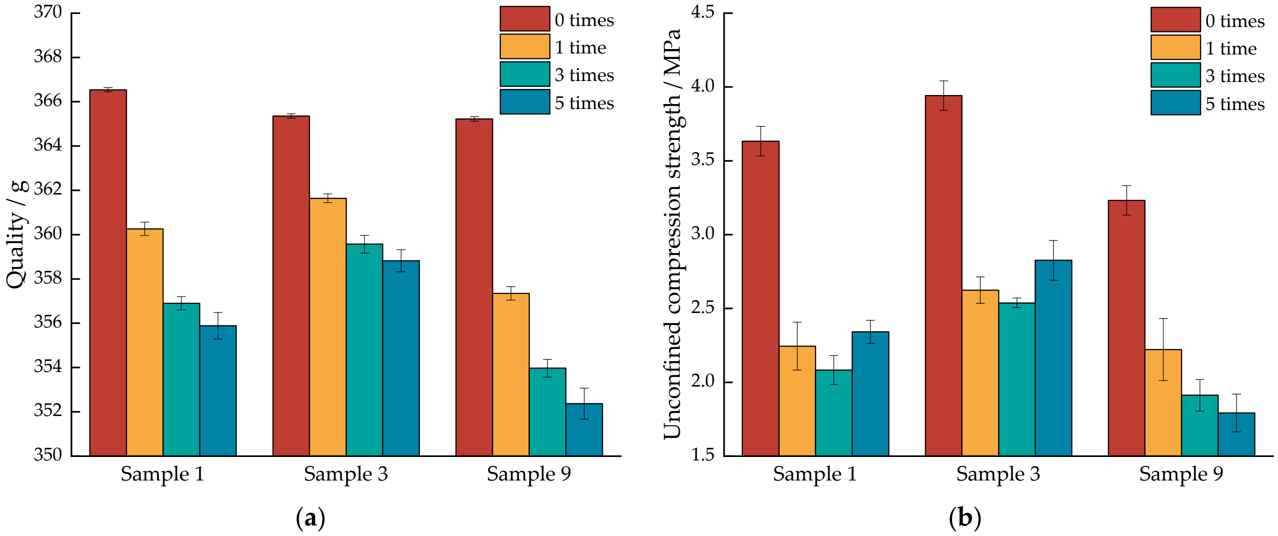

Figure 9. Quality and unconfined compressive strength vary with the number of dry–wet cycles, (**a**) Quality; (**b**) Unconfined compressive strength.

Regarding the reason for these findings, the dry–wet cycle, whereby the sample is repeatedly immersed in water, which is then evaporated, as well as the difference between the water content inside and outside the specimen, lead to the specimen's surface tensile stress. When the cementation between the specimen particles is insufficient to resist the tensile stress, holes appear on the specimen's surface. With the increase in the number of cycles, the holes further expand, the soil structure is damaged, and the strength decreases. It is worth noting that the unconfined compressive strength of Sample 1 and Sample 3 after five dry–wet cycles is higher than that after one dry–wet cycle; this is because the water that remains inside the specimen after immersion can promote a hydration reaction during the drying process, increasing the hydration products and improving the internal cementation capacity. The cementation produced between the particles in this process is sufficient to resist the tensile stress caused by the difference in moisture content inside and outside the specimen, and the strength then becomes higher than after the end of the first cycle. The water stability of shield muck cured with calcium carbide slag–fly ash is therefore better.

The stress–strain curves of the three specimens subjected to different numbers of dry–wet cycles are shown in Figure 10. The photos of the damage to the specimens after 28 days and 5 dry–wet cycles are shown in Figure 11.

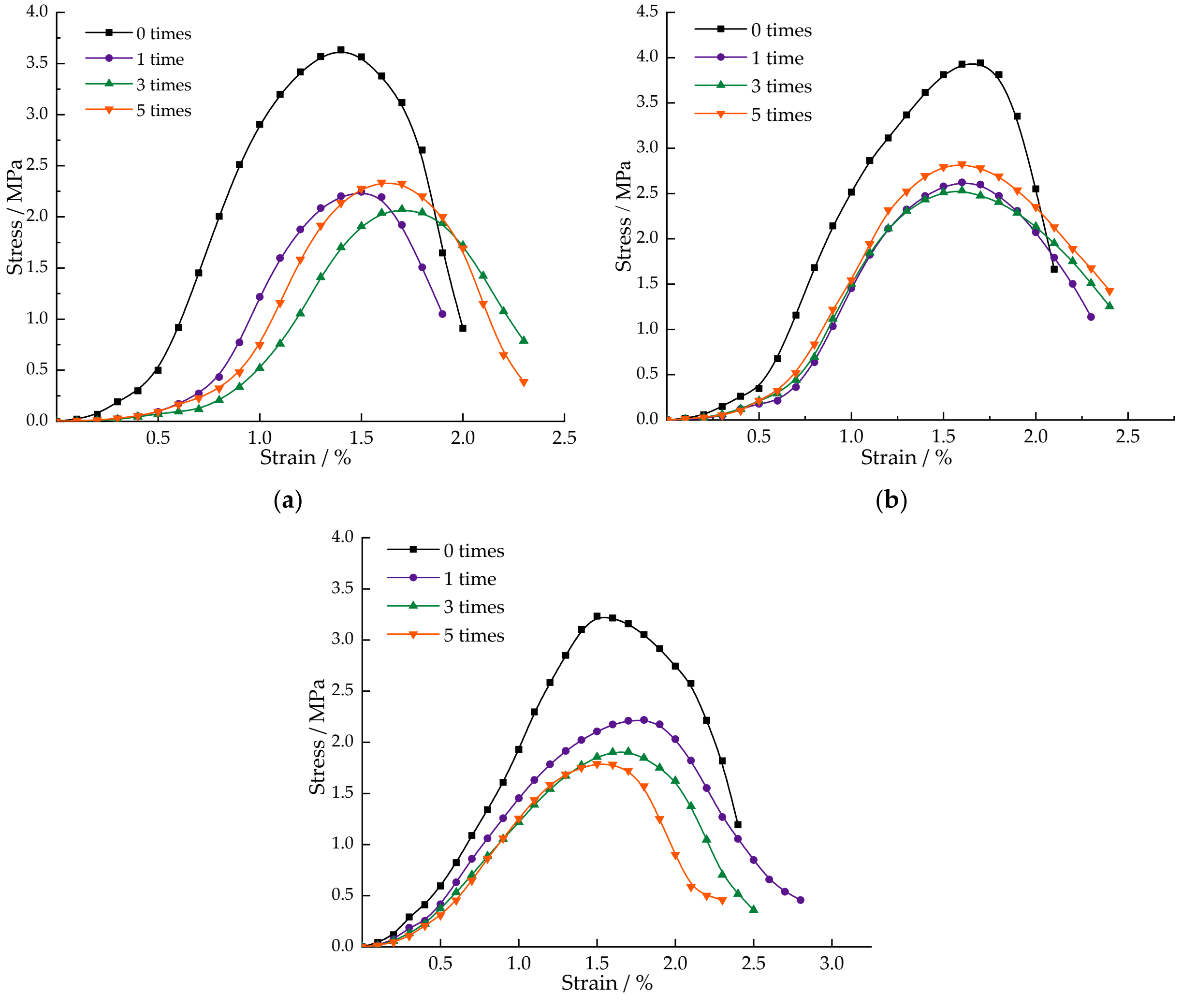

(**a**)

(**b**)

(**c**)

Figure 10. Stress-strain curve of the specimen under different dry–wet cycle times: (**a**) Sample 1; (**b**) Sample 3; (**c**) Sample 9.

Figure 10 shows that the ultimate strains of all three specimens were 1–2%. The more dry–wet cycles undergone by Sample 9, the lower its strength. Meanwhile, when maintained for 28 days, Sample 3 showed a rapid decrease in stress in the post-rupture phase; after dry–wet cycles, Sample 3 also showed a slower decrease in stress in the post-rupture phase, and the stress–strain curve after dry–wet cycles showed a strong plastic characteristic, which changed from strain hardening to strain softening. As shown in Figure 11a, the damage sustained by the specimens after 28 days of conditioning was mainly concentrated in the middle, forming through vertical (Sample 3) or oblique (Sample 1 and Sample 9) rupture surfaces. Moreover, after the dry–wet cycles, the damage was mainly situated at the ends of the samples, which were severely broken with a large amount of debris. Although vertical fractures were produced at the rupture surface of Sample 1 after the dry–wet cycles, the fractures did not penetrate the specimen (see Figure 11b), and, from a macroscopic point of view, the strength reduction of the specimen after the dry–wet cycles was mainly caused by the end being crushed first.

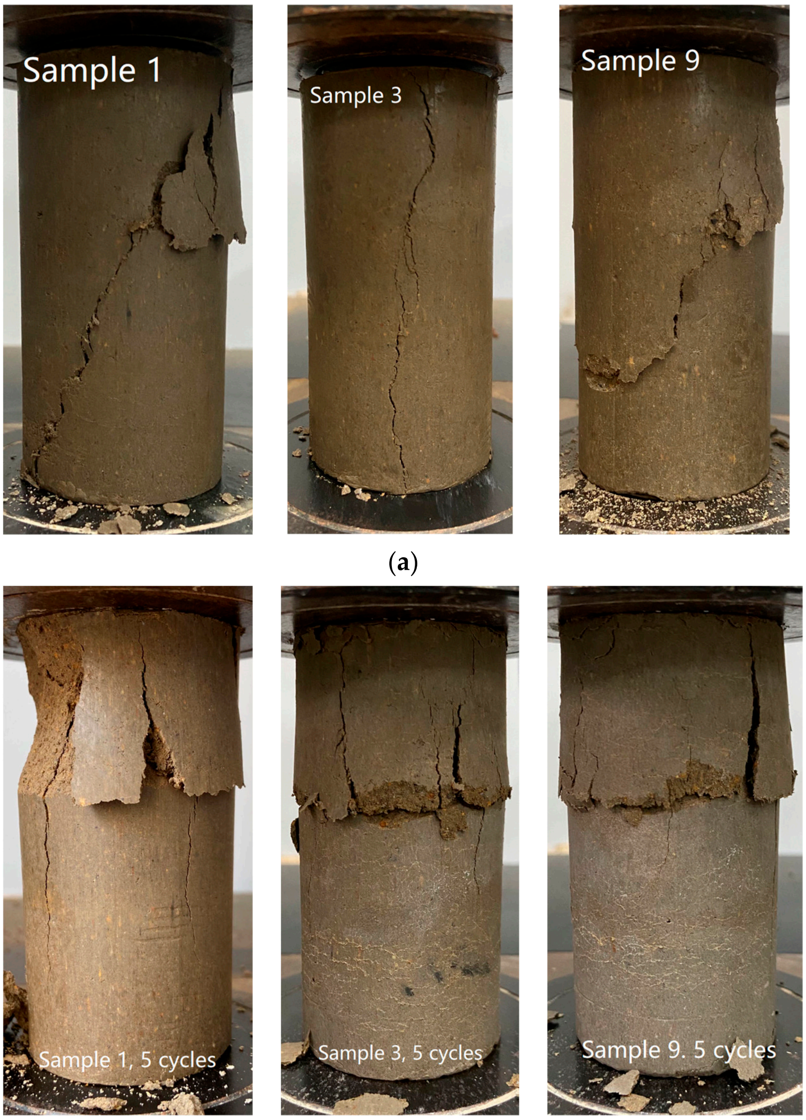

(**a**)

(**b**)

Figure 11. Photograph after specimen failure: (**a**) After 28 days of maintenance; (**b**) After dry–wet cycle.

4. Microscopic Test Results and Improvement Mechanism

4.1. X-ray Diffraction

Shield muck, calcium carbide slag, fly ash, cement, and representative specimens were selected for XRD analysis. The main components of each group of samples are shown in Figure 12. There is a $Ca(OH)_2$ diffraction peak in the carbide slag; there are SiO_2 diffraction peaks in the XRD pattern of fly ash; and aluminum silicate also exists in fly ash. The main minerals in cement are dicalcium silicate and tricalcium silicate. The XRD patterns of the cured soil specimens maintained for 28 days were compared with those of raw materials; a large number of diffraction peaks in the calcium carbide slag disappeared and $CaCO_3$ diffraction peaks appeared. In comparison with the XRD pattern of Control Group 2 and the raw materials, the diffraction peaks of dicalcium silicate and tricalcium silicate in cement disappeared, and $CaCO_3$ and SiS_2 diffraction peaks appeared. These substances react within the cured soil [32,33].

The XRD pattern shows that new crystalline phases appeared in Sample 1, Sample 3, and Control Group 2 at 28 days of maintenance, and $CaCO_3$ diffraction peaks appeared at 35.8° and 46.7° in Control Group 2, but these two $CaCO_3$ diffraction peaks disappeared in the soil cured with calcium carbide slag–fly ash. This is due to the reaction of the Ca^{2+} in the calcium carbide slag with the SiO_2 in the fly ash, resulting in a decrease in the $CaCO_3$ content. C-(A)-S-H diffraction peaks were observed at 38.5°, 46.3°, and 50.4° for Sample 3, confirming that these substances react to produce C-(A)-S-H.

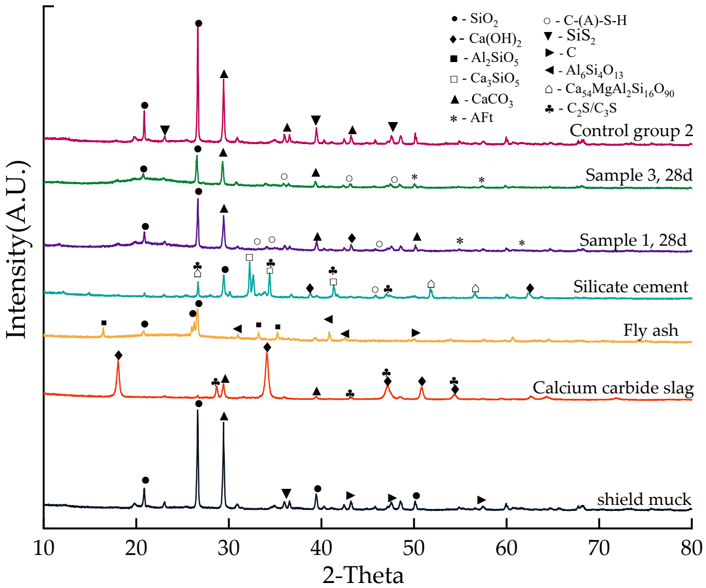

Figure 12. XRD diffraction comparison.

The results shown in Section 3.2 indicate that the higher compressive strength of the soil cured for 28 days with calcium carbide slag–fly ash at the optimum admixture is due to the generation of reaction products that can increase the strength of the specimens, such as hydrated calcium silicate, which is consistent with the test results and analysis presented in Sections 3.2 and 3.3 .

4.2. Scanning Electron Microscope

To further analyze the changes in the microstructure of the cured soil at different maintenance ages and different curing agent doses, the microstructure of the cured soil and the effect of the curing reaction on the pore structure were studied by scanning electron microscopy. The microstructure of the shield muck and Sample 3 at 7, 14, and 28 days with 2000 times magnification is shown in Figure 13.

Figure 13a, shows that the shield muck particles are mostly in face-to-face contact with each other. The mineral matrix is largely flat and continuous, and the flat particles are accumulated locally but are not dense. Many gaps exist between the particles. Sample 3 was maintained for 7 days with little generation of hydration products and uneven distribution. Figure 13e,f show the images of the same position shown in Figure 13a magnified 5000 and 10,000 times, respectively. The aggregation of needle-like and short columnar materials forming a similar net-like structure can be observed, which indicates the occurrence of a hydration reaction. At 14 days of curing, Sample 3 was much denser than at 7 days of curing, showing an obvious reticular structure. Figure 13d shows that many dense reticular C-(A)-S-H gels appear in the interstices of the soil particles and are connected to form a whole reticular gel. However, there are still a small number of pores in the reticular gel that are not completely connected, and the microstructure of the soil cured with calcium carbide slag–fly ash has changed significantly. This finding is consistent with the XRD test results, indicating the presence of C-(A)-S-H in the cured soil specimens.

The internal particles of the soil cured with calcium carbide slag–fly ash are all attached and cemented by the mesh-like C-(A)-S-H gel, and the soil particles are tightly polymerized by this action. The C-(A)-S-H gel, flaky AFm($3CaO{\cdot}Al_2O_3{\cdot}CaSO_2{\cdot}12H_2O$), and needle-rod AFt(Ettringite) bind and support the particle interstices, resulting in a significant reduction in the number and size of pores and a substantial increase in the soil's compactness and strength [34], as shown in Figure 14.

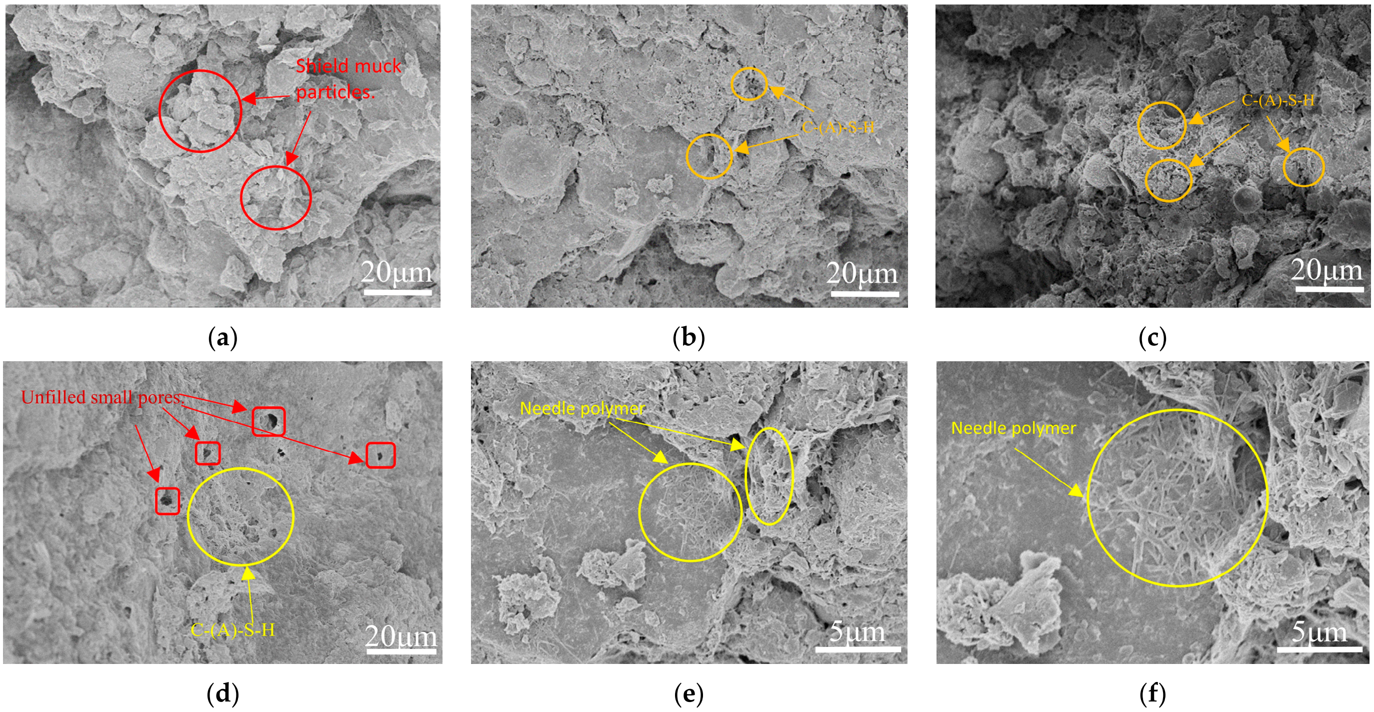

(**a**) (**b**) (**c**)

(**d**) (**e**) (**f**)

Figure 13. Microstructure of shield muck and sample 3: (**a**) Shield muck; (**b**) Sample 3, 7 days; (**c**) Sample 3, 14 days; (**d**) Sample 3, 28 days; (**e**) Sample 3, 7 days, 5000 times; (**f**) Sample 3, 7 days, 10,000 times.

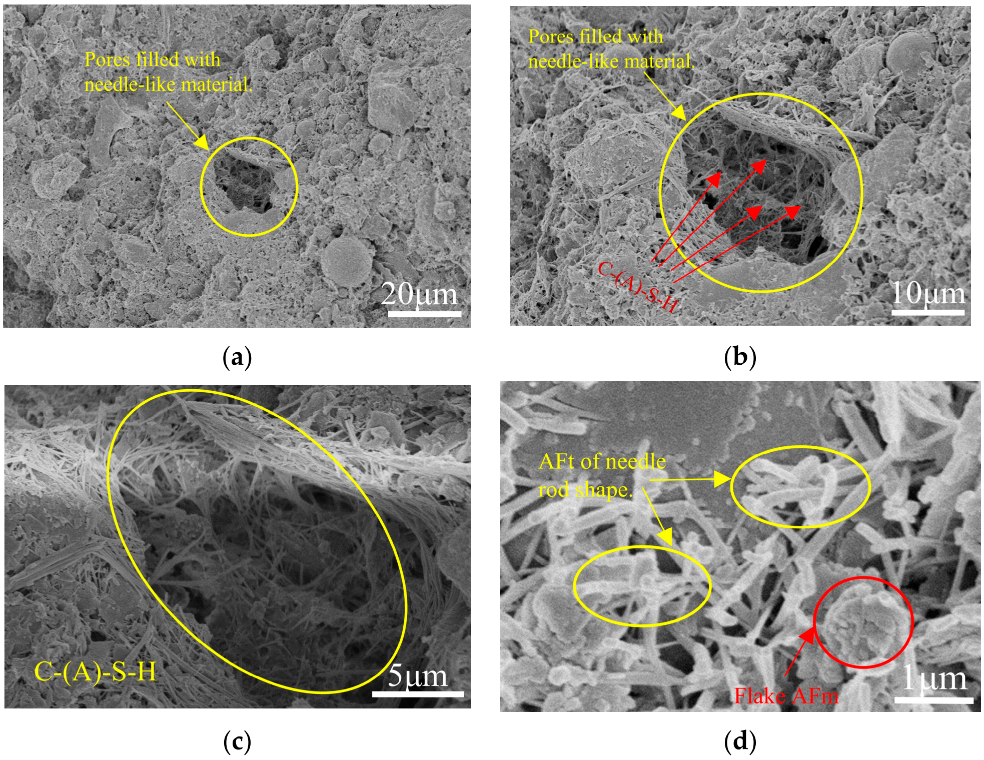

(**a**) (**b**)

(**c**) (**d**)

Figure 14. Internal cementation of pores: (**a**) Sample 3, 2000 times; (**b**) Sample 3, 5000 times; (**c**) Sample 3, 10,000 times; (**d**) AFt and AFm, 40,000 times.

The analysis based on the above microscopic tests shows that the main products ofthe reaction within the cured soil are gelled floccules, needles, and rod and mesh structures, which are favorable to the improvement of the strength of the cured soil samples. This finding is consistent with the strength test results shown in Sections 3.2 and 3.3.

4.3. Curing Mechanism Analysis

The results of the previous compaction test, strength test, XRD, and SEM tests were integrated, and it was found that the curing mechanism of the shield slag cured with calcium carbide slag–fly ash has three main manifestations: the hydration reaction, volcanic ash reaction, and ion exchange.

1. Hydration reaction: a large amount of the CaO in calcium carbide slag can react with water to generate $Ca(OH)_2$, and the generated $Ca(OH)_2$ can effectively fill the internal pores of the specimen. Meanwhile, dicalcium silicate and tricalcium silicate can react with water to generate C-S-H($3CaO\cdot 2SiO_2\cdot 3H_2O$) gel [35]. This is the hydration reaction.

$$3CaO\cdot SiO_2+3H_2O \rightarrow CaO\cdot SiO_2\cdot H_2O + 2Ca(OH)_2 \quad (1)$$

$$3CaO\cdot SiO_2+H_2O \rightarrow CaO\cdot 2SiO_2\cdot 3H_2O + Ca(OH)_2 \quad (2)$$

$$3CaO\cdot Al_2O_3+6H_2O \rightarrow 3CaO\cdot Al_2O_3\cdot 6H_2O \quad (3)$$

$$CaO + 2H_2O + SO_3 \rightarrow CaSO_4\cdot 2H_2O \quad (4)$$

$$3CaO\cdot Al_2O_3\cdot 6H_2O + 3(CaSO_4\cdot 2H_2O) + 6H_2O \rightarrow 3CaO\cdot Al_2O_3\cdot 3CaSO_4\cdot 32H_2O \quad (5)$$

2. Volcanic ash reaction: The main component of fly ash, SiO_2, further reacts with $Ca(OH)_2$, the hydration product of calcium carbide slag, to generate C-S-H($3CaO\cdot 2SiO_2\cdot 3H_2O$) gel; with the hydrolysis of SiO_2, C-A-S-H($CaO\cdot Al_2O_3\cdot 2SiO_2\cdot 6H_2O$) gel is gradually formed in the late maintenance period, which accelerates the hydration process of the mixture and thus improves the compressive strength of the cured soil.

$$SiO_2+Ca(OH)_2+H_2O \rightarrow C - S - H(gel) \quad (6)$$

$$SiO_2+Al_2SiO_5+Ca(OH)_2+H_2O \rightarrow C - A - S - H(gel) \quad (7)$$

3. Ion exchange reaction: the hydration reaction leads to the precipitation of OH^- ions, the OH^- concentration increases, and the Si^{2+} ions in the mixture react with OH^- and Ca^{2+} ions.

Through the above processes, the hydration products in the cured soil develop into a dense three-dimensional mesh structure through agglomeration, precipitation, and flocculation, so that the soil particles are glued to each other and gradually form a dense skeletal structure.

5. Conclusions

In this study, shield muck was cured with calcium carbide slag–fly ash, and the strength change law of the cured slag was investigated by an unconfined compression test, a dry–wet cycle test, X-ray diffraction, and an electron microscope scanning test under different calcium carbide slag and fly ash admixtures and maintenance ages. The curing mechanism was revealed by the microstructure evolution, and the main conclusions obtained are as follows:

(1) The compressive strength of the cured soil increases with the increase in the dosing of calcium carbide and fly ash, then decreases; it also increases with the increase in the curing age. For the shield slag soil used in this paper, the optimal doses of calcium carbide slag and fly ash are 10% and 15%, respectively, when the strength of the

cured soil is the highest. Under certain conditions, shield slag soil cured with calcium carbide slag–fly ash can achieve better results than cement. As the age increases, the peak stress of the specimen increases, the ultimate strain decreases, the stress–strain curve rises with an obvious change in the sudden drop, and the brittleness of the cured soil increases.

(2) The most significant effect of the first dry–wet cycle on the compressive strength of the specimens, compared with the specimens not subjected to a dry–wet cycle, was that the strength decreased by about a third; the strength of the samples subjected to subsequent dry–wet cycles remained unchanged. The shield slag soil cured with calcium carbide–fly ash exhibited good water stability. The ultimate strains of the 3 specimens that underwent dry–wet cycles were 1%~2%, and the rising and sudden falling trend of the stress–strain curve of the specimens became slower, showing stronger plasticity characteristics and the change from strain hardening to strain softening.

(3) Microscopic tests showed that with increasing age, gels, crystals, and precipitates gradually developed, agglomerated, and were cemented in the soil cured with calcium carbide slag–fly ash. The hydration products were well developed, needle and rod products increased significantly, a dense spatial mesh structure was formed, the soil integrity was improved, and the macroscopic expression showed improved mechanical strength.

(4) The reaction products mainly comprise hydrated calcium silicate polymeric colloid (C-S-H/C-A-S-H) and calcium alumina (AFt), which together support the inter-soil pores and form a skeletal structure that supports the inter-soil pores.

Author Contributions: Conceptualization, Y.F. and J.W.; methodology, Y.F. and J.W.; validation, Y.F. and J.W.; formal analysis, J.W.; investigation, J.W.; resources, Y.F.; data curation, J.W. and Y.F.; writing—original draft preparation, J.W.; writing—review and editing, Y.F. and X.X.; visualization, J.W. and F.Z.; supervision, Y.F. and F.Z.; project administration, J.W. and Y.F.; funding acquisition, Y.F. and X.X. All authors have read and agreed to the published version of the manuscript.

Funding: The authors are thankful for the financial support from the National Natural Science Foundation of China (No. 52108315), the National Science Foundation of Hubei Province of China (2021CFB286) and Hubei University of Technology Education Development Foundation.

Data Availability Statement: Data sharing is not applicable.

Acknowledgments: We wish to thank the anonymous referees for their careful reading and for providing insightful comments to improve the initial version of this paper. All individuals included in this section have consented to the acknowledgement.

Conflicts of Interest: The authors declare no conflict of interest.

References

1. Wang, S.Y.; Liu, P.F.; Hu, Q.X.; Huang, S.; Zhong, J.Z.; Liu, Z.R.; Yang, J.S. State-of-the-art on Theories and Technologies of Soil Conditioning for Shield Tunneling. *China J. Highw. Transp.* **2020**, *33*, 8–34.
2. Zhu, W.; Qian, Y.J.; Wang, L.; Wei, B.; Lu, K.J.; Fang, Z.K.; Meng, L.F. Classification, Treatment, and Utilization Techniques of Shield Tunnel Abandoned Soil and Related Issues. *Tunn. Constr.* **2021**, *41* (Suppl. S2), 1–13.
3. Xie, Y.P.; Zhang, C.; Yang, J.S.; Fu, J.Y.; Xiao, C.; Zhan, Y.J. Research and Prospect on Technology for Resource Recycling of Shield Tunnel Spoil. *Tunn. Constr.* **2022**, *42*, 188–207.
4. Li, W.T.; Ni, P.P.; Yi, Y.L. Comparison of reactive magnesia, quick lime, and ordinary Portland cement for stabilization/solidification of heavy metal-contaminated soils. *Sci. Total Environ.* **2019**, *671*, 741–753. [CrossRef] [PubMed]
5. He, L.; Wang, Z.; Gu, W.B. Evolution of freeze-thaw properties of cement-lime solidified contaminated soil. *Environ. Technol. Innov.* **2021**, *21*, 101189. [CrossRef]
6. Ahmed, A.; Issa, U.H. Stability of soft clay soil stabilised with recycled gypsum in a wet environment. *Soils Found.* **2014**, *54*, 405–416. [CrossRef]
7. Benhelal, E.; Zahedi, G.; Shamsaei, E.; Bahadori, A. Global strategies and potentials to curb CO_2 emissions in cement industry. *J. Clean. Prod.* **2013**, *51*, 142–161. [CrossRef]
8. Hussain, J.; Khan, A.; Zhou, K. The impact of natural resource depletion on energy use and CO_2 emission in Belt & Road Initiative countries: A cross-country analysis. *Energy* **2020**, *199*, 117409.

9. Noaman, M.F.; Khan, M.A.; Ali, K.; Hassan, A. A review on the effect of fly ash on the geotechnical properties and stability of soil. *Clean. Mater.* **2022**, *6*, 100151. [CrossRef]
10. Zhang, Y.J.; Wang, J.; Zhang, L.L.; Li, C.L.; Jiang, H.; Ba, X.Z.; Hou, D.S. Study on the preparation and properties of high-belite cementitious materials from shield slag and calcium carbide slag. *Constr. Build. Mater.* **2022**, *355*, 129082. [CrossRef]
11. Baskar, I.; Keerthana, K.; Sakthisri, K.; Sona, R. Effect of calcium carbide residue and fly ash in soil stabilization for sand mixed clayey soil. *Mater. Today Proc.* **2022**, *69*, 1253–1259. [CrossRef]
12. Xu, F.; Jiang, C.Z.; Zhang, S.J.; Yang, D.; Li, S.S. Experimental Study on Alkali Activated Slag Solidification of Earth Pressure Balance Shield Muck. *Chin. J. Undergr. Space Eng.* **2022**, *18*, 849–859.
13. Liu, Y.Y.; Chang, C.W.; Namdar, A.; She, Y.X.; Lin, C.H.; Yuan, X.; Yang, Q. Stabilization of expansive soil using cementing material from rice husk ash and calcium carbide residue. *Constr. Build. Mater.* **2019**, *221*, 1–11. [CrossRef]
14. Guo, Q.Y.; Li, B.Y.; Ding, J.W.; Chen, J.G.; Sun, S.; Ma, Y.L. Experimental study on the road performance of slurry shield tunnel residue improved by industrial waste residues. *J. Civ. Environ. Eng.* **2022**, *143*, 1–11.
15. *JTG 3430-2020*; Test Methods of Soils for Highway Engineering. Ministry of Transport of China: Beijing, China, 2020.
16. Cao, W.; Zhao, J.; Jiang, Z.Y.; Li, Y.Z.; Che, C. Reuse of Abandoned Shield Residues Stabilized by a Sustainable Binder: Assessment of Strength, Durability, and Environmental Properties. *Buildings* **2023**, *13*, 738. [CrossRef]
17. Ayodele, F.O.; Fajimi, M.S.; Alo, B.A. Stabilization of tropical soil using calcium carbide residue and rice husk ash. *Mater. Today Proc.* **2022**, *60*, 216–222. [CrossRef]
18. Horpibulsuk, S.; Phetchuay, C.; Chinkulkijniwat, A.; Cholaphatsorn, A. Strength development in silty clay stabilized with calcium carbide residue and fly ash. *Soils Found.* **2013**, *53*, 477–486. [CrossRef]
19. Latifi, N.; Meehan, C.L. Strengthening of Montmorillonite and Kaolinitic Clays with Calcium Carbide Residue: A Sustainable Additive for Soil Stabilization. In Proceedings of the Geotechnical Frontiers 2017, Orlando, FL, USA, 15 December 2017.
20. Ren, Y.W.; Cai, Y.X.; Liu, F.T. Experimental Study on Properties of Calcium Carbide Slag and Fly Ash Stabilized Coal Gangue Base Mixture. *Highw. Eng.* **2023**, *48*, 74–78+97.
21. Liang, S.H.; Zeng, W.H. Experimental Study of Nansha Silt Soil Reinforced with Cement and Fly Ash during Wetting-Drying Cycles. *Ind. Constr.* **2018**, *48*, 83–86+43.
22. Li, P.L.; Bi, J.Y.; Pei, Y.; Zhu, D.J. Analysis of Performance Improvement of Carbide Slag Stabilized Loess by Adding Fly Ash. *Highw. Eng.* **2022**, *47*, 146–152.
23. Cheng, Z.; Cui, G.H.; Gao, Y.H.; Gang, H.H.; Gao, Z.L.; Yang, Z.; Zhang, X. Mechanical Properties of Fly Ash Reinforced Subgrade Soil in Seasonally Frozen Area. *Bull. Chin. Ceram. Soc.* **2021**, *40*, 3854–3864,3875.
24. He, J.; Shi, X.K.; Li, Z.X.; Zhang, L.; Feng, X.Y.; Zhou, L.R. Strength properties of dredged soil at high water content treated with soda residue, carbide slag, and ground granulated blast furnace slag. *Constr. Build. Mater.* **2020**, *242*, 118126. [CrossRef]
25. Palomo, A.; Grutzeck, M.W.; Blanco, M.T. Alkali-activated fly ashes: A cement for the future. *Cem. Concr. Res.* **1999**, *29*, 1323–1329. [CrossRef]
26. Zhang, J.J.; Li, B.; Yu, C.; Zhang, M.Y. Mechanical properties of slag-fly ash based geopolymer stabilized sandy soil. *Rock Soil Mech.* **2022**, *43*, 2421–2430.
27. Zhao, H.; Xie, Y.J.; Long, G.C.; Li, N.; Zhang, J.W.; Cheng, Z.Q. Mechanical Characteristics and Stress and Strain Analysis of Concrete with Bonding Interface Under Impact Load. *J. Shanghai Jiaotong Univ.* **2022**, *56*, 1208–1217.
28. Li, L.H.; Han, Q.P.; Yang, X.; Xiao, H.L.; Li, W.T.; Huang, S.P. Mechanical properties and micro-mechanisms of RHA-cement solidified sludge. *China Civ. Eng. J.* **2022**. [CrossRef]
29. Li, L.H.; Zhang, H.Q.; Xiao, H.L.; Pei, Y.Y.; Wang, J.Z. Mechanical and microscopic properties of alkali-activated fly-ash-stabilised construction and demolition waste. *Eur. J. Environ. Civ. Eng.* **2020**, *27*, 2661–2677. [CrossRef]
30. Liang, R.W.; Zhang, M.; Bai, X.H. Analysis of laboratory test results of cemented soil. *Rock Soil Mech.* **2001**, *22*, 211–213.
31. Kun, D.; Bian, X.Y.; Chen, J.L.; Bai, J.L. Experimental investigation on clay stabilized by cement and waste brick fine aggregate. *Chin. J. Geotech. Eng.* **2021**, *43* (Suppl. S2), 174–177.
32. Chen, I.A.; Juenger, M.C.G. Incorporation of coal combustion residuals into calcium sulfoaluminate-belite cement clinkers. *Cem. Concr. Compos.* **2012**, *34*, 893–902. [CrossRef]
33. Bhagath Singh, G.V.P.; Subramaniam, K.V.L. Quantitative XRD study of amorphous phase in alkali activated low calcium siliceous fly ash. *Constr. Build. Mater.* **2016**, *124*, 139–147. [CrossRef]
34. Wei, G.Q.; Dong, B.Q.; Fang, G.H.; Wang, Y.S. Understanding reactive amorphous phases of fly ash through the acidolysis. *Cem. Concr. Compos.* **2023**, *140*, 105102. [CrossRef]
35. Su, Y.H.; Luo, B.; Luo, Z.D.; Xu, F.; Huang, H.; Long, Z.W.; Shen, C.P. Mechanical characteristics and solidification mechanism of slag/fly ash-based geopolymer and cement solidified organic clay: A comparative study. *J. Build. Eng.* **2023**, *71*, 106459. [CrossRef]

buildings

Article

Production of Large-Sized Ceramic Stones Based on Screenings from Waste Heap Processing Using the Technology of Stiff Extrusion for Molding Products

Khungianos Yavruyan * and Evgeniy Gaishun

Faculty "Engineering and Construction", Don State Technical University, 344003 Rostov-on-Don, Russia
* Correspondence: khungianos@mail.ru

Abstract: This article discusses the prospects for using large-format ceramic stones in the construction of contemporary homes, as well as an overview of raw materials and technologies for production. The most promising technology is stiff extrusion with the ability to load the raw products on firing trolleys and accelerate the processes of firing and drying. Characteristics of Eastern Donbass waste heaps processing screenings are given, which are coal mining by-products and are considered to be main raw material for the production of large-sized ceramic stone. It is shown that as a result of introduction of waste heaps into the production of ceramic stones with the lowest prime cost, the density of the resulting products will be less than 800 kg/m^3, the thermal conductivity will be less than 0.20 m·°C/W, and the strength grade will be M150 and higher. Thus, the use of ceramic stones in total volume of wall products for residential construction will reach the level of 80% and will increase the competitiveness of the material, especially when compared with gas silicate products, as used in Western Europe. High economic feasibility of the production of such materials based on by-products of waste heap processing is shown as well.

Keywords: ceramic block; screening; siltstone; coal; coal sludge; stiff technology; density; strength; water absorption

1. Introduction

At the beginning of this century, there was an intensive construction of new enterprises engaged in the manufacture of large-sized highly porous ceramic stones in the industry of wall ceramic materials. In Russian civil engineering, ceramic bricks with a lower density and thermal conductivity replaced concrete wall structures, but in Western Europe this happened in the 1980s and 1990s. An objective comparison of ceramic blocks with analogues in the use of structures and all stages of construction will justify this trend. Ceramic stones account for about 80% of the total volume of wall products used for housing construction in Western Europe. As for the Russian construction industry, this figure is significantly lower. The main factor in this case is the cost, which, when compared with gas silicate products, is slightly higher [1,2]. This is often the primary reason for builders, when evaluating only the construction itself without considering the long-term operation of the building [3–8].

In recent years, the most popular products in civil engineering appeared to be highly efficient ceramic blocks, which are classified as ceramic stones based on GOST 530-2012. The demand for ceramic blocks is explained by their properties: average density should be less than 800 kg/m^3, calculated thermal conductivity—less than 0.20 W/m·°C, high frost resistance, and a fairly high strength grade—M75 and higher, which allows them to be used for connecting load-bearing structures. The advantage of blocks is their size. The most popular are blocks with a length of 380 mm and 510 mm, a width of 250 mm, and thickness of 229 mm. In terms of ordinary bricks, this is 10.7 and 14.3 pieces of products.

A wall made of such blocks with a facing-in half a brick fully meets the requirements for thermal performance.

There are no factories for the production of ceramic blocks in the Rostov region, although the minimum requirement for the city of Rostov-on-Don alone is about 50 million pieces in terms of ordinary bricks. The region covers the need for blocks with deliveries from the Krasnodar Territory (Slavyansk-on-Kuban), Volgograd, Kabardino-Balkaria (Prokhladny). An important point for ceramic blocks to successfully compete with gas silicate blocks should be their cost—it should not exceed 3000 rubles per 1 m^3. This is in terms of an ordinary brick no more than six rubles apiece. The cost of freight transportation has recently risen significantly, which is why it is necessary to create a place for the manufacture of ceramic stones with lower cost products in the Rostov region. The implementation of this is possible only if the following cost conditions are reduced: technological operations, raw materials, firing, and the construction of new plants or improvement of old plants.

For many years VNIIStrom of P. P. Budnikova, JSC have been engaged in the technology of processing and using technogenic wastes of the coal series with different contents of the combustible component. Based on its mineral content it has been used as either the main raw material or as an additive. It has been established that when the content of the combustible component is 5–6%, coal waste can be used as the main raw material [9,10].

The Spanish company "Agemac" uses coal waste in the production of ceramic facing bricks. Products with increased strength characteristics were obtained (compressive strength 45 MPa). Fuel consumption during firing was reduced by 50% [11].

The French company "Ceric" has developed technology and equipment for the production of stiff molded bricks from coal waste [12].

The purpose of the research is to scientifically substantiate the feasibility of manufacturing reduced-density large-format ceramic blocks from by-products of waste heap (coal dumps) processing using stiff extrusion technology.

The novelty of the work is the scientific substantiation of production of ceramic stones from by-products of waste heap processing using technology of stiff extrusion.

2. Materials and Methods

A technological development with a goal of ceramic block production has recently taken place at Don State Technical University. It was conducted based on raw materials made from by-products of waste heap processing in Eastern Donbass, in order to achieve high profitability and minimize production costs.

Due to the economic aspect, screenings of waste heap disposal are considered to be extremely appealing raw material for the manufacture of wall ceramics and other products. They are obtained as a result of processing waste heaps during coal mining. During the processing other materials also appear, which are separated according to grain composition, the amount of coal component, and the mineralogical and petrographic composition [13,14].

Screenings are materials with medium grain size varying from 2–5 mm and are represented in the Eastern Donbass by siltstones mixed with mudstones. They do not contain more than 1% of coal. Therefore, they are the least of all in demand after waste heap processing. Coarse-grained materials with a grain size of more than 5 mm are widely used in industrial civil and road construction, and fine-grained material with a grain size of less than 2 mm serves as low-calorie fuel when screenings are already less in demand. They cost almost nothing, and factories have to spend money to store them. In relation to the prerequisites indicated earlier, we have performed a number of studies on the production of large-sized ceramic stones from screenings with reduced thermal conductivity and density.

Investigation of waste heap processing screenings to establish the possibility of producing ceramic blocks on their basis were carried out according to the following scheme:

- Determination of structural features, chemical and mineralogical composition;
- Study of pre-fired ceramic properties using plastic and compression-molding methods in relation to plastic and low-plastic stone-like raw materials;
- Study of firing ceramic properties;

- Selection of raw materials with testing of laboratory samples;
- Characteristics of finished products, establishing relationships, determining the influence of various technological factors on them;
- Development of primary technological production schemes.

Screenings from waste heap processing in the Eastern Donbass region do not practically differ from clay raw materials in terms of chemical composition (Table 1). They contain almost the same amount of silicon and aluminum oxides as semi-acidic clay raw materials. Iron oxide makes up the same proportion as it does in the composition of each dark-burning clay raw material. Due to the presence of potassium feldspars and feldspars with a predominance of potassium oxide, the presence of alkali oxides is almost the same as in refractory and low-melting clay raw materials.

Table 1. The average chemical composition of waste heap processing screenings excluding the coal content.

Loss on Ignition	SiO_2	Al_2O_3	Fe_2O_3	CaO	MgO	SO_3	K_2O	Na_2O
3.2–6.3	56.5–64.8	17.0–22.2	3.1–6.3	1.1–3.3	0.5–2.1	0.4–1.0	2.1–4.6	0.8–2.0

Screening minerals are represented by feldspars, quartz, micas and hydromicas. Albite and orthoclase make up the majority of feldspar. Pelletization and chloritization are two significant secondary alterations that they are susceptible to. Secondary ferrous minerals (oxides and hydroxides) are also present. A grain from screening is shown on an electron micrograph (Figure 1), where the sizes of the components can be clearly seen. Figure 2 shows X-ray diagrams of common screenings of waste heap processing from different companies of eastern Donbass.

Figure 1. Micrograph of a grain from screening from Pyramid LLC (Rostov region, Russia).

Diffraction peaks of around 10 and 5 Å can be used to identify hydromicas (illite) and micas. Peaks of diffraction for feldspar and plagioclase are 3.20, 4.04, and 2.96 Å. Quartz has good crystallinity, evidently apparent by the diffraction peaks at 4.25; 3.34; 2.45; 2.28; 2.12; 1.82 and 1.54 Å. Chlorite and kaolinite group minerals—at peaks of 7.12; 3.53; 14.2; 4.68, 2.33 Å, etc. It should be noted that all minerals are in close proximity to one another and appear to be joined by a mass of siliceous and ferrous cementing mass. Siltstones typically have a water absorption of 1–2% and a porosity of 3–5%. Compressive strength varies on average from 10 to 40 MPa.

The complete absence, or small amount, of clay minerals is the main difference between screenings and clays. Because of this, if the screenings contain argillite-like clays or mudstones they are of low plasticity or completely devoid of this property, even when being crushed. Despite the fact that fired samples based on screenings sinter well and with a rather high strength index, it is impossible to form products using extrusion technology. As a result, we noticed their poor formability. The firing temperature and the degree of grinding of screenings are the main factors that affect the characteristics of fired samples.

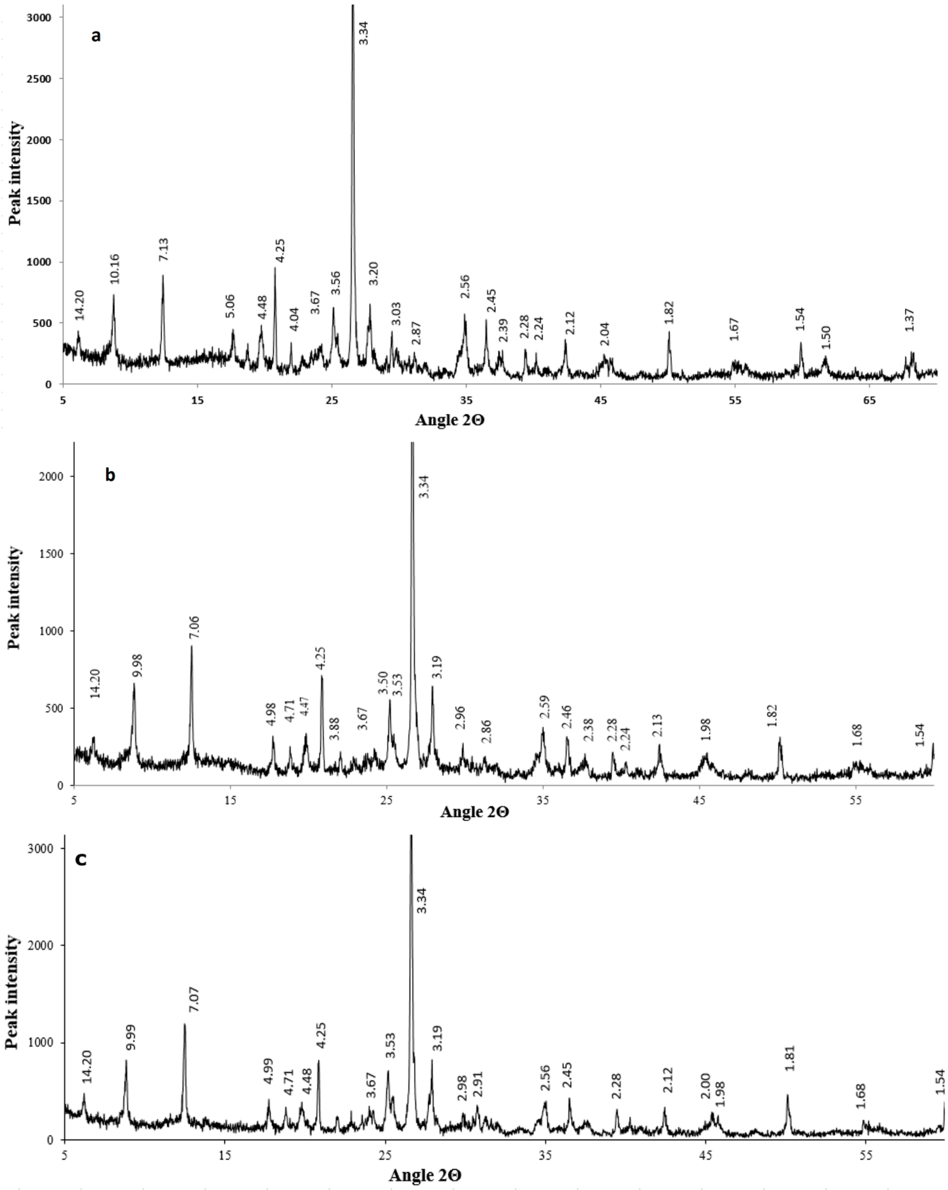

Figure 2. X-ray diagrams of common screenings of waste heap processing of different companies of Eastern Donbass. Rostov region, Russia: (**a**) Coal technologies LLC, (**b**) Sulinugol LLC, (**c**) Piramida LLC.

In order to optimize the composition of the raw charge, plastic clays were introduced into the mixture. Siliceous clays were chosen as a plasticizing additive. They have medium plasticity and medium dispersibility properties (47–53% filling below 1 micron) and are commonly used in the southern part of Russia.

Amongst significant tasks are the reduction of product costs and the cost of firing, which can reach up to 25%. The above prerequisites confirm that the introduction of finely dispersed products of waste heap processing into the composition of raw material mixtures can be called predominantly optimal. Initially, they appear in the form of a pulp from the technological cycle and dehydrate naturally later, which is why in most cases they are called coal sludge. The coal content in them is usually 30–50%. Most often, the mineral part is represented by mudstones, because they are moderately plastic. This property is present due to low strength and transitions to fine fractions during technological processing (crushing, screening, moisturizing). In our case, coal sludge performs three main functions in ceramic masses, acting as additives:

- Pore-forming, reducing the thermal conductivity and density of products;
- Plasticizing, known as "technological lubricant" because the external friction created during molding items is greatly reduced by finely dispersed coal particles;
- Fuel-like, leading to a significant reduction in the use of external fuel for firing (gas), or its complete reduction in use.

It should be emphasized that the cost of a calorie of heat from coal sludge, when compared with gas or pure coal, is 15–20 times lower. However, it should be taken into account that for firing wall products the coal content should not exceed 8–10% in the composition of the ceramic mass, otherwise more heat will be released than is necessary during firing [15–22].

Standard methods for testing samples were used in accordance with Russian GOSTs in order to provide a comprehensive study of the physical and mechanical properties and structure of ceramic materials based on the products of waste heap processing.

The chemical compositions of PPT and fired samples were determined in accordance with the requirements of GOST 21216-2014 "Clay raw materials. Methods of testing".

Laboratory and technological samples of PPT weighing 50–100 kg were taken in specific areas of their accumulation, storage, and processing. They were then formed from samples that did not contain plant, soil, or foreign inclusions. Basic samples of raw materials were preliminarily dried to an air-dry state if necessary, were crushed in a laboratory jaw crusher, and fractionated according to grain composition.

Using the compression test method, after grinding the raw material was moistened to the required molding moisture content and aged under conditions excluding drying of the mass for 24–48 h. Next, molding of standard samples was carried out: cubes with dimensions of 50 × 50 × 50 mm, bricks with dimensions of 67 × 30 × 15 mm and beams with dimensions of 135 × 30 × 15 mm and 160 × 40 × 40 mm. For control tests, brick samples of standard sizes with dimensions of 250 × 120 × 65 mm and 200 × 100 × 50 mm were made. The pressing pressure ranged from 10 to 50 MPa. The density in terms of the solid phase was determined by the calculation and control of dry samples.

Freshly molded samples were kept under natural conditions for a day in the absence of drafts, and then dried in a desiccator for 24 h at a maximum temperature of 90 ± 5 °C. After drying, the samples were examined with fixation of all changes in appearance, and air shrinkage was determined as well. Firing was carried out in laboratory electric furnaces with a chamber volume of 50–200 L, with automatic control of the firing mode with an average temperature rise rate of 1–3 °C/min, and exposure at a maximum temperature of 900–1150 °C for 1.5–2 h.

The reliability of the results obtained in the course of research was ensured by control using statistical methods. The data obtained obey the law of normal distribution of random errors.

When processing the obtained results, the confidence interval (with a confidence probability equal to 0.95) and the standard deviation were determined.

3. Results

The results of our previous studies [18–21] showed that the most appropriate materials for production of large-sized ceramic stones were medium-grained materials of waste heap processing and fine-grained materials—coal sludge. The first are the basic raw materials. Their secondary grinding to a fraction of less than 0.3–0.6 mm is the main technological operation. It is the degree of their grinding that largely determines the strength of the samples after firing. Figures 3 and 4 show how the degree of screen grinding and the firing temperature affect the compressive strength and water absorption of fired samples. It can be seen from the graphs that a fraction size of 0–0.315 and 0–0.63 mm guarantees the strength characteristics of products, taking into account their porosity up to 50% at firing temperatures of 950–1050 °C [22–30].

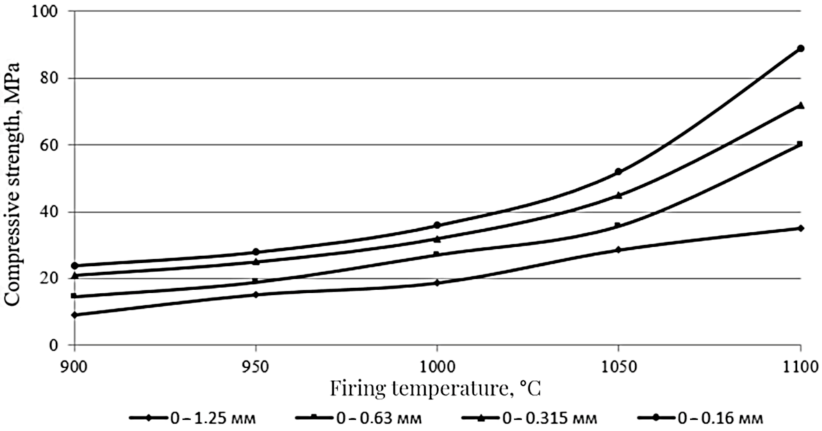

Figure 3. Dependence of the compressive strength of samples on firing temperature and degree of screening grinding.

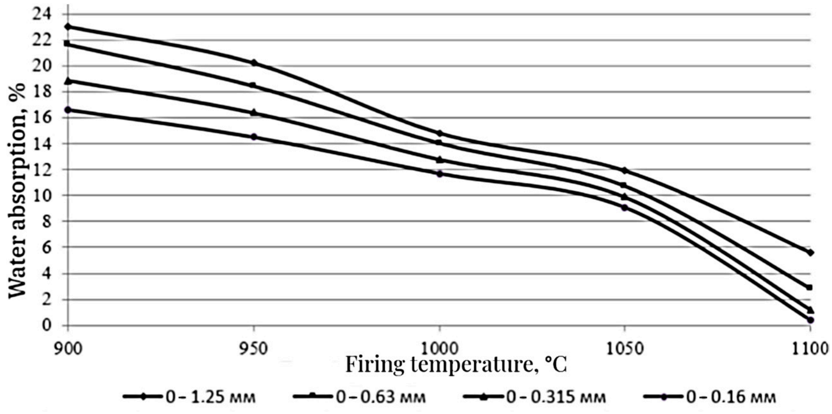

Figure 4. Dependence of water absorption of samples on firing temperature and degree of screening grinding.

Based on our previously conducted tests on the selection of the optimal composition of ceramic mass, it was established to take 60% of waste heap processing screenings, 25% of siliceous clay, and 15% of coal sludge. At the same time, the most suitable degree of screening grinding appeared to be from 0 to 0.315 mm and firing temperature—1000 °C.

Fine-grained materials obtained in the process of waste heap processing are a combined additive. They provide the necessary plasticity and cohesion of the raw mixture already at a content of 15–20%, and they are also a fuel-burning additive. This allows for a reduction in the density of the ceramic shard and a large decrease in the amount of gas required for firing.

However, the amount of coal sludge should not exceed 22% when the content of coal in the sludge is around 35%, so the amount of fuel introduced with the raw materials should not exceed 80%. At these ratios, the mass's plasticity only reaches 7–8 units, which is insufficient for the extrusion molding of products. For this reason, coal sludge has already been chosen as a combination additive. It also serves as a fuel-burning additive, which can reduce the density of ceramic shards and significantly reduce gas consumption for firing. Its cost per calorie of released heat is 15–20 times lower (200–400 rubles per ton) than that of gas and clean coal (7000–9000 rubles per ton).

Coal particle combustion during firing contributes to the formation of a porous structure of the ceramic material, which significantly reduces the density and thermal conductivity of products. However, the strength of the products decreases at the same time.

Therefore, determining the optimal amount of introduced sludge is quite a complicated technological task. The dependence of compressive strength of samples with 22% of coal sludge on firing temperatures of screenings with fractions of 0–0.63 and 0–0.315 mm is represented on Figure 5.

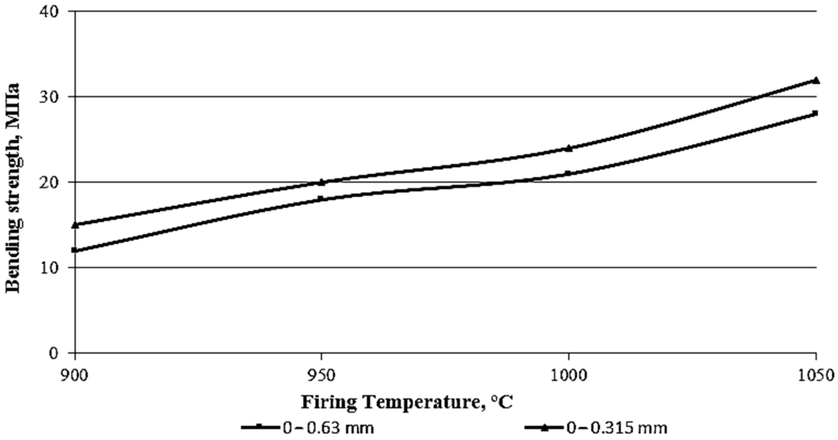

Figure 5. The dependence of compressive strength of samples with 22% of coal sludge on firing temperatures of screenings with fractions of 0–0.63 and 0–0.315 mm.

It can be seen that at 22% of coal sludge content in the raw mixture, the strength of samples is great enough to obtain highly effective large-sized ceramic blocks with 50% porosity and a strength grade of at least M100. The firing temperature should be between 950–1050 °C, depending on the desired strength. It should be noted that given the strength of the ceramic material itself, it is possible to improve the porosity of goods. Currently produced large-sized ceramic blocks with vertically arranged voids obtain porosity up to 60%, with the horizontally arranged voids up to 70%, however, their strength indicators are significantly lower.

Fuel can comprise up to 80% of the raw mixture composition. In terms of products, this means that up to 8–10% of pure coal can be contained in the dry raw material. Considering that, on average, the coal content in coal sludge is about 30%, then, accordingly, their content in the raw mixture can be up to 25–30%. The burning of coal particles during firing contributes to the formation of a finely porous structure of the shard, which can significantly reduce the thermal conductivity of products. However, along with this, the introduction of sludge contributes to a decrease in the strength of products and it is quite a difficult task to determine the optimal sludge content, taking into account all the necessary technological parameters. The density of the shard is 1500–1600 kg/m^3. Taking into account the stone porosity, the average density of products will be 750–800 kg/m^3. At the same time, there is a margin of safety of the shard to increase the porosity and reduce the density of products. Currently produced ceramic blocks with a vertical arrangement of voids have a porosity of about 60%, with a horizontal arrangement of voids up to 70%. However, the latter can only be used for building enclosed structures.

Our research in this area has contributed to the development of a concept that is especially pertinent for coal-mining and residing regions: the creation of large-sized porous ceramic stones using stiff extrusion technology and waste heap screens.

Stiff extrusion technology is the leader in most countries and is now regarded as the most progressive in the manufacture of ceramic wall goods. It appeared due to the introduction of powerful extruders that can mold raw products at a reduced humidity and under pressure of more than 2.5 MPa in the press head. Due to this, the molded raw products are endowed with strength, which contributes to their laying on kiln trolleys without being fully dry, which significantly reduces the cost of drying and delivery of raw material. If an operation such as transferring raw material from drying to firing trolleys is ignored, then it will be possible to significantly reduce technological costs, the number of machines, and to simplify the technological scheme. Capitalization for the construction of the newest brick shops and factories using the stiff extrusion technology is 30–35% less than when building shops using the ordinary plastic extrusion method, and less industrial space is also needed.

The technology for the production of large-format ceramic blocks from waste heap processing without auxiliary transportation equipment, using the technology of stiff extrusion for molding products, is shown in Figure 6.

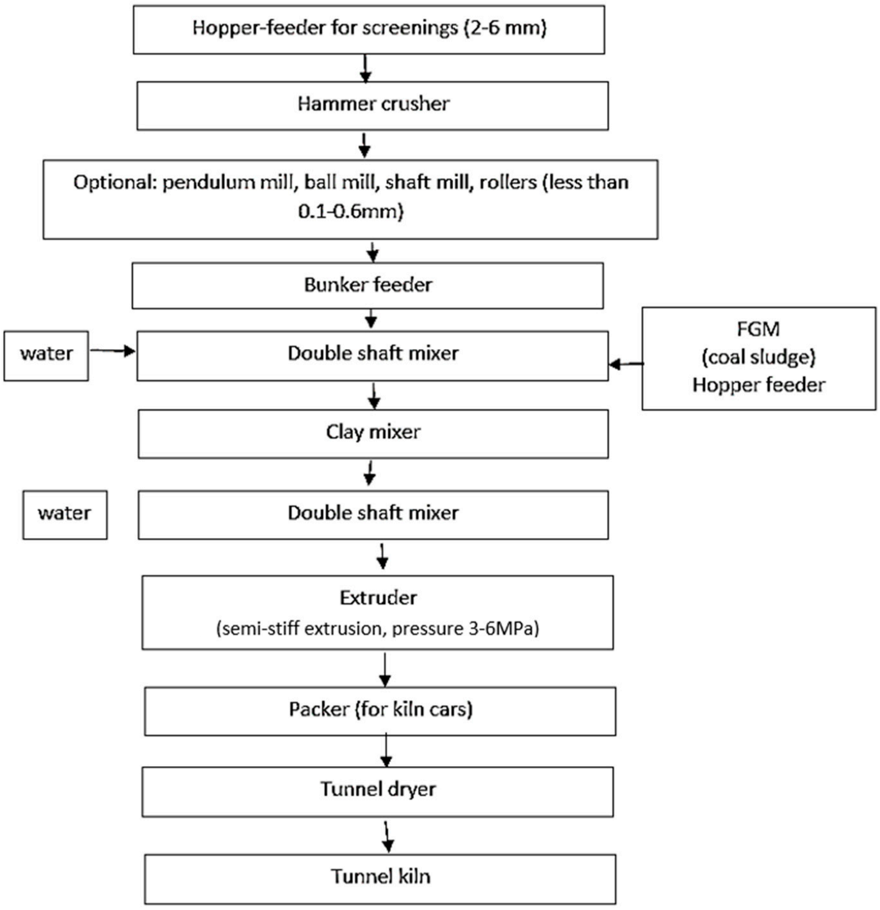

Figure 6. Technological scheme for the production of high-performance ceramic blocks based on products of waste heap processing.

4. Discussion

Distinctive features of our research and proposals from those available in this area [13, 22–37] are described in this section.

The main procedure in the preparation of the raw mixture is the grinding of screenings to a fractional composition ranging from 0.16 to 0–0.63 mm. It is most rational to use a hammer mill for primary grinding, for secondary—depending on the petrographic composition of the screenings and the required grain composition—one of the following can be chosen: a pendulum mill, a shaft mill, a ball mill, or rollers. Ultimately, everything will be determined by the initial operating costs. Fine-grained processing materials do not require grinding because they are finely dispersed in the initial state. The task is to thoroughly mix the mixture's components while carefully controlling its moisture content, which for the given raw masses and the molding method is 14–15%. Therefore, two mixers and a clay grinder are provided in the production line. Products are formed on extruder presses. The presence of a carbon component is especially beneficial for stiff extrusion, as the carbon is a kind of "lubricant" during molding. The main task is to select the technological parameters of molding (pressure in the press head, vacuum depth, steam temperature, molding temperature, beam output speed, etc.) to obtain defect-free products with strength sufficient for mounting on kiln trolleys. Robots should be used for product placement, since it is only with their help that it is possible to guarantee the laying of blocks without the risk of damage and deformation.

The absence of stacking products on drying trolleys and removing them from drying trolleys as a separate operation greatly simplifies the technological scheme of production. Drying as a separate operation may be eliminated for these raw masses with a sufficient length of the furnace (150 m or more). The main task during firing is to make sure that the coal component is completely burned out. According to the scheme, firing can be carried out entirely on coal in this case: 80% of the fuel in the products themselves, 20% of external fuel, and thus external combustion. It should be said that the presence of fuel inside the products contributes to uniform firing. The introduction of sawdust in the amount of 1–2% improves the firing conditions by increasing the combustion zone, since sawdust ignites at much lower temperatures than coal and has more volatile components in its composition. Waste heat of the furnace can be used for other needs of the enterprise.

The products which are ready to be fired are laid according to a certain scheme, fully corresponding to the type of fuel used and the design of the furnace.

In order to load and unload the stone, a special rack must be stable enough and convenient to use at the same time. Its design is important in the formation of heat exchange processes and heat distribution between products. The type of fuel affects the type of special rack [31,32].

The following are methods for laying high-performance ceramic stones of the 14.3 NF format on drying and kiln trolleys (Figures 7 and 8).

Figure 7. Stacking products on drying trolleys.

A rational firing mode is one in which the products are fired without defects, and in accordance with technical indicators in the shortest possible time, with minimal fuel consumption.

The totality of the results of laboratory and technical tests of raw materials and the results of experimental firing of products or their models, under conditions similar to those in real equipment for which this mode is set, is a predominantly advantageous and often used method for determining a rational mode.

Figure 8. Stacking products on kiln trolleys.

The firing cycle includes a period of heating, holding in the region of maximum temperatures, and cooling for ceramic products.

The firing temperature is the most important condition affecting the degree and speed of sintering. During solid-phase sintering in the process of firing wall ceramic products, an increase in the firing temperature accelerates the diffusion of the substance and, accordingly, the sintering process itself. An increase in temperature helps the system to achieve the conditions for liquid sintering, improving the wetting ability of the liquid phase and decreasing the viscosity [13,35,36].

We identified several key stages depending on the firing temperature in ceramic masses based on screenings:

1. Getting rid of free water. There is residual moisture in the products in the range of 2–4% after drying. It is removed in the temperature range up to 200 °C. Initially, the elimination of water occurs from larger pores, then from smaller ones, so this process occurs gradually;
2. Oxidation (burnout) of organic impurities contained in screenings, which begins at temperatures of 250–350 °C. This process is completed at 700–800 °C;
3. Clay dehydration begins at 400–600 °C—removal of chemically bound water;
4. Isolation of iron oxides;
5. At 650–700 °C anthracite ignites, heat is released, and the supply of external heat is interrupted;
6. The formation of a liquid phase is accompanied by sintering from approximately 950 °C. The liquid phase is very important in the sintering of a shard as it helps separate mineral particles to stick together into a single one [37].

The presence of iron content in raw materials with different firing environments leads to different reactions. Thus, the firing of clay in an oxidizing environment leads all the iron into its oxide form, and in the reducing one—into its reduced oxide form, coloring the products in a blue-greenish color. With an increase in the amount of iron in the composition of clay, it darkens more and more and may turn black after firing. In order to improve the quality of products redox firing has been widely used.

Water vapor is supplied to the installed burners at the end of the burning zone. Along with this, the air consumption coefficient decreases to 1. In the next half of the firing zone, there should be a section of the reducing environment covering more than four positions of the kiln. The oxygen content within this section should not be more than 0.3%, when the largest accumulation of reducing gases (CO + H_2) should range from 1.5% to 4%. It is necessary to limit the volume of secondary air entering the second half, along with a decrease in the supply of primary air to 5–6 pairs of the last burners: the firing zones of the kiln in the form of suction and directed through the kiln channel from the cooling zone to the firing zone. The supply of steam to the burners located at the end of the firing zone has an effect on reducing the temperature of the combustion flame when the burners operate with an air flow rate close to 1, thereby eliminating overheating of products at the points of action of the combustion flame.

The aerodynamic mode of the furnace guarantees an overpressure in the second half of the firing zone over the entire cross section of the special cage of about 3 Pa and supports a decrease in the content of secondary air entering the firing zone. This requires the competent use of sand gates, constant monitoring of the trolley fleet, the closest attention to the joints and aprons of the trolleys, as well as special control of the sealing of the firing channel in the mentioned area [38–41].

5. Conclusions

The conducted studies of waste heap processing screenings made it possible to identify the following significant conclusions for the production technology of large-sized ceramic blocks:

- Screenings of waste heap processing are raw materials for low-temperature sintering. Water absorption is less than 5% at firing temperatures up to 1100 °C;
- The grind size determines which group raw materials will be assigned to during firing;
- Screenings have a small sintering interval—no more than 50 °C, which is possible only when preparing screenings due to an increase in the content of fine fractions. Moreover, it is the degree of grinding of screenings that makes it possible to regulate the sintering process;
- In the manufacture of stones based on screenings and ordinary bricks, it is necessary to focus on temperatures of 1000—1050 °C;
- When choosing corrective additives for screenings, it is worth taking complex ones as a basis. They increase the plasticity and cohesion of the molding compositions and extend the sintering range. We decided to focus on siliceous clays and coal sludge in the form of such additives.

The key factors influencing the formation of the structure of a ceramic shard based on screenings are the degree of their grinding and the firing temperature. These data are confirmed by numerous laboratory tests.

Other factors also need to be taken into account, such as:

- Stone format, dimensions, porosity;
- Special rack shape;
- Type of firing unit;
- Firing mode;
- Firing environment.

As for the formats, sizes and porosity of ceramic stones, there are some rules: the shape of a ceramic block is a parallelepiped with different lengths of facets, which depends on the type of block. The porosity of ceramic stones can vary from 48 to 55%.

As a result, the conducted research revealed the potential of manufacturing large-sized ceramic blocks from waste heap screenings processing. At the same time, it is possible to reduce the cost of products and achieve an increase in technical and economic indicators for the construction industry as a whole. A technological regulation for the manufacturing process with an updated list of equipment is required for further development.

Author Contributions: Conceptualization, K.Y. and E.G.; methodology, K.Y. and E.G.; software, E.G.; validation, K.Y.; formal analysis, K.Y.; investigation, K.Y. and E.G.; resources, K.Y. and E.G.; data curation, K.Y.; writing—original draft preparation, K.Y. and E.G.; writing—review and editing, K.Y.;

visualization, K.Y. and E.G.; supervision, K.Y.; project administration, K.Y.; funding acquisition, K.Y. and E.G. All authors have read and agreed to the published version of the manuscript.

Funding: This research received no external funding.

Data Availability Statement: The data presented in this study are available on request from the corresponding author.

Conflicts of Interest: The authors declare no conflict of interest.

References

1. Komarov, A.K.; Filonenko, E.A. Influence of the type of wall material on the technical and economic indicators of the construction of a low-rise building. *Bull. ISTU* **2015**, *8*, 103.
2. Tilinin, Y.I.; Uvarov, G.D.; Bravy, A.Y. Improving the technology of building walls in low-rise housing construction. *Colloq. J.* **2019**, *24*, 48.
3. Tolegenov, D.T.; Yelubai, M.A.; Tolegenova, D.J.; Kulumbaev, N.K.; Tylyubaev, R.A. *Use of Man-Made Energy and Metallurgical Waste in Building Ceramics*; Vestnik Toraigyrov University: Pavlodar, Republic of Kazakhstan, 2022; Volume 2, pp. 310–321. [CrossRef]
4. Gadaev, R.S.; Esetova, A.M. Improvement of pricing methods in construction. *Reg. Probl. Econ. Transform.* **2022**, *3*, 33–41. [CrossRef]
5. Bozhko, Y.A.; Lazareva, Y.V.; Gaishun, E.S. Phase transformations of siliceous clays during the firing of ceramics. In Proceedings of the 63rd International Scientific Conference of the Astrakhan State Technical University, Dedicated to the 25th Anniversary of the Astrakhan State Technical University, Astrakhan, Russia, 15–19 April 2019.
6. Yavruyan, K.S.; Gaishun, E.S.; Teryokhina, Y.V.; Kotlyar, V.D. The research on the sifting from Donbass refuse heap for manufacturing wall ceramic goods. In *MATEC Web of Conferences 2018*; EDP Sciences: Les Ulis, France, 2018; pp. 4–55.
7. Yavruyan, K.S.; Gaishun, E.S.; Kotlyar, V.D.; Lotoshnikova, E.O. Raw Materials in East Donbass Based on Waste Piles Processing Screenings for the Large-Sized Ceramic Stones' Production. In *Materials and Technologies in Construction and Architecture III*, 1st ed.; Yazyev, B., Litvinov, S., Lapina, A., Kotesova, A., Akay, O., Eds.; Trans Tech Publications Ltd.: Zurich, Switzerland, 2020; pp. 116–122.
8. Yavruyan, K.S.; Gaishun, E.S.; Kotlyar, V.D.; Serebryanaya, I.A.; Filippova, A.A.; Gaishun, A.S. Selection of compositions of ceramic masses based on industrial wastes using mathematical planning methods. In *E3S Web of Conferences*; EDP Sciences: Les Ulis, France, 2020; Volume 164.
9. Ashmarin, G.D.; Kurnosov, V.V.; Lastochkin, V.G. Energy and resource-saving technology of ceramic wall materials. *Build. Mater.* **2010**, *4*, 24–27.
10. Ashmarin, G.D.; Livada, A.N. Expansion of the raw material base is an important factor in the development of ceramic wall materials industry. *Build. Mater.* **2008**, *4*, 22–23.
11. Ilyicheva, S.I.; Yaskevich, T.G. *Production of Bricks with the Use of Waste Coal*; Express Information. Series 19, Issue 10; VNIIESM: Moscow, Russia, 1986; pp. 10–11.
12. Loseva, G.I. *Production of Bricks from Coal Waste*; Express Information. Series 19, Issue 16; VNIIESM: Moscow, Russia, 1986; pp. 12–13.
13. Kotlyar, V.D.; Yavruyan, K.S.; Gaishun, E.S.; Terekhina, Y.V. Comprehensive Approach to the Processing of East Donbass Spoil Tip. In Proceedings of the 2018 IEEE International Conference "Management of Municipal Waste as an Important Factor of Sustainable Urban Development" (WASTE), St. Petersburg, Russia, 4–6 October 2018; Institute of Electrical and Electronics Engineers Inc.: Piscataway, NJ, USA; pp. 39–41.
14. Fomina, O.A.; Stolboushkin, A.Y. *Approbation of the Method for Studying the Core-Shell Transition Layer of Ceramic Matrix Composites on the Example of Coal Waste*; International participation, Novokuznetsk, 8–10 October 2019; Stolboushkina, A.Y., Aleshina, E.A., Matekhina, O.V., Blaginykh, E.A., Eds.; Siberian State Industrial University: Novokuznetsk, Russia, 2019; pp. 123–126. Available online: https://www.elibrary.ru/item.asp?id=41863738 (accessed on 19 March 2023).
15. Eliche-Quesada, D.; Martínez-García, C.; Martínez-Cartas, M.L.; Cotes Palomino, M.T.; P'erez-Villarejo, L.; Cruz-P'erez, N.; Corpas-Iglesias, F.A. The use of different forms of waste in the manufacture of ceramic bricks. *Appl. Clay Sci.* **2011**, *52*, 270–276. [CrossRef]
16. Stolboushkin, A.Y. Perspective direction of development of building ceramic materials from low-quality raw materials. *Stroit. Mater.* **2018**, *4*, 24–28.
17. Eckel, Z.C.; Zhou, C.; Martin, J.H.; Jacobsen, A.J.; Carter, W.B.; Schaedler, T.A. Additive manufacturing of polymer-derived ceramics. *Science* **2016**, *351*, 58–62. [CrossRef] [PubMed]
18. Gaishun, E.S.; Gaishun, A.S.; Yavruyan, K.S. Technogenic raw materials of the coal series for the production of coarse building ceramics. Actual problems of science and technology. In Proceedings of the National Scientific and Practical Conference, Rostov-on-Don, Russia, 26–28 March 2019; Don State Technical University: Rostov-on-Don, Russia, 2019; pp. 762–763. Available online: https://www.elibrary.ru/item.asp?id=39453330 (accessed on 19 March 2023).

19. Kotlyar, V.D.; Yavruyan, K.S. Wall ceramic products based on finely dispersed waste heap processing products. *Build. Mater.* **2017**, *4*, 38–41.
20. Yavruyan, K.S.; Kotlyar, V.D.; Gaishun, E.S. Medium-fraction materials for processing of coal-thread waste drains for the production of wall ceramics. *Mater. Sci. Forum* **2018**, *931*, 532–536. [CrossRef]
21. Yavruyan, K.S.; Gaishun, E.S.; Kotlyar, V.D.; Okhotnaya, A.S. Features of phase and mineralogical of conversions when burning wall ceramics on the basis of secondary materials for processing coal deposits of Eastern Donbass. In *Materials and Technologies in Construction and Architecture II. Materials Science Forum—CATPID 2019*; Trans Tech Publications Ltd.: Bäch, Switzerland, 2019; Volume 974, pp. 67–74. [CrossRef]
22. Guzman, I.Y. *Workshop on Ceramics Technology*; LLC RIF Stroymaterialy: Moscow, Russia, 2005; p. 336.
23. Padmalosan, P.; Vanitha, S.; Sampath Kumar, V.; Anish, M.; Rajesh, T.; Dhapekar, N.K.; Yadav, A.S. An investigation on the use of waste materials from industrial processes in clay brick production. *Mater. Proc.* **2023**. [CrossRef]
24. Kotlyar, V.D.; Terekhina, Y.V.; Kotlyar, A.V. Method of testing stone-likeraw materials for the production of wall products of compression molding. *Stroit. Mater.* **2014**, *4*, 24–27.
25. Hoppe Filho, J.; Pires, C.A.O.; Leite, O.D.; Garcez, M.R.; Medeiros, M.H.F. Red ceramic waste as supplementary cementitious material: Microstructure and mechanical properties. *Constr. Build. Mater.* **2021**, *296*, 123653. [CrossRef]
26. Fiala, L.; Konrád, P.; Fořt, J.; Keppert, M.; Černý, R. Application of ceramic waste in brick blocks with enhanced acoustic properties. *J. Clean. Prod.* **2020**, *261*, 121185. [CrossRef]
27. Kotlyar, V.D.; Ustinov, A.V.; Terekhina, Y.V.; Kotlyar, A.V. Features of the coal firing process for the production of wall ceramics. *Tech. Technol. Silic.* **2014**, *21*, 8–15.
28. Eterigho-Ikelegbe, O.; Trammell, R.; Bada, S. Preparation and characterization of ceramic composites from South Africa coal discard. *Constr. Build. Mater.* **2021**, *302*, 124164. [CrossRef]
29. Stolboushkin, A.Y.; Storozhenko, G.I. Coal waste as a raw material and energy base for factories that produce ceramic wall materials. *Build. Mater.* **2011**, *4*, 43–46.
30. Sun, J.; Zhou, H.; Jiang, H.; Zhang, W.; Mao, L. Recycling municipal solid waste incineration fly ash in fired bricks: An evaluation of physical-mechanical and environmental properties. *Constr. Build. Mater.* **2021**, *294*, 123476. [CrossRef]
31. Kotlyar, A.V.; Talpa, B.V.; Lazareva, Y.A.V. Features of the chemical composition of argillite-like and clays and argillites. *Stroymaterialy* **2016**, *4*, 10–13.
32. Kotlyar, V.D.; Ustinov, A.V.; Terekhina, Y.V.; Kotlyar, A.V. Peculiarities of the firing process of coal sludge in the production of wall ceramics. *Tekhnika Tekhnol. Silik.* **2014**, *4*, 8–15.
33. Fomina, O.A.; Stolboushkin, A.Y. Development of a novel mold design for manufacturing of hollow ceramic products from coal wastes. *Mater. Today Proc.* **2019**, *11*, 348–353. [CrossRef]
34. Luo, Y.; Wu, Y.; Ma, S.; Zheng, S.; Chu, P.K. An eco-friendly and cleaner process for preparing architectural ceramics from coal fly ash: Pre-activation of coal fly ash by a mechanochemical method. *J. Clean. Prod.* **2019**, *214*, 419–428. [CrossRef]
35. Terekhina, Y.V.; Talpa, B.V.; Kotlyar, A.V. Mineralogical and technological features of lithified clayey rocks and prospects for their use as a raw material for the production of building ceramics. *Stroit. Mater.* **2017**, *4*, 8–10.
36. Babisk, M.P.; Amaral, L.F.; da Silva Ribeiro, L.; Vieira, C.M.F.; do Prado, U.S.; Gadioli, M.C.B.; Oliveira, M.S.; da Luz, F.S.; Monteiro, S.N.; da Costa Garcia Filho, F. Evaluation and application of sintered red mud and its incorporated clay ceramics as materials for building construction. *J. Mater. Res. Technol.* **2020**, *9*, 2186–2195. [CrossRef]
37. Muñoz Velasco, P.; Morales Ortíz, M.P.; Medívil Giró, M.A.; Muñoz Velasco, L. Fired clay bricks manufactured by adding wastes as sustainable construction material—A review. *Constr. Build. Mater.* **2014**, *63*, 97–107. [CrossRef]
38. Storozhenko, G.I.; Stolboushkin, A.Y.; Ivanov, A.I. Processing of carbonaceous argillites for obtaining ceramic raw materials and technological fuel. *Build. Mater.* **2015**, *8*, 50–59.
39. Stolboushkin, A.Y.; Ivanov, A.I.; Fomina, O.A. A study on structure and phase composition of cellular ceramic materials from dispersed silicarich rocks. In *Solid State Phenomena*; Trans Tech Publications Ltd.: Bäch, Switzerland, 2018.
40. Kotlyar, A.V.; Talpa, B.V. Stone-like clayey rocks of the Eastern Donbass are a promising raw material for the production of wall ceramics. In *Proceedings of the Scientific Conference of Students and Young Scientists with International Participation "Actual Problems of the Earth Sciences"*; SFU Publishing House: Rostov-on-Don, Russia, 2015; pp. 49–51.
41. Stolboushkin, A.Y.; Akst, D.V.; Fomina, O.A.; Ivanov, A.I.; Syromyasov, V.A. Analysis of waste coal from the enterprises of Kemerovo region as raw materials for production of ceramic material. In *IOP Conference Series: Earth and Environmental Science*; IOP Publishing: Bristol, UK, 2017.

buildings

MDPI

Article

Study on the Effect of Supplementary Cementitious Material on the Regeneration Performance of Waste Fresh Concrete

Weicheng Wang [1], Daoming Zhang [2,*], Linqing Liu [3], Xueyuan Zhang [2] and Yue Wang [1]

[1] College of Materials Science and Engineering, Qiqihar University, Qiqihar 161006, China
[2] College of Architecture and Civil Engineering, Qiqihar University, Qiqihar 161006, China
[3] Chengbang Ecological Environment Co., Ltd., Hangzhou 310008, China
* Correspondence: zdmzdm@sina.com

Abstract: In the preparation of ready-mixed concrete, it is inevitable to produce waste fresh concrete (WFC). An efficient, low-cost and environmentally friendly recycling scheme is the key to WFC recycling. In this work, we directly added some unhardened WFC to fresh concrete to prepare recycled fresh concrete (RFC); on this basis, fly ash (FA) and nano-silica (NS) were added as supplementary cementitious material (SCM) to obtain modified recycled fresh concrete (RFC-SF). Then, the mechanical properties, slump, freeze–thaw resistance, phase structure of the hydration products and hydration process in RFC were studied. The results show that the addition of FA and NS significantly improved the comprehensive performance of RFC. Compared with RFC, the compressive strength of RFC-SF with 15% FA and 3% NS increased by 15.2% and 50.3% at 7 d and 90 d, respectively, and the splitting tensile strength increased by 20.5% and 76.4%, respectively. The slump remained above 155 mm, and the mass loss rate decreased by 42.6% after freeze–thaw cycles. XRD and FTIR analysis showed that the addition of FA and NS accelerated the hydration reaction process of RFC-SF, reduced the content of calcium hydroxide (CH) and refined the grain size of CH. RFC-SF had a denser microstructure and a lower calcium-silicon ratio in SEM and EDS tests.

Keywords: waste fresh concrete; recycled fresh concrete; supplementary cementitious material; mechanical properties; fly ash; nano-silica; microcharacterization

1. Introduction

As the main material in infrastructure construction, annual global concrete production has exceeded 27 billion tons [1,2], of which 3% of the daily output is abandoned due to improper mix ratio and over time during transportation and pouring [3,4]. Recycling and reusing waste construction materials can improve the recycling rate of building materials, reduce the space required to bury waste and reduce pollution to the air environment [5–9]. For the waste fresh concrete (WFC) produced during the production of ready-mixed concrete, the traditional regeneration method often uses aggregate washing and screening to separate the aggregate and mud to prepare recycled concrete [10–13], while the wastewater and residue produced during washing can be put into concrete production again [14,15]. The waste slurry in WFC can be used as a curing agent to fill in the soil and road base to improve the stability of the soil structure [16,17]. Since the waste slurry is alkaline and rich in calcium, it can also be used as a chemical adsorbent in CO_2 capture, phosphorus recovery and water purification [18–20].

Compared with the traditional regeneration method, the more novel and rapid way is to use WFC as a part of ready-mixed concrete, directly stirred in to prepare recycled fresh concrete (RFC), and modify the RFC to reapply it in the field of engineering construction [21]. This regeneration method has the characteristics of lower energy consumption, a simpler site environment and a shorter regeneration production cycle. Some researchers have added retarders and accelerators to the WFC to adjust the setting time of the WFC, and then mixed it with ready-mixed concrete to be used in construction projects again [22–25]. Xuan et al. put the unhardened WFC paste directly into cement and recycled aggregate to prepare concrete blocks, and then carbonized the prepared blocks to enhance the mechanical properties of the blocks [21].

The above WFC regeneration methods have improved the recycling rate of building materials. However, more efficient, convenient and low-cost modification methods must be explored. Adding supplementary cementitious material (SCM) for modification when preparing RFC directly from unhardened WFC may be a more convenient and inexpensive recovery method. With the rapid development of building materials, SCM has become an important measure to improve the regeneration performance of concrete [26]. Among them, the addition of CNT, GNPs and nano-silica (NS) as SCMs can significantly improve the mechanical properties of concrete [27–29]. Compared with CNT and GNPs, NS is low cost and simple to use; moreover, NS has the advantages of high permeability, high specific surface energy, nucleation and pozzolanic effect. Its incorporation into cement-based materials can effectively enhance hydration activity, accelerate the hydration rate and improve the mechanical properties of concrete [30,31]. However, a large number of unsaturated bonds in NS can easily absorb free water, which seriously affects the working performance of concrete [32]. The fly ash (FA) in SCM can significantly improve the working performance and durability of concrete due to its small size and the morphological characteristics of glass spheres [33,34]. On the other hand, the chemical activity of FA is lower than that of cement, and excessive incorporation is not conducive to the improvement of the early strength of concrete [35].

It can be seen that when these two materials are separately mixed with WFC for direct regeneration, the prepared RFC has problems such as low early strength and poor working performance. If these two materials are mixed together, however, then these problems may be mitigated [36]. In this study, FA and NS were mixed into RFC, and the effects of different proportions of FA and NS on the strength, slump and freeze–thaw resistance of RFC were analyzed as well as the changes of phase composition and microstructure after adding these two materials. The results of this study provide a valuable method for the direct recycling of WFC.

2. Materials and Methods

2.1. Materials

P.O42.5 ordinary Portland cement produced by Qiqihar Beijiang company (Qiqihar City and China) was used, and grade I ash was used for fly ash. Table 1 shows the chemical composition of the cement and fly ash used under XRF analysis, in which it can be seen that the fly ash was a low-calcium type. The sand was medium sand produced locally in Qiqihar, and the fineness modulus was 2.3. Gravel with a continuous gradation range of 5–25 mm was used. The model of water-reducing agent is 325C polycarboxylic superplasticizer (PS). The NS was a transparent liquid from Suzhou Nadi Microelectronics Co., LTD (Suzhou City and China). Table 2 gives the properties of the NS liquid.

Table 1. Chemical compositions of cement and fly ash (%).

Materials	SiO_2	Al_2O_3	CaO	Fe_2O_3	MgO	K_2O	Na_2O	Cr_2O_3	Others
cement	31.5	10.7	46.19	3.93	3.31	1.31	0.76	/	2.3
fly ash	40.1	29.3	3.69	14.9	0.81	1.13	0.58	5.94	3.55

Table 2. Performance parameters of NS (%).

Exterior	Average Particle Size/nm	Content/%	Solvent	pH Value
Transparent liquid	15 ± 5	30	Transparent liquid	9–11

The setting time of fresh concrete is an important factor affecting the working performance of concrete and the hydration performance of slurry [37]. Consequently, normal concrete (NC) with a water–binder ratio of 0.5 and cement paste with the same ratio (NC-J) were prepared, and each cubic meter contains 180 kg of water, 360 kg of cement, 760 kg of sand, 1100 kg of gravel and 2.52 kg of PS. Then, the slump of NC at 120 min, 180 min and 300 min was tested, and the performance changes of NC-J in these three time periods were analyzed with a Fourier transform infrared spectrometer. Figure 1 shows that the slump of NC presents a plummeting trend with the increase of setting time, and its morphology changes from plastic slurry to angular block with aggregate wrapped by slurry, which cannot be poured. Figure 2 shows that the absorption peak of C_3S dominated by Si-O bond vibration is mainly reflected at 930 cm^{-1} after mixing NC-J for 120 min. When the standing time was extended to 180 min and 300 min, the vibration absorption peak of Si-O bond did not migrate from the low wavenumber to a high wavenumber. This indicates that the slurry was stilled in the hydration induction period during this period [38], and C_3S did not enter the rapid hydration reaction period and still has strong reactivity. Considering that the initial setting time of cement used is 180 min, we collected concrete that lost its plasticity after being placed for 180 min as WFC.

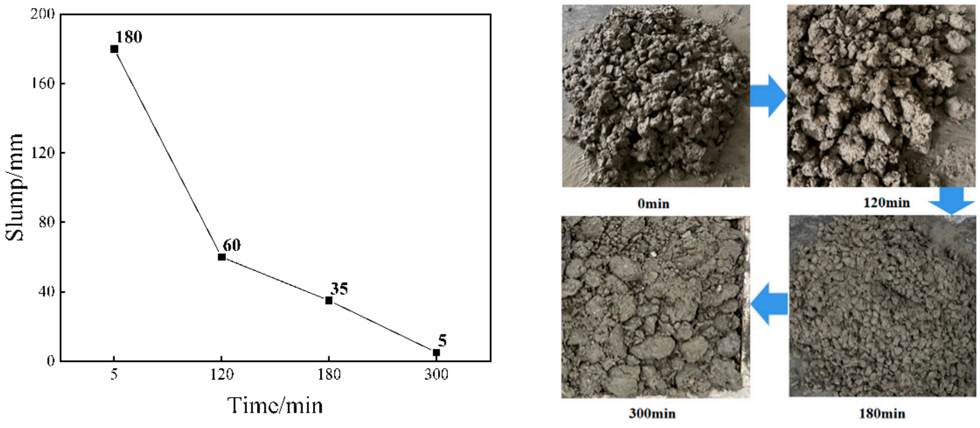

(**a**) (**b**)

Figure 1. Working performance of concrete under different placement times. (**a**) Slump of concrete; (**b**) Morphology of concrete.

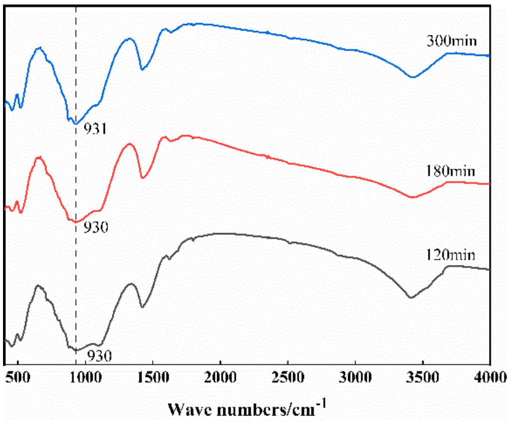

Figure 2. FTIR spectrum of NC-J at early hydration.

2.2. Methods

2.2.1. Proportioning of Concrete

In order to explore the effects of different FA and NS additions on RFC performance in this study, 14 groups of concrete mixing ratios were designed, and the water–binder ratio of each group was 0.5. Among these groups, NC was normal concrete; RFC was the concrete directly prepared with WFC replacing NC at a replacement rate of 30% of the total mass of NC; RFC-F was RFC with FA added separately as SCM; RFC-SF was the composite addition of FA and NS to the RFC. NC, RFC, RFC-F and RFC-SF all had variations designed with cement paste with the same ratio as concrete for microscopic performance testing, and they were recorded as NC-J, RFC-J, RFC-F-J and RFC-SF-J. For example, RFC-S3F15 represents the addition of 15% FA and 3% NS to RFC, and RFC-S5F20-J represents the addition of 20% FA and 5% NS to RFC-J. In order to effectively control the influence of the water–binder ratio, the additional water contained in NS was subtracted from the mixing water of RFC-SF. In addition, when preparing for mixing water, NS and PS were put into water to mix together and then dispersed with ultrasonic waves, which can eliminate the agglomeration phenomenon of nanomaterials due to the high specific surface energy [39]. Table 3 shows the mix ratios of concrete and cement pastes.

Table 3. Mixture proportions of concrete and the same proportion of cement pastes (kg/m^3).

Samples	Cement Paste						Aggregate		WFC
	Cement	Water	FA	NS	PS	Additional Water	Sand	Gravel	
NC	360	180	-	-	2.5	-	760	1100	-
RFC	252	126	-	-	1.8	-	532	770	720.7
RFC-F10	216	126	36	-	1.8	-	532	770	720.7
RFC-F15	198	126	54	-	1.8	-	532	770	720.7
RFC-F20	180	126	72	-	1.8	-	532	770	720.7
RFC-S1F10	214.9	123.5	36	3.6	1.8	2.5	532	770	720.7
RFC-S3F10	212.8	118.4	36	10.8	1.8	7.6	532	770	720.7
RFC-S5F10	210.6	113.4	36	18	1.8	12.6	532	770	720.7
RFC-S1F15	196.9	123.5	54	3.6	1.8	2.5	532	770	720.7
RFC-S3F15	194.8	118.4	54	10.8	1.8	7.6	532	770	720.7
RFC-S5F15	192.6	113.4	54	18	1.8	12.6	532	770	720.7
RFC-S1F20	178.9	123.5	72	3.6	1.8	2.5	532	770	720.7
RFC-S3F20	176.8	118.4	72	10.8	1.8	7.6	532	770	720.7
RFC-S5F20	174.6	113.4	72	18	1.8	12.6	532	770	720.7

2.2.2. Slump and Mechanical Properties

The concrete steps of the slump test conform to the Chinese standard GB/T 50080-2002. After the slump test, the concrete samples were put into concrete molds and then demolded after 24 h. In order to better meet the requirements of the specimen size in the frost resistance test, the concrete test blocks in this test were designed with a size of 100 mm × 100 mm × 100 mm. Then, the samples were placed in a curing room (T = 20 ± 2 °C, RH > 95%) for 7 days, 28 days and 90 days. After reaching the curing age, according to the Chinese standard GB/T 50081-2019, the compressive strength and splitting tensile strength of concrete samples were tested with the YAW-2000 pressure testing machine.

2.2.3. Freeze–Thaw Resistance

The freeze–thawing test of concrete adopted the slow-freezing method in Chinese standard GB/T 50082-2009. Firstly, as shown in Figure 3a, the concrete samples that had been cured for 24 days were immersed in water (T = 20 ± 2 °C) for 4 days. After the immersion was completed, the surface water of the samples was wiped off, and then the samples were weighed. Then, as shown in Figure 3a, the samples were put into the freeze–thaw testing machine for 150 freeze–thaw cycles, each freeze–thaw cycle taking 8 h. The temperature in the freeze–thaw machine was (−20~−18 °C) when frozen, and the water temperature was (18~20 °C) when melted. After 25 cycles, the test blocks were weighed. Finally, the mass loss rate of the concrete samples was calculated and averaged.

(**a**) (**b**)

Figure 3. Freeze–thaw testing. (**a**) Specimen immersion; (**b**) specimen freeze–thaw.

2.2.4. Microstructure Analysis

Various micro-experiments were conducted to evaluate the microstructure and components of concrete and its cement pastes, which helped to analyze the macro properties and regeneration mechanisms of each group of RFC samples. Phase analysis of the paste was performed at a scanning rate of 4°/min using an X-ray diffractometer (XRD, Smart Lab 9Kw, Rigaku, Tokyo, Japan) with CuKα radiation. The hydration process of RFC was analyzed with the Fourier transform infrared spectrometer (FTIR, Nicolet 6700, Thermo Scientific, Waltham, MA, USA) in the range of 400~4000 cm^{-1}. The microstructure of RFC was analyzed with a scanning electron microscope (SEM, S-4300, Hitachi, Tokyo, Japan) and an energy-dispersive X-ray spectrometer (EDS, Quantax75, Hitachi, Tokyo, Japan).

3. Results

3.1. Mechanical Properties

3.1.1. Effect of Adding Fly Ash Alone

It can be observed from Figure 4 that the strength of RFC at any curing age is lower than that of NC, and that the addition of FA alone has a negative effect on the early mechanical properties of RFC. Figure 4a shows that the compressive strength of RFC-F with FA is significantly lower than that of RFC at 7 d and 28 d, and this situation becomes more obvious with the addition of FA. When the curing age was extended to 90 d, the compressive strength of RFC-F exceeded that of RFC, and the compressive strength of RFC-F10, RFC-F15 and RFC-F20 increased by 22.8%, 25.6% and 17.3%, respectively. In addition, the increasing rate of compressive strength of RFC-F is greater than that of NC in 28~90 d.

A similar situation also occurs in splitting tensile strength. Figure 4b shows that the splitting tensile strength of RFC is lower than that of NC at any curing age; the splitting tensile strength of RFC-F at 7 d and 28 d is also lower than that of RFC. When the curing age increased to 90 d, the splitting tensile strength of RFC-F10, RFC-F15 and RFC-F20 increased by 39.7%, 44.2% and 32.2%, respectively, compared with RFC.

The reason for the above phenomenon is that the polymerization degree of $[SiO_4]^{4-}$ in FA is large, and most instances were long chain polymerization, which is not easy to disintegrate and fracture. Moreover, the surfaces of glass beads in FA were dense and smooth, and the erosion process of OH^- is slow, which delayed the reaction of Ca^{2+} and OH^- to form C-S-H, thus affecting the improvement of early strength. When age was increased, OH^- was eroded into the glass beads and a pozzolanic reaction occurred; this reaction increased the content of C-S-H and improved the strength of RFC-F.

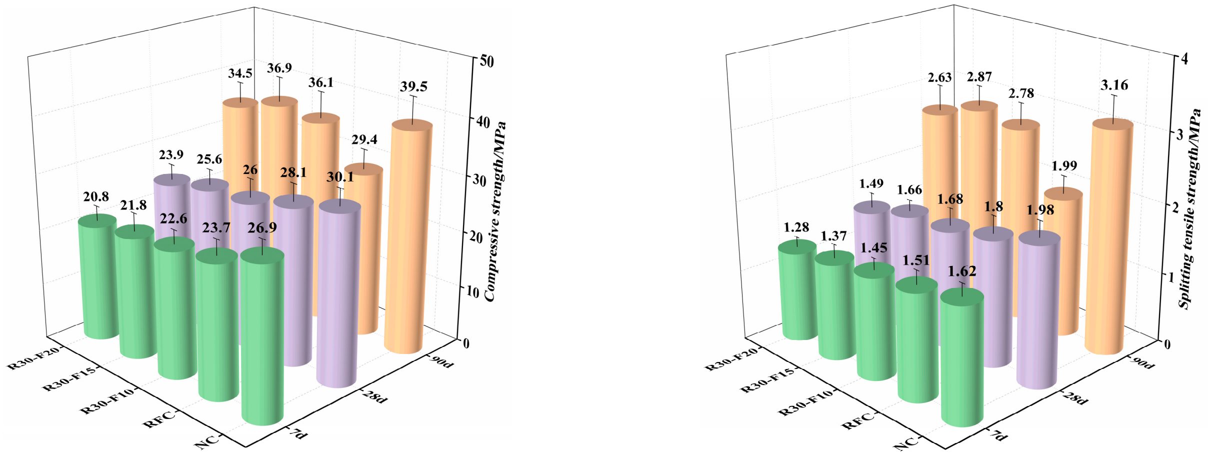

(**a**) (**b**)

Figure 4. Mechanical properties of RFC-F with FA. (**a**) Compressive strength; (**b**) splitting tensile strength.

3.1.2. Effect of Composite Addition of Fly Ash and Nano-Silica

On the basis of adding FA, FA and NS were mixed into RFC, and the effect of the two materials on RFC was tested. Figure 5a clearly shows the compressive strength change trend of RFC-SF with FA and NS. When the curing age was 7 d, the compressive strength of RFC-S3F15 was 15.2% higher than that of RFC. This indicates that the addition of NS effectively compensates for the deterioration of early compressive strength of RFC caused by fly ash. When the curing age was extended to 90 d, the compressive strength of RFC-SF increased by 9.5~50.3% compared with RFC. Figure 5b shows the splitting tensile strength of RFC-SF with two materials at 7 d, 28 d and 90 d. Similar to compressive strength, the splitting tensile strength of RFC-S3F15 at 7 d was 20.5% higher than that of RFC. The splitting tensile strength of RFC-SF increased by 10.1~76.4% at 90 d, and some results were higher than that of NC.

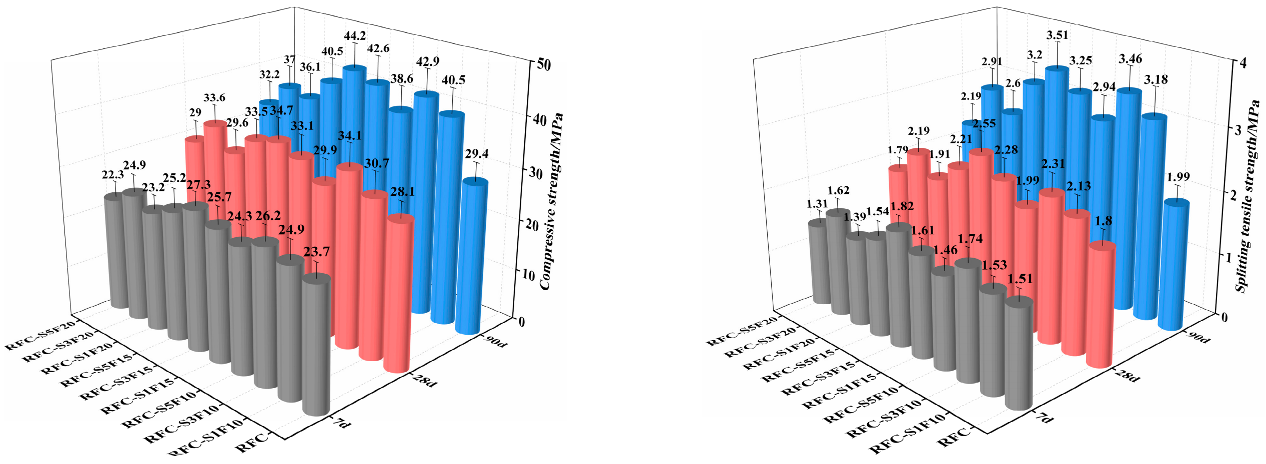

(**a**) (**b**)

Figure 5. Mechanical properties of RFC-SF with FA and NS. (**a**) Compressive strength; (**b**) splitting tensile strength.

The above strength improvement is due to the synergistic effect between FA and NS [40]. In the early stage of the reaction, the fine particles of FA are evenly distributed, which prevents the mutual cohesion between cement particles and provides them with a larger surface area for hydration reaction. The addition of highly active NS can significantly accelerate the hydration reaction rate of cement and improve the early strength of concrete. In addition, calcium hydroxide (CH) in cement hydration products can also undergo secondary hydration reactions with SiO_2 and increase the content of C-S-H in cement stone. In the later stages, the volcanic ash activity of FA is reflected. These measures provide RFC-SF with stronger mechanical properties.

It should be noted that with the increase of the amount of the two materials, the strength of RFC-SF first increases and then decreases. This is because too much nano SiO_2 agglomerates together, which absorbs free water and delays the hydration reaction of cement. Similarly, excessive introduction of low-activity FA will reduce hydration reactivity, which adversely affects the strength of RFC-SF.

3.2. Slump

The slump of concrete containing different contents of FA and NS is shown in Figure 6. After mixing for 5 min, the slumps of NC and RFC remained at about 180 mm and 150 mm, respectively. In contrast, the addition of FA increased the slump of RFC-F to above 185 mm, gradually increasing with the increase of FA content. When FA and NS were added together, the slump of RFC-SF was between 120 and 185 mm, and some of them were still larger than RFC. The reason for the decrease in slump is that NS has a very high specific surface energy, which makes a large number of unsaturated bonds absorb free water and form uneven hydration flocs [41], thereby reducing the free water content in RFC-SF. However, FA with smooth surfaces and fine particle size can disperse this part of the hydration flocs so that more water molecules absorbed by the flocs are freed, and its small spherical morphology makes it play a lubricating role in mixing, reducing the friction resistance between concrete aggregates.

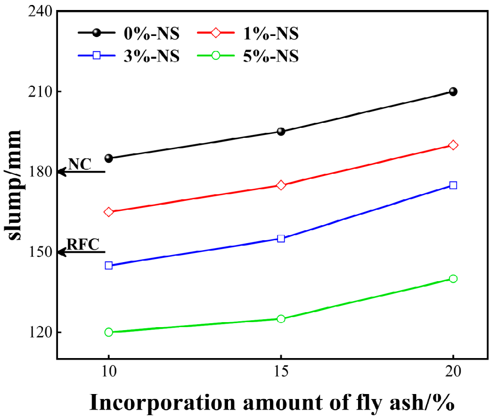

Figure 6. Slump of concrete with different contents of FA and NS.

3.3. Freeze–Thaw Resistance

Figure 7a shows the trend of mass loss rate of NC, RFC and RFC-F under 150 freeze–thaw cycles. In the early stage of freeze–thaw cycles, the mass loss rate of NC, RFC and RFC-F were negative. With the increase of freeze–thaw cycles, the mass loss rates gradually became positive and showed upward trends. After 150 freeze–thaw cycles, the mass loss rate of RFC-F with FA was between 0.32 and 0.43% as compared with RFC, and the mass loss rate of RFC-F15 decreased by 31.9%. In the early stage of the freeze–thaw cycle, high porosity concrete absorbed a lot of water when immersed in water, which increased the quality of concrete and led to a negative mass loss rate. After long-term freeze–thaw action, the water in the pores produced expansion stress and increased continuously when frozen, which caused the destruction of the concrete pore structure, made the cement paste and fine aggregate at the corner of the samples appear to be obviously spalling, and reduced the quality of concrete. This phenomenon is most obvious in unmodified RFC. However, FA with small particle size and microsphere morphology has filled the pores in RFC-F, which reduced the porosity of RFC and weakened the adverse effect of the expansion stress of freezing water on the pore structure, which makes RFC-F have a smaller mass loss rate and good freeze–thaw resistance.

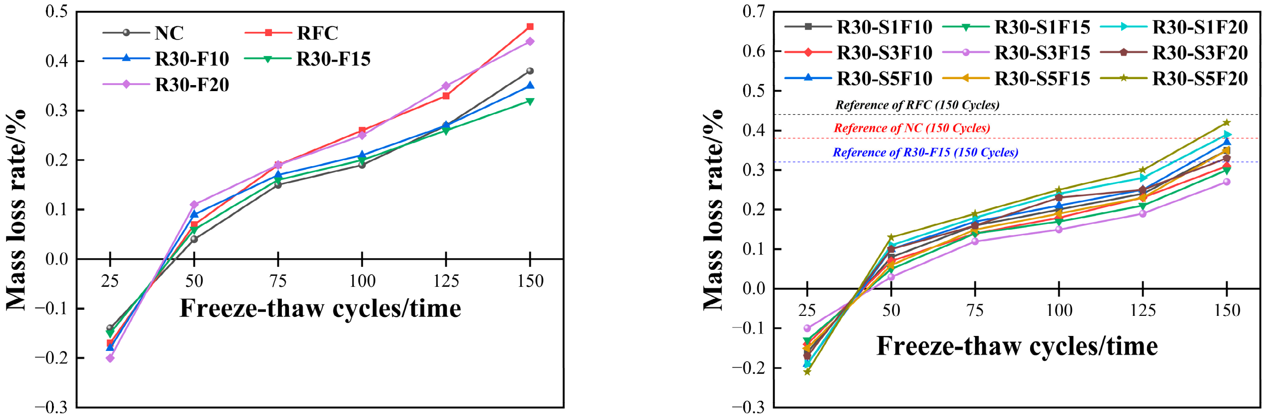

(**a**) (**b**)

Figure 7. Mass loss rates of RFC-F and RFC-SF after freeze–thaw cycles. (**a**) RFC-F; (**b**) RFC-SF.

Figure 7b shows that the composite addition of FA and NS can improve the freeze–thaw cycle performance of RFC-SF more obviously. The freeze–thaw cycle loss rate of RFC-SF was between 0.27 and 0.42%. Compared with RFC, the mass loss rate of RFC-S3F15 decreased by 42.6%. This is due to the addition of NS to generate more C-S-H on the basis of FA, which enhanced the strength of cement stone. At the same time, the nano-sized SiO_2 also filled some capillary pores, reduced the porosity and optimized the pore structure, which mitigated the damage caused by the expansion stress of freezing water to the pore structure and further improved the freeze–thaw resistance of RFC-SF.

3.4. Microstructure Analysis

3.4.1. XRD

The phase composition of different cement paste samples cured for 7 d and 28 d were measured with XRD, as shown in Figure 8a. It can be seen that the mineral types of RFC-F-J with FA added and RFC-SF-J with FA and NS added are basically the same as those of NC-J. However, the intensity of C_2S and C_3S in RFC-F15-J with FA is higher than that in NC-J and RFC-J, and the intensity of CH is lower than that in NC-J and RFC-J. This indicates that in the early stage of hydration reaction, the addition of FA with low activity delays the hydration reaction, resulting in a higher content of C_3S and C_2S in the unreacted cement clinker in the cement paste and lower C-S-H and CH content in the hydration products, which is an important factor in the poor early strength of RFC-F. In contrast, the intensities of the C_2S, C_3S and CH of RFC-S3F15-J with two materials are lower than that of RFC-J and RFC-F-J, which is because the addition of NS promotes the hydration reaction. In addition, CH also reacts with SiO_2 to further consume it, which increases the C-S-H content. The XRD spectrum of Figure 8b shows that the intensities of the C_3S, C_2S and CH of RFC-S3F15 are still lower than that of RFC after 28 days of cement paste curing, which indicates that the addition of the two materials is still helpful for the hydration reaction at a longer age. Moreover, the CH intensity of RFC-F15-J is lower than that of RFC, which may be due to the fact that the Si-O and Al-O bonds in FA are eroded by OH^- and Ca^{2+} with strong polarity, and CH is consumed by reaction with them.

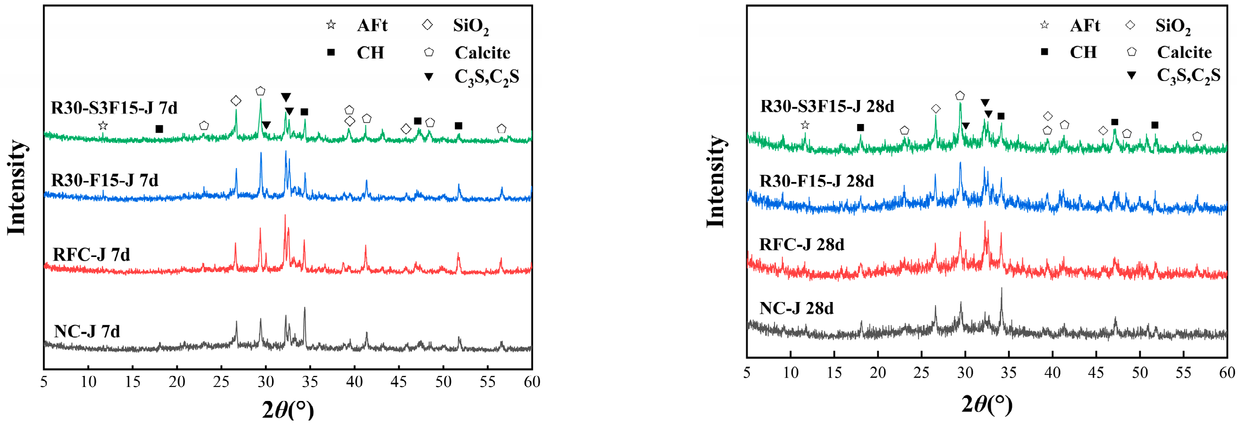

(**a**) (**b**)

Figure 8. XRD spectra of different cement pastes at different ages. (**a**) 7 d; (**b**) 28 d.

The particle size of the CH crystals in the cement paste was calculated by the Scherrer formula, and the equation of the Scherrer formula is as follows:

$$D = K \times \lambda / (B \times \cos\theta) \quad (1)$$

where D is the grain size (nm); K is the Scherrer constant, which generally takes 0.89; λ is the wavelength of the X-ray—the K_{a1} of Cu target radiation is 0.15405980 (nm); B is the peak half-width of the CH crystals; θ is the diffraction angle of the CH crystals.

As shown in Figure 9, the particle size of the CH crystals corresponding to the 101 crystal faces of RFC-J was larger than that of NC-J. The addition of FA alone and the combination of FA and NS made the particle size of the CH crystals smaller, and NS had a greater influence on the crystal size of CH. Compared with RFC-J, the particle size of the CH crystals in RFC-S3F15-J decreased by 21.7%, which indicated that the addition of FA and NS could refine the grain size of CH and avoid the problem of directional arrangement of CH in ITZ. Zhou et al. reached a similar conclusion [42].

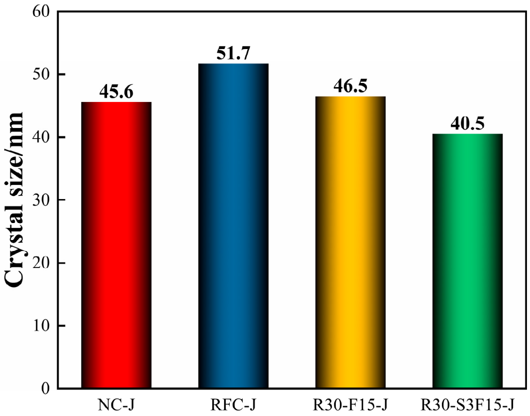

Figure 9. Particle size of CH crystals in different cement pastes.

3.4.2. FTIR

The FTIR spectra of NC-J, RFC-J, RFC-F15-J and RFC-S3F15-J pastes were compared in Figure 10a. It is obvious from the figure that the absorption peak at 875 cm^{-1} was caused by the out-of-plane bending vibration of CO_3^{2-} of $CaCO_3$, which may be due to the reaction of CH contained in the paste with CO_2 in the air and the formation of $CaCO_3$ during the preparation of the cement paste. The absorption peak at 976 cm^{-1} was caused by the Si-O stretching vibration of Q_2 representing $[SiO_4]^{4-}$, and the absorption peak at 3640 cm^{-1} was caused by the O-H stretching vibration representing CH. Figure 10b is a local enlarged image at 600–2000 cm^{-1}. The wave number of the Si-O stretching vibration in RFC-F15-J was lower than that in RFC-J, indicating that the hydration degree of RFC-F15-J is poor. A blue-shift phenomenon occurs for RFC-S3F15-J after the addition of FA and NS, and the wave number of the Si-O stretching vibration moves from 972 to 979 cm^{-1}. This indicates that the addition of two materials can increase the degree of polymerization of Q_2 and accelerate the degree of hydration reaction.

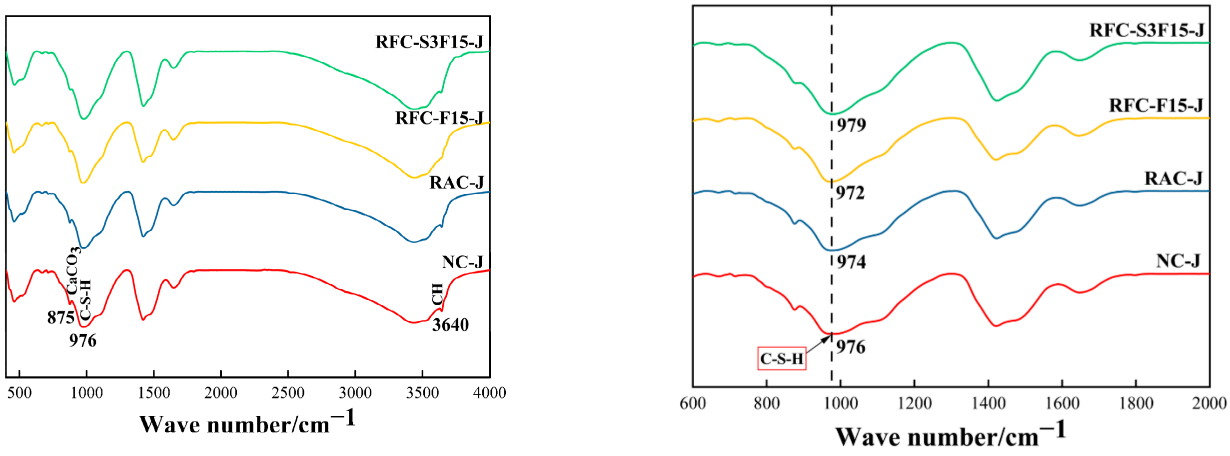

(**a**) (**b**)

Figure 10. FTIR spectra of different cement pastes. (**a**) 400–4000 cm^{-1}; (**b**) local amplification of 600–2000 cm^{-1}.

3.4.3. SEM

The microstructure of different concrete samples was measured with SEM, as shown in Figure 11. In the RFC samples, there were many large pores and cracks on the surface of the slurry, between the old and new cement pastes and between the slurry and the aggregate (Figure 11a). These pores and cracks may have been caused by uneven vibration during RFC preparation and aggregate detachment during compressive failure. After amplification, it can be seen that large amounts of block CH and needle ettringite (AFt) had grown in the pores, and the connection between the flocculent C-S-H and the crystal was loose, which made the pores poorly filled and prone to become empty again (Figure 11a). These phenomena made the gelation of the slurry in RFC poor, which ultimately degraded its mechanical properties. In contrast, RFC-F15 with fly ash still had obvious pores and cracks, and some of the pores had been filled with slurry (Figure 11c). It was found that the C-S-H in the slurry was wrapped with FA and AFt, and a small amount of bulk CH was embedded in the slurry, thus enhancing the cementitious property of the slurry (Figure 11d). However, RFC-S3F15 with FA and NS exhibited a denser microstructure, and the larger pores were gradually filled into small pores; this effectively alleviated the problem of pore structure damage caused by expansion stress of frozen water due to large pores (Figure 11e). A large amount of flocculent C-S-H wrapped in FA and irregular lumps of CH were found in the enlarged image (Figure 11f), as mentioned above, because the pozzolanic reaction consumes part of CH, and thus the number of CH presented in the image is small. These phenomena indicate that the composite addition of the two materials promoted the hydration reaction, and more C-S-H with strong connection was generated in the hydration products, which were closely combined with other hydration products to improve the cementitious properties of the slurry. Moreover, the secondary hydration reaction reduced the CH content in the hydration products, weakened the phenomenon of ITZ deterioration caused by the directional arrangement of CH, and enhanced the mechanical properties of concrete.

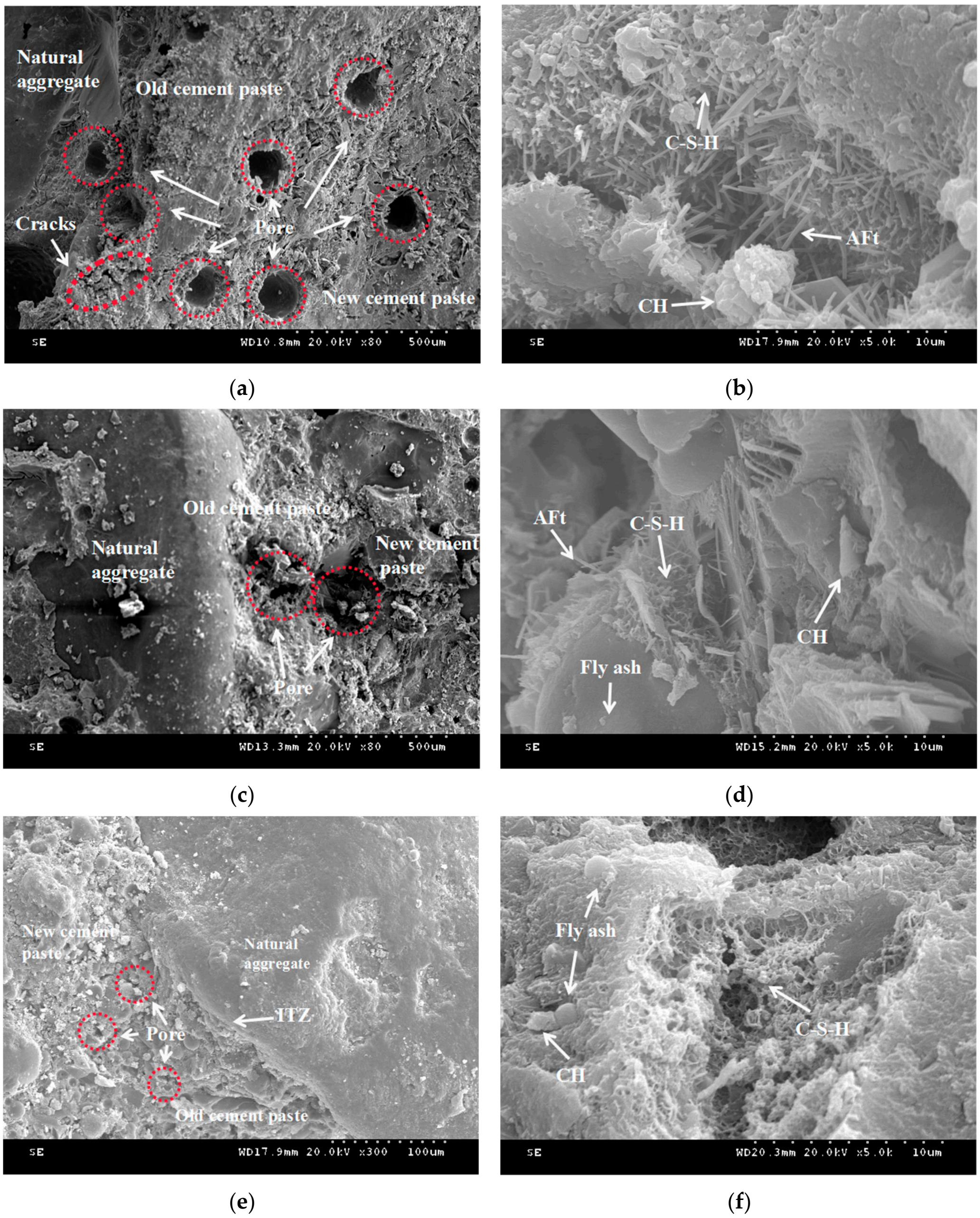

(**a**) (**b**)

(**c**) (**d**)

(**e**) (**f**)

Figure 11. SEM images of different concretes at 28 d. (**a**) RFC; (**b**) enlarged RFC; (**c**) RFC-F15; (**d**) enlarged RFC-F15; (**e**) RFC-S3F15; (**f**) enlarged RFC-S3F15.

3.4.4. EDS

The point scanning analysis of RFC-J, RFC-15 and RFC-S3F15-J cured for 28 days was carried out with EDS, as shown in Figure 12. RFC mainly contains the elements O, Mg, Al, Si, Ca, and Fe. The Ca/Si of RFC-J, RFC-F15-J and RFC-S3F15-J were 2.08, 1.69, 1.17, respectively, and the (Al + Fe)/Ca was 0.2 (Figure 12a,c,e). Taylor et al. found that when $0.8 \leq \text{Ca/Si} \leq 2.5$ and $(\text{Al} + \text{Fe})/\text{Ca} \leq 0.2$, C-S-H was the main hydration product of Portland cement [43]. With the increase of Ca/Si, the content of C-S-H will gradually decrease, while the content of CH and AFt will increase. Compared with RFC-J, the Ca/Si of RFC-F15-J and RFC-S3F15-J decreased by 0.39 and 0.91, indicating that the addition of FA and NS effectively promoted the production of C-S-H.

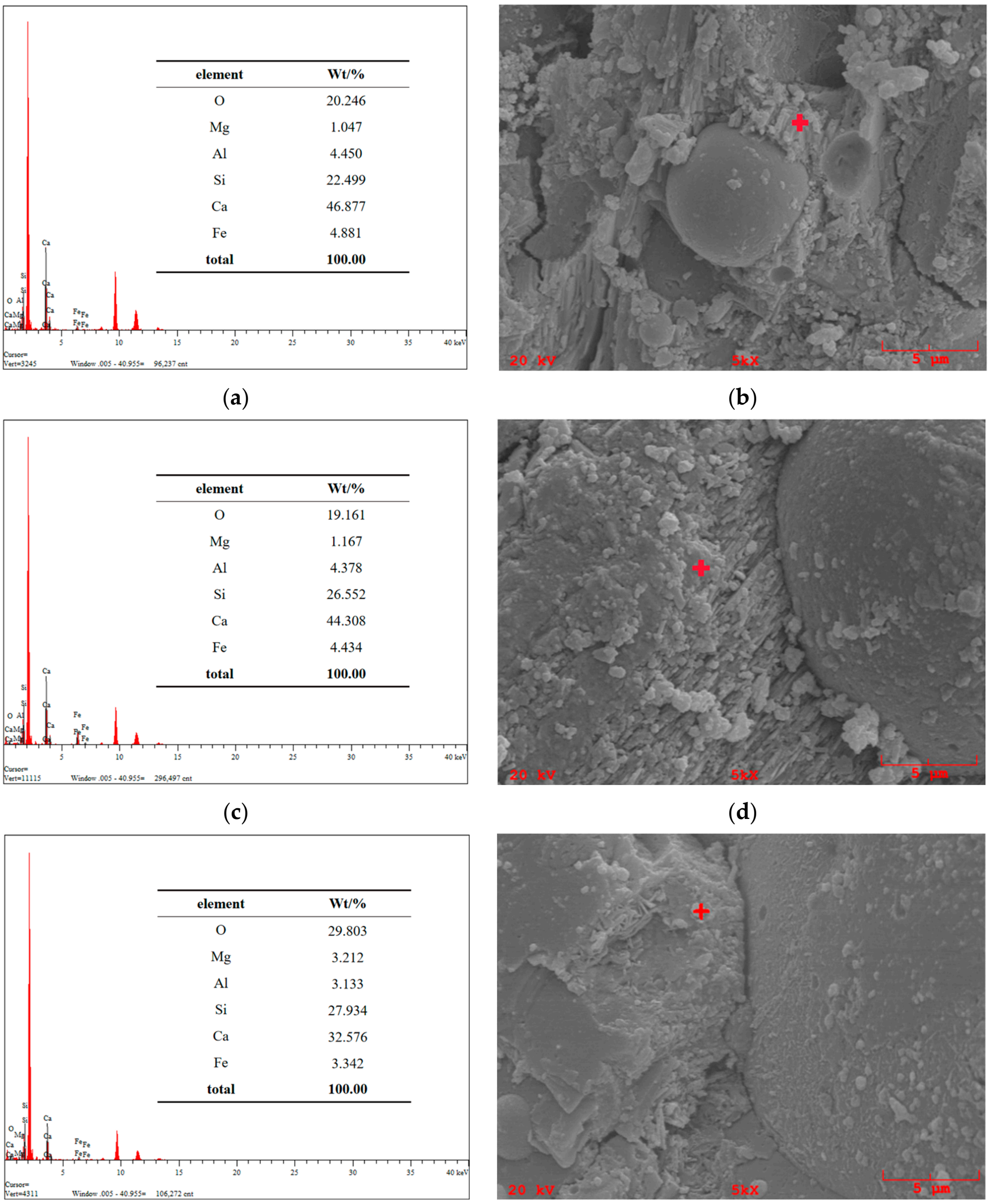

element	Wt/%
O	20.246
Mg	1.047
Al	4.450
Si	22.499
Ca	46.877
Fe	4.881
total	**100.00**

(**a**) (**b**)

element	Wt/%
O	19.161
Mg	1.167
Al	4.378
Si	26.552
Ca	44.308
Fe	4.434
total	**100.00**

(**c**) (**d**)

element	Wt/%
O	29.803
Mg	3.212
Al	3.133
Si	27.934
Ca	32.576
Fe	3.342
total	**100.00**

(**e**) (**f**)

Figure 12. Point scanning images of EDS of different cement pastes at 28d. (**a**) Element content of RFC-J; (**b**) point scanning image of RFC-J; (**c**) element content of RFC-F15-J; (**d**) point scanning image of RFC-F15-J; (**e**) element content of RFC-S3F15-J; (**f**) point scanning image of RFC-S3F15-J.

Figure 13 shows the elemental distribution of RFC and RFC-S3F15 cured for 28 days under EDS mapping scanning. There is a clear boundary between the slurry and the aggregate of RFC (red line area). The Ca element is located below the line, indicating that the area is a cement slurry, and the Si element is enriched above the line, indicating that the area is an aggregate. ITZ is a hollow area between the two elements, and only a small amount of Ca element and Si exist in this area (Figure 13a–c). In contrast, Ca element in RFC-S3F15 is located on both sides of the line, Si element is enriched in the center of the line, and the content of Si element in the Ca element region is significantly increased (Figure 13d–f). In addition, the content of Ca and Si elements in the ITZ region of RFC-S3F15 increased, which may have been caused by more C-S-H filling the ITZ.

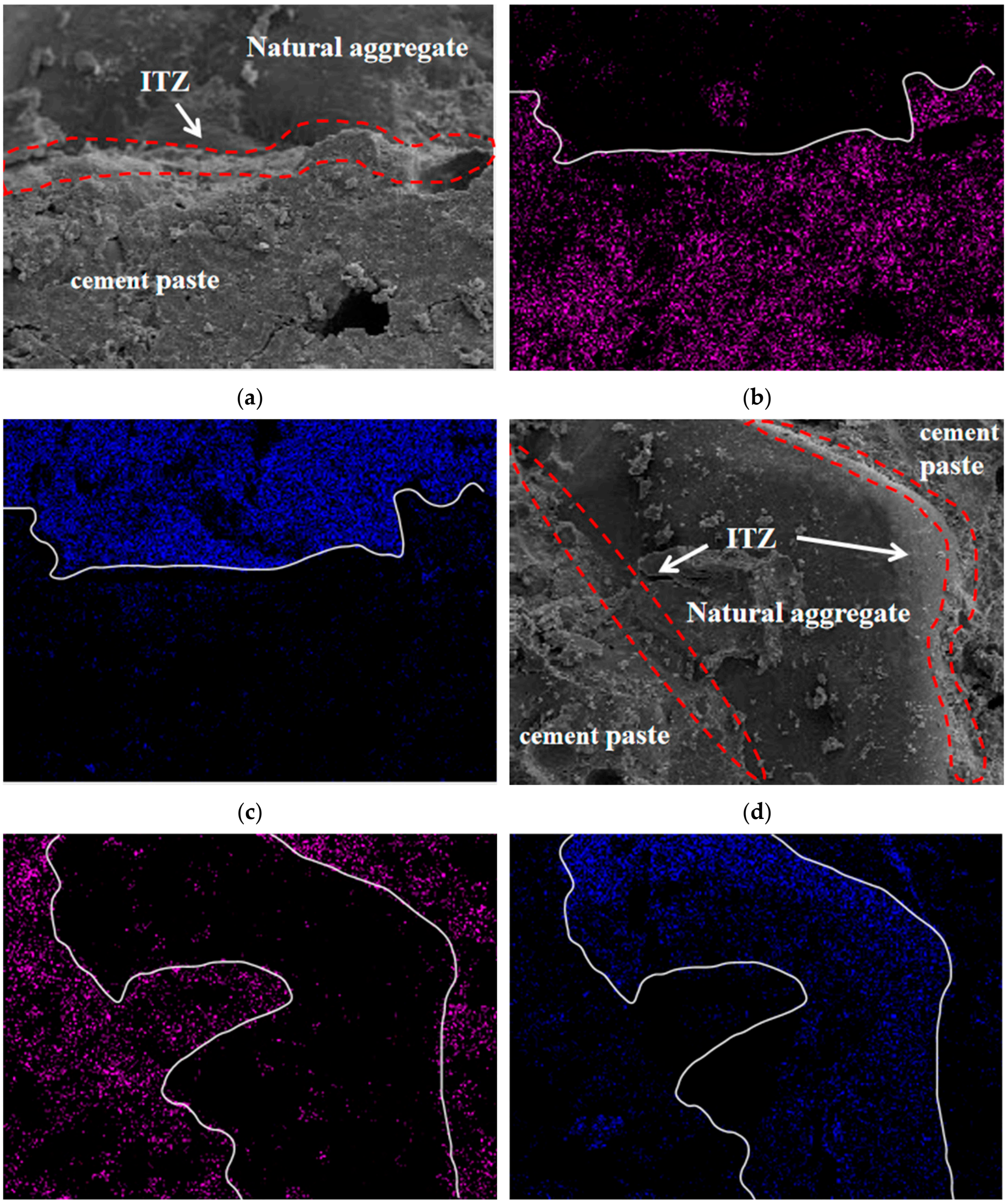

(**a**) (**b**)

(**c**) (**d**)

(**e**) (**f**)

Figure 13. Mapping scanning images of EDS of different concretes at 28 d. (**a**) Mapping scanning images of RFC; (**b**) distribution of Ca element in RFC; (**c**) distribution of Si element in RFC; (**d**) mapping scanning images of RFC-S3F15; (**e**) distribution of Ca element in RFC-S3F15; (**f**) distribution of Si element in RFC-S3F15.

4. Discussion

The results of this study indicated that the SCMs FA and NS have a significant effect on the hydration process and hardening state of RFC directly regenerated from WFC, which is caused by two factors.

4.1. Effect of Nano-Silica on Hydration and Hardening of RFC

Clinker minerals C_3S and C_2S in Portland cement will generate a large number of C-S-H in the hydration reaction, which is the main source of a certain strength of hardened cement stone. As mentioned above, WFC was placed for 180 min in the early hydration reaction, and its cement paste contained a large amount of unreacted C_3S and C_2S clinker minerals. When WFC was again mixed with cement and SCM, C_3S rapidly hydrolyzed in contact with water, and then Ca^{2+} and OH^- entered the solution and formed a calcium-deficient, silicon-rich layer on its surface. In order to maintain charge balance, the silicon-rich layer absorbed Ca^{2+} to the surface to form an electric double layer as shown in Figure 14. At this time, the dissolved Ca^{2+} and NS made the slurry strongly alkaline. In this alkaline environment, a large amount of $H_2SiO_4^{2-}$ in NS was released, which increased the content of $H_2SiO_4^{2-}$ in the silicon-rich layer. In order to maintain the charge balance again, the silicon-rich layer continuously absorbed Ca^{2+} in the solution, which made the cement particles continuously dissolve and effectively promote the hydration reaction. In addition, the volcanic ash reaction between NS and CH and its own physical filling gave RFC superior mechanical properties [44].

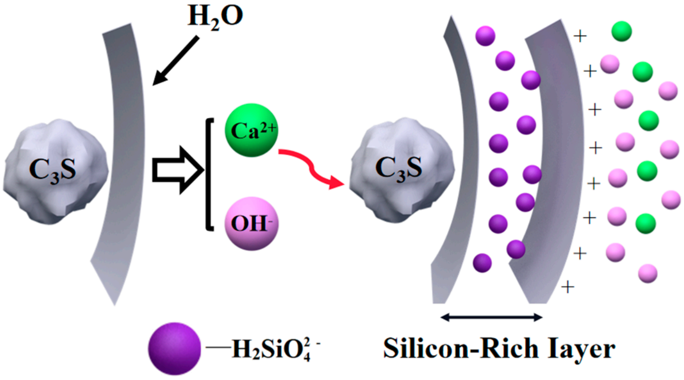

Figure 14. Diagram of silicon-rich layer.

4.2. Effect of Fly Ash on Hydration and Hardening of RFC

During the hydration process, the unevenly dispersed NS can easily cause self-agglomeration and absorb the newly dissolved cement particles in a block or flocculent shape, which hinders the hydration reaction. However, the addition of FA with its small size and smooth surface can effectively reduce the frictional resistance between cement particles and diffuse the cement particles that have been absorbed by NS. In addition, the morphological effect and micro-aggregate effect caused by FA improves the workability and compactness of the paste [45]. FA contains a large number of spherical floating beads and sinking beads, which can play a lubricating role in mixing concrete. In the early stage of hydration, the pozzolanic activity of FA was lower than that of Portland cement, which lead to the decrease of cement composition after replacing cement, delayed the hydration process, and reduced the mechanical properties of concrete. However, in the later stage of slurry hardening, the pozzolanic activity increased, and the floating beads and sinking beads were tightly wrapped by the hydration products C-S-H and AFt, filling in pores and cracks, which can be found in Figure 10f. This phenomenon further improves the mechanical properties of RFC under long-term service conditions.

5. Conclusions

In this paper, unhardened WFC was directly added into fresh concrete to prepare RFC, and FA and NS were added into RFC as SCMs to prepare modified RFC-F and RFC-SF. The effects of FA and NS on the mechanical properties, working performance and freeze–thaw performance of RFC were studied. The microstructure evolution of modified RFC was investigated by XRD, FTIR, SEM and EDS. This study concludes as follows:

(1) The early strength of RFC-F added with FA alone is poor. The synergistic effect of FA and NS added together makes the early and late mechanical properties of RFC-SF significantly improved. The compressive strength and splitting tensile strength at 7 d are increased by 15.2% and 20.5% at most, and the compressive strength and splitting tensile strength at 90 d are increased by 50.3% and 76.4% at most.

(2) Adding FA increased the slump of RFC from 150 mm to 185 mm or more; adding NS absorbed free water and reduced the fluidity of concrete. However, the slump of RFC-SF with two materials remains between 120 mm and 185 mm.

(3) The addition of FA alone improved the freeze–thaw performance of RFC-F, and the combined addition of FA and NS further improved the freeze–thaw performance of RFC-SF. Compared with RFC, the mass loss of RFC-F15 and RFC-S3F15 decreased by 31.9% and 42.6% after freeze–thaw cycles.

(4) XRD and FTIR showed that the addition of FA delayed the early hydration process of RFC-F. In contrast, the addition of FA and NS accelerated the hydration degree of RFC-SF, reduced the content of CH in the hydration products, and refined the grain size of CH.

(5) The results of SEM and EDS indicated that the microstructure of RFC-F15 with FA became denser, and the microstructure of RFC-S3F15 with FA and NS was improved obviously, as some pores were filled with C-S-H. Compared with RFC-J, the Ca/Si ratio of RFC-F15-J and RFC-S3F15-J decreased by 0.39 and 0.91.

(6) As an environmentally friendly material, RFC is conducive to promoting the sustainability of building materials. The effect of more solid wastes such as waste fiber and waste glass on the performance of RFC needs further study, and more efficient recovery methods of WFC need to be actively explored by engineers.

Author Contributions: W.W., D.Z., L.L. and X.Z. are the main contributors of this research work. They carried out the main experimental program, analyzed the experimental results and drafted the research paper; Y.W. mainly processed experimental data and proofread the paper. All authors have read and agreed to the published version of the manuscript.

Funding: This work was financially supported by the Horizontal Project of Qiqihar University. The funder is Qiqihar University, and the funding number is 220122222019.

Data Availability Statement: Data is contained within the article.

Acknowledgments: The authors are grateful for the financial support from Chengbang Ecological Environment Co., Ltd.

Conflicts of Interest: The authors declare no conflict of interest.

References

1. Wang, R.X.; Zhang, Y.X. Recycling fresh concrete waste: A review. *Struct. Concr.* **2018**, *19*, 1939–1955. [CrossRef]
2. Silva, D.O.F.; Quattrone, M.; Romano, R.C.O.; Angulo, S.C. Reuse of fines from ready-mix concrete washing slurries. *Resour. Conserv. Recycl.* **2020**, *155*, 104653. [CrossRef]
3. Vieira, L.D.P.; de Figueiredo, A.D.; Moriggi, T.; John, V.M. Waste generation from the production of ready-mixed concrete. *Waste Manag.* **2019**, *94*, 146–152. [CrossRef] [PubMed]
4. Nielsen, C.V.; Glavind, M. Danish experiences with a decade of green concrete. *J. Adv. Concert. Technol.* **2007**, *5*, 3–12. [CrossRef]
5. Zeybek, O.; Ozkilic, Y.O.; Karalar, M.; Celik, A.I.; Qaidi, S.; Ahmad, J.; Burduhos-Nergis, D.D.; Burduhos-Nergis, D.P. Influence of replacing cement with waste glass on mechanical properties of concrete. *Materials* **2022**, *15*, 7513. [CrossRef] [PubMed]
6. Karalar, M.; Bilir, T.; Çavuşlu, M.; Özkiliç, Y.O.; Sabri Sabri, M.M. Use of recycled coal bottom ash in reinforced concrete beams as replacement for aggregate. *Front. Mater.* **2022**, *9*, 1064604. [CrossRef]
7. Qaidi, S.; Najm, H.M.; Abed, S.M.; Ozkilic, Y.O.; Al Dughaishi, H.; Alosta, M.; Sabri, M.M.S.; Alkhatib, F.; Milad, A. Concrete containing waste glass as an environmentally friendly aggregate: A review on fresh and mechanical characteristics. *Materials* **2022**, *15*, 6222. [CrossRef]
8. Celik, A.I.; Ozkilic, Y.O.; Zeybek, O.; Karalar, M.; Qaidi, S.; Ahmad, J.; Burduhos-Nergis, D.D.; Bejinariu, C. Mechanical behavior of crushed waste glass as replacement of aggregates. *Materials* **2022**, *15*, 8093. [CrossRef]
9. Basaran, B.; Kalkan, I.; Aksoylu, C.; Özkılıç, Y.O.; Sabri, M.M.S. Effects of Waste Powder, Fine and Coarse Marble Aggregates on Concrete Compressive Strength. *Sustainability* **2022**, *14*, 14388. [CrossRef]
10. Audo, M.; Mahieux, P.Y.; Turcry, P. Utilization of sludge from ready-mixed concrete plants as a substitute for limestone fillers. *Constr. Build. Mater.* **2016**, *112*, 790–799. [CrossRef]
11. Xuan, D.X.; Poon, C.S.; Zheng, W. Management and sustainable utilization of processing wastes from ready-mixed concrete plants in construction: A review. *Resour. Conserv. Recycl.* **2018**, *136*, 238–247. [CrossRef]
12. He, X.Y.; Ma, Q.H.; Su, Y.; Zheng, Z.Q.; Tan, H.B.; Peng, K.; Zhao, R.X. Humid hardened concrete waste treated by multiple wet-grinding and its reuse in concrete. *Constr. Build. Mater.* **2022**, *350*, 128485. [CrossRef]

13. Vieira, L.D.P.; de Figueiredo, A.D. Evaluation of concrete recycling system efficiency for ready-mix concrete plants. *Waste Manag.* **2016**, *56*, 337–351. [CrossRef]
14. Wang, X.; Yan, Y.R.; Tong, X.F.; Gong, Y.F. Investigation of mineral admixtures on mechanical properties of alkali-activated recycled concrete powders cement. *Buildings* **2022**, *12*, 1234. [CrossRef]
15. Asadollahfardi, G.; Asadi, M.; Jafari, H.; Moradi, A.; Asadollahfardi, R. Experimental and statistical studies of using wash water from ready-mix concrete trucks and a batching plant in the production of fresh concrete. *Constr. Build. Mater.* **2015**, *98*, 305–314. [CrossRef]
16. Reiterman, P.; Mondschein, P.; Doušová, B.; Davidová, V.; Keppert, M. Utilization of concrete slurry waste for soil stabilization. *Case Stud. Constr. Mater.* **2022**, *16*, e00900. [CrossRef]
17. Zhang, J.; Fujiwara, T. Concrete sludge powder for soil stabilization. *Transp. Res. Rec. J. Transp. Res. Board* **2007**, *2026*, 54–59. [CrossRef]
18. Iizuka, A.; Sakai, Y.; Yamasaki, A.; Honma, M.; Hayakawa, Y.; Yanagisawa, Y. Bench-scale operation of a concrete sludge recycling plant. *Ind. Eng. Chem. Res.* **2012**, *51*, 6099–6104. [CrossRef]
19. Iizuka, A.; Sasaki, T.; Hongo, T.; Honma, M.; Hayakawa, Y.; Yamasaki, A.; Yanagisawa, Y. Phosphorus adsorbent derived from concrete sludge (PAdeCS) and its phosphorus recovery performance. *Ind. Eng. Chem. Res.* **2012**, *51*, 11266–11273. [CrossRef]
20. Sasaki, T.; Sakai, Y.; Iizuka, A.; Nakae, T.; Kato, S.; Kojima, T.; Yamasaki, A. Evaluation of the capacity of hydroxyapaptite prepared from concrete sludge to remove lead from water. *Ind. Eng. Chem. Res.* **2011**, *50*, 9564–9568. [CrossRef]
21. Xuan, D.X.; Zhan, B.J.; Poon, C.S.; Zheng, W. Innovative reuse of concrete slurry waste from ready-mixed concrete plants in construction products. *J. Hazard. Mater.* **2016**, *312*, 65–72. [CrossRef] [PubMed]
22. Lobo, C.; Guthrie, W.F.; Kacker, R. A Study on the reuse of plastic concrete using extended set-retarding admixtures. *J. Res. Natl. Inst. Stand. Technol.* **1995**, *100*, 575–589. [CrossRef] [PubMed]
23. Okawa, Y.; Yamamiya, H.; Nishibayashi, S. Study on the reuse of returned concrete. *Mag. Concr. Res.* **2000**, *52*, 109–115. [CrossRef]
24. Vieira, L.D.P.; Figueiredo, A.D. Implementation of the use of hydration stabilizer admixtures at a ready-mix concrete plant. *Case Stud. Constr. Mater.* **2020**, *12*, e00334. [CrossRef]
25. Kong, D.Y.; He, G.P.; Pan, H.W.; Weng, Y.H.; Du, N.; Sheng, J.S. Influences and mechanisms of nano-C-S-H gel addition on fresh properties of the cement-based materials with sucrose as retarder. *Materials* **2020**, *13*, 2345. [CrossRef]
26. Lothenbach, B.; Scrivener, K.; Hooton, R.D. Supplementary cementitious materials. *Cem. Concr. Res.* **2011**, *41*, 1244–1256. [CrossRef]
27. Wang, B.; Xiao, H.; Zhang, T. Autogenous shrinkage property of high-performance multi-walled cement-based carbon nanotubes composites. *J. Nanosci. Nanotechnol.* **2018**, *18*, 6894–6904. [CrossRef]
28. Gholampour, A.; Kiamahalleh, M.V.; Tran, D.N.H.; Ozbakkaloglu, T.; Losic, D. Revealing the dependence of the physiochemical and mechanical properties of cement composites on graphene oxide concentration. *RSC Adv.* **2017**, *7*, 55148–55156. [CrossRef]
29. Hasan-Nattaj, F.; Nematzadeh, M. The effect of forta-ferro and steel fibers on mechanical properties of high-strength concrete with and without silica fume and nano-silica. *Constr. Build. Mater.* **2017**, *137*, 557–572. [CrossRef]
30. Wang, J.B.; Du, P.; Zhou, Z.H.; Xu, D.Y.; Xie, N.; Cheng, X. Effect of nano-silica on hydration, microstructure of alkali-activated slag. *Constr. Build. Mater.* **2019**, *220*, 110–118. [CrossRef]
31. Shan, H.L.; Yu, Z.P. Strength, chloride ion penetration, and nanoscale characteristics of concrete prepared with nano-silica slurry pre-coated recycled aggregate. *Buildings* **2022**, *12*, 1707. [CrossRef]
32. Kong, D.Y.; Su, Y.; Du, X.F.; Yang, Y.; Wei, S.; Shah, S.P. Influence of nano-silica agglomeration on fresh properties of cement pastes. *Constr. Build. Mater.* **2013**, *43*, 557–562. [CrossRef]
33. Elahi, A.; Basheer, P.A.M.; Nanukuttan, S.V.; Khan, Q.U.Z. Mechanical and durability properties of high performance concretes containing supplementary cementitious materials. *Constr. Build. Mater.* **2010**, *24*, 292–299. [CrossRef]
34. Kim, K.; Shin, M.; Cha, S. Combined effects of recycled aggregate and fly ash towards concrete sustainability. *Constr. Build. Mater.* **2013**, *48*, 499–507. [CrossRef]
35. Yoshitake, I.; Zhang, W.B.; Mimura, Y.; Saito, T. Uniaxial tensile strength and tensile Young's modulus of fly-ash concrete at early age. *Constr. Build. Mater.* **2013**, *40*, 514–521. [CrossRef]
36. Cui, K.; Chang, J. Hydration, reinforcing mechanism, and macro performance of multi-layer graphene-modified cement composites. *J. Build. Eng.* **2022**, *57*, 104880. [CrossRef]
37. Gebremichael, N.N.; Karein, S.M.M.; Karakouzian, M.; Jadidi, K. Investigation of setting time and compressive strength of ready-mixed concrete blended with returned fresh concrete. *Constr. Build. Mater.* **2019**, *197*, 428–435. [CrossRef]
38. Feng, P.; Chang, H.L.; Liu, X.; Ye, S.X.; Shu, X.; Ran, Q.P. The significance of dispersion of nano-SiO_2 on early age hydration of cement pastes. *Mater. Des.* **2020**, *186*, 108320. [CrossRef]
39. Reches, Y.; Thomson, K.; Helbing, M.; Kosson, D.S.; Sanchez, F. Agglomeration and reactivity of nanoparticles of SiO_2, TiO_2, Al_2O3, Fe_2O_3, and clays in cement pastes and effects on compressive strength at ambient and elevated temperatures. *Constr. Build. Mater.* **2018**, *167*, 860–873. [CrossRef]
40. Wang, J.B.; Liu, M.L.; Wang, Y.G.; Zhou, Z.H.; Xu, D.Y.; Du, P.; Cheng, X. Synergistic effects of nano-silica and fly ash on properties of cement-based composites. *Constr. Build. Mater.* **2020**, *262*, 120737. [CrossRef]
41. Sun, H.L.; Zhang, X.Z.; Zhao, P.; Liu, D. Effects of nano-Silica particle size on fresh state properties of cement paste. *KSCE J. Civ. Eng.* **2021**, *25*, 2555–2566. [CrossRef]

42. Zhou, S.; Zhang, X.T.; Zhou, H.; Li, D.X. Effects of graphene oxide encapsulated silica fume and its mixing with nano-silica sol on properties of fly ash-mixed cement composites. *Crystals* **2022**, *12*, 144. [CrossRef]
43. Taylor, H.F.W.; Newbury, D.E. An electron-microprobe study of a mature cement paste. *Cem. Concr. Res.* **1984**, *14*, 565–573. [CrossRef]
44. Singh, L.P.; Karade, S.R.; Bhattacharyya, S.K.; Yousuf, M.M.; Ahalawat, S. Beneficial role of nanosilica in cement based materials—A review. *Constr. Build. Mater.* **2013**, *47*, 1069–1077. [CrossRef]
45. Bilir, T.; Gencel, O.; Topcu, I.B. Properties of mortars with fly ash as fine aggregate. *Constr. Build. Mater.* **2015**, *93*, 782–789. [CrossRef]

buildings

MDPI

Article

The Early Age Hydration Products and Mechanical Properties of Cement Paste Containing GBFS under Steam Curing Condition

Baoliang Li [1,*], Zhouyang Tang [1], Binbin Huo [2], Zejun Liu [1], Yongzhen Cheng [1], Baizhan Ding [3] and Peng Zhang [1,*]

[1] Faculty of Architecture and Civil Engineering, Huaiyin Institute of Technology, Huaian 223001, China
[2] State Key Laboratory of Coal Resources and Safe Mining, School of Mines, China University of Mining and Technology, Xuzhou 221116, China
[3] Huaian Construction Engineering Quality Testing Center Co., Ltd., Huaian 223003, China
* Correspondence: lbljndx@126.com (B.L.); zhangpeng87@hyit.edu.cn (P.Z.)

Abstract: The hydration products and strength of cement pastes incorporated with ground blast furnace slag (GBFS) (0% and 20% replacement) have been investigated under steam curing condition (80 °C for 7 h and 7 d) in comparison with normal curing condition (moist curing for 28 d). The results show that, during the initial 80 °C steam curing for 7 h, in addition to the filler effect, GBFS is still involved in cement hydration. The abundant available Al phase and Mg phase in GBFS promote the formation of flake-like hydrotalcite, foil-like C-(A)-S-H gels, as well as equant grain-shaped C-(A)-S-H gels. Prolonging the steam curing time to 7 d further improves the formation of hydrogarnet. Since the formation of both hydrogarnet and hydrotalcite can consume the available Al, steam curing for 7 d seems to favor the formation of low Al C-(A)-S-H gels. In addition, due to the formation of a large amount of hydration products, the influence of 20% GBFS addition on the demolding strength of initial steam-cured cement mortar (80 °C for 7 h) is almost negligible. However, further extending the steam curing time to 7 d increases the strength gap between 20% GBFS blended cement mortar and pure cement mortar, and the related mechanism is discussed.

Keywords: GBFS; steam curing; hydration products; strength

1. Introduction

Prefabricated concrete elements have attracted more attention due to their advantages of shortening construction time, reducing construction cost, and improving the construction quality of buildings [1], and are widely used in cross-sea bridges and municipal engineering. Currently, they account for around 20% of the world's total concrete production. In order to shorten the manufacturing cycle and improve the early strength of prefabricated concrete elements, steam curing is one of the common measures adopted [1,2]. Although steam curing accelerates the early hydration of cement, the "Hot Damage Effect (HDE)" triggered by thermal treatment will cause heterogeneous distribution of hydration products and form more micro-cracks and pores, resulting in higher permeability which is detrimental to the durability of concrete [3–5].

To alleviate the adverse effects of HDE and improve the durability of prefabricated components, previous studies have focused on improving steam curing regime and the use of supplementary cementitious material (SCM) to replace portions of cement. Typical steam curing regime is generally composed of a pre-curing period, heating period, constant temperature curing period, as well as the following cooling period [6]. It is reported that prolonging the time in the pre-curing period, slowing down the heating rate in the heating period, reducing the temperature in the constant temperature curing period, and adopting a lower cooling rate, have been proved to be effective in reducing the adverse effects brought on by steam curing [6–8]. In addition, it should be noted that subsequent curing also plays an important role in the performance development of steam-cured concrete, and a positive correlation between adequate subsequent curing and better macro-performance

Buildings **2022**, *12*, 1746. https://doi.org/10.3390/buildings12101746

has been found. Liu et al. [9] investigated that, in comparison with subsequent air curing, subsequent wet curing (including moist curing, water curing, as well as saturated lime water curing) is competitive in improving the pore structure of steam cured concrete, and the longer the subsequent wet curing time, the more effective it is to improve the durability of steam-cured concrete to a certain extent. In the process of steam curing, the covering measures of the concrete surface are also very important to the durability of concrete. Shi et al. [6] found that since a geotextile can use adsorbed water to replenish the concrete when the concrete is short of water, the concrete covered with a geotextile is denser than that covered with plastic film.

With the improvement of steam curing regimes, the role of SCM in improving the durability of steam-cured concrete has attracted a growing concern. Escalante-Garcia et al. [10] revealed that the raised temperature reduces the hydration degree of neat cement in the longer term; however, the presence of SCM is expected to change its hydration patterns. Wang et al. [11] indicated that fly ash (FA) addition lowers not only the drying shrinkage, but also the autogenous shrinkage of steam-cured concrete. Chen et al. [12] revealed that adding both metakaolin and limestone powder can reduce the sorptivity and improve the mechanical properties of the steam-cured concrete. Liu et al. [13] presented that in comparison with steam curing 80 °C for 8 h, steam curing 60 °C for 11 h can help concrete incorporated with phosphorus slag gain an ideal demolding strength and chloride permeability. The authors' investigation showed that adding lithium slag can improve demolding strength, ferronickel slag incorporation can promote the late strength, while steel slag addition is detrimental to the strength of steam-cured concrete [14–16]. Although these three SCMs have little influence on hydration products, they can improve the sulfate resistance of steam-cured concrete. However, compared with the SCMs mentioned above, ground blast furnace slag (GBFS) is the most widely used in prefabricated components at present [17–19].

The abundant amorphous phases endow GBFS with high pozzolanic reactivity, which is helpful to repair the thermal damage and compensate for strength loss caused by elevated temperature curing [20]. Escalante-Garcia et al. [10] reported that the presence of GBFS accelerates the hydration of alite from very early stages. A lower CH content appeared in 60 °C cured GBFS blended cement paste compared to that cured at normal curing suggested that the elevated temperature favors the pozzolanic reaction of GBFS in the early stages of hydration. Barnett et al. [21] implied that the early age strength of mortar blended with high level GBFS is much more sensitive to temperature; even a 10 °C increase can considerably enhance the mortar strength, so that its strength gained at 40~50 °C is basically equivalent to that pure cement mortar after 3 days. Yu et al. [22] found that the combination of GBFS and FA not only reduced the temperature difference between inside and outside of the specimen, but also lessened the concrete expansion caused by steam curing. Zhuang et al. [23] noted that large amounts of ultrafine slag contribute to better demolding strength, higher sulfate resistance, as well as lower permeability of steam-cured concrete.

Although GBFS addition can improve the durability of steam-cured concrete, the effect of GBFS on the early properties of steam-cured concrete, especially the early hydration products and mechanical properties, is still unclear. Generally, precast concrete is used immediately after demolding; therefore, the effect of GBFS on early age hydration products and mechanical properties is very important to understand the action mechanism of GBFS in steam-cured concrete.

GBFS contains around 10.6~15.1% Al_2O_3 and 8.0~9.4% MgO [1,20–23]. How such a large amount of Al_2O_3 and MgO affect the hydration products and microstructure of concrete during steam curing is rarely reported. Therefore, the hydration product composition and mechanical properties of GBFS-incorporated cement paste were studied under the conditions of steam curing (80 °C for 7 h and 7 d) compared with that of normal curing (standard curing for 28 d). This investigation revealed that the GBFS addition promoted the uptake of Al by C-S-H gels and the formation of hydrotalcite at elevated temperatures, and that the extension of steam curing time would further promote the production of hydrogarnet. These results are helpful for understanding the action mechanism of GBFS in steam-cured concrete.

2. Materials and Methods

2.1. Raw Materials

The cement used was PII52.5 Portland cement (PC) with loss-on-ignition (LOI) of 2.4% and specific surface area of 356 m^2/kg. Type S95 GBFS with LOI of 2.1% and specific surface area of 536 m^2/kg was used. The chemical compositions of PC and GBFS tested by XRF are shown in Table 1. The particle size distribution curves of cement and GBFS determined by a Microtrac S3500 laser particle size analyzer are shown in Figure 1. The maximum particle size of GBFS was 44.7 μm, and the average particle size was 6.34 μm, which was much smaller than the corresponding value (422.2 μm and 16.1 μm) in PC.

Table 1. Chemical composition of PC and GBFS, wt.%.

Oxide	CaO	SiO_2	Al_2O_3	SO_3	Fe_2O_3	MgO	Na_2O	K_2O
PC	64.47	20.87	4.87	2.52	3.59	2.13	0.11	0.65
GBFS	44.40	29.56	14.87	2.98	0.40	6.72	-	0.49

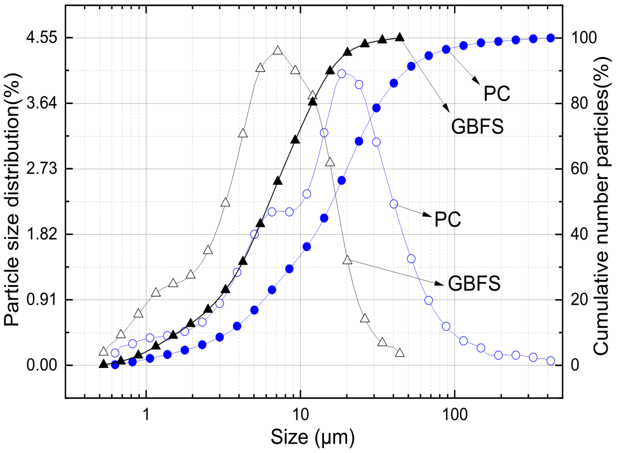

Figure 1. Particle size distribution of PC and GBFS.

The XRD analysis of the GBFS is shown in Figure 2. The GBFS was mainly composed of amorphous phase, which is responsible for its latent hydraulic or pozzolanic reactivity. Generally, the average amount of glassy phase in GBFS is often above 90% [24]; thus, the reactivity of GBFS was higher than other SCM. The 28 d strength activity index of GBFS used in this investigation reached 103%, which meets the requirements of Type S95 GBFS.

2.2. Sample Preparation and Test Methods

Previous studies have shown that the optimal substitution level of GBFS in cement is 10~20% [25]; therefore, 0% and 20% replacement were considered in this investigation. Under the condition of water-binder ratio of 0.3 [26], the cement paste was prepared according to the mix proportion in Table 2. In order to simulate the actual curing regime on site and activate the reactivity of GBFS, 80 °C steam curing for 7 h (S7h, steam curing at constant 80 °C for 7 h), and 80 °C steam curing for 7 d (S7d, steam curing at constant 80 °C for 7 d) were adopted in comparison with the condition of standard curing for 28 d (N28d, cured at 20 ± 2 °C, and relative humidity larger than 95% for 28 d). The corresponding steam curing regime can be referred to in Figure 3. The hydration of specimens at corresponding ages was terminated with anhydrous ethanol, then dried at 60 °C for 24 h in a vacuum-drying oven. Subsequently, the composition of hydration products in the cement paste containing GBFS were determined by XRD, SEM-EDS, and TG-DTG.

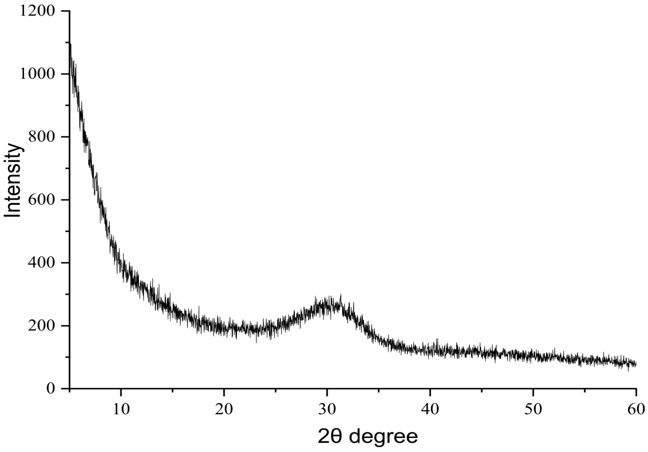

Figure 2. XRD result of GBFS.

Table 2. Mix proportion (wt. %) and physical properties of GBFS blended cement.

Sample	PC	GBFS	Water Demand (wt. %)	Setting Times (h: min)	
				Initial	Final
Ref	100	0	27.4	2:52	3:57
G20	80	20	28.0	2:45	3:32

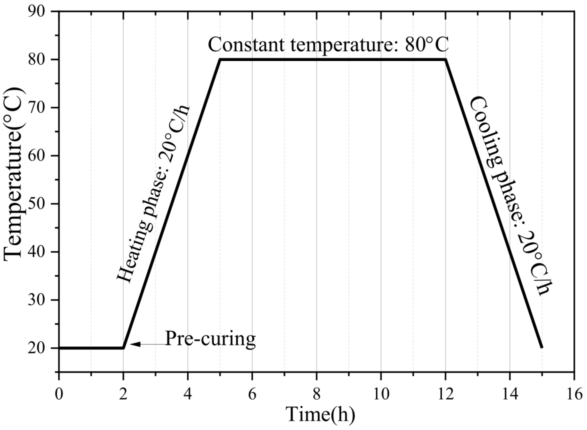

Figure 3. The regime for steam curing.

According to the mix proportion in Table 2, mortars with the same curing condition were prepared (binder: water: standard sand = 1:0.5:3). The mechanical properties of cement mortar were carried out according to Chinese standard GB/T 17671-1999. For steam-cured samples, mechanical properties were tested after demolding, whereas strength tests for standard cured samples were performed after 28 d of moist curing. The basic physical properties of PC and GBFS blended cement are also shown in Table 2, in which the shorter setting time of G20 is related to the larger specific surface area and the higher content of SO_3 in GBFS.

XRD test: the composition of GBFS and the hydration products in hardened cement paste were checked using a D8-Discover X-ray diffractometer (XRD) using CuKa1 radiation, 40 kV voltage, and 36 mA current with the scanning speed of 3°/min.

SEM-EDS test: the fresh and dry fracture surfaces of mortars were observed using a Sirion (FEI) field emission scanning electron microscope (SEM), and the related compositions were checked by energy dispersive X-ray spectra (EDS). It is worth noting that the samples were dried and sprayed with gold before the SEM-EDS test.

TG-DTG test: STA 449 F3 Jupiter® was used to carry out TG/DTG by heating cement paste from room temperature to 1000 °C at 10 °C/min under nitrogen atmosphere.

3. Results

3.1. XRD Analysis of Hydration Products

Figure 4 shows the XRD patterns of the hydration products of pure cement paste and composite cement paste blended with 20% GBFS, under steam curing condition and 28 d standard curing condition.

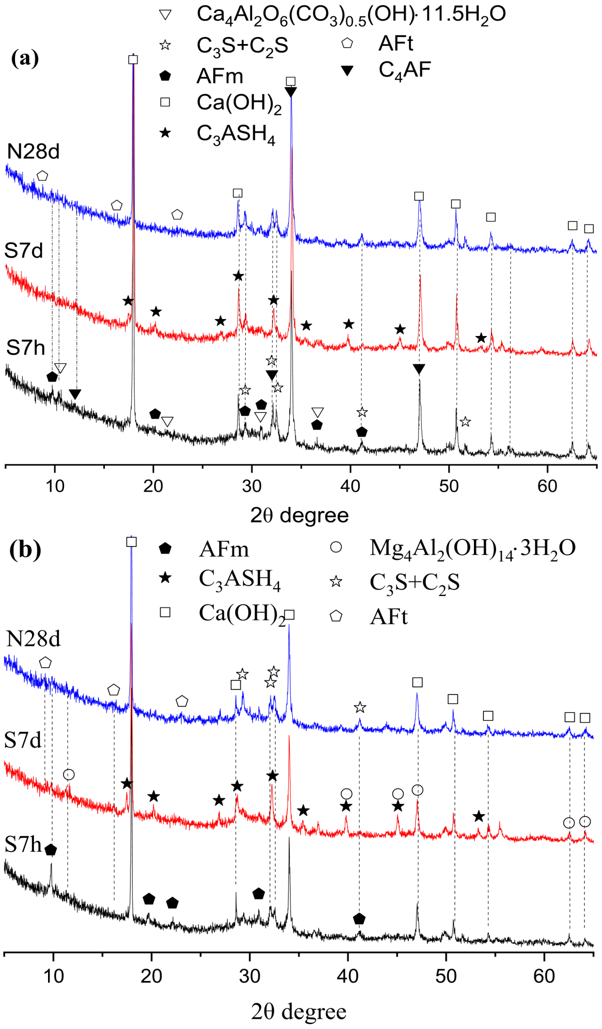

Figure 4. XRD of cement pastes under various curing conditions (**a**) Ref; (**b**) G20.

In addition to the C-S-H gels, the hydration products of pure cement paste (Figure 4a) under the condition of steam curing for 7 h included $Ca(OH)_2$, monosulfoaluminate hydrate (AFm), and semi-carbonate ($Ca_4Al_2O_6(CO_3)_{0.5}(OH)\cdot 11.5H_2O$). Different from steam curing for 7 h, hydrogarnet (C_3ASH_4) was formed in pure cement paste under steam curing for 7 d, while ettringite (AFt) was formed under standard curing for 28 d. Since AFt is unstable at elevated temperatures, there is no AFt produced under steam curing. Limestone powder is a common filler for cement, and consequently, the formation of semi-carbonates was found in pure cement paste, regardless of curing conditions.

From Figure 4b, it can be seen that the main hydration products of blended cement paste incorporated with GBFS were C-S-H gel, CH, AFt, AFm, and $Mg_4Al_2(OH)_{14}\cdot 3H_2O$ (hydrotalcite) at normal curing for 28 d, which is consistent with the study of Chen et al. [27].

Apart from C-S-H gels, the hydration products of S7h G20 also presented CH, AFm, and hydrotalcite. When the steam curing time was extended to 7 d, hydrogarnet appeared too. Nonetheless, AFt is unstable and will convert into AFm at 80 °C, the traces of AFt were still observed, which may be related to the high SO_3 content in GBFS [14].

The reactivity of GBFS principally depends on its source, chemical composition, pretreatment process (e.g., the content of amorphous phases, structure, cooling rate, particle size, etc.), and the pore solution of hardened cement paste [28]. In addition, it also depends on the curing temperature and the replacement level of GBFS. Under the conditions of higher curing temperature (>50 °C) and lower substitution ratio (<20%), cement paste can release a large amount of $Ca(OH)_2$, under such a high temperature and high alkali environment, GBFS dissolves quickly and has a high reactivity [29]. In this investigation, the more amorphous phase and higher specific surface area ensured the higher reactivity of GBFS under 80 °C steam curing [30]. In particular, GBFS contains a high content of reactive Al and Mg phases, which can affect the composition and type of hydration products; in consequence, hydrotalcite is generated under the condition of steam curing. It has been reported that hydrotalcite has a good chloride ion binding ability [31]. Moreover, the formation of hydrotalcite consumes the available Al that should be involved in AFm precipitation; thus, it reduces the content of AFm which can react with the intruded sulfate, and thereby improves the sulfate resistance [32].

Hydrogarnet (C_3AH_6) is transformed from metastable phases CAH_{10}, C_2AH_8, and C_4AH_{13}. This conversion rate is positively correlated with temperature: this conversion rate is slow at 5 °C, and very fast at temperatures above 50 °C. This transformation will lead to the decrease of solid volume and the increase of porosity [33]; therefore, the formation of hydrogarnet will result in the loss of late strength of high-aluminate cement or high-temperature cured concrete. It is worth noting that, due to the high content of SiO_2 in cement and the use of Si-rich SCMs, hydrogarnet in cement and concrete often exists in the form of C_3ASH_4, and its chemical formula is between C_3AH_6~C_3AS_3 [34]. Based on this, in order to avoid the formation of hydrogarnet phase, high-aluminate cement is often mixed with Si-rich additives, such as 40~60% GBFS or 17~20% natural zeolite [35], so that the C_2ASH_8 phase is preferred to form instead of hydrogarnet, thus avoiding the reduction of strength. At the same time, increasing the ratio of metakaolin to cement or the ratio of reactive Si to reactive Al in composite cement at room temperature is also conducive to the generation of C_2ASH_8 phase instead of C_4AH_{13}, thus inhibiting the transformation of C_4AH_{13} to hydrogarnet [36]. Nevertheless, whether increasing GBFS content can avoid or reduce the formation of hydrogarnet in blended cement under long-term high temperature curing needs further investigation.

3.2. Morphology and Composition of Hydration Products Determined by SEM-EDS

3.2.1. Hydration Products under 80 °C Steam Curing for 7 h

The hydration products of pure cement paste and composite cement paste mixed with 20% GBFS under the condition of steam curing for 7 h are shown in Figures 5 and 6, respectively. As can be seen from Figure 5, the hydration products of steam-cured 7 h pure cement paste were mainly loose fibrous C-S-H gels (Figure 5a), flake CH (Figure 5c), accompanied by many pores (Figure 5a,c).

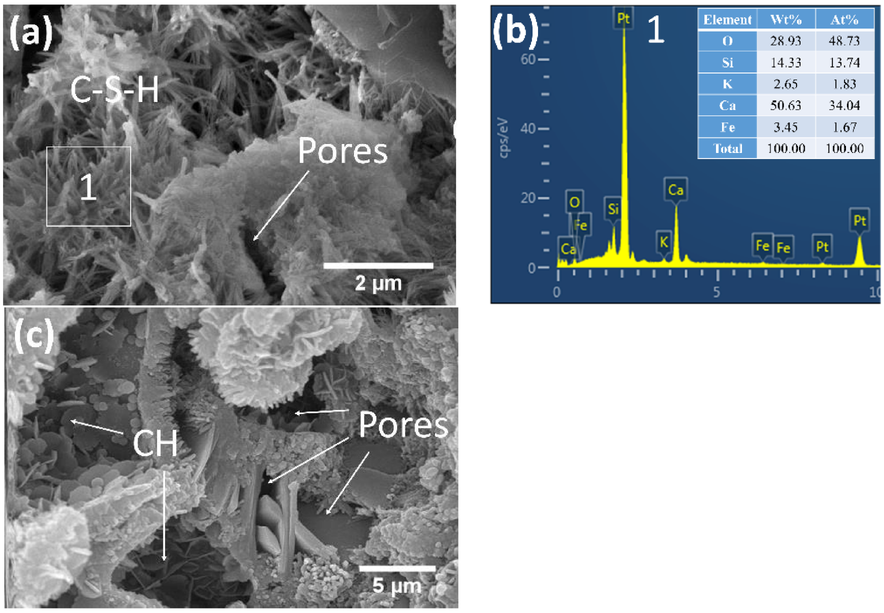

Figure 5. SEM images of pure cement paste after 80 °C steam curing for 7 h, (**a**) fibrous C-S-H gels; (**b**) EDS result of area 1; (**c**) pores. Note: Wt% represents the mass percentage, At% represents the atomic percentage.

As shown in Figure 6, in addition to fibrous C-S-H gels (Figure 6a), foil-like and equant grain-shaped C-S-H gels also appeared in cement-GBFS composite binder (Figure 6c). As can be seen from Figure 6d, the presence of Al and Mg have influenced the formation of C-S-H gels, which are considered to be responsible for the morphology change of C-S-H gels. In addition, flake-like hydration products (Figure 6e) were produced. According to its EDS result (Figure 6f), it contains high contents of Mg and Al, and its Mg/Al ratio is 1.67, close to 2; accordingly, it can be speculated that it is hydrotalcite ($Mg_4Al_2(OH)_{14}{\cdot}3H_2O$), which can be confirmed by the XRD results shown in Figure 4b. However, due to the short hydration time, there are still many pores in the GBFS-cement composite binder, as shown in Figure 6g.

Under the condition of 80 °C steam curing, a large amount of OH^- released by cement hydration can quickly invade into the network structure of amorphous phase in GBFS, dissolve Ca^{2+} and Mg^{2+} in the Ca-rich phase, and interact with Si^{4+} and Al^{3+} in the Si-rich phase, and thereby form C-S-H and C-A-H [37]. Additionally, in comparison with C-S-H gels in pure cement paste (Figure 5b), the uptake of Al in C-S-H gels in GBFS-blended cement paste is more evident and has been reported [38], which suggested that the C-(A)-S-H gels formation is easier in GBFS-blended cement under steam curing. Although the trace of Mg was also found in the EDS results (Figure 6b,d), it was still difficult to prove the uptake of Mg by C-S-H gels due to the different structure between M-S-H and C-S-H gels [38], and further study is needed to determine the role of Mg in the C-S-H gels formation. Moreover, according to the EDS results in S7h (Figures 5b and 6b,d), the Ca/Si ratio of C-S-H gels was around 2.17~2.49, indicating that the hydration degree of cement paste after steam curing for 7 h was relatively high, which is related to the accelerated cement hydration at steam curing.

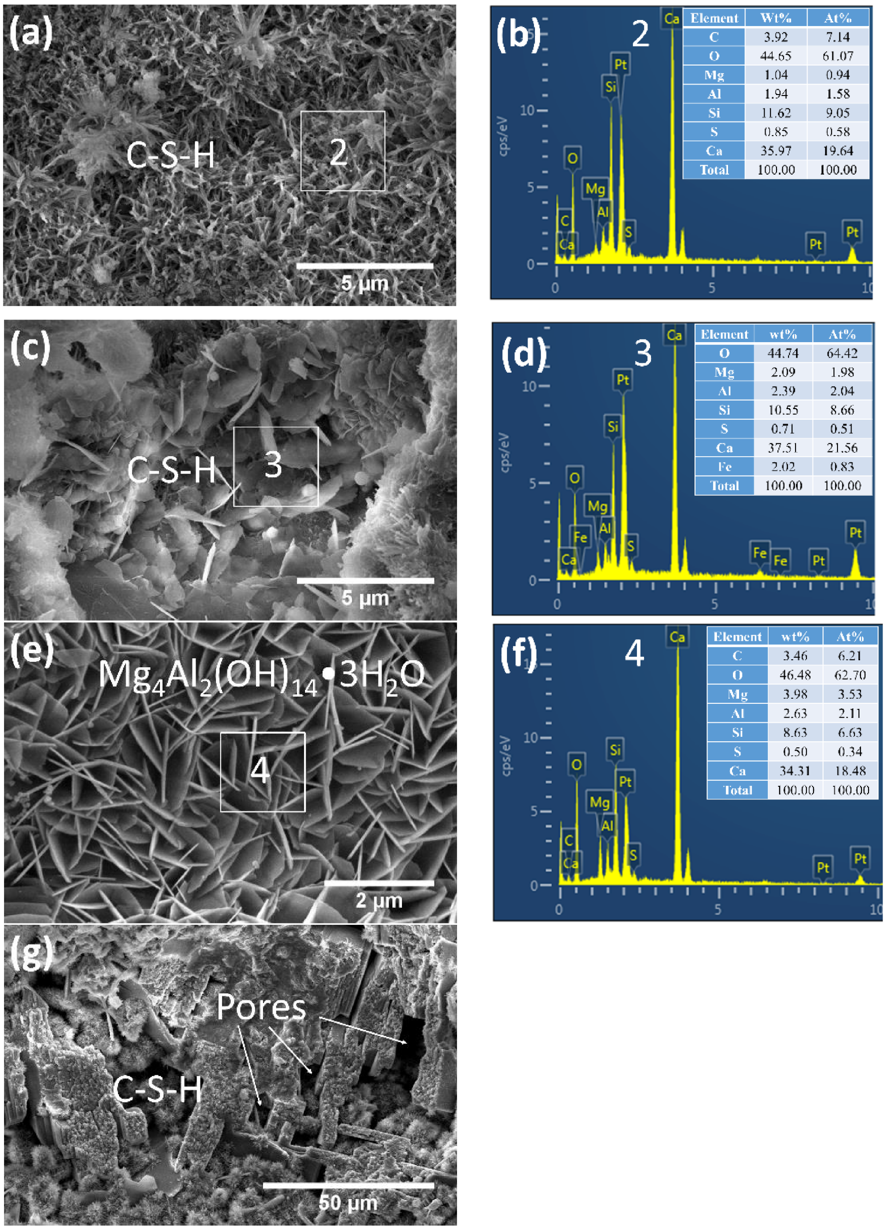

Element	Wt%	At%
C	3.92	7.14
O	44.65	61.07
Mg	1.04	0.94
Al	1.94	1.58
Si	11.62	9.05
S	0.85	0.58
Ca	35.97	19.64
Total	100.00	100.00

Element	wt%	At%
O	44.74	64.42
Mg	2.09	1.98
Al	2.39	2.04
Si	10.55	8.66
S	0.71	0.51
Ca	37.51	21.56
Fe	2.02	0.83
Total	100.00	100.00

Element	wt%	At%
C	3.46	6.21
O	46.48	62.70
Mg	3.98	3.53
Al	2.63	2.11
Si	8.63	6.63
S	0.50	0.34
Ca	34.31	18.48
Total	100.00	100.00

Figure 6. SEM images of cement-GBFS composite binder after 80 °C steam curing for 7 h, (**a**) fibrous C-S-H gels; (**b**) EDS result of area 2; (**c**) foil-like and equant grain-shaped C-S-H gels; (**d**) EDS result of area 3; (**e**) flake-like hydrotalcite; (**f**) EDS result of area 4; (**g**) pores.

3.2.2. Hydration Products under 80 °C Steam Curing for 7 d

The hydration products of pure cement paste and cement-GBFS composite binder under steam curing for 7 days are shown in Figures 7 and 8, separately. The hydration products of pure cement paste were mainly fibrous C-S-H gels (Figure 7a) and flake CH (Figure 7c), and obvious cracks occurred after a long time of steam curing (Figure 7c). In addition, the hydration products of spherical particles with the approximate size of 1 μm were generated, as shown in Figure 7c. Combined with the morphology [39] and the XRD results in Figure 4a, it can be confirmed that it is hydrogarnet.

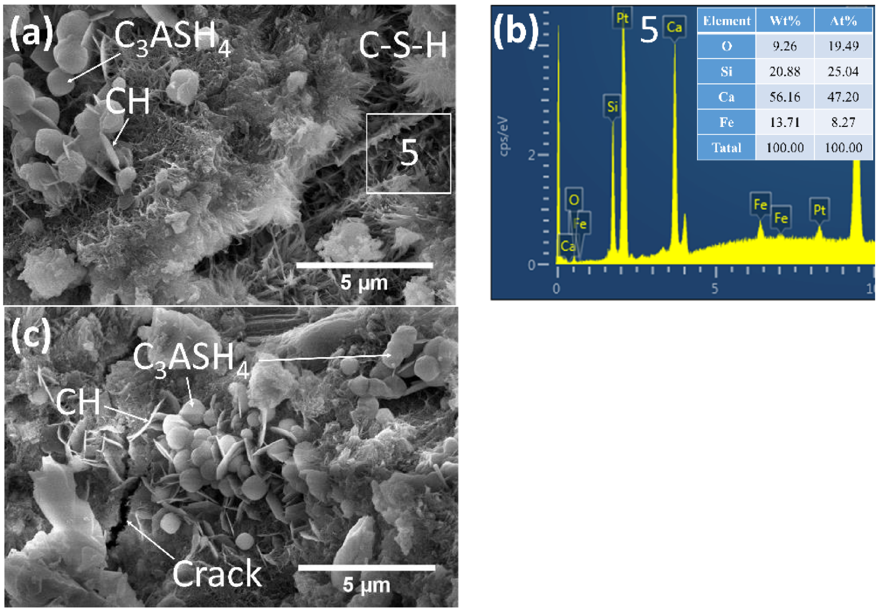

Element	Wt%	At%
O	9.26	19.49
Si	20.88	25.04
Ca	56.16	47.20
Fe	13.71	8.27
Tatal	100.00	100.00

Figure 7. SEM images of pure cement paste after 80 °C steam curing for 7 d, (**a**) fibrous C-S-H gels; (**b**) EDS result of area 5; (**c**) spherical hydrogarnet and crack.

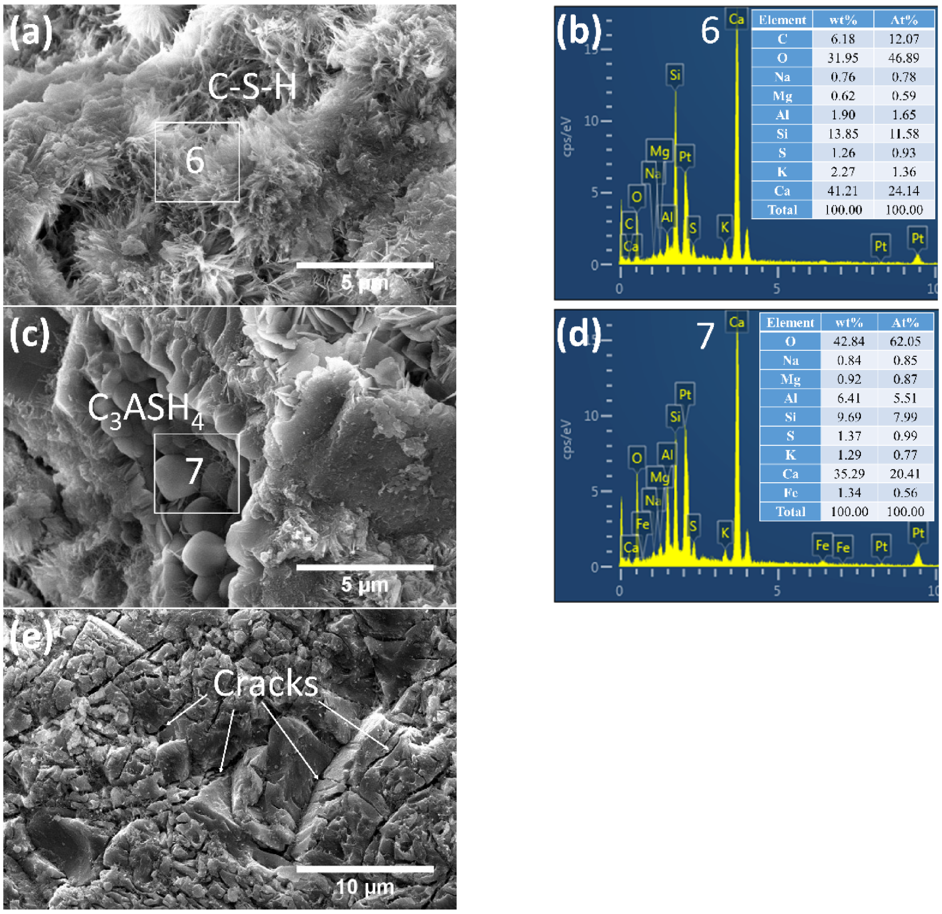

Element	wt%	At%
C	6.18	12.07
O	31.95	46.89
Na	0.76	0.78
Mg	0.62	0.59
Al	1.90	1.65
Si	13.85	11.58
S	1.26	0.93
K	2.27	1.36
Ca	41.21	24.14
Total	100.00	100.00

Element	wt%	At%
O	42.84	62.05
Na	0.84	0.85
Mg	0.92	0.87
Al	6.41	5.51
Si	9.69	7.99
S	1.37	0.99
K	1.29	0.77
Ca	35.29	20.41
Fe	1.34	0.56
Total	100.00	100.00

Figure 8. SEM images of cement-GBFS composite binder after 80 °C steam curing for 7 d, (**a**) fibrous C-S-H gels; (**b**) EDS result of area 6; (**c**) spherical hydrogarnet; (**d**) EDS result of area 7; (**e**) cracks.

The morphology of C-S-H gels in S7d G20 was mainly fibrous (Figure 8a). In addition, 1–2 µm granular hydration products (Figure 8c) appeared, whose Ca/Al ratio (3.70) and

Al/Si ratio (0.69) (Figure 8d) were close to the proportion of each element in C_3ASH_4. Consequently, combined with the results shown in Figure 4, it can be determined as hydrogarnet. However, it should be noted that the particle size of hydrogarnet in S7d G20 is larger than that in S7d Ref (1 μm), which may be related to the sufficient available Al in GBFS. At the same time, more obvious cracks in S7d G20 appeared, as shown in Figure 8e. In addition to long-term high temperature steam curing, whether it is also related to the production of more hydrogarnet needs to be further studied. Although steam curing is helpful for the uptake of Al by C-S-H gels, the prolongation of steam curing time seems to be more conducive to the formation of low-Al C-(A)-S-H gels (lower Al/Si ratio of C-(A)-S-H in Figure 6b,d compared to that in Figure 8b) which is attributed to more available Al participation in the formation of hydrotalcite and hydrogarnet at this time [40]. Furthermore, according to the EDS results in S7d (Figures 7b and 8b), the Ca/Si ratio of C-S-H gels was around 1.88~2.08, lower than that in S7h, indicating that the hydration degree of cement paste under S7d is higher than S7h, which is undoubtedly related to the prolonged steam curing time. Generally, the average polymerization degree of C-S-H gels increases when its Ca/Si ratio decreases [41], and at the same time, the compressive strength of the C-S-H paste also increases [42].

3.2.3. Hydration Products under 28 d Standard Curing

Hydration products of pure cement paste and cement-GBFS composite binder are shown in Figures 9 and 10, respectively. More hydration products (Figure 9a) appeared in pure cement paste after 28 d normal curing, and the C-S-H gel interwoven with CH made the structure relatively compact (Figure 9b).

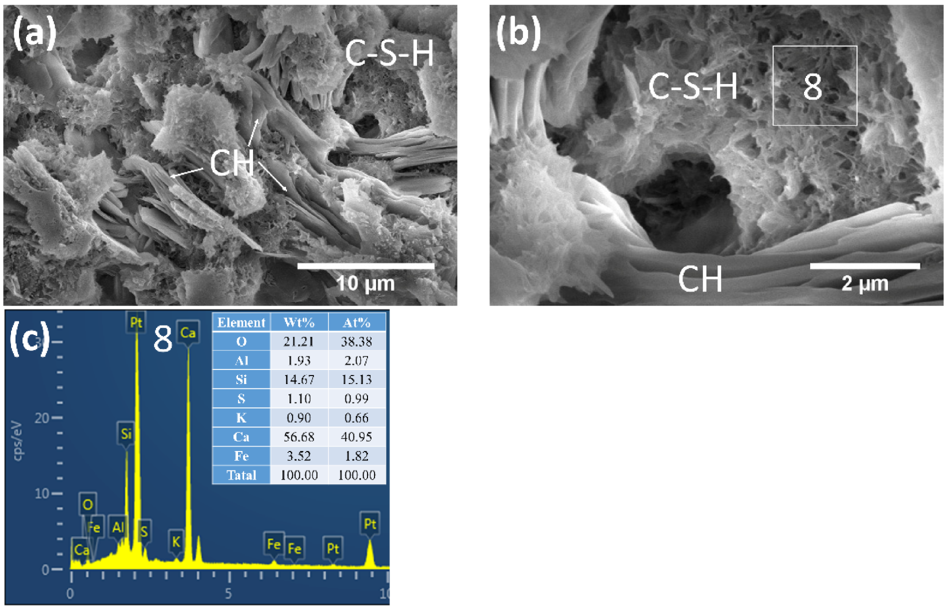

Element	Wt%	At%
O	21.21	38.38
Al	1.93	2.07
Si	14.67	15.13
S	1.10	0.99
K	0.90	0.66
Ca	56.68	40.95
Fe	3.52	1.82
Tatal	100.00	100.00

Figure 9. SEM images of pure cement paste after standard curing for 28 d, (**a**) reticular C-S-H gels and CH; (**b**) reticular C-S-H gels and CH; (**c**) EDS result of area 8.

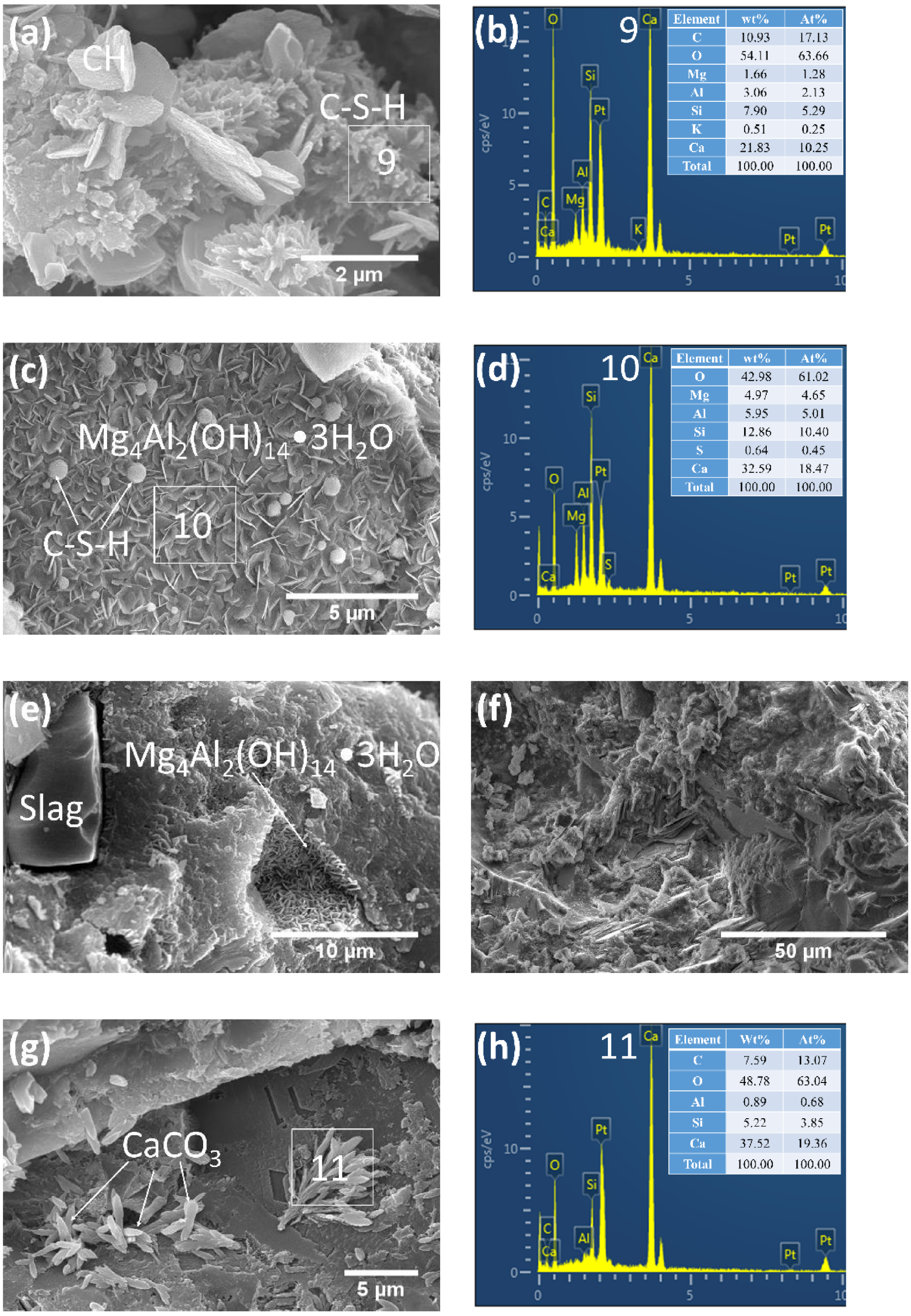

Element	wt%	At%
C	10.93	17.13
O	54.11	63.66
Mg	1.66	1.28
Al	3.06	2.13
Si	7.90	5.29
K	0.51	0.25
Ca	21.83	10.25
Total	100.00	100.00

Element	wt%	At%
O	42.98	61.02
Mg	4.97	4.65
Al	5.95	5.01
Si	12.86	10.40
S	0.64	0.45
Ca	32.59	18.47
Total	100.00	100.00

Element	Wt%	At%
C	7.59	13.07
O	48.78	63.04
Al	0.89	0.68
Si	5.22	3.85
Ca	37.52	19.36
Total	100.00	100.00

Figure 10. SEM images of cement-GBFS composite binder after standard curing for 28 d, (**a**) fibrous C-S-H gels; (**b**) EDS result of area 9; (**c**) flake-like hydrotalcite and quant grain-shaped C-S-H gels; (**d**) EDS result of area 10; (**e**) flake-like hydrotalcite; (**f**) dense microstructure; (**g**) tadpole-like $CaCO_3$; (**h**) EDS result of area 11.

Different from C-S-H gels in pure cement paste, fibrous and equant grain-shaped C-S-H (Figure 10a,c) and CH with smaller particle size (Figure 10a) appeared in standard-cured GBFS-blended cement paste. Furthermore, flake-like hydrotalcite was observed in Figure 10c,e, which agrees with the above XRD results. In accordance with the research of most studies, adding mineral powder can reduce the porosity of concrete and densify its microstructure (Figure 10f). It is interesting to note that tadpole-like and fibrous products also were produced in GBFS-mixed cement paste (Figure 10g). It can be seen from Figure 10h that this product was mainly composed of C, Ca, and O; thus, it can be determined as $CaCO_3$. The formation of tadpole-like $CaCO_3$ may be related to the use of anhydrous ethanol to terminate the hydration of the sample in this investigation [43]. It is well known that $CaCO_3$ usually has three types of structures: calcite, aragonite, and vaterite, with cubic, spherical, fibrous, flake, and petal-like morphologies, etc. [43]. The morphology of $CaCO_3$ is mainly affected by the pH value, foreign ions (Mg^{2+}, etc.), organic additives (alcohols, acids, amino acids, proteins, and sugars), and the supersaturation degree of the solution [43], of which alcohol additives mainly affect the morphology of $CaCO_3$ by affecting the dielectric constant of the medium, the attraction between ions and the interaction between solute and solvent [43].

Furthermore, according to the EDS results in N28d (Figures 9c and 10b), the Ca/Si ratio of C-S-H gels was around 1.94~2.71, which is similar to that in S7h, but lower than that in S7d, indicating that the hydration degree of cement paste in N28d is similar to that of S7h, but slightly lower than that of S7d.

3.3. Hydration Products Determined by TG/DTG Analysis

Figure 11 shows the TG/DTG curve of pure cement paste and GBFS-blended cement pastes under different curing conditions. As can be seen from Figure 11, under the conditions of S7h and N28d, the type of hydration products in Ref and G20 are basically the same. In comparison with the condition of S7h and N28d, the weight loss of pure cement paste at 300~390 °C under the condition of S7d is more obvious (Figure 11a), and it is reported that the weight loss between this interval is mainly caused by the decomposition of hydrogarnet [44], which closely matches the above XRD and SEM results. However, compared with Ref, the weight loss in G20 at 300~390 °C is more significant, which is related to the formation of hydrotalcite in addition to the hydrogarnet generation in G20 under S7d curing conditions. Furthermore, it can be seen that, due to the high SO_3 content in GBFS, there is still a small amount of ettringite in the steam-cured GBFS-mixed cement pastes.

The non-evaporable water and CH content of Ref and G20, calculated by using the mass loss of samples in specific temperature ranges in Figure 11, are tabulated in Table 3 [14]. Under the conditions of S7h and N28d, the non-evaporable water and CH content of G20 were basically the same, indicating that early steam curing promoted the reaction between cement and GBFS, which made its hydration degree equal to that of standard-cured for 28 d.

Table 3. Total mass loss, non-evaporable water, and CH content of cement pastes, wt.%.

Samples		Mass Loss	Non-Evaporable Water	CH
Ref	S7h	18.43	20.13	19.34
	S7d	20.75	23.72	24.07
	N28d	20.73	23.69	20.00
G20	S7h	19.29	21.52	13.40
	S7d	21.45	24.93	18.74
	N28d	19.26	21.47	13.29

In addition, under the conditions of S7h, S7d, and N28d, the non-evaporable water of G20 reached 106.9%, 105.1%, and 90.6% that of Ref, respectively, revealing that GBFS addition promotes the hydration of steam-cured pure cement paste, which is related to both the high content of SO_3 and the high activity of GBFS [45]. Under the above three curing conditions, the CH content of G20 was 69.3%, 77.9%, and 66.5% that of Ref, respectively. It suggests that GBFS participates in the cement hydration and consumes CH under steam curing condition, especially at steam curing for 7 h; however, prolonging the steam curing time from 7 h to 7 d is not conducive to the further reduction in the ratio of CH content in G20 to that in Ref (77.9%).

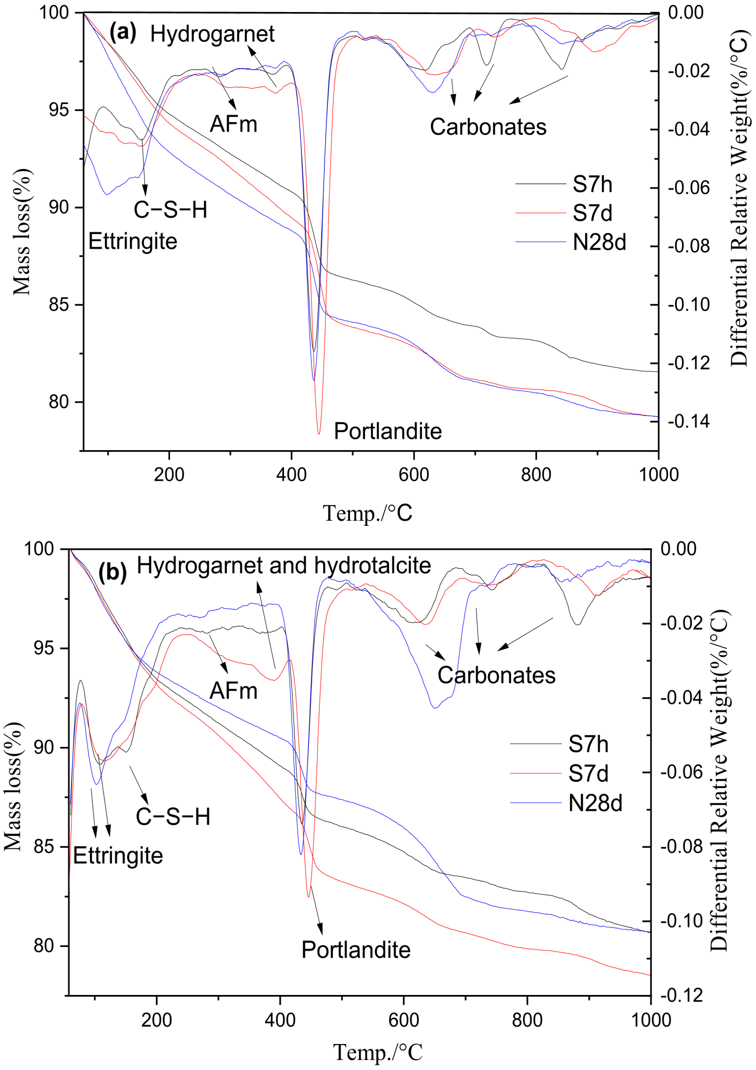

Figure 11. TG / DTG curves of Ref (**a**) and G20 (**b**) under different curing conditions.

3.4. Mechanical Property

The strengths of GBFS-blended cement mortar and pure cement mortar under various curing conditions are shown in Figure 12. It can be seen that the compressive strength of G20 mortar under three curing conditions were all lower than that of Ref mortar. The strength activity index (the strength ratio of G20 mortar to Ref mortar under the same curing condition) under various curing conditions was 92.6%, 82.0%, and 99.7%, respectively, while the corresponding flexural strength activity index was 103.1%, 81.9%, and 109.1%, separately. Despite the fact that the compressive strength activity index of S7h G20 mortar was lower than that of N28d, the difference was slight, indicating that early steam curing improves the hydration activity of GBFS, which is in good agreement with the result of non-evaporable water in Table 3. Although the non-evaporable water in S7d G20 is higher than that of S7d Ref (Table 3), the strength of G20 mortar was much lower than Ref, regardless of compressive strength or flexural strength. This may be related to the formation of a large number of hydrogarnet and more micro-cracks produced in GBFS-blended cement mortar during long-term steam curing (Figure 8e). It should be noted that, compared with compressive strength, flexural strength is more sensitive to cracks; therefore, although the compressive strength of G20 in S7d is higher than that in S7h, the flexural strength of G20 in S7d is less than that in S7h.

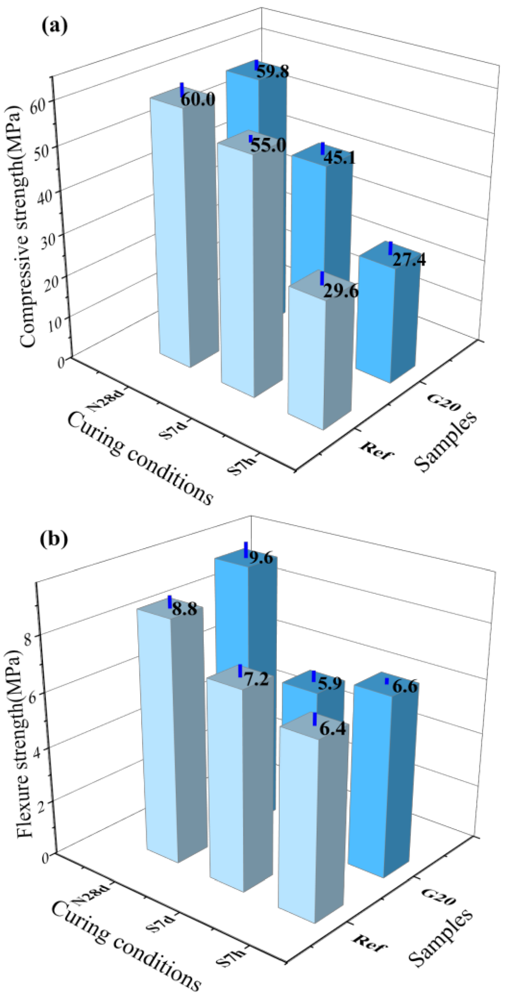

Figure 12. Strength of GBFS blended cement mortars, (**a**) compressive strength, (**b**) flexural strength.

Under the condition of standard curing for 28 d, G20 has the highest strength activity index including compressive strength and flexural strength, which is related to both the high content of non-evaporable water (Table 3) and its improved dense microstructure, as shown in Figure 10f. In addition, the G20 mortar has a high flexural strength under the conditions of S7h and N28d, which is attributed to the lower CH content, smaller crystal size of CH (Table 3 and Figure 10a) and the improved adherence at the aggregate-paste interface [30].

4. Discussion

The abundant amorphous phase content and the high specific surface area guarantee the high reactivity of GBFS; therefore, besides the filler effects, GBFS can also participate in cement hydration during 80 °C steam curing for 7 h. The presence of a high content of available Al_2O_3 and MgO not only changes the composition, but also changes the morphology of hydration products, so that hydrotalcite and the foil-like C-S-H gels were formed. Hydrotalcite can not only consolidate chloride ions, but also can consume the available Al phase required by ettringite formation during the ingress of sulfate; therefore, it is helpful to improve the durability of concrete [31,32]. In addition, a large amount of Al_2O_3 in GBFS will inevitably take part in the precipitation of C-S-H gels and form C-(A)-S-H gels under the condition of steam curing, so as to avoid being further sulfate attacked; therefore, the formation of C-(A)-S-H gels is also conducive to the improvement of sulfate resistance [15]. In addition, although the non-evaporable water of G20 under the conditions of S7h and N28d are basically the same, the strength of S7h G20 is much lower than N28d G20 due to the existence of pores under steam curing condition (Figure 6g).

Although the prolongation of steam curing time can improve the non-evaporable water, it also brings the risk of hydrogarnet (C_3ASH_4) formation, especially for the cement paste mixed with GBFS. Due to the large amount of available Al phase in GBFS, there is a high probability of aluminate hydrate formation which can be further converted to hydrogarnet in GBFS-mixed cement paste at elevated temperature. It is reported that hydrogarnet formation will cause the reduction of solid phase volume and increase the porosity of concrete [33], which is harmful to the strength improvement and durability of concrete. Accordingly, even though the hydration products of S7d G20 is more abundant (Table 3), its strength is still much lower than that of S7d Ref. Moreover, prolonging the steam curing time will also lead to the increase of cracks and is not conducive to the durability of concrete. Since the formation of hydrotalcite and hydrogarnet can consume the available Al, steam curing for 7 d seems to be more conducive to the formation of C-(A)-S-H with lower Al content than steam curing for 7 h in GBFS-blended cement paste [41].

Under standard curing for 28 d, the structure of G20 is denser and its strength is basically the same as that of Ref, due to both the pozzolanic effect and filler effect of GBFS. In addition, it is worth noting that GBFS incorporation can not only reduce the amount of CH, but also reduce the particle size of CH, so as to improve the structure of the interfacial transition zone and improve the flexural strength of G20 cured under both S7h and N28 conditions.

5. Conclusions

This study investigated the influence of GBFS with high content Al_2O_3 and MgO on the early age hydration products and mechanical properties of steam-cured concrete. The hydration products and mechanical properties of cement paste blended with GBFS (0% and 20% replacement) were studied under steam curing conditions (80 °C for 7 h and 7 d) in comparison with standard curing conditions for 28 d. According to the above results, the conclusions are as follows:

(1) GBFS addition promotes the formation of flake-like hydrotalcite and foil-shaped, equant grain-shaped C-S-H gels, of which hydrotalcite helps to improve the durability of concrete. However, extending the steam curing time to 7 days, more hydrogarnet with larger sizes are further formed due to the higher content of available Al in the GBFS. The generation of hydrogarnet will induce the formation of cracks and increase the porosity, which is detrimental to strength development and durability of concrete.

(2) The enhanced uptake of Al by C-S-H gels in GBFS-blended cement paste under steam curing promotes the formation of C-(A)-S-H gels, and thereby reduces the Al phase that can react with sulfate under sulfate attack, which is helpful to improve the sulfate resistance of concrete. However, since the formation of hydrotalcite and hydrogarnet reduces the available Al, the prolongation of steam curing time (to 7 d) seems to be more conducive to the formation of low Al C-(A)-S-H gels.

(3) The non-evaporable water and CH content of GBFS-blended cement paste are basically the same under 80 °C steam curing for 7 h and standard curing for 28 d, indicating that steam curing can significantly accelerate the interaction between cement and GBFS. Under the above three curing conditions, the compressive strength of G20 mortar is 92.6%, 82.0%, and 99.7% that of pure PC mortar, respectively, while the corresponding values for flexural strength are 103.1%, 81.9%, and 109.1%, separately. This indicates that 20% GBFS addition has almost no negative effect on the demolding strength under initial 80 °C steam curing for 7 h; however, extending the steam curing time to 7 d increases the strength gap between 20% GBFS-blended cement mortar and pure cement mortar, which is related to the formation of hydrogarnet and cracks.

Author Contributions: B.L.: conceptualization, data curation, investigation, methodology, validation, visualization, writing—original draft, writing—review &editing. Z.T.: data curation, software, investigation, writing—original draft, writing—review &editing. B.H.: formal analysis, investigation, validation, writing—original draft. Z.L.: formal analysis, methodology, validation, writing—review

&editing. Y.C.: formal analysis, methodology, validation, writing—original draft. B.D.: funding acquisition, investigation, resources, writing—original draft. P.Z. formal analysis, funding acquisition, supervision, visualization, writing—review & editing. All authors have read and agreed to the published version of the manuscript.

Funding: This research was funded by the Jiangsu Natural Science Foundation (BK20181061), the National Natural Science Foundation of China (No. 11902123, 51778132), Jiangsu Province Construction System Science and Technology Project (No. 2020ZD85, 2021ZD74, 2022ZD100) and the Huai Shang Ying Cai Project.

Institutional Review Board Statement: Not applicable.

Informed Consent Statement: Not applicable.

Data Availability Statement: All data generated or used during the study appear in the submitted article.

Acknowledgments: The authors would like to acknowledge the funding support from the Jiangsu Natural Science Foundation, the National Natural Science Foundation of China and Jiangsu Province Construction System Science and Technology Project, and thanks the support from the Huai Shang Ying Cai Project.

Conflicts of Interest: The authors declare no conflict of interest.

References

1. Cassagnabère, F.; Mouret, M.; Escadeillas, G. Early hydration of clinker–slag–metakaolin combination in steam curing conditions, relation with mechanical properties. *Cem. Concr. Res.* **2009**, *39*, 1164–1173. [CrossRef]
2. Kurpinska, M.; Grzyl, B.; Kristowski, A. Cost Analysis of Prefabricated Elements of the Ordinary and Lightweight Concrete Walls in Residential Construction. *Materials* **2019**, *12*, 3629. [CrossRef]
3. Aldea, C.-M.; Young, F.; Wang, K.; Shah, S.P. Effects of curing conditions on properties of concrete using slag replacement. *Cem. Concr. Res.* **2000**, *30*, 465–472. [CrossRef]
4. Ramezanianpour, A.; Esmaeili, K.; Ghahari, S.A. Influence of initial steam curing and different types of mineral additives on mechanical and durability properties of self-compacting concrete. *Constr. Build. Mater.* **2014**, *73*, 187–194. [CrossRef]
5. Lothenbach, B.; Winnefeld, F.; Alder, C.; Wieland, E.; Lunk, P. Effect of temperature on the pore solution, microstructure and hydration products of Portland cement pastes. *Cem. Concr. Res.* **2007**, *37*, 483–491. [CrossRef]
6. Shi, J.; Liu, B.; Wu, X.; Tan, J.; Dai, J.; Ji, R. Effect of steam curing on surface permeability of concrete: Multiple transmission media. *J. Build. Eng.* **2020**, *32*, 101475. [CrossRef]
7. Hooton, R.D.; Titherington, M. Chloride resistance of high-performance concretes subjected to accelerated curing. *Cem. Concr. Res.* **2004**, *34*, 1561–1567. [CrossRef]
8. Prem, P.R.; Bharatkumar, B.H.; Iyer, N.R. Influence of curing regimes on compressive strength of ultra high performance concrete. *Sadhana* **2013**, *38*, 1421–1431. [CrossRef]
9. Liu, B.; Jiang, J.; Shen, S.; Zhou, F.; Shi, J.; He, Z. Effects of curing methods of concrete after steam curing on mechanical strength and permeability. *Constr. Build. Mater.* **2020**, *256*, 119441. [CrossRef]
10. Escalante-García, J.; Sharp, J. Effect of temperature on the hydration of the main clinker phases in portland cements: Part ii, blended cements. *Cem. Concr. Res.* **1998**, *28*, 1259–1274. [CrossRef]
11. Wang, P.; Fu, H.; Guo, T.; Zuo, W.; Zhao, H.; Tian, L.; Chen, C. Volume deformation of steam-cured concrete with fly ash during and after steam curing. *Constr. Build. Mater.* **2021**, *306*, 124854. [CrossRef]
12. Chen, L.; Zheng, K.; Xia, T.; Long, G. Mechanical property, sorptivity and microstructure of steam-cured concrete incorporated with the combination of metakaolin-limestone. *Case Stud. Constr. Mater.* **2019**, *11*, e00267. [CrossRef]
13. Liu, J.; Wang, D. The Role of Phosphorus Slag in Steam-Cured Concrete. *Adv. Mater. Sci. Eng.* **2017**, *2017*, 8392435. [CrossRef]
14. Li, B.; Cao, R.; You, N.; Chen, C.; Zhang, Y. Products and properties of steam cured cement mortar containing lithium slag under partial immersion in sulfate solution. *Constr. Build. Mater.* **2019**, *220*, 596–606. [CrossRef]
15. Li, B.; Huo, B.; Cao, R.; Wang, S.; Zhang, Y. Sulfate resistance of steam cured ferronickel slag blended cement mortar. *Cem. Concr. Compos.* **2019**, *96*, 204–211. [CrossRef]
16. Li, B.; Wang, Y.; Yang, L.; Zhang, Y. Sulfate resistance and hydration products of steam cured steel slag blended cement mortar under dry–wet cycle. *J. Sustain. Cem. Mater.* **2019**, *8*, 353–366. [CrossRef]
17. Ho, D.W.S.; Chua, C.W.; Tam, C.T. Steam-cured concrete incorporating mineral admixtures. *Cem. Concr. Res.* **2003**, *33*, 595–601. [CrossRef]
18. Jung, W.; Choi, S.-J. Effect of High-Temperature Curing Methods on the Compressive Strength Development of Concrete Containing High Volumes of Ground Granulated Blast-Furnace Slag. *Adv. Mater. Sci. Eng.* **2017**, *2017*, 7210591. [CrossRef]
19. Gonzalez-Corominas, A.; Etxeberria, M.; Poon, C.S. Influence of steam curing on the pore structures and mechanical properties of fly-ash high performance concrete prepared with recycled aggregates. *Cem. Concr. Compos.* **2016**, *71*, 77–84. [CrossRef]

20. Kolani, B.; Lacarrière, L.; Sellier, A.; Escadeillas, G.; Boutillon, L.; Linger, L. Hydration of slag-blended cements. *Cem. Concr. Compos.* **2012**, *34*, 1009–1018. [CrossRef]
21. Barnett, S.; Soutsos, M.; Millard, S.; Bungey, J. Strength development of mortars containing ground granulated blast-furnace slag: Effect of curing temperature and determination of apparent activation energies. *Cem. Concr. Res.* **2006**, *36*, 434–440. [CrossRef]
22. Yu, Y.; Jin, Z.; Shao, S.; Zhang, X.; Li, N.; Xiong, C. Evolution of temperature stress and tensile properties of concrete during steam-curing process. *Constr. Build. Mater.* **2020**, *256*, 119441. [CrossRef]
23. Shiyu, Z.; Qiang, W.; Yuqi, Z. Research on the resistance to saline soil erosion of high-volume mineral admixture steam-cured concrete. *Constr. Build. Mater.* **2019**, *202*, 1–10. [CrossRef]
24. Kucharczyk, S.; Zajac, M.; Stabler, C.; Thomsen, R.M.; Ben Haha, M.; Skibsted, J.; Deja, J. Structure and reactivity of synthetic CaO-Al_2O_3-SiO_2 glasses. *Cem. Concr. Res.* **2019**, *120*, 77–91. [CrossRef]
25. Ahmad, J.; Kontoleon, K.J.; Majdi, A.; Naqash, M.T.; Deifalla, A.F.; Ben Kahla, N.; Isleem, H.F.; Qaidi, S.M.A. A Comprehensive Review on the Ground Granulated Blast Furnace Slag (GGBS) in Concrete Production. *Sustainability* **2022**, *14*, 8783. [CrossRef]
26. Li, L.; Feng, J.; Lu, Z.; Xie, H.; Xiao, B.; Kwan, A.; Jiao, C. Effects of aggregate bulking and film thicknesses on water permeability and strength of pervious concrete. *Powder Technol.* **2022**, *396*, 743–753. [CrossRef]
27. Chen, W.; Brouwers, H.J.H. The hydration of slag, part 2: Reaction models for blended cement. *J. Mater. Sci.* **2006**, *42*, 444–464. [CrossRef]
28. Bougara, A.; Lynsdale, C.; Milestone, N. Reactivity and performance of blastfurnace slags of differing origin. *Cem. Concr. Compos.* **2010**, *32*, 319–324. [CrossRef]
29. Escalante, J.; Gómez, L.; Johal, K.; Mendoza, G.; Mancha, H.; Méndez, J. Reactivity of blast-furnace slag in Portland cement blends hydrated under different conditions. *Cem. Concr. Res.* **2001**, *31*, 1403–1409. [CrossRef]
30. Özbay, E.; Erdemir, M.; Durmuş, H.I. Utilization and efficiency of ground granulated blast furnace slag on concrete properties—A review. *Constr. Build. Mater.* **2016**, *105*, 423–434. [CrossRef]
31. Yang, Z.; Fischer, H.; Polder, R. Modified hydrotalcites as a new emerging class of smart additive of reinforced concrete for anticorrosion applications: A literature review. *Mater. Corros.* **2013**, *64*, 1066–1074. [CrossRef]
32. Yan, X.; Jiang, L.; Guo, M.; Chen, Y.; Song, Z.; Bian, R. Evaluation of sulfate resistance of slag contained concrete under steam curing. *Constr. Build. Mater.* **2019**, *195*, 231–237. [CrossRef]
33. Quillin, K.; Osborne, G.; Majumdar, A.; Singh, B. Effects of w/c ratio and curing conditions on strength development in BRECEM concretes. *Cem. Concr. Res.* **2001**, *31*, 627–632. [CrossRef]
34. Jappy, T.G.; Glasser, F.P. Synthesis and stability of silica-substituted hydrogarnet $Ca_3Al_2\,Si_{3\text{-}x}O_{12\text{-}4x}(OH)_{4x}$. *Adv. Cem. Res.* **1991**, *4*, 1–8. [CrossRef]
35. Fu, Y.; Ding, J.; Beaudoin, J. Zeolite-based additives for high alumina cement products. *Adv. Cem. Based Mater.* **1996**, *3*, 37–42. [CrossRef]
36. Sha, W. Differential scanning calorimetry study of the hydration products in portland cement pastes with metakaolin replacement. *Adv. Build. Technol.* **2002**, *1*, 881–888. [CrossRef]
37. Song, S.; Sohn, D.; Jennings, H.M.; Mason, T.O. Hydration of alkali-activated ground granulated blast furnace slag. *J. Mater. Sci.* **2000**, *35*, 249–257. [CrossRef]
38. Bernard, E.; Lothenbach, B.; Cau-Dit-Coumes, C.; Chlique, C.; Dauzères, A.; Pochard, I. Magnesium and calcium silicate hydrates, Part I: Investigation of the possible magnesium incorporation in calcium silicate hydrate (C-S-H) and of the calcium in magnesium silicate hydrate (M-S-H). *Appl. Geochem.* **2018**, *89*, 229–242. [CrossRef]
39. Ríos, C.; Williams, C.; Fullen, M. Hydrothermal synthesis of hydrogarnet and tobermorite at 175 °C from kaolinite and metakaolinite in the $CaO–Al_2O_3–SiO_2–H_2O$ system: A comparative study. *Appl. Clay Sci.* **2009**, *43*, 228–237. [CrossRef]
40. Walkley, B.; Nicolas, R.S.; Sani, M.-A.; Bernal, S.A.; van Deventer, J.S.; Provis, J.L. Structural evolution of synthetic alkali-activated CaO-MgO-Na_2O-Al_2O_3-SiO_2 materials is influenced by Mg content. *Cem. Concr. Res.* **2017**, *99*, 155–171. [CrossRef]
41. Liu, L.; Sun, C.; Geng, G.; Feng, P.; Li, J.; Dähn, R. Influence of decalcification on structural and mechanical properties of synthetic calcium silicate hydrate (C-S-H). *Cem. Concr. Res.* **2019**, *123*, 105793. [CrossRef]
42. Kunther, W.; Ferreiro, S.; Skibsted, J. Influence of the Ca/Si ratio on the compressive strength of cementitious calcium–silicate–hydrate binders. *J. Mater. Chem. A* **2017**, *5*, 17401–17412. [CrossRef]
43. Manoli, F.; Dalas, E. Spontaneous precipitation of calcium carbonate in the presence of ethanol, isopropanol and diethylene glycol. *J. Cryst. Growth* **2000**, *218*, 359–364. [CrossRef]
44. Durdziński, P.T. *Hydration of Multi-Component Cements Containing Cement Clinker, Slag, Calcareous Fly Ash and Limestone*; EPFL: Lausanne, Switzerland, 2016. [CrossRef]
45. Liu, B.; Xie, Y.; Li, J. Influence of steam curing on the compressive strength of concrete containing supplementary cementing materials. *Cem. Concr. Res.* **2005**, *35*, 994–998. [CrossRef]

buildings

MDPI

Article

Partial Substitution of Binding Material by Bentonite Clay (BC) in Concrete: A Review

Jawad Ahmad [1], Karolos J. Kontoleon [2,*], Mohammed Zuhear Al-Mulali [3], Saboor Shaik [4], Mohamed Hechmi El Ouni [5,6] and Mohammed A. El-Shorbagy [7]

[1] Department of Civil Engineering, Swedish College of Engineering, Wah Cantt 47080, Pakistan; jawadcivil13@scetwah.edu.pk
[2] Laboratory of Building Construction & Building Physics, Department of Civil Engineering, Faculty of Engineering, Aristotle University of Thessaloniki, Gr-54124 Thessaloniki, Greece
[3] Department of Building and Construction Technologies Engineering, Al-Mustaqbal University College, Hillah 51001, Iraq; mohammed.zuhair@mustaqbal-college.edu.iq
[4] School of Mechanical Engineering, Vellore Institute of Technology (VIT), Vellore 632014, India; saboor.nitk@gmail.com
[5] Department of Civil Engineering, College of Engineering, King Khalid University, P.O. Box 394, Abha 61411, Saudi Arabia; melouni@kku.edu.sa
[6] Applied Mechanics and Systems Research Laboratory, Tunisia Polytechnic School, University of Carthage, La Marsa, Tunis 2078, Tunisia
[7] Department of Mathematics, College of Science and Humanities in Al-Kharj, Prince Sattam bin Abdulaziz University, Al-Kharj 11942, Saudi Arabia; ma.hassan@psau.edu.sa
* Correspondence: kontoleon@civil.auth.gr

Abstract: Concrete consumes millions of tons of cement, which causes global warming as cement factories emit huge amounts of carbon dioxide into the atmosphere. Thus, it is essential to explore alternative materials as a substitute of OPC, which are eco-friendly and at the same time cost-effective. Although there are different options available to use industrial waste instead of cement, such as waste glass, waste marble, silica fume fly ash, or agriculture waste such as rice husk ash, wheat straw ash, etc., but bentonite clay is also one of the best options to be used as a binding material. There are a lot of diverse opinions regarding the use of bentonite clay as a cement substitute, but this knowledge is scattered, and no one can easily judge the suitability of bentonite clay as a binding material. Accordingly, a compressive review is essential to explore the suitability of bentonite clay as a cementitious material. This review focuses on the appropriateness of bentonite clay as a binding material in concrete production. The attention of this review is to discuss the physical and chemical composition of BC and the impact of BC on the fresh and mechanical performance of concrete. Furthermore, durability performance such as water absorption, acid resistance and dry shrinkage are also discussed. The results indicate that bentonite clay increased the mechanical and durability performance of concrete up to some extent but decrease its flowability. The optimum proportion of bentonite clay varies from 15 to 20% depending on the source of bentonite clay. The overall study demonstrates that bentonite clay has the creditability to be utilized partially instead of cement in concrete.

Keywords: sustainable concrete; supplementary cementitious material; bentonite clay; strength; durability

1. Introduction

Concrete is widely utilized as a building material around the globe due to its exceptional stability and compressive strength [1–3]. The current practice of concrete construction is thought to be unsustainable as it consumes a huge amount of natural resources [4–6]. Cement factories face difficulties in minimizing carbon dioxide emissions, increasing the cost of energy rises, and the supply of raw materials (in particular maintaining a supply of raw materials of good quality) [7–9]. Demand for cement and concrete on a global scale has expanded dramatically in recent years, owing to the fast development of nations and the continuation of population growth in many parts of the world [10–12]. According to the World Cement Association, Pakistan manufactures 85 million tons of cement, which refers to 2% of global cement production. The cost of cement increasing continuously (i.e., more than 150 percent in ten years) [13]. Therefore, it is essential to explore alternative materials instead of cement.

Sustainable development is a kind of evaluation that seeks to enhance the quality of life, while also meeting the fundamental requirements of future generations. Its goals are to provide basic requirements, raise living standards, and promote the protection and management of ecosystems, among other things [14–16]. In response to growing public concerns about environmental degradation, fossil fuel depletion, and sustainable growth, the reusing of various industrial waste shows a rapid increase on a global scale [17–20]. Overall, the creation of OPC, which is a key component in concrete [21–23], is a significant supply of emissions of harmful gases such as carbon dioxide [24,25].

Currently, our planet produces around 3.6 billion metric tons of cement each year [26]. It is anticipated, that by 2030 the amount of cement would rise to greater than 5 billion metric tons [27,28]. Although this trend may vary across countries, almost part of the global OPC is used to create 11 billion metric tons of concrete each year; the remaining part is utilized in mortars, soil stabilization, coatings, etc. [14,29]. As it is well known that the concrete industry is a significant consumer of natural resources on a worldwide level. Consequently, reused aggregates and natural cementitious materials may be employed in the building sector to conserve energy and increase the sustainability of the overall structure [30–32]. Bentonite clay corresponds to one of the best possible solutions of integration in concrete, as a partial replacement as a substitute of OPC in a variety of applications.

BC is a highly colloidal ductile clay that is generated by the modification of volcanic ash (or glass) in situ. It is sometimes referred to as smectite-rich clay due to the presence of smectite in the clay (mostly montmorillonite) [33]. United States, China, India, Greece, Mexico, Turkey, Iran, Russia, Japan, Brazil, and Germany are the world's leading BC manufacturers, listed in decreasing order of manufacture [34]. Recently, researchers described bentonite as calcined clays that are not derived from kaolin and that are economical supplemental cementitious materials [35,36].

Various researchers have determined the appropriateness of bentonite clay for use in the construction of concrete [37]. A common clay-bentonite was employed as an addition in concrete in one research. Apart from investigating the impact of such clay elements on the mechanical characteristics of concrete, the authors investigated the chemical resistance of concrete to sulphates, carbonation, and chloride exposure as well. They detected that the resistance to carbonation in the bentonite-bearing material may be lower than the resistance to carbonation in the reference plain Portland cement concrete [37]. The addition of bentonite in concrete can significantly improve the durability of concrete and helps to prevent it from shrinkage cracking once it has been allowed to dry. Concrete's performance, strength, and durability are all greatly affected by the presence of specific minerals in pozzolanic materials [38]. The use of bentonite clay may aid to increase the compressive strength of a material. The early-age compressive strength of the concrete with additional bentonite did not demonstrate a substantial improvement. However, it increases to a level that is much greater than that of the control concrete specimen when the specimen is aged longer. Apart from that, the water to binder percentage was increased to 55% and the OPC content was increased to 340 kg/m^3, with the maximum bentonite replacement ratio set at 21%. Apart from compressive strength, other durability characteristics was studied. According to the findings, the specimens that had been treated with bentonite performed better in terms of acid corrosion resistance. A study conclude that the mechanical performance of concrete decreased with the substitution of bentonite clay [39]. The hydration process in a Portland cement mixture comprising metakaolin and sodium bentonite has been researched to determine the influence of pozzolanic elements on the final product. A combination of sodium bentonite and metakaolin enhanced the cement hydration, as measured by strength development, portlandite utilization, and the calcium-silicate hydrate (C-S-H) phase, as well as other parameters. In addition, the decomposition of metakaolin is speeded up in the existence of BC [40]. A study claims that BC based concrete needs more curing time to obtain strength [41]. The silane-modified BC had a greater pozzolanic activity as compared to without treated BC [42].

Several research efforts focus on utilizing bentonite clay in concrete instead of cement. However, the knowledge of bentonite clay in concrete is scattered and no one can easily judge the importance of bentonite clay in concrete. Therefore, this review focus on the physical and chemical composition of BC, fresh properties, mechanical and durability performance of concrete with bentonite clay instead of cement. The optimum dose is also important for better performance. A successful review will also give the idea for a new researcher to choose and apply bentonite clay in concrete.

2. Physical Properties

The physical properties of bentonite clay, including grain size, specific gravity, and fineness, assist in determining their applicability and ability to utilize as a binding material in concrete. BC is usually accessible in several colors and types. Table 1 shows lists some of the physical properties of bentonite clay indicated by various researchers. The specific gravity of bentonite clay is slightly lower than cement (3.1 to 3.16). The particle size of bentonite (4.75 μm) is much lower than cement (75 μm). Blain's fineness of bentonite clay varies greatly ranging from 1730 to 4800 (cm^2/g). Almost all authors described distinct values. It is due to a change in the location source of BC.

Table 1. Physical properties of bentonite clay.

Property Name	Achyutha et al. [43]	Memom et al. [44]	Rao et al. [45]
Specific Gravity	3.12	2.79	2.82
Particle Size (μm)	-	4.32	4.75
Blains Fineness (cm^2/g)	1730	4800	4800

The scanning electron microscope (SEM) was utilized to define the grain size of BC, which was previously unknown. The scanning electron micrographs of BC was shown in Figure 1 which indicate that the bentonite clay is flaky and elongated which decreased the flowability of fresh concrete.

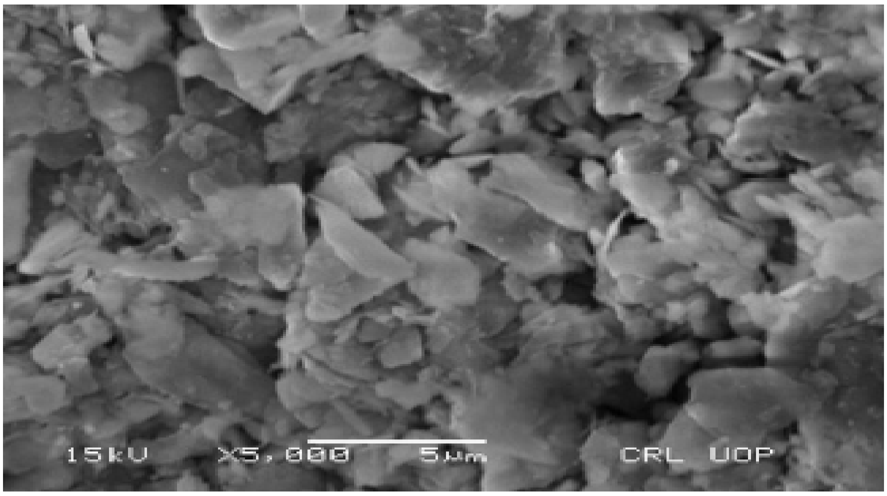

Figure 1. SEM of Bentonite Clay, reprinted from permission of Elsevier [44].

3. Chemical Composition of Bentonite Clay

Concrete made with bentonite clay has variable mechanical and durability characteristics depending on the number of different compounds contained in the bentonite clay.

According to one study, the chemical composition and particle size of SCM are the most important factors influencing its pozzolanic action [46]. According to previous investigations, the chemical makeup of bentonite clay is shown Table 2. It can be concluded that the primary constituent of bentonite clay is SiO_2. Figure 2 depicts the XRD results of BC. The amorphous nature of the silicon dioxide (SiO_2) included in bentonite clay has a considerable influence on the performance of concrete, from the initial hydration through the ultimate development of strength. ASTM [47] states that the addition of a chemical (SiO_2, CaO, Al_2O_3, MgO, and Fe_2O_3) more than 70% can be used as pozzolanic materials as bentonite clay exceeds 70%.

Table 2. Chemical properties of BC.

Chemical Name	Akbar et al. [48]	Vijay et al. [49]	Shabab et al. [50]
SiO_2	49.63	51.11	52.1
Al_2O_3	21.11	16.38	13.4
Fe_2O_3	3.23	7.65	7.5
MgO	12.56	7.57	2.64
CaO	3.59	7.12	12.0
K_2O	2.091	1.34	2.64
Na_2O	0.449	0.29	-
TiO_2	0.498	1.29	-
P_2O_5	0.119	0.29	-
LOI	-	6.75	8.61

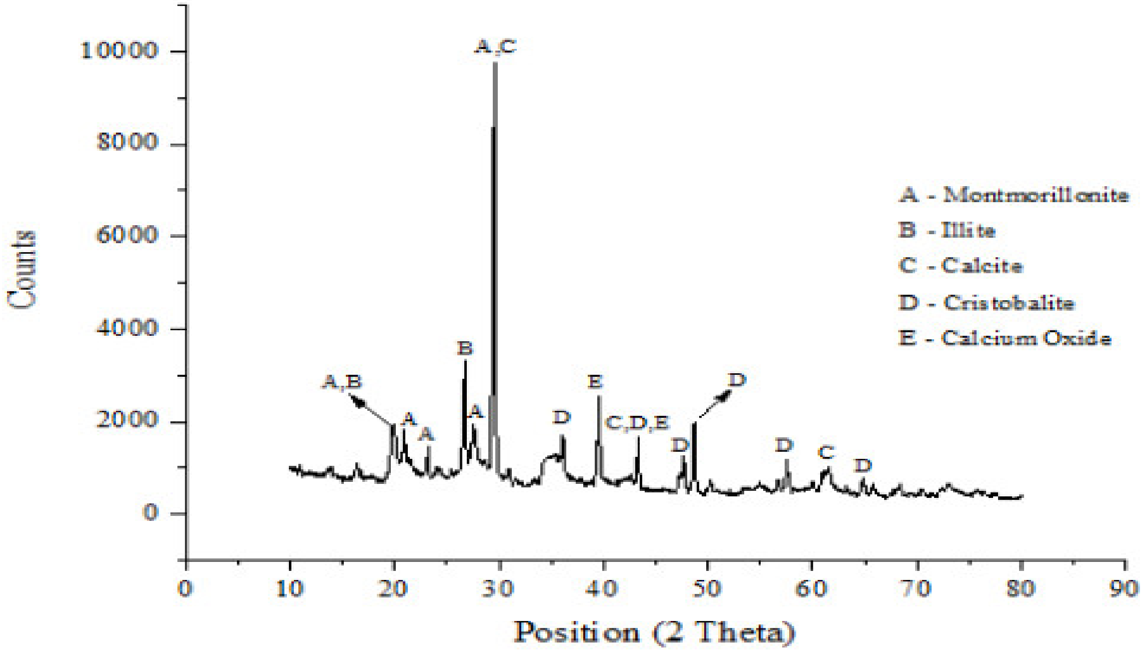

Figure 2. XRD Analysis of bentonite clay [43].

4. Fresh Properties

Workability and Fresh Density

The higher workable concrete in the construction sector results in ease of installation, increased filling ability, the use of dense reinforcement in highly congested concrete components, and a reduction in the cost of vibration in the building industry [51]. To produce highly workable concrete with exceptional segregation resistance, it is necessary to have sufficient flowability and rheological qualities. The flowability with various percentages of bentonite clay is given in Figure 3. It can be observed that the flowability of concrete is reduced with bentonite clay. The tiny grain size and relatively large surface area of BC particles contribute to the decrease in slump value. As a result, it can be inferred that, while using the same water to cement ratio, the flowability of concrete made with BC is lower as compared to the blank mix [44]. According to one research, the flowability of concrete deteriorated when BC was used instead of Portland cement. The large surface area of the clay elements, as well as the subsequent adsorption of free water within the combination, is responsible for the decreased flowability of the mixture. As a result, lubrication of the solid particles is hindered, and internal friction is increased due to Jess cement paste [35]. In contrast, some study claimed that the pozzolanic materials results increase in the flowability of concrete due to the micro filling effect which results in less cavities in concrete ingredients and hence free water are available in more quantity for lubrication, causing more flowable concrete [52]. With the use of a superplasticizer, it is possible to achieve the necessary flowability of concrete [44]. A also reported that the flowability of concrete reduced with the substitution of BC due to a larger surface area [53]. The flaky and elongated shape of BC as shown in Figure 1 also causes to decrease in the flowability of concrete by increasing friction between aggregates. A study also claims that BC is from clay material having high water absorption [54]. Therefore, less water is available for lubrication to reduce the friction between concrete ingredients.

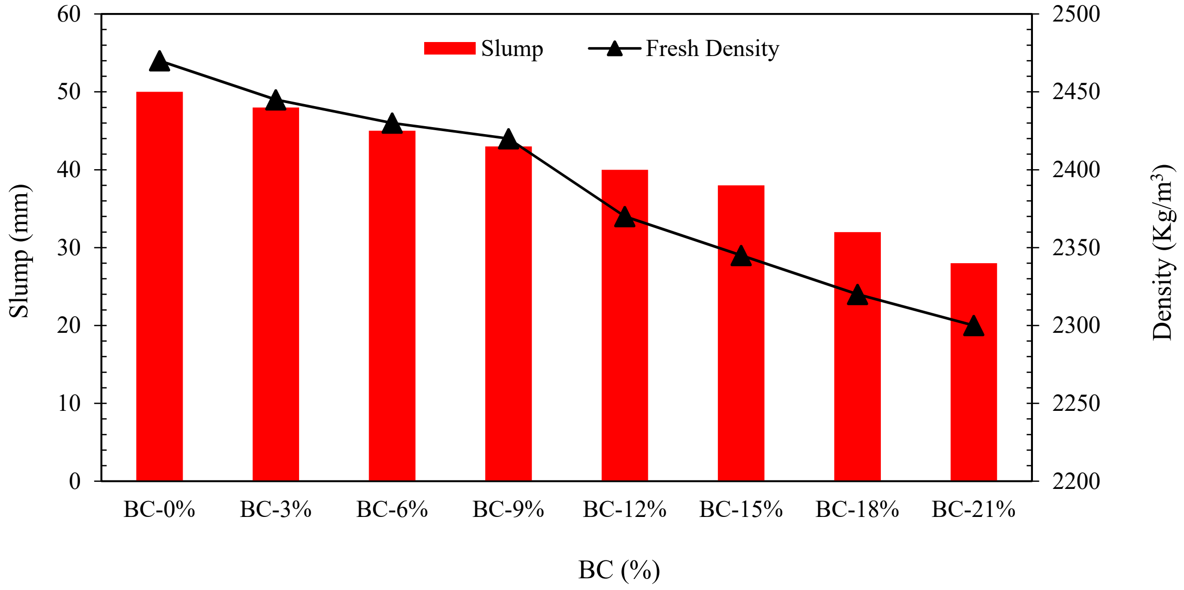

Figure 3. Workability and fresh density (data source [44]).

Figure 3 depicts the results of fresh density tests on various percentages of bentonite clay. Blank mix without bentonite clay shows the highest density (2470 kg/m^3), when it is in its fresh condition, as can be seen in Figure 3. The introduction of bentonite substitute resulted in a fall in density and the greater the bentonite percentage, the lower the density. This is due to the fact that density is a function of specific gravity. Since cement has higher specific gravity than bentonite, the density of the control mix (blank mix) is higher than that of the bentonite-based mixture [44].

With the inclusion of secondary cementitious materials (SCM), the density of concrete increases due to the micro-filling of gaps in the concrete components which results in a denser concrete mixture. Furthermore, the pozzolanic reaction of SCM improved the binding characteristics of cement paste, resulting in denser concrete [52]. However, some studies reported that a higher dose of SCM leads to a lower density of concrete due to lower workability [35,55]. A study also claimed that, as the BC in the concrete mix is increased, the workability of the concrete mix decreased which increased compaction affords, resulting in the fresh density of the concrete mix decreased [53].

Figure 4 shows a correlation between slump values and the density of concrete. As stated earlier that workability and density are correlated to each other. The lower workability increased the compaction affords and increased the number of voids in hardened concrete, resulting in a decreased density of concrete. As a result, a strong correlation between slump values and concrete density has been observed, with an R^2 of greater than 90%.

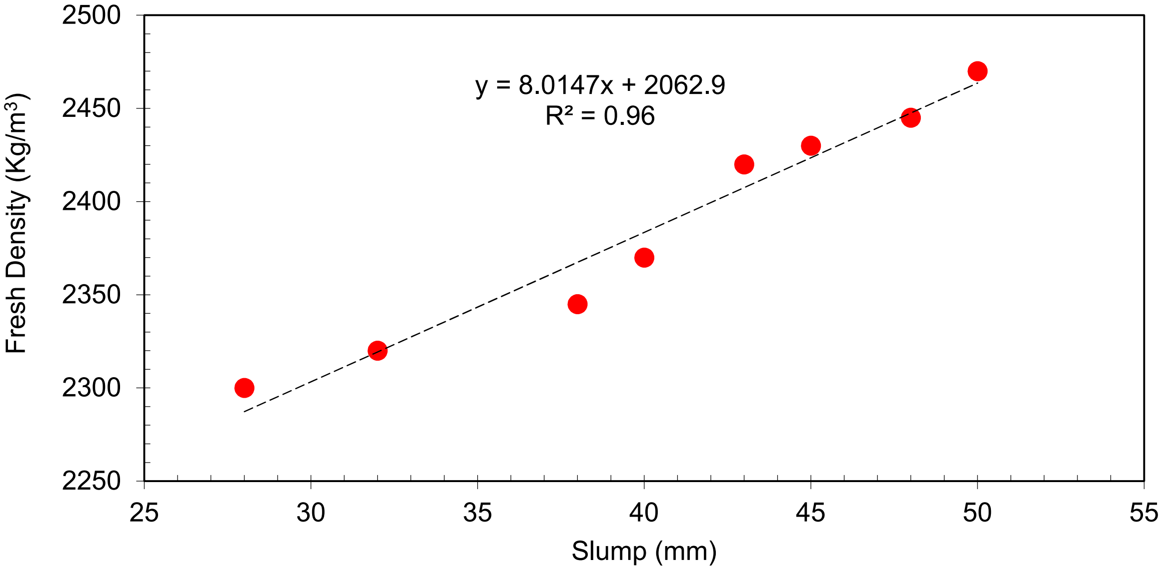

Figure 4. Correlation between slump and fresh density (data source [44]).

5. Mechanical Properties

5.1. Compressive Strength

The compressive capacity of concrete with varying doses of BC is given in Figure 5. It can be observed that the BC dose does not considerably affect the compressive capacity of concrete. All of the mixes of BC have a compressive capacity comparable to the reference concrete in terms of strength. Although no increase in compressive capacity was observed but the use of cement could be reduced up to 20%. Furthermore, the pozzolanic reaction of SCM proceeds slowly and the authors conduct compressive strength only up to 28 days. However, according to one research project, the compressive capacity of concrete reduced with the rise in the proportion of bentonite clay used as a cement substitute on all days of curing [56]. In contrast, according to the findings of the research. At 56 days, the proportion of improvement in strength was 0.9 percent, 1.5 percent, 1.8 percent, 2.7 percent, 2.5 percent, and 2.2 percent, respectively, when compared to the control group [44]. A researcher claim that the compressive capacity of concrete reduced with the rise in the proportion of BC used as a cement substitute at all ages of curing [56]. A study reported a considerable improvement in compressive strength with the substitution of BC [35]. One of the most important factors contributing to this improvement in compressive capacity is the pozzolanic reaction, which occurs at a slower rate than the rate of cement hydration and is combined with the filling voids in concrete ingredients effect induced by pozzolanic material [57]. These contrasting findings of bentonite clay will need to be investigated further in future research before being used practically.

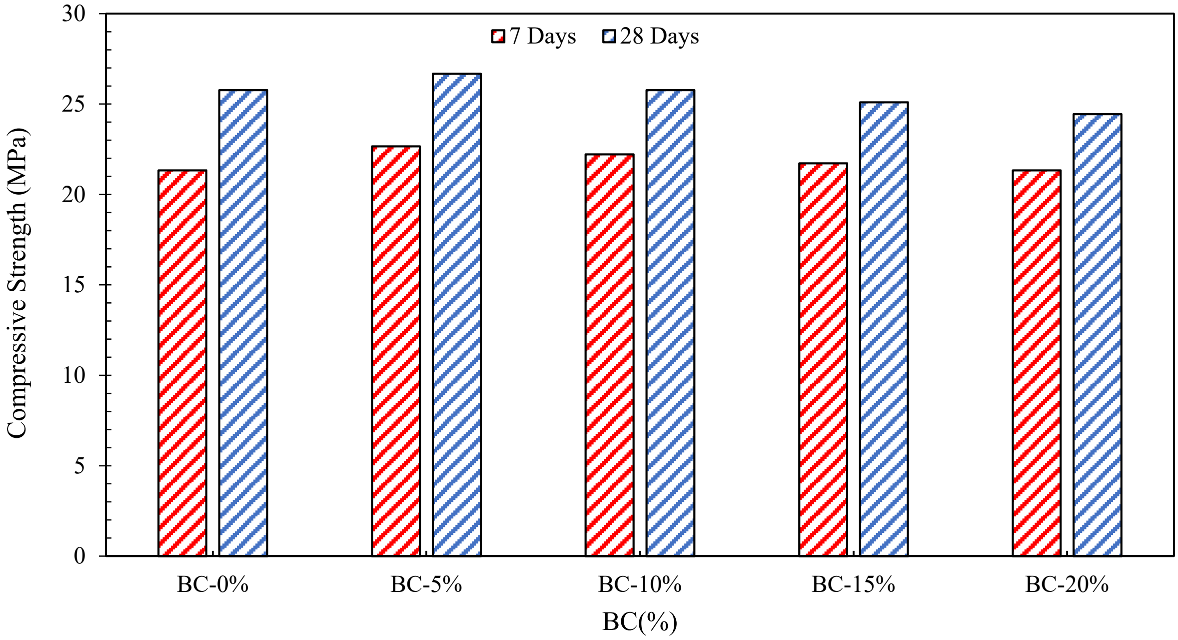

Figure 5. Compressive strength(data source [58]).

An analysis of compressive capacity gain with various days of curing is also provided in Figure 6, in which the compressive capacity of control concrete is used as a reference concrete. At seven days of curing, concrete compressive capacity is less than 14% from the blank mix at 10% substitution of BC while 20% substitution of BC shows 18% lower than blank mix. At 28 days, compressive capacity is just 4% more than blank mix at 5% substitution of BC while 20% substitution shows 6% lower than the reference strength. It has been established that BC could not improve the compressive capacity effectively but the strength is approximately equal to the reference concrete.

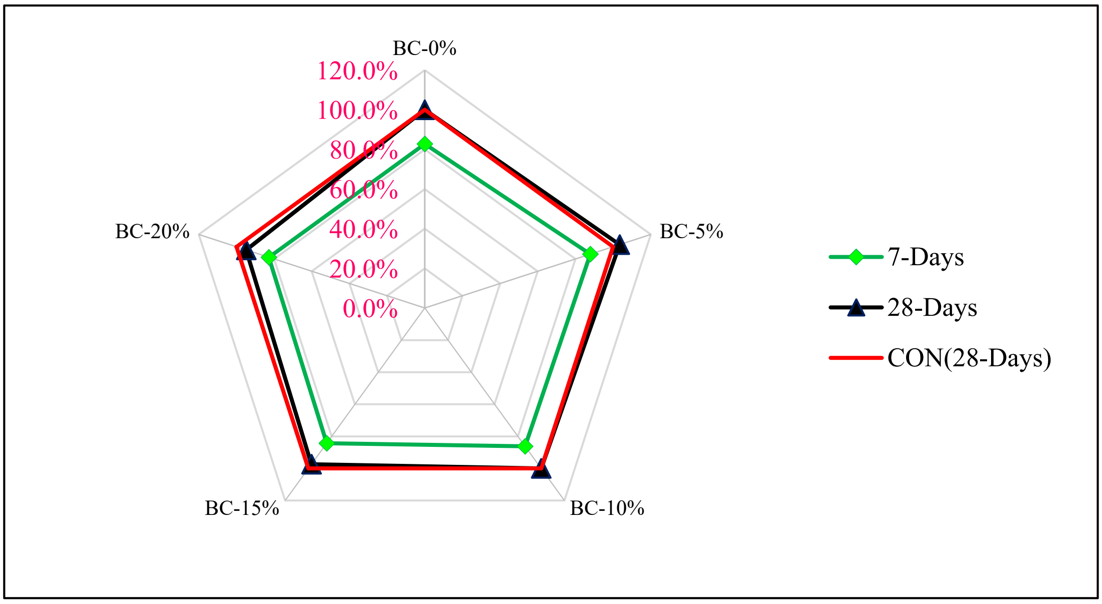

Figure 6. Relative analysis of compressive strength (data source [58]).

5.2. Split Tensile Strength

The split tensile capacity of mix with various doses of BC shows similar trends to the compressive capacity of concrete i-e the split tensile capacity of the mix is not enhanced with the substitution of BC; nonetheless, all of the BC mixes have split tensile strengths that are about equivalent to the reference concrete as indicated in Figure 7. Additionally, it has been shown that increasing the bentonite content of concrete degrades its performance, resulting in a significant reduction in both tensile strength and compressive strength (tensile strength) [39]. Based on the research, it was determined that the best bentonite replacement ratio by weight of cement in the concrete is 2.7 percent, which produces a satisfactory compressive and tensile strength. The concrete is appropriate for usage in low-rise buildings [59]. Using bentonite clay as a binding substance, A researcher discovered that split tensile strength decreased when the bentonite clay was substituted. It can be determined that the poor bond formation between the bentonite and cement particles is responsible for the decreased split tensile strength [43]. However, according to one research, the split tensile strength improved due to the replacement of BC. The pozzolanic reaction enhanced the binding qualities of the cement paste and thus raised the split tensile strength. Additionally, the presence of micro-filling gaps of BC also leads to increased split tensile strength. Overall, the combination of pozzolanic and micro-filling gaps in BC has a good effect on split tensile strength. Aside from that, the increased dosage of BC resulted in a drop in split tensile strength as a consequence of a lack of workability [35]. Almost all authors reported different values. The reason behind this attribute to changes in the location of the source.

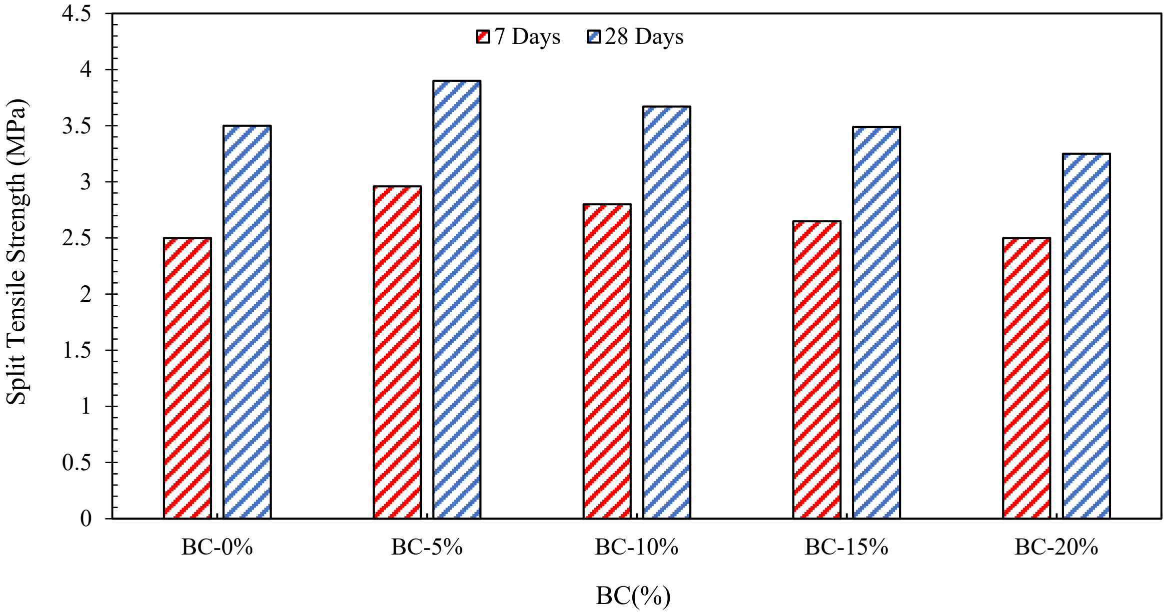

Figure 7. Split tensile strength (data source [58]).

A relative analysis of tensile strength with various days of curing is also shown in Figure 8. The 28 days tensile strength of the blank mix is taken as a reference strength. At seven days, the tensile capacity of concrete is less than 20% from the reference mix at 10% substitution of BC while 20% substitution of BC shows 29% lower split tensile strength than reference strength. At 28 days, tensile capacity is just 9% more than reference strength at 5% substitution of BC while 20% substitution shows 8% less tensile capacity than the reference strength. It has been noted that concrete with a partially substituted BC is still weak in tension.

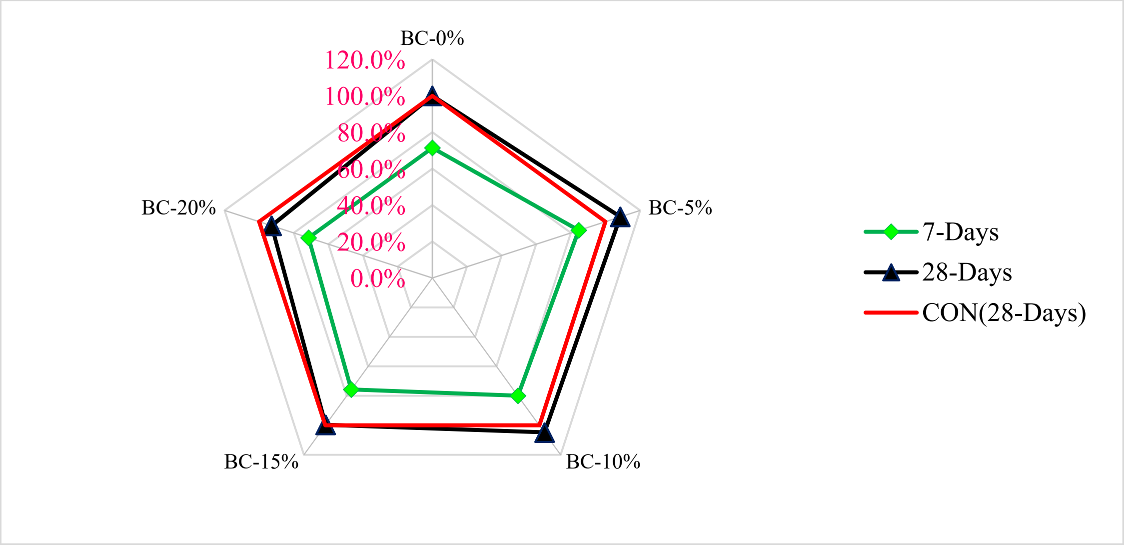

Figure 8. Relative analysis of split tensile strength (data source [58]).

Figure 9 shows a correlation between compressive and tensile capacity of mix with different replacement ratios of BC. Tensile strength depends on the compressive strength of concrete. It is estimated that the tensile capacity of concrete is around 10 to 15 percent of compressive capacity. A high link is existing between the compressive capacity of concrete and its split tensile capacity, even when the BC substitution ratios are varied. The regression model shows an R^2 value greater than 90%.

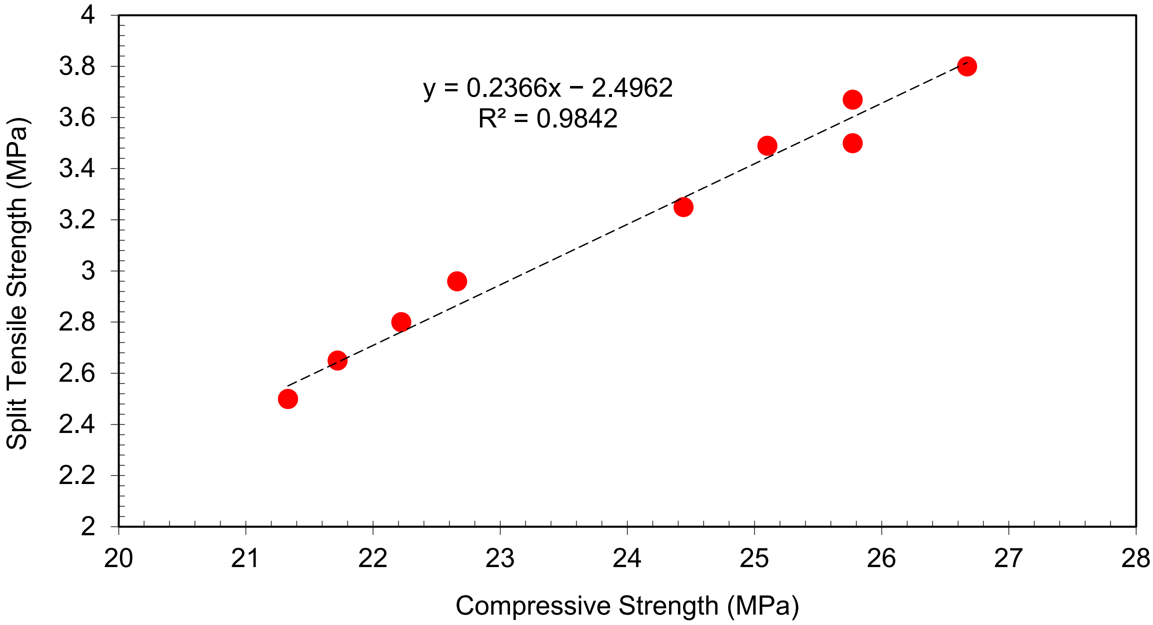

Figure 9. Correlation between compressive and split tensile strength (data source [58]).

5.3. Flexure Strength

The flexural capacity of concrete when treated with various doses of BC is displayed in Figure 10. Similar to the compressive capacity of concrete, the flexure capacity of the mix is not enhanced by the addition of BC, but all of the BC mixes have flexure strengths that are nearly equivalent to the reference concrete. Flexural strength of BC mixtures was shown to be lowered than from blank concrete, particularly at a higher dose of BC. In concrete, the flexural strength is inversely related to the amount of bentonite blended (after 20 percent) and the water to cement ratio (W/C). It may be linked to the creation of a weak connection between bentonite and cement particles during the manufacturing process [43]. After 28 days of curing, concrete beams with dimensions of 150 mm × 150 mm × 750 mm were cast to assess the modulus of rupture, commonly known as flexural strength of the concrete. The results show that the modulus of rupture reduced as the degree of cement substitution rate rise as a result of the addition of bentonite. However, the decrease was not significant. These results were almost the same for concrete beams containing 20 percent and 25 percent bentonites, respectively. Web shear cracks are developed in the same direction as flexural fractures. Final results showed that after being loaded, the control and bentonite-containing concrete beams failed at ten and eight tones, respectively [13]. A study suggests that, for high-strength concrete, it is important to add fiber with secondary cementitious materials (SCM) [52]. As compared to the reference concrete, when basalt fiber and bentonite clay were combined, the flexure strength of the concrete improved significantly, according to the researchers. Furthermore, the use of 10% bentonite replacement and 1.5 percent basalt fiber provided the best results possible [60]. However, less studies consider flexure strength in their research.

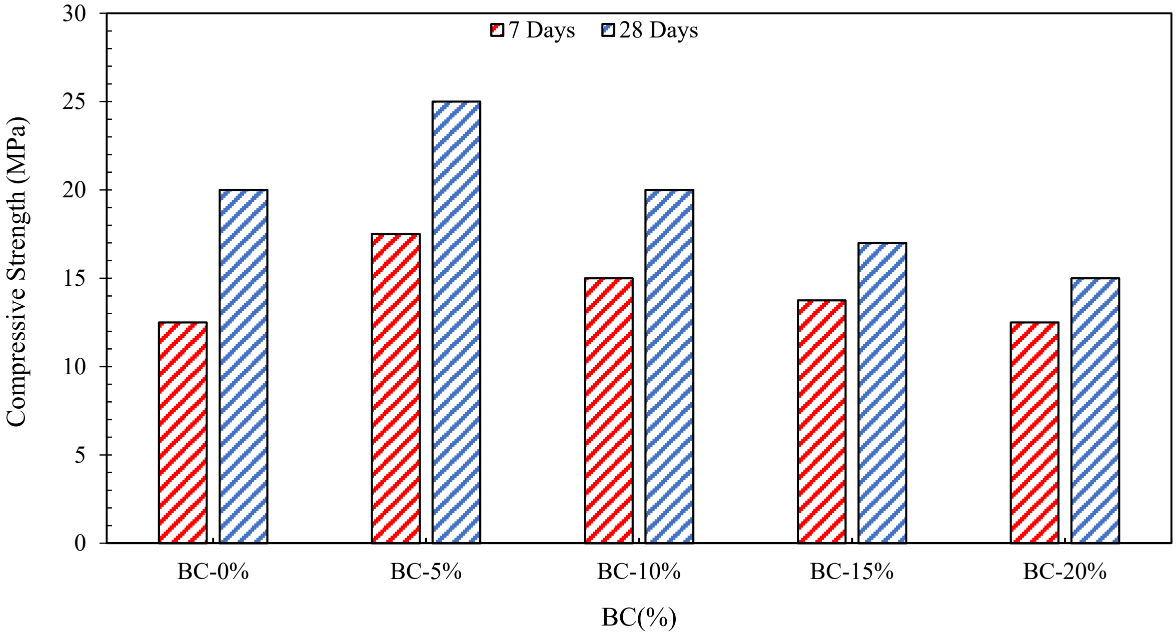

Figure 10. Flexure strength [58].

Figure 11 shows the strength age relation of flexure strength with various percentages of BC. The 28 days of reference concrete flexure capacity of concrete was taken as a benchmark flexure strength. At seven days of curing, flexure capacity of 5% replacement of BC is 13% lower than the reference flexure strength (28 days control concrete flexure strength) while 10% substitution of BC shows 25% less than flexure strength to the benchmark flexure strength (28 days blank concrete flexure strength). At 28 days, the flexure capacity of concrete is 25% more than the benchmark flexure strength. The increased flexure strength with the substitution of BC is due to the chemical reaction of BC which increased the binding characteristics of concrete and filling the cavities in concrete components, leading to more dense concrete [35].

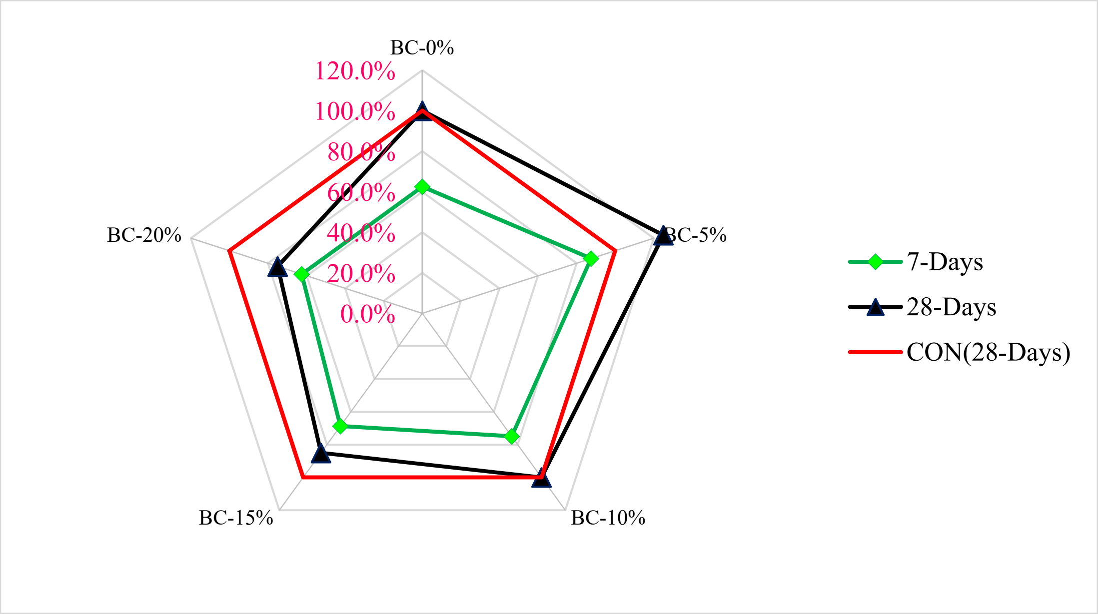

Figure 11. Relative analysis of flexure strength (data source [58]).

Figure 12 shows the correlation between compressive and f1exure strength on different days of curing. It can be noted that a strong correlation exists between compressive and flexure strength having an R^2 value approximately equal to 90% (78%).

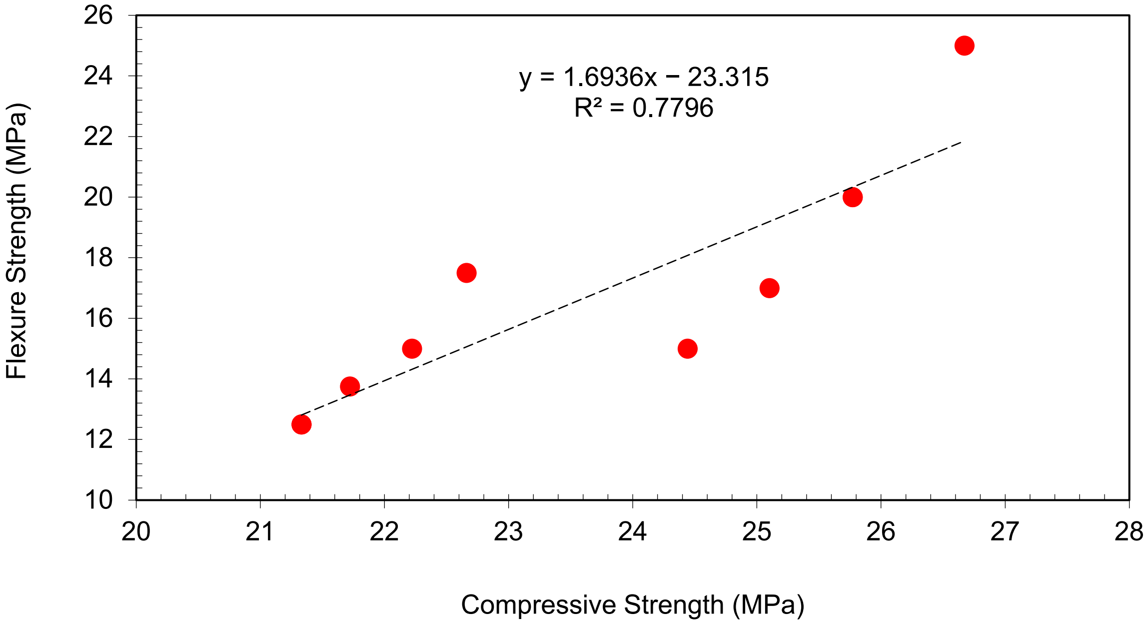

Figure 12. Correlation between compressive and flexure strength (data source [58]).

Load Deflection Curve and Ductility Ratio

Third point loading of 5.4 and 3.8 tons was observed at breaking of the control and BC beams, respectively, compared to design capacities of 4.1 and 4.0 tons. This fracture formed from the middle bottom region of the structure and was deflected by 3 mm. The crack width widened when the load increments were increased. Flexural fractures were observed by web shear cracks in the same direction. Ultimately, the control and BC concrete beams collapsed at 10 and 8 tons, respectively, when the loads were increased. Figure 13 displays the load versus deflection curves for the two beams for the third point loading, which were plotted against each other. The yield of steel reinforcement was exhibited in the control and bentonite concrete beams, which were loaded with 7.8 and 6.0 tons, respectively. Furthermore, the considerable deflection of the bentonite-containing concrete beam was observed in Table 3 which demonstrates the more ductility ratio. The high ductility important attribute in earthquakes since it allows energy to be dissipated quickly. An increase in area under the curve is associated with a higher ductility ratio, which enhances the ability to disperse force during an earthquake, which might have major ramifications for human life. Table 4 reveals the summary of slump, compressive, flexural and split tensile strength of mix with different doses of BC as per past researchers.

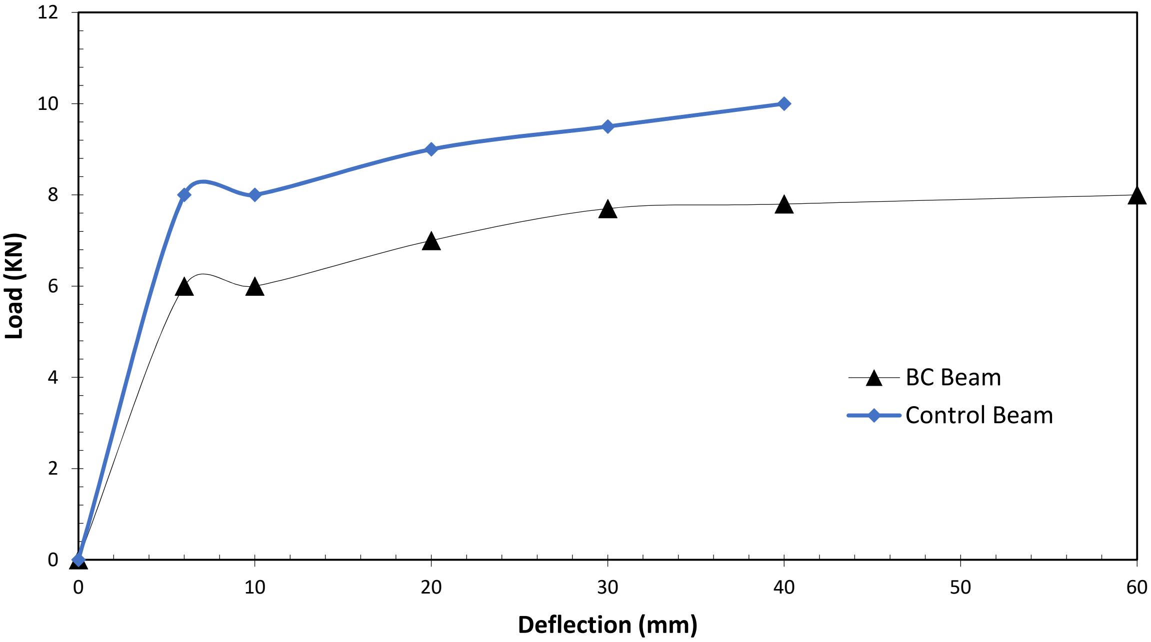

Figure 13. Load deflection curve [13].

Table 3. Ductility concrete with and without BC [13].

Beam Type	Deflection at Ultimate Point	Deflection at Yield Point	Ductility Ratio *
Control Beam	37.00	4.87	7.61
25% Bentonite Clay	56.83	5.66	10.05

* Ratio of the deflection at the ultimate point to the deflection at the yield point.

Table 4. Summary of mechanical performance of concrete with bentonite clay.

Authors	Remarks	Bentonite Clay (%)	Tensile Strength (MPa)	Compression Strength (MPa)	Flexure Strength (MPa)
Ahmad et al. [35]			14 days, 28 days	14 days, 28 days	-
		BC-5%	2.6, 3.5	20, 30	
		BC-10%	2.7, 3.6	21, 32	
		BC-15%	3, 4	24, 34	
		BC-20%	2.6, 3.2	17, 26	
Sumitha et al. [61]	Silica Fume 10%		7 days, 28 days	7 days, 28 days	7 days, 28 days
		0%	2.4, 3.3	38, 48	6, 8
		5%	2.5, 3.3	28, 42	5, 7
		10%	1.6, 2	25, 42	4.5, 5.5
		15%	1.4, 1.8	22, 35	3, 4.2

Table 4. *Cont.*

Authors	Remarks	Bentonite Clay (%)	Tensile Strength (MPa)	Compression Strength (MPa)	Flexure strength (MPa)
Liu et al. [62]	-	Ca-bent = 0%, 2%, 4%, 6%, 8%, 10% Na-bent = 0%, 2%, 4%, 6% 8%, 10% Mg-bent = 0%, 2%, 4%, 6%, 8%, 10%.	-	28 days 11, 12, 12.2, 14, 15, 16 11 13, 14, 17, 17, 18 11, 12, 13, 14, 16, 17	28 days 2.7, 2.8, 3, 3.5, 3.4, 3.7 2.7, 2.8, 3, 3.5, 3, 6, 3.7 2.7, 3.5, 3.4, 3.6, 3.7, 4
Akbar et al. [48]	Plasticizer (%) 1.5	0%, 20%	-	7 days 25, 30 14 days 32, 40 28 days 20, 22 56 days 24, 32	-
Rao et al. [45]	-	 Control 10% WSA 10% BC (H) 10% BC (R)	-	7 days, 28 days 55, 65 52, 68 50, 60 45, 50	7 days, 28 days 16, 18 15, 19 14, 16 10, 12
Kumar et al. [63]	Fly Ash 0% 5% 7.5% 12.5% 15%	 0% 5% 7.5% 12.5% 15%	7 days, 28 days 1.9, 2.3 1.4, 2 1.6, 2 1.5, 1.5 1.3, 1.3	7 days, 28 days 45, 90 25, 50 40, 70 30, 60 40, 65	-
Chandrakanth et al. [58]		 0% 5% 10% 15% 20%	7 days, 28 days 2.5, 3.5 2.96, 3.8 2.8, 3.67 2.65, 3.49 2.5, 3.25	7 days, 28 days 21.33, 25.77 22.66, 26.67 22.22, 25.77 21.72, 25.10 21.33, 24.44	7 days, 28 days 12.5, 20 17.5, 25 15, 20 13.75, 17 12.5, 15
Mirza et al. [13]		 0% 20% 25% 30% 40% 50% 100%	-	7 days, 28 days 16, 23 15, 19 15, 19 14, 16 13, 14 8, 10 4, 2	-
Khaliq et al. [64]		 0% 5% 10% 15% 20%	28 days 2.1 2.0 2.2 2.1 2.0	28 days 23.44 22.4 22 17.2 13.7	-
Adeboje et al. [65]	Rubber 0 0.75 0.50 0.25	 0 0.25 0.50 0.75	28 days 1.9 1.7 1.8 1.7	28 days 27 25 26 25	-

6. Durability

6.1. Water Absorption (WA)

The outcomes of the WA test are shown graphically in Figure 14. The results of the tests revealed that the water absorption reduced as the quantity of cement substituted by BC improved. Due to the chemical reaction among natural pozzolans and CH in hydrated cement paste consuming lime rather than lime producing calcium silicate hydrates (CSH) gel, the binding property of cement paste is increased, resulting in a more compact mass which decreased water absorption of concrete. Secondly, since the grain size of BC is smaller than OPC, it can give more compact mass by micro-filling voids and, as a result, a reduction in water absorption [57,66]. Additionally, research revealed that WA was reduced with BC substitutions of up to 30% [56]. Additionally, according to one research, SCM reduced water absorption due to micro filling, which improved the density of concrete, resulting in lower water absorption. However, with greater doses of BC, an increase in WA was found owing to a lack of flowability, which increased the compaction afforded, resulting in porous concrete, which eventually increased the water absorption of concrete [52].

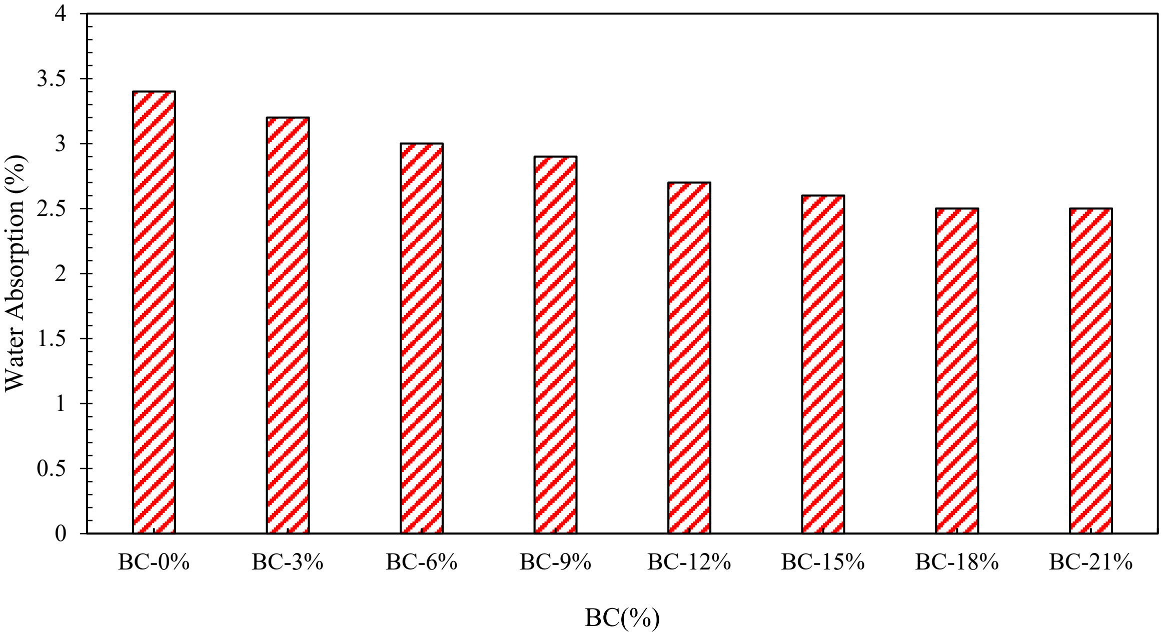

Figure 14. Water absorption (data source [44]).

6.2. Acid Resistance

The outcomes of the acid attack test with various replacement ratio of BC are shown in Figure 15. In the laboratory tests, it was discovered that the amount of weight loss experienced by blank mix was greatest in both sulfuric acid (H_2SO_4) and hydrochloric acid (HCL) solutions. The lower acid resistance of blank mix against acid attack may be attributed that it includes a big quantity of lime and during hydration emits a significant amount of free CH, which interacts with the acid and leaves a soft and mushy material behind. For bentonite mixes, the CH combines with the SiO_2 available in BC to produce CSH gel, resulting in a small quantity of CH and improved acid resistance capacity of BC concrete. When comparing the two acid solutions, the weight loss pattern was identical. Sulfuric acid, on the other hand, was shown to cause greater degradation than HCL. The greater degradation of H_2SO_4 is due to a product known as calcium sufflarninate (Ettringite) is created, which expands and produces rupture of the set cement paste [67]. In the case of hydrochloric acid, no such product is generated. An investigation into Pozzolanic reaction and micro filling SCM resulted in a reduction of cavities, which inhibited the rapid entry of acid. The dissolving of calcium aluminate and calcium hydroxide in concrete due to H_2SO_4 is the primary cause of erosion [68]. The concrete erosion is determined by the rate at which H_2SO_4 penetrates into the concrete body and the time it takes to achieve calcium hydroxide and calcium aluminate. As a consequence, a reduction in the voids of concrete due to the replacement of bentonite clay leads to a denser concrete mixture. It is anticipated that increased density will lead to a reduction in the rate of H_2S0_4 penetration into the concrete. However, higher acid resistance was examined at a higher substitution ratio of bentonite clay due to loss of flowability which results in porous concrete. The acid may readily permeate concrete via cavities, resulting in the destruction of the concrete structure. Further, bentonite is one of the most essential ingredients utilized in the construction of plastic concrete, where it serves to stabilize the concrete. It is made of clay components that have strong water absorption and swelling characteristics of 300 percent even after being in touch with water [54]. Swelled BC slurry will fill the voids and these water-saturated BC can block the further water absorption and permeability, thus decreasing the water absorption of water and increasing the acid resistance.

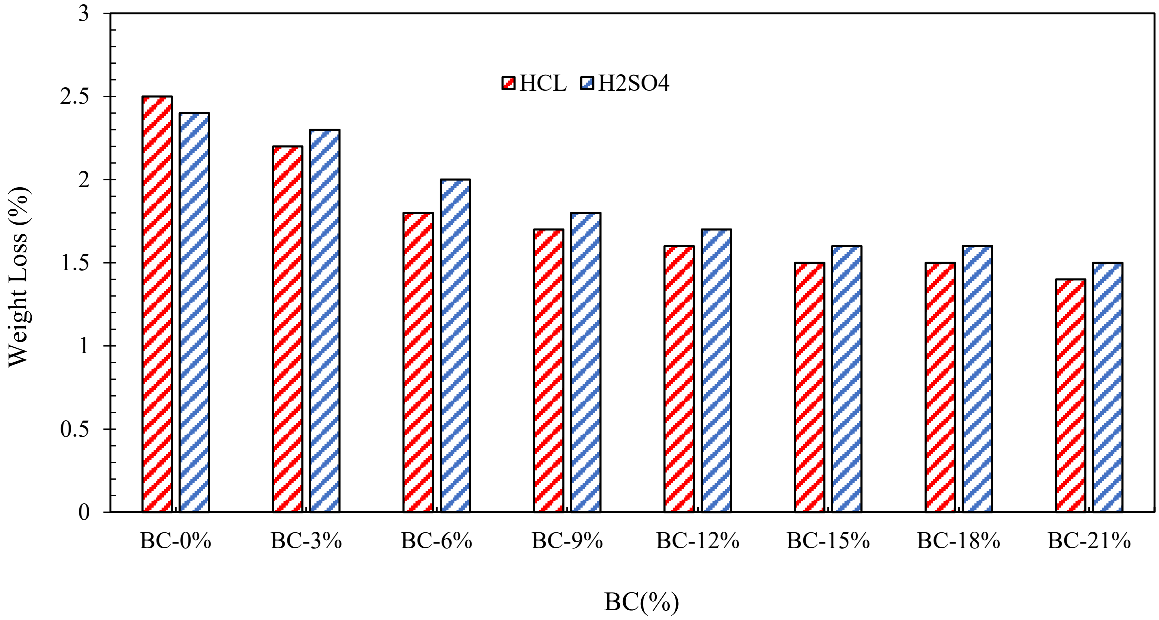

Figure 15. Acid resistance (data source [44]).

6.3. Dry Shrinkage

The shrinking of concrete is induced by the loss of moisture as a result of the drying process. To decrease cracking and the structural movement caused by drying shrinkage in concrete, shrinkage compensating concrete is utilized in its construction. It is dependent on the component materials, mixture proportions, curing time, drying environment, and constraint that the degree of drying shrinkage that happens in concrete buildings is determined. A study claims that the shrinkage of concrete is due to the movement of cement paste while aggregate restricts the movement of cement paste [55]. The findings of dry shrinkage of the five samples evaluated for initial days of hardening are assessed for evaluation. These specimens are the reference concrete, 5% BC, 10% BC, 15% BC, and 20% BC, respectively. Results indicate that the reference concrete experienced a large shrinkage when compared to the total amount of shrinkage experienced by all of the bentonite mixes. The maximal value of autogenous shrinkage strain obtained by the control mix was 135 macro strains. The shrinkage in B-5 and B-10 was 40 macro strain or 31 percent and 11 percent, respectively, but the shrinkage in B-15 and B-20 was 14 percent and 14 percent, respectively (Figure 16). The B-10 specimen produced the best results in terms of autogenous shrinkage strain. These findings are quite encouraging in terms of the decrease in linear shrinkage that may be obtained with the substitution of bentonite. The overall testing duration for the concrete beams was ten days, and no substantial fluctuation in autogenous strain was recorded beyond that time. The combined pozzolanic reaction and micro filling of mineral admixture improved the cement paste binding properties and density which ultimately decreased the dry shrinkage of concrete [57]. A study noted that the reduction of cement content in cement pastes results in a decrease in drying shrinkage of cement pastes [69]. In addition, the research found that the mineral additive lowered the heat of hydration which prevented the quick evaporation of water from the concrete surface and decreased the formation of dry shrinkage cracks [70]. It has also been observed that fly ash may significantly minimize drying shrinkage in concrete by plugging micropores in the concrete and hence increasing the internal compactness of the concrete mix [19].

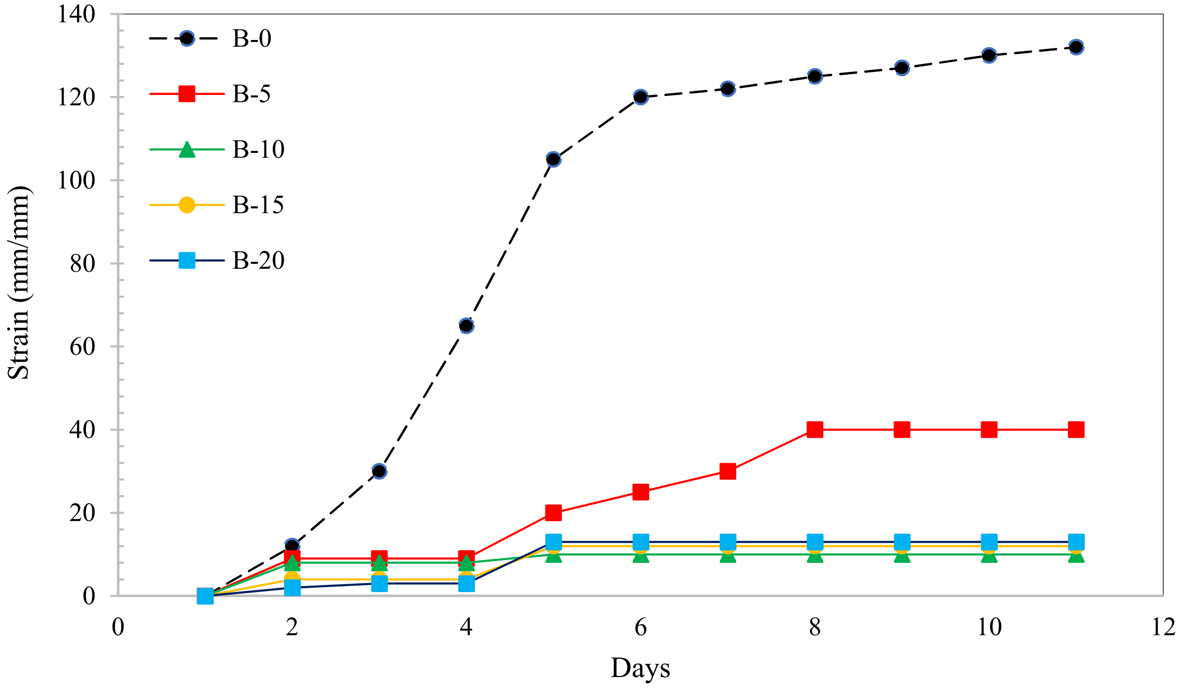

Figure 16. Dry shrinkage of concrete [71].

7. Conclusions

In a general sense, the incorporation of bentonite as pozzolan appears to be an environmentally friendly possibility. Technically and economically, BC presents various benefits to be used as a cement replacement in concrete. This review highlights the current research progress on bentonite clay in concrete. The main properties such as the physical and chemical composition of bentonite clay, fresh properties, and harden properties of concrete with varying doses of bentonite clay are the main focus of this review. Also, load defection and ductility were discussed. Furthermore, the durability of concrete with varying doses of bentonite clay was also a major concern of this review. The fundamental conclusions are as follows:

- Physical properties of bentonite clay show that the particle nature of bentonite clay is a rough and larger surface area than cement which negatively impacts the flowability of concrete.
- The chemical compounds of bentonite clay shows that it has the creditability to be utilized as a cement substitute.
- The flowability of concrete decreased with bentonite clay due to the larger surface area of bentonite clay which needed additional mortar to cover them and thus workability of concrete decreased.
- The fresh density was also noted to reduce with bentonite clay. The reduction in the fresh density is due to the lower specific gravity of bentonite clay as compared to cement.

- A reduction in mechanical performance was noted with bentonite clay. However, the decrease in strength was not significantly but approximately equal to the control. In contrast, some studies claim that strength was improved with bentonite clay due to pozzolanic reaction and micro filling voids, but more research is required in this regard.
- The load-deflection curve shows that the ductility of concrete is considerably improved with bentonite clay.
- Increased acid resistance and decreased dry shrinkage were observed with the substitution of bentonite clay instead of cement but still less studies are available on acid resistance and dry properties of concrete with substations of bentonite clay.

8. Future Perspective/Scope of BC

Although the overall review shows that bentonite clay has the creditability to be used as cement replacement in concrete up to some extent, less research focused on bentonite clay to be used as cement replacement in concrete as compared to other pozzolanic materials such silica fume, fly ash, etc. Furthermore, information on the long-term durability properties of concrete with bentonite clay is still scarce. No information is available on the alkali-silica reaction associated with bentonite clay. Therefore, this review recommends a detailed study on the durability aspects such as freezing and thawing action, dry shrinkage properties, and risk of alkali-silica reaction. Also, no information is available on microstructure analysis such as thermogravimetric analysis, and Fourier transforms infrared spectroscopy (FTIR). This review recommends a detailed study on microstructure analysis. Furthermore, the review also recommends fibers into bentonite clay-based concrete for high-strength concrete.

Author Contributions: Writing—original draft preparation, J.A.; Conceptualization, J.A., S.S. and K.J.K.; methodology, J.A.; software, J.A. and M.H.E.O.; validation, K.J.K., M.Z.A.-M. and M.A.E.-S.; formal analysis, J.A.; investigation, M.A.E.-S.; resources, M.Z.A.-M.; data curation, M.A.E.-S. and M.H.E.O.; writing—Formatting, M.H.E.O.; writing—review and editing, K.J.K. and S.S.; visualization, J.A. and M.H.E.O.; supervision, S.S. and M.H.E.O.; project administration, K.J.K.; funding acquisition, K.J.K. and M.H.E.O. All authors have read and agreed to the published version of the manuscript.

Funding: This paper is funded by the deanship of King Khalid University under grant number RGP. 2/5/43.

Institutional Review Board Statement: Not applicable.

Informed Consent Statement: Not applicable.

Data Availability Statement: All the data available in the manuscript.

Acknowledgments: The authors extend their appreciation to the Deanship of Scientific Research at King Khalid University for funding this work through Large Groups Project under grant number RGP.2/5/43.

Conflicts of Interest: The authors declare no conflict of interest.

References

1. Sankh, A.C.; Biradar, P.M.; Naghathan, S.J.; Ishwargol, M.B. Recent Trends in Replacement of Natural Sand with Different Alternatives. In Proceedings of the International Conference on Advances in Engineering and Technology, Singapore, 29–30 March 2014; pp. 59–66.
2. Svintsov, A.P.; Shchesnyak, E.L.; Galishnikova, V.V.; Fediuk, R.S.; Stashevskaya, N.A. Effect of Nano-Modified Additives on Properties of Concrete Mixtures during Winter Season. *Constr. Build. Mater.* **2020**, *237*, 117527. [CrossRef]
3. Fediuk, R. Reducing Permeability of Fiber Concrete Using Composite Binders. *Spec. Top. Rev. Porous Media Int. J.* **2018**, *9*, 79–89. [CrossRef]
4. Isler, J.W. *Assessment of Concrete Masonry Units Containing Aggregate Replacements of Waste Glass and Rubber Tire Particles*; University of Colorado at Denver: Denver, CO, USA, 2012; ISBN 1267297336.
5. Taskin, A.; Fediuk, R.; Grebenyuk, I.; Elkin, O.; Kholodov, A. Effective Cement Binders on Fly and Slag Waste from Heat Power Industry of the Primorsky Krai, Russian Federation. *Int. J. Sci. Technol. Res.* **2020**, *9*, 3509–3512.
6. Nassar, R.-U.-D.; Soroushian, P. Green and Durable Mortar Produced with Milled Waste Glass. *Mag. Concr. Res.* **2012**, *64*, 605–615. [CrossRef]

7. Benhelal, E.; Zahedi, G.; Shamsaei, E.; Bahadori, A. Global Strategies and Potentials to Curb CO_2 Emissions in Cement Industry. *J. Clean. Prod.* **2013**, *51*, 142–161. [CrossRef]
8. Oh, D.-Y.; Noguchi, T.; Kitagaki, R.; Park, W.-J. CO_2 Emission Reduction by Reuse of Building Material Waste in the Japanese Cement Industry. *Renew. Sustain. Energy Rev.* **2014**, *38*, 796–810. [CrossRef]
9. Agency, I.E.; Agency, I.E. *Tracking Industrial Energy Efficiency and CO_2 Emissions*; OECD: Paris, France, 2007; ISBN 9789264030169.
10. Berriel, S.S.; Favier, A.; Domínguez, E.R.; Machado, I.R.S.; Heierli, U.; Scrivener, K.; Hernández, F.M.; Habert, G. Assessing the Environmental and Economic Potential of Limestone Calcined Clay Cement in Cuba. *J. Clean. Prod.* **2016**, *124*, 361–369. [CrossRef]
11. Kou, S.C.; Poon, C.S. Properties of Self-Compacting Concrete Prepared with Coarse and Fine Recycled Concrete Aggregates. *Cem. Concr. Compos.* **2009**, *31*, 622–627. [CrossRef]
12. Si, R.; Dai, Q.; Guo, S.; Wang, J. Mechanical Property, Nanopore Structure and Drying Shrinkage of Metakaolin-Based Geopolymer with Waste Glass Powder. *J. Clean. Prod.* **2020**, *242*, 118502. [CrossRef]
13. Mirza, J.; Riaz, M.; Naseer, A.; Rehman, F.; Khan, A.N.; Ali, Q. Pakistani Bentonite in Mortars and Concrete as Low Cost Construction Material. *Appl. Clay Sci.* **2009**, *45*, 220–226. [CrossRef]
14. Smith, R.A.; Kersey, J.R.; Griffiths, P.J. The Construction Industry Mass Balance: Resource Use, Wastes and Emissions. *Construction* **2002**, *4*, 680.
15. Jiang, Y.; Ling, T.-C.; Mo, K.H.; Shi, C. A Critical Review of Waste Glass Powder—Multiple Roles of Utilization in Cement-Based Materials and Construction Products. *J. Environ. Manag.* **2019**, *242*, 440–449. [CrossRef] [PubMed]
16. Anwar, A. The Influence of Waste Glass Powder as a Pozzolanic Material in Concrete. *Int. J. Civ. Eng. Technol.* **2016**, *7*, 131–148.
17. Zhang, T.; Yang, Y.-L.; Liu, S.-Y. Application of Biomass by-Product Lignin Stabilized Soils as Sustainable Geomaterials: A Review. *Sci. Total Environ.* **2020**, *728*, 138830. [CrossRef]
18. Park, S.B.; Lee, B.C.; Kim, J.H. Studies on Mechanical Properties of Concrete Containing Waste Glass Aggregate. *Cem. Concr. Res.* **2004**, *34*, 2181–2189. [CrossRef]
19. Rahma, A.; El Naber, N.; Issa Ismail, S. Effect of Glass Powder on the Compression Strength and the Workability of Concrete. *Cogent Eng.* **2017**, *4*, 1373415. [CrossRef]
20. Somasri, M.; Kumar, B.N. Graphene Oxide as Nano Material in High Strength Self-Compacting Concrete. *Mater. Today Proc.* **2021**, *43*, 2280–2289. [CrossRef]
21. Siddique, R.; Singh, G.; Singh, M. Recycle Option for Metallurgical by-Product (Spent Foundry Sand) in Green Concrete for Sustainable Construction. *J. Clean. Prod.* **2018**, *172*, 1111–1120. [CrossRef]
22. Idir, R.; Cyr, M.; Tagnit-Hamou, A. Use of Waste Glass As Powder and Aggregate in Cement-Based Materials. In Proceedings of the SBEIDCO-1st International Conference on Sustainable Built Environment Infrastructures in Developing Countries, Oran, Algeria, 12–14 October 2009; pp. 109–116.
23. Kumar, R.; Goel, P.; Mathur, R. Suitability of Concrete Reinforced with Synthetic Fiber for the Construction of Pavements. In Proceedings of the 3rd International Conference on Sustainable Construction Materials and Technologies, Kyoto, Japan, 18–21 August 2013; pp. 18–22.
24. Amin, S.K.; Allam, M.E.; Garas, G.L.; Ezz, H. A Study of the Chemical Effect of Marble and Granite Slurry on Green Mortar Compressive Strength. *Bull. Natl. Res. Cent.* **2020**, *44*, 19. [CrossRef]
25. Jani, Y.; Hogland, W. Waste Glass in the Production of Cement and Concrete—A Review. *J. Environ. Chem. Eng.* **2014**, *2*, 1767–1775. [CrossRef]
26. Humphreys, D. Long-Run Availability of Mineral Commodities. *Miner. Econ.* **2013**, *26*, 1–11. [CrossRef]
27. Müller, N.; Harnisch, J. *How to Turn Around the Trend of Cement Related Emissions in the Developing World*; WWF: Gland, Switzerland, 2008.
28. Imbabi, M.S.; Carrigan, C.; McKenna, S. Trends and Developments in Green Cement and Concrete Technology. *Int. J. Sustain. Built Environ.* **2012**, *1*, 194–216. [CrossRef]
29. McEwan, A.E. From Cottages to 'Skyscrapers': The Architecture of AE & ES Luttrell in Tasmania and New Zealand. Master's Thesis, University of Canterbury, Christchurch, New Zealand, 1988.
30. Okeke, K.L.; Adedeji, A.A. A Review on the Properties of Concrete Incorporated with Waste Glass as a Substitute for Cement. *Epistem. Sci. Eng. Technol.* **2016**, *5*, 396–407.
31. Idir, R.; Cyr, M.; Tagnit-Hamou, A. Use of Fine Glass as ASR Inhibitor in Glass Aggregate Mortars. *Constr. Build. Mater.* **2010**, *24*, 1309–1312. [CrossRef]
32. Rashad, A.M. Recycled Waste Glass as Fine Aggregate Replacement in Cementitious Materials Based on Portland Cement. *Constr. Build. Mater.* **2014**, *72*, 340–357. [CrossRef]
33. Pusch, R. *Bentonite Clay: Environmental Properties and Applications*; CRC Press: Boca Raton, FL, USA, 2015; ISBN 148224344X.
34. Arslan, M.; Abdioğlu, E.; Kadir, S. Mineralogy, Geochemistry, and Origin of Bentonite in Upper Cretaceous Pyroclastic Units of the Tirebolu Area, Giresun, Northeast Turkey. *Clays Clay Miner.* **2010**, *58*, 120–141. [CrossRef]
35. Ahmad, J.; Tufail, R.F.; Aslam, F.; Mosavi, A.; Alyousef, R.; Faisal Javed, M.; Zaid, O.; Khan Niazi, M.S. A Step towards Sustainable Self-Compacting Concrete by Using Partial Substitution of Wheat Straw Ash and Bentonite Clay Instead of Cement. *Sustainability* **2021**, *13*, 824. [CrossRef]
36. Fernandez, R.; Martirena, F.; Scrivener, K.L. The Origin of the Pozzolanic Activity of Calcined Clay Minerals: A Comparison between Kaolinite, Illite and Montmorillonite. *Cem. Concr. Res.* **2011**, *41*, 113–122. [CrossRef]

37. Andrade, C.; Martínez-Serrano, A.; Sanjuán, M.Á.; Tenorio Ríos, J.A. Reduced Carbonation, Sulfate and Chloride Ingress Due to the Substitution of Cement by 10% Non-Precalcined Bentonite. *Materials* **2021**, *14*, 1300. [CrossRef]
38. Ramezanianpour, A.A.; Pourkhorshidi, A.R. Durability of Concretes Containing Supplementary Cementing Materials under Hot and Aggressive Environment. *Spec. Publ.* **2004**, *221*, 633–646.
39. Reddy, G.V.K.; Rao, V.R.; Reddy, M.A.K. Experimental Investigation of Strength Parameters of Cement and Concrete by Partial Replacement of Cement with Indian Calcium Bentonite. *Int. J. Civ. Eng. Technol.* **2017**, *8*, 512–518.
40. Wei, J.; Gencturk, B. Hydration of Ternary Portland Cement Blends Containing Metakaolin and Sodium Bentonite. *Cem. Concr. Res.* **2019**, *123*, 105772. [CrossRef]
41. Ashraf, M.; Iqbal, M.F.; Rauf, M.; Ashraf, M.U.; Ulhaq, A.; Muhammad, H.; Liu, Q. Developing a Sustainable Concrete Incorporating Bentonite Clay and Silica Fume: Mechanical and Durability Performance. *J. Clean. Prod.* **2022**, *337*, 130315. [CrossRef]
42. Khandelwal, S.; Rhee, K.Y. Evaluation of Pozzolanic Activity, Heterogeneous Nucleation, and Microstructure of Cement Composites with Modified Bentonite Clays. *Constr. Build. Mater.* **2022**, *323*, 126617. [CrossRef]
43. Reddy, M.A.K.; Rao, V.R.; Chaitanya, K.N.; Khed, V.C. Optimization of Bentocrete Parameters Using Response Surface Methodology (RSM). *AIMS Mater. Sci.* **2021**, *8*, 221–247. [CrossRef]
44. Memon, S.A.; Arsalan, R.; Khan, S.; Lo, T.Y. Utilization of Pakistani Bentonite as Partial Replacement of Cement in Concrete. *Constr. Build. Mater.* **2012**, *30*, 237–242. [CrossRef]
45. Khushnood, R.A.; Rizwan, S.A.; Memon, S.A.; Tulliani, J.-M.; Ferro, G.A. Experimental Investigation on Use of Wheat Straw Ash and Bentonite in Self-Compacting Cementitious System. *Adv. Mater. Sci. Eng.* **2014**, *2014*, 832508. [CrossRef]
46. Ahmad, J.; Martínez-García, R.; De-Prado-Gil, J.; Irshad, K.; El-Shorbagy, M.A.; Fediuk, R.; Vatin, N.I. Concrete with Partial Substitution of Waste Glass and Recycled Concrete Aggregate. *Materials* **2022**, *15*, 430. [CrossRef]
47. *ASTM D6868*; Specification for Biodegradable Plastics Used as Coatings on Paper and Other Compostable Substrates. ASTM International: West Conshohocken, PA, USA, 2017.
48. Akbar, J.; Alam, B.; Ashraf, M.; Afzal, S.; Ahmad, A.; Shahzada, K. Evaluating the Effect of Bentonite on Strength and Durability of High Performance Concrete. *Int. J. Adv. Struct. Geotech. Eng.* **2013**, *2*, 1–5.
49. Vijay, C.; Reddy, M.A.K. Optimization of Bentonite Modified Cement Mortar Parameters at Elevated Temperatures Using RSM. In *IOP Conference Series: Materials Science and Engineering*; IOP Publishing: Bristol, UK, 2021; Volume 1197, p. 12040.
50. Shabab, M.E.; Shahzada, K.; Gencturk, B.; Ashraf, M.; Fahad, M. Synergistic Effect of Fly Ash and Bentonite as Partial Replacement of Cement in Mass Concrete. *KSCE J. Civ. Eng.* **2016**, *20*, 1987–1995. [CrossRef]
51. Mousavi, S.S.; Dehestani, M.; Mousavi, S.M. Bond Strength and Development Length of Glass Fiber-Reinforced Polymer Bar in Unconfined Self-Consolidating Concrete. *J. Reinf. Plast. Compos.* **2016**, *35*, 924–941. [CrossRef]
52. Ahmad, J.; Zaid, O.; Shahzaib, M.; Abdullah, M.U.; Ullah, A.; Ullah, R. Mechanical Properties of Sustainable Concrete Modified by Adding Marble Slurry as Cement Substitution. *AIMS Mater. Sci.* **2021**, *8*, 343–358. [CrossRef]
53. Waqas, R.M.; Butt, F.; Danish, A.; Alqurashi, M.; Mosaberpanah, M.A.; Masood, B.; Hussein, E.E. Influence of Bentonite on Mechanical and Durability Properties of High-Calcium Fly Ash Geopolymer Concrete with Natural and Recycled Aggregates. *Materials* **2021**, *14*, 7790. [CrossRef] [PubMed]
54. Fadaie, M.A.; Nekooei, M.; Javadi, P. Effect of Dry and Saturated Bentonite on Plastic Concrete. *KSCE J. Civ. Eng.* **2019**, *23*, 3431–3442. [CrossRef]
55. Ahmad, J.; Aslam, F.; Martinez-Garcia, R.; De-Prado-Gil, J.; Qaidi, S.M.A.; Brahmia, A. Effects of Waste Glass and Waste Marble on Mechanical and Durability Performance of Concrete. *Sci. Rep.* **2021**, *11*, 21525. [CrossRef] [PubMed]
56. Ahmad, S.; Barbhuiya, S.A.; Elahi, A.; Iqbal, J. Effect of Pakistani Bentonite on Properties of Mortar and Concrete. *Clay Miner.* **2011**, *46*, 85–92. [CrossRef]
57. Ahmad, J.; Aslam, F.; Martinez-Garcia, R.; El Ouni, M.H.; Khedher, K.M. Performance of Sustainable Self-Compacting Fiber Reinforced Concrete with Substitution of Marble Waste (MW) and Coconut Fibers (CFs). *Sci. Rep.* **2021**, *11*, 23184. [CrossRef]
58. Chandrakanth, M.; Rao, N.P.C.; Rao, K.S. Experimental Studies on Concrete with Bentonite as Mineral Admixture. *GRD J.* **2016**, *1*, 7–10.
59. Taklymi, S.M.Q.; Rezaifar, O.; Gholhaki, M. Investigating the Properties of Bentonite and Kaolin Modified Concrete as a Partial Substitute to Cement. *SN Appl. Sci.* **2020**, *2*, 2023. [CrossRef]
60. Ashish, P.; Srinivasarao, C. Influence of Bentonite as Partial Replacement of Cement in Basalt Fiber Concrete. In *IOP Conference Series: Materials Science and Engineering*; IOP Publishing: Bristol, UK, 2021; Volume 1185, p. 12015.
61. Sumitha, Y.; Abraham, R. Experimental Study on Bentonite Clay Powder with Silica Fume and GGBS as Partial Replacement of Cement in M40 Grade Concrete. *Int. J. Eng. Res. Technol.* **2016**, *5*. [CrossRef]
62. Liu, M.; Hu, Y.; Lai, Z.; Yan, T.; He, X.; Wu, J.; Lu, Z.; Lv, S. Influence of Various Bentonites on the Mechanical Properties and Impermeability of Cement Mortars. *Constr. Build. Mater.* **2020**, *241*, 118015. [CrossRef]
63. Kumar, B.P.; Rao, V.R.; Reddy, M.A.K. Effect on Strength Properties of Concrete by Partial Replacement of Cement with Calcium Bentonite and Fly Ash. *Technology* **2017**, *8*, 450–455.
64. Khaliq, S.U.L.; Jamil, I.; Ullah, H. Evaluating Permeability and Mechanical Properties of Waste Marble Dust Mix Concrete and Bentonite Mix Concrete. In Proceedings of the International Structural Engineering and Construction, Brisbane, Australia, 3–5 December 2018. [CrossRef]
65. Adeboje, A.O.; Kupolati, W.K.; Sadiku, E.R.; Ndambuki, J.M.; Kambole, C. Experimental Investigation of Modified Bentonite Clay-Crumb Rubber Concrete. *Constr. Build. Mater.* **2020**, *233*, 117187. [CrossRef]

66. Shannag, M.J. High Strength Concrete Containing Natural Pozzolan and Silica Fume. *Cem. Concr. Compos.* **2000**, *22*, 399–406. [CrossRef]
67. Rawal, P. Development of Durable Concrete from Pulverized Fly Ash and Pozzolan Derived from Agricultural Wastes. Master's Thesis, Asian Institute of Technology, Bangkok, Thailand, 2003.
68. Fediuk, R.; Pak, A.; Kuzmin, D. Fine-Grained Concrete of Composite Binder. In *IOP Conference Series: Materials Science and Engineering*; IOP Publishing: Bristol, UK, 2017; Volume 262, p. 12025.
69. Bheel, N.; Abbasi, S.A.; Awoyera, P.; Olalusi, O.B.; Sohu, S.; Rondon, C.; Echeverría, A.M. Fresh and Hardened Properties of Concrete Incorporating Binary Blend of Metakaolin and Ground Granulated Blast Furnace Slag as Supplementary Cementitious Material. *Adv. Civ. Eng.* **2020**, *2020*, 8851030. [CrossRef]
70. Ahmad, J.; Zaid, O.; Siddique, M.S.; Aslam, F.; Alabduljabbar, H.; Khedher, K.M. Mechanical and Durability Characteristics of Sustainable Coconut Fibers Reinforced Concrete with Incorporation of Marble Powder. *Mater. Res. Express* **2021**, *8*, 075505. [CrossRef]
71. Afzal, S.; Shahzada, K.; Fahad, M.; Saeed, S.; Ashraf, M. Assessment of Early-Age Autogenous Shrinkage Strains in Concrete Using Bentonite Clay as Internal Curing Technique. *Constr. Build. Mater.* **2014**, *66*, 403–409. [CrossRef]

buildings

Article

Strength Properties of Cement-Solidified Dredged Sludge Affected by Curing Temperature

Yupeng Cao [1,2], Jing Zhang [3], Zengfeng Zhao [4,*], Junxia Liu [5] and Hui Lin [5]

[1] College of Civil Engineering and Architecture, Weifang University, Weifang 261061, China
[2] Key Laboratory of Ministry of Education for Geomechanics and Embankment Engineering, Hohai University, Nanjing 210098, China
[3] Zibo Planning and Information Center, Zibo 255022, China
[4] College of Civil Engineering, Tongji University, Shanghai 200092, China
[5] School of Civil Engineering and Architecture, East China University of Technology, Nanchang 330013, China
* Correspondence: zengfengzhao@tongji.edu.cn

Abstract: In this study, unconfined compressive strength (q_u) tests were conducted to explore the coupling effect of organic matter content (3.7%, 7.7%, 10.7%, and 13.7%) and curing temperature (18 °C, 36 °C, 46 °C) on the development of early and mid-late strength of cement-solidified dredged sludge (cement-stabilized clay, or CSC). The microstructure of the CSC containing organic matter at different curing temperatures was also analyzed. The results show that q_u of CSC decreases with the increase in organic matter content (C_o). The strength growth rate of CSC in the mid-late stage ($\geq$14 days) is small when $C_o \geq 7.7\%$, and it is difficult to increase this strength growth rate even if the curing temperature is increased up to 46 °C. There is a cement incorporation ratio threshold of 15% for q_u of CSC containing organic matter ($C_o = 7.7\%$), which is not affected by curing temperature; increasing the cement incorporation ratio (to 20%) cannot increase q_u significantly. The CSC with high curing temperature has more hydration products and higher structural compactness, and it can obtain higher q_u in the early and mid-late stages. A high curing temperature can increase the early strength growth rate and shorten the curing age for CSC containing organic matter.

Keywords: organic matter; curing temperature; cement-solidified dredged sludge; unconfined compressive strength; microstructure

1. Introduction

More than 100 million cubic meters of dredged sludge are produced every year in China's coastal areas from harbor dredging, waterway widening and water quality improvements [1–6]. Dredged sludge generally has high clay content and high water content, due to using a cutter suction dredger. Currently, the dredged sludge is often abandoned in cofferdams, occupying a large amount of land resources for a long time, which leads to social conflicts and environmental pollution [7]. In order to transform the sludge into suitable engineering materials, achieve waste utilization and sustainable economic development, chemical solidification technology using cementitious materials such as cement and lime is generally proposed and has been already applied in some construction projects, such as ports, road subbases and airports [8–16].

In recent years, fluid-plastic cement-solidified dredged sludge (cement-stabilized clay, or CSC) has been pumped into reclamation areas to form construction sites that meet a certain mechanical strength for reclamation projects, which could solve the problem of the shortage of resources, and it is one important way to use this waste material in large-scale applications [17–19]. Except for the characteristics of low cement content and high initial water content of CSC in reclamation projects [14,20], there are also the following two distinctive features: (1) Sludge (especially for marine sediments) usually contains a certain amount of organic matter [21–25], affecting the development of strength; (2) CSC is usually directly poured underwater, and the seawater temperature is used as the ambient temperature. Taking the waters near Hainan and Guangdong provinces of China as an example, the ambient temperature is higher than 25 °C for more than 6 months per year, and the maximum temperature is 30 °C [26]. In addition, CSC technology usually has a large filling volume and fast construction speed, which leads to the heat generated by cement hydration gathering inside the CSC, making the temperature of the whole pouring area significantly higher than the external temperature. The internal hydration heat of large-volume CSC is high, the seawater temperature varies in different sea areas, and the ambient temperature varies in different areas (e.g., the highest temperature recorded in Singapore in 2017 was 35.7 °C) [17,27,28], all of which factors are different from those in the curing environment of traditional CSC.

The main representative material of organic matter is humic acid [29–32], which will adsorb on the surface of soil particles, lowering the pH value of pore water and hindering cement hydration and pozzolanic reactions [31,33,34]. Calcium humate formed by hydration reaction will deposit on the surface of cement particles, preventing the formation of chemical products and soil-cement [35]. Organic matter has a large number of functional groups, which affect the stability of the soil skeleton formed by clay particles and hydration products [36]. Tremblay et al. [37] analyzed the influence of different organic compounds on the strength of cement-solidified soil from the perspective of a curing mechanism through laboratory tests and pointed out that the existence of organic matter can seriously affect the strength development. When the pH value is less than 9.0, cement products do not form in the presence of high sulfate content. A large number of previous results showed that the presence of organic matter significantly reduced the strength of cement-solidified soil [24,36,38,39]. Du et al. [24] investigated the 28-day unconfined compressive strength with organic matter content in the range of 0–21% and found that the strength decreased (the strength loss was increased) with the increase of organic matter content. When the organic matter content was 21%, the strength was about 40% compared to the solidified soil system without organic matter. However, for foundation soil rich in organic matter (e.g., peat foundation), the unconfined compressive strength did not reach 300 kPa even when the cement content reached 30% [35]. Kang et al. [29] found that the strength development of cement-solidified soil is controlled by both cement and humus content. For a given humic acid content, there was a threshold cement content at which the adverse effect of humic acid on strength development could be overcome. All these conclusions showed that organic matter has a negative effect on cement-solidified soil, but the effect of curing temperature was not considered in the previous studies.

Curing temperature will affect the mechanical behavior of cement-stabilized material [40]. Concrete and mortar generally have higher early strength at higher curing temperatures, but the long-term strength will decrease [41]. For cement stabilized sludge, the high curing temperature can reduce the pH requirement for the pozzolanic reaction between clay particles and $Ca(OH)_2$, and thus the quantity of pozzolanic reactions between the $Ca(OH)_2$ and kaolinite is increased. High curing temperature can accelerate the cement hydration, which accumulates more strength in reinforced material, and lead to a higher early and long-term strength. These conclusions are confirmed by the measured data [28,42–45]. However, few studies have focused on the long-term behavior of cement-stabilized clays at different temperatures. The important factors affecting the strength of solidified soil (organic matter and curing temperature) have opposite effects on the strength development of solidified soil. Current studies mainly focus on the independent influence of a single factor on the strength behavior of solidified soil, and few studies have been devoted to solidified dredged sludge. The coupling effect of the two factors on the strength performance of CSC is still unclear. Thus, it is important to clarify the influence of curing temperature and organic matter on the strength development of CSC to better use it in industrial applications.

The unconfined compressive strength tests of CSC with different cement incorporation ratios, initial water content, organic matter content and curing temperature are carried out in the laboratory. The influences of the coupling effect of organic matter and curing temperature on the strength growth of CSC at the early and mid-late stages are comprehensively evaluated. In addition, the microstructure of CSC containing organic matter is analyzed by Scanning Electron Microscopy (SEM). This study will provide knowledge on the strength development of large-volume underwater pouring projects using CSC as filler at different curing temperatures.

2. Materials and Experimental Program

2.1. Materials

The dredged sludge used in this study was obtained from Huaihe River bank sediment (located in Bengbu City, Anhui Province, China). Table 1 shows the physical properties of dredged sludge. According to ASTM D2487, the tested sludge was a high liquid limit clay [46]. According to the potassium dichromate method, the organic matter content in the sludge was measured as 3.7%. Adding high-purity humic acid (HA) to soil was the main method to prepare cement-solidified organic-containing soil [47]. Therefore, the effect of organic matter on the strength of CSC was investigated by adding HA to the sludge. The organic matter used is 95% pure powder HA from Jinan Luhui Chemical Co., Ltd. (Jinan, Shandong Province, China). The cement used in this study (P.S.A 32.5) is mainly composed of 49% Portland cement, 39% slag, and 7% fly ash, which is provided by Zhucheng Yangchun Cement Co., Ltd. (Weifang, Shandong Province, China). The physical and chemical properties of cement are shown in Table 2.

Table 1. Physical properties of dredged sludge.

Soil Type	Natural Water Content (%)	Organic Matter Content (%)	Plastic Limit (%)	Liquid Limit w_L (%)	Specific Gravity	Clay ($\leq$0.002 mm) (%)	Sand ($\geq$0.06 mm) (%)
Dredged sludge	73.9	3.7	26.9	58.8	2.7	35.0	4.4

Table 2. Physical properties and chemical properties of cement used in this study.

Physical Index	Measured Value
Fineness 0.08 mm sieve residue (%)	2.6
Initial setting time (min)	226
Final setting time (min)	317
Standard consistency (%)	31.80
Chemical composition	Measured value
Sulphur trioxide SO_3(%)	2.30
Magnesium oxide MgO (%)	3.45
Slag (%)	39.0
Fly ash (%)	7.0
Chloride (%)	0.038
Gypsum (%)	5.0

2.2. Test Scheme

In the practical engineering of CSC, the cement incorporation ratio A_w is usually 10–20% [48]. According to the different organic matter contents present in the sludge from different regions and the solidification test of the organic matter reported in the sludge [21–24], the corresponding organic matter contents used in this study were chosen as 3.7%, 7.7%, 10.7% and 13.7%, respectively. Since the organic matter content (C_o) of the original sludge is 3.7%, the amount of HA added (C_{HA}) is 0%, 4%, 7% and 10%, respectively [24]. The curing temperature range of the existing research ranges from 10 to 50 °C [49,50], so 18 °C, 36 °C and 46 °C are selected as the curing temperatures in this study.

To investigate the effects of initial water content w, cement incorporation ratio A_w, and organic matter content C_o on strength, the mixture conducted in this study is shown in Table 3. The CSC samples designed with the above different mixing ratios were cured at three curing temperatures (T = 18 °C, 36 °C, 46 °C), and the curing ages used were 3, 7, 14, 28, and 60 days, respectively. About 480 samples of different mixes were evaluated in this study. Each group has two parallel samples, and the average value is presented in the results and discussion section.

Table 3. Test scheme used in this study.

Series	Cement Incorporation Ratio A_w (%)	Water Content w (times w_L)	Organic Matter Content C_o (%)	Curing Temperature (°C)	Curing Age (d)
1	15	1.50	3.7	18, 36, 46	3, 7, 14, 28, 60
2	15	1.50	7.7	18, 36, 46	3, 7, 14, 28, 60
3	15	1.50	10.7	18, 36, 46	3, 7, 14, 28, 60
4	15	1.50	13.7	18, 36, 46	3, 7, 14, 28, 60
5	10	1.50	7.7	18, 36, 46	3, 7, 14, 28, 60
6	13	1.50	7.7	18, 36, 46	3, 7, 14, 28, 60
7	20	1.50	7.7	18, 36, 46	3, 7, 14, 28, 60
8	15	1.75	7.7	18, 36, 46	3, 7, 14, 28, 60
9	15	2.00	7.7	18, 36, 46	3, 7, 14, 28, 60
10	15	2.25	7.7	18, 36, 46	3, 7, 14, 28, 60

The dosage of each material (e.g., cement, HA, water) was calculated based on the experimental design of each mixing ratio. Powdered HA and purified water were added to the sludge, then they were mechanically stirred until homogenous states were reached. A proper amount of cement was added to the sludge-HA-water mixture and mixed for 6–8 min. The well-mixed cement-sludge-HA-water mixture was poured in three layers into a cylindrical PVC mold ($\varphi \times h$ = 4 cm × 8 cm) which was evenly coated with Vaseline. In order to eliminate the influence of bubbles, each layer of the mixture was poured and vibrated on a shaking table for 30 s. The molds were stored in the standard curing box and demolded after 6 h. The demolded samples were stored in the curing tank by adjusting the different curing temperatures. After a specific curing age, the unconfined compressive strength test was carried out. The strength of CSC was measured by using a YYW-II strain controlled unconfined compression gauge, and the data were collected by a TMR-200 multi-data acquisition system. Scanning electron microscopy (SEM) was used to examine the sections of the fractured specimens after 60 days of curing. For SEM tests, the images were taken with a Zeiss EVO 18 at a magnification of 2000 to 20,000. In order to get a more ideal solid section, the broken sample was knocked open and small pieces with flat surfaces were selected from the center. Before the SEM test, the sample was soaked in anhydrous alcohol and then dried at a low temperature for 8 h. To prevent charge accumulation on the sample surface, a layer of conductive adhesive was sprayed onto the observation sample. Finally, the sample was placed on the holder, and the flat part of the sample was selected for the SEM observation.

3. Results and Discussion

3.1. Influences of Cement Incorporation Ratio and Water Content on the Unconfined Compressive Strength

Figure 1 shows the relationship between unconfined compressive strength q_u and cement incorporation ratio A_w of CSC. For a given water content, the q_u of CSC at each curing age increases with the increase of A_w. The increasing trend of q_u with A_w of CSC at different curing ages is different. The q_u of CSC with 3 d, 7 d and 14 d curing ages increases linearly with the increase of A_w, while the q_u of CSC with 28 d and 60 d curing ages increases nonlinearly with A_w. The strength growth rate can be obtained by taking the derivative of the fitting formula of the q_u-A_w curve at different ages. The strength growth rate of 3 d, 7 d and 14 d increases with the increase of curing age. For the samples at 28 d and 60 d, the strength growth rate of CSC gradually decreases with the increase of A_w. When A_w is less than 15%, the longer the curing age and the greater the strength growth rate. However, when A_w is greater than 15%, the strength growth trend of 28 d and 60 d becomes slower, even lower than the strength growth rate of 7 d and 14 d.

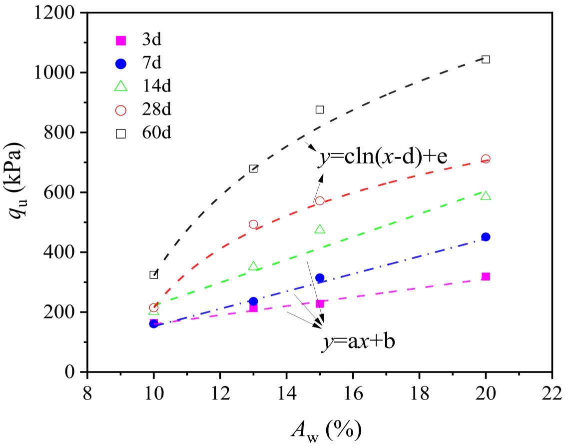

Figure 1. Relationship of q_u-A_w (T = 18 °C, w = 1.5 w_L, C_o = 3.7%).

Figure 2 shows the variation of q_u as a function of the initial water content w of CSC at different curing ages. For a given cement content, the strength of solidified sludge decreases nonlinearly with the increase of w. Combined with the change law of q_u with A_w analyzed above, q_u increases and decreases nonlinearly with the increase of A_w and w, respectively, which is consistent with the previous research results [51]. In CSC, cement hydration products are mainly calcium silicate hydrate (CSH) and calcium hydroxide ($Ca(OH)_2$), which contribute to the strength development. The initial water content is high in the solidified sludge samples (minimum 1.5 w_L), and the samples are in a saturated state during the curing process. When the initial water content increases, the corresponding water distribution in the pores of soil particles and cementation products increases, which leads to a decrease of the interaction between particle clusters.

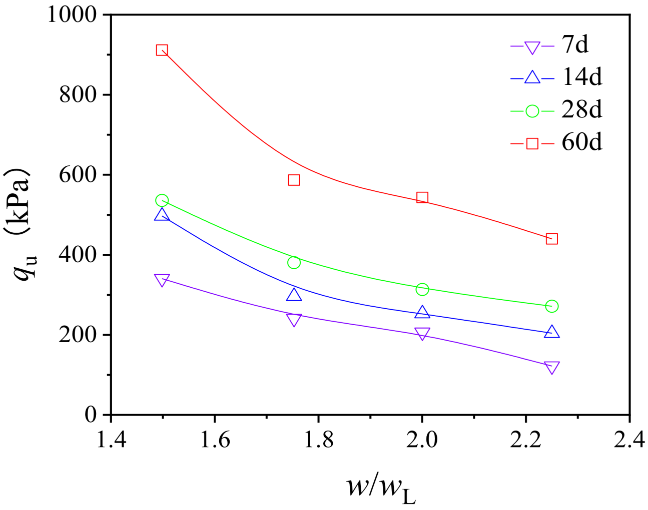

Figure 2. Relationship of q_u-w/w_L (T = 18 °C, A_w = 15%, C_o = 3.7%).

3.2. Influence of Organic Matter Content on the Unconfined Compressive Strength

Figure 3 shows the variation of unconfined compressive strength as a function of organic matter content C_o of solidified sludge at different temperatures and curing ages. In general, the influence of C_o on the q_u at each curing age is negative. When C_o is between 3.7% and 13.7%, q_u decreases with the increase of C_o. When the curing age exceeds 14 days, q_u decreases significantly when C_o is less than 7.7%, and the reduction trend of q_u slows down when C_o is greater than 7.7%.

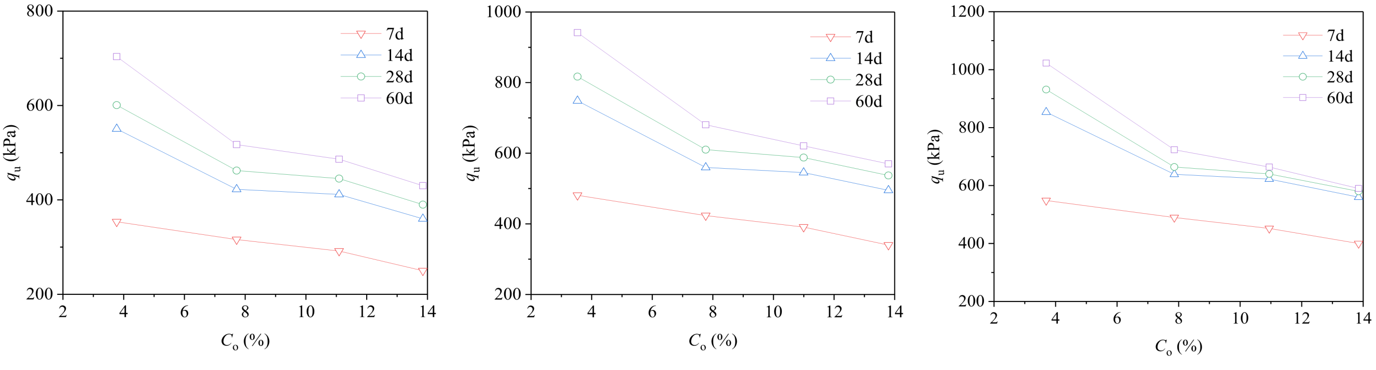

(**a**) (**b**) (**c**)

Figure 3. Relationship of q_u-C_o at different *temperatures*: (**a**) T = 18 °C; (**b**) T = 36 °C; (**c**) T = 46 °C.

For a given curing temperature, the strength of CSC mixed with a certain amount of organic matter increases in different ranges with the curing age. When C_o is larger than 7.7%, the growth range of q_u in the mid-late stage is limited. When the curing temperature rises, the increase of the strength of CSC in the mid-late stage is very small. At the curing temperature of 46 °C, the q_u of CSC after 28d with a C_o of 7.7%, 10.7% and 13.7% are 664, 640 and 580 kPa, respectively, while the q_u of CSC after 60d with a C_o of 13.7% is 590 kPa, which is only 10 kPa higher than that of q_u at 28d. It shows that the strength of CSC at high curing temperature and high organic matter content does not increase in the mid-late stage. Organic matter affects the strength growth of CSC in the mid-late stage, and high curing temperature will further aggravate the effect.

In order to quantitatively compare the effect of adding amount of HA on the strength development of CSC, the retention coefficient of strength is defined as $RCT = q_{u,ct}/q_{u,t}$ where $q_{u,ct}$ and $q_{u,t}$ are the unconfined compressive strengths of CSC with and without HA at a certain curing temperature and age, respectively. Figure 4 shows the development law of *RCT* with the added amount of HA (C_{HA}). For a given curing temperature, the change of *RCT* with C_{HA} shows a similar tread to the q_u-C_o curve of CSC, i.e., *RCT* decreases with the increase of C_{HA} (seen in Figure 4a). The longer the curing age, the more obvious is the reduction of *RCT*. The *RCT* values of 7 d, 28 d and 60 d curing ages with C_{HA} = 7% are 0.81, 0.72 and 0.66, respectively, which indicate that the effect of organic matter on the strength of CSC in the mid-late stage is greater than that in the early stage. In the alkaline environment of cement hydration, humic acid will exchange ions with calcium, magnesium, iron, aluminum and other metal ions, resulting in the reduction of hydroxide ion OH^- in pores of CSC, which makes it difficult to excite the pozzolanic reaction. Thus, the mid- and late-stage strength growth of CSC is greatly reduced [38,52].

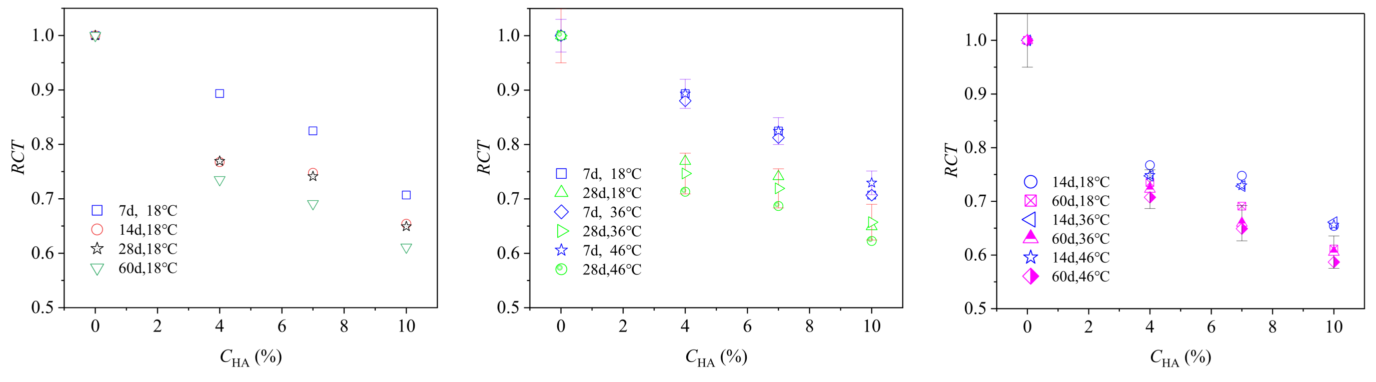

(**a**) (**b**) (**c**)

Figure 4. Relationship of *RCT*-C_{HA}: (**a**) T = 18 °C; (**b**) 7 d, 28 d curing age; (**c**) 14 d, 60 d curing age.

In addition, Figure 4b,c shows that, for a given C_o (or C_{HA}) and curing age, the *RCT* values at different curing temperatures are similar, which indicates that the reduction degree of organic matter on the strength of CSC is not affected by the temperature. When predicting the strength of CSC in practical projects, the independent variables C_o and T corresponding to organic matter content and curing temperature can be considered, respectively [43].

Figure 5 shows the variation of unconfined compressive strength with cement incorporation content at different temperatures when organic matter content is 7.7%. When A_w is not larger than 15%, the q_u-A_w curve of CSC with added HA shows an increasing trend, which is similar to that of CSC with C_{HA} = 0%. However, when A_w is greater than 15%, the q_u-A_w curve stops growing. This indicates that for organic-containing sludge, there is a cement incorporation ratio threshold, which is not affected by temperature, and when A_w is greater than this threshold, the increase of A_w does not increase its q_u significantly. The hyperbolic model is commonly used to predict the change of unconfined compressive strength with curing age. However, due to the existence of the A_w threshold in organic-containing sludge, there will be a large error if the model is still used to predict the strength growth.

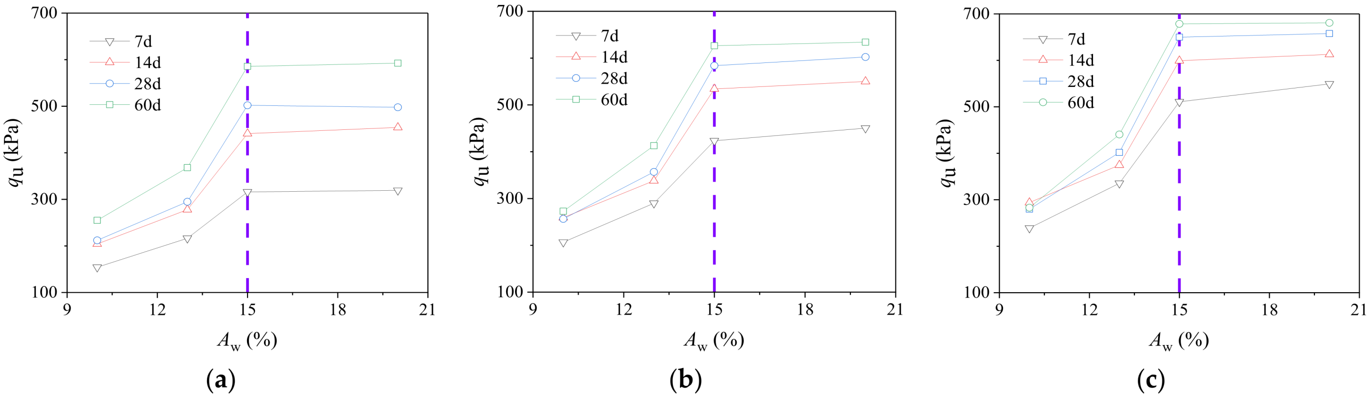

Figure 5. Relationship of q_u-A_w with C_o = 7.7% at different T. (**a**) T = 18 °C; (**b**) T = 36 °C; (**c**) T = 46 °C.

Figure 6 shows SEM images with different C_{HA}. Compared with the CSC without HA (C_{HA} = 0%), the sample with HA (C_{HA} = 4%) shows a lower density. Although the pore size of the sample doped with HA (C_{HA} = 4%) is relatively high, hydration products can also be observed around the clay particles, which are mutually cemented with the soil particles and improve the strength of CSC. However, with the increase of organic matter content (C_{HA} = 7%), the needle-like CSH in the SEM image of CSC is almost not observed. In addition, the structure is relatively loose (the porosity is relatively high), and so the strength of the sample is low. This may be due to the acid produced by organic matter consuming a large amount of $Ca(OH)_2$ in cement hydration products, which leads to the decrease of pozzolanic reaction. The hydrate products such as CSH and calcium aluminate hydrate (CAH) are decreased, which can reduce the strength of the specimens.

3.3. Influence of Curing Temperature on the Unconfined Compressive Strength

Figure 7 shows the strength development of solidified sludge containing organic matter at different temperatures. For a given mix ratio and curing age, the samples at higher curing temperatures can always obtain higher q_u in the early and mid-late stages, indicating that curing temperature can improve the strength of CSC. The increasing polymerization rate of silicate products and the formation of denser cementitious products are the main reasons for the early strength increase. The higher curing temperature is conducive to the dissociation of silicate and aluminate, which makes more $Ca(OH)_2$ participate in the pozzolanic reaction and produces more strengthening products, thus further increasing the strength in the mid-late stage [42].

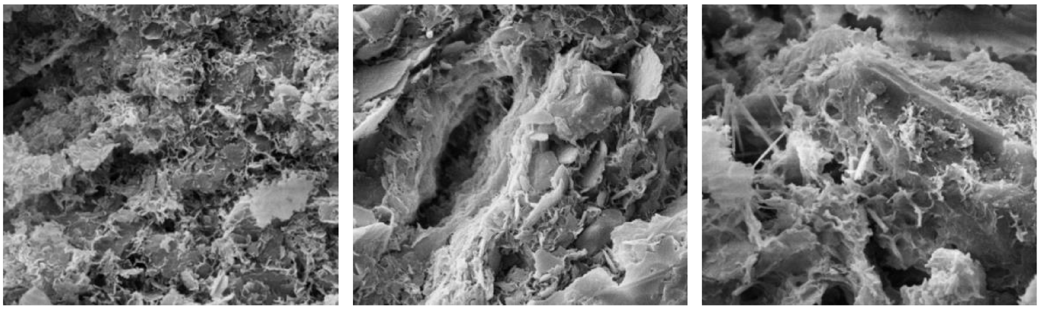

(**a**) (**b**) (**c**)

Figure 6. SEM images at different C_{HA} (at a magnification of 20K): (**a**) C_{HA} = 0%; (**b**) C_{HA} = 4%; (**c**) C_{HA} = 7%.

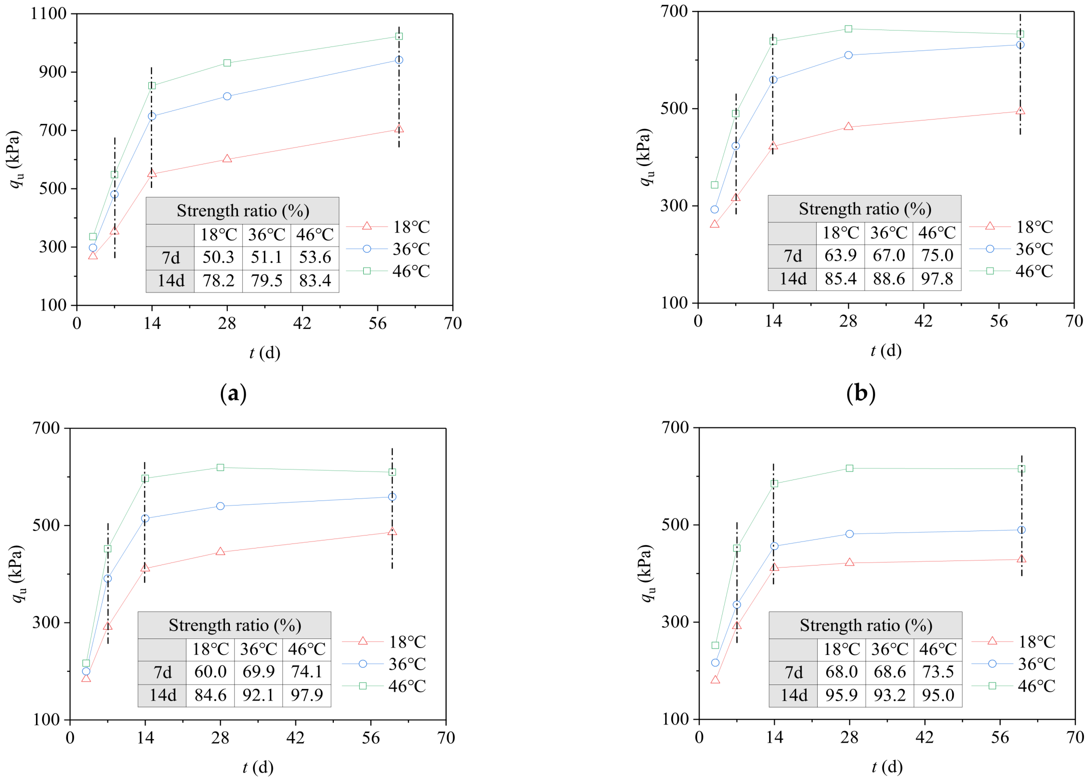

(**a**) (**b**)

(**c**) (**d**)

Figure 7. Relationship of q_u-t at different C_{HA}. (**a**) C_{HA} = 0%; (**b**) C_{HA} = 4%; (**c**) C_{HA} = 7%; (**d**) C_{HA} = 10%.

The strength ratio is defined as the ratio of the strength at different ages to the strength at 60 d age. The addition of HA can affect the development of curve shape and strength. Without adding HA, the strength of CSC at 7 d age can reach 50% of the compressive strength at 60 d age, while the strength at 14 d age can reach 80% of that at 60d age, and q_u increases with curing age. The strength ratios at 7 d and 14 d of CSC mixed with HA are higher than those without HA at the same age and curing temperature, indicating that organic matter increases the strength growth rate at the early stage of CSC. At the same curing age, the strength ratio of CSC with different organic matter content increases with the increase of curing temperature. When the curing temperature is 46 °C, the 14 d strength ratios are more than 95%, indicating that the curing age of the CSC containing organic matter can be greatly shortened by increasing the curing temperature.

In order to explain the effect of temperature on the strength of CSC, SEM tests were carried out on 60-day specimens with C_{HA} = 4%. Figures 8 and 9 show SEM images of CSC at 18 °C, 36 °C and 46 °C, respectively. The soil structure of solidified sludge samples at 18 °C has the worst compactness at lower magnification (2K), and large intergranular voids can be observed. With the increase in temperature, the samples show fewer voids and higher compactness. Using a higher magnification (20K), the bonding materials between the soil particles—calcium silicate hydrate CSH and calcium hydroxide CH—can be observed, specifically as aggregates of elongated spicules and anchor sheets. The samples at 18 °C show the lowest amount of fine gel or mesh products in the soil-cement body. In the 36 °C samples, a higher density network structure can be observed, indicating that a large amount of solidified soil is formed in the CSC. In the 46 °C samples, most of the soil particles are observed to be covered with fine gel-like reinforcing material with only a few unfilled pores. Bi and Chian (2021) found through XRD patterns that the hydration products were mainly $Ca(OH)_2$ and CSH. At a lower curing temperature (less than 23 °C), the content of $Ca(OH)_2$ in the solidification products was high. However, at a higher curing temperature (48 °C), $Ca(OH)_2$ was consumed by the pozzolanic reaction with silicate SiO_2 and aluminate Al_2O_3 in soil minerals [28]. The high curing temperature reduces the pH requirement for the pozzolanic reaction to occur [42]. The increase of curing temperature accelerates cement hydration and increases the amount of pozzolanic reactions between $Ca(OH)_2$ and clay minerals, both of which can produce strength-reinforced CSH material. As can be seen from Figure 9, with the increase of temperature, the amount of CSH increases. The observed positive relationship between the amount of binding material and curing temperature is consistent with the relationship observed by other studies [28]. In addition, in the case of relatively low cement content, a cement particle is likely to be surrounded by multiple clay particles; cement hydration products will more easily bond with clay particles and make reinforcement materials (such as CSH) distribute evenly [28], giving the CSC high strength at high curing temperatures.

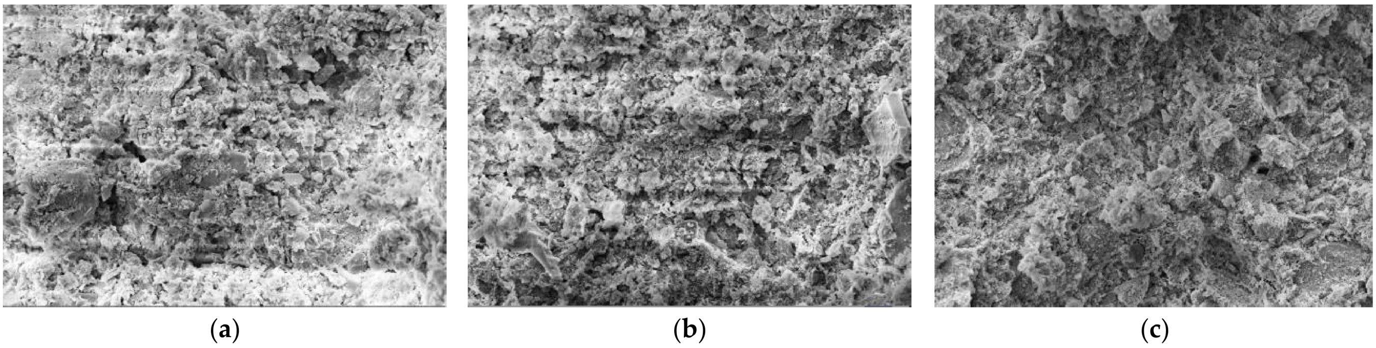
(**a**) (**b**) (**c**)

Figure 8. SEM images at different curing temperatures (at a magnification of 2K): (**a**) *T* = 18 °C; (**b**) *T* = 36 °C; (**c**) *T* = 46 °C.

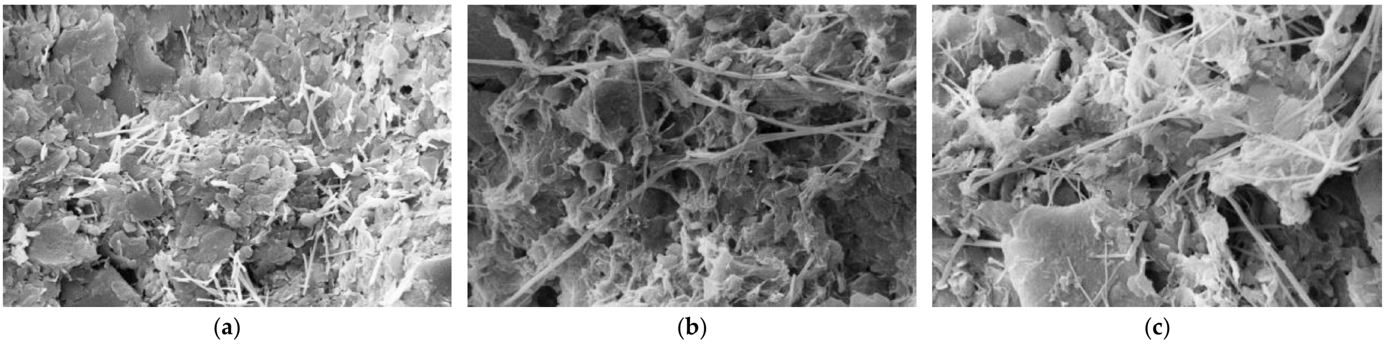
(**a**) (**b**) (**c**)

Figure 9. SEM images at different curing temperatures (at a magnification of 20K): (**a**) *T* = 18 °C; (**b**) *T* = 36 °C; (**c**) *T* = 46 °C.

4. Conclusions

In this study, the influences of organic matter content and curing temperature on the strength evolution of cement-solidified sludge are investigated by conducting unconfined compressive strength tests of CSC with different mixing ratios. The main conclusions are as follows:

1. The unconfined compressive strength q_u increases with the increase of cement incorporation ratio A_w and decreases with the increase of water content w. When the organic matter content C_o is 7.7%, there is the same threshold of A_w (15%) in the CSC at different temperatures. When A_w is greater than the threshold, the increase of A_w value (to 20%) does not increase the q_u at different curing ages significantly.
2. The overall effect of organic matter content on the q_u of CSC is negative. Organic matter reduces the strength growth of CSC in the mid-late stage, but it increases the strength growth rate of CSC in the early stage, and high curing temperature will further aggravate this effect.
3. The retention coefficient of strength value RCT decreases with the increase of C_{HA}, and the longer the curing age, the more obvious the reduction of RCT. The effect of organic matter on the q_u of CSC in the mid-late stage is greater than in the early stage.
4. The high curing temperature can improve the unconfined compressive strength in the early and mid-late stages of CSC, which can accelerate the formation of hydration products, improve the structural compactness, and greatly shorten the curing age of cement-solidified dredged sludge. This study will provide knowledge on the strength development of large-volume underwater pouring projects using CSC as filler in different curing temperatures.

Author Contributions: Y.C.: Conceptualization, methodology, writing—original draft preparation, supervision, project administration, funding acquisition; J.Z.: investigation, formal analysis, data curation; Z.Z.: writing—review and editing, funding acquisition, validation; J.L.: investigation, visualization, formal analysis; H.L.: writing—review and editing, validation, investigation. All authors have read and agreed to the published version of the manuscript.

Funding: This research was funded by the National Natural Science Foundation of China with grant number 52178347; the project ZR2021ME068 supported by Shandong Provincial Natural Science Foundation; Key Laboratory of Ministry of Education for Geomechanics and Embankment Engineering, Hohai University, grant number 2021006; Excellent Doctor Young Teacher Support Program of Weifang University; Scientific Research Foundation of Weifang University, grant number 2021BS32; Fundamental Research Funds for the Central Universities, funding numbers: 22120220084 (Tongji University).

Data Availability Statement: Not applicable.

Conflicts of Interest: The authors declare no conflict of interest.

References

1. Huang, Y.H.; Zhu, W.; Qian, X.D.; Zhang, N.; Zhou, X.Z. Change of Mechanical Behavior between Solidified and Remolded Solidified Dredged Materials. *Eng. Geol.* **2011**, *119*, 112–119. [CrossRef]
2. Cao, Y.P.; Xu, J.W.; Bian, X.; Xu, G.Z. Effect of Clogging on Large Strain Consolidation with Prefabricated Vertical Drains by Vacuum Pressure. *KSCE J. Civ. Eng.* **2019**, *23*, 4190–4200. [CrossRef]
3. Cao, Y.P.; Zhang, R.; Xu, G.Z.; Xu, J.W. Axisymmetric Large Strain Consolidation by Vertical Drains Considering Well Resistance under Vacuum Pressure. *Arab. J. Geosci.* **2021**, *14*, 2016. [CrossRef]
4. Cao, Y.P.; Zhang, J.; Xu, J.W.; Xu, G.Z. A Large-Strain Vacuum-Assisted Radial Consolidation Model for Dredged Sludge Considering Lateral Deformation. *KSCE J. Civ. Eng.* **2020**, *24*, 3561–3572. [CrossRef]
5. Bian, X.; Zeng, L.L.; Li, X.Z.; Hong, J.T. Deformation Modulus of Reconstituted and Naturally Sedimented Clays. *Eng. Geol.* **2021**, *295*, 106450. [CrossRef]
6. Bian, X.; Zeng, L.L.; Li, X.Z.; Shi, X.S.; Zhou, S.M.; Li, F.Q. Fabric Changes Induced by Super-Absorbent Polymer on Cement and Lime Stabilized Excavated Clayey Soil. *J. Rock Mech. Geotech. Eng.* **2021**, *13*, 1124–1135. [CrossRef]
7. Cao, Y.P.; Ding, J.W.; Zhang, R.; Xu, G.Z. Effect of Vertical Flow on Consolidation Degree of Foundation with Vertical Drains in Large-Strain Consolidation Theory. *KSCE J. Civ. Eng.* **2021**, *25*, 3264–3272. [CrossRef]

8. Kitazume, M.; Satoh, T. Development of a Pneumatic Flow Mixing Method and its Application to Central Japan International Airport Construction. *Proc. Inst. Civ. Eng.-Ground Improv.* **2003**, *7*, 139–148. [CrossRef]
9. Gao, Y.; Wang, Y.H. Experimental and DEM Examinations of K_0 in Sand under Different Loading Conditions. *J. Geotech. Geoenvironmental Eng.* **2014**, *140*, 1–11. [CrossRef]
10. Ma, C.; Qin, Z.H.; Zhuang, Y.C.; Chen, L.Z.; Chen, B. Influence of Sodium Silicate and Promoters on Unconfined Compressive Strength of Portland Cement-Stabilized Clay. *Soils Found.* **2015**, *55*, 1222–1232. [CrossRef]
11. Horpibulsuk, S.; Suksiripattanapong, C.; Samingthong, W.; Rachan, R.; Arulrajah, A. Durability against Wetting–Drying Cycles Of Water Treatment Sludge–Fly Ash Geopolymer and Water Treatment Sludge–Cement and Silty Clay–Cement Systems. *J. Mater. Civ. Eng.* **2016**, *28*, 04015078. [CrossRef]
12. Cecchin, I.; Reddy, K.R.; Thomé, A.; Tessaro, E.F.; Schnaid, F. Nanobioremediation: Integration of Nanoparticles and Bioremediation for Sustainable Remediation of Chlorinated Organic Contaminants in Soils. *Int. Biodeterior. Biodegrad.* **2017**, *119*, 419–428. [CrossRef]
13. Nordin, N.S.; Chan, C.M. Undrained Shear Strength of Low Dosage Cement-Solidified Dredged Marine Soils (DMS) for Reclamation Works. *Int. J. Geomate* **2017**, *13*, 180–186. [CrossRef]
14. Khalid, U.; Liao, C.C.; Ye, G.L.; Yadav, S.K. Sustainable Improvement of Soft Marine Clay Using Low Cement Content: A Multi-Scale Experimental Investigation. *Constr. Build. Mater.* **2018**, *191*, 469–480. [CrossRef]
15. Lee, H.; Kim, S.J.; Kang, B.H.; Lee, K.S. Long-Term Settlement Prediction of Ground Reinforcement Foundation Using a Deep Cement Mixing Method in Reclaimed Land. *Buildings* **2022**, *12*, 1279. [CrossRef]
16. Zhang, G.; Ding, Z.; Zhang, R.; Chen, C.; Fu, G.; Luo, X.; Wang, Y.; Zhang, C. Combined Utilization of Construction and DemolitionWaste and Propylene Fiber in Cement-Stabilized Soil. *Buildings* **2022**, *12*, 350. [CrossRef]
17. Zhang, R.; Qiao, Y.; Zheng, J.; Dong, C.A. Method for Considering Curing Temperature Effect in Mix Proportion Design of Mass Cement-Solidified Mud at High Water Content. *Acta Geotech.* **2020**, *16*, 279–301. [CrossRef]
18. Bian, X.; Zeng, L.L.; Ji, F.; Xie, M. Plasticity Role in Strength Behaviour of Cement-Phosphogypsum Stabilized Soils. *J. Rock Mech. Geotech. Eng.* 2022; *in press*. [CrossRef]
19. Bian, X.; Zhang, W.; Li, X.Z.; Shi, X.S.; Deng, Y.F.; Peng, J. Changes in Strength, Hydraulic Conductivity and Microstructure of Superabsorbent Polymer Stabilized Soil Subjected to Wetting-Drying Cycles. *Acta Geotech.* **2022**, *17*, 5043–5057. [CrossRef]
20. Liu, W.B.; Chen, Q.S.; Chiaro, G.; Jiang, H.M. Effect of a Cement-Lignin Agent on the Shear Behavior of Shanghai Dredged Marine Soils. *Mar. Georesources Geotechnol.* **2017**, *35*, 17–25. [CrossRef]
21. Gu, Z.; Hua, S.D.; Zhao, W.X.; Li, S.S.; Gao, Z.; Shan, H.T. Using Alkali-Activated Cementitious Materials to Solidify High Organic Matter Content Dredged Sludge as Roadbed Material. *Adv. Civ. Eng.* **2018**, *2018*, 2152949. [CrossRef]
22. Schmidt, F.; Hinrichs, K.U.; Elvert, M. Sources, Transport, and Partitioning of Organic Matter at a Highly Dynamic Continental Margin. *Mar. Chem.* **2010**, *118*, 37–55. [CrossRef]
23. Detzner, H.D.; Schramm, W.; Döring, U.; Bode, W. New Technology of Mechanical Treatment of Dredged Material from Hamburg Harbour. *Water Sci. Technol.* **1998**, *37*, 337–343. [CrossRef]
24. Du, C.; Zhang, J.L.; Yang, G.; Yang, Q. The Influence of Organic Matter on the Strength Development of Cement-Stabilized Marine Soft Clay. *Mar. Georesources Geotechnol.* **2020**, *1*, 1–11. [CrossRef]
25. Masciandaro, G.; Di Biase, A.; Macci, C.; Peruzzi, E.; Iannelli, R.; Doni, S. Phytoremediation of Dredged Marine Sediment: Monitoring of Chemical and Biochemical Processes Contributing to Sediment Reclamation. *J. Environ. Manag.* **2014**, *134*, 166–174. [CrossRef] [PubMed]
26. Tang, Y.X.; Miyazaki, Y.; Tsuchida, T. Practices of Reused Dredgings by Cement Treatment. *Soils Found.* **2001**, *41*, 129–143. [CrossRef]
27. Yun, J.M.; Song, Y.S.; Lee, J.H.; Kim, T.H. Strength Characteristics of the Cement-Stabilized Surface Layer in Dredged and Reclaimed Marine Clay, Korea. *Mar. Georesources Geotechnol.* **2006**, *24*, 29–45. [CrossRef]
28. Bi, J.R.; Chian, S.C. Modelling Strength Development of Cement-Stabilised Clay and Clay with Sand Impurity Cured under Varying Temperatures. *Bull. Eng. Geol. Environ.* **2021**, *80*, 6275–6302. [CrossRef]
29. Kang, G.O.; Tsuchida, T.; Kim, Y.S.; Baek, W.J. Influence of Humic Acid on the Strength Behavior of Cement-Treated Clay during Various Curing Stages. *J. Mater. Civ. Eng.* **2017**, *29*, 04017057. [CrossRef]
30. Lipczynska-Kochany, E. Humic Substances, Their Microbial Interactions and Effects on Biological Transformations of Organic Pollutants in Water and Soil: A Review. *Chemosphere* **2018**, *202*, 420–437. [CrossRef]
31. Beddaa, H.; Ben Fraj, A.; Lavergne, F.; Torrenti, J.M. Effect of Potassium Humate as Humic Substances from River Sediments on the Rheology, the Hydration and the Strength Development of a Cement Paste. *Cem. Concr. Compos.* **2019**, *104*, 103400. [CrossRef]
32. Ge, S.Q.; Zang, J.C.; Wang, Y.C.; Zheng, L.W.; Xie, X.Y. Combined Stabilization/Solidification and Electroosmosis Treatments for Dredged Marine Silt. *Mar. Georesources Geotechnol.* **2020**, *39*, 1157–1166. [CrossRef]
33. Saride, S.; Puppala, A.J.; Chikyala, S.R. Swell-Shrink and Strength Behaviors of Lime and Cement Stabilized Expansive Organic Clays. *Appl. Clay Sci.* **2013**, *85*, 39–45. [CrossRef]
34. Kamon, M. On the stabilization of Hydro by using cement group hardening materials. *J. Soc. Mater. Sci. Jpn.* **1989**, *38*, 1092–1097. [CrossRef]
35. Chen, H.E.; Wang, Q. The Behaviour of Organic Matter in the Process of Soft Soil Stabilization Using Cement. *Bull. Eng. Geol. Environ.* **2006**, *65*, 445–448. [CrossRef]

36. Ma, C.; Chen, B.; Chen, L.Z. Effect of Organic Matter on Strength Development of Self-Compacting Earth-Based Construction Stabilized with Cement-Based Composites. *Constr. Build. Mater.* **2016**, *123*, 414–423. [CrossRef]
37. Tremblay, H.; Duchesne, J.; Locat, J.; Leroueil, S. Influence of the Nature of Organic Compounds on Fine Soil Stabilization with Cement. *Can. Geotech. J.* **2002**, *39*, 535–546. [CrossRef]
38. Pan, Y.Z.; Rossabi, J.; Pan, C.G.; Xie, X.Y. Stabilization/solidification Characteristics of Organic Clay Contaminated by Lead when Using Cement. *J. Hazard. Mater.* **2019**, *362*, 132–139. [CrossRef]
39. Yilmaz, O.; Ünlü, K.; Cokca, E. Solidification/stabilization of Hazardous Wastes Containing Metals and Organic Contaminants. *J. Environ. Eng.* **2003**, *362*, 132–139. [CrossRef]
40. Du, Y.; Wang, S.; Hao, W.; Shi, F.; Wang, H.; Xu, F.; Du, T. Investigations of the Mechanical Properties and Durability of Reactive Powder Concrete Containing Waste Fly Ash. *Buildings* **2022**, *12*, 560. [CrossRef]
41. Chitambira, B. *Accelerated Ageing of Cement Stabilised/Solidified Contaminated Soils with Elevated Temperatures*. Ph.D. Thesis, University of Cambridge, London, UK, 2004.
42. Zhang, R.J.; Lu, Y.T.; Tan, T.S.; Phoon, K.K.; Santoso, A.M. Long-term Effect of Curing Temperature on the Strength Behavior of Cement-stabilized Clay. *J. Geotech. Geoenvironmental Eng.* **2014**, *140*, 04014045. [CrossRef]
43. Cao, Y.P.; Zhang, J.; Xu, G.Z.; Li, M.D.; Bian, X. Strength Properties and Prediction Model of Cement-Solidified Clay Considering Organic Matter and Curing Temperature. *Front. Mater.* **2022**, *9*, 965975. [CrossRef]
44. Porbaha, A.; Shibuya, S.; Kishida, T. State of the Art in Deep Mixing Technology. Part III: Geomaterial Characterization. *Proc. Inst. Civ. Eng. Ground Improv.* **2000**, *4*, 91–110. [CrossRef]
45. Marzano, I.P.; Al-Tabbaa, A.; Grisolia, M. Influence of Curing Temperature on the Strength of Cement-Stabilised Artificial Clays. In *Geotechnics of Soft Soils-Focus on Ground Improvement*; Karstunen, M., Leoni, M., Eds.; Taylor & Francis: London, UK, 2009; pp. 257–262.
46. ASTM. Standard Practice for Classification of Soils for Engineering Purposes (Unified Soil Classification System). ASTM: ASTM D2487-10; In *Standard Practice for Classification of Soils for Engineering Purposes (Unified Soil Classification System)*; ASTM: Montgomery County, PA, USA, 2010.
47. Suits, L.D.; Sheahan, T.C.; Tan, T.S.; Goh, T.L.; Yong, K.Y. Properties of Singapore Marine Clays Improved by Cement Mixing. *Geotech. Test. J.* **2002**, *25*, 422–433. [CrossRef]
48. Zhang, R.J.; Santoso, A.M.; Tan, T.S.; Phoon, K.K.; ASCE, F. Strength of High Water-Content Marine Clay Stabilized by Low Amount of Cement. *J. Geotech. Geoenvironmental Eng.* **2013**, *139*, 2170–2181. [CrossRef]
49. Porbaha, A.; Raybaut, J.L.; Nicholson, P. State of the Art in Construction Aspects of Deep Mixing Technology. *Proc. Inst. Civ. Eng.-Ground Improv.* **2001**, *5*, 123–140. [CrossRef]
50. Van Impe, W.F.; Flores, R.V. Deep Mixing in Underwater Conditions: A Laboratory and Field Investigation. *Proc. Inst. Civ. Eng.-Ground Improv.* **2006**, *10*, 15–22. [CrossRef]
51. Dahal, B.K.; Zheng, J.J.; Zhang, R.J.; Song, D.B. Enhancing the Mechanical Properties of Marine Clay Using Cement Solidification. *Mar. Georesources Geotechnol.* **2019**, *37*, 755–764. [CrossRef]
52. Kipton, H.; Powell, J.; Town, R.M. Solubility and Fractionation of Humic Acid; Effect of pH and Ionic Medium. *Anal. Chim. Acta* **1992**, *267*, 47–54. [CrossRef]

MDPI AG
Grosspeteranlage 5
4052 Basel
Switzerland
Tel.: +41 61 683 77 34

Buildings Editorial Office
E-mail: buildings@mdpi.com
www.mdpi.com/journal/buildings

MDPI

Academic Open
Access Publishing

mdpi.com

ISBN 978-3-7258-4430-2